Porous Sulfur-Based Materials for Photocatalytic Applications

October 2023

Doctoral Thesis

Candidate: Beatriz Silva Gaspar

Directors: Avelino Corma Canós
Urbano Díaz Morales

Acknowledgements

Living in a foreign country, where my language is barely spoken and contact with the Portuguese culture is scarce, the fear of losing my identity and my cultural roots was something that haunted me. However, the Portuguese friendships I have made over the years have been there to remind me that I will always be Portuguese, regardless of where I live or how far I am from my motherland. I would like to take this opportunity to thank you. The friendships I made during my time at the Instituto Superior Tecnico were a constant reminder of who I am. To Carmo Silva and Leonor Piloto, who have become my support network, especially in the most difficult moments of adapting to my Valencian routine, thank you. To Joana and Carolina Richheimer, for being by my side for the last ten years, from the moment I started university until I finished my doctorate, I know that you will always be by my side, regardless of the distance between us. To Carolina van der Vaz, thank you for the hours spent discussing intellectual issues in the most diverse areas, from converting the GDP of the G20 countries into one-dollar notes and their volume into Olympic swimming pools to possible alternatives to a capitalist system, and for becoming someone with whom I don't feel insecure about showing vulnerability. I'd also like to thank two other people who were fundamental in bringing me back to my origins. To Liliana Vaz, although we met in Ghent, you were my greatest discovery of 2022. Thank you for putting up with my constant dramas and ethical and moral doubts and I will never forget the moment we lived in Calp. And finally, Beatriz Ribeiro. It's hard to put our friendship into words. Despite the ups and downs and the distance that has always been between us, looking back on almost ten years of friendship, having you in my life fills me with happiness and I can say that you have become the sister I never had.

Valencia, which has become my third home, has taught me many lessons. The pleasure of having a fresh orxata at the end of a summer's day with a good friend is an unforgettable experience and something that wouldn't be possible in any other city. However, and perhaps the most important lesson, was to appreciate the little things in life, regardless of how fleeting they may be. Living in a city with people from so many parts of the world has taught me that sometimes people have a limited time in my life, but that doesn't take away from their importance. It has been the most diverse people who, over these four years, have taught me the importance of living in the present. To Vėja Palubinskaitė and Arina Seliukova for being able to offer me an anxiety-free space and for helping me simplify adult life. To Marthe Rombaut for unlocking a part of me that I thought would be inert forever. To Katariina Kriipsalu for making me the person I am today. Without her influence, I wouldn't be able to enjoy the simple things that life has to offer.

Fortunately, I don't have only transitory people. When you live in a foreign city, it's human nature to create a core groups, which eventually becomes your family, your

Abstract

The present doctoral thesis, developed in collaboration between IFP Energies Nouvelles (Lyon, France) and ITQ (Valencia, Spain), focused on the development and modification of metal sulfide based microstructured materials for the solar fuels production.

Two new materials, IZM-5 and ITQ-75 made of tin and zinc sulfide, were obtained and characterized. Since it is intended to use such materials on solar-driven processes, it was necessary to fine tune their electronic structure, through a doping strategy, and their accessibility, through the modification of the synthesis gel composition or by post synthesis methods. Different doping agents, such as copper, cobalt, nickel and iron, as well as the insertion of a ruthenium complex were tested. The most successful ones were copper and cobalt, since with their presence it is possible to reduce the optical band gap value to 2,0 eV, a value within the optimal range of optical band gaps for solar fuel production processes. When such doping agents were present into the IZM-5 gel, it was found that the expected diffraction pattern was not obtained, but one of a new material, entitled ITQ-76.

As with zeolites, the firsts attempts to allow accessibility to photoactive sites was about releasing the microporosity, the internal surface, by removing the organic structure directing agent used during the synthesis process. Because no strategy was successful, it was alternatively attempted to enhance the external surface (grain surface or mesoporosity). Of the different strategies tested, it was found that varying the gel composition was the most successful one. The insertion of saccharides, previously studied in the literature as mesoporosity agents, and increasing the synthesis gel viscosity in order to decrease the final crystal size were

tested. However, the presence of saccharides did not lead to the formation of a mesoporous system. The improvement in accessibility was due to the decrease of particle sizes. By increasing the gel viscosity it was also possible to decrease the average size of the crystals and consequently increase the external surface area.

After the modification of the structures under study in order to obtain a wide range of properties, their photocatalytic performance was evaluated. Two reactions were tested, CO_2 photoreduction and water splitting. Regarding the first one, the results were inconclusive, since even using TiO_2 or TiO_2 with 1wt.% of Pt photodeposited, two widely study photocatalyts, no carbon products were detected, only H_2. It is suspect that the experimental unit or the experimental conditions used were not the most appropriate. As such, the photocatalytic performance of the different samples was evaluated by using the water splitting reaction. A volcano-like relationship seemed to exist between photocatalytic performance and the external surface area. According to the literature reviewed, this behavior might be explained by the balance between the increase of available active centers and the increase of surface defects which are potential recombination sites. Regarding the relation between the photocatalytic performance and the optical band gap value, again a volcano-like relationship seems to exist. According to the reviewed bibliography, it was found that with the reduction of the optical band gap value the number of absorbed photons increases and, as such, the performance is expected to increase. However, it is necessary that the photogenerated charges have a sufficient potential to participate in the desired reaction. As a result, below a certain optical band gap value, the photogenerated charges no longer have sufficient potential and, as such, the performance decreases.

Of the different samples tested, those modified with sucrose stand out as having the best performance. So far it was not possible to unravel the phenomenon behind those enhanced reactivity. Hence, a more detailed characterization of these samples is necessary in order to understand how the presence of the organic component influences the electronic structure of the material and, consequently, its performance. It would also be important to assess the stability of the organic component during the reaction, more specifically to verify that it does not undergo an oxidation process that might produce protons, which are then able to form dihydrogen.

Throughout this thesis, different materials have been obtained and optimized in terms of optical and photocatalytic behavior. These solids have the advantage of being simple to handle and to synthesize, contain no toxic or noble compounds and are obtained from widely available raw materials. With the different doping techniques used, it was found that their optical band gap is tunable. Therefore, and

considering the preliminary photocatalytic results, these materials seem promising photocatalysts to be used in the solar fuels production.

Resumen

La presente tesis doctoral, desarrollada en colaboración entre IFP Energies Nouvelles (Lyon, Francia) e ITQ (Valencia, España), se centró en el desarrollo y modificación de materiales microestructurados basados en sulfuros metálicos para la producción de combustibles solares.

Se obtuvieron y caracterizaron dos nuevos materiales laminares basados en sulfuro de estaño y zinc, IZM-5 e ITQ-75. Dado que se pretende utilizar dichos materiales en procesos basados en el uso de energía solar, fue necesario ajustar su estructura electrónica mediante una estrategia de dopaje y su accesibilidad mediante la modificación de la composición del gel de síntesis o mediante métodos posteriores a la síntesis. Se probaron diferentes agentes dopantes como cobre, cobalto, níquel y hierro, así como la inserción de un complejo de rutenio. Los más exitosos fueron el cobre y el cobalto, ya que con su presencia es posible reducir el valor de la band gap a 2,0 eV, un valor dentro del rango óptimo para procesos de producción de combustibles solares. Cuando estos agentes dopantes estuvieron presentes en el gel de síntesis de IZM-5, se descubrió que no se obtenía el patrón de difracción esperado, sino uno de un nuevo material, denominado ITQ-76.

Al igual que con las zeolitas, los primeros intentos para permitir el acceso a los centros fotoactivos consistieron en liberar la microporosidad, la superficie interna, mediante la eliminación del agente orgánico director de estructura utilizado durante el proceso de síntesis. Se intentó alternativamente mejorar la superficie externa (tamaño de partícula o mesoporosidad). De las diferentes estrategias probadas, se descubrió que variar la composición del gel de síntesis fue la más exitosa. Se probaron la inserción de sacáridos, previamente estudiados en la literatura como

agentes inductores de mesoporosidad, y el aumento de la viscosidad del gel de síntesis para disminuir el tamaño de cristal final. Sin embargo, la presencia de sacáridos no condujo a la formación de un sistema mesoporoso; la mejora en la accesibilidad se debió a la disminución del tamaño de partícula. Al aumentar la viscosidad del gel, también fue posible disminuir el tamaño promedio de los cristales y, en consecuencia, aumentar la superficie externa.

Después de la modificación de las estructuras estudiadas con el fin de obtener una amplia gama de propiedades, se evaluó su rendimiento fotocatalítico. Se probaron dos reacciones, la fotorreducción de CO_2 y la ruptura de la molécula de agua. En cuanto a la primera, los resultados fueron inconclusos, ya que incluso utilizando TiO_2 o TiO_2 con un 1% wt de Pt fotodepositado, dos fotocatalizadores ampliamente estudiados, no se detectaron productos de carbono, solo H_2. Se sospechó que el sistema de reacción o las condiciones experimentales utilizadas no fueron las más adecuadas. Por lo tanto, el rendimiento fotocatalítico de las diferentes muestras se evaluó mediante la reacción de ruptura de la molécula de agua. Parecía existir una relación tipo "volcano" entre el rendimiento fotocatalítico y la superficie externa. Según la literatura revisada, este comportamiento podría explicarse por el equilibrio entre el aumento de los centros activos disponibles y el aumento de los defectos en la superficie, los cuales son centros potenciales de recombinación. En cuanto a la relación entre el rendimiento fotocatalítico y el valor de la band gap, nuevamente parece existir una relación tipo "volcano". Según la bibliografía revisada, se encontró que con la reducción del valor de la band gap aumenta el número de fotones absorbidos y, como tal, se espera que aumente el rendimiento. Sin embargo, es necesario que las cargas fotogeneradas tengan un potencial suficiente para participar en la reacción deseada. Como resultado, por debajo de cierto valor de band gap, las cargas fotogeneradas ya no tienen un potencial suficiente y, por ello, el rendimiento disminuye.

De las diferentes muestras probadas, las modificadas con sacarosa destacaron por tener el mejor rendimiento. Hasta ahora no ha sido posible desentrañar el fenómeno detrás de esta mayor reactividad. Por lo tanto, se requiere una caracterización más detallada de estas muestras para comprender cómo la presencia del componente orgánico influye en la estructura electrónica del material y, en consecuencia, en su rendimiento. También sería importante evaluar la estabilidad del componente orgánico durante la reacción, específicamente para verificar que no sufra un proceso de oxidación que pueda producir protones, que luego sean capaces de formar hidrógeno.

A lo largo de esta tesis, se obtuvieron y optimizaron diferentes materiales en términos de su comportamiento óptico y catalítico. Estos sólidos tienen la ventaja de ser fáciles de manejar y sintetizar, no contienen compuestos tóxicos ni metales

nobles y se obtienen a partir de materias primas ampliamente disponibles. Con las diferentes técnicas modificación utilizadas, se descubrió que su band gap es ajustable. Por lo tanto, considerando los resultados preliminares fotocatalíticos, estos materiales resultan prometedores como fotocatalizadores para su uso en la producción de combustibles solares.

Resum

La present tesi doctoral, desenvolupada en col·laboració entre IFP Energies Nouvelles (Lyon, França) i ITQ (València, Espanya), es va centrar en el desenvolupament i modificació de materials microestructurats basats en sulfurs metàl·lics per a la producció de combustibles solars.

Es van obtenir i caracteritzar dos nous materials lamel·lars basats en sulfur d'estany i zinc, IZM-5 i ITQ-75. Com que es pretén utilitzar aquests materials en processos basats en l'ús d'energia solar, va ser necessari ajustar la seua estructura electrònica mitjançant una estratègia de dopatge i la seua accessibilitat mitjançant la modificació de la composició del gel de síntesi o mitjançant mètodes posteriors a la síntesi. Es van provar diferents agents dopants com coure, cobalt, níquel i ferro, així com la inserció d'un complex de ruteni. Els més reeixits van ser el coure i el cobalt, ja que amb la seua presència és possible reduir el valor de la band gap a 2,0 eV, un valor dins de l'abast òptim per a processos de producció de combustibles solars. Quan aquests agents dopants van estar presents en el gel de síntesi d'IZM-5, es va descobrir que no s'obtenia el patró de difracció esperat, sinó un de nou material, anomenat ITQ-76.

Al igual que amb les zeolites, els primers intents per a permetre l'accés als centres fotoactius van consistir en alliberar la microporositat, la superfície interna, mitjançant l'eliminació de l'agent orgànic director d'estructura utilitzat durant el procés de síntesi. Es va intentar alternativament millorar la superfície externa (mida de partícula o mesoporositat). De les diferents estratègies provades, es va descobrir que variar la composició del gel de síntesi va ser la més reeixida. Es van provar la inserció de sacàrids, prèviament estudiats en la literatura com a agents

inductors de mesoporositat, i l'augment de la viscositat del gel de síntesi per a disminuir la dimensió del cristall final. No obstant això, la presència de sacàrids no va conduir a la formació d'un sistema mesoporós; la millora en l'accessibilitat va ser a causa de la disminució de la mida de partícula. Augmentant la viscositat del gel, també es va poder disminuir la mida mitjana dels cristalls i, en conseqüència, augmentar la superfície externa.

Després de la modificació de les estructures estudiades amb l'objectiu d'obtenir una àmplia gamma de propietats, es va avaluar el seu rendiment fotocatalític. Es van provar dues reaccions, la fotoreducció de CO_2 i la ruptura de la molècula d'aigua. Pel que fa a la primera, els resultats van ser inconclusos, ja que fins i tot utilitzant TiO_2 o TiO_2 amb un 1% wt de Pt fotodepositat, dos fotocatalitzadors àmpliament estudiats, no es van detectar productes de carboni, només H_2. Es va sospitar que el sistema de reacció o les condicions experimentals utilitzades no eren les més adequades. Per tant, el rendiment fotocatalític de les diferents mostres es va avaluar mitjançant la reacció de ruptura de la molècula d'aigua. Hi semblava haver una relació tipus "volcà" entre el rendiment fotocatalític i la superfície externa. Segons la literatura revisada, aquest comportament podria explicar-se per l'equilibri entre l'augment dels centres actius disponibles i l'augment de les defectes en la superfície, els quals són centres potencials de recombinació. Pel que fa a la relació entre el rendiment fotocatalític i el valor de la band gap, de nou sembla existir una relació tipus "volcà". Segons la bibliografia revisada, es va trobar que amb la reducció del valor de band gap augmenta el nombre de fotons absorbits i, com a tal, s'espera que augmenti el rendiment. No obstant això, és necessari que les càrregues fotogenerades tinguin un potencial suficient per a participar en la reacció desitjada. Com a resultat, per sota d'un cert valor de band gap, les càrregues fotogenerades ja no tenen un potencial suficient i, per tant, el rendiment disminueix.

De les diferents mostres provades, les modificades amb sacarosa van destacar per tenir el millor rendiment. Fins ara no ha estat possible desxifrar el fenomen darrere d'aquesta major reactivitat. Per tant, es requereix una caracterització més detallada d'aquestes mostres per a comprendre com la presència del component orgànic influeix en l'estructura electrònica del material i, en conseqüència, en el seu rendiment. També seria important avaluar l'estabilitat del component orgànic durant la reacció, específicament per a verificar que no patisca un procés d'oxidació que puga produir protons, que després siguen capaços de formar hidrogen.

Al llarg d'aquesta tesi, es van obtenir i optimitzar diferents materials en termes del seu comportament òptic i catalític. Aquests sòlids tenen l'avantatge de ser fàcils de manejar i sintetitzar, no contenen compostos tòxics ni metalls nobles i s'obtenen a partir de matèries primeres àmpliament disponibles. Amb les diferents tècniques

de modificació utilitzades, es va descobrir que la seua band gap és ajustable. Per tant, considerant els resultats preliminars fotocatalítics, aquests materials semblen prometedors com a fotocatalitzadors per a la seua utilització en la producció de combustibles solars.

Table des Matières

Ces travaux de thèse, réalisés en collaboration avec IFP Energies Nouvelles (Lyon, Espagne) et ITQ (Valence, Espagne), avaient pour objet le développement et la modification de matériaux microstructurés à base de sulfures métalliques pour la production de carburants solaires.

Deux nouveaux matériaux lamellaires à base de sulfure de zinc et d'étain, IZM-5 et ITQ-75, ont été obtenus et caractérisés. Afin de mettre en œuvre ces matériaux dans des processus photo-induits, il a été nécessaire d'optimiser leurs structures électroniques par une stratégie de dopage, et leur accessibilité par la modification de la composition du gel de synthèse ou par des méthodes de post-traitement. Différents agents dopants tels que le cuivre, le cobalt, le nickel et le fer, ainsi que l'insertion d'un complexe de ruthénium ont été évalués. Le cuivre et le cobalt ont été les plus prometteurs, car leur présence permet de réduire la valeur de la bande interdite optique à 2,0 eV, une valeur qui se situe dans la plage optimale des bandes interdites optiques pour les processus de production de carburant solaire. Lorsque ces agents dopants étaient présents dans le gel de synthèse du matériau IZM-5, il a été constaté que le schéma de diffraction obtenu n'était pas celui attendu, mais celui d'un nouveau matériau, appelé ITQ-76.

De manière analogue aux zéolithes, les premières tentatives pour permettre l'accès aux sites photoactifs ont consisté à libérer la microporosité, la surface interne, en éliminant le l'agent structurant organique utilisé pendant le processus de synthèse. Aucune stratégie n'ayant été couronnée de succès, une stratégie alternative a été mise en œuvre pour tenter d'augmenter la surface externe (surface de grain ou mésoporosité). Parmi les différentes stratégies testées, la variation de la composi-

tion du gel s'est avérée la plus efficace. L'insertion de saccharides, précédemment étudiés dans la littérature comme agents de mésoporosité, et l'augmentation de la viscosité du gel de synthèse afin de diminuer la taille finale des cristaux ont été testées. Cependant, dans notre cas la présence de saccharides n'a pas conduit à la formation d'un système mésoporeux, l'amélioration de l'accessibilité est due à diminution de la taille des particules. En augmentant la viscosité du gel, il a également été possible de diminuer la taille moyenne des cristaux et par conséquent d'augmenter la surface externe.

Après la modification des structures étudiées afin d'obtenir une large gamme de propriétés, leurs performances photocatalytiques ont été évaluées. Deux réactions ont été testées, la photoréduction de CO_2 et la réaction de dissociation de l'eau. En ce qui concerne la première, les résultats n'ont pas été concluants, car même en utilisant TiO_2 ou TiO_2 avec 1wt.% de Pt photodéposé, deux photocatalyseurs largement étudiés, aucun produit carboné n'a été détecté, seulement H_2. On soupçonne que l'unité expérimentale ou les conditions expérimentales utilisées n'étaient pas suffisamment appropriées. Ainsi, la performance photocatalytique des différents échantillons a été évaluée en utilisant la réaction de séparation de l'eau. Une relation de type courbe en volcan semble exister entre la performance photocatalytique et la surface externe développée par les matériaux. D'après la littérature, ce comportement pourrait s'expliquer par l'équilibre entre le nombre de centres actifs disponibles et celui des défauts de surface qui sont des sites de recombinaison potentiels. En ce qui concerne la relation entre la performance photocatalytique et la valeur de la bande interdite optique, une relation de type courbe en volcan semble également exister. D'après la bibliographie, il a été constaté qu'avec la réduction de la valeur de la bande interdite optique, le nombre de photons absorbés augmente et, par conséquent, les performances devraient s'accroître. Toutefois, il est nécessaire que les charges photogénérées aient un potentiel suffisant pour participer à la réaction souhaitée. Par conséquent, en dessous d'une certaine valeur de bande interdite optique, les charges photogénérées n'ont plus un potentiel suffisant et, par conséquent, les performances diminuent.

Parmi les différents échantillons testés, ceux qui ont été modifiés avec du saccharose se sont révélés les plus performants. Jusqu'à présent, il n'a pas été possible d'élucider le phénomène à l'origine de cette réactivité accrue. Une caractérisation plus détaillée de ces échantillons est donc nécessaire pour comprendre comment la présence du composant organique influence la structure électronique du matériau et, par conséquent, ses performances. Il serait également important d'évaluer la stabilité du composant organique au cours de la réaction, plus précisément de vérifier qu'il ne subit pas un processus d'oxydation susceptible de produire des protons capables ensuite de former le dihydrogène.

Tout au long de cette thèse, différents matériaux ont été obtenus et optimisés en termes de réponse optique et catalytique. Ces solides présentent l'avantage d'être simples à manipuler et à synthétiser, ils ne contiennent pas de composés toxiques ou nobles et sont obtenus à partir de matières premières largement disponibles. Les différentes techniques de dopage utilisées ont permis de constater qu'il était possible d'optimiser leur bande interdite optique. Par conséquent, et compte tenu des résultats photocatalytiques préliminaires, ces matériaux semblent des photo-catalyseurs prometteurs à utiliser dans la production de carburants solaires.

Contents

Chapter 1

Social Context

It seems to be encoded in human DNA that a foreseeable future crisis is not to be considered significant until it is at the door.

Josef Michl

1.1   Introduction

According to the Encyclopedia Britannica, Energy is the *capacity for doing work* [1]. Although this definition seems a bit general, it shows how difficult it is to define energy, this term that is becoming one of the main problems of today's society. Looking at any media platform available, this is not the only concerning situation happening at the moment. Food and water availability, access to adequate education and proper health care, pollution, and war are among the many different problems affecting the contemporary society. Taking a closer look at the problematic situations listed above, one can noted that they are strongly related on energy availability [2].

Energy consumption is associated with any kind of consumer goods and is necessary to produce any type of service. It is therefore normally related to the well-being of society. However, it has been demonstrated that the quality of life is closely correlated with the energy consumption per capita only in the initial phases of economic development. For industrialized countries, it has been found that such correlation does not apply [2]. The relation between quality of living and energy use is neither linear nor does it follow a simple and direct connection [3].

The reduction of energy consumption, namely in affluent countries, is a topic increasingly being addressed. Reducing consumption of consumer goods, by not buying non-essential items or by increasing its lifetimes would allow enormous energy savings. However, the reduction in consumption is not in line with the current economic paradigm of infinite economic growth [2].

Wiedmann et al. [4] discuss the positive connection between biophysical resources and affluence, showing that consumption needs to be reduce in order to maintain the integrity of the environment that surrounds us, similar conclusions to those reached by Smiil [5] in 2003. In order to achieve this, a model based on the reduction of consumption taking into account the basic needs of society is suggested (see Figure 1.1). Different strategies to reduce consumption that guarantee the society's sustainability and safeguard human needs are presented and discussed. The different policies analyzed range from reformist policies [6, 7], which argue that transformations can be made within the current economic paradigm, to more radical ones, such as eco-socialism [8, 9] and eco-anarchism [10, 11], which claim that the necessary transformations are not compatible with a capitalist society.
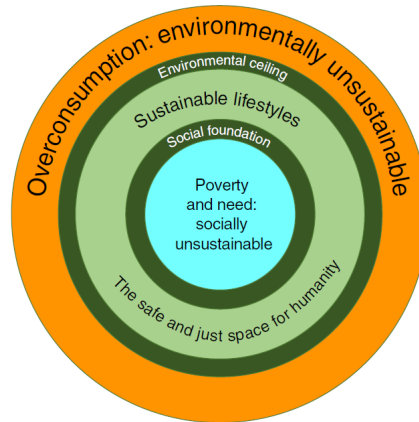
Figure 1.1: Sustainable model suggested by Wiedmann et al. (adapted from [4])

Looking at recent European news, the reduction of energy consumption is something widely talked about. Since the invasion of Ukraine, the European Union intends to reduce its energy consumption by 15% in order to become fully independent from Russian gas [12]. To this end, the European Commision presented the REPowerEU Plan. By energy saving, diversification of energy supplies and accelerated roll-out of renewable energy this plan aims to make the European Union more energy independent and, at the same time, to tackle the climate crisis [13].

1.2 Current Energy Matrix

Presently, almost 90% of the energy consumed has non-renewable origins (see Table 1.1). In 2021 the highest recorded growth in energy consumption was observed associated with the economic recovery following the COVID-19 pandemic [14].

Comparing 2019 and 2021, thus eliminating 2020, the year in which the impacts of the COVID-19 pandemic were most severe, an increase in energy consumption of 2% was observed. Evaluating the energy sources, it can be seen that this growth was motivated by the development of renewable energy sources, registering an increase of 27%, the highest among the different energy sources. Concerning fossil fuels consumption, this remained relatively stable, with a reduction in the oil consumption, compensated by an increase in the natural gas and coal utilization [14].

The reduction in oil consumption was strongly driven by the drop in aviation fuel consumption, being about 33% lower than the 2019 figures. Regarding natural gas, its consumption exceeded 4 trillion cubic meters for the first time with a generalized price increase across the globe. As for coal, its price has also increased. Around 70% of the growth in demand was recorded in India and China. There was also an increase in consumption in Europe and North America, after 10 years of decline [14].

Table 1.1: World primary energy consumption, broken down by energy source, from 2019 to 2021 [14]

Energy Source	Energy Consume per Year (EJ)			Growth Rate	
	2019	2020	2021	2019-2021	2020-2021
Oil	193,0	174,2	184,2	-5%	+5%
Natural Gas	141,5	138,4	145,4	+3%	+5%
Coal	157,9	151,1	160,1	+1%	+6%
Nuclear Energy	24,9	24,4	25,3	+2%	+4%
Hydropower	37,6	41,1	40,3	+7%	-2%
Renewables	29,0	34,8	39,9	+27%	+13%
Total	583,9	564,0	595,2	+2%	+5%

Considering the energy consumption over time, it can be observed that an exponential growth of energy consumption and population marked the 20th century (see Figure 1.2). The past century was the first era dominated by fossil fuels [15]. With the emergence of new technologies, particularly in the transport, food production, and electrical appliances sectors, humankind became dependent on fossil fuels (see Figure 1.2b) [16].
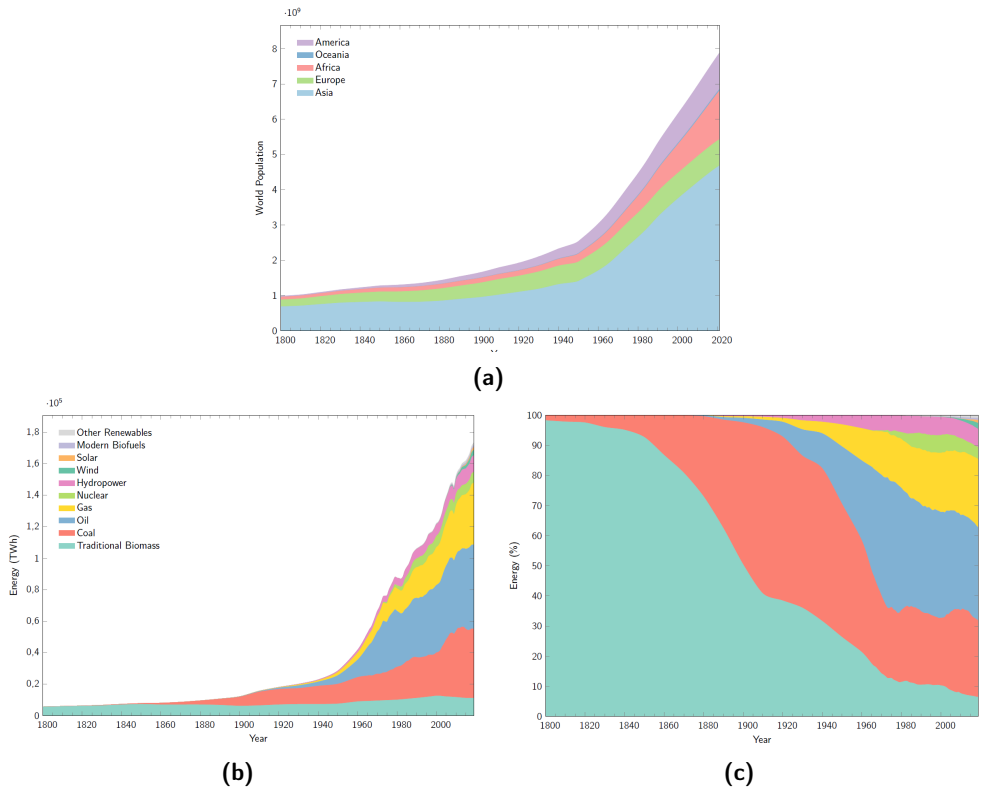
Figure 1.2: (1.2a) World population evolution and (1.2b) global primary energy consumption by source and (1.2c) its relative values [17, 18]

Until the middle of the 19th century, the principal source of energy was the traditional biomass, via solid fuels burning such as wood, charcoal and crop waste. After the industrial revolution at the beginning of the 20th century, which brought the development of the steam engine and consequently power plants, there was a dramatic increase in the coal consumption as an energy primary source. As the 20th century progressed, there was a greater dependence on coal, but oil consumption began to increase due to the introduction of internal combustion engines and oil-powered ships [18, 19].

The technological development of the 20th century has allowed the insertion of new sources of energy in the energy matrix. After oil, gas, hydropower and later nuclear. At the beginning of the 1980s wind and solar energy were introduced. Today, society uses a wide variety of primary energy sources, although most are

non-renewable. Observing the transitions between the different energy sources, it can be seen that in the past it took several decades for an energy source to become the main one. Today, and taking the case of coal as an example, the energy transitions are becoming faster [18, 19].

Looking to the world energy consumption profile (see Figure 1.2b), although it has an exponential behavior, there are some moments when consumption has remained stable or even decreased. These are associated with particular moments in history, such as oil crisis in 1973 and 1979, or moments of economic recession, such as the financial crisis of 2008. Recently, due to the COVID-19 pandemic and the subsequent economic crisis, there was a reduction in primary energy consumption of 4%, the largest drop in consumption on record [20].

1.3 Human and Environmental Consequences of Energy Consumption

Energy consumption is of enormous importance for the development of a society in its pre-industrial stages. However, this consumption has negative consequences for human health and the environment [5].

The first impact is air pollution. Exposure to air pollutants, such as particulate matter, increases the risk of developing cardiovascular and respiratory diseases and cancer. As a result of exposure to air pollutants, millions of people have poor health and millions of deaths associated with it are registered every year. Comparing the different energy sources, fossil fuel and traditional biomass combustion are responsible for most of these deaths, as they are the dirtiest energy sources [21, 22].

The second impact to be highlighted is the accidents associated with raw materials extraction and transport, construction and maintenance of power plants [21].

Ritchie [21], to evaluate the impact on short-therm human health concerns, compared the different energy sources with the estimated number of deaths (from air pollution and accidents in the supply chain) per terawatt-hour of electricity produced (see Figure 1.3). Comparing the different sources, it is easy to see that fossil fuels, with coal being the most prominent, are responsible for many more deaths than renewable or nuclear energy sources [21].
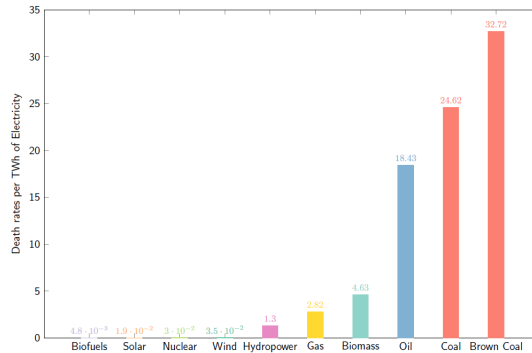
Figure 1.3: Death rates per TWh of electricity according to the energy source [21]

The third impact of energy consumption is the emission of greenhouse gases, the main driver of climate change [23].

1.3.1 Greenhouse Gas Emissions and Climate Change

A greenhouse gas is a gas that absorbs and emits infrared thermal radiation, causing a greenhouse effect [24]. The main greenhouse gases in the Earth's atmosphere are water vapor, carbon dioxide, methane, nitrous oxide and ozone. It is because of the presence of these gases that the average temperature at the Earth's surface is 15°C and not -18°C.

Of the different greenhouse gases listed above, carbon dioxide stands out due to its atmospheric concentration and lifetime. Observing the evolution of this gas at the atmosphere (see Figure 1.4a), after the 18th century, with the start of the Industrial Revolution, its content began to increase, until it reached 418 ppm in 2021, the highest level ever recorded in 3 million years [23]. Evaluating the global emissions of greenhouse gases and separating them by sector (see Figure 1.4b), it is observed that the electricity and heating production are the main greenhouse gases emitters [25].
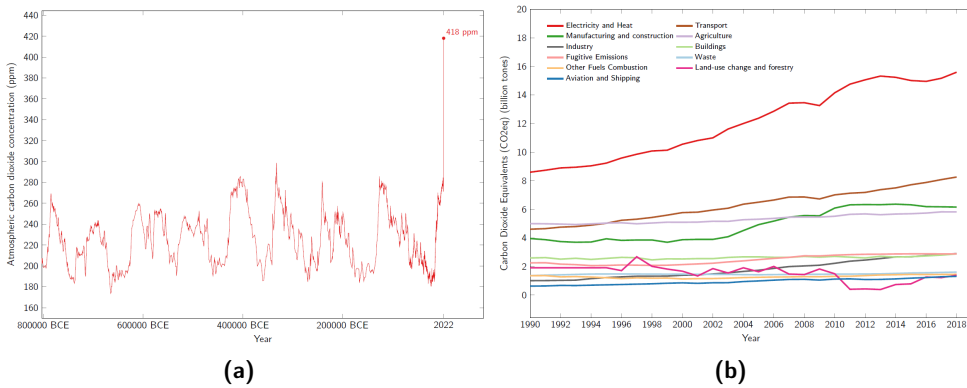
Figure 1.4: (1.4a) Atmospheric carbon dioxide concentration over time [23] and (1.4b) greenhouse gas emissions (in CO$_2$ eq) by sector [25]

Different factors influence the climate, namely solar activity and large volcanic eruptions. Due to the current increase in the atmospheric concentration of greenhouse gases of anthropogenic origin, there are numerous studies linking this increase with the climate change that's already affecting society. Human activity also plays a dominant role in ocean's warming, sea ice melting and in the pattern of warming in the lower atmosphere and cooling in the stratosphere. Current climate models can only reproduce the increase in the Earth's temperature when the effects of human activity are combined with natural causes (compare the gray area with the black line on Figure 1.5) [24].
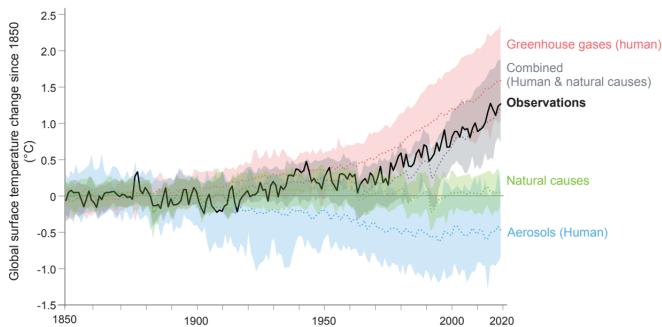
Figure 1.5: Observed global surface temperature change (black line) and respective climate models, where the effects of natural causes, aerosols, greenhouse gas emissions and the combination of natural and human causes are considered (adapted from [24])

Therefore, *it is unequivocal that human influence has warmed the atmosphere, ocean and land* [24].

1.4   Reducing Carbon Dioxide Emissions to Net Zero by 2050

It is estimated that human activity was responsible for favoring 1,0°C increase on global surface temperature already observed (see Figure 1.5). If it continues to follow the same profile, a 1,5°C increase is likely to be reached between 2030 and 2052. The consequences of the antropogenic emissions recorded up to the present will be felt for centuries to come and will continue to have an impact on the climate system. However, these alone are unlikely to cause a warming greater than 0,5°C in the next two to three decades. Therefore, by achieving and maintaining zero antropogenic carbon dioxide emissions would allow to halt global warming and to avoid the worst impacts of climate change [26, 27].

Since the energy sector is responsible for about three-quarters of greenhouse gas emissions (see Figure 1.4b), in order to reach zero net by 2050 a complete transformation in the way energy is produced, transported and consumed is necessary. The International Energy Agency (IEA) [27] has produced a report presenting a strategy to achieve such objective. The strategy presented allows to maintain economic growth and ensures access to energy sources, while maximizing technical feasibility, acceptance by society and cost-effectiveness. It is emphasized that this is not the only possible path to achieve the desired objective, but that the chosen strategy is heavily dependent on technological development, on the acceptability of citizens to change their behavior and on international collaboration.

According to projections, by 2050 the world's population will have increased by two billion people and the world economy will double (see Figure 1.6).
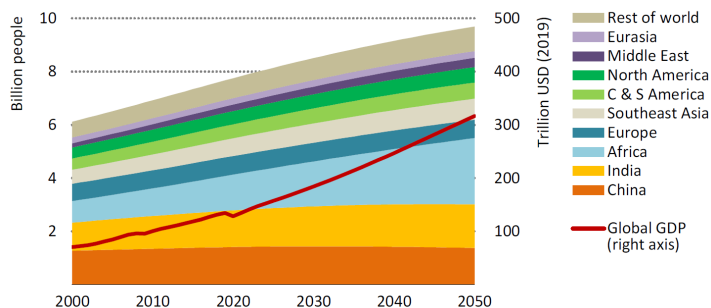

Figure 1.6: Estimated world population and economic growth up to 2050 (adapted from [27])

In order to meet net zero by 2050 and ensure that the nearly 10 billion people have access to energy, it is therefore necessary to reduce the world's energy needs by 8% through a more efficient energy use and behavioral change. Energy efficiency is one of the main factors that will enable to reduce energy consumption and emissions in the 2030 period.

The IEA highlights some key moments on their Net-Zero Emissions Scenario (NZE):

- The global energy and industrial carbon dioxide emissions are reduced by 40% between 2020 and 2030 and net zero by 2050 (see Figure 1.7) and the methane emissions from fossil fuels by 75% until 2030;

- Solar photovoltaic and wind energies are the leading electricity producers, responsible for 75% of it by 2050;

- As for fossil fuels, coal demand is reduced by 90%, oil by 75% and natural gas by 55% until 2050 (see Figure 1.8a);

- Until 2030, energy efficiency, wind and solar energies will be the responsible for reducing emissions in 50%. From 2030 to 2050, electrification, hydrogen use and Carbon capture, utilization and storage (CCUS) deployment, where not all technologies are commercialized at the moment, will be responsible for half of the emissions saving (see Figure 1.7).
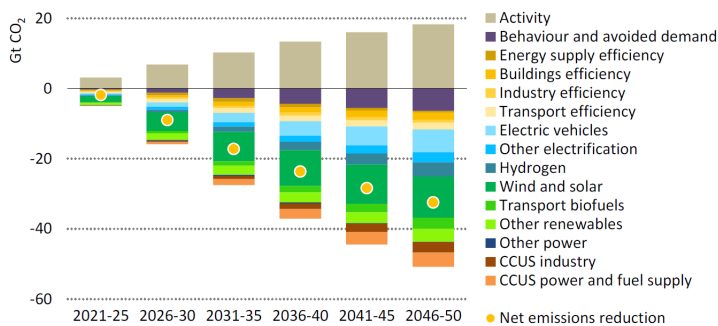

Figure 1.7: Carbon dioxide average annual reductions according to the NZE scenario (adapted from [27])

According to the NZE scenario, the energy mix in 2050 will be quite different from today. Nowadays oil accounts for one third of energy supply, while coal and natural gas 27% and 24%, respectively (see Table 1.1). In 2050 about two thirds of energy

consumption will be provided by renewable energies and nuclear energy will see a growth between 2020 and 2050 (see Figure 1.8a).

Although there will be a drastic reduction in the usage of fossil fuels, its consume will not be zero (see Figure 1.8a). Fossil fuels consumption will be mainly for non-energy purposes that do not involve its combustion, thus avoiding carbon dioxide emissions, coupled with CCUS technology or in sectors where the technological options are lacking, like aviation (see Figure 1.8b).

(a)   (b)
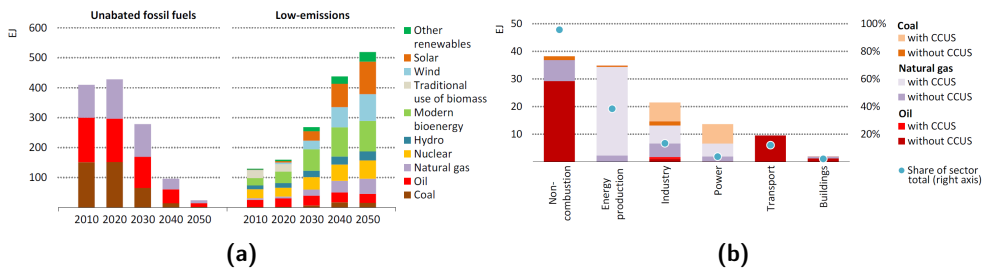
Figure 1.8: (1.8a) Total energy supply of unabated fossil fuels and low-emissions (includes fossil fuels with CCUS technology) energy sources and (1.8b) fossil fuel share and usage in 2050 according to the NZE scenario (adapted from [27])

The volume of carbon dioxide captured over the years gradually increases. In 2030 an estimated 1,6 Gt per year is captured, rising to 7,6 Gt in 2050, where 95% is estimated to be stored in permanent geological storage and the rest used as raw material. .

1.4.1   Carbon Dioxide as a Raw Material

As presented earlier, CCUS technology will play an important role in achieving sustainable development and reaching net zero carbon dioxide emissions by 2050. One of the possible uses for the captured carbon dioxide is its storage in geological formations, such as depleted oil reservoirs or sedimentary basins, or mineral carbonation by reacting carbon dioxide with silicate minerals containing calcium or magnesium [28].

The storage of the captured carbon dioxide is seen only as a temporary solution, since it only displaces the carbon dioxide from the atmosphere to another location. In addition, there are long-term ecological consequences of using the Earth as a carbon dioxide storage and the technologies available today are expensive and require a high energy input [29, 30, 31].

Instead of sequestering CO_2, the use of captured CO_2 as a raw material for the production of value-added chemicals has been seen as an attractive alternative [32, 33, 34, 35, 36]. It is now possible to find processes where CO_2 is used as feedstock, for example in the production of urea, salicyclic acid and polycarbonates [34, 37]. The urea production capacity from CO_2 and NH_3 is about 100 Mt/a, covering about 94% of CO_2 utilization at an industrial level [36, 38]. However, only about 0,5% of the CO_2 emitted by human sources is used in industry [39].

Captured CO_2 has the potential to be used in different processes (see Figure 1.9). It can be used without chemical conversion, for example as a yield boosting on algae production or as a solvent, or with chemical conversion (by thermal catalysis, electrocatalysis or photocatalysis), that would allow to produce valuable chemicals, fuels or building materials [36, 40].
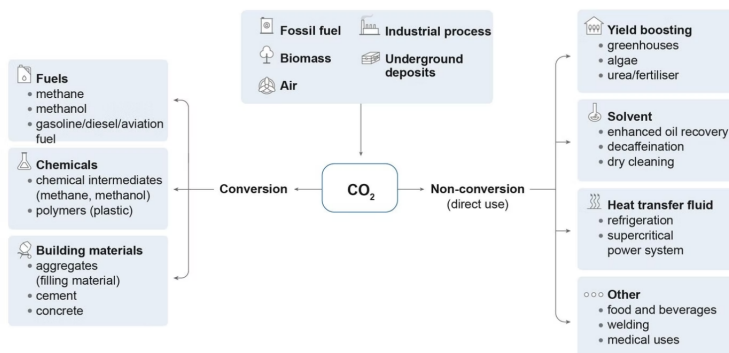
Figure 1.9: Simplified scheme of possible CO_2 applications (adapted from [40, 41])

Comparing the theoretical potential of different CO_2 applications and their impact on the climate, fuel production has the highest impact due to its market size [41].

It is possible to use CO_2 to produce fuels currently used, such as methane, methanol, gasoline or jet fuel. One possibility would be to hydrogenate CO_2, producing a product that is easier to transport and use than pure hydrogen. This hydrogen would be produced for example by electrolysis of water using low-carbon electricity, namely wind or photovoltaic energies [36, 41]. Due to the intermittency of these energy sources and the difficulty of energy storage, hydrocarbon production is being seen as a possible solution to stabilize the power grid. The technologies that allow such a process to be done are generally referred to as "Power-to-X", where X can be gas, liquids or chemicals [42]. It is already possible to find a first industrial scale demonstration of methanol production from CO_2, water and solar energy [43].

Alternatively, it is possible to use the captured CO_2 in electro- or photocatalytic reactions. The electroreduction of CO_2 is an attractive and promising pathway, that would allow to store electricity in a chemical form. This would be a two-step process. First, the sunlight is converted into electricity by means of photovoltaics. This electricity would be used afterwards to electro reduced the CO_2 [44]. At the moment, products that involve the transfer of two electrons, such as CO or formic acid, can be obtainable with low over potentials and high Faradaic efficiencies. However, products that involve multi-electron transfer need higher over potentials and are obtained with lower selectivity [44]. The low stability of the catalyst, the reaction mechanism and the limited energy efficiency area problems that need to be addressed for this strategy to become viable [36, 44].

Another possible use of captured CO_2 would be artificial photosynthesis. Plants, through photosynthesis, are able to convert solar into chemical energy. By mimicking this process, it would be possible to photoreduce CO_2 by using water as proton source, thus obtaining formic acid, formaldehyde, methanol or equivalents [44, 45]. The direct solar-assisted conversion of CO_2 into hydrocarbon fuels is quiet attractive, since it allows to obtain, on a renewable basis, an energy dense portable fuel compatible with the current energy infrastructure [46]. However, due to thermodynamic and kinetic considerations, the CO_2 photoreduction occurs with low efficiencies. In order to address such problem, currently the tendencies is to design a photocatalyst with better substrate adsorption, light harvesting capabilities and charge carriers transport [44].

References

[1] The Editors of Encyclopaedia Britannica. "Energy". In: *Encyclopaedia Britannica* (Nov. 2021. Accessed 12 July 2022).

[2] Nicola Armaroli and Vincenzo Balzani. "The Future of Energy Supply: Challenges and Opportunities". In: *Angewandte Chemie International Edition* 46.1-2 (2007), pp. 52–66. DOI: https://doi.org/10.1002/anie.200602373.

[3] Vaclav Smil. "Elusive links: energy, value, economic growth and quality of life". In: *OPEC Review* 16.1 (1992), pp. 1–21. DOI: https://doi.org/10.1111/j.1468-0076.1992.tb00418.x.

[4] Thomas Wiedmann et al. "Scientists' warning on affluence". In: *Nature Communications* 11.1 (2020), p. 3107. DOI: 10.1038/s41467-020-16941-y.

[5]   Vaclav Smil. *Energy at the Crossroads: Global Perspectives and Uncertainties*. The MIT Press, 2003.

[6]   Peter A. Victor. *Managing without Growth - Slower by Design, Not Disaster*. Advances in Ecological Economics series. Edward Elgar Publishing, 2008.

[7]   Jeroen C. J. M. van den Bergh. "A third option for climate policy within potential limits to growth". In: *Nature Climate Change* 7.2 (2017), pp. 107–112. DOI: 10.1038/nclimate3113.

[8]   Giorgos Kallis. "In defence of degrowth". In: *Ecological Economics* 70.5 (2011), pp. 873–880. DOI: https://doi.org/10.1016/j.ecolecon.2010.12.007.

[9]   Richard Smith. *Green Capitalism: the God that Failed*. World Economics Association Book Series. World Economics Association, 2015.

[10] Anitra Nelson and Frans Timmerman. *Life Without Money - Building Fair and Sustainable Economies*. PlutoPress, 2011.

[11] Ted Trainer. *The Simpler Way*. Ed. by Samuel Alexander and Jonathan Rutherford. Simplicity Institute, 2020.

[12] Virginie Malingre. *Brussels wants to reduce EU energy consumption by 15% to break its dependence on Russian gas*. https://www.lemonde.fr/en/economy/article/2022/07/21/brussels-wants-to-reduce-eu-energy-consumption-by-15-to-break-its-dependence-on-russian-gas_5990901_19.html. Online. Accessed 2nd August 2022. 2022.

[13] European Comission. *REPowerEU: A plan to rapidly reduce dependence on Russian fossil fuels and fast forward the green transition*. https://ec.europa.eu/commission/presscorner/detail/en/IP_22_3131. Online. Acessed 25th August 2022. 2022.

[14] BP. *Statistical Review of World Energy*. https://www.bp.com/en/global/corporate/energy-economics/statistical-review-of-world-energy.html. Online. Acessed on 15th July 2022.

[15] Vaclav Smil. "Energy in the Twentieth Century: Resources, Conversions, Costs, Uses, and Consequences". In: *Annual Review of Energy and the Environment* 25.1 (2000), pp. 21–51. DOI: 10.1146/annurev.energy.25.1.21.

[16] Chunshan Song. "Global challenges and strategies for control, conversion and utilization of CO_2 for sustainable development involving energy, catalysis, adsorption and chemical processing". In: *Catalysis Today* 115.1 (2006). Proceedings of the 8th International Conference on Carbon Dioxide Utilization, pp. 2–32. DOI: https://doi.org/10.1016/j.cattod.2006.02.029.

[17] Max Roser, Hannah Ritchie, and Esteban Ortiz-Ospina. *World Population Growth*. https://ourworldindata.org/world-population-growth. Online. Accessed 15th August 2022. 2021.

[18] Max Roser and Hannah Ritchie. *Energy*. https://ourworldindata.org/energy. Online. Accessed 13th July 2022. 2021.

[19] Jean-Paul Rodrigue. *The Geography of Transport Systems*. Routledge, 2020.

[20] International Energy Agency. *CO_2 Emissions in 2020*. https://www.iea.org/articles/global-energy-review-co2-emissions-in-2020. Online. Accessed 14th July 2022. 2020.

[21] Hannah Ritchie. *What are the safest and cleanest sources of energy?* https://ourworldindata.org/safest-sources-of-energy. Online. Accessed 15th July 2022. 2020.

[22] Max Roser. *Data Review: How many people die from air pollution?* https://ourworldindata.org/data-review-air-pollution-deaths. Online. Accessed 19th July 2022. 2021.

[23] Hannah Ritchie, Max Roser, and Pablo Rosado. *CO_2 and Greenhouse Gas Emissions*. https://ourworldindata.org/co2-and-other-greenhouse-gas-emissions. Online. Accessed 19th July 2022. 2020.

[24] IPCC. *Climate Change 2021: The Physical Science Basis. Contribution of Working Group I to the Sixth Assessment Report of the Intergovernmental Panel on Climate Change*. Vol. In Press. Cambridge, United Kingdom and New York, NY, USA: Cambridge University Press, 2021. DOI: 10.1017/9781009157896.

[25] Hannah Ritchie and Max Roser. *Emissions by Sector*. https://ourworldindata.org/emissions-by-sector. Online. Acessed 19th July 2022. 2020.

[26] IPCC. *Global Warming of 1.5°C. An IPCC Special Report on the impacts of global warming of 1.5°C above pre-industrial levels and related global greenhouse gas emission pathways, in the context of strengthening the global response to the threat of climate change, sustainable development, and efforts to eradicate poverty*. Cambridge, United Kingdom and New York, NY, USA: Cambridge University Press, 2018. DOI: `10.1017/9781009157940.001`.

[27] IEA. *Net Zero by 2050*. `https://www.iea.org/reports/net-zero-by-2050`. Online. Accessed 20th July 2022. 2021.

[28] Eric H. Oelkers and David R. Cole. "Carbon Dioxide Sequestration A Solution to a Global Problem". In: *Elements* 4.5 (Oct. 2008), pp. 305–310. DOI: `10.2113/gselements.4.5.305`.

[29] Amin Taheri Najafabadi. "CO_2 chemical conversion to useful products: An engineering insight to the latest advances toward sustainability". In: *International Journal of Energy Research* 37.6 (2013), pp. 485–499. DOI: `10.1002/er.3021`.

[30] Stefan Bachu and Michael A. Celia. "Assessing the potential for CO_2 leakage, particularly through wells, from geological storage sites". In: *Carbon Sequestration and Its Role in the Global Carbon Cycle*. Ed. by Brian J. McPherson and Eric T. Sundquist. Vol. 183. Geophysical Monograph Series. Washington, D. C.: American Geophysical Union, 2009, pp. 203–216. DOI: `10.1029/2005GM000338`.

[31] Wei-Ning Wang et al. "Comparison of CO_2 Photoreduction Systems: A Review". In: *Aerosol and Air Quality Research* 14.2 (2014), pp. 533–549. DOI: `10.4209/aaqr.2013.09.0283`.

[32] Hironori Arakawa et al. "Catalysis Research of Relevance to Carbon Management: Progress, Challenges, and Opportunities". In: *Chemical Reviews* 101.4 (2001), pp. 953–996. DOI: `10.1021/cr000018s`.

[33] Devin T. Whipple and Paul J. A. Kenis. "Prospects of CO_2 Utilization via Direct Heterogeneous Electrochemical Reduction". In: *The Journal of Physical Chemistry Letters* 1.24 (2010), pp. 3451–3458. DOI: `https://doi.org/10.1021/jz1012627`.

[34] Mingyuan He, Yuhan Sun, and Buxing Han. "Green Carbon Science: Scientific Basis for Integrating Carbon Resource Processing, Utilization, and Recycling". In: *Angewandte Chemie International Edition* 52.37 (2013), pp. 9620–9633. DOI: `https://doi.org/10.1002/anie.201209384`.

[35] Avelino Corma. "Preface to Special Issue of ChemSusChem on Green Carbon Science: CO_2 Capture and Conversion". In: *ChemSusChem* 13.23 (2020), pp. 6054–6055. DOI: `https://doi.org/10.1002/cssc.202002323`.

[36] Mingyuan He, Yuhan Sun, and Buxing Han. "Green Carbon Science: Efficient Carbon Resource Processing, Utilization, and Recycling towards Carbon Neutrality". In: *Angewandte Chemie International Edition* 61.15 (2022), e202112835. DOI: `https://doi.org/10.1002/anie.202112835`.

[37] Toshiyasu Sakakura, Jun-Chul Choi, and Hiroyuki Yasuda. "Transformation of Carbon Dioxide". In: *Chemical Reviews* 107.6 (2007), pp. 2365–2387. DOI: `10.1021/cr068357u`.

[38] Jens Artz et al. "Sustainable Conversion of Carbon Dioxide: An Integrated Review of Catalysis and Life Cycle Assessment". In: *Chemical Reviews* 118.2 (2018), pp. 434–504. DOI: `10.1021/acs.chemrev.7b00435`.

[39] Mette Mikkelsen, Mikkel Jørgensen, and Frederik C. Krebs. "The teraton challenge. A review of fixation and transformation of carbon dioxide". In: *Energy & Environmental Science* 3 (1 2010), pp. 43–81. DOI: `10.1039/B912904A`.

[40] IEA. *About CCUS*. `https://www.iea.org/reports/about-ccus`. Online. Accessed 21st July 2022. 2021.

[41] IEA. *Putting CO_2 to Use*. `https://www.iea.org/reports/putting-co2-to-use`. Online. Accessed 22nd July 2022. 2019.

[42] Lothar Mennicken, Alexander Janz, and Stefanie Roth. "The German R&D Program for CO_2 Utilization—Innovations for a Green Economy". In: *Environmental Science and Pollution Research* 23 (2016), pp. 11386–11392. DOI: `https://doi.org/10.1007/s11356-016-6641-1`.

[43] Chinese Academy of Sciences. *Thousand-tonne Scale Demonstration of Solar Fuel Synthesis Starts Operation in Lanzhou, China*. `https://english.cas.cn/newsroom/research_news/chem/202001/t20200113_229335.shtml`. Online. Accessed 28th September 2022.

[44] Avelino Corma and Hermenegildo Garcia. "Photocatalytic reduction of CO_2 for fuel production: Possibilities and challenges". In: *Journal of Catalysis* 308 (2013). 50th Anniversary Special Issue, pp. 168–175. DOI: `https://doi.org/10.1016/j.jcat.2013.06.008`.

[45] Josef Michl. "Towards an artificial leaf?" In: *Nature Chemistry* 3 (2011), pp. 268–269. DOI: `https://doi.org/10.1038/nchem.1021`.

[46] Somnath C. Roy et al. "Toward Solar Fuels: Photocatalytic Conversion of Carbon Dioxide to Hydrocarbons". In: *ACS Nano* 4.3 (2010), pp. 1259–1278. DOI: `10.1021/nn9015423`.

Chapter 2

State of Art

The decisions we make now will determine the course of the next 30 years and beyond

*António Guterres*

2.1   Introduction

The dependence on burning fossil fuels as the main energy source and consequent emission of CO_2, its main combustion product, has become the main contributor to the current climate changes. In order to minimize the impact of anthropogenic CO_2 emissions on the climate, the IEA has presented a proposal to achieve net zero emissions by 2050. The proposal is based on the use of renewable energies as the main electricity producers and a strong reduction in the fossil fuels usage. These will be used coupled with CCUS technology, as chemical feedstocks or in sectors where electrification is complicated, such as aviation.

Something interesting to consider in the development of a more sustainable energy mix would be the production of fuels with the same properties as fossil fuels but by employing renewable sources. To do this, it would be necessary to collect energy in a renewable form and convert H_2O and CO_2 into gaseous or liquid fuels. Thus, it would not be necessary to retrofit existing technology. There are several technologies available to do it but, due to the high production costs, they are not competitive yet [1].

The different technologies available can be divided into four categories, depending on how the renewable energy is collected: concentration, transformation, natural photosynthesis and artificial photosynthesis.

Through solar concentration it is possible to generate high temperatures that can be used for the production of electricity (through a steam turbine), hydrogen or syngas (through water gas shift reaction). Syngas can later be used to produce methanol or in the Fisher-Tropsch reaction [1].

The second production method is the transformation of renewable energies, such as solar or wind power, into electricity which will participate in subsequent electroconversion processes (see Figure 2.1). These processes are generally referred as "Power to X", where X can be gas, liquids or chemicals [2].
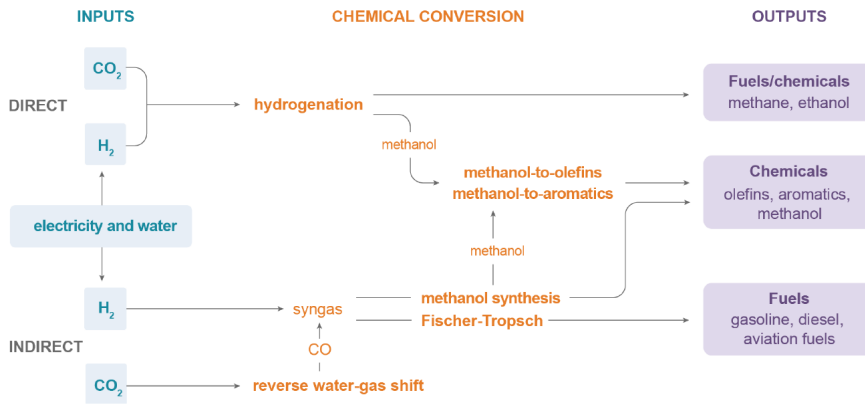
Figure 2.1: Scheme of the different "Power to X" configurations (adapted from [3])

Due to the intermittency of renewable energies, the development of large distribution and storage systems is necessary. The Power-to-Gas (PtG) technology, by converting electricity into hydrogen or methane, is one possibility to meet such needs. The renewable energy is used to electrolyze water, producing oxygen and hydrogen. Oxygen can then be released into the atmosphere or used in industrial processes. As for hydrogen, it can be used directly as a fuel or in industrial processes. However, the hydrogen production is limited by the existence of infrastructure for its storage and transport. One possibility to overcome this limitation is the production of methane instead of hydrogen as PtG end product. The methane is produced by CO_2 hydrogenation that could be previously captured by carbon capture technology (see Figure 2.1) [4, 5].

Yilmaz et al. [5] carry out a techno-economic assessment of the use of PtG technology for methane production as a way to decarbonise the European electrical grid. It is concluded that by taxing carbon emissions at 160€/tCO_2 and combining it with energy storage through methane production (using PtG technology) it is possible to decarbonise the European electrical grid in an economically feasible way by 2050. The economic reliability of this model depends on the taxation of CO_2 emissions, the CO_2 source and the development and improvement of PtG technology.

In Power-to-Liquids (PtL) technology there are three essential steps (see Figure 2.1). The first, similar to PtG technology, is the production of hydrogen by water electrolysis. The second step is the conversion of CO_2 into CO through the water-gas shit reaction. When CO and H_2 are combined, syngas is obtained, which

can be used in the Fischer–Tropsch reaction for the fuels production [6, 7, 8] or for producing methanol. The methanol can later be used for the production of chemicals with an industrial interest, such as aromatics or olefins [2, 9, 10].

Another way in which it is possible to obtain fuels is by using solar energy. The power provided by the sun, about 120 000 TW of electromagnetic radiation, far exceeds the current energy needs of humankind. Solar energy has enormous potential as an economical, abundant and clean energy source. However, it cannot be used directly. Since solar energy is diffuse and intermittent, the conversion of solar energy into useful energy should also involve concentration and storage [11]. Algae, plants and other organisms are able, through photosynthesis, to collect solar energy and produce biomass or biofuels [12]. It is possible to produce fuels, chemicals, heat or electricity generation. There is also the possibility of using micro-organisms as "small factories". These organisms have been genetically engineered to excrete out of their cells interesting compounds such as hydrogen, ethanol or other high value-added chemical compounds [1, 12] (see Figure 2.2).
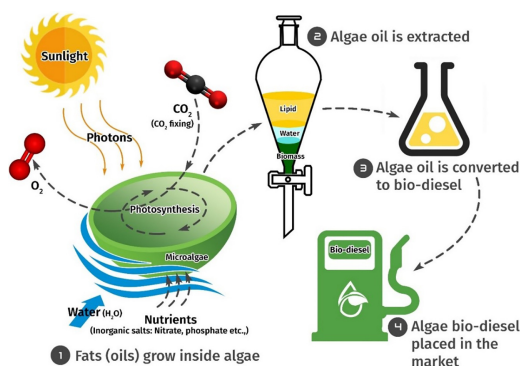
Figure 2.2: Scheme of fuel production from CO_2 sequestered algal biomass (adapted from [12])

However, natural photosynthesis evolved in order to ensure the survival and not the maximize light-to-product conversion. The typical solar-to-biomass efficiency is between 0,1% to 2%, which is too low to meet the global energetic demand. Additionally, it is observed that only 48,7% of the solar energy is in the photosynthetically active band and there is an energy loss associated with internal metabolic inefficiencies [13, 14, 15].

Inspired by the natural photosynthesis, artificial photosynthesis systems (APS's) have been developed in order to increase the efficiency of the process [15]. The APS's combine photochemical and enzimatic reactions, that allow to mimic the

natural photosynthetic process (see Figure 2.3 for comparison between both processes). On natural photosynthesis the first step, the water splitting, happens at the thylakoid membrane. In artificial photosynthesis this step, the photochemical one, occurs in the photocatalysts. Different materials can be used as photocatalysts, namely organic dyes, inorganic materials or organic-inorganic hybrid materials. The last step, CO_2 fixation, is carried out by redox enzymes in both processes using the H_2 previously produced as proton carrier. It is the first step, the water splitting, the responsible for storing solar energy [16].

(a)   (b)
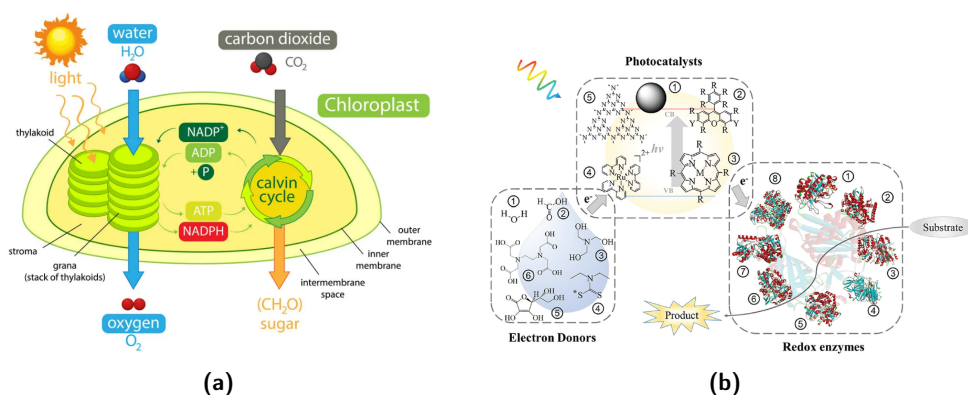
Figure 2.3: (2.3a) Natural and (2.3b) artificial photosynthesis processes (adapted from [15])

One example of APS's is the artificial leaf developed by Daniel Nocera and his team [17, 16, 18, 19]. Nocera's team designed a solar water-splitting cell based on earth abundant elements with efficiencies up to 4,7 % [17]. This cell was combined with *Ralstonia eutropha* in order to produce C compounds, thus obtaining a true photosynthetic analogue [18, 19]. The hybrid system developed has a solar-to-biomass performance of 9,7%, solar-to-bioplastics of 7,6% and solar-to-fuel alcohols of 7,1%. These efficiencies greatly exceed the natural photosynthesize performance [19].

The combination of a photocatalyst with a redox enzyme in the same system is quite complex, since they usually work under very different conditions. Different configurations have been tested that allow maximizing the charge carriers transportation and the stability. However, these systems are still in the early stages of development and involve different challenges, namely on the scale-up of lab-scale devices [15].

2.2   Photocatalysis

Although it is used worldwide, the term photocatalysis is misleading, since it suggests that light is the catalyst for the reaction. By definition, a catalyst should be recovered after the chemical reaction without, theoretically, being modified in the process and can be used several times. In a photochemical reaction, it is observed that light is absorbed and cannot be recovered at the end of the chemical reaction. Thus, photocatalysis refers to the acceleration of a photoreaction through the presence of a catalyst, and not a reaction catalyzed by light [20].

Taking into account the solar energy availability and the increasing environmental challenges, the development of sustainable processes that produce fuels and chemical feedstocks from H_2O and CO_2 is highly desired [21]. Solar fuels can be defined as the H_2 produced from water or the conversion of CO_2 into fuels through the direct use of solar energy [22].

2.2.1   Photocatalytic configurations

Solar fuels can be produce by different device's configuration - electrochemical, photoelectrochemical or photocatalytic powder dispersion.

In the electrochemical configuration an electrolyser, with a catalysts that drives the desired reaction, is connected to a photovoltaic panel - PV-EC - (see Figure 2.4). The electrolyser and photovoltaic panel performances are of primary importance to achieve high performances [23]. It is possible to find in the literature devices that present a solar-to-hydrogen (STH) efficiency of 22% [24] and when connecting different electrolysers in series it is possible to reach an STH efficiency up to 30% [25]. As for the CO_2 reduction, its efficiency quantification is more complicated, since it is possible to obtain different products, and not all publications provide this value. For example, Schreier et al. [26] reported one of the highest solar-to-CO efficiency of 6,5% and a STH of 7% as a secondary product. The disadvantage of this configuration is the high complexity of photovoltaic panels, although it is a mature and commercialized technology [23].
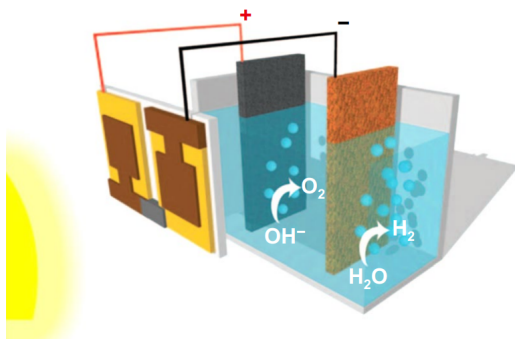
Figure 2.4: Electrochemical configuration (adapted from [27])

The second configuration, the photoelectrochemical device (PEC), consists on one or two photoelectrodes and auxiliary metal immersed in an electrolyte (see Figure 2.5 for wired and wireless PEC devices) [21, 28]. This configuration allows oxidation and reduction reactions to taken place in different physical positions, allowing a better optimization of each reaction and reducing charge recombination. It is possible to find in the literature different PEC cell's configurations, with different degrees of complexity. For example, Kang et al. [29] by using a photoanode-photocatode tandem PEC cell could obtain a STH efficiency of 13%. When using a photoelectrode combined with a photovoltaic technology it is possible to obtain a STH efficiency of 19% [30]. Regarding CO_2 photoreduction, it is already possible to find in the literature self-bias configurations that allow to obtain a solar-to-CO efficiency of 7% and STH of 3,5% [31]. The main disadvantages of this configuration are the complexity, the cost and the low stability of the electrodes [22, 32, 33].
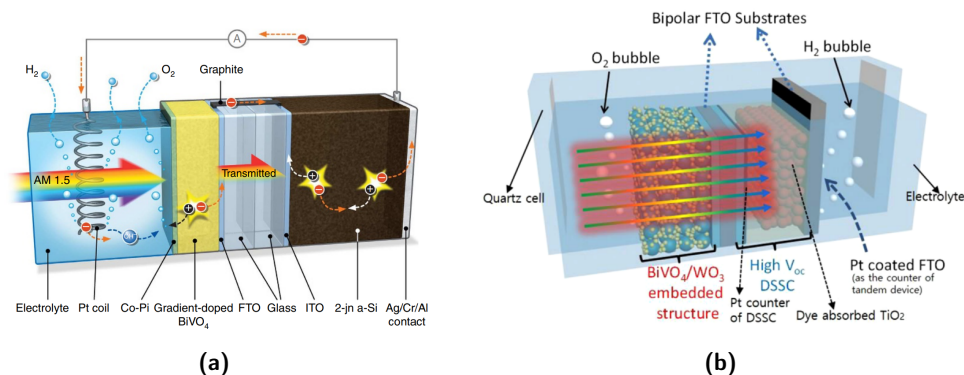
Figure 2.5: (2.5a) Wired and (2.5b) wireless photoelectrochemical cells (adapted from [34, 35])

The last configuration is the dispersion of a photocatalyst directly in the reaction medium - PC - (see Figure 2.6). This configuration has recently attracted interest, as it allows direct use of sunlight without the need to use solar cells and electrolysis units [36, 23]. Although this is the simplest configuration, different semiconductor characteristics, such as appropriate band structure and stability in the reaction medium, have to be taken into account. The oxidation and reduction reactions occur at different points of the photocatalyst surface, thus having a mixture of the final products and the possibility of product oxidation. As for the application of this configuration in water splitting, it is possible to find STH efficiencies of 2% for semiconductors with one-step excitation [37] and 3% for semiconductors with two-step excitation [38].
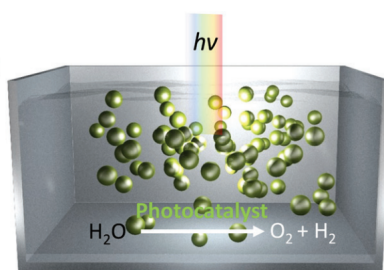
Figure 2.6: Photocatalyst dispersed directly on the reaction medium (adapted from [23])

In order to compare the different configurations available, Kim et al. [23] plotted a technology map for water splitting technologies available (see Figure 2.7). It

can be observed that PC technologies present the lowest complexity but the lowest efficiency. PV-EC presents the highest efficiency, but the highest complexity, which means a higher cost. As for PEC cells, at the current level of development, they are not competitive with PV-EC devices. For this, it would be necessary that their STH efficiency would be higher than 10% and with a lifetime longer than 10 years.
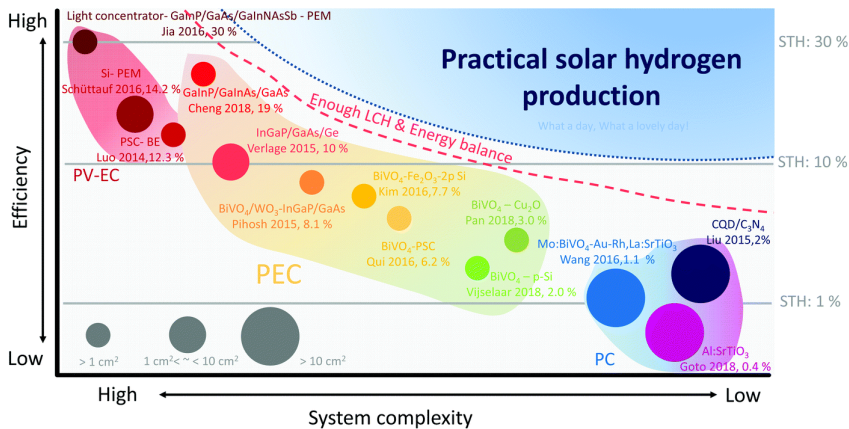
Figure 2.7: Comparison of different photon-driver water splitting technologies (adapted from [23])

The US Department of Energy has estimated that for a STH efficiency of 5% it is possible to produce H_2 by PC at a cost of \$2,30 per kilogram. Currently, H_2 obtained by steam reforming of natural gas costs \$1 per kilogram and by water electrolysis \$5,5 per kilogram. Taking into consideration the simplicity and the potentiality of PC configuration, there is high interest in increasing its efficiency [23].

2.2.2   *Photocatalytic process*

The process begins when the photocatalyst is irradiated by sunlight. When the photons from the solar radiation have a higher energy than the band gap of the photocatalyst, electrons and holes are produced. Subsequently, the charge carriers are partly transported to the surface of the photocatalyst, where the electrons may participate in a reduction reaction (see path A in Figure 2.8) and the holes in an oxidation process (see path B in Figure 2.8) [39, 40, 41, 42, 43].
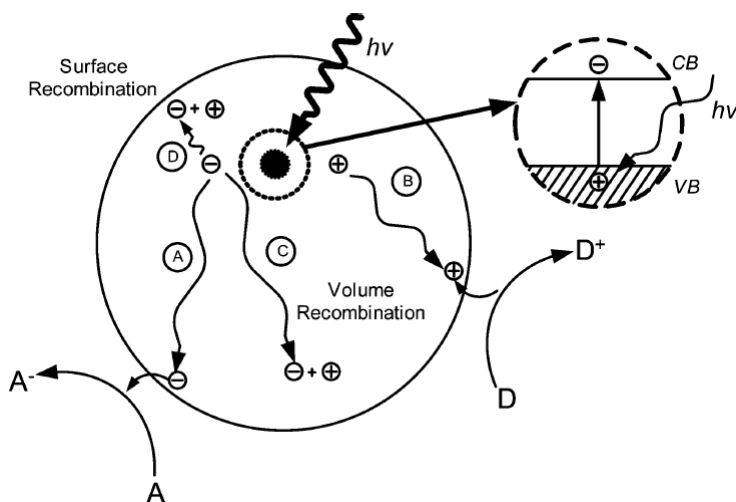
Figure 2.8: Schematic of a redox process through photocatalysis, where A is an electron acceptor species and D is an electron donor (adapted from [43])

In addition to participating in redox reactions, charge carriers can also undergo recombination (see paths C and D in Figure 2.8). Charge recombination competes directly with the redox reactions that occur at the surface of the photocatalyst, becoming one of the main factors responsible for the low yield of the process [42].

To ensure that the desired reaction process takes place as efficiently as possible, charge separation has to be maximized and redox reactions to the surface have to occur within the average lifetime of the charges [39]. In order to decrease charge recombination rate, a semiconductor with high crystallinity should be used, since the defects and the boundaries in the crystalline framework act as traps, thus facilitating the electron-hole recombination [42]. However, it was observed that the presence of deffects could have a positive impact on photocatalytic performance [44]. It was shown that decreasing the concentration ratio of bulk defects to surface defects could improve the separation efficiency of photogenerated electrons and holes, enhance the light absorption and increase the donor density [45, 46]. Therefore, since it is possible to find in the literature conflicting opinions on the effect of defects on photocatalytic performance, further studies are needed to understand their true influence [44].

For a semiconductor to be used as a photocatalyst, it is required that it presents a set of properties that make it suitable for such application. It is necessary that the base of the semiconductor conduction band is located at a more negative

potential than the reduction potential of the acceptor species and that the top of the valence band is located at a more positive potential than the oxidation potential of the donor species [32, 36, 40, 43] (see Figure 2.9). Therefore, in order to attain high photocatalytic performance, the photocatalyst should have excellent light harvesting, generation and charge separation properties.

2.2.3   Photocatalysts

The first compound found to show photocatalytic activity was TiO_2 in 1972 [47] and, since then, different ways to increase photocatalytic performance have been investigated.

Different materials, such as metal oxides, metal and oxy-nitrides, metal chalcogenides, alkali metal base, polyoxometalate-based strucutres, with sometimes very specific combined structural arrangements between materials such as Z-scheme systems or others with interfaces forming Schottky barriers and organic materials, are being investigated for use as photocatalysts [48, 49, 50, 51, 52, 53, 54, 55, 56, 57, 58, 59]. Among the materials presented, the metal oxides, metal chalcogenides and their composites stand out [39].

The vast majority of oxides show high values for the optical band gap and can only absorb radiation in the UV region. Bearing in mind that only 5% of the solar spectrum is made up of UV radiation and about 43% of the visible radiation, the synthesis of materials with band gaps more adapted to solar radiation becomes essential to meet high yields of conversion, especially for the solar-to-fuel route [60]. Metal chalcogenides comprise a viable alternative to metal oxides, as they have a band gap more suitable for solar radiation [61] (see Figure 2.9).

In particular, while the conduction band of transition metal oxides and transition metal sulfides materials is primarily derived from the metal s orbitals, the valence band is primarily derived from oxygen $2p$ orbitals for transition metal oxides [62] and for transition metal sulfides it derives from sulfur $3p$ orbitals [63], allowing substantially narrowed band gaps for the latter.

Analyzing the band structure of the most common metal oxides (see Figure 2.9), it is easy to conclude that these are not the best candidates to be used as photocatalysts for solar fuels production, since the position of their valence and conduction bands is not the more appropriate to the redox potentials of the species involved. Moreover, most of the oxides have a wide band gap value, since their valence band consists of O $2p$ orbital, and the holes have a large effective mass and a low dielectric constant, being unfavorable for charge separation [64]. Assessing now the band position of the metal sulfides, one can see that they are in more suitable positions

(see Figure 2.9). In addition, these materials have a less positive valence band, since it is occupied by S $3p$ orbital, Thus, lower band gap, and still thermodynamically able to oxidize water [39]. Hence, metal sulfides have an enormous potential as candidates to be used on the solar fuels production. It is already possible to find in the literature reference to the use of metal chalcogenides as photocatalysts in processes of pollutants degradation but also for the production of fuels [65, 66, 67, 68, 69, 70, 71, 72, 73].
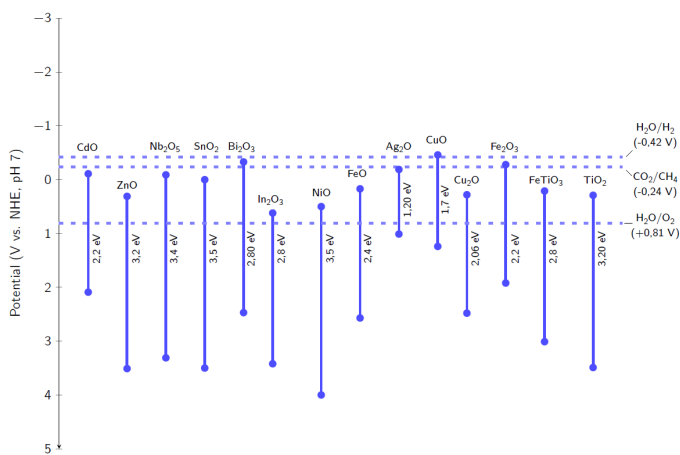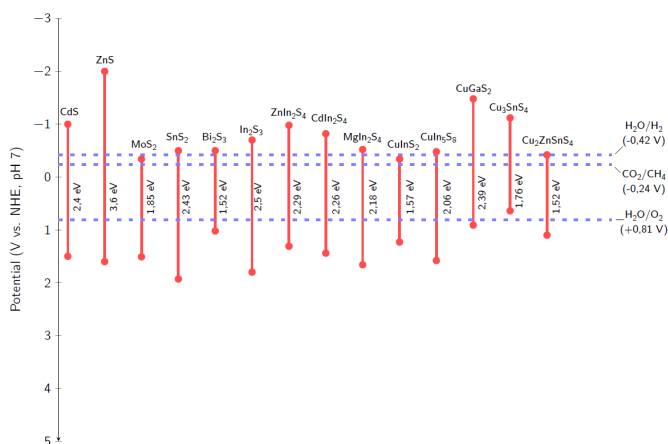
Figure 2.9: Band position of common (2.9a) metal oxides and (2.9b) metal sulfides [61, 74]

Besides, microporous materials have, over time, attracted enormous interest in both scientific and technological fields. Since they allow the interaction with atoms, molecules and ions at the surface but also withing the porosity, these materials have innumerable applications, namely in gas separation, ionic exchange and petrochemical industries [75].

Since the applications of these materials are closely related to their topology and chemical composition, intense research has been carried out on the synthesis of new materials. According to Zheng et al. [76] there are several advantages in using crystalline microporous materials as active photocatalysts. The open framework architecture helps, due to the high surface area, increase the number of active sites, but is also likely to reduce the electron-hole recombination rate since it reduces the average carrier path to reach the surface of the catalysts particle where the reaction occurs. However, oxide based porous materials are mainly insulators (typically silica or silica-alumina) [77], presenting limitations for applications involving photon absorption. Thus, in order to expand such applications, the synthesis of porous materials with semiconducting properties became desirable [78].

Recently, porous chalcogenides materials have received special attention, as they combine the presence of an open framework with semiconductivity, hence making it possible to use such materials in optoelectronic devices, photocatalysis and fast ionic conduction materials [79].

2.3   Porous Chalcogenide Materials

The term "chalcogen" was first used in 1930 by Werner Fischer and derived from the Greek words $\chi\alpha\lambda\kappa\acute{o}\zeta$, copper, and $\gamma\epsilon\upsilon\upsilon\acute{\omega}$, giving birth. By definition, this term refers to the elements of group 16 of the periodical table - oxygen, sulfur, selenium, telurium and polonium. However, it is generally used to treat all the elements of this group except oxygen, since the chemistry of this element was generally discussed in separate chapters in common chemical inorganic textbooks [80, 81]. Hence, in order to follow the trend followed by the other authors, when the word "chalcogen" or its derivatives are used it is referring to the elements of group 16 excluding oxygen.

The main difference between oxygen and the other elements of group 16 is the presence of vacant d orbitals. The heavier elements can use these orbitals in bonding, so their coordination number is not limited to four nor their valence limited to two as in oxygen [81, 82]. Open framework chalcogenides present themselves as a particular system since both cations and anions in the framework tend to adopt a tetrahedral coordination. In the case of zeolites or zeotype materials

only metal cations tend to adopt a tetrahedral coordination while oxygen atoms generally adopt a bi- or tricoordination [83]. This tetrahedral arrangement allows the formation of clusters that are not observed in oxygen-based materials [84].

Therefore, it is observed that chalcogenide materials with an open framework present as building units M_xS_y clusters, where M is a metal cation, generally from Groups 12-14 (such as Zn, Cd, Ga, In, Ge and Sn), instead of TX_4 tetrahedra that can be found in zeolite or zeolite-like materials. One of the immediate consequences of using M_xS_y clusters instead of the TO_4 is the increase pore size [85].

Given that the framework consists of clusters, which can be seen as large artificial atoms, an extra structural level associated with each cluster arises, allowing to fine tune the material properties [83, 84]. Of the many known clusters [86], the tetrahedrally shaped clusters stand out, since they are able to form links through their vertices.

Since the discovery in 1989 by Bedard et al. [87, 88] of microporous sulfides through hydro(solvo) thermal methods, intensive research has been carried out in order to obtain new materials with controlled chemical compositions and architectures, so that their physical and chemical properties are better adapted to a specific application [89].

2.3.1   Clusters Topologies

Open framework chalcogenides are crystalline materials consisting of clusters that are connected by chalcogen bridges or metal ions. The porous volume is usually occupied by organic or inorganic components. The clusters that constitute these structures, due to their dimensions, are on the quantum dots[1] scale. These materials thus have properties that depend on their dimensions, in particular the electronic structure and electronic properties [84, 86]. Considering that the periodic arrangement of clusters can be seen as dots and the cavities as antidots, these materials allow to the study the interactions between individual dots and, due to the regular distance between them, the interdot coupling [91]. The electronic properties become particularly valuable as most of these clusters are semiconductors with a band gap and band structures suitable to be used with radiation with a wavelength between 400 to 800 nm.

These clusters, which are essentially made up of metals and chalcogen atoms, can be synthesized from a wide variety of methods. The simplest one is the association, in the appropriate proportions, of metal cations and chalcogen anions in solution.

---

[1]Quantum dots are semiconductor nanocrystals that, due to their dimensions, have unique optical and electronic properties [90]

Since both components can achieve different oxidation states, it is still possible to obtain these clusters from a redox reaction using a metal reductor and a chalcogen oxidant [86].

The clusters, after formed, can connect, originating open frameworks. These frameworks can be seen as decorated nets. A decorated net is based on atoms that were replaced by clusters, while maintaining the connection pattern [92]. Figure 2.10 presents some examples of topologies presented by 3-dimensional structures. It is observed that the most common topology in this family of materials is the diamond topology, simple or double interpenetrated. Interpenetration refers to two or more nets, with the same or different chemical composition, connected with each other [93].

(a) Diamond

(b) Sodalite

(c) CrB_4

(d) Cubic carbon nitride

(e) Gismondine

(f) Nabesite

(g) ABW
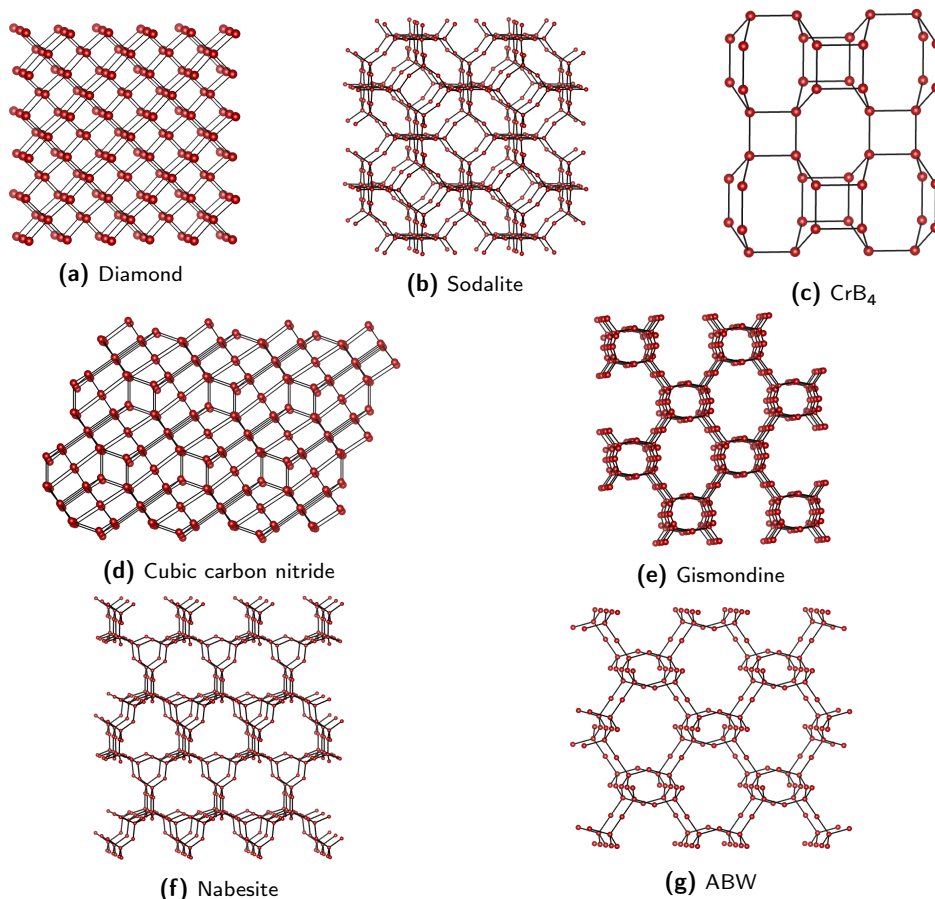
Figure 2.10: Representation of diamond (D), sodalite (SOD), CrB_4, cubic carbon nitride (C_3N_4), gismondine (GIS), nabesite (NAB) and ABW topologies

2.3.1.1 Tetrahedral Clusters

This type of cluster is the most common building unit in open framework chalcogenide materials. They are usually composed of cations from groups 12 to 14, and may also have other elements such as Fe, Mn, Co, Cu or Li.

There are different types of tetrahedron clusters, namely supertetrahedral Tn, super supertetrahedral $T_{p,q}$, pentasupertetrahedral Pn, capped supertetrahedral Cn and oxyclusters.

i. Supertetrahedral Clusters Tn

The simplest and most common series of tetrahedral clusters are called superte-trahedral clusters. These clusters are fragments of the cubic ZnS-type lattice and denoted as Tn by Li et al. [94], where n represents the number of metal layers. Figure 2.11 shows the diagrams of different Tn clusters for n=2, 3, 4, 5.
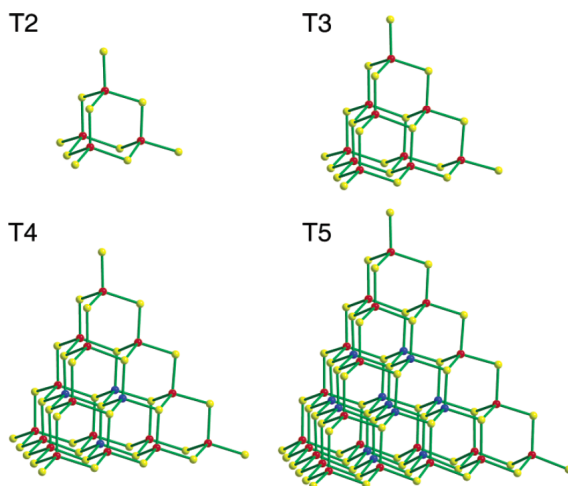
Figure 2.11: Diagrams for different Tn clusters ($n = 2$, 3, 4 and 5) where the red balls represent the cations and the yellow balls the anions. In clusters where two types of cations coexist, the blue balls represent the divalent cations (adapted from [83])

The number of cations in a Tn cluster is given by $t_n = n(n + 1)(n + 2)/6$. The number of anions per cluster is given by $t_{n+1} = (n + 1)(n + 2)(n + 3)/6$. The formulas for discrete Tn ($n = 2$-6) clusters are M_4X_{10}, $M_{10}X_{20}$, $M_{20}X_{35}$, $M_{35}X_{56}$ and $M_{56}X_{82}$, respectively. Taking into account that in a continuous network of clusters the four vertices of the supertetrahedron are shared with another supertetrahedron, the final composition of the structure is M_xX_y, where x= t_n and y= $t_{n+1} - 2$.

Regarding coordination, all cations have a coordination equal to 4. The same is no longer true for anions. They may have a coordination of 2 if they are at the vertices of the cluster, coordination of 3 if they are on the face of the cluster, or coordination of 4 if they are within the cluster. The number of anions with 2-coordination is given by $6n - 4$, with 3-coordination given by $2(n - 1)(n - 2)$ and with 4-coordination given by $(n-3)(n-2)(n-1)/6$. Table 2.1 shows the number of cations and anions present in an isolated Tn cluster or when it participates

in a network, as well as the number of anions with coordination 2, 3 and 4. It is observed that anions with 4-coordination only exist for n greater or equal to 4. In order to ensure the compliance with Brown's equal valence rule [95], the 4-coordinated chalcogen atoms are only bonded to divalent cations in order to ensure that the four bonds have a bond valence of 1/2, thus explaining the need to use divalent cations to obtain clusters with n greater or equal to 4. The number of divalent cations in the cluster as a function of n is given by $t_n - 6n + 8$ [91, 96].

Table 2.1: Composition of Tn clusters

Cluster Tn	t_n	t_{n+1}	Number of Cations x	Number of Anions y	Anion coordination 2	3	4
1	1	4	1	2	2	0	0
2	4	10	4	8	8	0	0
3	10	20	10	18	14	4	0
4	20	35	20	33	20	12	1
5	35	56	35	54	26	24	4
6	56	84	56	82	32	40	10

As the size of the cluster increases, the overall negative charge increases, making it difficult to stabilize clusters with higher dimensions [84]. Therefore, only structures consisting of clusters up to $n = 6$ are known.

It is observed that the presence of low-valence cations in M^{3+}-S system promotes the formation of larger-sized clusters and high-valence cations promotes the formation of smaller clusters. When only trivalent cations are present it is common to obtain T3 clusters.

i.a. T2 and T3 chalcogenide based materials

In 1994 Yaghi et al. [97] presented the first synthesis of an open framework microporous sulfide based on Ge containing the T2 Ge_4S_{10} cluster as building unit. The material obtained has the formula $[(CH_3)_4N]_2[MnGe_4S_{10}]$ and presents a non-interpenetrating framework with a diamond topology. The crystalline structure is based on the presence of T2 Ge_4S_{10} clusters which are connected by MnS_4 tetrahedra (see Figure 2.12). In order to achieve the 3-dimensional structure it was necessary to add mono or divalent cations, such as Mn, Cu [97, 98, 99], Ag [100], Fe [97] or Cd [97] which will be responsible for connecting the different building units, hence avoiding the formation of a layered material.
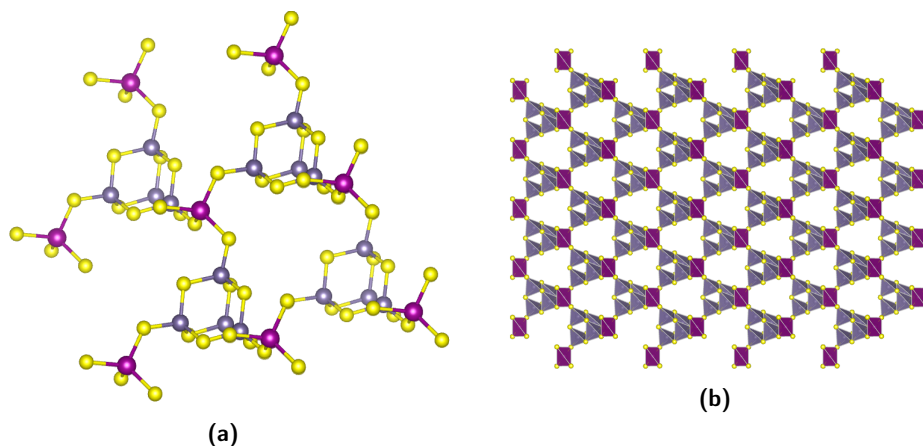
Figure 2.12: (2.12a) Representation of the connection of the T2 Ge_4S_{10} clusters through MnS_4 tetrahedra. (2.12b) Structure of $MnGe_4S_{10}\cdot2(CH_3)_4N$ where the organic part was not presented (Mn - pink; Ge - gray, S - yellow) [97]

Also based on the T2 Ge_4S_{10} cluster, Cahill et. al [101] obtained a material entitled QUI-MnGS-1 with a diamond lattice. Although QUI-MnGS-1 is also based on Ge_4S_{10} cluster, the presence of MnS_4 tetrahedral is not observed. The connection between the Ge_4S_{10} clusters is made by sulfur atoms at the vertices through a sulfur bridge. It was observed that it is possible to eliminate part of the structure directing agent (SDA) through calcination at a temperature between 240°C and 360°C without destroying the framework. At temperatures above 360°C the structure collapses.

In the Ge-S system the largest synthesized cluster is type T2. This is justified by the fact that the cations charge is too high to satisfy the coordination environment of a tricoordinated anion that exists for clusters bigger than $n = 2$. The number of known 3-dimensional frameworks is low, perhaps because fully connected M^{4+}-S framework would be neutral, not allowing the electrostatic interaction with a SDA [83, 102].

The chemical system In-S have been extensively studied by Cahill et al. [85, 103]. Several materials with different dimensions, from isolated clusters to 3-dimensional frameworks, based on the T2 In_4S_{10} and T3 $In_{10}S_{20}$ clusters were obtained. As for the materials based on the T3 clusters, it was concluded that such cluster could be obtained over a range of SDA's, and the presence of water played an important role in defining the final topology of the material, but not on the type of cluster formed (see Table 2.2). When using dimethylamine (DMA) or diethylamine (DEA)

as SDA one obtains a 3-dimensional structure. When the SDA used is the DEA and water exists in the initial gel one gets a laminar structure instead of a 3-dimensional structure. Therefore, it can be said that, for this system, the SDA is not the only one responsible for the final topology of the material.

Li et al. [94, 104] also synthesized 3-dimensional microporous solids based on In, which presents the T3 clusters as building units in its structure. Three crystalline structures, ASU-31, ASU-32 and ASU-34, were obtained, since different types of SDA were used (see Figure 2.13).

(a)

(b)

(c)
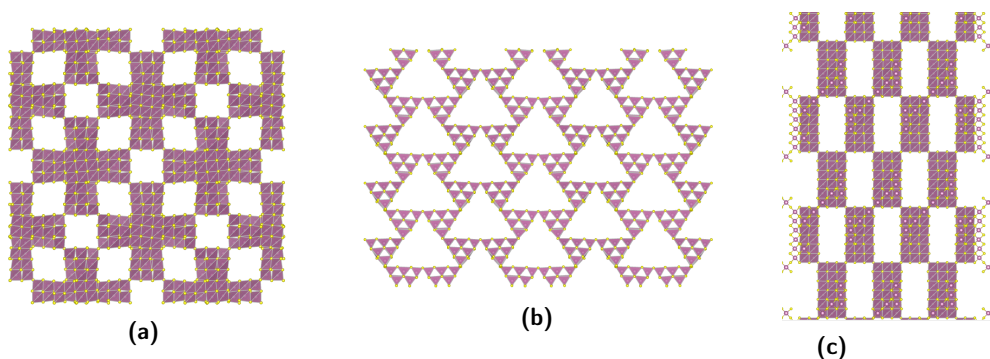
Figure 2.13: Representations of (2.13a) ASU-31, (2.13b) ASU-32 and (2.13c) ASU-34 where the organic component was not presented (In - pink, S - yellow) [94, 104]

Comparing the structures obtained by Cahill [85, 103] and Li [94, 104] (see Table 2.2), the structures synthesized by the first exhibited an interpenetrated framework. This type of framework occurs when the pore size is too large to support the framework. This is not the case with the structures obtained by Li, since the SDA's used allowed to obtain the giant cavities.

Table 2.2: Different materials based on T3 $In_{10}S_{20}$ cluster and their gels compositions and final topology (adapted from [85])

Material	SDA	Gel composition (mol)				Cluster	Structure	Interpenetration	Ref.
		In	S	Organic	H_2O				
DMA-InS-SB1	DMA[1]	1	2,3	4,4	16,6	T3	3D - DD[2]	Yes	[103]
DEA-InS-SB1	DEA[3]	1	2,3	6,8	trace	T3	3D - DD[2]	Yes	[85]
DEA-InS-SB2	DEA[3]	1	2,3	3,4	14,0	T3	2D	No	[85]
ASU-31	HPP[4]	1	2,5	n/a[5]	n/a[5]	T3	3D - SOD[6]	No	[94]
ASU-32	DPM[7]	1	2,5	n/a[5]	n/a[5]	T3	3D - CrB_4[8]	No	[94]
ASU-34	HMA[9]	1	2,5	n/a[5]	n/a[5]	T3	3D - CrB_4[8]	No	[104]

[1] Dimethylamine. [2] Double Diamond. [3] Diethylamine. [4] 1,3,4,6,7,8-hexahydro-2H-pyrimido[l,2-a]pyrimidine. [5] n/a - not available. [6] Sodalite (see Figure 2.10b). [7] Dipiperidinomethane. [8] (see Figure 2.10c). [9] Hexamethyleneimine.

The Ga-S system was also studied. Zheng et al. [105] being obtained for the first time a structure based on the T3 $Ga_{10}S_{18}$ cluster, called UCR-7. Depending on the SDA used, they were able to obtain a structure based on cluster T3 $Ga_{10}S_{17,5}(S_3)_{0,5}$, known as UCR-18, that presented for the first time a polysulfide linkage between the clusters (see Figure 2.14).
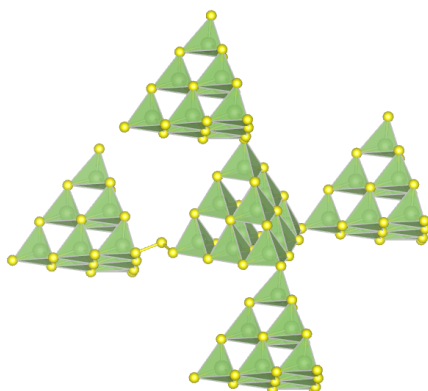
Figure 2.14: Representation of the connection mode between the clusters of the UCR-28 structure (Ga - green, S - yellow) [105]

When using 1-(2-aminoethyl)piperazine (AEP) as a SDA in the Ga-S system, clusters connected by a polysulfide bridge are obtained. However, when the same SDA is used in the In-S system, one obtains a structure where the clusters are connected through the common bisulfide bridge. According to Zheng et al. [105], this situation is explained by the different sizes between Ga and In. Due to the small size of

Ga when compared with In, a contraction of the framework occurs, making it more difficult to accommodate the AEP molecule. Thus, the presence of the polysulfide bridge allows the framework to expand, associated to its natural contraction due to the presence of Ga instead of In.

More recently, a 3-dimensional interrupted structure based on the combination of Sn, In and S has been synthesized [106]. A structure is considered to be interrupted when the clusters that constitute it are only connected to three other clusters, instead of four (see Figure 2.15a). The obtained material, entitled SCU-36, has as framework based on 3-connected T2 clusters and has a *etc* topology (see Figure 2.15b). Other interesting features about SCU-36 is the presence of extra-large channels, consisting of 36-MR, and a very low framework density. As for the exchange properties of the material, after 12 hours of exchange with CsCl the N_2 absorption is negligible. When the time of exchange or the CsCl concentration were increased, the crystal structure collapsed.

(a)   (b)
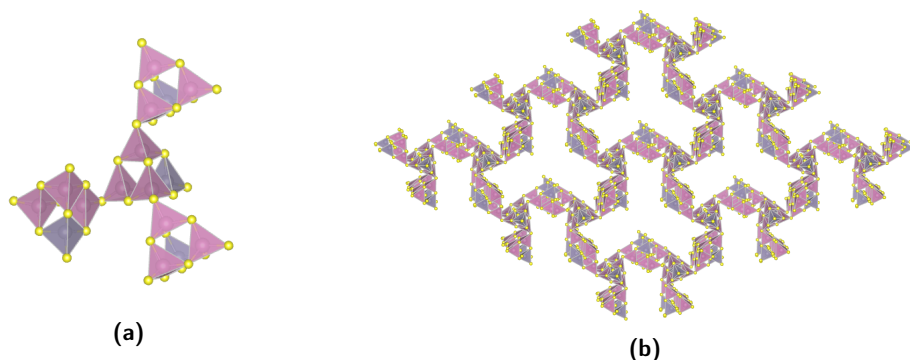
Figure 2.15: Representations of (2.15a) an interrupted framework and of (2.15b) SCU-36 where the organic component was not presented (In - pink, Sn - gray, S - yellow) [106]

According to Wu et al. [107], when partial replacement of In by Sn occurs, the high negative charge of corner sites of clusters decreases, increasing the possibility of formation of interrupted structures.

Continuing the research to obtain more complex structures, Wang et al. [108] synthesized for the first time a structure based on the extended spiro-5 unit, which are expanded through the fusion of five T3-InSnS clusters. The obtained compound, entitled SOF-27, exhibits for the first time a NAB topology (see Figure 2.10f). Comparing the structure obtained with nabasetie, the only known natural zeolite

with the NAB structure, the ring size is increased three times due to the use of T3 clusters instead of TO_4 tetrahedra.

Turning to selenium-based materials, there is a reduced number of crystalline 3-dimensional selenium-based frameworks. The first known structure [109] is based on the T2 cluster Ge_4Se_{10} where the addition of divalent metal cations is required to connect the different clusters in order to achieve a 3-dimensional framework with an analogous structure to that obtained by Yaghi et al. [97].

Continuing the search for larger clusters, the first T3 cluster based on the In-Se system was obtained by Wang et al. [110]. Later, Xue et al. [111] were able to obtain a family of compounds also based on the In-Se which presented polyselenides bridges as a way to connect the different clusters.

As for the Ga-Se chemical system, the first 3-dimensional open frameworks based on T3 clusters as building units were first obtained by Bu et al. [112]. Two different materials were obtained: OCF-6 and OCF-13. The first one presents a diamond topology and a ring size of 18 T atoms while the second one presents a CrB_4 topology and a ring size of 24 T atoms. The synthesized structures present non-interpenetrating frameworks while the ones obtained for the Ga-S system are all interpenetrating nets (see Table 2.3). As for the synthesis conditions, the presence of water promotes the crystal growth while in the Ga-S system the synthesis must be held in a non-aqueous medium (see Table 2.3).

Table 2.3: Different materials based on T3 $Ga_{10}X_{20}$ (X = S, Se) cluster and their gels compositions and final topology

Material	SDA	Gel composition (mol)					Cluster	Structure	Interpenetration	Ref.
		Ga	S	Se	Organic	H_2O				
UCR-7-GaS-TETA	TETA[1]	n/a[2]	n/a[2]	-	n/a[2]	-	T3	3D	Yes	[105]
UCR-7-GaS-TAE	TAE[3]	n/a[2]	n/a[2]	-	n/a[2]	-	T3	3D	Yes	[105]
UCR-7-GaS-DBA	DBA[4]	n/a[2]	n/a[2]	-	n/a[2]	-	T3	3D	Yes	[105]
UCR-18-GaS-AEP	AEP[5]	1	3,3	-	8,6	-	T3	3D	Yes	[105]
-	DEA[6]	1	2,1	-	33,0	-	T3	3D - DD[7]	Yes	[113]
OCF-6-GaSe-TMDP	TMDP[8]	1	-	2,5	4,9	152,9	T3	3D - D[9]	No	[112]
OCF-13-GaSe-DPM	DPM[10]	1	-	2,5	5,2	207,5	T3	3D - CrB_4[11]	No	[112]

[1] Triethylenetetramine. [2] n/a - not available. [3] Tris(2-aminoethyl)amine. [4] Di-n-butylamine. [5] 1-(2-aminoethyl)piperazine. [6] Diethylamine. [7] Double Diamond. [8] 4,4'-trimethylenedipiperidine. [9] Diamond (see Figure 2.10a). [10] Dipiperidinomethane. [11] CrB_4 (see Figure 2.10c).

i.b. Supertetrahedral clusters with $n > 3$

The need to obtain structures with large pores has led to the development of materials consisting of Tn clusters with n greater than 3, since the size of the ring is increased n times, thus leading to structures with a highly open framework [112]. Although Tn are the most commonly used type of clusters, there are some limitations in their use. The first is the way to connect the different clusters. Generally, the connection between two clusters is made through bi-coordinated chalcogen bridge. When using this type of clusters the formed structures tend to be interpenetrated, in order to reduce the potential energy and stabilize the structure, leading to a reduction in pore size and pore volume [114, 115]. Another difficulty that arises is the drastically increase of negative charges with increasing n, making it difficult to synthesize clusters with large dimensions. Although the metal cations are always coordinated with four anions, the same cannot be said for anions at the surface. Thus, as the cluster size increases, so does the number of underbonded anions, contributing to the huge increase in the global negative charge of the cluster [116].

The first material based on a T4 cluster was synthesized in 2001 by Li et al. [96]. This interpenetrating structure is formed by clusters of the type $In_{16}Cd_4S_{35}$, where Cd^{2+} presents a fundamental role in obtaining such structure. It is due to the addition of the divalent cation that the local charge balance at the core tetrahedral anion is achieved. Continuing the research on the synthesis of structures based on T4 clusters, Bu et al. [114] managed to synthesize a structure where a sulfur atom was connecting three T4 clusters.

Wang et al. [117, 118] was able to synthesize a family of T4-based 3-dimensional sulfides as well as using transition metals, such as Fe and Co, to join the different T4 clusters into a 2-dimensional framework. Taking into account the mentioned materials (see Table 2.4), it is possible to obtain the structure of CrB_4 from a diverse range of SDAs, provided they contain a piperazine ring. However, the cubic carbon nitride and UCR-1 topologies are more rigid, since they can only be obtained from di-n-butylamine and 4,4'-trimethylenedipiperidine, respectively, as SDA. It is also interesting to note that when using 1,2-diaminocyclohexane as SDA in the chemical systems In-Fe-S or In-Co-S, the final material presents a 2-dimensional structure instead of a 3-dimensional structure.

Table 2.4: Different materials based on T4 $In_{16}X_4S_{35}$ (X = Zn, Cd, Fe, Co, Mn) cluster and their gels compositions and final topology

Material	SDA	Gel composition (mol)				Cluster	Structure	Interpenetration	Ref.
		In	S	X	Organic				
CdInS-44	BAPP[1]	1	2,5	0,3	4,3	$In_{16}Cd_4S_{35}$	3D - CrB_4[2]	Yes	[96]
UCR-8FeInS-DBA	DBA[3]	n/a[4]	n/a	n/a	n/a	$In_{16}Fe_4S_{35}$	3D - C_3N_4[5]	No	[114]
UCR-8CoInS-DBA	DBA	n/a	n/a	n/a	n/a	$In_{16}Co_4S_{35}$	3D - C_3N_4	No	[114]
UCR-8ZnInS-DBA	DBA	1	3,5	0,4	15,1	$In_{16}Zn_4S_{35}$	3D - C_3N_4	No	[114]
UCR-8CdInS-DBA	DBA	n/a	n/a	n/a	n/a	$In_{16}Cd_4S_{35}$	3D - C_3N_4	No	[114]
UCR-1CdInS	TMDP[6]	1	2,9	0,3	3,9	$In_{16}Cd_4S_{35}$	3D - UCR-1[7]	No	[117]
UCR-1ZnInS	TMDP	n/a	n/a	n/a	n/a	$In_{16}Zn_4S_{35}$	3D - UCR-1	No	[117]
UCR-1MnInS	TMDP	n/a	n/a	n/a	n/a	$In_{16}Mn_4S_{35}$	3D - UCR-1	No	[117]
UCR-1CoInS	TMDP	n/a	n/a	n/a	n/a	$In_{16}Co_4S_{35}$	3D - UCR-1	No	[117]
UCR-5ZnInS-1	BAPP	n/a	n/a	n/a	n/a	$In_{16}Zn_4S_{35}$	3D - CrB_4	No	[117]
UCR-5ZnInS-2	AEPP[8]	n/a	n/a	n/a	n/a	$In_{16}Zn_4S_{35}$	3D - CrB_4	No	[117]
UCR-5ZnInS-3	ATMP[9]	n/a	n/a	n/a	n/a	$In_{16}Zn_4S_{35}$	3D - CrB_4	No	[117]
UCR-5MnInS	BAPP	n/a	n/a	n/a	n/a	$In_{16}Mn_4S_{35}$	3D - CrB_4	No	[117]
UCR-5CoInS	BAPP	n/a	n/a	n/a	n/a	$In_{16}Co_4S_{35}$	3D - CrB_4	No	[117]
-	DACH[10]	1	2,0	0,5	132,9	$In_{16}Fe_4S_{35}$	2D	No	[118]
-	DACH	1	4,0	0,5	149,5	$In_{16}Co_4S_{35}$	2D	No	[118]

[1]1,4-bis(3-aminopropyl)piperazine. [2]CrB_4 (see Figure 2.10c). [3]Di-n-butylamine. [4] n/a - not available. [5]Cubic carbon nitride (see Figure 2.10d). [6]4,4'-trimethylenedipiperidine. [7]UCR-1 topology (see [117] for more information regarding this topology). [8]1-(2-aminoethyl)piperazine. [9]4-amino-2,2,6,6-tetramethylpiperidine. [10]1,2-diaminocyclohexane.

Wu et al. [116] managed to synthesize a family of materials based on the complex Sn-Ga-M-X (M = Mn, Cu, Zn; X = S, Se) chemical system. It was found that in the systems under study there was a phase transformation from a 3-dimensional interpenetrated diamond framework composed of T4 clusters, OCF-5 (see Figure 2.16a), to isolated and highly stable T4 clusters, OCF-40 (see Figure 2.16b). It was observed that OCF-5 has highly disordered dipiperidinomethane (DPM) molecules and OCF-40 highly ordered protonated piperidine. Thus, it is assumed that the driving force controlling the transformation of OCF-5 into OCF-40 is the gradual decomposition of DPM into piperidine, which causes the dissolution of OCF-5 and subsequent formation of OCF-40. When pyridine is used as SDA instead of DPM only OCF-40 is obtained. In this system, the SDA does not influence the type of cluster obtained, but rather the dimension of the material obtained. It is also referred that in order to obtain large clusters, the relative concentrations of the cations involved must be carefully controlled. The cations involved have distinct functions. The cations M^{2+} or M^+ serve to counterbalance the charge requirements of the anions at the cluster core and the high-valence cations, M^{4+} and M^{3+}, serve to stabilize the unbound anions at the cluster surface.

(a)   (b)
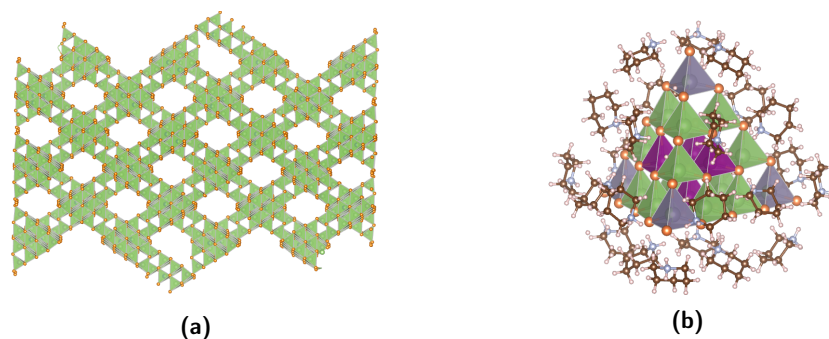
Figure 2.16: Representations of (2.16a) OCF-5 and (2.16b) OCF-40 obtained by Wu et al. (Ga - green, N - light gray, Se - orange, H - light pink, C - brown, Sn - gray) [116]

It is important to remark that all 3-dimensional structures based on T4 clusters composed by three different metals have diamond as topology, regardless of the SDA used [119].

The first synthesized T5 cluster had a missing core atom [120]. As there is no core atom, there are no sulfur atoms with 4-coordination, so the existence of divalent cations is not necessary. Thus, it is possible to achieve large-sized clusters without the need to incorporate divalent cations in the structure, provided that the clusters have at least one missing core atom. To synthesize a true T5 cluster it was necessary to add Cu to the In-S system, obtaining a cluster with the formula $In_{30}Cu_5S_{54}$ [121]. With this type of clusters it was possible to synthesize two distinct structures, one with a 2-dimensional framework, entitled UCR-16 (see Figure 2.17a), and another with a 3-dimensional framework, the UCR-17 (see Figure 2.17b). Both structures are obtained in the same batch, with UCR-16 as the dominant phase.
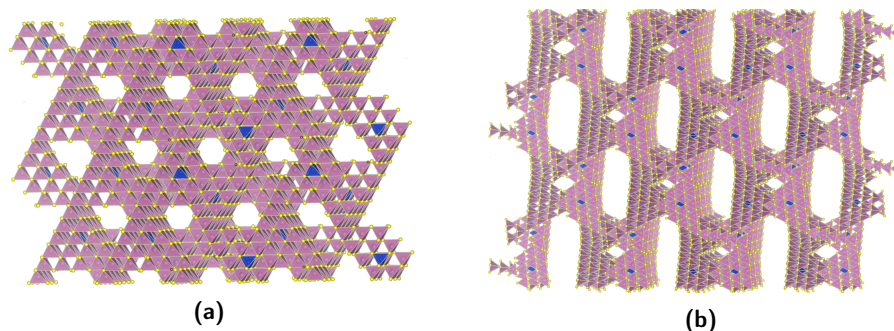
Figure 2.17: Representations of (2.17a) UCR-16 and (2.17b) UCR-17 obtained by Bu et al. where the organic part is not presented (In - pink, Cu - blue, S - yellow) [121]

From the T5 clusters obtained so far only the combination M^{3+}/M^{2+} has been observed to be possible.

Some years after the synthesis of a true T5 cluster, a T6 cluster was obtained (see Figure 2.18a) [122]. In order to achieve a cluster of that size without adding organic ligands to stabilize the negative charges, a mixed metal strategy is used, in order to have some high valence cations at the corners of the cluster that allow to reduce the global charge. In order to achieve that, the ratio M^{2+}/M^{3+} of an ideal T6 cluster should be one. In the obtained T6-based 2-dimensional structure (see Figure 2.18b), named OCF-100, all Zn ions are located at the core or at the faces of the cluster and the edges are occupied by In^{3+}.
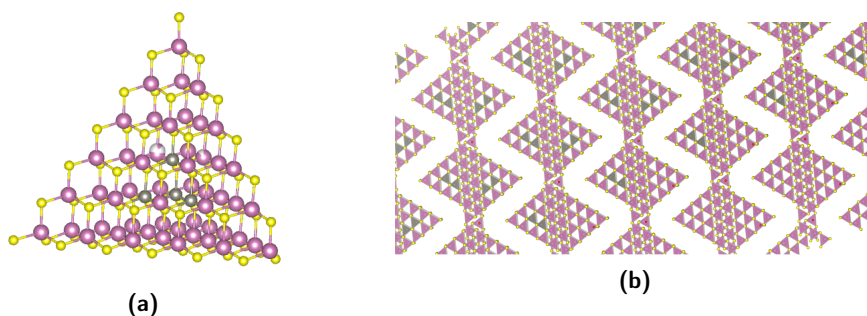
Figure 2.18: Representations of (2.18a) a T6 cluster and (2.18b) UCF-100 obtained by Xue et al. where the organic part is not presented (In - pink, Zn - black, S - yellow) [122]

ii. Pentasupertetrahedral Clusters Pn

Another example of tetrahedral clusters are the penta-supertetrahedral clusters Pn. Each Pn cluster can be seen as an assembly of four Tn tetrahedrally distributed into the four faces of one anti-Tn cluster. In an anti-Tn cluster the positions of cations and anions are exchanged in comparison with a Tn cluster. P1 (see Figure 2.19a) and P2 (see Figure 2.19b) clusters can be found as building blocks in a wide variety of open frameworks. Comparing to a Tn cluster of the same order, a Pn cluster has larger dimensions. For that reason, it is harder to prepare materials that uses Pn clusters as building units [83, 102, 123].

The number of cations in a Pn cluster is given by $t_n = [4n(n+1)(n+2)/6] + [(n+1)(n+2)(n+3)/6]$ and the number of anions is given by $x_n = [4(n+1)(n+2)(n+3)/6] + [n(n+1)(n+2)/6]$ (see Table 2.5).

Table 2.5: Composition of Pn clusters

Cluster Pn	t_n	x_n
1	8	17
2	26	44
3	60	90

(a)

(b)
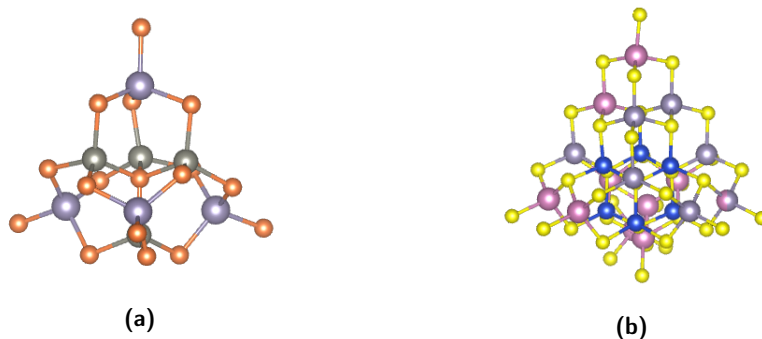
Figure 2.19: Representation of (2.19a) P1 and (2.19b) P2 clusters (In - pink, Cu - blue, S - yellow, Se - orange, Zn - gray, Sn - dark purple) [124, 125]

A P1 cluster consists of four T1 MX_4 clusters and one anti-T1 XM_4 at the core, resulting in a P1 cluster with the composition M_8X_{17} [123]. Zimmermann et al. [126] and Dehnen et al. [124] obtained P1 clusters of the type $M_4Sn_4Se_{17}$ (M = Zn, Mn, Co). A 3-dimensional structure was then obtained based on the $Cd_4Sn_3Se_{13}$ cluster, which derives from $Cd_4Sn_4Se_{17}$, originating a polar open-framework [127]. The extra-framework is occupied by K^+ cations which can be exchanged with other cations such as Li^+, Na^+ or Rb^+, while maintaining the structure of the material.

Continuing the research to obtain P1 clusters, Palchik et al. [128] obtained clusters based on sulfur instead of selenium, presenting the chemical formula $M_4Sn_4S_{17}$ (M = Zn, Mn, Co, Fe). Also based on the $Zn_4Sn_4S_{17}$ cluster, Manos et al. [129, 130] obtained a 3-dimensional structure in which each cluster is connected to four Sn atoms through the four terminal sulfur atoms. In turn, each Sn atom is connected to four clusters. The connection of clusters through metal centers is somewhat rare when it comes to methods of connection between clusters. Regarding the topology of the structure, the diamond type with three different sizes of cavities was detected (see Figure 2.20a). Each cavity has a distinct chemical reactivity, since the distribution of K^+ cations is different in each one (see Figure 2.20b). Due to the difference in cavity chemical reactivity, the structure has a high Cs^+ selectivity, even in the presence of large excess of Li^+, Na^+, K^+ or Rb^+. In the absence of Cs^+, the structure has a high ion-exchange capacity for NH_4^+, comparable to that of natural zeolites.

| (a) | (b) |
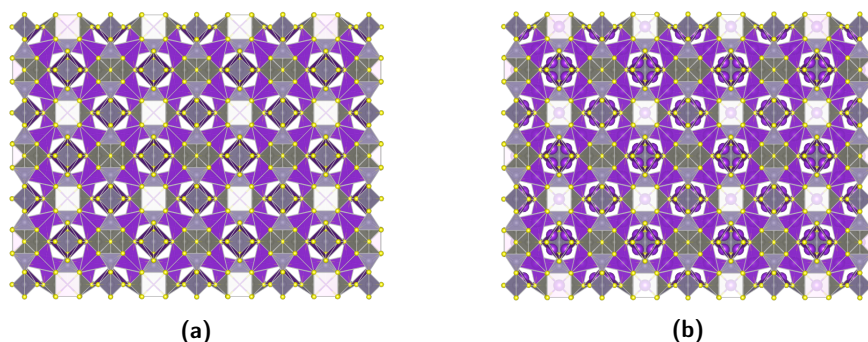
Figure 2.20: Representation of the structure obtained by Manos et al. [129, 130], (2.20a) without and (2.20b) with the presence of K^+ (Zn - gray, K - purple, S - yellow)

As for 3-dimensional structures based only on P2 clusters (see Figure 2.19b), Lv et al. [125] were able to synthesize such structures, entitled it MCOF-1 (see Figure 2.21a) and MCOF-2 (see Figure 2.21b). Both materials are based on a combination of Sn-In-Cu. MCOF-2 presents an interrupted open framework, which

is somewhat peculiar for these of type of structures. Both structures collapse after an ion exchange with Cs^+.

(a)

(b)
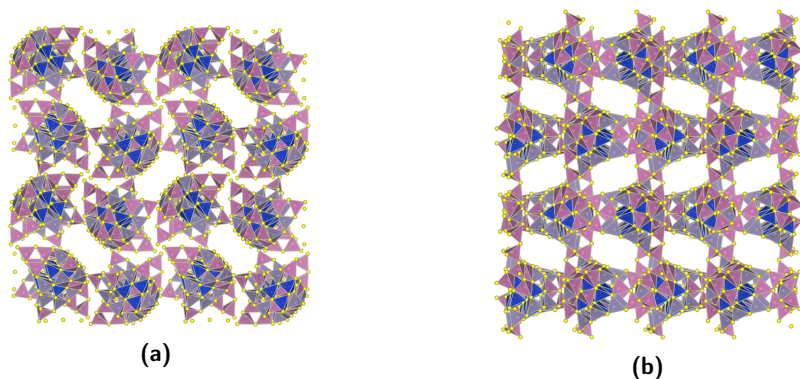
Figure 2.21: Representation of the structures (2.21a) MCOF-1, with a chiral *srs* topology, and (2.21b) MCOF-2, with a double diamond topology (Sn - gray, In - pink, Cu - Blue, S - yellow) [125]

As can be seen, most of the materials obtained are isolated clusters, and there is no example of a laminar structure composed by this type of clusters.

iii. Capped Supertetrahedral Clusters Cn

A third example of tetrahedral clusters is the Capped Supertetrhaedral series Cn. Each one of Cn cluster consists of a Tn clusters covered by a shell of atoms. Each face of the individual Tn cluster is covered by the bottom atomic sheet of a T$(n + 1)$ cluster and each corner covered by a metal-chalcogenide group. Thus, the stoichiometry of a M_xX_y type Cn cluster is equal to $x = [n(n+1)(n+2)]/6 + [4(n+1)(n+2)]/2 + 4$ and $y = [(n+1)(n+2)(n+3)]/6 + [4(n+2)(n+3)]/2 + 4$ (see Table 2.6) [83]. Representations of clusters C1 and C2 can be found in Figure 2.22.

Table 2.6: Composition of Cn clusters

Cluster Cn	x	y
1	17	32
2	32	54
3	54	84

(a)   (b)
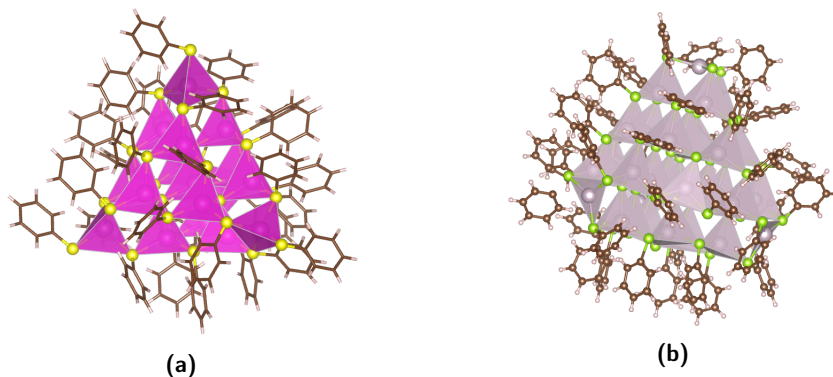
Figure 2.22: Representation of (2.22a) C1 [131] and (2.22b) C2 [132] clusters (Cd - pink, C - carbon, S - yellow, Se - green, H - light pink, Hg - gray)

Lee at al. [133] obtained for the first time a C1 cluster with the composition $S_4Cd_{17}(SPh)_{28}$. Later, a 3-dimensional double interpenetrated diamond structure based on the C1 $Cd_{17}S_4(SCH_2CH_2OH)_{26}$ cluster [131] and a 3-dimensional polymeric complex based on $[S_4Cd_{17}(SPh)_{24}(CH_3OCS_2)_{4/2}]_n \cdot n\ CH_3OH$ [134] were also synthesized.

The first material based on C2 cluster, with the composition $Cd_{32}S_{14}(SC_6H_5)_{36} \cdot DMF_4$, was obtained by Herron et al. [135]. Vossmeyer et al. [136] obtained a similar structure but with different organic parts. The C2 cluster was stabilized by the presence of $SCH_2CH(OH)CH_3$ instead of SC_6H_5. It was observed that the organic residue has a direct influence on the final architecture as well as on its optical properties of the final material. Other examples of materials based on the C2 cluster can be found in the literature [132, 137].

It can therefore be concluded that clusters of this series have not yet been obtained without the presence of an organic component and that the materials obtained are

only the result of the combination M^{2+}-X (X = S, Se). With the exception of the materials synthesized by Behrens et al. [137] and Eichhöfer et al. [132], all the others have in their composition Cd, a chemical element known for its toxicity.

iv. Oxyclusters

The addition of oxygen atoms to the clusters is a technique used to obtain large clusters, since it allows to diffuse the bond valence associated to the chalcogen anions. It is thus possible to obtain Tn clusters with $n > 2$ with only tetravalent metals [138]. Regarding more practical applications, metal chalcogenides may present stability problems, namely when used as photocatalysts. Therefore, it is expected that the formation of oxycluster-based structures will have a superior stability, being able to maintain the electronic properties, such as suitable band structures and favorable absorption on the visible region [139].

The first isolated $Sn_{10}O_4S_{20}^{8-}$ oxycluster (see Figure 2.23) was obtained in 1975 by Schiwy et al. [140].
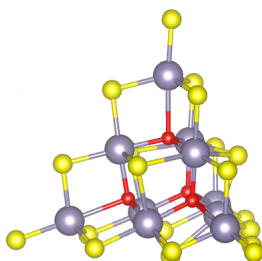
Figure 2.23: Representation of the T3 $Sn_{10}O_4S_{20}$ oxycluster (Sn - gray, O - red, S - yellow) [141]

Parise et al. [142] obtained for the first time a 3-dimensional structure with a 4-connected porous system using as building units the clusters previously obtained by Schiwy et al. [140]. The material obtained, refered as TETN-SnOS-SB2, presents a two-interpenetrating network and a topology analogous to cristobalite (see Figure 2.24). Continuing the research to obtain structures based on the T3 $Sn_{10}O_4S_{20}^{8-}$ cluster, the same research team obtained a layered material, called TMA-SnOS-SB3 [143]. It was observed that it is possible to obtain the TETN-SnOS-SB2 or TMA-SnOS-SB3 structures from the analogous non-oxygen frameworks. Although the source of oxygen is not known, one possible hypotheses for the origin of this element is the decomposition of the water used as a solvent in the syntheses gel.
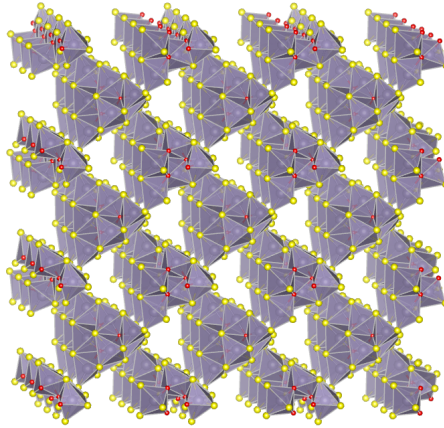
Figure 2.24: Representation of the structure TETN-SnOS-SB2 (Sn - gray, O - red, S - yellow) [142]

Aharia et al. [144] studied the Sn-Se chemical system. It was observed that there is a change of phases between a laminar material $TMA_2Sn_3Se_7$ to $TMA_2Sn_5Se_{10}O$, a 3-dimensional structure. What differentiates the achievement of the different phases are temperature and synthesis time. It was observed that for two days of synthesis, a laminar monocyclic phase is the only phase present. On the fourth day of synthesis, three distinct phases coexist: two laminar orthorombic and monocyclic phases and a third unknown phase. On the seventh day of synthesis there is a fourth phase associated with a 3-dimensional tetragonal material which becomes the only phase present after sixteen days of synthesis. The 3-dimensional material consists of T2 $Sn_4Se_{10}O$ clusters with the oxygen atom located at the center (see Figure 2.25).

(b)

(a)
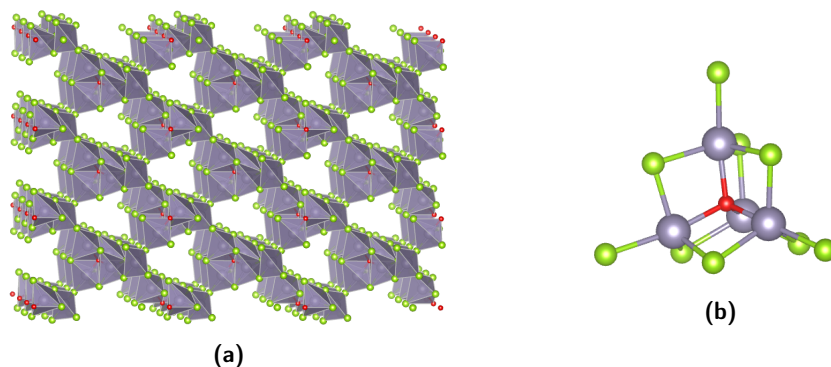
Figure 2.25: Representation of (2.25a) $TMA_2Sn_5Se_{10}O$ 3-dimensional material and (2.25b) its bulding unit (Sn - gray, O - red, Se - green) [144]

2.3.1.2   Non Tetrahedral Clusters

Due to the tetrahedral coordination of Tn, Pn and Cn clusters series, these units become the ideal candidates for the construction of open frameworks. However, the number of clusters available is limited. Moreover, clusters in the Pn and Cn series tend to maintain their isolated form rather than forming open frameworks. It is therefore desirable to create other series of clusters in order to enrich the cluster-based chalcogenide open frameworks [145].

i. Semi-cube Clusters

Regarding this type of clusters, two possible compositions stand out: Sb_3S_6 and Sn_3S_4 (see Figure 2.26) [85].

Figure 2.26: Representation of (2.26a) Sb_3S_6 and (2.26b) Sn_3S_4 building units [146] [147]

Parise et al. [148] obtained for the first time a layered material based on the Sb_3S_6 cluster. When tetramethylammonium ion is used as a SDA, a 3-dimensional structure is obtained [149]. Research continued into this chemical system, using large tertiary amines in order to try to produce materials with larger cavities [146]. When tetrapropylammonium hydroxide or triethylenetetramine is used, no 3-dimensional materials are obtained, but 1-dimensional and 2-dimensional structures, respectively.

The materials obtained by Bedard et al. [87, 88] in 1989 are the first examples of layered materials composed by the semicube Sn_3S_4 clusters. Jiang et al. [147, 150, 151, 152, 153] have studied the Sn-S system, obtaining layered materials based on the periodic arrangement of Sn_3S_4 clusters. Two types of layered materials were obtained: SnS-1 and SnS-3. The difference between the two is based on the way the clusters are connected. SnS-1 presents a hexagonally shaped 24-atom rings (see Figure 2.27a) and SnS-3 (see Figure 2.27b) has an elliptically shaped 32-atom rings.

(a)   (b)
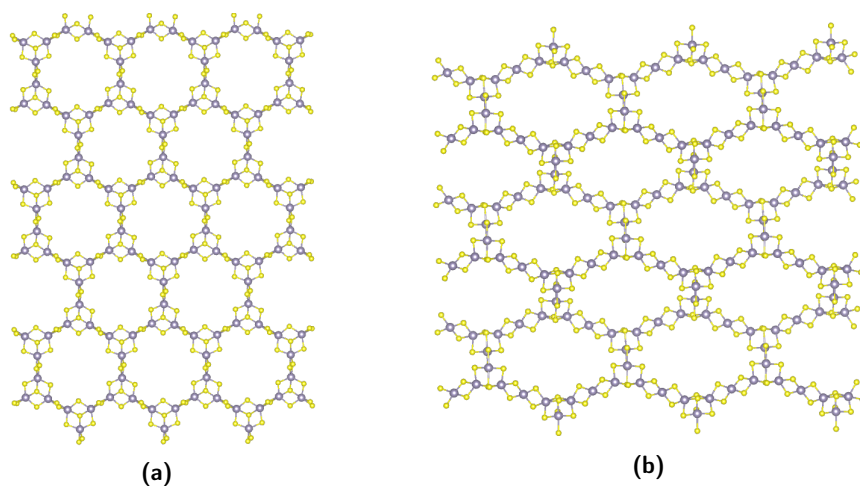
Figure 2.27: Representation of (2.27a) SnS-1 and (2.27b) SnS-3 laminar structures where the organic part was not represented (Sn - gray, S - yellow) [147]

It has been observed that when using small size SDAs, such as tetrabutylammonium hydroxide, SnS-1 is obtained and large size SDAs, for example tetrapropylammonium or tetrabutylammonium hydroxides, originate SnS-3. Both structures have a surprising flexibility. In order to accommodate SDAs with different shapes or dimensions, the synthesized materials may undergo a certain elastic deformation, changing the interlaminar spacings instead of forming a structure with a new topology. Another important characteristic of these materials is their thermal stability when removing the SDA used during their synthesis. SnS-1 was also subjected to an ion-exchange study. When tetramethylammonium hydroxide is located in the interlaminar space, it is possible to exchange part of the organic component with Na^+, Ca^{2+}, Co^{2+} or Ni^{2+}. However, the structure collapses when trying to exchange with Cu^{2+} or Ag^+ [154].

Bowes et al. [155] performed a more in-depth study of the SnS-1 structure. It was noted that it is possible to use tetramethylammonium (TMA), tert-butylammonium (TBA) or quinuclidinium (QUIN) as SDA's to obtain these structures. Such species occupy the interlaminar space, being responsible for counterbalancing the charge of the framework, but also to support it. The size and shape of the SDA is responsible for controlling the interlaminar distance, but also the thermal stability, adsorption and sieving properties of the material. The SnS-1 structure is able, to a certain extent, to exchange with other species, occurring swelling of the structure. When the species are too large, they are simply excluded, thus having a sieving effect.

2.3.1.3 Final Considerations

As can be seen from the examples presented above, there is a great variability of materials composed by different combinations of chemical elements and type of clusters. The materials obtained can have different dimensions, from isolated clusters, 1-dimensional chains of clusters, 2-dimensional lamelar and 3-dimensional materials. Due to the use of M_xX_y clusters instead of TO_4 tetrahedron, materials with a superior pore opening are obtained.

The most common method of connection between clusters is through bichalcogeneos bridges. However, it is still possible to find examples of materials where clusters are connected through polychalcogeneos bridges or metals. Evaluating the two chalcogens studied, S and Se, sulfur is the most common chalcogen present in the studied materials. The number of structures with Se is quite small in relation to the number of structures constituted by S.

For 3-dimensional materials, the typical topology is diamond, and most materials have an interpenetrated network, since it reduces the potential energy of the structure. As such, the extraframework volume, as well as the pore opening, tends to decrease.

Regarding the combination Ge-S or Ge-Se, it is observed that the number of 3-dimensional structures obtained is reduced, often requiring the use of other metals, such as Mn, Cu, or Ag to connect the different clusters. As for Sn-S or Sn-Se combinations, it is only possible to obtain laminar structures that have as building unit the semicube cluster. Two distinct laminar structures, SnS-1 and Sn-3, were synthesized and widely studied. Both structures are quite elastic, i.e. they can be obtained using a wide variety of SDAs. It is observed that when the SDA is altered, it will affect the interlaminar space, instead of obtaining a new topology. SnS-3 is obtained when large SDA's are used and SnS-1 is obtained when small SDA's are used.

It is also observed that M^{4+}-X^{2+} combinations originate small clusters, such as T2 and semicube clusters. In order to increase the size of the obtained clusters without the addition of other metals, oxygen is added to the system. Thus, it is already possible to find of T3 and T4 clusters consisting of the Sn, O and S or Se.

Both in the Ga-S and Ga-Se system the synthesized materials are composed of T3 clusters. It is observed that to obtain 3-dimensional structures composed by Ga and Se the gels should not present water in their composition and the final structures are not interpenetrated. On the contrary, for the the Ga-S system, the

gels should contain water in their composition and until now only interpenetrated 3-dimensional structures have been obtained.

By increasing the degree of complexity, it is possible to obtain structures where the clusters are composed of two types of metals. The addition of M^{2+} or M^+ cations to a M^{3+}-X^{2-} system allows the cluster size to be increased, from T3 to T4, T5 or T6. When inserting a M^{2+} or M^+ cation in an M^{4+}-X^{2-} system, the size of the Tn type clusters is not increased. P1 clusters are obtained when M^{4+} is Sn. It was also observed that when a M^{4+} cation is inserted in a M^{3+}-X^{2-} system, there is the probability of interrupted structures forming, since the overall negative charge of the cluster decreases.

2.3.2 Zeolite Analogue Structures

Zeolites are an important family of microporous crystalline inorganic materials, with numerous applications, namely in adsorption and separation processes and in the petrochemical industry as catalysts. Zeolites present the general formula A$_{x/n}$-[Si$_{1-x}$Al$_x$O$_2$]·m H$_2$O, where A is a metal cation with a valence n. Regarding their structure, two hundred and forty eight different architectures are known [156] based on the connection through the vertices of the tetrahedrons TO$_4$, where T, can be Si or Al. It is possible to find numerous porous materials based on zeolites, where the T atom is replaced by other elements, such as Ga, Ge or P [157]. However, these materials, because they are TO$_4$-based, are insulating and therefore have limited applications in photo, electro and optical fields.

In recent years, chalcogenide-based semiconductor zeolite analogs have been synthesized, where the oxygen is replaced by another chalcogen (such S, Se or Te), and the T atom by another tetracoordinated metallic cation. This strategy has been successful in obtaining semiconductor structures with high surface area and microporosity. However, the number of such structures with the IZA structure code remains small. Although there are many 3-dimensional microporous chalcogenide structures, as noted earlier, the presence of different anion coordination and the possible absence of tetravalent metal ions leads to the creation of non-zeolite structures [158]. As the size of the cluster increases, some characteristics appear that make the structure non-zeolite, such as anions with three or four coordination. Thus, the structures analogous to zeolites are generally based on T2 clusters, where metallic ions with high valence are used to balance the overall charge of the structure [159].

The first reference to a material with an analogue structure to a zeolite is from 1997. The material obtained by Cahil et. al [160] consists on the presence of T2

Ge_4S_{10} clusters that are connected by Mn. Using 1,4-diazabicyclo[2.2.2]-octane as SDA it is possible to obtain an analogous structure to Li-A (ABW, following the IZA code) zeolite where the SiO_4 and AlO_4 were substituted by MnS_4 and Ge_4S_{10}, respectively.

Zheng et al. [78] obtained a series of zeolite analogous materials based on the combination of M^{4+} and M^{3+} in the same Tn cluster. In order to synthesize clusters involving both cations and to avoid the formation of two types of clusters consisting only of M^{4+} or M^{3+}, Zheng et al. resorted to a synthesis in a non-aqueous medium in order to overcome such problem. The zeolite analogues materials obtained were design through a triple replacement of O^{2-} by S^{2-} or Se^{2-}, Si^{4+} by Ge^{4+} or Sn^{4+}, and Al^{3+} by Ga^{3+} or In^{3+}. Any M^{4+}/M^{3+} combination is possible. Due to the different possible combinations, it is feasible to customize the physical properties of the final material, such as band gap, luminescence, pore size, surface area, ion exchange and chemical stability. The previously synthesized 3-dimensional structures generally have a low thermal stability, collapsing at temperatures below 300°C. In order to avoid such a situation, the M^{4+}/M^{3+} ratio should preferably be between 0,2 and 1,2. This is contrary to the Loewenstein's rule of stability of zeolites, which states that the M^{4+}/M^{3+} ratio should not be less than 1 [161].

All materials can be described as a network of Tn clusters composed of M^{4+}-M^{3+}-X^{2-} which are connected to each other through the vertices by a bichalcogenide bridge. The different synthesized samples were grouped into four families: UCR-20, UCR-21, UCR-22 and UCR-23. Each family refers to materials with the same framework topology but different chemical compositions. UCR-20, UCR-21 and UCR-23 have as building units T2 type clusters while UCR-22 presents a pseudo-T4 cluster as building unit. Regarding topology, UCR-20 presents the sodalite framework (see Figure 2.28a), UCR-21 has a diamond structure, UCR-22 exhibits two interpenetrating diamond conformations and UCR-23 presents a CrB_4 type topology (see Figure 2.28). UCR-20 and UCR-21 show a large pore size, consisting of 12 T atoms, while UCR-22 and UCR-23 have an extra-large pore size, consisting of 24 and 16 T atoms, respectively. The main characteristics of the different obtained materials are summarized in the Table 2.7.

(a)

(b)

(c)

(d)
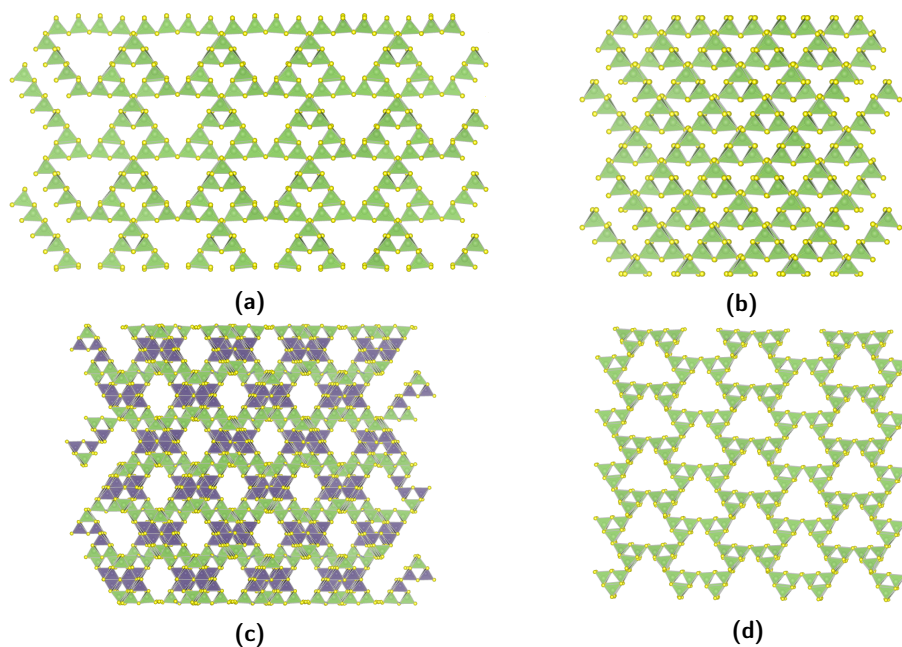
Figure 2.28: Representation of the different structures obtained by Zheng et al. [78] - (2.28a) UCR-20, (2.28b) UCR-21, (2.28c) UCR-22 and (2.28d) UCR-23 (Ga - green, Sn - grey, S - yellow)

The samples UCR-20GaGeS-AEP, UCR-20GaGeS-TAEA, UCR-20-InGeS-TMDP, UCR-20-InSnS-TMDP, UCR-21GaGeS-AEM, UCR-22InGeS-AEP, UCR-22GaSnS-AEP and UCR-23GaGeS-AEM were able to keep their structure after heating with air at 300°C for 1 hour. After a calcination at 350°C under N_2 atmosphere, 77 % of the nitrogen and 81 % of the hydrogen were eliminated from UCR-20-GaGeS-TAEA without collapsing of the structure. It was also observed that an ion exchange with CsCl is also able to eliminate the SDA. After the ionic exchange, it was observed that the sample exhibit a type I isotherm. As for the textural properties, it presents a Langmuir surface area of 807 m^2/g, a micropore volume of 0,23 m^3/g and an average pore diameter of 9,5 Å. For the remaining samples, there is no reference to whether they have been subjected to a calcination under N_2 atmosphere, ionic exchange or other technique to eliminate the SDA present in the framework.

Table 2.7: Different zeolite analogue materials obtained by Zheng et al. [78] and their chemical composition, final topology and pore size

Material	SDA	Composition			Cluster Composition	Structure	Pore Size
		M^{4+}	M^{3+}	X^{2-}			
UCR-20-GaGeS-TAEA	TAEA[1]	Ge	Ga	S	$Ga_{2,67}Ge_{1,33}S_8$	3D - SOD[2]	12 T Atoms
UCR-20-GaSnS-TMDP	TMDP[3]	Sn	Ga	S	$Ga_{1,8}Sn_{2,2}S_8$	3D - SOD	12 T Atoms
UCR-20-InGeS-TMDP	TMDP	Ge	In	S	$In_3Ge_1S_8$	3D - SOD	12 T Atoms
UCR-20-InSnS-TMDP	TMDP	Sn	In	S	$In_{2,5}Sn_{1,5}S_8$	3D - SOD	12 T Atoms
UCR-20-GaGeSe-TMDP	TMDP	Ge	Ga	Se	$Ga_xGe_{4-x}Se_8$	3D - SOD	12 T Atoms
UCR-21-GaGeS-APO	APO[4]	Ge	Ga	S	$Ga_{3,3}Ge_{0,7}S_8$	3D - D[5]	12 T Atoms
UCR-21-GaSnS-TAEA	TAEA[6]	Sn	Ga	S	$Ga_{2,32}Sn_{1,6}S_8$	3D - D	12 T Atoms
UCR-21-InGeS-APP	APP[7]	Ge	In	S	$In_{1,84}Ge_{2,16}S_8$	3D - D	12 T Atoms
UCR-21-InSnS-AEP	AEP[8]	Sn	In	S	$In_xSn_{4-x}S_8$	3D - D	12 T Atoms
UCR-21-GaSnSe-TAEA	TAEA[6]	Sn	Ga	Se	$Ga_{2,47}Sn_{1,53}Se_8$	3D - D	12 T Atoms
UCR-22-GaGeS-AEP	AEP	Ge	Ga	S	$Ga_{3,33}Ge_{0,67}S_8$	3D - DD[9]	24 T Atoms
UCR-22-GaSnS-AEP	AEP	Sn	Ga	S	$Ga_{2,13}Sn_{1,87}S_8$	3D - DD	24 T Atoms
UCR-22-InGeS-AEP	AEP	Ge	In	S	$In_{2,69}Ge_{1,31}S_8$	3D - DD	24 T Atoms
UCR-22-GaSnSe-TOTDA	TOTDA[10]	Sn	Ga	Se	$Ga_{1,73}Sn_{2,27}Se_8$	3D - DD	24 T Atoms
UCR-23-GaGeS-AEM	AEM[11]	Ge	Ga	S	$Ga_{2,67}Ge_{1,3}S_8$	3D - CrB$_4$[12]	16 T Atoms
UCR-23-GaSnS-AEM	AEM	Sn	Ga	S	$Ga_{2,29}Sn_{1,71}S_8$	3D - CrB$_4$	16 T Atoms
UCR-23-InGeS-AEM	AEM	Ge	In	S	$In_{1,84}Ge_{2,16}S_8$	3D - CrB$_4$	16 T Atoms

[1]Tris(2-aminoethyl)amine. [2]Sodalite (see Figure 2.10b). [3]4,4'-trimethylenedipiperidine. [4]dl-1-amino-2-propanol. [5]Diamond (see Figure 2.10a). [6]Tris(2-aminoethyl)amine. [7]1-(3-aminopropyl)-2-pipecoline. [8]1-(2-aminoethyl)piperazine. [9]Double Diamond. [10]4,7,10-trioxa-1,13-tridecanediamine. [11]N-(2-aminoethyl)morpholine. [12] (see Figure 2.10c).

Lin et al. [162] obtained structures rich in Ge or Sn, thus managing to obtain truly high silica zeolite analogous structures. It was observed that a small portion of divalent cations induce crystallization of Sn/Ge rich structures. Four different materials, CPM-120, CPM-121, CPM-122 and CPM-123 with different topologies were obtained. All the materials have as building units T2 clusters composed by M^{4+}-M^{2+}-X^{2-} and connected by a bichalcogenide bridge through the clusters vertices. The clusters of CPM-120 are organized to form the sodalite topology, obtaining the zeolite-type RWY framework. CPM-121 presents a non-interpenetrated diamond framework. Regarding CPM-122, it has a doubly-diamond framework. Finally, CPM-123 exhibits a CrB$_4$ type structure, the same as the zeolite framework code BCT. The main characteristics of the different obtained materials are summarized in the Table 2.8.

Table 2.8: Different zeolite analogue materials obtained by Lin et al. [162] and their chemical composition and final topology

Material	SDA	Composition			Cluster Composition	Structure
		M^{4+}	M^{3+}	X^{2-}		
CPM-120-ZnGeS	AEM[1]	Ge	Zn	S	$Zn_{0,81}Ge_{3,19}S_8$	3D - SOD[2]
CPM-121-ZnGeS	AEM, TBA[3]	Ge	Zn	S	$Zn_{0,93}Ge_{3,07}S_8$	3D - D[4]
CPM-122-ZnCdGeS	AEM, LTD[5], DBU[6]	Ge	Zn, Cd	S	$Zn_{0,65}Cd_{0,41}Ge_{2,9}S_8$	3D - DD[7]
CPM-123-ZnGeS	AEM, HA[8]	Ge	Zn	S	$Zn_{1,21}Ge_{2,79}S_8$	3D - CrB$_4$[9]
CPM-120-ZnSnSe	BPP[10]	Sn	Zn	Se	$Zn_{0,99}Sn_{3,01}Se_8$	3D - SOD
CPM-120-CdSnSe	BPP	Sn	Cd	Se	$Cd_{0,68}Sn_{3,32}Se_8$	3D - SOD

[1]N-(2-aminoethyl)morpholine. [2]Sodalite (see Figure 2.10b). [3]Tributylamine. [4]Diamond (see Figure 2.10a). [5]2,6-Lutidine [6]1,8-diazabicyclo[5.4.0]undec-7-ene. [7]Double Diamond. [8]1-hexylamine. [9] (see Figure 2.10c). [10]1,3-bis(4-piperidinyl)propane.

After the synthesis, due to the blocking of the porous system by the used SDAs, the samples show negligible gas adsorption. However, after exchange with Cs^+, the synthesized materials show an isotherm type I. For thermal stability, e.g. CPM-120-ZnGeS sample maintains structural and mechanical integrity when heated in air at $310°C$ for at least 1 hour, presenting itself as a thermally and chemically stable solid. Further studies have been conducted on the CPM-120-ZnGeS-AEM structure [163], namely on its charge selectivity. After performing an ionic exchange with Cs^+, it was observed that the structure presents a selectivity towards cationic organic molecules, and can thus be used to respond selectively according to the charge properties of the compounds. It was also observed that this chalcogenide material presents, besides charge selectivity, size selectivity.

Lin et al. [158] synthesized a structure that presented ordered interrupted sites, allowing to precisely doping the material and to help the creation of extra-large pores. The structure, called CSZ-5, is composed of tetracoordinated In and bico-ordinated Se making up a T2 cluster with a new boracite-related topology. Due to the method of connection between the clusters, this structure presents a multiple channel system. On the <100> direction it is possible to find an aperture of 12-MR and on the <110> direction the aperture is 16-MR. It is possible, due to the presence of interrupted sites, to dope the structure in order to adapt the electronic structure and the photoelectric characteristics of the material to a specific given applications.

So far, zeolite-like structures are all made up of type T2 clusters and result from the combination of M^{4+}/M^{3+} or M^{4+}/M^{2+}. Chen et al. [164] were able to synthesize a structure analogues to a zeolite based on the system $M^{4+}/M^{3+}/M^{2+}$ still using the T2 clusters as building units. Starting with the precursor gels previously used

by Lin et al. [162], these were doped with Ga^{3+}, In^{3+}, Sn^{4+} or Cd^{2+}. Through progressive additions of Ga precursor into the gel it is observed that it helps to improve the morphology of the CPM-120 crystals. A transition from irregularly block shaped crystals to regular rhombic-dodecahedron crystals is observed with the increase of Ga content. Regarding the location of Ga in the T2 cluster, it can occupy different positions, as it is shown that depending on the amount of Ga precursor added, it can substitute Ge or Zn. Ga will first substitute Ge and then it will replace Zn. For the addition of In, small quantities result in no uniform CPM-120 crystals being obtained. When the amount of In precursor increases, the formation of CPM-121 crystals is observed. After optimization of the experimental conditions, it was possible to obtain the CPM-121 structure where Ge and Sn coexist in the same cluster. The same was observed after the addiction of Cd, being possible to obtain the structure CPM-121 where Zn and Cd coexist in the same cluster. Figure 2.29 shows the main experimental results obtained.
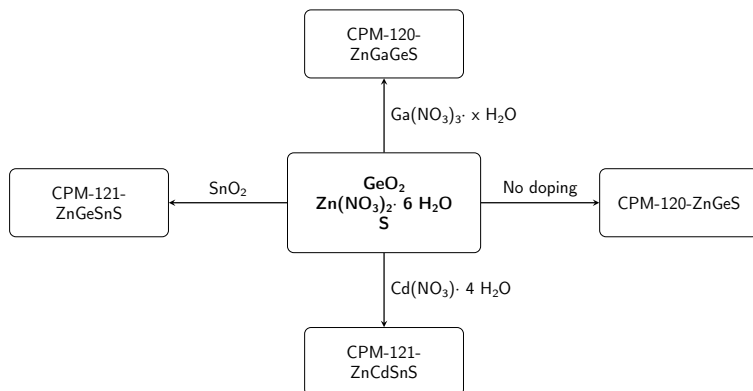
Figure 2.29: Scheme of the different forms of doping as well as the experimental results obtained in [164]

The stability of the structures after ion exchange with Cs^+ was also studied. It was found that the CPM-120 structure is much more stable than the CPM-121 structure, with a thermal stability up to 610°C and a highly porous framework.

Several 3-dimensional cluster-based structures have been synthesized, as can be seen in the first section of this chapter. However, for a structure to be considered analogous to a zeolite it is necessary that it contains M^{4+} cations in its composition and the anions of the structure must present a coordination equal to two. In view of these definitions, structures analogous to zeolites are limited to small clusters, since,

as seen above, with the increase in cluster size anions with different coordination numbers appear. Thus, most of the structures presented are clusters of type T2.

Of the different possible combinations of cations, the most similar to a zeolitic structure is the combination M^{4+}/M^{3+}, where M^{4+} can be Ge or Sn and M^{3+} Ga or In. It is also possible to find structures rich in M^{4+} cations, which are intended to be analogous to zeolitic structures rich in Si. It should be noted that in order to facilitate the crystallization of structures rich in M^{4+} cations, the addition of small quantities of M^{2+} cations is necessary. This technique, the addition of M^{2+} cations to M^{4+}-X^{2-} systems, is something that had already been done previously, namely in the first publication regarding the synthesis of a 3-dimensional structure based on the T2 Ge_4S_{10} cluster [97].

Although there are materials with a topology that corresponds to an IZA approved topology, it is possible to obtain architectures that are not accessible through the use of TO_4 tetrahedrons, since the system under study has different physical and chemical characteristics from those presented by a more usual zeolitic system. It is possible to find examples of structures with more exotic structures, with multiple channels of different dimensions, large pores or with different pores openings.

One of the great problems of these structures is their low thermal stability. It was observed that, in order to overcome this problem, the M^{4+}/M^{3+} ratio should be lower than one, an observation that goes against the Löwenstein's rule, which states that the M^{4+}/M^{3+} ratio should be higher than one. Although it has been shown that M^{4+}/M^{3+} ratios lower than one lead to an increase in the thermal stability of the structures, no justification has been provided so far for the violation of this rule.

Another issue associated with these structures is the difficulty of eliminating the SDA. The most commonly used technique for pore volume recovery is ion exchange with a cesium salt. Although this technique showed the best results, several structures collapse when trying to eliminate the SDA.

2.3.3 SDA free synthesis

The materials presented so far were obtained through traditional methods of synthesis. The method that stands out is the hydro(solvo)thermal. This methodology, based on the use of polar solvents, organic amines and temperatures below 200°C, is currently the most used to prepare crystalline metal chalcogenides with various structures. Similar to the zeolite synthesis, it is possible to find examples of synthesis of these materials where metal ions instead of organic amines are used as SDAs.

When a typical calcination is used to eliminate the organic component, most of the structures collapse due to the low thermal stability. On some cases, those organic compounds could be exchanged with other inorganic cations, such as Cs^+, without destroying the framework, thus releasing the porous volume of the structure. The synthesis of a system without the use of SDA's is still subject of research, both for environmental and economic reasons.

The only purely inorganic systems, which are known, consist of In^{3+}, In^{3+}/Cu^+ or In^{3+}/M^{2+} (M^{2+} = Mn, Zn, Cd) and are generally composed by T2, T4, T5 or P2 clusters. All materials were synthesized in the presence of alkali or alkaline earth metal cations under highly alkaline conditions. The synthesis conditions used lead to the crystallization of chalcogenides with encapsulated inorganic cations in their cavities. Seven different 3-dimensional frameworks were synthesized and may present different chemical compositions: ICF-5, ICF-17, ICF-21, ICF-22, ICF-24, ICF-25, ICF-26, ICF-27 and ICF-29 [123, 165, 166]. A great diversity of clusters can be observed, as well as topologies of the different synthesized structures (see Table 2.9).

Table 2.9: Different SDA's free materials obtained by Zheng et al. [123, 165, 166] and their chemical composition, final topology and pore size

Material	Composition				Cluster Composition	Structure	Pore Size	Ref.
	M^{3+}	M^{2+}	M^+	X^{2-}				
ICF-5-CuInS-Na	In	Cu	Na	S	T4 - $Cu_3In_{17}S_{33}$	3D - DD[1]	-	[165]
ICF-5-CdInS-Na	In	Cd	Na	S	T4 - $Cd_4In_{16}S_{33}$	3D - DD	-	[165]
ICF-5-MnZnInS-Na	In	Mn, Zn	Na	S	T4 - $Mn_{1,8}Zn_{2,2}In_{16}S_{33}$	3D - DD	-	[165]
ICF-5-CdInS-Li	In	Cd	Li	S	T4 - $Cd_4In_{16}S_{33}$	3D - DD	-	[165]
ICF-5-ZnInS-Na	In	Zn	Na	S	T4 - $Zn_4In_{16}S_{33}$	3D - DD	-	[165]
ICF-5-MnInS-Li	In	Mn	Li	S	T4 - $Mn_4In_{16}S_{33}$	3D - DD	-	[165]
ICF-17-InZnS-Na	In	Zn	Na	S	T5 - $In_{22}Zn_{13}S_{54}$	3D - DD	-	[165]
ICF-21-InSe-Na	In	-	Na	Se	T2 - In_4Se_{842}	3D - D[2]	-	[165]
ICF-22-InS-Li	In	-	Li	S	pseudo T4 - $In_{16}S_{32}$	3D - DD	-	[165]
ICF-24-InSSe-Na	In	-	Na	S, Se	T2 - $In_4S_{2,9}Se_{5,1}$	3D - ICF-24[3]	20 T Atoms	[165]
ICF-25-InS-SrCaLi	In	-	Sr, Ca, Li	S	T2 - In_4S_8	3D - ICF-25[4]	16 T Atoms	[165]
ICF-26-InLiS-Ca	In	-	Li, Ca	S	P2 - $Li_4In_{22}S_{44}$	3D - DD	-	[123]
ICF-27-InS-SrLi	In	-	Sr, Li	S	$In_{15}S_{29}$	3D	-	[165]
ICF-29-InS-Na	In	-	Na	S	$SIn_4(InS_4)_{6/2}$	3D - Perovskite	-	[166]

[1]Double Diamond. [2]Diamond (see Figure 2.10a). [3]ICF-24 topology (see Figure 2.30a). [4]ICF-25 topology (see Figure 2.30b)

ICF-5 consists of T4 clusters as building units and presents two interpenetrating diamond-type lattices. ICF-17 presents the biggest cluster as building unit, i. e. the T5. Regarding the topology, ICF-17 presents the same as ICF-5. ICF-21 consists of the connection of T2 clusters into a non-interpenetrating diamond-type lattice and it is the first selenium based structure with a 4-connected, 3-dimensional structure. The ICF-22 structure is composed of two interpenetrating lattices, whose building block is a pseudo T4 cluster. Both ICF-24 and ICF-25 present as building unit

the T2 cluster and a spiro-5 unit. ICF-24 has a ring size of 20 T atoms, being the first 4-connected, 3-dimensional framework with such ring size. ICF-25 also exhibits a large pore size, having a ring size of 16 T atoms. Like ICF-21, ICF-24 and ICF-25 present a 3-dimensional non-centrosymmetric framework structures (see Figures 2.30a and 2.30b, respectively). Regarding the last framework, ICF-27 shows a 6-connected network (see Figure 2.30c) where the $In_{18}S_{41}$ clusters can be consider as the octhaedral unit. Although there is enormous variability in terms of the obtained clusters, no structure was synthesized that had as a building unit the T3 cluster. According to Feng et al. [83], it is likely that for sulfur sites exposed to extraframework inorganic cations the coordination with other three M^{3+} becomes unfavorable due to the increase in bond valence sum, thus becoming unstable. As Loewenstein's rule, which states that the M^{4+}/M^{3+} ratio has to be higher than one [161], is not fulfilled, the concentration of extraframework mobile cations is higher, allowing the increase of ionic conductivity of the materials. As the synthesized structures present the limit situation, i.e. the M^{4+}/M^{3+} ratio is zero, as well as having an open porous system, the synthesized chalcogenides materials present a surprisingly high ionic conductivity.

(a)

(b)

(c)
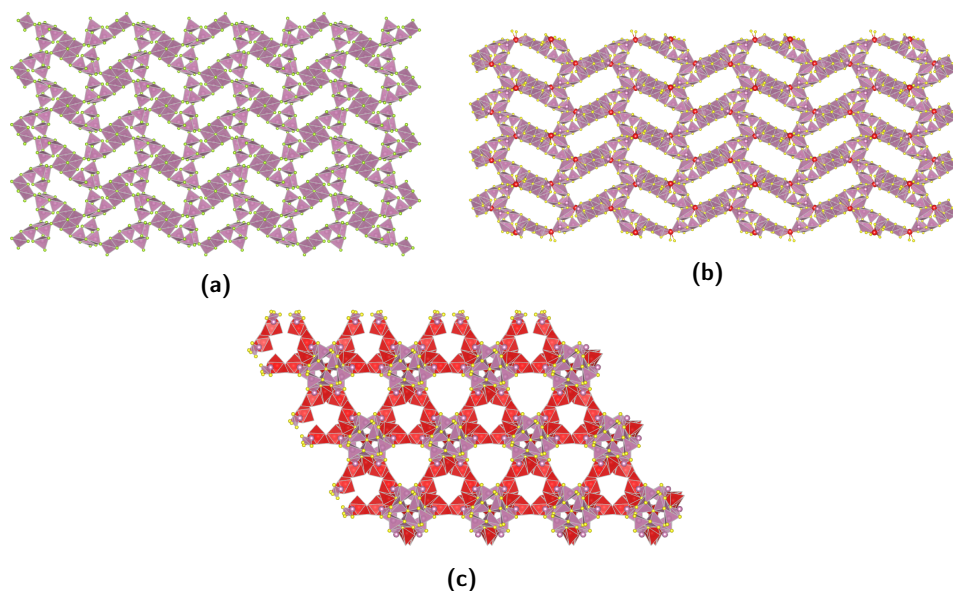
Figure 2.30: Representation of (2.30a) ICF-24, (2.30b) ICF-25 and (2.30c) ICF-27 (In - pink, S - yellow, Se - green, Sr - red) [165]

Another example of a structure obtained without the use of organic compounds as structural agents is ICF-26 [123]. ICF-26 is based on the P2 $Li_4In_{22}S_{44}$ cluster where Ca was used as countercation to stabilize the structure. As for the topology, it presents a double diamond topology. Due to the highly mobile extraframework cations, ICF-26 presents a fast ion condutivity like the structures presented in [165].

Continuing the research in this subject, Zheng et al. [166] synthesized a sodium indium sulfide hydrate, called ICF-29 (see Figure 2.31). The topology of this material can be derived from the perovskite, $CaTiO_3$. In order to obtain the ICF-29 structure from $CaTiO_3$ a triple substitution is performed: Ti^{4+} by SIn^{4+}, O^{2-} by InS_4^{5-} and Ca^{2+} by $Na_5(H_2O)_6^{5+}$. This material presents for the first time sulfur tetrahedrally bonded to four In ions. The remaining sulfurs have a 2-coordination, none with a 3-coordination. This absence is explained by the presence of the unusual SIn_4 unit. The existence of a tetracoordinated sulfur by four In ions can be explained by Brown's bond valence rule [95]. The In-S bond length is slightly longer than expected (2,55 Å instead of 2,44 Å), so the valence sum is 2,24, close to the theoretical value of two. This lengthening of the bond is explained by the fact that the remaining three In-S bonds involve bicoordenated sulfur, with a higher bond valence value than expected. The cavities of the synthesized material are occupied by $[Na_5(H_2O)_6]^{5+}$ clusters. Since the extraframework species are highly ordered when compared to previously synthesized ICF materials, ICF-29 showed a low ion conductivity.
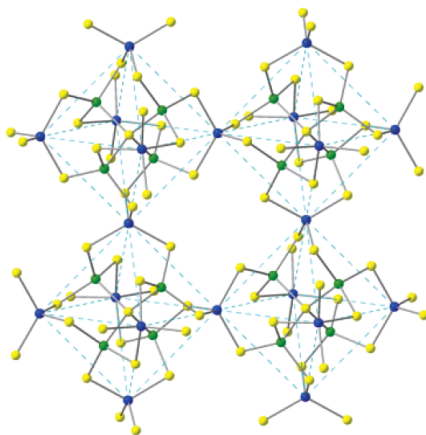
Figure 2.31: ICF-29 structure (blue: In^{3+}; yellow: S^{2-}; green: In^{3+} around tetrahedral S^{2-}) [166]

2.4   Photocatalytic Applications

Porous chalcogenides materials, as they allow to combine semiconductivity with open framework, become interesting structures for photocatalytic applications. As mentioned earlier (see Section 2.2.3), these materials, due to their electronic properties, have a band gap more suitable for the solar spectrum than metal oxides, the materials most studied as photocatalysts.

2.4.1   Band gap

The band gap of a material corresponds to the energy difference between the top of the valence band and the bottom of the conduction band. This parameter corresponds to the minimum energy that must be supplied to the material to promote an electron from the valence band to the conduction band. Thus, the band gap is closely related to the electrical conductivity. A material with a high band gap corresponds to an insulator and when the band gap is very small or when the valence and conduction bands overlap the material is called a conductor. A semiconductor has an intermediate band gap value and, as such, exhibits an electrical conductivity between that of a conductor and that of an insulator [167].

This property of semiconductors gains special attention when it comes to using such materials as photocatalysts. The performance of a photocatalyst depends strongly on the band structure and the value of the band gap. To use solar radiation efficiently as a source of radiation in a photocatalytic process, the band gap should be less than 3 eV in order to absorb light into the visible region [168].

The value of the band gap is highly influenced by clusters chemical composition, dimensions and the component present on the extra framework volume. The connection mode between clusters and consequent final topology of the material do not influence so strongly the band gap value [169, 170]. Taking into account the materials synthesized so far, it is possible to obtain materials with band gap values ranging from 0,69 eV [171] to 4,10 eV [113] and it is currently possible to modulate the value of this parameter as needed.

2.4.1.1 Chemical composition

The chemical composition of clusters is one of the main factors that influence the band gap value and it is through its variation that it is possible to customize the electronic properties of the structure. The two materials synthesized by Wu et al. [172] are two examples that show the importance of chemical composition in the value of band gap. SOF-20 and SOF-21 are two 3-dimensional materials composed by T2 clusters which, although they are composed of In, Sn and S, the Sn/In ratio is distinct. SOF-20 has a band gap value equal to 3,25 eV and SOF-21 equal to 3,07 eV and, according to the authors, what justifies such difference is the different Sn/In ratio.

Comparing the Ga-Se and Ga-S systems [112] (see Figure 2.32 and Table 2.3 for more information about this materials), it can be seen that the Ga-Se system band gap varies between 1,4 eV and 1,7 eV. Turning to the Ga-S system, the values of the band gap almost double, varying between 2,6 eV and 2,8 eV. Even with the insertion of Zn in the Ga-S system, the band gap still presents values higher than 2 eV. Thus, in this system, the framework anions have a greater impact on the value of the band gap than the framework cations.
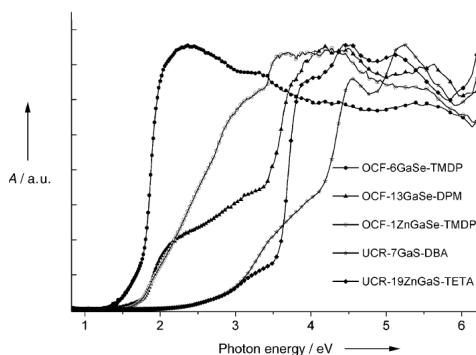
Figure 2.32: Optical absorption spectra of OCF-6GaSe-TMDP ($E_g = 1,43$ eV), OCF-13GaSe-DPM ($E_g = 1,76$ eV), OCF-1ZnGaSe-TMDP ($E_g = 1,71$ eV), UCR-7GaS-DBA ($E_g = 2,84$ eV) and UCF-19ZnGaS-TETA ($E_g = 2,60$ eV) (adapted from [112])

The doping of a certain chemical system allows to customize the electronic properties of the final material. When ISC-10-CdInS, isolated T5 clusters obtained in [173], are Cu-doped the band gap is reduced from 3,01 eV to 2,11 eV. It is also observed that when clusters are composed only by In-Cu-S the value of the band gap is 2,29 eV. Thus, the combination of Cu and Cd allows to obtain the lowest band gap value. Although a reduction in the band gap value is observed when

doping ISC-10-CdInS with Mn, from 3,01 eV to 2,87 eV, this reduction is not as significant as when doping with Cu [174].

It was possible to synthesize different isolated T4 clusters [116] and to compare the effect of Zn, Cu, S and Se in the band gap value. Looking at Figure 2.33a it is easy to conclude that when Cu and Se are present a lower value for the band gap is guaranteed. The type of amine present on the surface of the cluster also influences the final electronic properties (see Figure 2.33b).
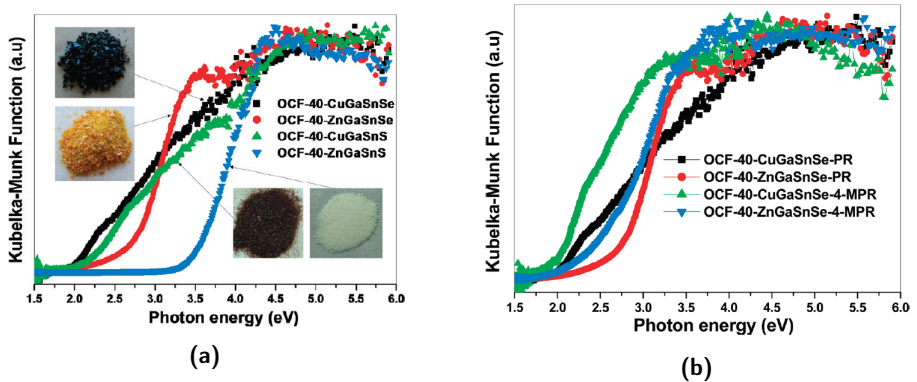
Figure 2.33: Optical absorption spectra of (2.33a) OCF-40-CuGaSnSe ($E_g = 1,91$ eV), OCF-40-ZnGaSnSe ($E_g = 2,71$ eV), OCF-40-CuGaSnS ($E_g = 2,11$ eV), OCF-40-ZnGaSnS ($E_g = 3,59$ eV), (2.33b) OCF-40-CuGaSnSe-PR ($E_g = 1,91$ eV), OCF-40-ZnGaSnSe-PR ($E_g = 2,71$ eV), OCF-40-CuGaSnSe-4-MPR ($E_g = 1,80$ eV) and OCF-40-ZnGaSnSe-4-MPR ($E_g = 2,60$ eV) (adapted from [116])

Since metal selenides and tellurides tend to have a lower band gap than sulfides, multi-chalcogen doping has been seen as a technique to customize electronic properties. Shen et al. [175] synthesized a set of isolated T3 clusters with different contents of chalcogen and observed that there is a systematic reduction of the band gap value along with the change from only S to the presence of Se and Te in the final material's composition (see Figure 2.34).
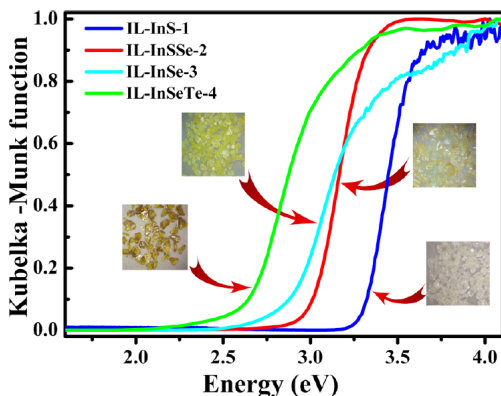
Figure 2.34: Optical absorption spectra of IL-InS-1 ($E_g = 3,31$ eV), IL-InSSe-2 ($E_g = 3,00$ eV), IL-InSe-3 ($E_g = 2,89$ eV) and IL-InSeTe-4 ($E_g = 2,65$ eV) (adapted from [175])

Wu et al. [176] synthesized a series of materials with the same topology but with different chemical composition in order to evaluate the impact that the chemical composition has on band structure. Thus, the Zn-Ga-Se was doped with Sn, S or both elements. When the system is doped with Sn, a red shift in the band gap is observed, evidenced by the reduction of OCF-5 band gap from 3,23 eV to 2,49 eV (see Figure 2.35a). However, when doping with S takes place, a blue shift of the band gap occurs, since OCF-1 band gap goes from 1,71 eV to 3,37 eV. Since doping showed opposite effects on the value of the band gap, it becomes interesting to evaluate the consequences of dual-doping. It is concluded that the direction of the shift depends on which of the elements is dominant. However, when comparing the undoped OCF-5-ZnGaSe-AEP ($E_g = 3,23$ eV) and OCF-5-ZnGaSnSeS-ECHA ($E_g = 2,54$ eV) it seems to suggest that Sn plays a dominant role against S. It was also evaluated the influence of the extra framework amine exhibits on the electronic properties. For the same topology, the nature of the amine on the band gap value presents less influence than doping phenomena (see Figure 2.35b).
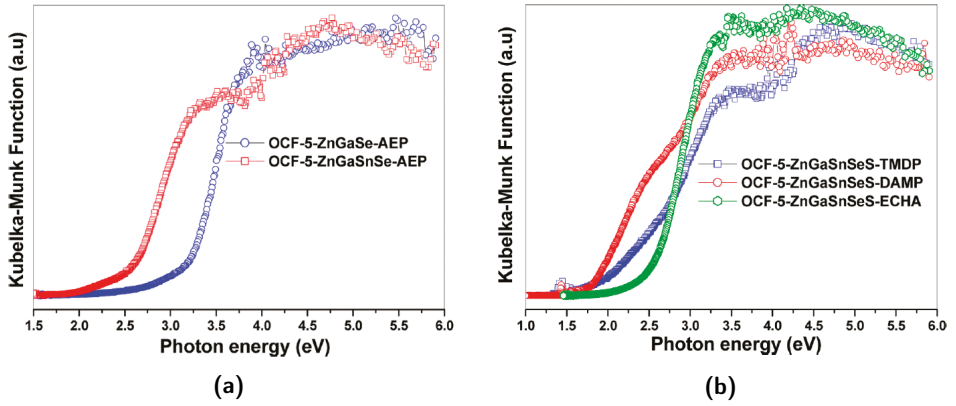
Figure 2.35: Optical absorption spectra of (2.35a) OCF-5-ZnGaSe-AEP ($E_g = 3{,}23$ eV), OCF-5-ZnGaSnSe-AEP ($E_g = 2{,}49$ eV) and (2.35b) OCF-5-ZnGaSnSeS-TMDP, OCF-5-ZnGaSnSeS-DAMP and OCF-5-ZnGaSnSeS-ECHA ($E_g = 2{,}54$ eV) (adapted from [176])

Although the clusters's chemical composition is one of the main characteristics that influence the band gap's value, Chen. et al [164] showed that the position of the dopant in the clusters influences the direction of the band gap shift. When CPM-120-ZnGeS-AEM is doped with Ga and this will subsist Ge, an increase in the band gap is observed. CPM-120-ZnGeS-AEM presents a band gap equal to 1,90 eV and when it is doped with Ga that will replace Ge, the band gap increases 2,30 eV. However, when Ga replaces Zn, a red shift of the band gap is observed. The band gap shift will depend on the amount of Ga added (see Figure 2.36).
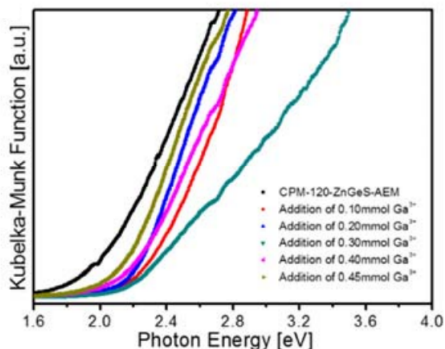
Figure 2.36: Optical absorption spectra of CPM-120-ZnGeS-AEM (E_g = 1,87 eV) and Ga-doped analogues (for an addition of 0,10 mmol Ga^{3+} - E_g = 2,30 eV, 0,20 mmol Ga^{3+} - E_g = 2,20 eV, 0,30 mmol Ga^{3+} - E_g = 2,12 eV, 0,40 mmol Ga^{3+} - E_g = 2,13 eV, 0,45 mmol Ga^{3+} - E_g = 2,16 eV) (adapted from [164])

The influence that the species present in the extra framework space has on the final electronic properties was also studied by other authors. Qi et al. [177], when studying the SnS-1 laminar structure, observed that there is a decrease in the value of the band gap when the structure is exchanged with Cs$^+$ or Sr^{2+}. The value of the band gap when it presents the organic compound in the interlaminar space is 2,92 eV. After ionic exchange with Cs$^+$ the value decreases to 2,82 eV or after ionic exchange with Sr^{2+} decreases to 2,60 eV. Filso et al. [178] compared the presence of two distinct organic species in the interlaminar space. They observed that when tris(2-aminoethyl)amine is located in the interlaminar space the band gap of the structure is 2,96 eV. When this species is exchanged with 1-(2-aminoethyl)piperidine the band gap increases to 3,21 eV.

2.4.2 Solar Fuels Production

2.4.2.1 H$_2$ Generation

The use of H$_2$ as an energy vector has been the subject of growing interest, as its oxidation produces only water and releases large amounts of energy (see Equation 2.1) [179, 180].

$$\tfrac{1}{2}O_2(g) + H_2(g) \rightarrow H_2O(l) \quad \Delta G^0 = -237 \, \text{kJ mol}^{-1} \quad \Delta H^0 = -286 \, \text{kJ mol}^{-1}$$
$$(2.1)$$
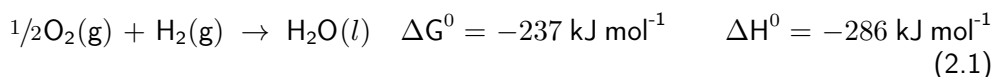
Currently, the production of H_2 is done through natural gas reforming. Besides having a non-renewable origin and requiring high temperatures, CO_2 and traces of CO are co-obtained. Consequently, in order to obtain H_2 without the need of non-renewable sources as well as avoiding the production of greenhouse gases, the dissociation of water has been seen as a viable alternative [179].

Whether the energy source comes from electricity (a electrochemical process) or sunlight (a photochemical process), the decomposition of water in liquid state to form H_2 starts with the adsorption of H^* on the surface of the catalyst, which can be described by Volmer's reaction for an acidic (see Equation 2.2) or a basic medium (see Equation 2.3). In the Equations 2.2 and 2.3, $*$ represents an empty active site and H^* a hydrogen atom connected to an active site [36].

$$H_3O^+\,(aq)\,+\,e^-\,+\,*\,\rightleftharpoons\,H^*\,+\,H_2O\,(l) \qquad \text{(Volmer reaction - acidic)} \quad (2.2)$$

$$H_2O\,(l)\,+\,e^-\,+\,*\,\rightleftharpoons\,H^*\,+\,OH^-\,(aq) \qquad \text{(Volmer reaction - basic)} \quad (2.3)$$
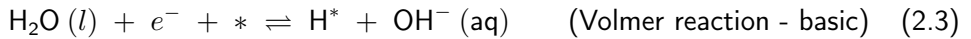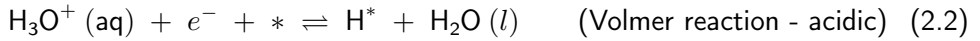
Depending on the nature of the catalyst, the reaction may be between two adsorbed hydrogen, i.e. it may be described by the Tafel equation (see Equation 2.4), or it may be between an adsorbed hydrogen atom and a H^+ from the electrolyte, which can be described by the Heyrovsky equations (see Equations 2.5 and 2.6 for acidic and basic medium, respectively) [36].

$$H^*\,+\,H^*\,\rightleftharpoons\,H_2\,(g)\,+\,2\,* \qquad \text{(Tafel reaction - acidic and basic)} \quad (2.4)$$

$$H^*\,+\,H_3O^+\,(aq)\,+\,e^-\,\rightleftharpoons\,H_2\,(g)\,+H_2O\,(l)\,+\,* \qquad \text{(Heyrovsky reaction - acidic)}$$
$$(2.5)$$

$$H^*\,+\,H_2O\,(l)\,+\,e^-\,\rightleftharpoons\,H_2\,(g)\,+OH^-\,(aq)\,+\,* \qquad \text{(Heyrovsky reaction - basic)}$$
$$(2.6)$$
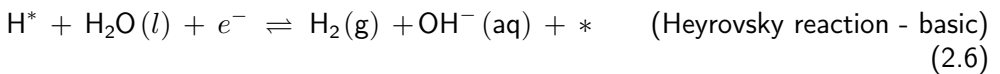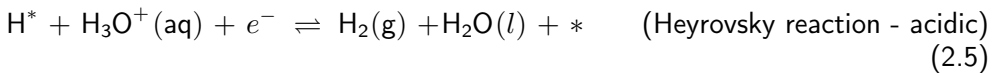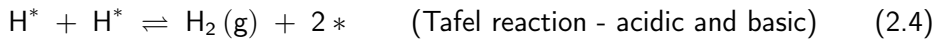
i. Photocatalytic Water Splitting

The decomposition of water is a non-spontaneous reaction, that is, it presents a $\Delta G^0 > 0$ (see Equation 2.1). A catalyst allows the alteration of the kinetics of a reaction, but not its thermodynamics. Thus, it only promotes spontaneous reactions, i.e., reactions with negative ΔG^0. Photocatalysis, by converting light into chemical energy, makes the process of water decomposition feasible. In this way, it is possible to produce a clean fuel, H_2, from an abundant and cheap source, H_2O [181]. Equations 2.7 and 2.8 illustrate the two reactions that occur during the photodegradation of water, the hydrogen evolution reaction (HER) and the oxygen evolution reaction (OER) respectively [182].

$$2H^+ + 2e^- \rightarrow H_2 \tag{2.7}$$

$$2\,H_2O + 4\,h^+ \rightarrow O_2 + 4\,H^+ \tag{2.8}$$
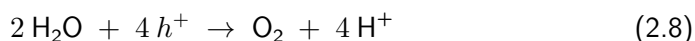
Generally, HER involves adsorbing hydrogen intermediates to the surface of a catalyst and recombination-desorption of molecular hydrogen [183].

OER involves a process of four charge carriers transfer and is more complicated than HER. Therefore, OER is considered to be the rate-determining step in the whole reaction [183]. According to Nørskov et al. [184, 185, 186], the molecular oxygen is generated via a surface HOO* intermediate and the reaction happens at the coordinatively unsaturated atoms. According to this computation, OER involves four elementary steps, each step involving the electron transfer coupled with electron removal (see Equations 2.9, 2.10, 2.11 and 2.12 where $*$ represents a surface cite and Y^* an attached Y intermediate on the surface). It was also found that the water chemisorbetion or the O^* formation could be the limiting step (see Equation 2.9 and 2.11).

$$H_2O + * \rightarrow HO^* + H^+ + e^- \tag{2.9}$$

$$HO^* \rightarrow O^* + H^+ + e^- \tag{2.10}$$

$$O^* + H_2O \rightarrow HOO^* + H^+ + e^- \tag{2.11}$$

$$HOO^* \rightarrow * + O_2 + H^+ + e^-$$ (2.12)
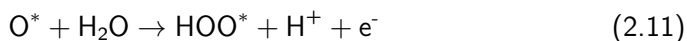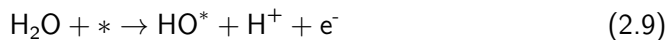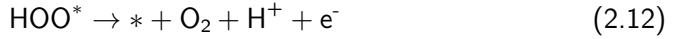
Dionigi et al. [187] studied the gas phase photocatalytic water splitting with $Rh_{2-y}Cr_yO_3/GaN:ZnO$ and its mechanism. It was concluded that the photocatalytic activity is proportional to the relative humidity of the gas instead of the absolute water pressure. The BET adsorption model predicts a linear relationship between the amount of molecule adsorbed and the relative humidity. Therefore, it possible to relate the photocatalytic hydrogen production rate with the chemisorbed water coverage (see Equation 2.13 where k_{H_2} represents the rate constant of the water splitting reaction and H_2O_{surf} the chemisorbed water coverage). It was also observed that the initial reaction rate is higher at the beginning of the reaction, something similar observed by Shearer et al. [188]. As the reaction proceeds, the water coverage is reduced compared to the initial water coverage and, therefore, the reaction rate also decreases (see Equation 2.13 and Figure 2.37).

$$r_{H_2} = k_{H_2} \cdot H_2O_{surf}$$ (2.13)

(a) Dark equilibrium	(b) UV on initial	(c) UV on equilibrium

quantity of chemisorbed H_2O = $H_2O_{surf,dark}$

$r(H_2)_{initial} = k(H_2).H_2O_{surf,dark}$

$r(H_2)_{UV} = k(H_2).H_2O_{surf, UV}$
$H_2O_{surf,UV} < H_2O_{surf,dark}$
$r(H_2)_{UV} < r(H_2)_{initial}$
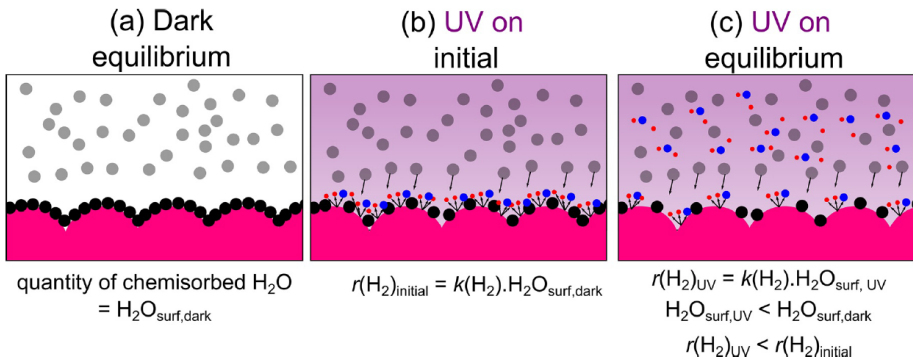
Figure 2.37: Scheme of gas phase photocatalytic hydrogen production (adapted from [188])

Comparing the quantum efficiencies between liquid and gas phases, gas phases usually present a lower efficiency. According to Dionigi et al. [187] this can be explained by limitations on the surface conduction of protons H^+ for OER centers to the HER centers. The conduction of protons is easier in an acid pH solution (something that can be controlled on liquid phase and not of gaseous phase) and a higher relative humidity is also beneficial, since it allows the creation of a more connected water film covering the particles increasing the protons mobility.

Considering the reduction potential of H^+ to H_2 ($E^0 = $ -0,41 V vs. normal hydrogen electrode (NHE) at pH 7,00) and the oxidation potential of H_2O in O_2 ($E^0 = $ 0,82 V vs. NHE at pH 7,00), the photon's minimum theoretical potential is 1,23 V. However, it is observed that there is an activation barrier when transferring the charges from the photocatalyst to the water molecules. Taking into account the overpotential associated with the oxidation and reduction reactions, a band gap between 1,7 eV and 2,2 eV is required to decompose the water [32, 36, 40].

When only pure water is used in the reaction system the process is generally inefficient (see Equation 2.8) [179]. As such, in order to increase the production of H_2, sacrificial agents are usually used as electron donors. These compounds, by scavenging the holes, allow a more favorable kinetic and therefore enhance the global redox mechanism. Electron donors have to react faster with the holes than water in order to avoid water oxidation. Moreover, no O_2 is produced, since the water oxidation reaction does not occur, so there is no need to purify the final gas. Usually, CH_3OH or a mixture of NaS/Na_2SO_3 is added to the aqueous system for that purpose. However, it produces waste products, thereby reducing the sustainability of the process [40, 181]. An alternative to the use of sacrificial agents is the use of co-catalysts (such as Pt), which allow to decrease the activation energy and enhancing global efficiency.

ii. Cluster-based chalcogenide materials

As presented earlier, open framework metal chalcogenides, due to their band structure, band gap value and open architecture, are excellent candidates to be used on the solar fuel production processes.

Table 2.10 presents several chalcogenide cluster-based materials that were used as photocatalysts in the generation of H_2. Different authors use this reaction to show that the material they synthesized can be used as a photocatalyst [162, 189, 190, 191].

Table 2.10: Summary of cluster-based chalcogenide materials for H_2 photogeneration

Photocatalysts	Cluster	Chemical Composition	Band gap (eV)	Dimension	Light Source	Co-catalyst	Reactant solution	Activity (μmol h^{-1} g^{-1})	Ref.
ICF-5CuInS-Na	T4	In-Cu-S	2	3D	Xe 300W (λ>420 nm)	-	Na$_2$S (0,5 M) Na$_2$SO$_3$ (O,5 M)	18 1,8	[76]
UCR-28	T2, T1	Ge-Zn-S	3,4	2D	Xe 300 W	-	Na$_2$SO$_3$ (O,5 M)	6,5	[189]
CPM-120-ZnGeS	T2	Ge-Zn-S	1,87	3D	Xe 300 W	-	Na$_2$S (0,25 M), Na$_2$SO$_3$ (0,1M) CH$_3$OH	2000 300	[162]
CPM-121-ZnCdGeS	T2	Ge-Cd-Zn-S	1,95	3D	Xe 300 W	-	Na$_2$S (0,25 M), Na$_2$SO$_3$ (0,1M)	1417,2	[164]
CPM-120-ZnGaGeS	T2	Ge-Ga-Zn-S	2,13	3D	Xe 300 W	-	Na$_2$S (0,25 M) & Na$_2$SO$_3$ (0,1M)	1130,6	[164]
CPM-121-ZnGeSnS	T2	Ge-Sn-Zn-S	2,18	3D	Xe 300 W	-	Na$_2$S (0,25 M) & Na$_2$SO$_3$ (0,1M)	950	[164]
-	T2	Ge-S	-	0D	Xe 5 W (λ>420 nm)	Ag	Na$_2$S (0,1 M), Na$_2$SO$_3$ (0,1M)	0,95	[192]
Cluster + Ag NWs	T2	Ge-S	-	0D/1D/1D	Xe 5 W (λ>420 nm)	Ag	Na$_2$S (0,1 M), Na$_2$SO$_3$ (0,1M)	4,57	[192]
-	T3	In-S	-	0D	Xe 5 W (λ>420 nm)	Ag	Na$_2$S (0,1 M), Na$_2$SO$_3$ (0,1M)	2,68	[192]
Cluster + Ag NWs	T3	In-S	-	0D/1D/1D	Xe 5 W (λ>420 nm)	Ag	Na$_2$S (0,1 M) & Na$_2$SO$_3$ (0,1M)	9,42	[192]
-	T4	Sn-Ga-Zn-Mn	-	0D	Xe 5 W (λ>420 nm)	Ag	Na$_2$S (0,1 M), Na$_2$SO$_3$ (0,1M)	1,55	[192]
Cluster + Ag NPs	T4	Sn-Ga-Zn-Mn	-	0D/0D/0D	Xe 5 W (λ>420 nm)	Ag	Na$_2$S (0,1 M), Na$_2$SO$_3$ (0,1M)	20,09	[192]
Cluster + Ag NWs	T4	Sn-Ga-Zn-Mn	-	0D/1D/1D	Xe 5 W (λ>420 nm)	Ag	Na$_2$S (0,1 M), Na$_2$SO$_3$ (0,1M)	35,68	[192]
-	T5	In-Mn-S	-	0D	Xe 5 W (λ>420 nm)	Ag	Na$_2$S (0,1 M), Na$_2$SO$_3$ (0,1M)	0,47	[192]
Cluster + Ag NWs	T5	In-Mn-S	-	0D/1D/1D	Xe 5 W (λ>420 nm)	Ag	Na$_2$S (0,1 M), Na$_2$SO$_3$ (0,1M)	7,14	[192]
-	T5	In-Cu-S	-	0D	Xe 5 W (λ>420 nm)	Ag	Na$_2$S (0,1 M), Na$_2$SO$_3$ (0,1M)	1,92	[192]
Cluster + Ag NWs	T5	In-Cu-S	-	0D/1D/1D	Xe 5 W (λ>420 nm)	Ag	Na$_2$S (0,1 M), Na$_2$SO$_3$ (0,1M)	5,42	[192]
T4-1	T4	In-Cd-S	3,25	3D	Xe 300 W (λ>420 nm)	Pt	Triethanolamine	3,5	[193]
T4-2	T4	In-Cd-S-Se	2,76	3D	Xe 300 W (λ>420 nm)	Pt	Triethanolamine	5,6	[193]
T4-3	T4	In-Cd-Se	2,6	3D	Xe 300 W (λ>420 nm)	Pt	Triethanolamine	15,9	[193]
T4-1	T4	In-Cd-S	Pt	0D	Xe 300 W (λ>420 nm)	Pt	Triethanolamine	6,1	[193]
T4-2	T4	In-Cd-S-Se	Pt	0D	Xe 300 W (λ>420 nm)	Pt	Triethanolamine	27,5	[193]
T4-3	T4	In-Cd-Se	Pt	0D	Xe 300 W (λ>420 nm)	Pt	Triethanolamine	91,5	[193]
T5-3	T5	In-Cd-Se	2,67	0D	Xe 300 W (λ>420 nm)	Pt	Triethanolamine	8,1	[74]
T5-4	T5	In-Cd-S-Se	2,79	0D	Xe 300 W (λ>420 nm)	Pt	Triethanolamine	17,3	[74]
T5-5	T5	In-Cd-S-Se	2,85	0D	Xe 300 W (λ>420 nm)	Pt	Triethanolamine	44,5	[74]

ii.a. Effect of open architecture

It can be observed that, by shifting from a dense structure to an open architecture structure, it is possible to obtain materials with a band structure suitable for water splitting.

Of the different structures previously obtained in Refs. [78] and [165], the one that stands out most is the ICF-5InCuS-Na structure, since it has a chemical composition similar to $CuInS_2$, a material with important photovoltaic applications [194]. ICF-5CuInS-Na is capable of producing up to 18 μmol h^{-1} g^{-1} of H_2 when irradiated with visible light and while using Na_2S (0,5 M) as a sacrificial agent (see Figure 2.38). This catalyst has a quantum efficiency of 3,7% at 420 nm. Although it has a lower quantum efficiency than the Pt/CdS photocatalyst ($\sim$ 28%) [195], the quantum efficiency is much higher when compared with the dense phases of $CuIn_5S_8$ ($\sim$ 0,02% while using AgS_2 as a co-catalysts) or $CuInS_2$ (lower than the one presented by $CuIn_5S_8$) [65].
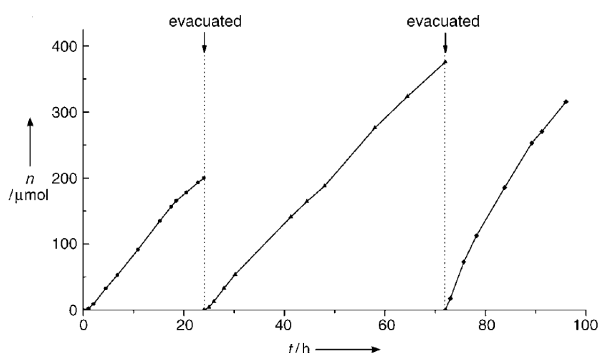
Figure 2.38: Photocatalytic H_2 evolution of ICF-5CuInS-Na (0,5 g) using as sacrificial agents aqueous solutions of Na_2S (0,5 M) and using as light source 300 W Xe lamp, λ>420 nm (adapted from [76])

The open architecture also allows the incorporation of optically active organic molecules or metal complexes that improve visible-light absorption. The [Fe(2,2'-bipyridine)$_2$]$^{3+}$ complex was incorporated into UCR-20GaGeS-TAEA by means of an ion exchange. After the ion exchange, the hybrid material obtained has an absorption that extends from the UV to the visible-light region (see Figure 2.39). When irradiating UCR-20 GaGeS-TAEA with UV light it presents catalytic activity, and no activity occurs when irradiating the structure with visible light. However,

the hybrid material already shows photocatalytic activity with visible light for at least 24 hours.
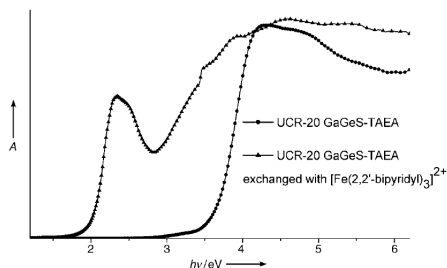
Figure 2.39: UV/Vis diffuse reflectance spectra of UCR-20 GaGeS-TAEA before and after an ionic exchange with the $[Fe(2,2'-bipyridine)_2]^{3+}$ complex (adapted from [76])

ii.b. Impact of the chemical composition and cluster size

Chen. et al [164] used the materials CPM-120 and CPM-121 as photocatalysts for H_2 generation. The structures CPM-121-ZnCdGeS, CPM-120-ZnGaGeS and CPM-121-ZnGeSnS were evaluated (see Figure 2.40). CPM-121-ZnCdGeS presents the highest activity, showing that the presence of Cd^{2+} in the T2 cluster exhibits a positive effect on the photocatalytic performance.
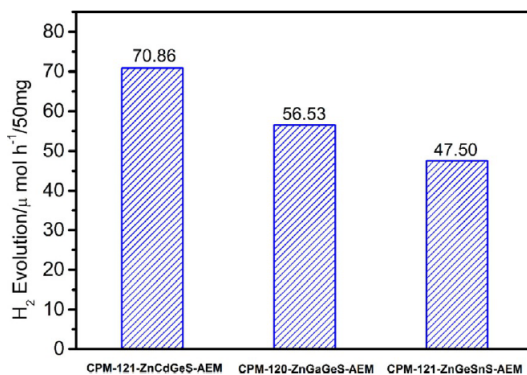
Figure 2.40: Photocatalytic H_2 evolution of CPM-121-ZnCdGeS, CPM-120-ZnGaGeS and CPM-121-ZnGeSnS (50 mg) in the presence of Na_2S (0,25 M) and Na_2SO_3 (0,10 M) as sacrificial agents and using 300 W Xe lamp as light source [164]

Hao et al. [193] synthesized three distinct 3-dimensional structures, named T4-1 ([BMMIm]$_9$[Cd$_3$In$_{17}$S$_{31}$Cl$_4$]), T4-2 ([BMMIm]$_9$[Cd$_3$In$_{17}$S$_{13}$Se$_{18}$Cl$_4$]) and T4-3 ([BMMIm]$_9$[Cd$_3$In$_{17}$Se$_{31}$Cl$_4$][4,4'-bpy]), and these structures were treated with ultrasounds in DMSO in order to obtain isolated and highly dispersed T4 clusters in solution. Figure 2.41a shows the results of the photocatalytic tests of the samples, before and after the ultrasonic treatment. Before this process, the samples show low photocatalytic, which gradually increases during the 5 hours of the test. After the ultrasonic treatment, it was observed that T4-2 and T4-3 present a photocatalytic activity about five times higher than the solid samples. However, the T4-1 sample does not present such an increase in photocatalytic activity since this sample presented difficulties of dispersion in most common solvents.
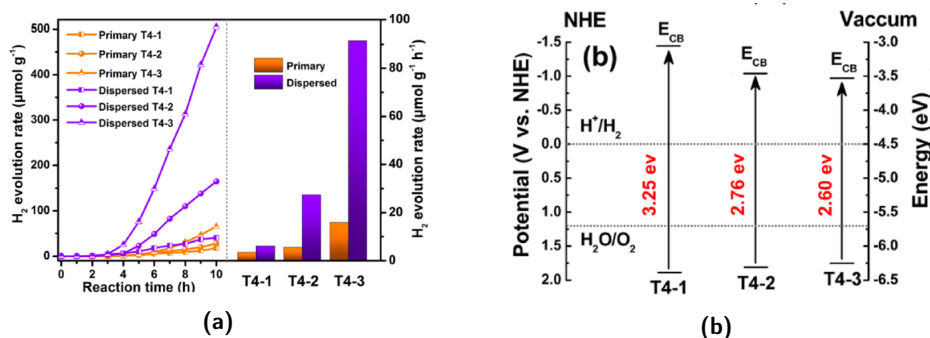
Figure 2.41: (2.41a) Photocatalytic H$_2$ evolution of T4-1, T4-2 and T4-3 (25 mg) in the presence of triethanolamine (TEOA) as sacrificial agent, Pt as co-catalyst and using 300 W Xe lamp with a cutoff filter (λ>420 nm) as light source. (2.41b) Band structures of T4-1, T4-2 and T4-3 obtained by impedance-potential measurements (adapted from [193])

The differences in photocatalytic activities can be explained due to different factors. Different chemical compositions and cluster sizes lead to changes in the position of the bands (see Figure 2.41b), directly affecting the photocatalytic generation of H$_2$. As seen before, selenides usually have a lower band gap than sulfides. Thus, through the insertion of Se in the clusters it is expected that the band gap of the structures decreases, a phenomenom that occurs in the three structures studied. Isolated T4 clusters allow a larger number of surface sites to be exposed and the average mean-path of the electrons is reduced, so the probability of charges recombination is reduced and the electrons reach the surface with more energy.

It is also possible, by analyzing the transient photocurrent response of a structure, to make observations regarding its capacity to create and separate charges. This analysis was performed on the isolated clusters T4-2 and T4-3 (see Figure 2.42)

and it was observed that, since T4-3 presents an induced photocurrent higher than T4-2, T4-3 presents a higher production capacity and charge separation, thus explaining why it exhibits a higher photocatalytic activity.
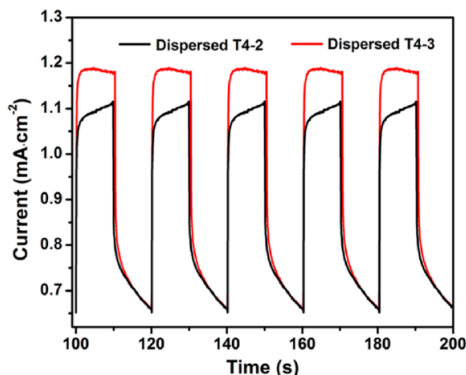
Figure 2.42: Current vs. time curves of T4−2 and T4−3 isolated clusters [193]

Regarding the stability of photocatalysts, it was observed that there were no changes in the UV−vis spectra after 10 hours of photocatalytic reaction, and the production rate of H_2 remained practically constant after five cycles.

Wang et al. [74] by using ionic liquids, obtained six structures based on T5 clusters: T5-1 ($[BMMIm]_{12}[Cu_5In_{30}Se_{52}Cl_3(Im)]$), T5-2 ($[BMMIm]_{12}[Cu_5In_{30}Se_{48\cdot5}S_{3\cdot5}Cl_3(Im)]$), T5-3 ($[BMMIm]_{11}[Cd_6In_{28}Se_{52}Cl_3(MIm)]$), T5-4 ($[BMMIm]_{11}[Cd_6In_{28}Se_{28\cdot5}S_{23\cdot5}Cl_3(MIm)]$), T5-5 ($[BMMIm]_{11}[Cd_6In_{28}Se_{16}S_{36}Cl_3(MIm)]$) and T5-6 ($[BMMIm]_9[Cd_6In_{28}Se_8S_{44}Cl_3(MIm)_3]$). By analyzing the structure of the bands of the synthesized materials (see Figure 2.43b), T5-1 and T5-2 cannot be used in the photodegradation of water, since the valence band does not present an adequate potential. It is observed again that the higher the sulfur content in the structure, the higher the band gap, although was also observed greater photocatalytic activity (see Figure 2.43a). One of the possible explanations presented by the authors is that a higher sulfur content is associated with a more negative conduction band, so the driving force of the photogenerated electrons to reduce H^+ is higher. Hence, there is a balance between the band gap value and the conduction band position [196]. Again, in order to evaluate the capacity of charge generation and separation, the photocurrent densities were measured (see Figure 2.43c) and the results are in accordance with the photocatalytic activity shown by the samples.
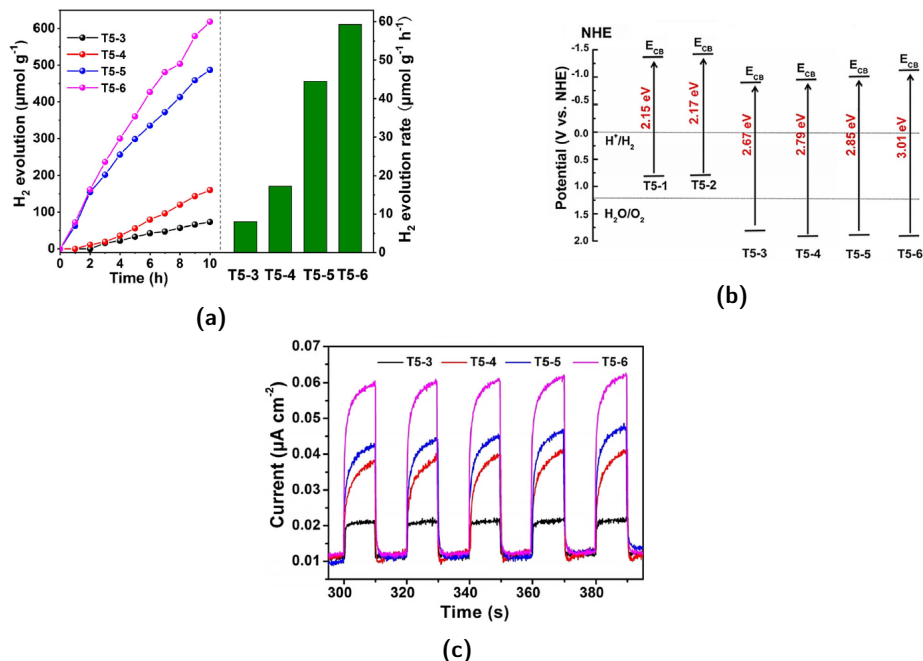
Figure 2.43: (2.43a) Photocatalytic H_2 evolution of T5−3, T5−4, T5−5 and T5−6 (10 mg) in the presence of TEOA as sacrifical agent, Pt as co-catalyst and using 300 W Xe lamp with a cutoff filter (λ>420 nm) as light source. (2.43b) Band structures of T5−1 to T5−6 obtained by impedance-potential measurements. (2.43c) Current vs. time curves of T5−3 to T5−6 (adapted from [74])

ii.c. Hybrid architectures

Hybrid structures based on metals and semiconductors have been the subject of intense research, since the presence of metal-semiconductor heterojunction improves the charge separation of the material.

Liu et al. [192] have developed hybrid materials consisting of silver nanowires (Ag-NWs) whose surface is evenly coated by T4 Mn-Zn-Ga-Sn-S clusters. In this way, a 0D/1D/1D material, referred as T4/Ag$_2$S/Ag-NW, was obtained. This material consists of silver nanowires covered with T4 clusters with an ultra thin layer of Ag$_2$S between them, which serves as a connector between the two materials. Besides testing the photocatalytic activity of T4/Ag$_2$S/Ag-NW, other clusters, such as T2, T3 and T4, and the Ag-NWs and Ag$_2$S nano particles without any cluster

were also evaluated. Regardless of the type of cluster used, there is always an increase in activity when these are deposited in Ag-NWs (see Figure 2.44a). The structure with the highest photocatalytic activity is $T4/Ag_2S/Ag$-NW. Different Zn : Mn mass ratios were also evaluated in the clusters and how they affects the photocatalytic activity of the final material. A 7:8 ratio leads to maximum photocatalytic activity (see Figure 2.44b). A material containing T4 Zn-Ga-Sn-S and Mn-Ga-Sn-S clusters was also synthesized in order to find out what the impact of having Zn and Mn in different clusters is. It was observed that the photocatalytic activity of the sample containing the Zn and Mn in separate clusters is much lower than the sample containing both metals in the same cluster (see Figure 2.44b). It was thus concluded that the synergistic effect between the different metals plays a fundamental role in the photocatalytic activity of the material. However, the mechanism of this synergistic effect is not yet known. In order to evaluate the importance that the thickness of the cluster layer presents in the photocatalytic activity, materials with different amount of clusters were obtained. It was observed that the photocatalytic activity is dependent on the amount of clusters present in the material, presenting a maximum activity for a loading amount equal to 9,13 % wt (see Figure 2.44c).
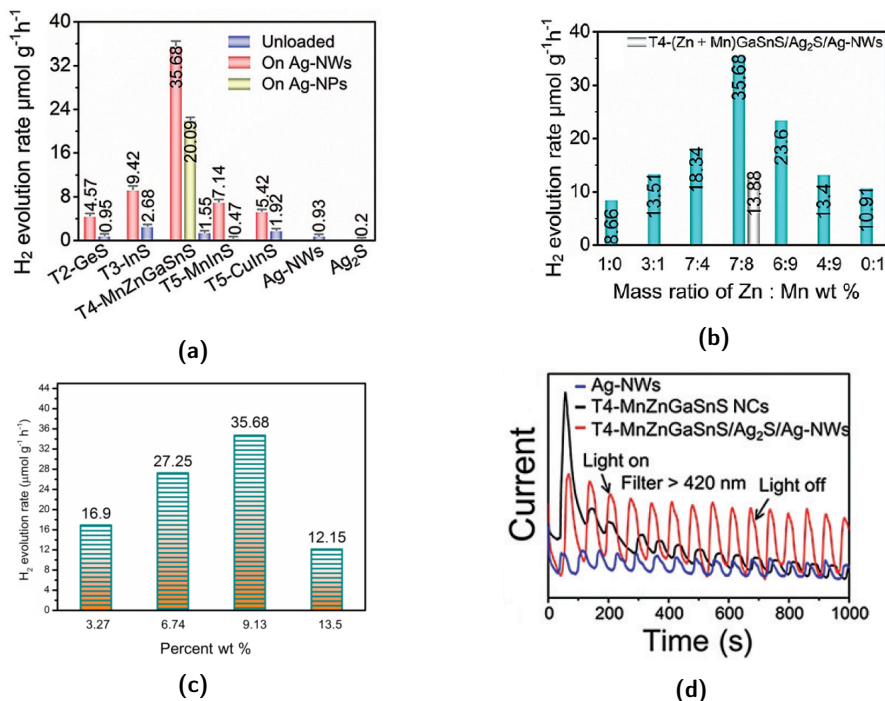
Figure 2.44: Photocatalytic H$_2$ evolution of (2.44a) materials with different clusters and their corresponding heterojuntions (5 mg), (2.44b) T4/Ag$_2$S/Ag-NW with different Zn:Mn mass ratios (5 mg) and (2.44c) T4/Ag$_2$S/Ag-NW with different loading amounts (5 mg) in the presence of Na$_2$S (0,1 M) and Na$_2$SO$_3$ (0,1M) as sacrifical agent and using 5 W Xe lamp with a cutoff filter (λ>420 nm) as light source. (2.44d) Current vs. time curves of silver nanowires, discrete T4 clusters and T4/Ag$_2$S/Ag-NW (adapted from [192])

The photocurrent response properties of Ag-NWs, discrete T4 clusters and T4/Ag$_2$S/ Ag-NW were measured in order to assess the charge production capacity and charge separation of the materials, as well as their stability. For the discrete T4 clusters, a rapid increase of the photocurrent is observed at first, followed by a rapid decrease (see Figure 2.44d). This rapid decrease can be explained by the photocorrosion that occurs. T4/Ag$_2$S/Ag-NW presents an increase in photocurrent regarding Ag-NWs, managing to keep the photocurrent more or less constant (see Figure 2.44d), thus overcoming the stability problems associated with photocorrosion of the discrete T4 clusters.

2.4.2.2 CO_2 Photoreduction

Since CO_2 is a relatively stable and inert compound, most reduction procedures involve high pressures or temperatures [43]. Photocatalysis has been seen as an alternative to these processes. The conversion of CO_2 into hydrocarbons or alcohols at room temperature and atmospheric pressure using sunlight has been seen as a very feasible option to close the carbon cycle.

Inoue et al. [197], using several photocatalysts such as WO_3, TiO_2, ZnO, CdS, GaP and SiC, photoreduced CO_2 for the first time in aqueous phase, obtaining formaldehyde, formic acid, methyl alcohol and traces of methane.

Most publications suggest that the first step towards the CO_2 photoreduction is the formation of the species $H^\bullet$ (Equation 2.14) and $CO_2^{\bullet-}$ (Equation 2.15) [198]. The most energetic stage, and often the limiting step, is the formation of the species $CO_2^{\bullet-}$, which has a reduction potential equal to $E^0 = -1,90$ V vs NHE at a pH = 7,00 [199]. Since this potential is quite high and never reached by any semiconductor, it is suggested by some researchers that $CO_2^{\bullet-}$ is not an intermediate of this reaction, thus passing through a bi-electronic mechanism that does not need such high activation potential [200, 201].

$$H^+ + e^- \rightarrow H^\bullet \qquad\qquad (2.14)$$

$$CO_2 + e^- \rightarrow CO_2^{\bullet-} \qquad\qquad (2.15)$$

Although the formation of $CO_2^{\bullet-}$ presents a high reduction potential, the transfer of multiple electrons (see Equations 2.16 to 2.21)[2] with the assistance of H^+ presents reduction potentials comparable to its own reduction potential (see Equation 2.22) [198, 201, 202]. Looking at Equations 2.16 to 2.21, it is easy to infer that there are kinetic challenges regarding the reduction of CO_2 to obtain more complex products. It is possible to find proof of concept that allows the obtention of carbon monoxide and formate from CO_2. However, more complex products, such as methane and methanol, require multiple transfers of both electrons and protons. Currently, it is possible to obtain such products but with a low efficiency [199, 203]. Besides obtaining the desired products, it is also possible to observe some inverse reactions. For example, due to the strong oxidative potential of the holes and the presence of O_2, it is possible to oxidize the desired hydrocarbons formed to CO_2 back [204].

---

[2]The redox potentials presented in Equations 2.16 to 2.22 are vs. NHE at pH 7,00

$$CO_2 + 2H^+ + 2e^- \rightarrow CO + H_2O \qquad E^0 = -0,53 \text{ V} \qquad (2.16)$$

$$CO_2 + 2H^+ + 2e^- \rightarrow HCOOH \qquad E^0 = -0,61 \text{ V} \qquad (2.17)$$

$$CO_2 + 4H^+ + 4e^- \rightarrow HCHO + H_2O \qquad E^0 = -0,48 \text{ V} \qquad (2.18)$$

$$CO_2 + 6H^+ + 6e^- \rightarrow CH_3OH + H_2O \qquad E^0 = -0,38 \text{ V} \qquad (2.19)$$

$$CO_2 + 8H^+ + 8e^- \rightarrow CH_4 + 2H_2O \qquad E^0 = -0,24 \text{ V} \qquad (2.20)$$

$$2CO_2 + 12H^+ + 12e^- \rightarrow CH_3CH_2OH + 3H_2O \qquad E^0 = 0,08 \text{ V} \qquad (2.21)$$
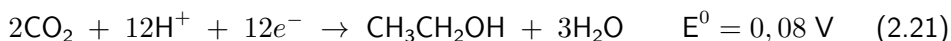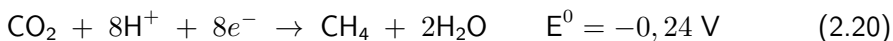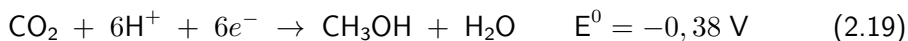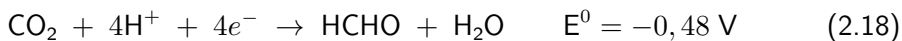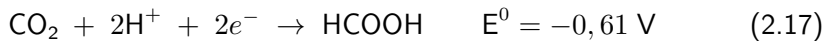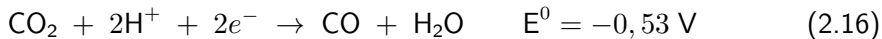
When the photoreduction of CO_2 is performed in water, liquid or gas phase, it is in direct competition with H_2 (see Equation 2.7) and H_2O_2 formation by O_2 reduction (see Equation 2.23). Although thermodynamically the reduction of CO_2 is favored over H_2 formation, in kinetic terms the formation of H_2 is favored since it requieres less electrons. The competition between these two reactions is partly responsible for the low efficiency of the CO_2 photoreduction process [205, 206].

$$2H^+ + 2e^- \rightarrow H_2 \qquad E^0 = -0,41 \text{ V} \qquad (2.22)$$

$$O_2 + 2H^+ + 2e^- \rightarrow H_2O_2 \qquad E^0 = 0,69 \text{ V} \qquad (2.23)$$
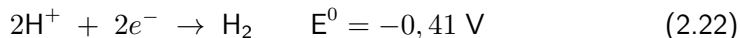
i. Materials for CO_2 photoreduction

Since the first use of photocatalysis to reduce CO_2, several studies on various photocatalysts, such as TiO_2 with or without doping [207, 208, 209, 210, 211, 212, 55], Bi_2WO_6 [213], Zn_2GeO_4 [214] or CeO_2 [215] have been carried out. However, most of these materials only show a response in the ultraviolet region or present low stability when irradiated. In addition, bulk materials have a high electron-hole recombination [216]. In order to obtain materials that are more efficient in

the CO_2 photoreduction process, the use of quantum dots [108, 217], hierarchical nanostructures or laminar materials [218, 219] as alternatives to traditional photocatalysts have been investigated.

Quantum dots have been seen recently as promising photocatalysts candidates. Compared to other commonly used photocatalysts, such as organic donor–acceptor molecules or transition metal complexes, quantum dots have greater stability and photoactivity. The phenomenon of multi-exciton generation was also observed in some quantum dots, namely on PbS, PbSe and PbTe. Normally, a photon generates an electron and a hole. However, it was observed that in some materials, when the energy of the incident photon has at least twice the band gap energy, multiple charges are generated [220]. This phenomenon can therefore increase the efficiency of photocatalytic systems based on quantum dots. However, most of the quantum dots studied so far contain heavy metals in their composition, such as Cd and Pb, not being good candidates for practical applications, namely green applications [217]. It is therefore imperative to develop this class of materials without the presence of heavy metals. Previously, several examples of isolated Tn clusters without heavy metals were presented, as well as their use as photocatalysts in H_2 production. These structures can be seen as a special type of quantum dots, as they have a high surface/volume ratio, exact chemical composition, precise structure, uniform size and a light response over a broad spectrum range [193]. Although these structures have already been used for the production of H_2 [74, 193], it is not possible to find substantial literature on their use for CO_2 photoreduction.

Another class of materials that presents high potentialities in CO_2 photoreduction is the hierarchical nanostructures one. These structures have a high CO_2 adsorption capability, a high surface area, improved molecular diffusion and enhanced light harvesting due to scattering effect [218]. Such characteristics make it possible to obtain a photocatalyst for the CO_2 photoreduction with superior activities. From this class of materials there are several examples that contain sulfur in their composition such as CdS multicavity hollow particles [221], CdS nanoparticles dispersed on WO_3 hollow spheres [222], $CuInS_2$ [223] or MoS_2 [224] dispersed into TiO_2 nanofibers, In_2S_3-$CdIn_2S_4$ [216] or $ZnIn_2S_4$-In_2O_3 [225] nanotubes and the combination of mesoporous TiO_2 and layers of MoS_2 into 3D graphene [226].

Layered materials have also been seen as potential candidates, as they have high surface areas compared to their bulk structures and, therefore, present a high number of active sites on the surface. 2-dimensional composites resulting from the combination of two laminar materials may also present an enhanced photocatalytic activity due to possibility of band gap tunnig and heterojunction formation [227]. The synthesis of thin films allows the reduction of the average mean path of charge carriers, reducing or even eliminating its recombination [228]. It is possible to find

examples in the literature of the use of thin films made of $CuInS_2$ [229], $ZnIn_2S_4$ [228, 230] and $CuIn_5S_8$ [231] in CO_2 photoreduction.

i.a. Cluster-based chalcogenide materials

As seen before, cluster-based chalcogenide materials are marked by an enormous diversity of both chemical composition and types of structure. Since it is possible to obtain materials with characteristics similar to quantum dots, nanostructured and layered materials, structures that have been reviewed recently for presenting promising results in CO_2 photoreduction, it makes sense to investigate them as active photocatalysts. However, it was only possible to find one example of the use of cluster based materials as photocatalyst in CO_2 photoreduction.

Using the CPM-120-ZnGeS structure previously obtained by Lin et al. [162], Sasan et al. [232] tested it in the CO_2 photoreduction reaction. Through ionic exchange, the SDA was exchanged with Au^{3+} or Pd^{2+} in order to evaluate the impact that the extraframework cations have on the band gap of the materials and its consequence on the photocatalytic performance of the material. The structure with the SDA, designated as AEM@GeZnS, has a band gap of 2,8 eV. After ion exchange with Au^{3+} (sample entitled Au@GeZnS) or with Pd^{2+} (sample entitled Pd@GeZnS), a reduction of the band gap to 2,6 eV and 2,5 eV is observed, respectively. In order to evaluate the photogeneration and charge separation properties, PEC measurements were carried out (see Figure 2.45a). It is noted that the sample with the highest photocurrent density is the Au@GeZnS sample, with a density about five times higher that of AEM@GeZnS and about twice to that of Pd@GeZnS.
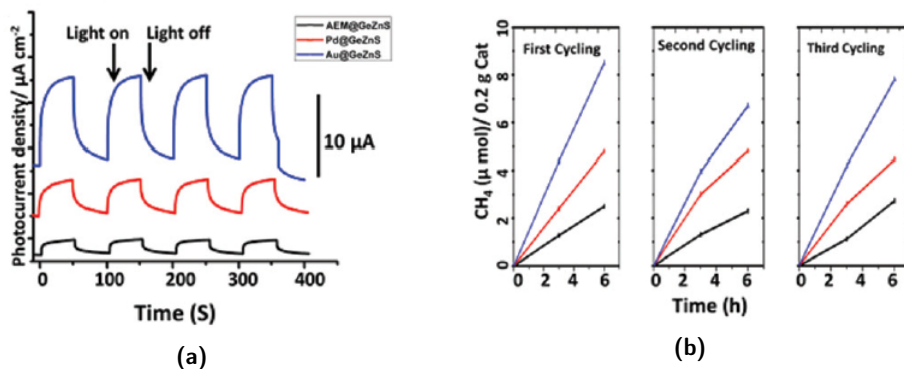
Figure 2.45: (2.45a) Current vs. time curves of AEM@GeZnS, Pd@GeZnS and Au@GeZnS. (2.45b) Photocatalytic CH_4 evolution of AEM@GeZnS, Pd@GeZnS and Au@GeZnS (0,2 g) in a gas-solid system and using 300 W Xe lamp as light source [232]

In order to assess the photocatalytic performance of the samples AEM@GeZnS, Pd@GeZnS and Au@GeZnS, CO_2 photoreduction to produce CH_4 in the presence of H_2O vapor over a gas-solid system was performed (see Figure 2.45b). The samples with metal incorporation present a higher photocatalytic activity. Under the same experimental conditions, the Au@GeZnS sample exhibits a superior photocatalytic activity. It was also observed that any of the materials is capable of keeping photocatalytic activity after three cycles without appreciable degradation. According to the authors, the samples with incorporated metals present a superior photocatalytic performance due to two reasons. First, it is observed that the ion exchange with metals leads to a reduction of the band gap of the materials. Secondly, with the incorporation of metals, an increase in photocurrent density is observed. Such phenomenon is associated with a better charge generation and separation properties, thus contributing to a better photocatalytic performance. However, such effect that cannot be excluded from the co-catalyst effect that the added metals might have. The added metal can be acting as a co-catalysts, hence reducing the activation energy and enhancing the reaction's kinetics.

2.4.2.3   Final Considerations

Cluster-based chalcogenide materials are suitable to be used as photocatalysts for the production of H_2 from water decomposition. Regarding CO_2 photoreduction, although it is possible to find one example of the use of these materials, further research is still needed.

For H_2 production, it has been observed that these materials have a quantum yield higher than dense phases composed by the same chemical elements. Although structures with an open architecture present a band gap superior to their dense phase, such increase is not necessarily a negative consequence. For example, In_2S_3 does not present photocatalytic activity even when irradiated with UV radiation. On the other hand, even though UCR-7InS-AEP exhibits a band gap superior to In_2S_3, it can produce H_2 even when irradiated with visible radiation. The presence of a porous system also allows the insertion of dyes or metal complexes, thus increasing its light absorption properties.

Looking at Table 2.10 it can be seen that even though the structures are capable of producing H_2, the production rate is low. This may be due to the fact that in 3-dimensional structures, the porous volume is partially occupied by the SDA, thus reducing the active sites available for participation in the reaction.

One solution found to circumvent the problem of eliminating the SDA was the use of isolated clusters instead of structures with higher dimensions. These clusters have characteristics similar to quantum dots and might be stabilized by the ionic liquids used during the synthesis process. However, the used technique implied their dispersion in solvents. Thus, although this solution works in gas-liquid approaches, it may not be the best methodology when it comes to synthesizing photocatalysts to be used in gas-solid systems. As can be seen, the value of the band gap as well as the position of the valence and conduction bands have a huge impact on photocatalytic performance. The chemical composition of the material seems to be one of the parameters that most influences the band gap. Copper is one of the metals that seems to lead to a red shift in the band gap. It was also possible to establish a relationship between the chalcogen composition and the band gap value. Higher sulfur contents lead to a larger band gap, with the conduction band becoming more negative. On the contrary, a higher selenium content in the clusters leads to a lower band gap. The content of these two elements allows the customization of the band structure of the final material, taking into account two factors: the position of the bands and the band gap value. A more negative conduction band will produce charge carries with more reductive potential. However, higher band gaps mean that more energetic photons are needed to generate charges and losses in energetic yields. Thus, there is a balance between the two phenomena that must

be taken into account when synthesizing a material to be used as a photocatalyst for a specific reaction. Although the connection mode between the clusters does not seem to have much influence on the value of the band gap, it does seem to influence the charge separation properties of the material, as shown in [172].

Hence, there are three factors that influence the photocatalytic performance of a material: the characteristics associated with the band structure (band gap value and band's position) and light absorption capacity together with the porosity of the samples.

The synthesis of hybrid materials is a great way to improve photocatalytic performance. The existence of a synergy between the multimetalic clusters dispersed in a metallic substrate was observed. This effect contributes to the increase in photocatalytic activity and has yet to be scientifically explained.

2.5   Conclusions

Photocatalytic processes are regarded as a sustainable and environmental-friendly way to attenuate humankind's strong dependence on fossil fuels, which are the main responsible for high pollution levels in our planet and the climate changes we are starting to feel.

Intensive research is being done on the synthesis of new materials that could present superior photocatalytic performance. Recently, quantum dots, nanostructured or laminar materials have been investigated as photocatalysts, as they present optimal properties for applications in this field of science. Nevertheless, the use of new oxide-based materials remains the most common. Materials based on less conventional species, such as sulfur and selenium, are increasingly being seen as possible alternatives to oxides. It is observed that chalcogenide-based materials have electronic properties, namely band structure and band gap value, more suitable to be used in solar-power driven processes than oxide-base materials. There are already several studies regarding the usage of chalcogenide-based materials as photocatalysts for the production of H_2 through water splitting. Although it is possible to find in the literature examples of the use of sulfur-based materials in CO_2 photoreduction, the use of cluster-based materials in this reaction is still at a very early stage. Since it is possible to find materials consisting of clusters with characteristics similar to quantum dots, nanostructured and laminar materials, it is imperative to study their use as photocatalysts in CO_2 reduction, both in gas-liquid and gas-solid photocatalytic systems.

Nowadays it is possible to obtain materials based on chalcogenide clusters with an enormous diversity, both in terms of chemical composition, that leads to a wide range of band gap values, but also structures with uncommon topologies. However, there are some problems associated with these cluster-based materials. These materials generally have low thermal stability, i.e. they tend to collapse at temperatures above 300°C. The difficult elimination of the SDA used during the synthesis, which occupies an extra framework position, is another problem, since it does not allow to take full advantage of the structure's open architecture. Large parts of these materials have in their composition toxic or non-abundant metals, which makes their use in a green process ethically questionable. Taking into account the limitations of the use of these materials, it is suggested a set of possible improvements, that could result in increased photocatalytic performance, since the current performance does not justify their marketing on a large scale.

The presence of SDA in the porous system is one of the main problems, since it obstructs the porous volume, with a consequent decrease in active sites available. The most used technique is an ionic exchange with a cesium salt. However, such a technique does not always guarantee success. The use of non-conventional SDAs, namely compounds that can be used in sulfides or selenides systems and are not suitable for oxides, which are easier to degrade can be seen as a solution.

One of the challenges in obtaining a photocatalyst adapted to a given reaction, using a specific radiation, is to have a band structure suitable for the reaction under study and a band gap fitted for incident radiation. Taking into account the enormous diversity of known cluster-based materials, it would be interesting to perform a band structure engineering by manipulating the cluster chemical composition, in order to obtain a band gap value more suitable to a specific reaction.

The radiation absorption properties, in addition to band structure features, is another characteristic to take into account when someone engineers a photocatalyst. The use of organic dyes, which act as antennas, is commonly used to increase the photocatalyts absorption capability. There is a lack of exploration of the inherent characteristics of laminar materials and how these same characteristics could be used to increase photocatalytic performance, namely the possibility of inserting organic dyes in the interlaminar space.

References

[1] R. J. Detz, J. N. H. Reek, and B. C. C. van der Zwaan. "The future of solar fuels: when could they become competitive?" In: *Energy Environ. Sci.* 11 (7 2018), pp. 1653–1669. DOI: 10.1039/C8EE00111A.

[2] Lothar Mennicken, Alexander Janz, and Stefanie Roth. "The German R&D Program for CO_2 Utilization—Innovations for a Green Economy". In: *Environmental Science and Pollution Research* 23 (2016), pp. 11386–11392. DOI: https://doi.org/10.1007/s11356-016-6641-1.

[3] IEA. *Putting CO_2 to Use*. https://www.iea.org/reports/putting-co2-to-use. Online. Accessed 22nd July 2022. 2019.

[4] Markus Lehner et al. *Power-to-Gas: Technology and Business Models*. Springer, 2014.

[5] Hasan Ümitcan Yilmaz et al. "Power-to-gas: Decarbonization of the European electricity system with synthetic methane". In: *Applied Energy* 323 (2022), p. 119538. DOI: https://doi.org/10.1016/j.apenergy.2022.119538.

[6] Tiejun Lin et al. "Advances in Selectivity Control for Fischer–Tropsch Synthesis to Fuels and Chemicals with High Carbon Efficiency". In: *ACS Catalysis* 0.0 (0), pp. 12092–12112. DOI: 10.1021/acscatal.2c03404.

[7] Sandra Adelung. "Global sensitivity and uncertainty analysis of a Fischer-Tropsch based Power-to-Liquid process". In: *Journal of CO_2 Utilization* 65 (2022), p. 102171. DOI: https://doi.org/10.1016/j.jcou.2022.102171.

[8] Yujun Suo et al. "Recent advances in cobalt-based Fischer-Tropsch synthesis catalysts". In: *Journal of Industrial and Engineering Chemistry* (2022). DOI: https://doi.org/10.1016/j.jiec.2022.08.026.

[9] Michael Stöcker. "Methanol to Olefins (MTO) and Methanol to Gasoline (MTG)". In: *Zeolites and Catalysis*. John Wiley & Sons, Ltd, 2010. Chap. 22, pp. 687–711. DOI: https://doi.org/10.1002/9783527630295.ch22.

[10] Manuel Moliner, Cristina Martínez, and Avelino Corma. "Synthesis Strategies for Preparing Useful Small Pore Zeolites and Zeotypes for Gas Separations and Catalysis". In: *Chemistry of Materials* 26.1 (2014), pp. 246–258. DOI: 10.1021/cm4015095.

[11] Nicola Armaroli and Vincenzo Balzani. "The Future of Energy Supply: Challenges and Opportunities". In: *Angewandte Chemie International Edition* 46.1-2 (2007), pp. 52–66. DOI: https://doi.org/10.1002/anie.200602373.

[12] Jayaseelan Arun et al. "Technical insights into the production of green fuel from CO_2 sequestered algal biomass: A conceptual review on green energy". In: *Science of The Total Environment* 755 (2021), p. 142636. DOI: `https://doi.org/10.1016/j.scitotenv.2020.142636`.

[13] Xin-Guang Zhu, Stephen P Long, and Donald R Ort. "What is the maximum efficiency with which photosynthesis can convert solar energy into biomass?" In: *Current Opinion in Biotechnology* 19.2 (2008). Food biotechnology / Plant biotechnology, pp. 153–159. DOI: `https://doi.org/10.1016/j.copbio.2008.02.004`.

[14] Nikolay Kornienko et al. "Interfacing nature's catalytic machinery with synthetic materials for semi-artificial photosynthesis". In: *Nature Nanotechnology* 13 (2018), pp. 890–899. DOI: `https://doi.org/10.1038/s41565-018-0251-7`.

[15] Zhenfu Wang et al. "Artificial photosynthesis systems for solar energy conversion and storage: platforms and their realities". In: *Chem. Soc. Rev.* 51 (15 2022), pp. 6704–6737. DOI: `10.1039/D1CS01008E`.

[16] Daniel G. Nocera. "The Artificial Leaf". In: *Accounts of Chemical Research* 45.5 (2012), pp. 767–776. DOI: `10.1021/ar2003013`.

[17] Steven Y. Reece et al. "Wireless Solar Water Splitting Using Silicon-Based Semiconductors and Earth-Abundant Catalysts". In: *Science* 334.6056 (2011), pp. 645–648. DOI: `10.1126/science.1209816`.

[18] Chong Liu et al. "Water splitting & biosynthetic system with CO_2 reduction efficiencies exceeding photosynthesis". In: *Science* 352.6290 (2016), pp. 1210–1213. DOI: `10.1126/science.aaf5039`.

[19] Dilek K. Dogutan and Daniel G. Nocera. "Artificial Photosynthesis at Efficiencies Greatly Exceeding That of Natural Photosynthesis". In: *Accounts of Chemical Research* 52.11 (2019), pp. 3143–3148. DOI: `10.1021/acs.accounts.9b00380`.

[20] "Chapter 1 Introduction". In: *Chemistry and Light*. Ed. by Paul Suppan. The Royal Society of Chemistry, 1994, pp. 1–10.

[21] Joseph H. Montoya et al. "Materials for solar fuels and chemicals". In: *Nature Materials* 16 (2017), pp. 70–81. DOI: `https://doi.org/10.1038/nmat4778`.

[22] Gabriele Centi and Siglinda Perathoner. "Towards Solar Fuels from Water and CO_2". In: *ChemSusChem* 3.2 (2010), pp. 195–208. DOI: `https://doi.org/10.1002/cssc.200900289`.

[23]   Jin Hyun Kim et al. "Toward practical solar hydrogen production – an artificial photosynthetic leaf-to-farm challenge". In: *Chem. Soc. Rev.* 48 (7 2019), pp. 1908–1971. DOI: 10.1039/C8CS00699G.

[24]   Shannon A. Bonke et al. "Renewable fuels from concentrated solar power: towards practical artificial photosynthesis". In: *Energy Environ. Sci.* 8 (9 2015), pp. 2791–2796. DOI: 10.1039/C5EE02214B.

[25]   Jieyang Jia et al. "Solar water splitting by photovoltaic-electrolysis with a solar-to-hydrogen efficiency over 30%". In: *Nature Communications* 7 (2016), p. 13237. DOI: https://doi.org/10.1038/ncomms13237.

[26]   Marcel Schreier et al. "Efficient photosynthesis of carbon monoxide from CO_2 using perovskite photovoltaics". In: *Nature Communications* 6 (2015), p. 7326. DOI: https://doi.org/10.1038/ncomms8326.

[27]   Xiao Li et al. "Water Splitting: From Electrode to Green Energy System". In: *Nano-Micro Letters* 12.131 (2020). DOI: https://doi.org/10.1007/s40820-020-00469-3.

[28]   F. Decker and S. Cattarin. "Photoelectrochemical Cells - Overview". In: *Encyclopedia of Electrochemical Power Sources*. Ed. by Jürgen Garche. Amsterdam: Elsevier, 2009, pp. 1–9. DOI: https://doi.org/10.1016/B978-044452745-5.00035-6.

[29]   Dongseok Kang et al. "Printed assemblies of GaAs photoelectrodes with decoupled optical and reactive interfaces for unassisted solar water splitting". In: *Nature Energy* 2.17043 (2017). DOI: https://doi.org/10.1038/nenergy.2017.43.

[30]   Wen-Hui Cheng et al. "Monolithic Photoelectrochemical Device for Direct Water Splitting with 19% Efficiency". In: *ACS Energy Letters* 3.8 (2018), pp. 1795–1800. DOI: 10.1021/acsenergylett.8b00920.

[31]   Tobias A. Kistler et al. "Monolithic Photoelectrochemical CO_2 Reduction Producing Syngas at 10% Efficiency". In: *Advanced Energy Materials* 11.21 (2021), p. 2100070. DOI: https://doi.org/10.1002/aenm.202100070.

[32]   Kazuhiko Maeda and Kazunari Domen. "New Non-Oxide Photocatalysts Designed for Overall Water Splitting under Visible Light". In: *The Journal of Physical Chemistry C* 111.22 (2007), pp. 7851–7861. DOI: 10.1021/jp070911w.

[33]   Deng Li et al. "Powering the World with Solar Fuels from Photoelectrochemical CO_2 Reduction: Basic Principles and Recent Advances". In: *Advanced Energy Materials* 12.31 (2022), p. 2201070. DOI: https://doi.org/10.1002/aenm.202201070.

[34] Fatwa F. Abdi et al. "Efficient solar water splitting by enhanced charge separation in a bismuth vanadate-silicon tandem photoelectrode". In: *Nature Communications* 4.2195 (2013). DOI: `https://doi.org/10.1038/ncomms3195`.

[35] Xinjian Shi et al. "Unassisted photoelectrochemical water splitting beyond 5.7% solar-to-hydrogen conversion efficiency by a wireless monolithic photoanode - dye-sensitised solar cell tandem device". In: *Nano Energy* 13 (2015), pp. 182–191. DOI: `https://doi.org/10.1016/j.nanoen.2015.02.018`.

[36] Anders B. Laursen et al. "Molybdenum sulfides—efficient and viable materials for electro - and photoelectrocatalytic hydrogen evolution". In: *Energy & Environmental Science* 5 (2 2012), pp. 5577–5591. DOI: `10.1039/C2EE02618J`.

[37] Juan Liu et al. "Metal-free efficient photocatalyst for stable visible water splitting via a two-electron pathway". In: *Science* 347.6225 (2015), pp. 970–974. DOI: `10.1126/science.aaa3145`.

[38] Faqrul A. Chowdhury et al. "A photochemical diode artificial photosynthesis system for unassisted high efficiency overall pure water splitting". In: *Nature Communications* 9.1707 (2018). DOI: `https://doi.org/10.1038/s41467-018-04067-1`.

[39] Sundaram Chandrasekaran et al. "Recent advances in metal sulfides: from controlled fabrication to electrocatalytic, photocatalytic and photoelectrochemical water splitting and beyond". In: *Chemical Society Reviews* 48 (15 2019), pp. 4178–4280. DOI: `10.1039/C8CS00664D`.

[40] Mohammad Reza Gholipour et al. "Nanocomposite heterojunctions as sunlight-driven photocatalysts for hydrogen production from water splitting". In: *Nanoscale* 7 (18 2015), pp. 8187–8208. DOI: `10.1039/C4NR07224C`.

[41] Nick Serpone. "Relative photonic efficiencies and quantum yields in heterogeneous photocatalysis". In: *Journal of Photochemistry and Photobiology A: Chemistry* 104.1 (1997), pp. 1–12. DOI: `https://doi.org/10.1016/S1010-6030(96)04538-8`.

[42] Dan Kong et al. "Recent advances in visible light-driven water oxidation and reduction in suspension systems". In: *Materials Today* 21.8 (2018), pp. 897–924. DOI: `https://doi.org/10.1016/j.mattod.2018.04.009`.

[43] Phairat Usubharatana et al. "Photocatalytic Process for CO_2 Emission Reduction from Industrial Flue Gas Streams". In: *Industrial & Engineering Chemistry Research* 45.8 (2006), pp. 2558–2568.

[44] Zaiba Zafar et al. "Recent Development in Defects Engineered Photocatalysts: An Overview of the Experimental and Theoretical Strategies". In: *Energy & Environmental Materials* 5.1 (2022), pp. 68–114. DOI: `https://doi.org/10.1002/eem2.12171`.

[45] Ming Kong et al. "Tuning the Relative Concentration Ratio of Bulk Defects to Surface Defects in TiO_2 Nanocrystals Leads to High Photocatalytic Efficiency". In: *Journal of the American Chemical Society* 133.41 (2011). PMID: 21923140, pp. 16414–16417. DOI: `10.1021/ja207826q`. eprint: `https://doi.org/10.1021/ja207826q`.

[46] Hao Zhang et al. "Insights into the effects of surface/bulk defects on photocatalytic hydrogen evolution over TiO_2 with exposed 001 facets". In: *Applied Catalysis B: Environmental* 220 (2018), pp. 126–136. DOI: `https://doi.org/10.1016/j.apcatb.2017.08.046`.

[47] Akira Fujishima and Kenichi Honda. "Electrochemical Photolysis of Water at a Semiconductor Electrode". In: *Nature* 238 (1972), pp. 37–38. DOI: `https://doi.org/10.1038/238037a0`.

[48] Canan Acar, Ibrahim Dincer, and Greg F. Naterer. "Review of photocatalytic water-splitting methods for sustainable hydrogen production". In: *International Journal of Energy Research* 40.11 (2016), pp. 1449–1473. DOI: `https://doi.org/10.1002/er.3549`.

[49] Jeannie Z. Y. Tan and M. Mercedes Maroto-Valer. "A review of nanostructured non-titania photocatalysts and hole scavenging agents for CO_2 photoreduction processes". In: *J. Mater. Chem. A* 7 (16 2019), pp. 9368–9385. DOI: `10.1039/C8TA10410G`.

[50] Shao-Hong Guo et al. "Enhanced CO_2 photoreduction via tuning halides in perovskites". In: *Journal of Catalysis* 369 (2019), pp. 201–208. ISSN: 0021-9517. DOI: `https://doi.org/10.1016/j.jcat.2018.11.004`.

[51] Mohammed-Ibrahim Jamesh, Yun Kuang, and Xiaoming Sun. "Constructing Earth-abundant 3D Nanoarrays for Efficient Overall Water Splitting – A Review". In: *ChemCatChem* 11.6 (2019), pp. 1550–1575. DOI: `https://doi.org/10.1002/cctc.201801783`.

[52] Amit Mishra et al. "Graphitic carbon nitride (g–C_3N_4)–based metal-free photocatalysts for water splitting: A review". In: *Carbon* 149 (2019), pp. 693–721. DOI: `https://doi.org/10.1016/j.carbon.2019.04.104`.

[53] Yu Zhang et al. "Polyoxometalate-based materials for sustainable and clean energy conversion and storage". In: *EnergyChem* 1.3 (2019), p. 100021. DOI: `https://doi.org/10.1016/j.enchem.2019.100021`.

[54]   Ch Venkata Reddy et al. "Hetero-nanostructured metal oxide-based hybrid photocatalysts for enhanced photoelectrochemical water splitting – A review". In: *International Journal of Hydrogen Energy* 45.36 (2020). Waste and Biomass-derived Hydrogen Synthesis and Implementation, pp. 18331–18347. DOI: https://doi.org/10.1016/j.ijhydene.2019.02.109.

[55]   Stefanie Kreft et al. "Recent advances on TiO_2-based photocatalytic CO_2 reduction". In: *EnergyChem* 2.6 (2020), p. 100044. DOI: https://doi.org/10.1016/j.enchem.2020.100044.

[56]   Jiajia Wang et al. "Earth-abundant transition-metal-based bifunctional catalysts for overall electrochemical water splitting: A review". In: *Journal of Alloys and Compounds* 819 (2020), p. 153346. DOI: https://doi.org/10.1016/j.jallcom.2019.153346.

[57]   Dong-Cheng Liu, Di-Chang Zhong, and Tong-Bu Lu. "Non-noble metal-based molecular complexes for CO_2 reduction: From the ligand design perspective". In: *EnergyChem* 2.3 (2020), p. 100034. DOI: https://doi.org/10.1016/j.enchem.2020.100034.

[58]   Xiaofang Li and Qi-Long Zhu. "MOF-based materials for photo- and electrocatalytic CO_2 reduction". In: *EnergyChem* 2.3 (2020), p. 100033. DOI: https://doi.org/10.1016/j.enchem.2020.100033.

[59]   Eder Moisés Cedeño Morales, Boris I. Kharisov, and Miguel A. Méndez-Rojas. "CO_2 photoreduction by MOF-derived carbon nanomaterials: A review". In: *Materials Today: Proceedings* 46 (2021). International Conference on Advances in Material Science and Chemistry – 2020 (ICAMSC-2020), pp. 2982–2997. DOI: https://doi.org/10.1016/j.matpr.2020.12.702.

[60]   Lina Nie and Qichun Zhang. "Recent progress in crystalline metal chalcogenides as efficient photocatalysts for organic pollutant degradation". In: *Inorganic Chemistry Frontiers* 4.12 (2017), pp. 1953–1962. DOI: DOIhttps://doi.org/10.1039/C7QI00651A.

[61]   Martin A. A. Schoonen Yong Xu. "The absolute energy positions of conduction and valence bands of selected semiconducting minerals". In: *American Mineralogist* 85 (2000), pp. 543–556. DOI: https://doi.org/10.2138/am-2000-0416.

[62]   R. T. Shuey. *Semiconducting ore minerals*. 1st. Elsevier scientific Publishing Company, 1975.

[63]   David J. Vaughan and James R. Craig. *Mineral chemistry of metal sulfides*. Cambridge University, 1978.

[64] Y. Shiga et al. "A metal sulfide photocatalyst composed of ubiquitous elements for solar hydrogen production". In: *Chem. Commun.* 52 (47 2016), pp. 7470–7473. DOI: 10.1039/C6CC03199D.

[65] K. Kobayakawa et al. "Photocatalytic Activity of $CuInS_2$ and $CuIn_5S_8$". In: *Electrochimica Acta* 37 (1992), pp. 465–467. DOI: https://doi.org/10.1016/0013-4686(92)87037-Z.

[66] Zhibin Lei et al. "Photocatalytic water reduction under visible light on a novel $ZnIn_2S_4$ catalyst synthesized by hydrothermal method". In: *Chemical Communications* 17 (2003), pp. 2142–2143. ISSN: 1359-7345. DOI: https://doi.org/10.1039/B306813G.

[67] Di Chen and Jinhua Ye. "Photocatalytic H_2 evolution under visible light irradiation on $AgIn_5S_8$ photocatalyst". In: *Journal of Physics and Chemistry of Solids* 68.12 (2007), pp. 2317–2320. DOI: https://doi.org/10.1016/j.jpcs.2007.07.059.

[68] Zhixin Chen et al. "Low-temperature and template-free synthesis of $ZnIn_2S_4$ microspheres". In: *Inorganic Chemistry* 47.21 (2008), pp. 9766–9772. DOI: https://doi.org/10.1021/ic800752t.

[69] Wenjuan Li et al. "High-efficient Degradation of Dyes by $Zn_xCd_{1-x}S$ Solid Solutions under Visible Light Irradiation". In: *The Journal of Physical Chemistry C* 112.38 (2008), pp. 14943–14947. DOI: https://doi.org/10.1021/jp8049075.

[70] Yao Li, Xiaoyan He, and Minhua Cao. "Micro-emulsion-assisted synthesis of ZnS nanospheres and their photocatalytic activity". In: *Materials Research Bulletin* 43.11 (2008), pp. 3100–3110. DOI: https://doi.org/10.1016/j.materresbull.2007.11.016.

[71] Meng Sun et al. "New Photocatalyst, Sb_2S_3 , for Degradation of Methyl Orange under Visible-Light Irradiation". In: *The Journal of Physical Chemistry C* 112.46 (2008), pp. 18076–18081. DOI: https://doi.org/10.1021/jp806496d.

[72] Yunhui He et al. "A New Application of Nanocrystal In_2S_3 in Efficient Degradation of Organic Pollutants under Visible Light Irradiation". In: *The Journal of Physical Chemistry C* 113.13 (2009), pp. 5254–5262. DOI: https://doi.org/10.1021/jp809028y.

[73] Wenjuan Zhang et al. "Microwave hydrothermal synthesis and photocatalytic activity of $AgIn_5S_8$ for the degradation of dye". In: *Journal of Solid State Chemistry* 183.10 (2010), pp. 2466–2474. DOI: https://doi.org/10.1016/j.jssc.2010.08.011.

[74]   Jingjing Wang et al. "Nanostructured Metal Sulfides: Classification, Modification Strategy, and Solar-Driven CO_2 Reduction Application". In: *Advanced Functional Materials* (), p. 2008008. DOI: https://doi.org/10.1002/adfm.202008008.

[75]   Mark E. Davis. "Ordered porous materials for emerging applications". In: *Nature* 417 (2002), pp. 813–821. DOI: https://doi.org/10.1038/nature00785.

[76]   Nanfeng Zheng et al. "Open-Framework Chalcogenides as Visible-Light Photocatalysts for Hydrogen Generation from Water". In: *Angewandte Chemie (International ed. in English)* 44 (33 2005), pp. 5299–5303. DOI: https://doi.org/10.1002/anie.200500346.

[77]   Kohsuke Mori, Hiromi Yamashita, and Masakazu Anpo. "Photocatalytic reduction of CO_2 with H_2O on various titanium oxide photocatalysts". In: *RSC Adv.* 2 (8 2012), pp. 3165–3172. DOI: 10.1039/C2RA01332K.

[78]   Nanfeng Zheng et al. "Microporous and Photoluminescent Chalcogenide Zeolite Analogs". In: *Science* 298.5602 (2002), pp. 2366–2369. DOI: 10.1126/science.1078663.

[79]   Silke Santner, Johanna Heine, and Stefanie Dehnen. "Synthesis of Crystalline Chalcogenides in Ionic Liquids". In: *Angewandte Chemie (International ed. in English)* 55.3 (2016), pp. 876–893. DOI: 10.1002/anie.201507736.

[80]   William B. Jensen. "A Note on the Term "Chalcogen"". In: *Journal of Chemical Education* 74.9 (1997), p. 1063.

[81]   Mirtat Bouroushian. "Chalcogens and Metal Chalcogenides". In: *Electrochemistry of Metal Chalcogenides*. Berlin, Heidelberg: Springer Berlin Heidelberg, 2010, pp. 1–56. ISBN: 978-3-642-03967-6. DOI: 10.1007/978-3-642-03967-6_1.

[82]   Uzma I Zakai. "Design, Synthesis, and Evaluation of Chalcogen Interactions". PhD thesis. The University of Arizona, 2007.

[83]   Pingyun Feng, Xianhui Bu, and Nanfeng Zheng. "The Interface Chemistry between Chalcogenide Clusters and Open Framework Chalcogenides". In: *Accounts of Chemical Research* 38.4 (2005), pp. 293–303. DOI: https://doi.org/10.1021/ar0401754.

[84]   J.A. Brant, C.D. Brunetta, and J.A. Aitken. "5.09 - Chalcogenides and Nonoxides". In: *Comprehensive Inorganic Chemistry II (Second Edition)*. Ed. by Jan Reedijk and Kenneth Poeppelmeier. Second Edition. Amsterdam: Elsevier, 2013, pp. 213–283. DOI: https://doi.org/10.1016/B978-0-08-097774-4.00510-6.

[85] Christopher L. Cahill and J. B. Parise. "On the formation of framework indium sulfides". In: *Journal of the Chemical Society, Dalton Transactions* (9 2000), pp. 1475–1482. DOI: https://doi.org/10.1039/A909005C.

[86] Ian Dance and Keith Fisher. "Metal Chalcogenide Cluster Chemistry". In: *Progress in Inorganic Chemistry*. Ed. by Kenneth D.Editor Karlin. Vol. 41. John Wiley, 1994, pp. 637–803. DOI: https://doi.org/10.1002/9780470166420.ch9.

[87] R. L. Bedard et al. "Crystalline microporous metal sulfide compositions". December 6, 1988, US 4,880,761.

[88] R.L. Bedard et al. "The Next Generation: Synthesis, Characterization, and Structure of Metal Sulfide-Based Microporous Solids". In: *Zeolites: Facts, Figures, Future Part A - Proceedings of the 8th International Zeolite Conference*. Ed. by P.A. Jacobs and R.A. van Santen. Vol. 49. Studies in Surface Science and Catalysis. Elsevier, 1989, pp. 375–387. DOI: https://doi.org/10.1016/S0167-2991(08)61735-8.

[89] Robert W.J. Scott, Mark J. MacLachlan, and Geoffrey A. Ozin. "Synthesis of metal sulfide materials with controlled architecture". In: *Current Opinion in Solid State and Materials Science* 4.2 (1999), pp. 113–121. DOI: https://doi.org/10.1016/S1359-0286(99)00014-5.

[90] Alejandro Simón de Dios and Marta Elena Díaz-García. "Multifunctional nanoparticles: Analytical prospects". In: *Analytica Chimica Acta* 666.1 (2010), pp. 1–22. DOI: https://doi.org/10.1016/j.aca.2010.03.038.

[91] Gérard Férey. "Supertetrahedra in sulfides: matter against mathematical series?" In: *Angewandte Chemie (International ed. in English)* 42.23 (2003), pp. 2576–2579. DOI: https://doi.org/10.1002/anie.200201621.

[92] M. O'Keeffe et al. "Frameworks for Extended Solids: Geometrical Design Principles". In: *Journal of Solid State Chemistry* 152.1 (2000), pp. 3–20. DOI: https://doi.org/10.1006/jssc.2000.8723.

[93] Yun-Nan Gong, Di-Chang Zhong, and Tong-Bu Lu. "Interpenetrating metal–organic frameworks". In: *CrystEngComm* 18 (15 2016), pp. 2596–2606. DOI: https://doi.org/10.1039/C6CE00371K.

[94] Hailian Li et al. "Supertetrahedral Sulfide Crystals with Giant Cavities and Channels". In: *Science* 283.5405 (1999), pp. 1145–1147. DOI: 10.1126/science.283.5405.1145.

[95] O. Slupecki and I. D. Brown. "Bond-valence–bond-length parameters for bonds between cations and sulfur". In: *Acta Crystallographica Section B* 38.4 (Apr. 1982), pp. 1078–1079. DOI: 10.1107/S0567740882005007.

[96] Hailian Li et al. "20 Å $Cd_4In_{16}S_{3514}$ - Supertetrahedral T4 Clusters as Building Units in Decorated Cristobalite Frameworks". In: *Journal of the American Chemical Society* 123.20 (2001), pp. 4867–4868. DOI: `https://doi.org/10.1021/ja010413f`.

[97] O. M. Yaghi et al. "Directed Transformation of Molecules to Solids: Synthesis of a Microporous Sulfide from Molecular Germanium Sulfide Cages". In: *Journal of the American Chemical Society* 116.2 (1994), pp. 807–808. DOI: `https://doi.org/10.1021/ja00081a067`.

[98] Kemin Tan, Alex Darovsky, and John B. Parise. "Synthesis of a novel open-framework sulfide, $CuGe_2S_5.(C_2H_5)_4N$, and its structure solution using synchrotron imaging plate data". In: *Journal of the American Chemical Society* 117.26 (1995), pp. 7039–7040. DOI: `https://doi.org/10.1021/ja00131a042`.

[99] Kemin Tan et al. "Hydrothermal Growth of Single Crystals of TMA-CuGS-2, $[C_4H_{12}N]_6[(Cu_{0.44}Ge_{0.56}S_{2.23})_4(Ge_4S_8)_3]$ and Their Characterization Using Synchrotron/Imaging Plate Data". In: *Chemistry of Materials* 8.2 (1996), pp. 448–453. DOI: `https://doi.org/10.1021/cm950375x`.

[100] Carol L. Bowes et al. "Dimetal Linked Open Frameworks: $(CH_3)_4N]_2(Ag_2Cu_2)Ge_4S_{10}$". In: *Chemistry of Materials* 8.8 (1996), pp. 2147–2152. DOI: `https://doi.org/10.1021/cm960280a`.

[101] Christopher L. Cahill et al. "Structure of Microporous QUI-MnGS-1 and in Situ Studies of Its Formation Using Time-Resolved Synchrotron X-ray Powder Diffraction". In: *Chemistry of Materials* 10.5 (1998), pp. 1453–1458. DOI: `https://doi.org/10.1021/cm980026d`.

[102] Xianhui Bu, Nanfeng Zheng, and Pingyun Feng. "Tetrahedral Chalcogenide Clusters and Open Frameworks". In: *Chemistry – A European Journal* 10.14 (2004), pp. 3356–3362. DOI: `https://doi.org/10.1002/chem.200306041`.

[103] Christopher L. Cahill, Younghee Ko, and John B. Parise. "A Novel 3-Dimensional Open Framework Sulfide Based upon the $[In_{10}S_{20}]^{10-}$ Supertetrahedron: DMA-InS-SB1". In: *Chemistry of Materials* 10.1 (1998), pp. 19–21. DOI: `https://doi.org/10.1021/cm9705707`.

[104] Hailian Li et al. "Noninterpenetrating Indium Sulfide Supertetrahedral Cristobalite Framework". In: *Journal of the American Chemical Society* 121.25 (1999), pp. 6096–6097. DOI: `10.1021/ja990410r`.

[105] Nanfeng Zheng, Xianhui Bu, and Pingyun Feng. "Nonaqueous Synthesis and Selective Crystallization of Gallium Sulfide Clusters into Three-Dimensional Photoluminescent Superlattices". In: *Journal of the American Chemical Society* 125.5 (2003), pp. 1138–1139. DOI: https://doi.org/10.1021/ja021274k.

[106] Wei Wang et al. "A 36-Membered Ring Metal Chalcogenide with a Very Low Framework Density". In: *Inorganic Chemistry* 56.24 (2017), pp. 14730–14733. DOI: https://doi.org/10.1021/acs.inorgchem.7b02109.

[107] Zhou Wu et al. "New 2D Assemblage of Supertetrahedral Chalcogenide Clusters with Tetravalent-Metal-Induced Interrupted Sites". In: *Crystal Growth & Design* 19.7 (2019), pp. 4151–4156. DOI: https://doi.org/10.1021/acs.cgd.9b00605.

[108] Wei Wang et al. "An Unusual Metal Chalcogenide Zeolitic Framework Built from the Extended Spiro-5 Units with Supertetrahedral Clusters as Nodes". In: *Inorganic Chemistry* 57.3 (2018), pp. 921–925. DOI: https://doi.org/10.1021/acs.inorgchem.7b03057.

[109] Homayoun Ahari et al. "Self-assembling iron and manganese metal – germanium – selenide frameworks: $[NMe_4]_2MGe_4Se_{10}$ where M = Fe or Mn". In: *Journal of the Chemical Society, Dalton Transactions* (12 1998), pp. 2023–2028. DOI: https://doi.org/10.1039/A800449H.

[110] Cheng Wang et al. "Indium selenide superlattices from $(In_{10}Se_{18})^6$ supertetrahedral clusters". In: *Chemical Communications* (13 2002), pp. 1344–1345. DOI: https://doi.org/10.1039/B203253H.

[111] Chaozhuang Xue et al. "Supertetrahedral Cluster-Based In–Se Open Frameworks with Unique Polyselenide Ion as Linker". In: *Crystal Growth & Design* 18.5 (2018), pp. 2690–2693. DOI: https://doi.org/10.1021/acs.cgd.8b00185.

[112] Xianhui Bu et al. "Three-dimensional frameworks of gallium selenide supertetrahedral clusters". In: *Angewandte Chemie (International ed. in English)* 43.12 (2004), pp. 1502–1505. DOI: https://doi.org/10.1002/anie.200352880.

[113] Paz Vaqueiro and M. Lucia Romero. "Three-dimensional gallium sulphide open frameworks". In: *Journal of Physics and Chemistry of Solids* 68.5 (2007). 7th International Conference of Solids State Chemistry 2006 (SSC 2006), pp. 1239–1243. DOI: https://doi.org/10.1016/j.jpcs.2006.11.031.

[114] Xianhui Bu et al. "Templated Assembly of Sulfide Nanoclusters into Cubic-C_3N_4 Type Framework". In: *Journal of the American Chemical Society* 125.20 (2003), pp. 6024–6025. DOI: `https://doi.org/10.1021/ja030103s`.

[115] Chaozhuang Xue et al. "Highly open chalcogenide frameworks built from unusual defective supertetrahedral clusters". In: *Dalton Transactions* 48 (29 2019), pp. 10799–10803. DOI: `https://doi.org/10.1039/C9DT01754B`.

[116] Tao Wu et al. "Largest Molecular Clusters in the Supertetrahedral Tn Series". In: *Journal of the American Chemical Society* 132.31 (2010), pp. 10823–10831. DOI: `https://doi.org/10.1021/ja102688p`.

[117] Cheng Wang et al. "Three-Dimensional Superlattices Built from $(M_4In_{16}S_{33})^{10-}$ (M = Mn, Co, Zn, Cd) Supertetrahedral Clusters". In: *Journal of the American Chemical Society* 123.46 (2001), pp. 11506–11507. DOI: `https://doi.org/10.1021/ja011739r`.

[118] Yu-Hong Wang et al. "Transition Metal Complexes as Linkages for Assembly of Supertetrahedral T4 Clusters". In: *Inorganic Chemistry* 49.21 (2010), pp. 9731–9733. DOI: `https://doi.org/10.1021/ic100088n`.

[119] B. Silva-Gaspar et al. "Open-Framework Chalcogenide Materials - from isolated clusters to highly ordered structures - and their photocalytic applications". In: *Coordination Chemistry Reviews* 453 (2022), p. 214243. DOI: `https://doi.org/10.1016/j.ccr.2021.214243`.

[120] Cheng Wang et al. "Nanocluster with One Missing Core Atom: A Three-Dimensional Hybrid Superlattice Built from Dual-Sized Supertetrahedral Clusters". In: *Journal of the American Chemical Society* 124.35 (2002), pp. 10268–10269. DOI: `https://doi.org/10.1021/ja020735z`.

[121] Xianhui Bu et al. "Pushing Up the Size Limit of Chalcogenide Supertetrahedral Clusters: Two- and Three-Dimensional Photoluminescent Open Frameworks from $(Cu_5In_{30}S_{54})^{13-}$ Clusters". In: *Journal of the American Chemical Society* 124.43 (2002), pp. 12646–12647. DOI: `https://doi.org/10.1021/ja021009z`.

[122] Xiaofan Xu et al. "Pushing up the Size Limit of Metal Chalcogenide Supertetrahedral Nanocluster". In: *Journal of the American Chemical Society* 140.3 (2018), pp. 888–891. DOI: `https://doi.org/10.1021/jacs.7b12092`.

[123] Nanfeng Zheng, Xianhui Bu, and Pingyun Feng. "Pentasupertetrahedral clusters as building blocks for a three-dimensional sulfide superlattice". In: *Angewandte Chemie (International ed. in English)* 43.36 (2004), pp. 4753–4755. DOI: `https://doi.org/10.1002/anie.200460386`.

[124] Stefanie Dehnen and Michael K. Brandmayer. "Reactivity of Chalcogenostannate Compounds: Syntheses, Crystal Structures, and Electronic Properties of Novel Compounds Containing Discrete Ternary Anions [MII$_4$(μ_4-Se)(SnSe$_4$)$_4$]$^{10-}$ (MII = Zn, Mn)". In: *Journal of the American Chemical Society* 125.22 (2003), pp. 6618–6619. DOI: https://doi.org/10.1021/ja029601b.

[125] Jing Lv et al. "Two Penta-Supertetrahedral Cluster-Based Chalcogenide Open Frameworks: Effect of the Cluster Spatial Connectivity on the Electron-Transport Efficiency". In: *Inorganic Chemistry* 58.6 (2019), pp. 3582–3585. DOI: https://doi.org/10.1021/acs.inorgchem.8b03503.

[126] Christian Zimmermann, Maike Melullis, and Stefanie Dehnen. "Reactivity of Chalcogenostannate Salts: Unusual Synthesis and Structure of a Compound Containing Ternary Cluster Anions [Co$_4$(μ_4-Se)(SnSe$_4$)$_4$]$^{10-}$". In: *Angewandte Chemie (International ed. in English)* 41 (2002), pp. 4269–4272. DOI: https://doi.org/10.1002/1521-3773(20021115)41:22<4269::AID-ANIE4269>3.0.CO;2-8.

[127] Nan Ding, Duck-Young Chung, and Mercouri G. Kanatzidis. "K$_6$Cd$_4$Sn$_3$Se$_{13}$: A polar open-framework compound based on the partially destroyed supertetrahedral [Cd$_4$Sn$_4$Se$_{17}$]^{10} cluster". In: *Chemical Communications* (10 2004), pp. 1170–1171. DOI: 10.1039/B402686A.

[128] Oleg Palchik et al. "K$_{10}$M$_4$Sn$_4$S$_{17}$ (M = Mn, Fe, Co, Zn): Soluble Quaternary Sulfides with the Discrete [M$_4$Sn$_4$S$_{17}$]$^{10-}$ Supertetrahedral Clusters". In: *Inorganic Chemistry* 42.17 (2003), pp. 5052–5054. DOI: https://doi.org/10.1021/ic0346001.

[129] Manolis J. Manos et al. "SnZn$_4$Sn$_4$S$_{17}$$^{6-}$: a robust open framework based on metal-linked penta-supertetrahedral Zn$_4$Sn$_4$S$_{17}$$^{10-}$ clusters with ion-exchange properties". In: *Angewandte Chemie (International ed. in English)* 44.23 (2005), pp. 3552–3555. DOI: 10.1002/anie.200500214.

[130] Manolis J. Manos, Konstantinos Chrissafis, and Mercouri G. Kanatzidis. "Unique Pore Selectivity for Cs$^+$ and Exceptionally High NH^{4+} Exchange Capacity of the Chalcogenide Material K$_6$Sn[Zn$_4$Sn$_4$S$_{17}$]". In: *Journal of the American Chemical Society* 128.27 (2006), pp. 8875–8883. DOI: https://doi.org/10.1021/ja061342t.

[131] T. Vossmeyer et al. "A "Double-Diamond Superlattice" Built Up of Cd$_{17}$S$_4$(SCH$_2$CH$_2$OH)$_{26}$ Clusters". In: *Science* 267.5203 (1995), pp. 1476–1479. ISSN: 0036-8075. DOI: 10.1126/science.267.5203.1476.

[132] Andreas Eichhöfer et al. "Synthesis, structure and physical properties of the manganese(ii) selenide/selenolate cluster complexes [Mn$_{32}$Se$_{14}$(SePh)$_{36}$(PnPr$_3$)$_4$] and [Na(benzene$-_{15}$-crown$-_5$)(C$_4$H$_8$O)$_2$]$_2$[Mn$_8$Se(SePh)$_{16}$]". In: *Chemical Communications* (13 2008), pp. 1596–1598. DOI: `https://doi.org/10.1039/B714582A`.

[133] Garry S. H. Lee et al. "[S$_4$Cd$_{17}$(SPh)$_{28}$]$^{2-}$, the first member of a third series of tetrahedral [SWMX(SR)y]z- clusters". In: *Journal of the American Chemical Society* 110.14 (1988), pp. 4863–4864. DOI: `10.1021/ja00222a075`.

[134] Xianglin Jin et al. "Synthesis and crystal structure of a polymeric complex [S$_4$Cd$_{17}$(SPh)$_{24}$(CH$_3$OCS$_2$)$_{4/2}$]n·nCH$_3$OH". In: *Polyhedron* 15.15 (1996), pp. 2617–2622. DOI: `https://doi.org/10.1016/0277-5387(95)00544-7`.

[135] N. Herron et al. "Crystal Structure and Optical Properties of Cd$_{32}$S$_{14}$(SC$_6$H$_5$)$_{36}$. DMF4, a Cluster with a 15 Angstrom CdS Core". In: *Science* 259.5100 (1993), pp. 1426–1428. DOI: `10.1126/science.259.5100.1426`.

[136] T. Vossmeyer et al. "Double-Layer Superlattice Structure Built Up of Cd$_{32}$S$_{14}$(SCH$_2$CH(OH)$_4$H$_2$O Clusters". In: *Journal of the American Chemical Society* 117.51 (1995), pp. 12881–12882. DOI: `10.1021/ja00156a035`.

[137] Silke Behrens et al. "Synthesis and Structure of the Nanoclusters [Hg$_{32}$Se$_{14}$(SePh)$_{36}$], [Cd$_{32}$Se$_{14}$(SePh)$_{36}$-(PPh$_3$)$_4$],[P(Et)$_2$(Ph)C$_4$H$_8$OSiMe$_3$]$_5$-[Cd$_{18}$I$_{17}$(PSiMe$_3$)$_{12}$], and [N(Et)$_3$C$_4$H$_8$OSiMe$_3$]$_5$[Cd$_{18}$I$_{17}$(PSiMe$_3$)$_{12}$]". In: *Angewandte Chemie International Edition in English* 35.19 (1996), pp. 2215–2218. DOI: `10.1002/anie.199622151`.

[138] Shan-Lin Huang et al. "A wide pH-range stable crystalline framework based on the largest tin-oxysulfide cluster [Sn$_{20}$O$_{10}$S$_{34}$]". In: *Chemical Communications* 55 (74 2019), pp. 11083–11086. DOI: `https://doi.org/10.1039/C9CC05736F`.

[139] Qipu Lin, Xianhui Bu, and Pingyun Feng. "An infinite square lattice of super-supertetrahedral T6-like tin oxyselenide clusters". In: *Chemical Communications* 50 (31 2014), pp. 4044–4046. DOI: `https://doi.org/10.1039/C4CC00583J`.

[140] Willy Schiwy and Bernt Krebs. "Sn$_{10}$O$_4$S$_{20}$$^{8-}$: A New Type of Polyanion". In: *Angewandte Chemie (International ed. in English)* 14 (1975), p. 436. DOI: `https://doi.org/10.1002/anie.197504361`.

[141] Thomas Kaib, Manuel Kapitein, and Stefanie Dehnen. "Synthesis and Crystal Structure of [Li$_8$(H$_2$O)$_{29}$][Sn$_{10}$O$_4$S$_{20}$]·$_2$H$_2$O". In: *Zeitschrift für anorganische und allgemeine Chemie* 637.12 (2011), pp. 1683–1686. DOI: `10.1002/zaac.201100268`.

[142] John B. Parise and Younghee Ko. "Material Consisting of Two Interwoven 4-Connected Networks: Hydrothermal Synthesis and Structure of [Sn$_5$S$_9$O$_2$] [HN(CH$_3$)$_3$]$_2$". In: *Chemistry of Materials* 6.6 (1994), pp. 718–720. DOI: https://doi.org/10.1021/cm00042a002.

[143] John B. Parise et al. "Structural evolution from Tin Sulfide (selenide) layered structures to nove 3- and 4- connected Tin Oxy sulfides". In: *Journal of Solid State Chemistry* 117 (1995), pp. 219–228. DOI: https://doi.org/10.1006/jssc.1995.1267.

[144] Homayoun Ahari et al. "Modular assembly and phase study of two- and three-dimensional porous tin(IV) selenides". In: *Journal of Materials Chemistry* 9 (6 1999), pp. 1263–1274. DOI: 10.1039/A807660J.

[145] Wei Wang et al. "Three-Dimensional Superlattices Based on Unusual Chalcogenide Supertetrahedral In–Sn–S Nanoclusters". In: *Inorganic Chemistry* 58.1 (2019), pp. 31–34. DOI: https://doi.org/10.1021/acs.inorgchem.8b02574.

[146] John B. Parise and Younghee Ko. "Novel antimony sulfides: synthesis and x-ray structural characterization of Sb$_3$S$_5$·N(C$_3$H$_7$)$_4$ and Sb$_4$S$_7$·N$_2$C$_4$H$_8$". In: *Chemistry of Materials* 4.6 (1992), pp. 1446–1450. DOI: https://doi.org/10.1021/cm00024a056.

[147] Tong Jiang, Geoffrey A. Ozin, and Robert L. Bedard. "Nanoporous tin(IV) sulfides: Mode of formation". In: *Advanced Materials* 6.11 (Nov. 1994), pp. 860–865. DOI: https://doi.org/10.1002/adma.19940061114.

[148] John B. Parise. "Novel sulphide frameworks: synthesis and X-ray structural characterization of Cs$_6$Sb$_{10}$S$_{18}$·12 H$_2$O". In: *Journal of the Chemical Society, Chemical Communications* (22 1990), pp. 1553–1554. DOI: https://doi.org/10.1039/C39900001553.

[149] John B. Parise. "An Antimony Sulfide with a Two-Dimensional, Intersecting System of Channels". In: *Science* 251.4991 (1991), pp. 293–294. DOI: 10.1126/science.251.4991.293.

[150] Tong Jiang, Geoffrey A. Ozin, and Robert L. Bedard. "Nanoporous tin(IV) sulfides: Thermochemical properties". In: *Advanced Materials* 7.2 (Feb. 1995), pp. 166–170. DOI: https://onlinelibrary.wiley.com/doi/abs/10.1002/adma.19950070214.

[151] Tong Jiang et al. "Synthesis and Structure of the Novel Nanoporous Tin(IV) Sulfide Material TPA-SnS-3". In: *Chemistry of Materials* 7.2 (1995), pp. 245–248. DOI: https://doi.org/10.1021/cm00050a001.

[152]   Tong Jiang et al. "Synthesis and structure of microporous layered tin(IV) sulfide materials". In: *Journal of Materials Chemistry* 8 (3 1998), pp. 721–732. DOI: `https://doi.org/10.1039/A706279F`.

[153]   Tong Jiang and Geoffrey A. Ozin. "New directions in tin sulfide materials chemistry". In: *Journal of Materials Chemistry* 8 (1998), pp. 1099–1108. DOI: `https://doi.org/10.1039/A709054D`.

[154]   John B. Parise et al. "Novel layered sulfides of tin: synthesis, structural characterization and ion exchange properties of TMA-SnS-1, $Sn_3S_7 \cdot (NMe_4)_2 \cdot H_2O$". In: *Journal of the Chemical Society, Chemical Communications* (4 1994), pp. 527–527. DOI: `10.1039/C39940000527`.

[155]   Carol L. Bowes et al. "Microporous layered tin sulfide, SnS-1: molecular sieve or intercalant?" In: *Journal of Materials Chemistry* 8 (3 1998), pp. 711–720. DOI: `10.1039/A706278H`.

[156]   IZA. *Database of Zeolite Structures - Zeolite Framework Types.* `http://europe.iza-structure.org/IZA-SC/ftc_table.php`. 2017 (acessed June 1, 2020).

[157]   Anthony K. Cheetham, Gérard Férey, and Thierry Loiseau. "Open-Framework Inorganic Materials". In: *Angewandte Chemie (International ed. in English)* 38.22 (Nov. 1999), pp. 3268–3292. DOI: `https://doi.org/10.1002/(SICI)1521-3773(19991115)38:22<3268::AID-ANIE3268>3.0.CO;2-U`.

[158]   Jian Lin et al. "Interrupted chalcogenide-based zeolite-analogue semiconductor: atomically precise doping for tunable electro-/photoelectrochemical properties". In: *Angewandte Chemie (International ed. in English)* 54.17 (2015), pp. 5103–5107. DOI: `https://doi.org/10.1002/anie.201500659`.

[159]   Chaozhuang Xue et al. "Two Unique Crystalline Semiconductor Zeolite Analogues Based on Indium Selenide Clusters". In: *Inorganic Chemistry* 56.24 (2017), pp. 14763–14766. DOI: `https://doi.org/10.1021/acs.inorgchem.7b02718`.

[160]   Christopher L. Cahill and John B. Parise. "Synthesis and Structure of $MnGe_4S_{10} \cdot (C_6H_{14}N_2) \cdot 3H_2O$: A Novel Sulfide Framework Analogous to Zeolite Li-A(BW)". In: *Chemistry of Materials* 9.3 (1997), pp. 807–811. DOI: `https://doi.org/10.1021/cm960484r`.

[161]   Walter Loewenstein. "The distribution of aluminum in the tetrahedra of silicates and aluminates". In: *American Mineralogist* 39.1-2 (Feb. 1954), pp. 92–96.

[162] Qipu Lin et al. "Mimicking High-Silica Zeolites: Highly Stable Germanium- and Tin-Rich Zeolite-Type Chalcogenides". In: *Journal of the American Chemical Society* 137.19 (2015), pp. 6184–6187. DOI: https://doi.org/10.1021/jacs.5b03550.

[163] Xitong Chen et al. "Selective Ion Exchange and Photocatalysis by Zeolite-Like Semiconducting Chalcogenide". In: *Chemistry – A European Journal* 23.49 (Sept. 2017), pp. 11913–11919. DOI: https://doi.org/10.1002/chem.201702418.

[164] Xitong Chen et al. "Charge- and Size-Complementary Multimetal-Induced Morphology and Phase Control in Zeolite-Type Metal Chalcogenides". In: *Chemistry – A European Journal* 24.42 (July 2018), pp. 10812–10819. DOI: https://doi.org/10.1002/chem.201801571.

[165] Nanfeng Zheng et al. "Synthetic design of crystalline inorganic chalcogenides exhibiting fast-ion conductivity". In: *Nature* 426 (2003), pp. 428–432. DOI: https://doi.org/10.1038/nature02159.

[166] Nanfeng Zheng, Xianhui Bu, and Pingyun Feng. "$Na_5(In_4S)(InS_4)_3 \cdot 6H_2O$, a Zeolite-like Structure with Unusual SIn_4 Tetrahedra". In: *Journal of the American Chemical Society* 127.15 (2005), pp. 5286–5287. DOI: https://doi.org/10.1021/ja050281g.

[167] Jacob Millman and Christos C. Halkias. *Integrated Electronics: Analog and Digital Circuits and Systems*. McGraw-Hill, 1972.

[168] Ibrahim Dincer and Calin Zamfirescu. "Chapter 5 - Hydrogen Production by Photonic Energy". In: *Sustainable Hydrogen Production*. Ed. by Ibrahim Dincer and Calin Zamfirescu. Elsevier, 2016, pp. 309–391. DOI: https://doi.org/10.1016/B978-0-12-801563-6.00005-4.

[169] Hongxiang Wang et al. "Assembly of supertetrahedral clusters into a Cu–In–S superlattice via an unprecedented vertex–edge connection mode". In: *CrystEngComm* 19 (32 2017), pp. 4709–4712. DOI: https://doi.org/10.1039/C7CE00849J.

[170] Le Wang et al. "Coassembly between the Largest and Smallest Metal Chalcogenide Supertetrahedral Clusters". In: *Inorganic Chemistry* 52.5 (2013), pp. 2259–2261. DOI: https://doi.org/10.1021/ic301965w.

[171] Konstantina Tsamourtzi et al. "Straightforward Route to the Adamantane Clusters $[Sn_4Q_{10}]^4$ (Q = S, Se, Te) and Use in the Assembly of Open-Framework Chalcogenides $(Me_4N)_2M[Sn_4Se_{10}]$ (M = MnII, FeII, CoII, ZnII) Including the First Telluride Member $(Me_4N)_2Mn[Ge_4Te_{10}]$". In: *Inorganic Chemistry* 47.24 (2008), pp. 11920–11929. DOI: https://doi.org/10.1021/ic801762h.

[172] Zhou Wu et al. "A new cluster-based chalcogenide zeolite analogue with a large inter-cluster bridging angle". In: *Inorganic Chemistry Frontiers* 6 (11 2019), pp. 3063–3069. DOI: https://doi.org/10.1039/C9QI01051C.

[173] Tao Wu et al. "Monocopper Doping in Cd-In-S Supertetrahedral Nanocluster via Two-Step Strategy and Enhanced Photoelectric Response". In: *Journal of the American Chemical Society* 135.28 (2013), pp. 10250–10253. DOI: https://doi.org/10.1021/ja404181c.

[174] Jian Lin et al. "Atomically Precise Doping of Monomanganese Ion into Coreless Supertetrahedral Chalcogenide Nanocluster Inducing Unusual Red Shift in Mn^{2+} Emission". In: *Journal of the American Chemical Society* 136.12 (2014), pp. 4769–4779. DOI: https://doi.org/10.1021/ja501288x.

[175] Nan-Nan Shen et al. "Discrete Supertetrahedral T3 InQ Clusters (Q = S, S/Se, Se, Se/Te): Ionothermal Syntheses and Tunable Optical and Photodegradation Properties". In: *Crystal Growth & Design* 18.2 (2018), pp. 962–968. DOI: https://doi.org/10.1021/acs.cgd.7b01437.

[176] Tao Wu et al. "Phase Selection and Site-Selective Distribution by Tin and Sulfur in Supertetrahedral Zinc Gallium Selenides". In: *Journal of the American Chemical Society* 133.24 (2011), pp. 9616–9625. DOI: https://doi.org/10.1021/ja203143q.

[177] Xing-Hui Qi et al. "A two-dimensionally microporous thiostannate with superior Cs^+ and Sr^{2+} ion-exchange property". In: *Journal of Materials Chemistry A* 3.10 (2015), pp. 5665–5673. DOI: 10.1039/C5TA00566C.

[178] Mette Ø. Filsø et al. "The structure-directing amine changes everything: structures and optical properties of two-dimensional thiostannates". In: *Acta Crystallographica Section B* 73.5 (Oct. 2017), pp. 931–940. DOI: 10.1107/S2052520617010630.

[179] Juan M. Coronado et al. *Design of Advanced Photocatalytic Materials for Energy and Environmental Applications*. London: Springer London, 2013.

[180] M. Tomkiewicz and H. Fay. "Photoelectrolysis of water with semiconductors". In: *Journal of Applied Physics* 18.1 - 28 (1979). DOI: https://doi.org/10.1007/BF00935899.

[181] María D. Hernández-Alonso et al. "Development of alternative photocatalysts to TiO_2: Challenges and opportunities". In: *Energy & Environmental Science* 2 (12 2009), pp. 1231–1257. DOI: 10.1039/B907933E.

[182] Murielle Schreck and Markus Niederberger. "Photocatalytic Gas Phase Reactions". In: *Chemistry of Materials* 31.3 (2019), pp. 597–618. DOI: 10.1021/acs.chemmater.8b04444.

[183] Yidan Wang et al. "Unraveling the Mechanism of Photocatalytic Water Splitting in α-Ga_2O_3 Loaded with a Nickel Oxide Cocatalyst: A First-Principles Investigation". In: *The Journal of Physical Chemistry C* 123.14 (2019), pp. 8990–9000. DOI: 10.1021/acs.jpcc.9b00047.

[184] J. Rossmeisl et al. "Electrolysis of water on oxide surfaces". In: *Journal of Electroanalytical Chemistry* 607.1 (2007). Theoretical and Computational Electrochemistry, pp. 83–89. DOI: https://doi.org/10.1016/j.jelechem.2006.11.008.

[185] Á. Valdés et al. "Oxidation and Photo-Oxidation of Water on TiO_2 Surface". In: *The Journal of Physical Chemistry C* 112.26 (2008), pp. 9872–9879. DOI: 10.1021/jp711929d.

[186] Isabela C. Man et al. "Universality in Oxygen Evolution Electrocatalysis on Oxide Surfaces". In: *ChemCatChem* 3.7 (2011), pp. 1159–1165. DOI: https://doi.org/10.1002/cctc.201000397.

[187] Fabio Dionigi et al. "Gas phase photocatalytic water splitting with Rh_{2y} $CryO_3$/GaN:ZnO in µ-reactors". In: *Energy Environ. Sci.* 4 (8 2011), pp. 2937–2942. DOI: 10.1039/C1EE01242H.

[188] Cameron J. Shearer et al. "Gas phase photocatalytic water splitting of moisture in ambient air: Toward reagent-free hydrogen production". In: *Journal of Photochemistry and Photobiology A: Chemistry* 401 (2020), p. 112757. DOI: https://doi.org/10.1016/j.jphotochem.2020.112757.

[189] Nanfeng Zheng, Xianhui Bu, and Pingyun Feng. "Two-dimensional organization of $[ZnGe_3S_9(H_2O)]^4$ supertetrahedral clusters templated by a metal complex". In: *Chemical Communications* (22 2005), pp. 2805–2807. DOI: https://doi.org/10.1039/B501775K.

[190] Tao Wu et al. "A Large Indium Sulfide Supertetrahedral Cluster Built from Integration of ZnS-like Tetrahedral Shell with NaCl-like Octahedral Core". In: *Journal of the American Chemical Society* 133.40 (2011), pp. 15886–15889. DOI: https://doi.org/10.1021/ja2066994.

[191] Zhenyu Zhang et al. "Three-Dimensional Open Framework Built from CuS Icosahedral Clusters and Its Photocatalytic Property". In: *Journal of the American Chemical Society* 130.46 (2008), pp. 15238–15239. DOI: https://doi.org/10.1021/ja805449p.

[192] Dongliang Liu et al. "Highly Tunable Heterojunctions from Multimetallic Sulfide Nanoparticles and Silver Nanowires". In: *Angewandte Chemie (International ed. in English)* 57.19 (2018), pp. 5374–5378. DOI: 10.1002/anie.201800848.

[193] Minting Hao et al. "Soluble Supertetrahedral Chalcogenido T4 Clusters: High Stability and Enhanced Hydrogen Evolution Activities". In: *Inorganic Chemistry* 58.8 (2019), pp. 5126–5133. DOI: `https://doi.org/10.1021/acs.inorgchem.9b00207`.

[194] Claudia Coughlan et al. "Compound Copper Chalcogenide Nanocrystals". In: *Chemical Reviews* 117.9 (2017), pp. 5865–6109. DOI: `https://doi.org/10.1021/acs.chemrev.6b00376`.

[195] Michio Matsumura et al. "Cadmium sulfide photocatalyzed hydrogen production from aqueous solutions of sulfite: effect of crystal structure and preparation method of the catalyst". In: *The Journal of Physical Chemistry* 89.8 (1985), pp. 1327–1329. DOI: `https://doi.org/10.1021/j100254a001`.

[196] Min-Ting Hao et al. "Ionothermal synthesis of $Zn_{1x}Cd_xS$ solid solutions with efficient photocatalytic H_2 production via elemental-direct-reactions". In: *Inorganic Chemistry Communications* 93 (2018), pp. 20–24. DOI: `https://doi.org/10.1016/j.inoche.2018.04.027`.

[197] Tooru Inoue et al. "Photoelectrocatalytic reduction of carbon dioxide in aqueous suspensions of semiconductor powders". In: *Nature* 277 (1979), pp. 637–638. DOI: `https://doi.org/10.1038/277637a0`.

[198] Vignesh Kumaravel, John Bartlett, and Suresh C. Pillai. "Photoelectrochemical Conversion of Carbon Dioxide (CO_2) into Fuels and Value-Added Products". In: *ACS Energy Letters* 5.2 (2020), pp. 486–519. DOI: `10.1021/acsenergylett.9b02585`.

[199] Bhupendra Kumar et al. "Photochemical and Photoelectrochemical Reduction of CO_2". In: *Annual Review of Physical Chemistry* 63.1 (2012), pp. 541–569. DOI: `https://doi.org/10.1146/annurev-physchem-032511-143759`.

[200] Sophie Bernadet et al. "Bulk Photodriven CO_2 Conversion through TiO_2 @Si(HIPE) Monolithic Macrocellular Foams". In: *Advanced Functional Materials* 29.9 (2019), p. 1807767. DOI: `https://doi.org/10.1002/adfm.201807767`.

[201] Severin N. Habisreutinger, Lukas Schmidt-Mende, and Jacek K. Stolarczyk. "Photocatalytic Reduction of CO_2 on TiO_2 and Other Semiconductors". In: *Angewandte Chemie International Edition* 52.29 (2013), pp. 7372–7408. DOI: `10.1002/anie.201207199`.

[202] Z. Goren et al. "Selective photoreduction of carbon dioxide/bicarbonate to formate by aqueous suspensions and colloids of palladium-titania". In: *The Journal of Physical Chemistry* 94.9 (1990), pp. 3784–3790. DOI: `10.1021/j100372a080`.

[203] Kan Li, Bosi Peng, and Tianyou Peng. "Recent Advances in Heteroge-neous Photocatalytic CO_2 Conversion to Solar Fuels". In: *ACS Catalysis* 6.11 (2016), pp. 7485–7527. DOI: 10.1021/acscatal.6b02089.

[204] Wei-Ning Wang et al. "Comparison of CO_2 Photoreduction Systems: A Review". In: *Aerosol and Air Quality Research* 14.2 (2014), pp. 533–549. DOI: 10.4209/aaqr.2013.09.0283.

[205] Venkata Pradeep Indrakanti, James D. Kubicki, and Harold H. Schobert. "Photoinduced activation of CO_2 on Ti-based heterogeneous catalysts: Cur-rent state, chemical physics-based insights and outlook". In: *Energy & En-vironmental Science* 2 (7 2009), pp. 745–758. DOI: 10.1039/B822176F.

[206] Xiaoxia Chang, Tuo Wang, and Jinlong Gong. "CO_2 photo-reduction: in-sights into CO_2 activation and reaction on surfaces of photocatalysts". In: *Energy & Environmental Science* 9 (7 2016), pp. 2177–2196. DOI: 10.1039/C6EE00383D.

[207] M. Halmann et al. "Photoassisted carbon dioxide reduction on aqueous suspensions of titanium dioxide". In: *Solar Energy Materials* 10.1 (1984), pp. 85–91. DOI: https://doi.org/10.1016/0165-1633(84)90010-8.

[208] K. Tennakone. "Photoreduction of carbonic acid by mercury coated n-titanium dioxide". In: *Solar Energy Materials* 10.2 (1984), pp. 235–238. DOI: https://doi.org/10.1016/0165-1633(84)90063-7.

[209] Teng-feng Xie et al. "Application of surface photovoltage technique in pho-tocatalysis studies on modified TiO_2 photo-catalysts for photo-reduction of CO_2". In: *Materials Chemistry and Physics* 70.1 (2001), pp. 103–106. DOI: https://doi.org/10.1016/S0254-0584(00)00475-2.

[210] I-Hsiang Tseng, Wan-Chen Chang, and Jeffrey C.S. Wu. "Photoreduction of CO_2 using sol–gel derived titania and titania-supported copper catalysts". In: *Applied Catalysis B: Environmental* 37.1 (2002), pp. 37–48. DOI: https://doi.org/10.1016/S0926-3373(01)00322-8.

[211] I-Hsiang Tseng, Jeffrey C.S Wu, and Hsin-Ying Chou. "Effects of sol–gel procedures on the photocatalysis of Cu/TiO_2 in CO_2 photoreduction". In: *Journal of Catalysis* 221.2 (2004), pp. 432–440. DOI: https://doi.org/10.1016/j.jcat.2003.09.002.

[212] Shengwei Liu, Jiaguo Yu, and Mietek Jaroniec. "Tunable Photocatalytic Selectivity of Hollow TiO_2 Microspheres Composed of Anatase Polyhedra with Exposed 001 Facets". In: *Journal of the American Chemical Society* 132.34 (2010), pp. 11914–11916. DOI: https://doi.org/10.1021/ja105283s.

[213]   Hefeng Cheng et al. "An anion exchange approach to Bi2WO6 hollow microspheres with efficient visible light photocatalytic reduction of CO_2 to methanol". In: *Chemical Communications* 48 (78 2012), pp. 9729–9731. DOI: 10.1039/C2CC35289C.

[214]   Qi Liu et al. "High-Yield Synthesis of Ultralong and Ultrathin Zn_2GeO_4 Nanoribbons toward Improved Photocatalytic Reduction of CO_2 into Renewable Hydrocarbon Fuel". In: *Journal of the American Chemical Society* 132.41 (2010), pp. 14385–14387. DOI: https://doi.org/10.1021/ja1068596.

[215]   Ping Li et al. "Hexahedron Prism-Anchored Octahedronal CeO_2: Crystal Facet-Based Homojunction Promoting Efficient Solar Fuel Synthesis". In: *Journal of the American Chemical Society* 137.30 (2015), pp. 9547–9550. DOI: https://doi.org/10.1021/jacs.5b05926.

[216]   Sibo Wang et al. "Formation of Hierarchical In_2S_3–$CdIn_2S_4$ Heterostructured Nanotubes for Efficient and Stable Visible Light CO_2 Reduction". In: *Journal of the American Chemical Society* 139.48 (2017), pp. 17305–17308. DOI: https://doi.org/10.1021/jacs.7b10733.

[217]   Hao-Lin Wu et al. "Semiconductor Quantum Dots: An Emerging Candidate for CO_2 Photoreduction". In: *Advanced materials (Deerfield Beach, Fla.)* 31.36 (2019), p. 1900709. DOI: 10.1002/adma.201900709.

[218]   Chaitanya Hiragond, Shahzad Ali, and Sorcar Saurav. "Hierarchical Nanostructured Photocatalysts for CO_2 Photoreduction". In: *Catalysts* 9.4 (2019), p. 370. DOI: https://doi.org/10.3390/catal9040370.

[219]   Jingjing Wang et al. "Nanostructured Metal Sulfides: Classification, Modification Strategy, and Solar-Driven CO_2 Reduction Application". In: *Advanced Functional Materials* (2020), p. 2008008. DOI: https://doi.org/10.1002/adfm.202008008.

[220]   Yong Yan et al. "Multiple exciton generation for photoelectrochemical hydrogen evolution reactions with quantum yields exceeding 100%". In: *Nature Energy* 2.5 (2017). DOI: https://doi.org/10.1038/nenergy.2017.52.

[221]   Peng Zhang et al. "Fabrication of CdS hierarchical multi-cavity hollow particles for efficient visible light CO_2 reduction". In: *Energy & Environmental Science* 12 (1 2019), pp. 164–168. DOI: https://doi.org/10.1039/C8EE02538J.

[222]   Jian Jin et al. "A Hierarchical Z-Scheme CdS-WO_3 Photocatalyst with Enhanced CO_2 Reduction Activity". In: *Small (Weinheim an der Bergstrasse, Germany)* 11.39 (2015), pp. 5262–5271. DOI: https://doi.org/10.1002/smll.201500926.

[223] Feiyan Xu et al. "CuInS$_2$ sensitized TiO$_2$ hybrid nanofibers for improved photocatalytic CO$_2$ reduction". In: *Applied Catalysis B: Environmental* 230 (2018), pp. 194–202. DOI: https://doi.org/10.1016/j.apcatb.2018.02.042.

[224] Feiyan Xu et al. "1D/2D TiO$_2$ /MoS$_2$ Hybrid Nanostructures for Enhanced Photocatalytic CO$_2$ Reduction". In: *Advanced Optical Materials* 6.23 (2018), p. 1800911. DOI: https://doi.org/10.1002/adom.201800911.

[225] Sibo Wang, Bu Yuan Guan, and Xiong Wen David Lou. "Construction of ZnIn$_2$S$_4$–In$_2$O$_3$ Hierarchical Tubular Heterostructures for Efficient CO$_2$ Photoreduction". In: *Journal of the American Chemical Society* 140.15 (2018), pp. 5037–5040. DOI: ttps://doi.org/10.1021/jacs.8b02200.

[226] Hyunju Jung et al. "Highly Efficient and Stable CO$_2$ Reduction Photocatalyst with a Hierarchical Structure of Mesoporous TiO$_2$ on 3D Graphene with Few-Layered MoS$_2$". In: *ACS Sustainable Chemistry & Engineering* 6.5 (2018), pp. 5718–5724. DOI: https://doi.org/10.1021/acssuschemeng.8b00002.

[227] Jingxiang Low et al. "Two-dimensional layered composite photocatalysts". In: *Chemical Communications* 50 (74 2014), pp. 10768–10777. DOI: 10.1039/C4CC02553A.

[228] Xingchen Jiao et al. "Defect-Mediated Electron–Hole Separation in One-Unit-Cell ZnIn$_2$S$_4$ Layers for Boosted Solar-Driven CO$_2$ Reduction". In: *Journal of the American Chemical Society* 139.22 (2017), pp. 7586–7594. DOI: https://doi.org/10.1021/jacs.7b02290.

[229] Jiongliang Yuan and Cunjiang Hao. "Solar-driven photoelectrochemical reduction of carbon dioxide to methanol at CuInS$_2$ thin film photocathode". In: *Solar Energy Materials and Solar Cells* 108 (2013). Selected publications from the 22nd Space Photovoltaic Research and Technology (SPRAT) Conference, pp. 170–174. DOI: https://doi.org/10.1016/j.solmat.2012.09.024.

[230] Jingshuai Chen et al. "Synthesis of hexagonal and cubic ZnIn$_2$S$_4$ nanosheets for the photocatalytic reduction of CO$_2$ with methanol". In: *RSC Advances* 5 (5 2015), pp. 3833–3839. DOI: 10.1039/C4RA13191F.

[231] Xiaodong Li et al. "Selective visible-light-driven photocatalytic CO$_2$ reduction to CH$_4$ mediated by atomically thin CuIn$_5$S$_8$ layers". In: *Nature Energy* 4.8 (2019), pp. 690–699. DOI: 10.1038/s41560-019-0431-1.

[232] Koroush Sasan et al. "Open framework metal chalcogenides as efficient photocatalysts for reduction of CO$_2$ into renewable hydrocarbon fuel". In: *Nanoscale* 8 (21 2016), pp. 10913–10916. DOI: 10.1039/C6NR02525K.

Chapter 3

Thesis Objectives

I am convinced that the old growth-model that is based on fossil-fuels and pollution is out of date, and it is out of touch with our planet.

Ursula von der Leyen

The world is changing. Climate change and its consequences are no longer just something you can read about in sci novels.

As was presented in Chapter 1, there is already an open debate about what to do to mitigate these changes and their consequences for society. From a more drastic visions, which include the debate on the compatibility of the current economic model with sustainable development, to the outline of a practical plans that would allow to halt the climate changes, the discussion is already present in most branches of modern society and cannot be ignored.

The strategy presented by the IEA to achieve net zero emissions by 2050 is based on different cornerstones, notably the increase in energy efficiency, a change in society's behavior, a shift in the energy paradigm, through the reduction of fossil fuel consumption and the increase in renewable and nuclear energy sources, and the deployment of CCUS technology. With the wide use of CCUS the CO_2 final destination is being discussed. One of the possibilities, besides its storage, would be its use as a raw material.

CO_2 photoreduction has been seen as one of the possible uses of captured CO_2, as it is an elegant, sustainable and direct way of closing the carbon cycle. However, a

solar-driven photocatalytic process presents limitations that motivate the low yield normally associated with photocatalysis. The semiconductor used as a photocatalyst must have an electronic structure, namely a band gap value, suitable for the solar spectrum. When the solar photon with proper energy is absorbed and charge carriers are formed, they have a greater tendency to recombine rather than move to the surface. When these recombine, the photon energy is wasted. Thus, the band gap value of the material and the charge recombination are the main contributors to the low yields.

Although metal oxides, notably TiO_2, are the most studied materials as photocatalysts, other classes are being evaluated in order to develop processes with better performances. Open framework chalcogenides stand out, since they might have a band gap more suited to the solar power and, due to their open architecture, the charge carriers recombination is expected to be reduced, considering the aspects evidenced in Chapter 2. Thus, the main photocatalysis limitations are being address.

While these materials have very attractive characteristics to be used as photocatalysts, they present some limitations. As discussed in Chapter 2, open framework chalcogenides have low thermal stability, typically collapsing at temperatures above 300°C, and tend to collapse when the structuring agent used during their synthesis is eliminated. It was also observed that although several two-dimensional structures are described in the literature, the exploration of their properties or post modifications is nonexistent to our knowledge. As for the use of these structures in the solar fuels production, it is possible to find in the literature their use for the production of hydrogen through water splitting but as for the CO_2 photoreduction there is little information available.

In view of the above, **the objective of this thesis is the development of open framework chalcogenide materials with suitable characteristics to be used as photocatalysts for solar fuels processes.** This objective can be divided into two main subjects. The first, based on material science, will focus on the synthesis, modification and characterization of the new structures obtained. After obtaining the structures, their photocatalytic performance will be evaluated.

The first point taken into account when it comes to the materials synthesis will be the selection of safe and optimal synthesis methods and the use of suitable, low cost and abundant reagents in order to try to obtain sustainable materials. After obtaining them, they will be characterized with several techniques, in order to evaluate their crystallinity, morphology, chemical composition, porous system and electronic properties.

Given the desired application, the structures previous studied will be post-modified. As presented in Chapter 2, in order to maximize the photocatalytic performance three things are important: band structure (band gap value and band's position adequate to solar spectrum), light absorption capacity together with the porosity of the samples. In order to modify the porous system, two techniques will be chosen. The first one consists in modifying the synthesis gel, through the addition of a mesoporosity agent or changing the gel viscosity. The second route chosen consists on post-synthesis modifications, techniques that involve eliminating the SDA present (e.g. thermal treatment) or reducing the crystal size (e.g. by ball mill). The band structure and light absorption capacity were modified by adding doping agents, such as metals or chalcogenides, and to complexes to the synthesis gel, respectively.

After obtaining, characterizing and modifying the structures, the last step is to evaluate their photocatalytic performance. For this purpose, the materials were tested in a batch photocatalytic unit in gas-solid system without the use of a sacrificial agent. Two reactions were studied, CO_2 photoreduction and water splitting for the production of H_2, which could be combined with CO_2 for further valorization.

Chapter 4

IZM-5 and ITQ-75 Materials: Screening Synthesis Conditions

4.1   Introduction

The syntheses, performed according to the methodology presented in the Chapter 4, can be considered as a hydro(solvo)thermal synthesis, a methodology already widely used in the synthesis of microporous oxides, such as zeolites [1]. Hydro(solvo)thermal synthesis can be defined as the synthesis of materials in a sealed and heated aqueous solution or organic solvent at appropriate temperature and pressure. Normally this type of synthesis is performed in a specially sealed container or high-pressure autoclave [2].

As previously mentioned, there is no reference in the literature as to how the parameters of synthesis influence the final properties of the chalcogenide-type materials under study. Thus, the first stage of this thesis was the screening of different conditions of synthesis, by analyzing the main parameters. The first parameter to be considered was the choice of SDA to be used. Taking into account that organic nitrogen compounds are widely used as SDAs in zeolite synthesis and considering the tests performed previously at IFPEN and in previous works (namely the one performed by Lin et al. [3]), 1,3-bis(4-piperidyl)propane, formerly referred as Compound A (see Table A.2) was chosen as a promising SDA to start the study.

4.2   Synthesis of IZM-5 Material. 1,3-Bis(4-piperidyl)propane ($C_{13}H_{26}N_2$) - Compound A as SDA

Using compound A as SDA (see Table A.2), a material named IZM-5 is obtained. This new ordered and crystalline material was first synthesized at IFPEN [4] in 2019 and it is one of the few metal sulfide materials without the presence of Ga, Ge, In or Cd, chemical elements known for their toxicity and/or rarity.

The IZM-5's PXRD pattern is present on Figure 4.1 and exhibits its characteristic diffraction peaks at 2θ equal to 8,0°, 10,2°, 11,1° and 11,7°. IZM-5's crystalline structure and its analysis was not present at its original patent and will be discussed below.
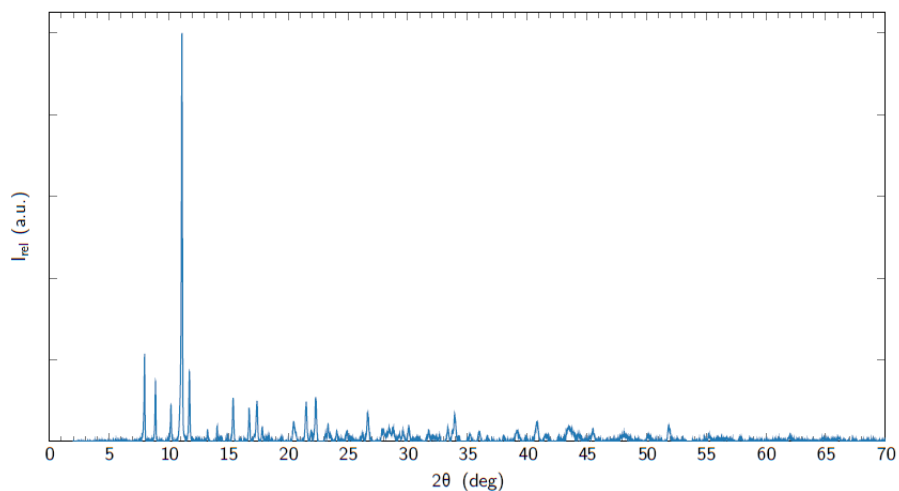
(a)
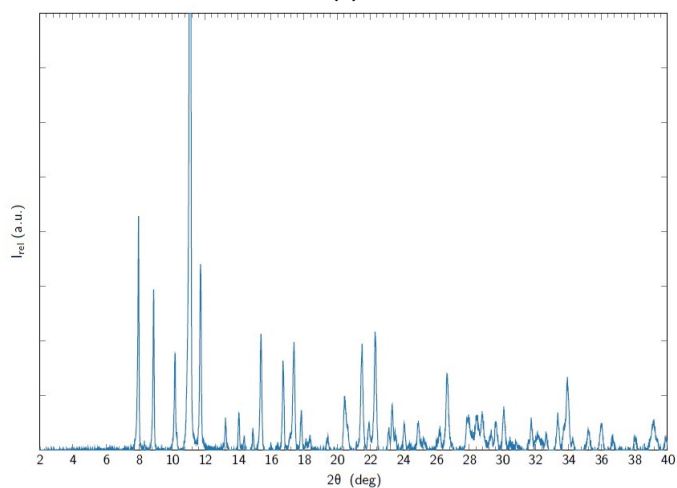
(b)

Figure 4.1: (4.1a) PXRD pattern of IZM-5 and (4.1b) respective zoom between 2θ equal to 2°
and 40°, highlighting the main diffraction peaks

This material was synthesized from a gel with the molar composition of 1 SnO_2
: 0,32 $Zn(NO_3)_2$: 5,72 S : 6,29 $C_{13}H_{26}N_2$ (Compound A) : 132,64 $C_2H_6O_2$:
138,08 H_2O. After 12 days of synthesis and at a temperature of 190°C, under au-

togenus pressure and static conditions, a yellow powder with the chemical formula $Sn_{3,4}Zn_{0,62}S_8 \cdot C_{13,68}H_{29,22}N_{2,05}$ was obtained according to the original patent [4].

Comparing IZM-5 with CPM-120-ZnSnSe [3], both obtained with the same SDA and metallic species, it is easily observed that the materials have different diffraction patterns (see Figure 4.2). Looking closely at the molar composition of the synthesis' gels and the final materials obtained, the main differences between the two are the Sn/Zn molar ratio (the synthesis gel that originates CPM-120 has a Sn/Zn molar ratio equal to 4,2 and the one that originates IZM-5 a molar ratio equal to 3,1) and the use of a different chalcogenide and Sn-source. This shows that it is possible to obtain structures with different topologies, not by changing the SDA used, but due to the chemical composition of the initial synthesis gel.
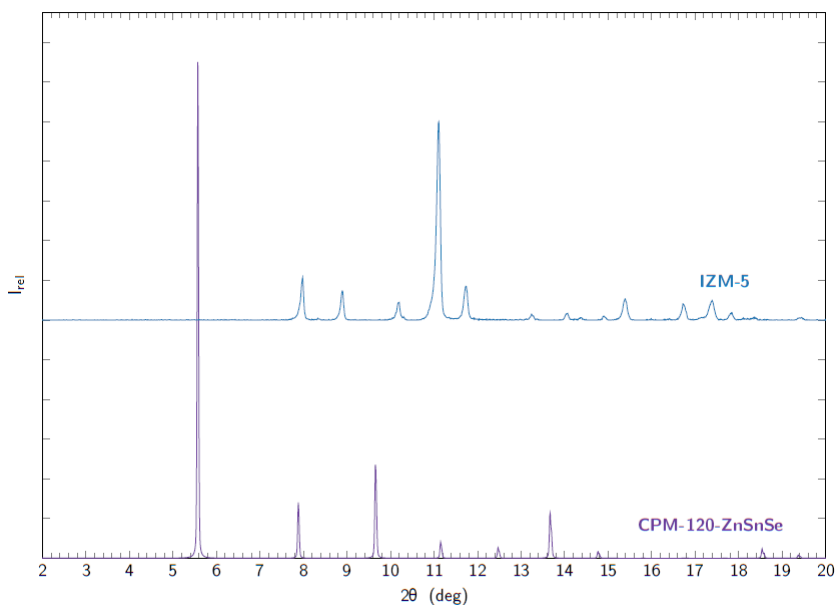
Figure 4.2: Comparison between CPM-120-ZnSnSe [3], with Sn : 0,24 Zn(NO$_3$)$_2$: 4,32 Se : 4,75 $C_{13}H_{26}N_2$ (Compound A) : 99,9 $C_2H_6O_2$: 105,32 H_2O as synthesis gel, and IZM-5, with 1 SnO$_2$: 0,32 Zn(NO$_3$)$_2$: 5,72 S : 6,29 $C_{13}H_{26}N_2$ (Compound A) : 132,64 $C_2H_6O_2$: 138,08 H_2O as synthesis gel, PXRD patterns

In terms of morphology, IZM-5 is composed of small regular prisms (see Figures 4.3b and 4.3d) or hexagonal plates (see Figures 4.3a and 4.3c) with dimensions between 6 and 9 μm.

(a)

(b)

(c)

(d)
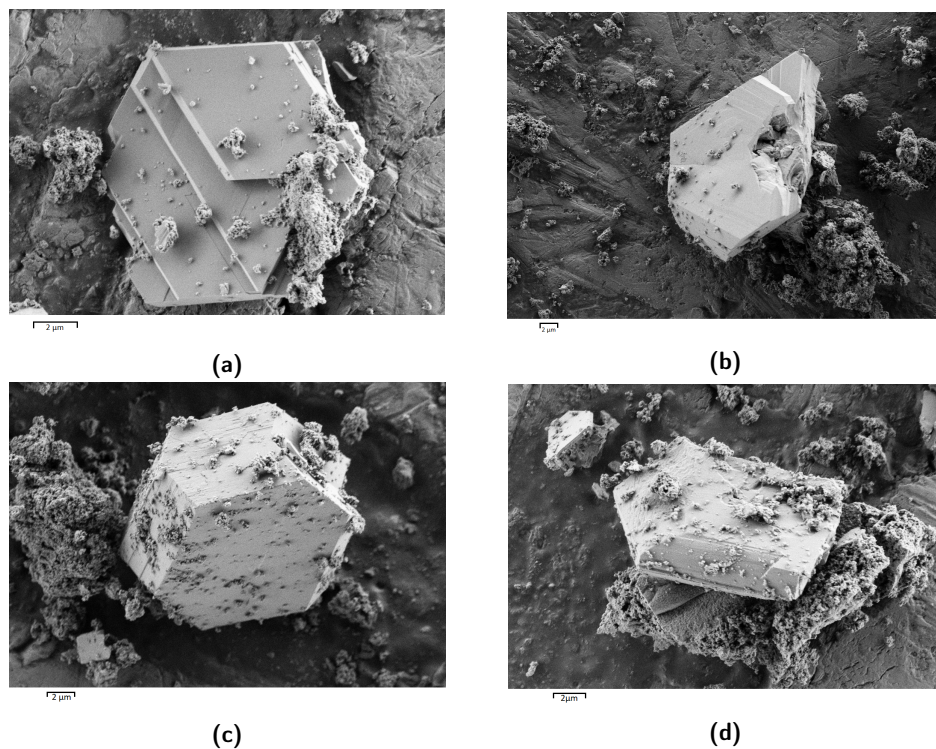
Figure 4.3: IZM-5's SEM images

In order to have more insight on the environment where the SDA is located in the structure, IR spectroscopy and ^{13}C NMR were performed. For this, two NMR spectra were analyzed, the isolated SDA and the IZM-5 in each case (see Figure 4.4).

(a)   **(b)**
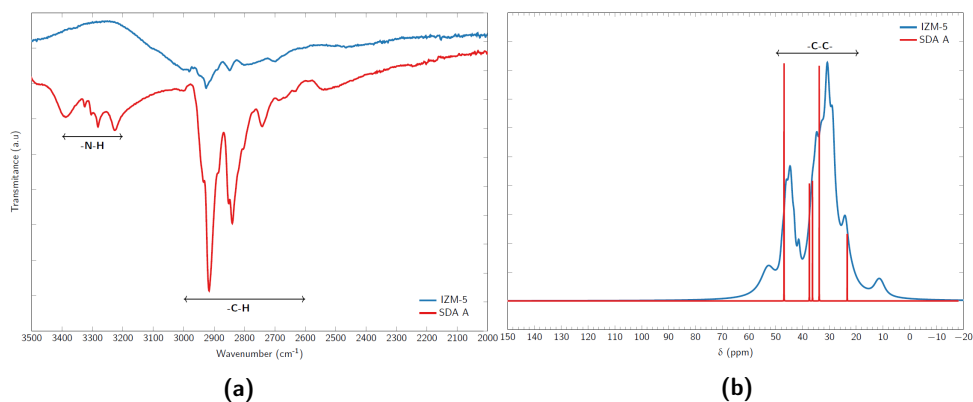
Figure 4.4: (4.4a) IR and (4.4b) ^{13}C NMR spectra of IZM-5 (in blue) and Compound A (in red)

Observing the IR spectrum of the isolated SDA (Figure 4.4a, spectrum in red) two zones stand out. A first one, between 3000 and 2600 cm^{-1}, can be associated with the C-H vibrations. The second zone, between 3300 and 3200 cm^{-1}, is associated with the N-H vibrations. Comparing now with IZM-5 IR spectrum (Figure 4.4a, spectrum in blue) the main difference is the disappearance of the vibration bands associated with the N-H bond. This could mean that the SDA present in the sample is interacting with the inorganic structure of IZM-5. Regarding the ^{13}C NMR spectra (see Figure 4.4b), it is observed that the peaks are in a region of the spectra associated with aliphatic carbons. Thus, it seems that the SDA carbon chain remains intact after the synthesis process as it was suggested earlier by elemental analysis.

4.2.1 IZM-5 Structure

According to single crystal XRD (SCXRD)[2], it was possible to solve the structure and simulate a diffraction pattern. A table with all diffraction peaks can be found in the Appendix C. Comparing the simulated pattern with the experimental one (see Figure 4.5a and Table 4.1), it can be seen that there is a good agreement between both diffractograms.

---

[2]SCXRD was carried out on a Bruker D8 VENTURE PHOTON-III using a Cu Kα (λ= 1,54178 Å) radiation at 100 K. The structure resolution was done in RIAIDT-USC analytical facilities

(a)

(b)

(c)
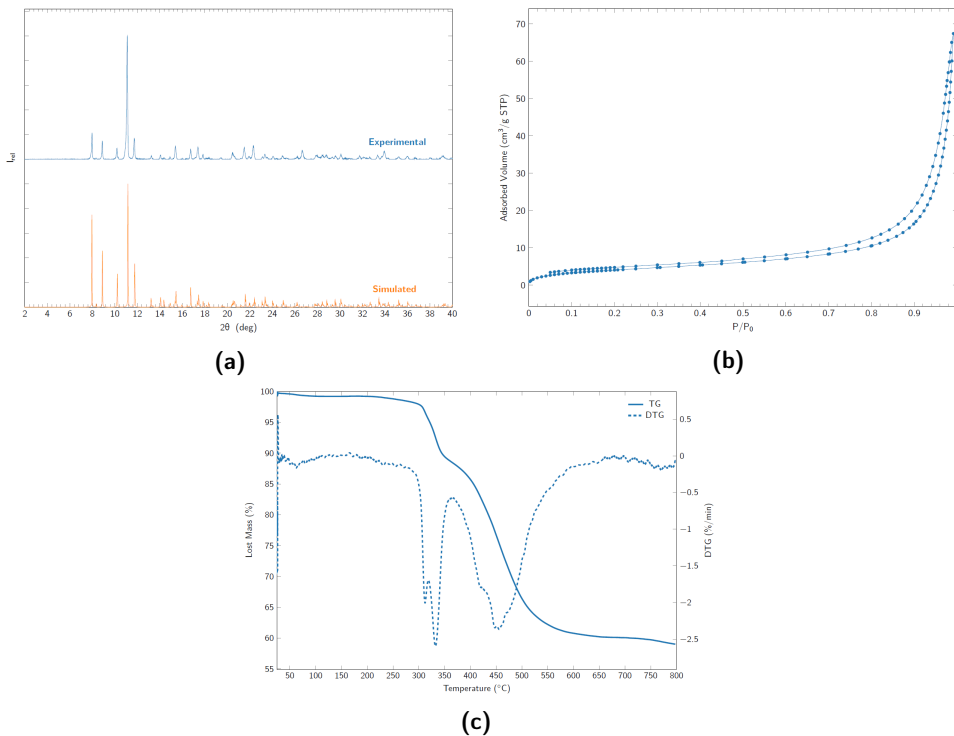
Figure 4.5: (4.5a) IZM-5 calculated and experimental diffraction patterns, (4.5b) N_2 adsorption-desorption isotherm and (4.5c) TG-DTG

Table 4.1: IZM-5's simulated diffraction peaks, and respective crystallographic planes, and experimentally observed diffraction peaks

h	k	l	Simulated 2θ (deg)	d (Å)	I rel (%)	Experimental 2θ (deg)	d (Å)	I rel (%)
1	1	0	7,96	11,10	65,5	7,94	11,14	37,4
2	0	0	8,92	9,93	20,8	8,93	9,91	21,3
2	0	-2	10,24	8,65	12,9	10,26	8,62	11,3
0	0	2	11,16	7,92	100,0	11,11	7,96	100,0
1	1	-2	11,76	7,52	37,5	11,73	7,55	28,0
0	2	0	13,22	6,69	7,9	13,23	6,69	4,6
3	1	-2	14,10	6,29	4,4	14,12	6,27	7,5
3	1	0	14,91	5,94	3,7	14,92	5,94	6,0
2	2	-1	15,36	5,76	4,7	15,37	5,77	22,2

			Simulated			Experimental		
h	k	l	2θ (deg)	d (Å)	I rel (%)	2θ (deg)	d (Å)	I rel (%)
3	1	-3	16,72	5,30	1,0	16,69	5,31	17,7
0	2	2	17,37	5,11	2,8	17,39	5,10	19,5
4	0	0	17,89	4,97	2,8	17,98	4,93	5,7
2	0	-4	19,52	4,54	1,6	19,51	4,55	1,1
4	2	-1	20,65	4,30	3,0	20,65	4,30	14,6
0	2	3	21,47	4,15	0,2	21,50	4,13	22,6
4	2	-3	21,86	4,06	0,8	21,85	4,07	5,3
4	2	0	22,33	3,99	1,2	22,30	3,99	19,5
6	0	-2	23,35	3,81	10,2	23,31	3,82	13,4
3	3	0	24,03	3,70	7,0	23,82	3,74	9,5
3	3	0	24,09	3,70	3,5	24,05	3,70	5,6
3	3	-3	25,22	3,53	1,7	25,23	3,53	8,2
0	2	4	26,12	3,41	1,8	26,05	3,42	2,9
2	4	-1	27,85	3,21	1,8	27,81	3,21	19,8
7	1	-4	28,84	3,09	7,9	28,77	3,10	12,4
3	3	2	29,33	3,04	3,3	29,14	3,07	18,7
2	4	1	29,58	3,02	9,1	29,57	3,02	8,9
0	4	3	31,63	2,83	3,0	31,59	2,83	10,2
1	5	0	33,76	2,65	1,1	33,71	2,66	20,0
7	3	-2	34,22	2,62	1,0	34,22	2,62	7,2
7	3	-4	34,62	2,59	0,0	34,59	2,59	3,9
9	1	-4	35,91	2,50	0,8	35,96	2,50	17,6
2	4	-5	36,73	2,45	2,3	36,67	2,45	8,7
3	5	1	37,79	2,38	0,2	37,78	2,38	1,0
7	3	-6	38,73	2,33	0,0	38,73	2,33	8,4
0	4	5	39,12	2,30	2,5	39,11	2,30	10,3

Table 4.1 continued from previous page

Concerning the structure, IZM-5 belongs to the monoclinic group, space group $C2/c$ and with $a = 22,9522(11)$Å, $b = 13,3899(11)$Å, $c = 18,2932(10)$Å, $\alpha = \gamma = 90°$ and $\beta = 119,969°$ as lattice parameters. IZM-5 can be classified as a microporous layered material with a semicube as building unit (see Figure 2.26b in Chapter 2) and with SDA located in the interlaminar space (see Figure 4.6). The SDA is responsible for the low microporous volume observed (see Figure 4.5b) due to their location in the free porous volume. The layers, which have a thickness of about 6 Å, are spaced by about 5 Å and are oriented parallel to plane ab.
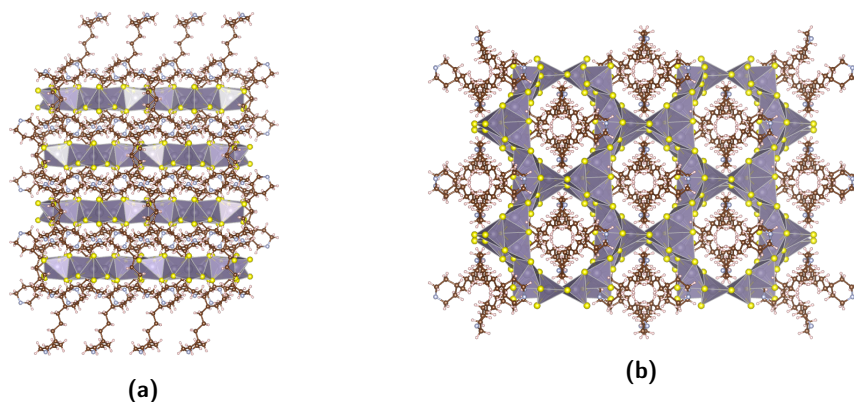
Figure 4.6: IZM-5 representations along (4.6a) a or (4.6b) c planes (Sn - gray, S - yellow, C - brown, N - pink, H - silver)

The different semi-cube clusters are connected by double bridge sulfur bonds (see Figure 4.7a). The connection of the different clusters leads to the formation of individual layers with a honeycomb structure. Each pore, with a hexagonal shape (see Figure 4.7b), presents as dimensions 13,2788(7) Å $\times$ 10,988(11) Å.
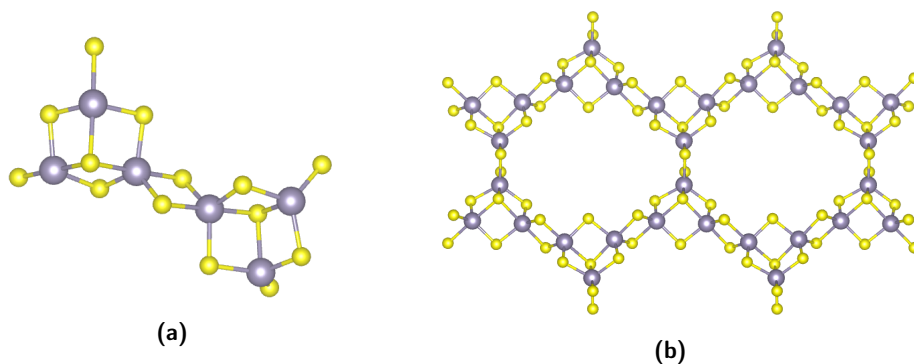
Figure 4.7: (4.7a) Connection between two clusters and (4.7b) hexagonal-shaped porous system

According to the structural resolution, IZM-5 should exhibit a composition equal to $Sn_3S_7 \cdot C_{13}H_{28}N_2$, thus not presenting Zn in its composition, although this metal is present in the synthesis gel. This raises the question about the location of Zn in the material. It may indeed be in the sample, but not in the structure, and might even be an impurity. In order to better understand Zn location and distribution on

the sample, semi-quantitative EDS was performed. Examining the IZM-5 crystal closely (see Figure 4.8), it is observed that Sn, Zn and S are present and evenly distributed. Thus, there seems to be Zn in the final structure, being necessary a more exhaustive consideration.
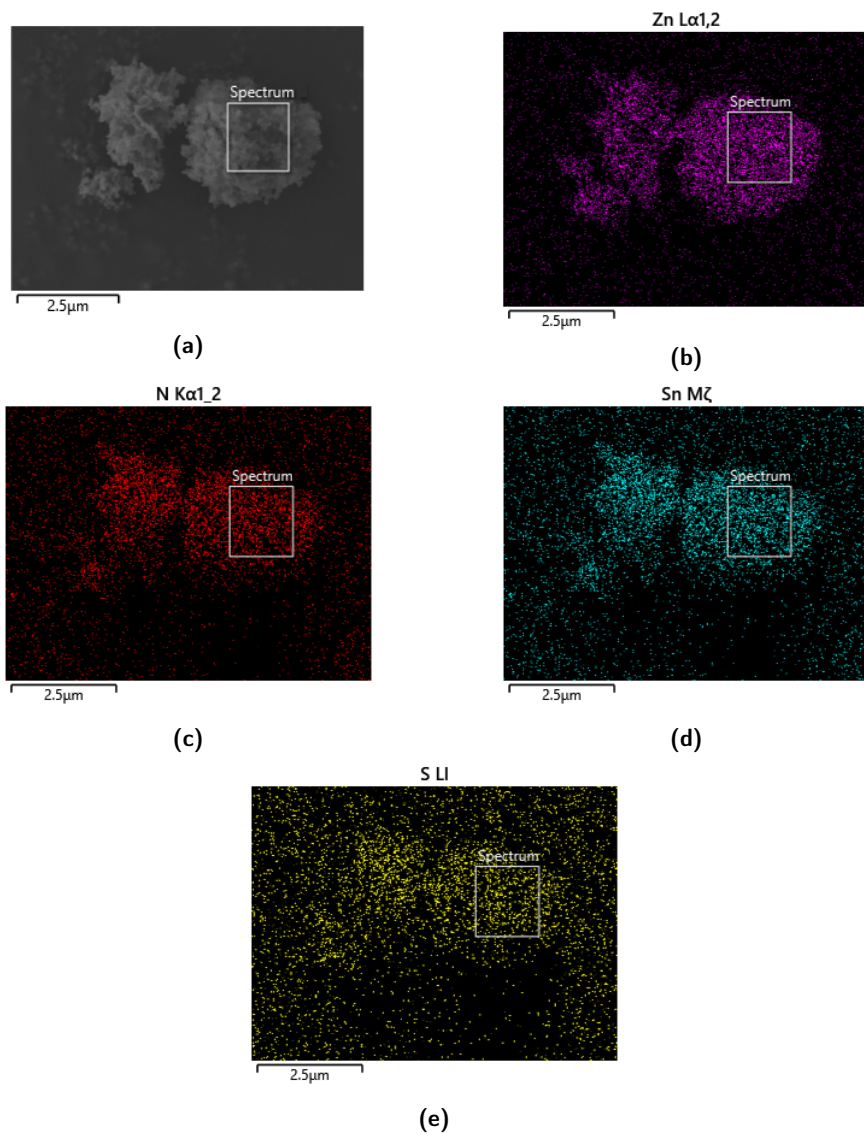
Figure 4.8: EDS mapping of a IZM-5 crystal: 4.8b - Zn content; 4.8c - N content; 4.8d - Sn content; 4.8e - S content

In order to better understand the importance of zinc in the structure, IZM-5 was synthesized without the presence of the zinc precursor in the synthesis gel. The PXRD of the resulting solid is shown in Figure 4.9.
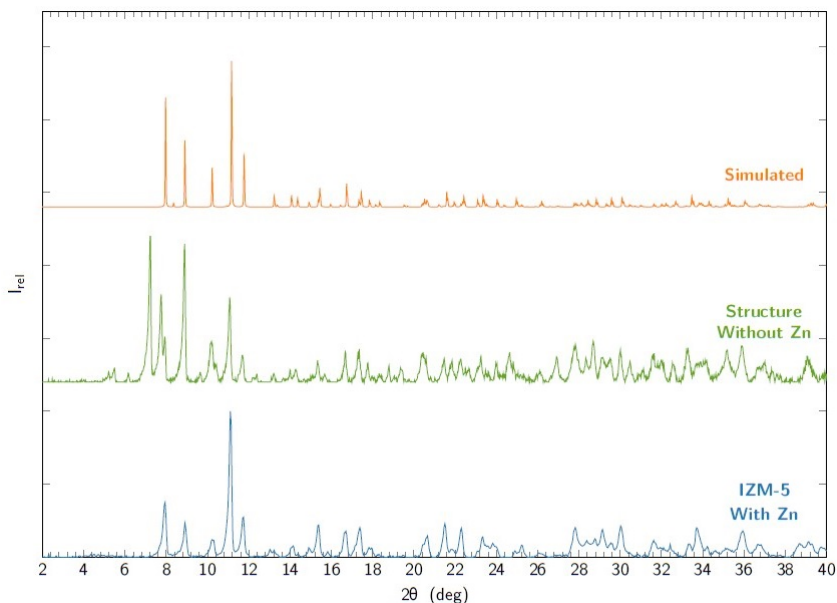
Figure 4.9: PXRD patterns of IZM-5 synthesized with Zn precursor on the synthesis gel (in blue), without Zn precursor on the synthesis gel (in green) and IZM-5 simulated pattern, according to SCXRD (in orange)

Looking at the diffractograms present in Figure 4.9, it can be seen that a structure with a crystalline diffraction pattern is obtained regardless of the presence of zinc in the synthesis gel. Comparing the experimental diffraction patterns obtained, a similarity is observed with respect to the position of the diffraction peaks, but not their intensity. IZM-5 characteristic peaks located at 2θ equal to 8,0°, 10,2°, 11,1° and 11,7° are present on the structure obtained without zinc. However, there are two diffraction peaks, located at 2θ equal to 7,2° and 7,7°, that are not present on IZM-5 experimental or simulated diffraction patterns. Evaluating now the peak's relative intensity, the most intense peak in IZM-5 is located at 2θ equal to 11,1° while the most intense peak obtained in the structure without zinc is at 7,2°, a peak non-existent on IZM-5's diffraction pattern. Therefore, it seems that when zinc is not present on the synthesis gel, IZM-5 and an unknown crystaline phase are obtained.

The chemical composition of the materials under study was then determined, through elemental analysis and ICP, to confirm the metal and organic content (see Table 4.2). On Table 4.3 it is possible to find the molar ratios of the synthesis gel and on the final structures.

Table 4.2: Chemical composition of different IZM-5 samples with and without Zn present in the synthesis gel ([1]Determined by elemental analysis. [2]Determined by ICP)

Material	Formula	Mass composition (%)					
		N[1]	C[1]	H[1]	S[1]	Sn[2]	Zn[2]
IZM-5 with Zn	$Sn_{3,13}Zn_{1,26}S_8 \cdot C_{15,01}H_{31,49}N_{2,24}$	3,09	17,80	3,11	25,34	36,68	8,12
Structure without Zn	$Sn_{3,60}S_8 \cdot C_{16,38}H_{33,92}N_{2,08}$	2,94	19,82	3,42	25,86	43,11	-

Table 4.3: Different molar ratios on the synthesis gel and on the final IZM-5 structures

	Gel Molar Ratios			Material Molar Ratios		
	Sn/Zn	Sn/S	C/N	Sn/Zn	Sn/S	C/N
IZM-5 with Zn	3,1	0,2	6,5	2,5	0,4	6,7
Structure without Zn	-	0,2	6,5	-	0,5	7,9

Assessing the chemical composition of IZM-5 prepared with zinc, it is observed that about 8% of the sample is composed of this element, confirming again its presence in the final material and corroborating the EDS results previously presented (see Figure 4.8). Looking now to the C/N molar ratio, this is similar of the original SDA, so it seems that this compound maintain its integrity during the synthesis procedure. Comparing the gel ratios with those of the material (see Table 4.3), it is possible to observe a decrease in the Sn/Zn molar ratio, from 3,1 to 2,5, and an increase in the Sn/S molar ratio, from 0,2 to 0,4. These results suggest that there is an excess of Sn and S precursors on the synthesis gel.

Concerning the material obtained without zinc, ICP confirms the absence of this metal in the final structure. Regarding the molar ratios Sn/S and C/N, an increase after the synthesis process. The most significant increase is in the C/N ratio, from 6,7 to 7,9.

Subsequently, XPS was performed on the two structures to better understand the environment where the zinc is located, its influence on the other elements present and their oxidation state (see Figure 4.10).
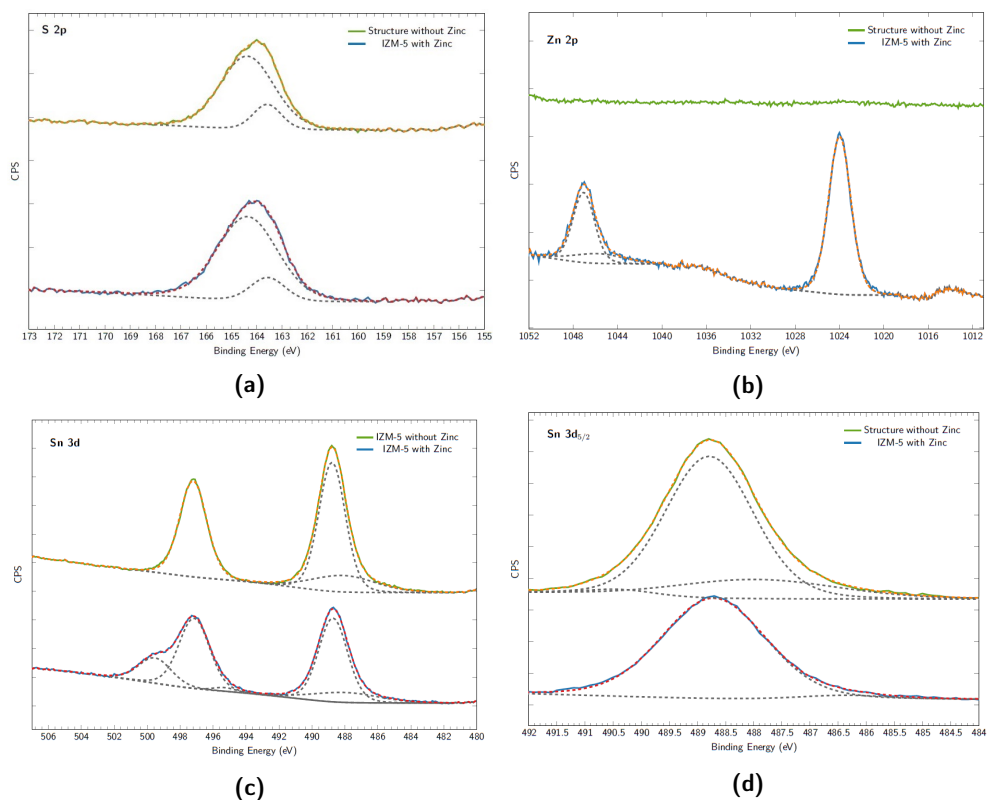
Figure 4.10: Regions S 2p (4.10a), Zn 2p (4.10b), Sn 3d (4.10c) and Sn $3d_{5/2}$ (4.10d) of the different XPS spectra of the structure obtained without zinc (in green) and IZM-5 with zinc (in blue)

Figure 4.10a shows the spectrum of S 2p associated with a S^{2-} ion [5]. The spectrum of this element is known to contain two spin-orbit doublets - S $2p_{3/2}$ and S $2p_{1/2}$ [6]. The S $2p_{1/2}$ component usually lies at a binding energy between 160,0 and 161,2 eV. However, in the samples under study, this component is found at 163,6 eV. According to Smart et al. [5], there is an increase on binding energy with increasing oxidized sulfur species, from S^{2-} (160,1-161,2 eV), S_2^{2-} (162,1-162,6 eV), S_n^{2-} (161,9-163,2 eV) to S_n^0 (163,0-164,2 eV). In metal polysulfide materials it is observed that the sulfur atoms adjacent to the ones bonded to the metal present a binding energy higher than expected, approximately 1 eV greater. The sulfur atoms more remote from the metal have a binding energy closer to, but still less, S_n^0 [7]. Hence, the sulfur species of the samples under study can be associated to a metal polysulfide material.

As for the spectrum of Zn 2p (see Figure 4.10b), two peaks, one at 1047,1 eV and the other at 1024,0 eV, can be associated with Zn $2p_{1/2}$ and $2p_{3/2}$, respectively [6]. This behavior can be assign to Zn^{2+} [8]. It is observed the nonexistence of such peaks in the sample IZM-5 obtained without zinc (spectrum in green in Figure 4.10b), confirming the absence of these metal species in the studied sample.

Finally, the Sn 3d spectra is presented (see Figure 4.10c). Both spectra show two peaks at 488,8 eV and 497,2 eV, associated with Sn $3d_{5/2}$ and Sn $3d_{3/2}$ respectively [6]. According to La Rocque et al. [9], the position of the Sn $3d_{5/2}$ peak makes it possible to distinguish whether Sn^{2+} or Sn^{4+} is present. The position of the peak at 488,7 eV confirms the presence of Sn^{4+}. Furthermore, the position of the S $2p_{1/2}$ component at 163,6 eV was associated by Minniam Reddy et al. [10] as a S connected to Sn^{4+}.

The impact that the presence of zinc has on the interaction with UV-Vis radiation was also evaluated. To this end, UV-Vis spectroscopy was used to plot the material's reflectance as a function of wavelength (see Figure 4.11).
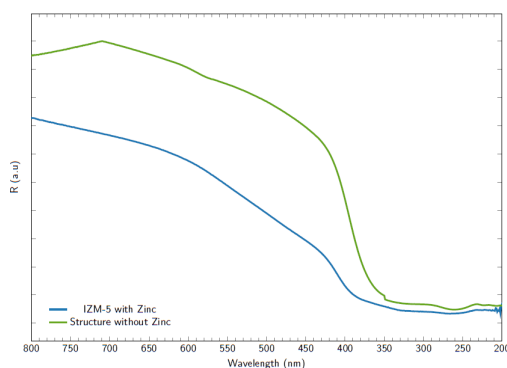
Figure 4.11: UV-Vis spectra of IZM-5 with Zn (in blue) and the structure without Zn (in green)

As can be seen in Figure 4.11, the presence of zinc allows for a decrease in the reflectance of the final structure and, as a consequence, a greater interaction with the longer wavelength radiation, i.e. the less energetic one. As such, the optical band gap of the structure with zinc is lower than the one without zinc, something desired for the final photocatalytic application.

In determining the optical band gap of the structures under study it was necessary, according to the method described by Zannata [11], to fit a sigmoidal curve to the transition (see Figure 4.12).

(a)　　　　　　　　　　　　　　**(b)**
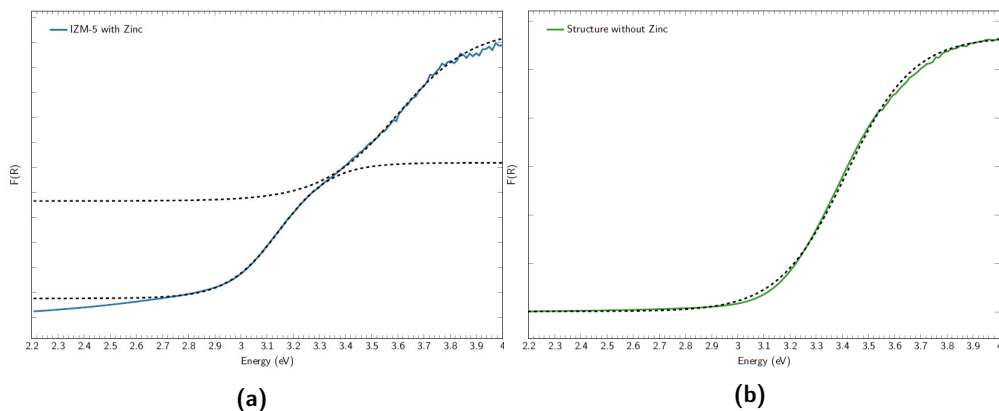
Figure 4.12: Kubelka Munk function representation for (4.12a) IZM-5 with zinc and for (4.12b) the structure without zinc

As can be seen from Figure 4.12a, it was necessary to fit two sigmoidal curves to the material's observed transaction. The same is not observed for the material obtained without zinc, where it is possible to fit only one sigmoidal curve (see Figure 4.12b). Hence, it is observed that the transition of IZM-5 with zinc shows two contributions, something not observed for the other material. Since IZM-5 with zinc has two transitions, two optical band gap values can be determined. The first transition is associated with a optical band gap equal to 3,1 eV and the second one with a optical band gap equal to 3,6. Regarding the remaining material, it has a optical band gap equal to 3,4 eV. This information is systematized in the Table 4.4.

Table 4.4: Optical band gap (E_g) of IZM-5 materials

Material	E_g (eV)
IZM-5 with zinc	3,1 & 3,6
Structure without zinc	3,4

4.2.1.1 Literature structure comparation

Comparing the structure of IZM-5 with others present in the literature, IZM-5 exhibits the structure typical of SnS-1 material, a structure previously studied by Jiang et al. [12, 13, 14, 15, 16]. Diverse SDAs were used to obtain the SnS-1 structure, which shows its flexibility. According to Jiang et al. [15], SnS-1 is obtained when using small cations such as $DABCOH^+$ (1,4-diazabicyclo[2.2. 2]octane), NH_4^+ / Et_4N^+, Et_4N^+, trimethylammonium and tetramethylammonium. In order to accommodate the different SDAs, SnS-1 tends to modify the space between, and within the layers, in order to stabilize the new species, instead of creating a new structure. Therefore, it is possible to observe in the literature the presence of several polymorphs of SnS-1, that is, SnS-1 frameworks with different unit cell parameters and space groups. Of the three SnS-1 polymorphs studied by Jiang et al. [15], DABCOH-SnS-1, obtained with 1,8-diazabicyclooctane (DABCO) as SDA, stands out, since crystallizes with the same space group as IZM-5. Comparing the porous dimensions, DABCOH-SnS-1 has pores with smaller dimensions (10,98 Å × 9,95 Å). With the information present in [15] it was possible to simulate the DABCOH-SnS-1 diffraction pattern and compare it with IZM-5 diffraction pattern (see Figure 4.13).
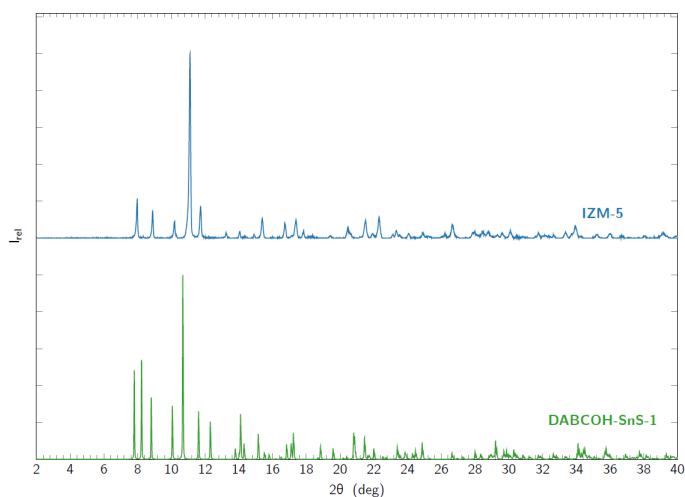
Figure 4.13: DABCOH-SnS-1 [15] and IZM-5 PXRD patterns

Comparing the two diffraction patterns, it can be seen that up to 2θ equal to 12°, where the main diffraction peaks of IZM-5 are located, both materials present the same diffraction peaks, except a peak at 2θ equal to 8,2° and 12,5°. Only

a slight displacement towards high diffraction angles is being observed for IZM-5 material. The IZM-5 highest intensity peak is displaced towards higher diffraction angles about 0,4°, which is significant in this range of 2θ.

4.2.2 Analysis of IZM-5 structure. Influence of synthesis conditions

A systematic study of this structure follows. For this, the impact of three important variables was assessed: crystallization time, cooling rate and chemical composition of the gel.

4.2.2.1 Impact of synthesis duration

According to the original IZM-5 patent [4], the time of synthesis of this material is 12 days. In order to evaluate the crystallization kinetics, i. e., if there would be the formation of other crystalline phases or the transformation of intermediate phases, a reduction on synthesis time was performed. The diffraction patterns of the samples obtained with 1, 2, 3, 6 and 8 days of synthesis time are presented in Figure 4.14.
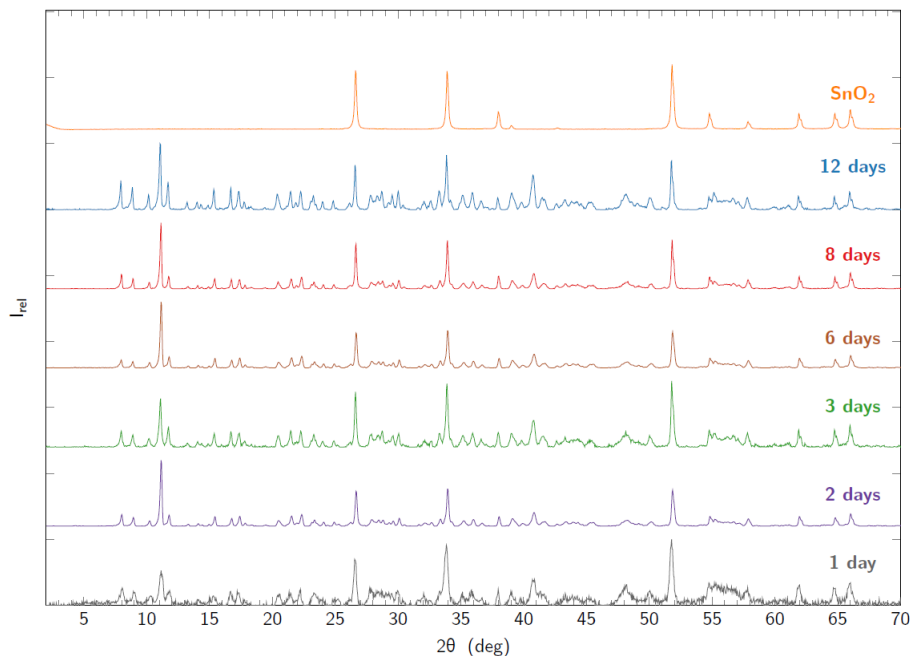
Figure 4.14: PXRD patterns of IZM-5 with reduced time of synthesis - 1 day (gray), 2 days (purple), 3 days (green), 6 days (brown), 8 days (red), 12 days (blue) - and SnO_2 (orange)

By evaluating the diffractograms present in Figure 4.14 different conclusions can be extrapolated. The relative intensity of the peaks associated with IZM-5 is increased up to 6 days of synthesis. After the sixth day of synthesis, these peaks do not suffer alterations in their intensity. It is thus observed that there is no intermediate crystalline phase during the crystallization process of IZM-5. Evaluating now at the intensity of the peaks associated with SnO_2 phase, the main impurity of this material, it is inferred that it varies little with the different synthesis times. This means that either SnO_2 is in excess in the initial gel, or it is not very soluble in the solvent used. Therefore, and using the composition of the gel present in the patent and 190°C as the temperature of synthesis, after 6 days of synthesis it is possible to obtain a fully crystallized IZM-5, albeit still presenting SnO_2 as the main impurity.

4.2.2.2 Impact of cooling rate

The rate at which the crystalline phases are cooled may have an impact on the final phase obtained after filtration. There are two fundamental steps in the crystallization process, nucleation and crystal growth. Nucleation is the step where the nuclei, clusters of microscopic dimensions that originate from atoms or molecules dispersed in the solvent, are formed. This step is followed by the crystal growth stage, where the growth of the previously formed nuclei occurs. Depending on the conditions, nucleation or crystal growth can be predominantly over each other. When rapid cooling takes place, the growth stage is stopped, and thus crystals with small crystal size are obtained. On the contrary, when the cooling is slow, the crystals have time to grow [17, 18]. The cooling rate may also have an impact on the final crystal structure in systems where there is a competition between kinetically and thermodynamic controlled routes [19, 20].

According to the original patent [4], in order to obtain IZM-5, cooling must be done using water and ice. This methodology, classified as fast cooling, allows the obtention of the diffraction pattern previously presented (see Figure 4.1a).

Two other forms of cooling have been tested: super fast cooling, where acetone and dry ice were used instead of water and ice, and cooling at room temperature. The diffractograms of the obtained samples are showed in Figure 4.15.
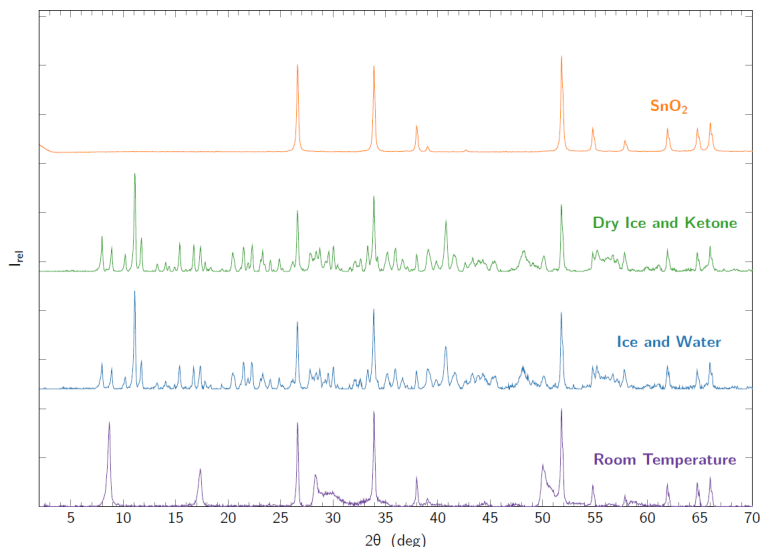
Figure 4.15: PXRD patterns of IZM-5 with different forms of cooling - room temperature cooling (purple), quick cooling, with water and ice (blue), very quick cooling, with dry ice and ketone (green) and SnO_2 (orange)

Evaluating Figure 4.15, it is concluded that the autoclaves cooling method influences the obtained final structure. When a slow cooling occurs, i.e. cooling at room temperature, a diffractogram with a pattern associated to a laminar structure is obtained. This diffraction pattern can be associated with a layered conformation when the basal spacing of the second diffraction peak is equal to half of the basal spacing of the first diffraction peak [21]. The first diffraction peak of the pattern represented in purple in Figure 4.15 is located at 2θ equal to 8,71° and exhibits a basal spacing equal to 10,15 Å. The second diffraction peak, located at 2θ equal to 17,41°, has a basal spacing equal to 5,09 Å.

Fast cooling, with water and ice, and very fast cooling, with acetone and dry ice, lead to a diffraction pattern associated with IZM-5, with no significant differences noted between these two types of cooling. Taking into account the results obtained with the different cooling methods tested, it is possible to say that IZM-5 is a kinetic controlled structure instead of thermodynamic one, something already observed for materials of the same type as IZM-5 [15].

4.2.2.3 Impact of gel composition

Continuing the systematical approach started earlier, the impact that the gel composition has in the obtained crystalline structure is now evaluated. For that purpose, modifications to the gel composition were performed. As can be seen in Figures 4.14 and 4.15, when following the experimental methodology presented above (see Section A.2), in a gel with the molar composition 1 SnO$_2$: 0,322 Zn(NO$_3$)$_2$: 5,72 S : 6,29 C$_{13}$H$_{26}$N$_2$: 132,64 C$_2$H$_6$O$_2$: 138,08 H$_2$O, peaks associated with an SnO$_2$ extra phase are clearly present in the IZM-5's diffraction pattern.

It was chosen to study the impact that the Sn source, the Sn and SDA contents and the solvent composition have on the final structure and on the extra SnO$_2$ present. It was chosen to replace SnO$_2$ with SnCl$_2$ as a source of Sn, since SnO$_2$ is not soluble in water, one of the solvents used, which could make its dissolution in the gel difficult. SnCl$_2$, being soluble in water, presents an easier dissolution in the gel and, as such, more active species should be formed that can participate in the IZM-5 crystallization process. Furthermore, SnCl$_2$ is soluble in ethanol, the solvent used when washing and filtering IZM-5, which facilitates the elimination of SnCl$_2$ that did not react during the crystallization process.

The effect of each of these parameters was first evaluated individually. The compositions of the gels studied, as well as the diffractograms obtained can be found in Appendix B.

Regarding the impact that the Sn source and content have (see Figure 4.16), it is observed that when using SnCl$_2$ instead of SnO$_2$ the disappearance of the peaks associated with SnO$_2$ occurs. As for the Sn content in the initial gel, it can be observed that even reducing the Sn content by 40% a similar diffraction pattern is obtained. Hence, Sn was in large excess in the used original gel composition.
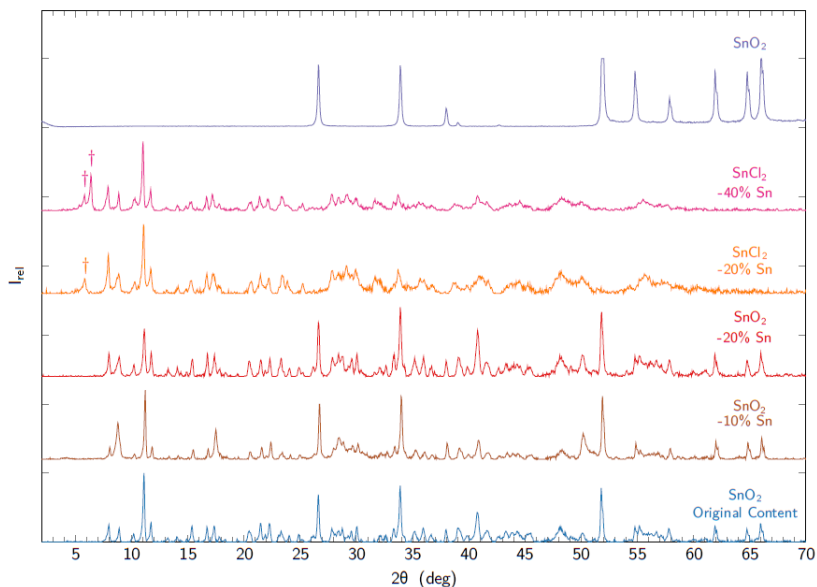
Figure 4.16: PXRD patterns of IZM-5 with SnO_2 as Sn source and the original Sn content (in blue), with -10% (in brown) and -20% Sn content (in red), with $SnCl_2$ as Sn source and -20% (in orange) and -40% (in pink) Sn content and SnO_2 (purple), where † denotes an unknown impurity

Concerning the influence that the solvent composition has on the obtained product, two alterations were studied. The first one consisted on decreasing the ethylene glycol-water ratio. The second consisted in maintaining the ethylene glycol-water molar ratio constant, increasing the water-tin ratio. For the two strategies studied (see Figure B.3), it is concluded that they do not influence the extra SnO_2 phase formation. However, when the water-tin molar ratio is increased to 300, an improving in the difractogram definition is observed, i.e., the intensity of the characteristic peaks of IZM-5 is maintained and the presence of peaks that could be associated with impurities is minimized.

The last parameter studied, the SDA gel content, has a great impact on the formation of the crystalline structure and on the extra SnO_2 phase (see Figure 4.17). When the SDA content increases by 20%, the intensity of the peaks associated with IZM-5 decreases. Regarding the SnO_2 phase, this becomes the most predominant phase. When the SDA content is decreased by 20%, the opposite is observed. When the SDA content is decreased, the intensity of the SnO_2 peaks is drastically reduced, making IZM-5 as the predominant crystalline phase in the final material. Therefore, the SDA was in excess in the original gel composition used.
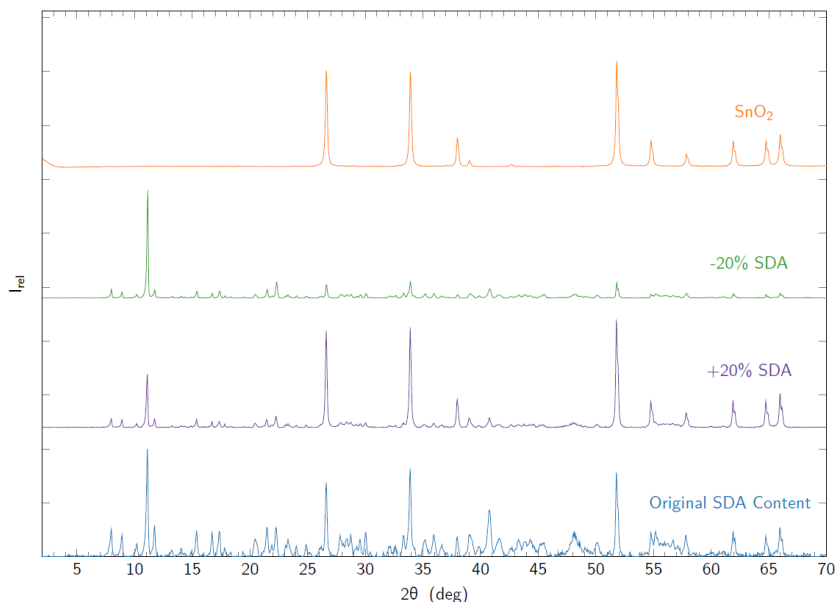
Figure 4.17: PXRD patterns of IZM-5 with original SDA content (in blue), with +20% SDA (in purple), -20% SDA (in green) and SnO$_2$ (in orange)

The parameters with the greatest impact on the SnO$_2$ extra phase were selected and combined (see Figure B.5). It was concluded that when using SnCl$_2$ as a Sn source instead of SnO$_2$, reducing the Sn and SDA content by 20% and increasing the H$_2$O/Sn molar ratio from 138 to 300, while keeping the EG/H$_2$O molar ratio equal to 0,96, it favors the elimination of the peaks associated with the SnO$_2$ phase (see Figure 4.18). Hence, it can be considered that the more optimal molar composition of the gel, which leads to the elimination of the SnO$_2$ peaks is 1 SnCl$_2$: 0,33 Zn(NO$_3$)$_2$: 5,84 S : 5,13 C$_{13}$H$_{26}$N$_{2}$: 230,03 C$_2$H$_6$O$_2$: 239,96 H$_2$O (see Figure 4.18 to compare the diffractograms before and after optimization of the gel composition).
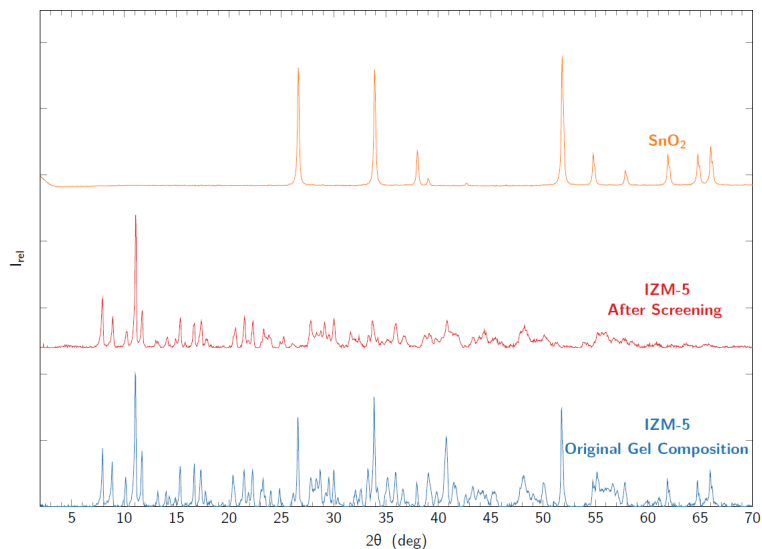
Figure 4.18: PXRD patterns of IZM-5 with the original gel composition (blue), IZM-5 after screening gel composition (red) and SnO_2 (orange)

4.3 Synthesis of ITQ-75. Aromatic Compounds as SDA
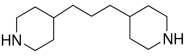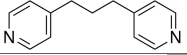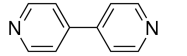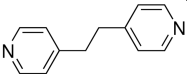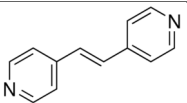
After the study of the synthesis conditions, where the Compound A was used as SDA to obtain IZM-5 material, other organic compounds were tested (see Table 4.5). Comparing the compounds present in Table 4.5, it can be observed that Compound A is the only one that does not present a conjugated Π system. It was thus decided to study the effect that SDAs with aromatic moieties would have on the crystallization process. SDAs' with a conjugated system, due to the electronic delocatization, are more stable and tend to have a planar conformation [22]. Therefore, the SDA interactions with IZM-5 precursors will be different, and may lead to modifications to the crystallization mechanism and over the final formed achitecture.

In a conjugated Π system, electrons are able to interact with photons with a certain wavelength. Generally, the more conjugated the system is, the longer the wavelength (and therefore less energetic) of the photon capable of interacting with the system. In this way, in order to increase the interaction with visible light, it is desirable that the system is as conjugated as possible [22]. Looking at the SDAs with conjugated Π system, Compounds C and E are the ones that present a greater

electrons delocalization, since they allow the delocalization of electrons between the two aromatic rings. Hence, it is expected that when these two SDAs are used, materials obtained present a greater interaction with the visible light. This is an important property to take into account, since the materials are intended to be used as photocatalysts.

Besides evaluating the impact that a conjugated Π system will have on the final product, the consequences of using different chain length between cycles was also studied. By using SDAs with different chain length, it was postulated that structures with different porosity could be obtained, that is, SDAs with longer chain length would originate structures with a more open architecture (Compound B and D).

Table 4.5: Different SDA's used

SDA	Reference	Chemical Formula	Chemical Representation	C/N Molar Ratio	pKa
1,3-Bis(4-piperidyl)propane	Compound A	$C_{13}H_{26}N_2$		6,5	11,0
1,3-Bis(4-pyridyl)propane	Compound B	$C_{13}H_{14}N_2$		6,5	6,3
4,4'-Dipyridyl	Compound C	$C_{10}H_8N_2$		5	3,2; 4,8
1,2-Bis(4-pirydyl)ethane	Compound D	$C_{12}H_{12}N_2$		6	6,1
1,2-Di(4-pyridyl)ethylene	Compound E	$C_{12}H_{10}N_2$		6	5,5

In the previous section, where the IZM-5 systematic study was carried out, a more optimal gel composition was determined, that allowed to eliminate the presence of a SnO_2 phase as impurity. To test the compounds present in the Table 4.5 as SDA it was thus used the IZM-5 optimal gel composition, changing only the SDA used and incorporated in the synthesis gel. Figure 4.19 shows the diffractograms of the samples obtained with the optimal gel composition (previously determined in Section 4.2.2.3), but using the different SDAs present on Table 4.5.
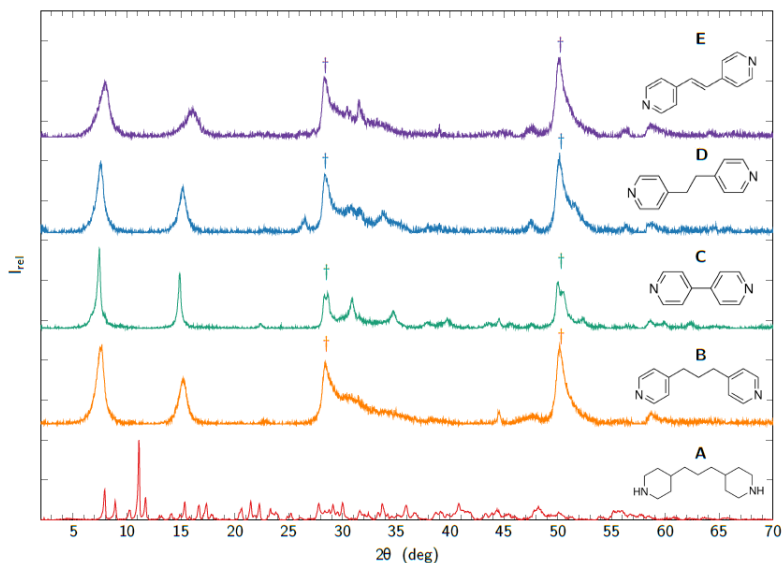
Figure 4.19: PXRD patterns of the chalcogenide-type materials obtained with different SDAs - IZM-5 in red obtained with Compound A as SDA, ITQ-75 obtained with Compound B, C, D and E in orange, green, blue and purple, respectively, where † denotes a ZnS phase

It is observed that when SDAs with aromatic rings are used, regardless of the length of the carbon chain that links them, a diffraction pattern is obtained that can be associated to a traditional pattern of a laminar material due to the basal distance oberved of the first two diffraction peaks [21]. This class of materials were named ITQ-75, assumed to be a new ordered and structured solids, and it is patent by IFPEN, CSIC and UPV [23]. However, there are some differences between them.

The diffraction pattern obtained when Compound B is used as SDA presents three main peaks located at 2θ equal to 7,5°, 15,2° and 50,2°. When using Compound C as SDA, the two first diffraction peaks move slightly towards lower angles. For the remaining peak, it maintains its position, but coupled with these arise a second peak. When using Compound D as SDA, the peak displacement observed before is not verified. The material obtained with Compound D as SDA shows the three peaks at 2θ equal to 7,5°, 15,2° and 50,2°, the same positions as in Compound B. Finally, in respect to the last compound studied as SDA, by using Compound E as SDA a small displacement of the first two peaks towards greater angles is observed. Thus, the material's diffraction patterns obtained with the different SDAs under study are very similar and there are only slight shifts in the first diffraction peaks associated with laminar ordering.

The chemical composition of the different samples, determined by elemental analysis and ICP, is present on Table 4.6. Table 4.7 presents the molar ratios on the original synthesis gel and on the final material.

Table 4.6: Chemical composition of the synthesized structures when using the different compounds as SDAs ([1]Determined by elemental analysis. [2]Determined by ICP)

Material	Formula	Mass composition (%)					
		N^1	C^1	H^1	S^1	Sn^2	Zn^2
ITQ-75 (B)	$Sn_{3,52}Zn_{1,27}S_8 \cdot C_{10,59}H_{12,24}N_{1,68}$	2,33	12,57	1,210	25,36	41,50	8,83
ITQ-75 (C)	$Sn_{3,05}Zn_{1,33}S_8 \cdot C_{11,54}H_{9,97}N_{2,24}$	2,81	12,41	0,90	22,95	32,41	7,78
ITQ-75 (D)	$Sn_{3,53}Zn_{1,45}S_8 \cdot C_{9,82}H_{10,37}N_{1,53}$	2,18	11,99	1,05	26,07	42,64	9,65
ITQ-75 (E)	$Sn_{2,86}Zn_{1,21}S_8 \cdot C_{11,61}H_{13,27}N_{1,65}$	2,58	15,54	1,48	28,61	37,88	8,80

Table 4.7: Different molar ratios in the synthesis gel and on the final structures

	Gel Molar Ratios			Material Molar Ratios		
	Sn/Zn	Sn/S	C/N	Sn/Zn	Sn/S	C/N
ITQ-75 (B)	3,2	0,2	6,5	2,6	0,4	6,3
ITQ-75 (C)	3,0	0,2	5,0	2,3	0,4	5,2
ITQ-75 (D)	3,2	0,2	6,0	2,4	0,4	7,0
ITQ-75 (E)	3,3	0,2	6,0	2,4	0,4	7,0

Concerning the chemical composition of ITQ-75, and considering once again that Sn, Zn and S are in the crystal framework, the inorganic frameworks may have a positive charge instead of a negative one, depending on the SDA used. ITQ-75 obtained with Compound C has an apparent negative charge of -1, similar to IZM-5. The other three structures, obtained with Compounds B, D and E have an apparent positive charge of +1. Taking into account that the oxygen content has not been determined and that the sum of the different elements is less than 100, it is possible that this element is present in the structure, thus changing the final charge of the structure.

Regarding the molar ratios of the different synthesis gels and those obtained in the final structures, a similar behavior to that earlier remarked for IZM-5 (see Table 4.3) is observed. The final materials present a higher Sn/S molar ratio and a lower Sn/Zn molar ratio than the synthesis molar ratios. Thus, there is an excess of Sn and S in the synthesis gel. Concerning the C/N molar ratios, the structures obtained with SDAs B and C maintain it after the synthesis. As for the other two

materials obtained with the remaining SDAs, D and E, there is a small increase, from 6,0 to 7,0.

In order to ascertain the SDA environment in the final material, IR and NMR spectroscopy were performed (see Figures 4.20 to 4.23).

(a)

(b)

(c)
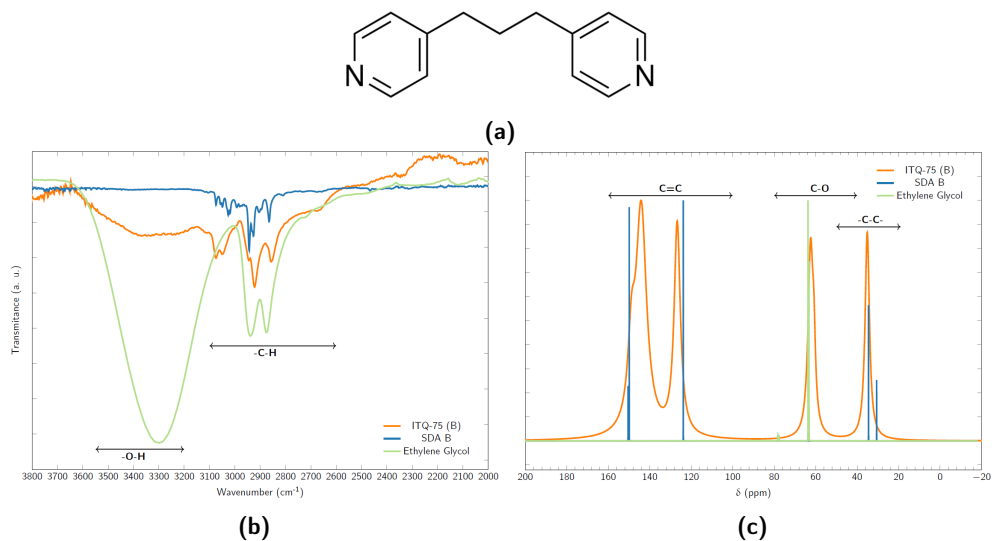
Figure 4.20: (4.20a) Representation of SDA B, (4.20b) IR and (4.20c) ^{13}C NMR spectra of ITQ-75 obtained with Compound B as SDA (in orange), Compound B (in blue) and Ethylene Glycol (in green)
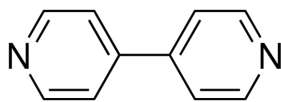
(a)
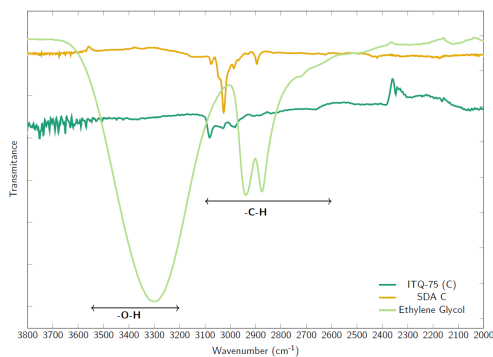
(b)
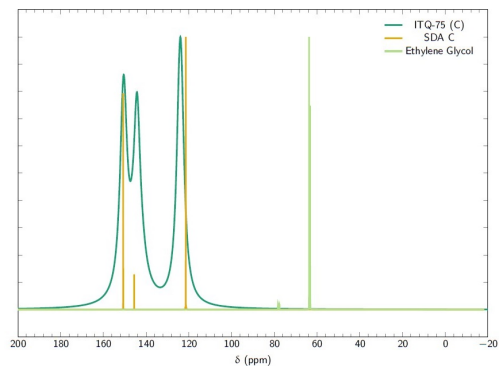
(c)

Figure 4.21: (4.21a) Representation of SDA C, (4.21b) IR and (4.21c) ^{13}C NMR spectra of ITQ-75 obtained with Compound C as SDA (in yellow) and Compound C (in green)
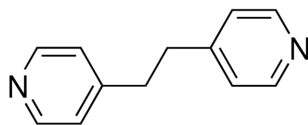
(a)
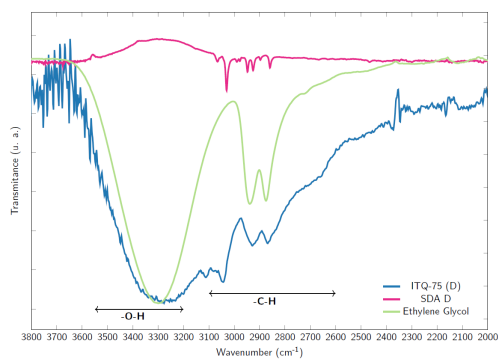
(b)
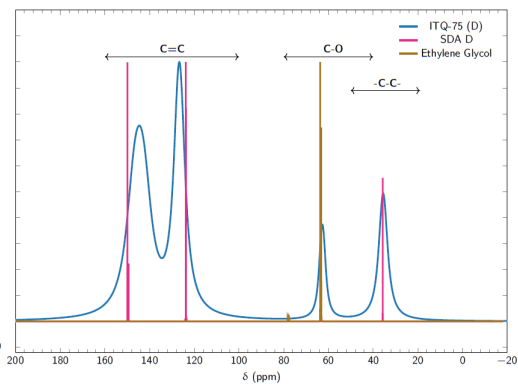
(c)

Figure 4.22: (4.22a) Representation of SDA D, (4.22b) IR and (4.22c) ^{13}C NMR spectra of ITQ-75 obtained with Compound D as SDA (in blue), Compound D (in pink) and Ethylene Glycol (in green)

(a)

(b)

(c)
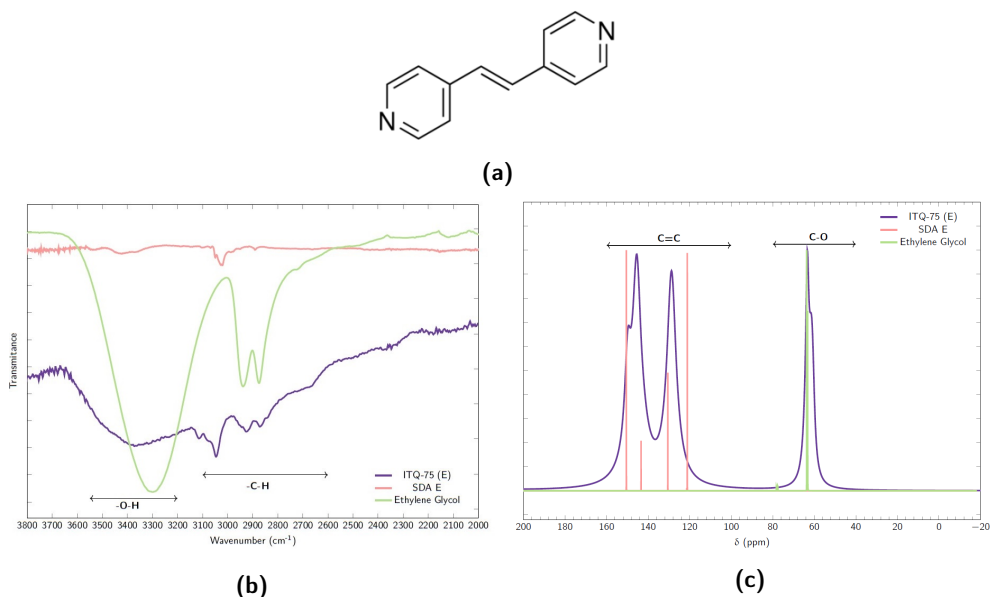
Figure 4.23: (4.23a) Representation of SDA E, (4.23b) IR and (4.23c) ^{13}C NMR spectra of ITQ-75 obtained with Compound E as SDA (in purple), Compound E (in pink) and Ethylene Glycol (in green)

Observing the previous figures, it is possible to see two types of behavior of the structures under study. The ITQ-75 obtained with Compound C (see Figure 4.21) does not show a peak at chemical shift equal to 62 ppm, chemical shift associated with the presence of ethylene glycol (see Figure 4.21c). The remaining samples show such a peak and, looking at their IR spectra, the presence of a broad peak at a wavenumber region from 3000 cm^{-1} to 3500 cm^{-1}, associated with the presence of hydroxyl groups, is present. In order to confirm that the ethylene glycol detected is in the structure and is not just a synthesis residue, the final solid was washed with ethanol for a period of three days. After the washing time, it was observed that there was no change in the IR spectrum. Hence, it appears that the samples that have an apparent positive framework charge (ITQ-75 obtained with Compounds B, D and E) contain ethylene glycol inserted in it, which would explain the possible presence of oxygen in the material.

The impact of the SDA present in the chalcogenide-type materials on the optical properties of the final material obtained was evaluated, namely on the optical band gap value. This property of the material is of extreme importance when one intends to use it as a photocatalyst, as long as as-made material are considered for

photoconversion experiments. For this, a UV-Vis spectra was drawn and the Tauc plot was calculated and plotted (see Figure 4.24 and Appendix D, respectively), allowing the determination of the optical band gap value (see Table 4.8) according to [11].
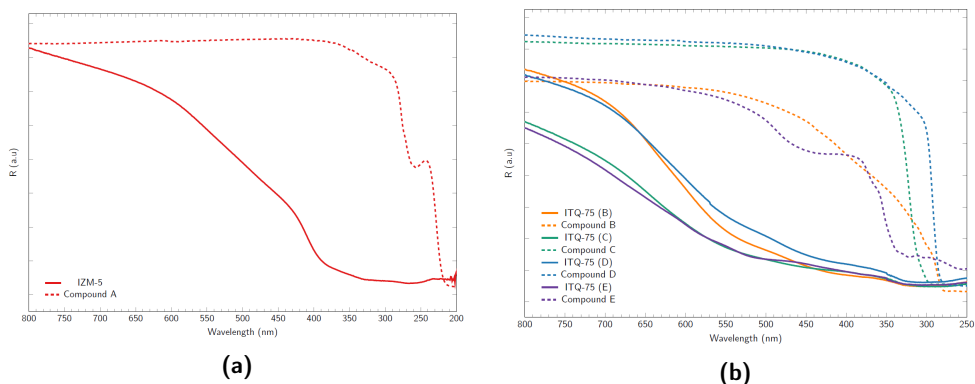
Figure 4.24: (4.24a) UV-Vis spectra of IZM-5, (4.24b) ITQ-75 family and respective SDAs

Table 4.8: Bandgap (E_g) of synthesized materials

Material	E_g (eV)
IZM-5	3,6
ITQ-75 (B)	2,7
ITQ-75 (C)	2,2
ITQ-75 (D)	2,5
ITQ-75 (E)	2,2

By first evaluating the UV-Vis spectra (see Figure 4.24), it can be observed that the five studied materials have different interactions with the UV-Vis radiation. IZM-5, material obtained with Compound A as SDA, presents the highest reflectance range. The samples obtained with Compounds B and D, compounds with two aromatic rings, present an intermediate reflectance range. The materials with the lowest reflectance range are those with Compounds C and E as SDAs. These two SDAs are the ones that, besides presenting two aromatic rings, allow the electronic displacement between them. Thus, it is concluded that, for a greater electronic dislocation, the peak of the reflectance occurs at longer wavelengths, i.e., occurs with less energetic radiation. This fact is of extreme importance for

these materials, since they are intended to be used as photocatalysts using solar radiation, thus making the properties of absorbing radiation strongly important, particularly in the visible region, since about 47% of the sunlight is composed of visible radiation. Moreover, looking at the band gap values of the different samples (see Table 4.8), it is easy to see that from materials synthesized with non-aromatic SDAs to aromatic ones, there is a reduction of the band gap between 0,4 to 0,7 eV.

Considering the impact that the SDA has on the radiation absorption properties of the final material, the question arises: is the presence of this organic compound in the structure necessary to maintain low band gap values? The UV-Vis spectra of the SDAs was measured (see Figure 4.24) and it was observed that their optical band gap is greater than 3,3 eV (see Appendix D for more information regarding their optical band gap values). Thus, although the SDA used has an impact on the material's electronic properties, its presence alone does not explain the observed interaction with UV-Vis radiation., being decisive the interaction between the inorganic matrix and the organic SDA compounds.

4.3.1 ITQ-75 Structure

Due to the potential that these new materials show, namely in their interaction with UV-Vis radiation, more details on their topology were necessary to be investigated. HRTEM analysis was performed first, in order to assess whether or not the materials had a laminar topology, as was previously hypothesized due to the values of the basal space associated with the first two diffraction peaks. Figure 4.25 shows the HRTEM images.

(a)

(b)

(c)

(d)
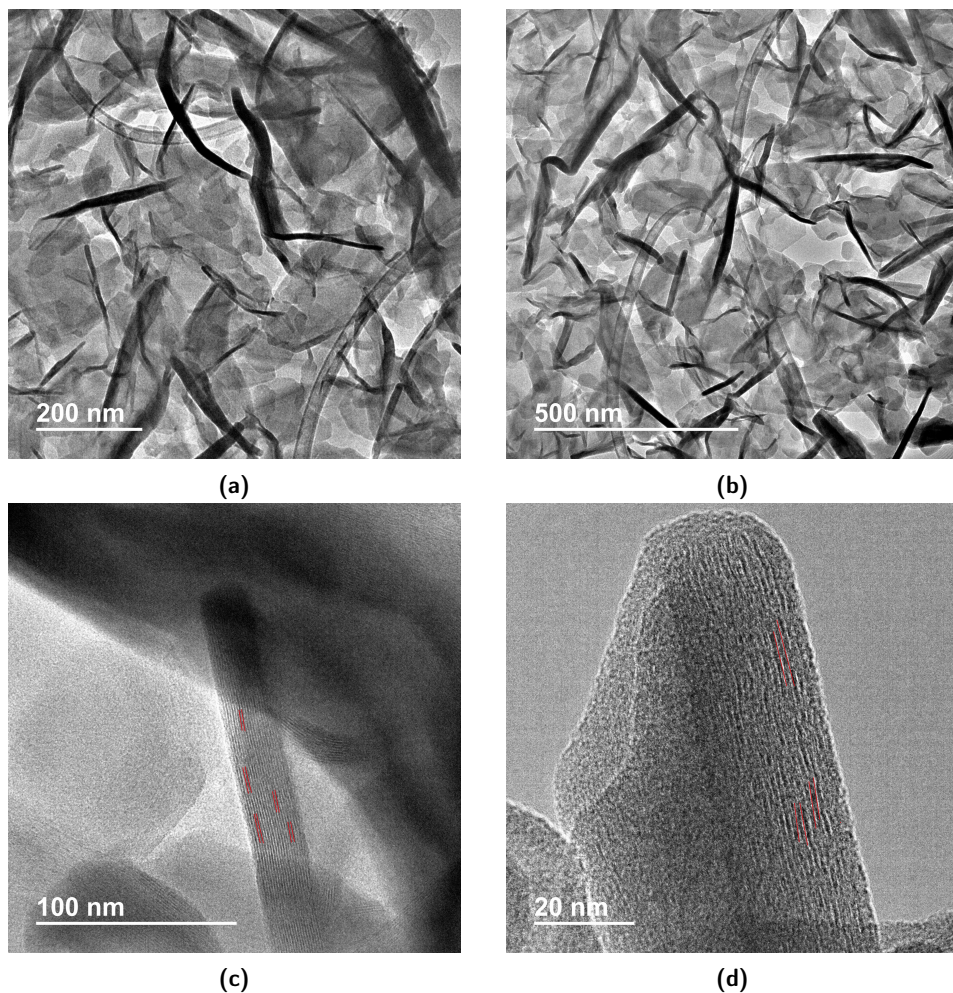
Figure 4.25: ITQ-75' HRTEM images, obtained with Compound C as SDA, where (4.25a) and (4.25b) highlights its morphology and (4.25c) and (4.25d) the laminar planes, marked in red

Looking at Figures 4.25a and 4.25b it can be seen that ITQ-75 can be seen as a fiber-like particles organized into a ball. Regarding its laminar profile, Figures 4.25c and 4.25d confirms it. The intercalary laminae are 1,0 $\pm$0,2 nm apart.

In order to learn more about ITQ-75 crystal's morphology, as well as their dimension, a FESEM analysis was performed (see Figure 4.26).

(a)

(b)

(c)

(d)
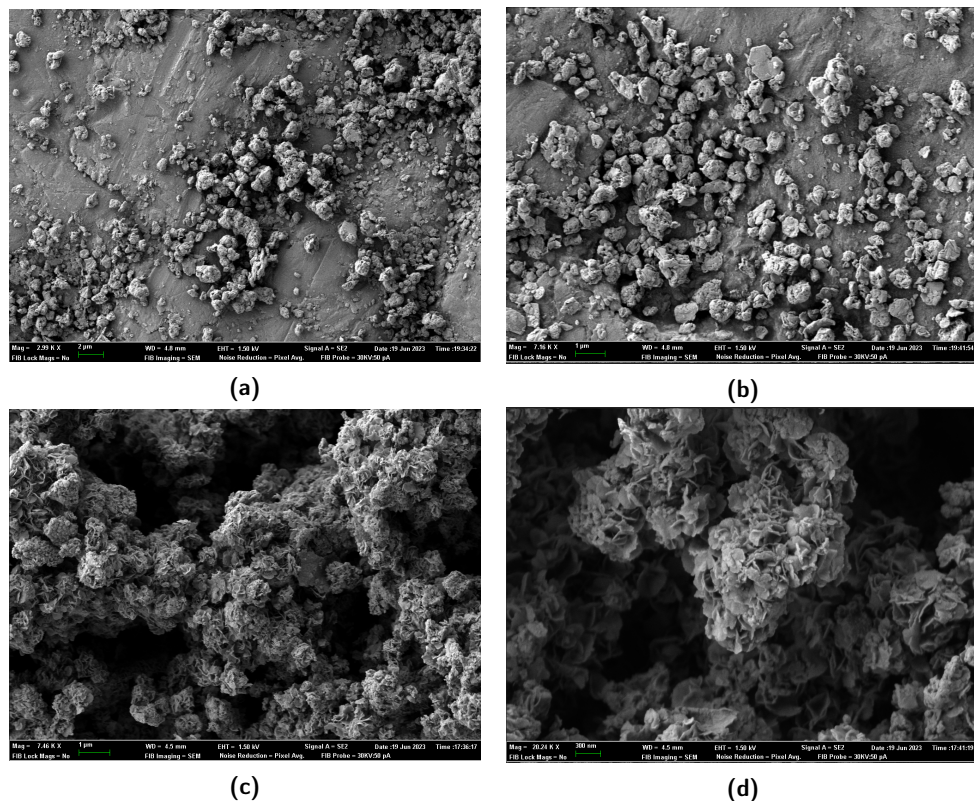
Figure 4.26: ITQ-75 FESEM images, obtained with (4.26a and 4.26b) Compound C or (4.26c and 4.26d) Compound B as SDA

Regarding the ITQ-75 crystal's morphology, it is possible to verify that they are spherical resulting from the accumulation of laminae with different orientation. Looking particularly at Figure 4.26d, some crystals present a flower-like morphology. ITQ-75 crystal size is 1,4 $\pm$0,5 µm, when obtained with Compound B as SDA, and 1,8 $\pm$0,6 µm, when obtained with Compound C as SDA.

Due to the small crystal size and the low amount of well-defined peaks it makes it impossible, up to now, to solve ITQ-75 structure by conventional methods, such as the one previously used on IZM-5.

However, a literature review on inorganic layered materials suggest that ITQ-75 structure might be related to the triclinic misfit layer compounds MTX_3 [24, 25]. This class of materials consists of two different materials layered on each other,

originating an ordered superstructure. Usually, MTX_3 materials can be seen as alternately double layers of MX (where M represents Sn, Pb or rare earth metals and X S or Se) and sandwiches of TX_2 (where T represents transition metals) (see Figure 4.27) [26]. $(SnS)_{1,2}(TiS_2)$ [26], $(BiS)(NbS_2)$ [27] or $(LaSe)_{1,14}(NbSe_2)$ [28] are examples of chalcogenide-layered materials with the MTX_3 structure.
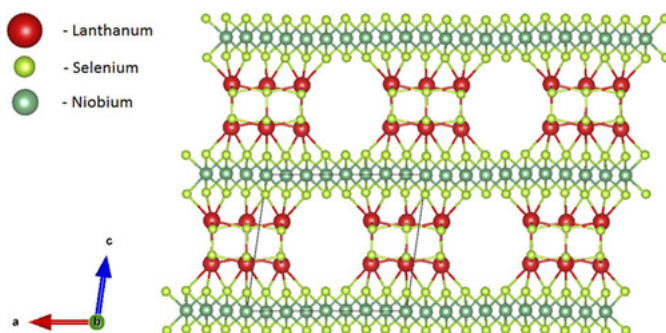
Figure 4.27: Crystal structure representation of $(LaSe)_{1,14}(NbSe_2)$ (adapted from [28])

Regarding ITQ-75, and assuming as an initial hypothesis for its structure the MTX_3 one, can be seen as SnS layers alternated with ZnS_2 layers that are partly replaced by the organic component present.

Concerning ITQ-75 textural properties (see Figure 4.28a and Table 4.9), this class of materials presents a negligible microporous area, between 0,5 and 4,6 m²/g. It is thus verified that the accessibility of these materials is due to their external surface area, which varies between 11,4 and 50,0 m²/g. It is also noted that depending on the compound used as SDA, the accessibility of the samples varies. When Compound B is used as SDA, the structure has the smallest external surface area. When Compounds D or E are used, their surface accessibility is greater, associated with the different flexibility of the SDA compounds.
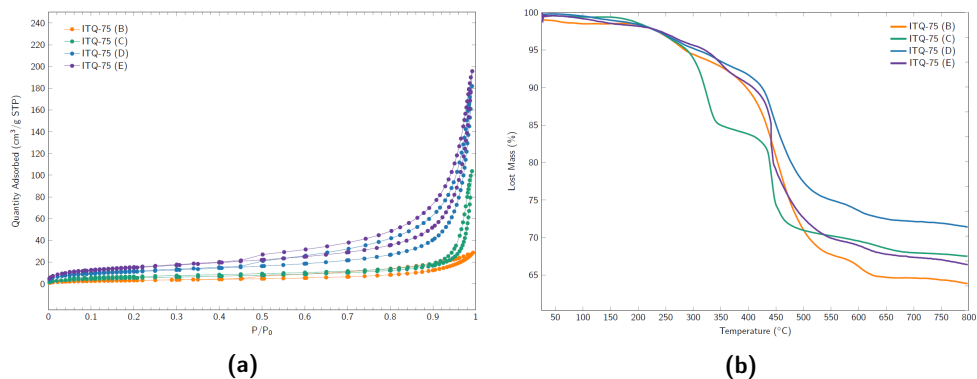
Figure 4.28: (4.28a) N_2 adsorption-desorption isotherms and (4.28b) TG-DTG of the different ITQ-75 materials

Table 4.9: ITQ-75 textural properties (n.a. - not available. [1]Determined by FESEM (see Appendix F)

	Pore Volume (cm³/g)	BET surface area (m²/g)	t-plot Micropore Area (m²/g)	t-plot External Surface Area (m²/g)	Crystal Size (μm)[1]
ITQ-75 (B)	n.a	11,9	0,5	11,4	1,4 ±0,5
ITQ-75 (C)	0,140	20,2	2,9	17,3	1,8 ±0,6
ITQ-75 (D)	0,255	40,5	3,3	37,2	1,6 ±0,6
ITQ-75 (E)	0,277	54,6	4,6	49,9	1,4 ±0,5

As for the thermal stability (see Figure 4.28b), the largest mass variation is observed for temperatures between 440°C and 450°C. However, for ITQ-75 obtained with Compound C a behavior slightly different from the others is observed. This material presents a first mass loss at 327°C, followed by the most preponderant one at 441°C (see Figure E.9), probably due to the lower thermal stability of the Compound C used as SDA.

4.4 SDA free synthesis

Finally, it was assessed whether it is possible to synthesize this class of materials without the presence of SDA in the gel. This fact should allow to know the importance of the SDA compounds into the final achieved structure. Currently there is a growing concern regarding the synthesis of structures without the use of SDA, due to its high economic and environmental costs [29].

As mentioned before, these materials tend to collapse when the SDA is eliminated. Furthermore, the SDA occupies an intra framework position, being the main responsible for clogging the porous system. Hence, the synthesis of materials without SDA would avoid the occlusion of the porous system and, by extension, the post-synthesis treatments necessary to remove said SDA, which often lead to the collapse of the crystalline structure.

Two experimental approaches were tested for this: the presence of Na^+ and the effect of seeding, hoping that both methodologies would favor the formation of a new ordered chalcogenide-type material, similar to IZM-5 or ITQ-75.

4.4.1 Na^+ presence

As can be seen above (see Table 2.9), the structures obtained until now without the presence of SDA had in its gel monocations, namely Na^+, a monocation widely used to replace SDA in the synthesis of materials such as zeolites [30]. Figure 4.29 shows the diffractograms of the samples synthesized with different S/Na^+ molar ratios. All samples obtained with different Na^+ molar contents were synthesized at a temperature equal to 190°C, six days as synthesis time, SnO_2 as Sn source and with a ethylene glycol - water molar ratio of 0,96.
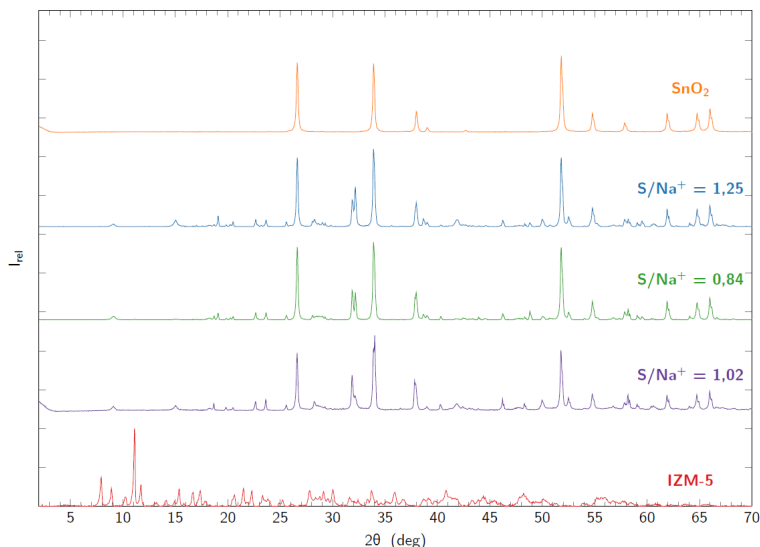
Figure 4.29: PXRD patterns of the different materials obtained with different Na contents - IZM-5 in red obtained with Compound A as SDA and no Na present on the gel, S/Na^+ molar ratio equal to 1,02 in purple (1 SnO_2 : 0,33 $Zn(NO_3)_2$: 5,98 S : 2,94 Na_2O : 134,61 $C_2H_6O_2$: 150,81 H_2O), S/Na^+ molar ratio equal to 0,84 in green (1 SnO_2 : 0,32 $Zn(NO_3)_2$: 5,76 S : 2,31 Na_2O : 132,13 $C_2H_6O_2$: 138,96 H_2O), S/Na^+ molar ratio equal to 1,25 in blue - and SnO_2 in orange (1 SnO_2 : 0,32 $Zn(NO_3)_2$: 5,71 S : 3,40 Na_2O : 131,08 $C_2H_6O_2$: 138,54 H_2O)

When using Na^+ on the gel without the presence of SDA, the SnO_2 diffraction pattern is obtained in all tested compositions. It should be noted that for 2θ around 9° and 15°, it is possible to observe two small peaks, which may be associated with a possible laminar phase. However, their intensity is so low, in relation to the peaks associated with SnO_2, that their presence is almost insignificant. Although small peaks not associated with SnO_2 can be seen, they are negligible in relation to the SnO_2 phase, so this strategy was considered not successful.

4.4.2 Seeding effect

The second technique tested in the synthesis of materials without the presence of SDA was seeding, a technique widely used in the SDA free synthesis of zeolites [29, 31]. Seeding is based on the use of seeds, material previously obtained in the presence of SDA, that will help with the nucleation phase of the new structure. In addition to not requiring the use of SDA, seeding also allows to reduce the time of synthesis, changing the size of crystallites and eliminating possible impurities [29].

The seeds used were obtained from a gel with the molar composition 1 SnO_2 : 0,32 $Zn(NO_3)_2$: 5,71 S : 6,41 $C_{13}H_{26}N_2$: 131,67 $C_2H_6O_2$: 145,23 H_2O, 6 days as synthesis time and 190°C as synthesis temperature. After obtaining the seeds, they were placed in a gel with the molar composition 1 SnO_2 : 0,330 $Zn(NO_3)_2$: 5,12 S : 133,70 $C_2H_6O_2$: 147,53 H_2O, where they represented 0,30% (mass percentage) of the final gel. Since seeding allows the reduction of the synthesis time, it was decided to shorten that period to one day, whilst keeping the temperature at 190°C. Figure 4.30 shows the diffractogram of the sample as-synthesized in the presence of seeds and without SDA.
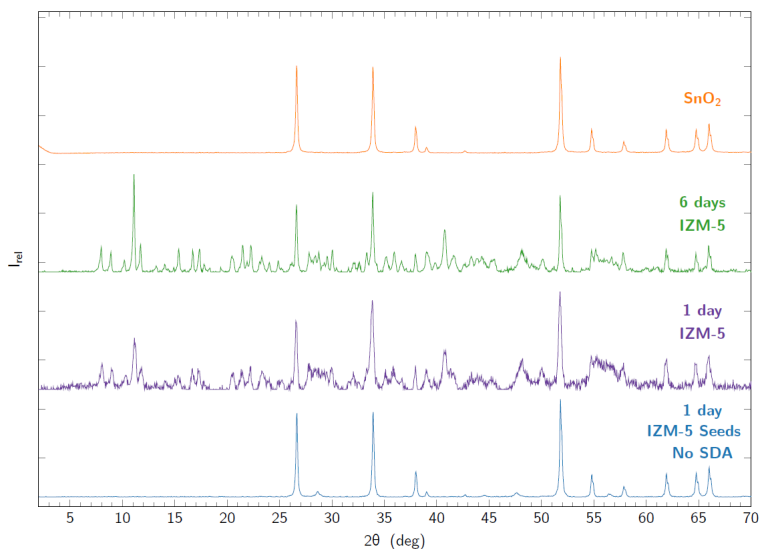
Figure 4.30: PXRD patterns of the material obtained with IZM-5 seeds and one day as synthesis time (in blue), IZM-5 with Compound A as SDA and one (in purple) or six days (in green) as synthesis time and SnO_2 (in orange)

As can be seen in Figure 4.30, through seeding it is not possible to obtain a crystalline structure, observing only the presence of diffraction peaks associated with SnO_2. It would be interesting to evaluate what would be obtained if $SnCl_2$ was used as a source of Sn. However, this preliminary result suggest that the use of seeds, in the absence of SDA molecules, does not favor the formation of chalcogenides.

This methodology was also used by using ITQ-75 seeds. Two type of seeds were used, ITQ-75 obtained with Compound B and Compound C, in order to evaluate the influence of SDA. ITQ-75 (B) seeds used were obtained from a gel with the

molar composition 1 $SnCl_2$: 0,31 $Zn(NO_3)_2$: 5,71 S : 6,37 $C_{13}H_{14}N_2$: 226,98 $C_2H_6O_2$: 239,41 H_2O, 6 days as synthesis time and 190°C as synthesis temperature. ITQ-75 (C) seeds used were obtained from a gel with the molar composition 1 $SnCl_2$: 0,32 $Zn(NO_3)_2$: 5,69 S : 5,11 $C_{10}H_{12}N_2$: 227,20 $C_2H_6O_2$: 238,24 H_2O, 6 days as synthesis time and 190°C as synthesis temperature. These seeds were placed in a gel with the molar composition 1 $SnCl_2$: 0,32 $Zn(NO_3)_2$: 5,67 S : 226,78 $C_2H_6O_2$: 238,20 H_2O, where they represented 0,30% (mass percentage) of the final gel.

Figure 4.31 shows the diffractogram of the sample synthesized in the presence of ITQ-75 seeds, obtained with Compounds B or C as SDA, and without SDA.
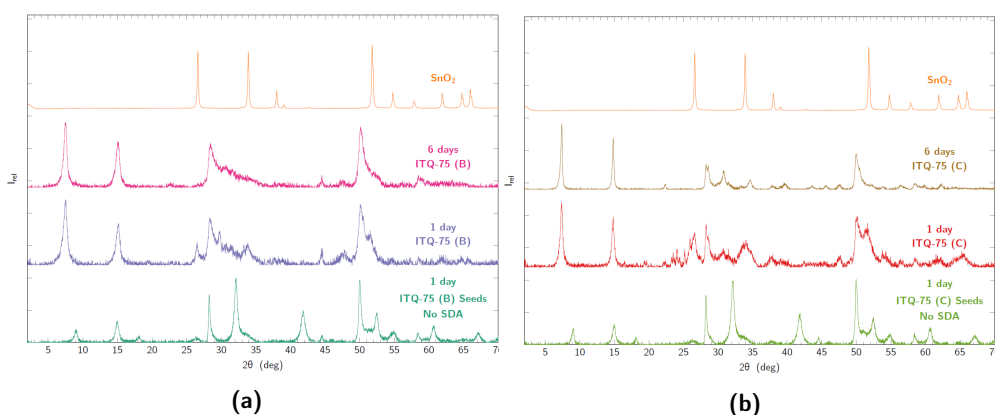
(a)   **(b)**

Figure 4.31: (4.31a) PXRD patterns of the material with ITQ-75 seeds, obtained with Compound B as SDA, and one day as synthesis time (in green), ITQ-75 with Compound B as SDA and one (in purple) or six days (in purple) as synthesis time and SnO_2 (in orange); (4.31b) PXRD patterns of the material with ITQ-75 seeds, obtained with Compound C as SDA, and one day as synthesis time (in green), ITQ-75 with Compound C as SDA and one (in red) or six days (in brown) as synthesis time and SnO_2 (in orange)

Although two peaks are observed around 2θ around 9° and 15° that could be associated with a possible laminar phase, their intensity is much lower than that of the other diffraction peaks. These peaks may be due to the ITQ-75 seeds present in the synthesis gel. It is also observed that, although there is no SnO_2 in either the synthesis gel or the seeds, the final structure shows peaks at 2θ at 26,7°, 34,0° and 51,3° that can be associated with a SnO_2 crystalline phase.

It is therefore concluded that, under the synthesis conditions aforementioned, a seeding strategy is not favorable for obtaining this class of chalcogenide materials.

4.5   Conclusions

In this chapter, a new sulfur-based material recently patented by IFPEN [4] and designated by IZM-5 was studied. As it is a new material, the only information available was its chemical composition and diffraction pattern. After structural resolution via SCXRD, IZM-5 can be seen as laminar material with a semicube building unit. According to the structural resolution, IZM-5 does not have Zn integrated in the structural framework. It was observed that when Zn is not present in the synthesis gel, a material with a diffraction pattern similar to IZM-5 is obtained. It can be noted that the presence of Zn is not essential to obtain a crystalline structure, but it is necessary to obtain a pure IZM-5 material. However, the presence of this element allows to reduce the optical band gap, something to be taken into account since the structure is intended to be used in solar-driven applications.

Since IZM-5 is a recent material and there is no systematic study available on the influence of the synthesis parameters in this class of materials, the first stage of this thesis was to understand how the conditions of synthesis influence the final structure. To this end, the impact that the synthesis time, cooling rate and chemical gel composition have on the final product obtained were evaluated.

Table 4.10 systematizes the impact of each of the parameters studied in obtaining IZM-5, and the presence of SnO_2 in the final material.

Table 4.10: Systematization of the main screening results obtained regarding the IZM-5 synthesis and the presence of the extra SnO_2 phase

	Strucuture	
	IZM-5	SnO_2
Synthesis time	Medium impact	No impact
Cooling method	High impact	No impact
Sn source	No impact	High impact
Sn content	No impact	No impact
Solvent composition	Medium impact	No impact
SDA content	High impact	High impact

The parameters that proved to have the greatest impact in obtaining IZM-5 were the cooling method and the SDA content in the gel. Already in relation to the extra SnO_2 phase, this is strongly influenced by the Sn source used and the SDA

content, which favors IZM-5 formation without impurities, namely an extra SnO_2 crystalline phase.

After studying the impact of the different parameters, the optimized synthesis conditions were used to tested other organic compounds as SDA. These showed aromaticity and different lengths of carbon chains linking the aromatic rings. These SDAs were chosen because, due to their aromaticity, they have different chemical properties that may lead to different structures and properties. The aromaticity, caused by the presence of a conjugated Π system, allows an electronic displacement not observed with other SDAs, thus improving the interaction with UV-Vis radiation, a very important property taking into consideration the intended photocatalytic application for the materials. The materials obtained with these compounds appear to be laminar and were named ITQ-75, a class of materials patented by IFPEN, CSIC and UPV [23]. However, due to its small crystal size and the reduced number of well-defined diffraction peaks, it was impossible to solve its structure by convectional methods.

Finally, the possibility of obtaining materials of this class without the presence of SDA in the gel was evaluated. Two techniques were tested, the replacement of SDA by a monocation, Na^+, or seeding. None of the techniques was completely successful, under the synthesis conditions studied, in obtaining a crystalline material similar to ITQ-75 lamellar chalcogenide-type solids.

References

[1] Colin S. Cundy and Paul A. Cox. "The Hydrothermal Synthesis of Zeolites: History and Development from the Earliest Days to the Present Time". In: *Chemical Reviews* 103.3 (2003), pp. 663–702. DOI: 10.1021/cr020060i.

[2] S.-H. Feng and G.-H. Li. "Chapter 4 - Hydrothermal and Solvothermal Syntheses". In: *Modern Inorganic Synthetic Chemistry (Second Edition)*. Ed. by Ruren Xu and Yan Xu. Second Edition. Amsterdam: Elsevier, 2017, pp. 73–104. ISBN: 978-0-444-63591-4. DOI: https://doi.org/10.1016/B978-0-444-63591-4.00004-5.

[3] Qipu Lin et al. "Mimicking High-Silica Zeolites: Highly Stable Germanium- and Tin-Rich Zeolite-Type Chalcogenides". In: *Journal of the American Chemical Society* 137.19 (2015), pp. 6184–6187. DOI: https://doi.org/10.1021/jacs.5b03550.

[4] Antoine Fecant and Raquel Martinez Franco. "Solide cristallise IZM-5 et son procede de preparation". June 28, 2019, FR 3 097 859.

[5]   Roger St. C. Smart, William M. Skinner, and Andrea R. Gerson. "XPS of sulphide mineral surfaces: metal-deficient, polysulphides, defects and elemental sulphur". In: *Surface and Interface Analysis* 28.1 (1999), pp. 101–105. DOI: `https://doi.org/10.1002/`.

[6]   J.F. Moulder and J. Chastain. *Handbook of X-ray Photoelectron Spectroscopy: A Reference Book of Standard Spectra for Identification and Interpretation of XPS Data*. Physical Electronics Division, Perkin-Elmer Corporation, 1992. ISBN: 9780962702624.

[7]   S.C. Termes, A.N. Buckley, and R.D. Gillard. "2p electron binding energies for the sulfur atoms in metal polysulfides". In: *Inorganica Chimica Acta* 126.1 (1987), pp. 79–82. ISSN: 0020-1693. DOI: `https://doi.org/10.1016/S0020-1693(00)81243-8`.

[8]   Xia Yang et al. "Synthesis of Porous $ZnS:Ag_2S$ Nanosheets by Ion Exchange for Photocatalytic H_2 Generation". In: *ACS Applied Materials & Interfaces* 6.12 (2014), pp. 9078–9084. DOI: `10.1021/am5020953`.

[9]   Adriana Gheorghiu-de La Rocque et al. "X-ray spectroscopy investigation of the electronic structure of SnS_x and $Li_{0,57}SnS_2$ compounds". In: *Philosophical Magazine B* 80.11 (2000), pp. 1933–1942. DOI: `10.1080/13642810008216515`.

[10] Vasudeva Reddy Minnam Reddy et al. "Development of sulphurized SnS thin film solar cells". In: *Current Applied Physics* 15.5 (2015), pp. 588–598. ISSN: 1567-1739. DOI: `https://doi.org/10.1016/j.cap.2015.01.022`.

[11] A. R. Zanatta. "Revisiting the optical bandgap of semiconductors and the proposal of a unified methodology to its determination". In: *Scientific Reports* 9 (2019), p. 11225. DOI: `10.1038/s41598-019-47670-y`.

[12] Tong Jiang, Geoffrey A. Ozin, and Robert L. Bedard. "Nanoporous tin(IV) sulfides: Mode of formation". In: *Advanced Materials* 6.11 (Nov. 1994), pp. 860–865. DOI: `https://doi.org/10.1002/adma.19940061114`.

[13] Tong Jiang, Geoffrey A. Ozin, and Robert L. Bedard. "Nanoporous tin(IV) sulfides: Thermochemical properties". In: *Advanced Materials* 7.2 (Feb. 1995), pp. 166–170. DOI: `https://onlinelibrary.wiley.com/doi/abs/10.1002/adma.19950070214`.

[14] Tong Jiang et al. "Synthesis and Structure of the Novel Nanoporous Tin(IV) Sulfide Material TPA-SnS-3". In: *Chemistry of Materials* 7.2 (1995), pp. 245–248. DOI: `https://doi.org/10.1021/cm00050a001`.

[15] Tong Jiang et al. "Synthesis and structure of microporous layered tin(IV) sulfide materials". In: *Journal of Materials Chemistry* 8 (3 1998), pp. 721–732. DOI: `https://doi.org/10.1039/A706279F`.

[16]   Tong Jiang and Geoffrey A. Ozin. "New directions in tin sulfide materials chemistry". In: *Journal of Materials Chemistry* 8 (1998), pp. 1099–1108. DOI: https://doi.org/10.1039/A709054D.

[17]   A. Mersmann, ed. *Crystallization Technology Handbook*. CRC Press, 2001.

[18]   Qiang Zeng et al. "Effect of Cooling Rate on Crystallization Behavior of $CaO-SiO_2-MgO-Cr_2O_3$ Based Slag". In: *High Temperature Materials and Processes* 39.1 (2020), pp. 74–80. DOI: doi:10.1515/htmp-2020-0023.

[19]   Kunfeng Chen et al. "Polymorphic crystallization of Cu_2O compound". In: *CrystEngComm* 16 (24 2014), pp. 5257–5267. DOI: 10.1039/C4CE00339J.

[20]   Anthony K. Cheetham, G. Kieslich, and H. H.-M. Yeung. "Thermodynamic and Kinetic Effects in the Crystallization of Metal–Organic Frameworks". In: *Accounts of Chemical Research* 51.3 (2018), pp. 659–667. DOI: 10.1021/acs.accounts.7b00497.

[21]   José María Moreno et al. "Single-Layered Hybrid Materials Based on 1D Associated Metalorganic Nanoribbons for Controlled Release of Pheromones". In: *Angewandte Chemie International Edition* 55.37 (2016), pp. 11026–11030. DOI: https://doi.org/10.1002/anie.201602215.

[22]   Pedro Paulo Santos. *Quimica Organica*. 3rd. Vol. I. IST Press, 2019.

[23]   Beatriz Silva Gaspar et al. "ITQ-75 Crystallised Solid and Method for Preparing Same". December 15, 2022, WO/2022/258472.

[24]   Alain Meerschaut. "Misfit layer compounds". In: *Current Opinion in Solid State and Materials Science* 1.2 (1996), pp. 250–259. ISSN: 1359-0286. DOI: https://doi.org/10.1016/S1359-0286(96)80092-1.

[25]   Nicholas Ng and Tyrel M. McQueen. "Misfit layered compounds: Unique, tunable heterostructured materials with untapped properties". In: *APL Materials* 10.10 (2022), p. 100901. DOI: 10.1063/5.0101429.

[26]   G A Wiegers et al. "X-ray crystal structure determination of the triclinic misfit layer compound $(SnS)_{1.20}TiS_2$". In: *Journal of Physics: Condensed Matter* 3.16 (Apr. 1991), p. 2603. DOI: 10.1088/0953-8984/3/16/001.

[27]   Masanori Nagao et al. "Growth and anisotropy evaluation of $NbBiCh_3$ (Ch = S, Se) misfit-layered superconducting single crystals". In: *Solid State Communications* 321 (2020), p. 114051. ISSN: 0038-1098. DOI: https://doi.org/10.1016/j.ssc.2020.114051.

[28]   Drake Niedzielski et al. "First principles electronic properties predictions of incommensurately layered 2D transition metal dichalcogenides". In: *APS March Meeting Abstracts*. Vol. 2022. APS Meeting Abstracts. Jan. 2022, S60.007.

[29]   Rishabh Jain and Jeffrey D. Rimer. "Seed-Assisted zeolite synthesis: The impact of seeding conditions and interzeolite transformations on crystal structure and morphology". In: *Microporous and Mesoporous Materials* 300 (2020), p. 110174. ISSN: 1387-1811. DOI: `https://doi.org/10.1016/j.micromeso.2020.110174`.

[30]   Yeqing Wang et al. "Insights into the Organotemplate-Free Synthesis of Zeolite Catalysts". In: *Engineering* 3.4 (2017), pp. 567–574. ISSN: 2095-8099. DOI: `https://doi.org/10.1016/J.ENG.2017.03.029`.

[31]   Robert W. Thompson. "Chapter 2 - Nucleation, growth, and seeding in zeolite synthesis". In: *Verified Syntheses of Zeolitic Materials*. Ed. by Harry Robson and Karl Petter Lillerud. Amsterdam: Elsevier Science, 2001, pp. 21–23. ISBN: 978-0-444-50703-7. DOI: `https://doi.org/10.1016/B978-044450703-7/50100-9`.

Chapter 5

Materials Modification

5.1   Adjusting Interaction with UV-Vis Radiation

Since the synthesized materials will be used as photocatalysts, their electronic properties, namely the optical band gap value, are of extreme importance. As for the optical band gap value, which is relatively easy to determine, it should be between 1,5 and 2,0 eV in order to take advantage of the solar radiation and to be suitable for solar fuels production. In this way, the value of the optical band gap is low enough to maximize the number of absorbed photons, but high enough to allow the photoproduced charge carriers to be thermodynamically feasible to participate in the desired processes. Taking into account the value of the optical band gaps presented previously (see Table 4.8), these structures were doped in order to obtain an optical band gap value more suitable for the desired application.

According to the state of the art presented earlier (see Section 2.4.1), the addition of Se or Cu leads to band gap reduction. Thus, small amounts of Se or Cu were added to the gels during the synthesis process. The addition of other metals as dopants, such as Fe, Ni and Co was also studied, since these metals are cheap, earth abundant elements and were previously studied as photocatalysts on solar fuel production [1, 2, 3, 4, 5].

Another methodology used to alter the electronic properties of the materials under study was the insertion of organic compounds into the synthesis gel that have a dual function, i.e., that can act as both an SDA and as a light-harvesting antenna. The compound chosen was a Ru complex, cis-dichlorobis(2,2-bipyridine)ruthenium(II), since this class of compounds is widely known for their use in dye-sensitized solar cells [6, 7, 8, 9]. However, it is important to note that Ru is not a common element in the earth's crust, which could jeopardize its use in a sustainable application [1].

5.1.1   IZM-5 Electronic Structure Tuning

During the synthesis process, small amounts of dopants were added to the gels in order to change its interaction with radiation. Different dopants and dopant's concentrations were tested.

As for the use of the Ru complex, it was tested in the absence, on the synthesis gel, of Compound A as SDA, in order to verify if it would be possible to obtain a crystalline structure, and also mixed with SDA A, i. e., the organic compound used for the synthesis of IZM-5 material.

5.1.1.1 Dopping with Selenium

Using Se as a dopant, three different molar concentrations were tested: 0,03% (Se/S molar ratio equal to 0,01), 0,2% (Se/S molar ratio equal to 0,1) and 0,4% (Se/S molar ratio equal to 0,2). Figure 5.1 shows the diffraction patterns of IZM-5 doped with different Se contents.
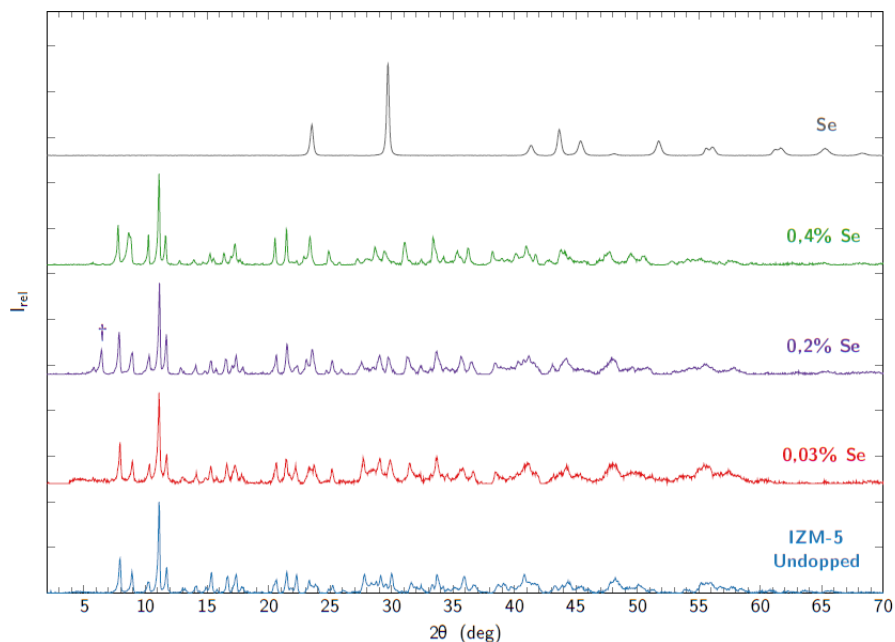
Figure 5.1: PXRD patterns of undopped IZM-5 (in blue), IZM-5 dopped with 0,03% Se (in red), 0,2% Se (in purple), 0,4% Se (in green) and Se (in grey), where † denotes an unknown impurity

Looking at Figure 5.1, the insertion of Se in the structure seems successful, since there is no change in the diffraction pattern with the different amounts of Se in the initial gel and there is no presence of diffraction peaks that could be related to an extra Se phase.

Since the Se doping allowed the structure integrity to be maintained, further characterization techniques, namely chemical composition, UV-Vis and XPS, were carried out in order to understand the consequences of the doping on IZM-5 final properties.

Table 5.1 shows the chemical composition of the different IZM-5 Se doped samples and their molar ratios on the synthesis gel and on the final structure (see Table 5.2).

Table 5.1: Chemical composition of the IZM-5 Se-doped samples ([1] Molar composition (%) on the initial gel. [2]Determined by elemental analysis. [3]Determined by ICP)

SDA	Dopant[1]	Formula	Mass composition (%)						
			N[2]	C[2]	H[2]	S[2]	Sn[3]	Zn[3]	Se[3]
	Undoped	$Sn_{3,13}Zn_{1,26}S_8 \cdot C_{15,01}H_{31,49}N_{2,24}$	3,09	17,80	3,11	25,34	36,68	8,12	-
Compound A	0,03% Se	$Sn_{2,84}Zn_{1,03}S_{7,63}Se_{0,37} \cdot C_{16,93}H_{34,12}N_{2,34}$	3,27	20,33	3,41	24,48	33,74	6,73	2,92
	0,2% Se	$Sn_{3,15}Zn_{1,25}S_{6,45}Se_{1,55} \cdot C_{16,23}H_{39,19}N_{3,34}$	3,86	21,85	3,77	19,90	36,00	7,86	11,76
	0,4% Se	$Sn_{3,44}Zn_{0,85}S_{5,12}Se_{2,88} \cdot C_{15,10}H_{36,37}N_{2,85}$	2,81	17,32	2,98	13,45	33,42	4,53	18,62

Table 5.2: Molar ratios of the different IZM-5 Se doped samples on the synthesis gel and on the final structure

	Gel Molar Ratios				Material Molar Ratios			
	Sn/Zn	Sn/S	Se/S	C/N	Sn/Zn	Sn/S	Se/S	C/N
IZM-5	3,1	0,2	-	6,5	2,5	0,4	-	6,7
0,03 % Se	3,2	0,2	0,02	6,5	2,8	0,4	0,1	7,2
0,2 % Se	3,1	0,2	0,09	6,5	2,5	0,5	0,2	6,6
0,4 % Se	3,1	0,2	0,2	6,5	4,1	0,7	0,6	7,2

It is observed that, along the different samples, the Sn mass percentage remains quite similar. As for the S content, it decreases as the Se content increases. When 0,4% of Se is added to the initial gel there is a drastic increase in the Sn/Zn and Sn/S molar ratios. It is therefore suggested that with the increase of Se in the gel, the assimilation of Zn and S by the final material decreases.

Afterwards, the UV-Vis spectra of the different Se-dopped samples were plotted in order to evaluate the influence of this dopant in the iteration with the UV-Vis radiation (see Figure 5.2) and its consequences on the optical band gap value (see Table 5.3).
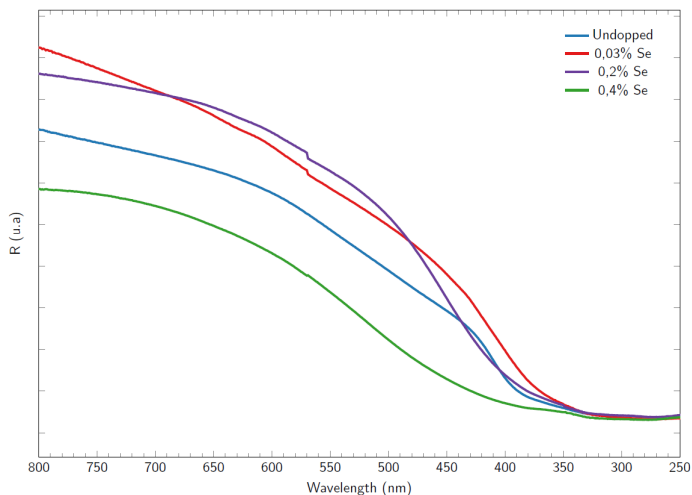
Figure 5.2: UV-Vis spectra of IZM-5 (in blue) and Se-dopped IZM-5 samples with different Se contents - 0,03% (in red), 0,2% (in purple) and 0,4% (in green)

Table 5.3: Bandgap (E_g) of IZM-5 Se-doped samples

	E_g (eV)
Undopped	3,1
0,03% Se	3,5
0,2% Se	3,4
0,4% Se	2,9

Looking at Table 5.3, it is concluded that a reduction in the optical band gap value is only observed when the Se molar percentage on the initial gel is equal to 0,4%. Therefore, it appears that doping with Se only yields changes in electronic properties towards the desired outcome above the 0,4% threshold. This increase is contrary to expectations, since according to the literature [10, 11], the insertion of Se into the structure should lead to marked a decrease in the optical band gap.

There are two possible justifications for such discordance with the literature. The first is the calculation method used to determine the optical band gap value. This was done by using the method presented by Zanatta [12], based on fitting a sigmoidal curve to the experimental data. Although it is a method that is meant to solve the disadvantages of using the Tauc plot method [13], it requires the fitting of a sigmoidal curve, which sometimes may not be the most appropriate for the

given situation. It is also necessary to know whether the material has a direct or indirect band gap. As this information is not known, since it is a new structure, it is assumed that the structure under study presents a direct band gap. This assumption could be wrong and therefore add a possible error to the calculated value. Another possible explanation would be the position that the dopant occupies in the crystal lattice. As noted in the state of the art [14, 15, 16], in addition to the chemical nature of the dopant, the position it occupies influences the final electronic properties. Therefore, it is possible that, with the first two concentrations of Se tested, the position it occupies leads to a blue shift on the band gap value.

5.1.1.2   Dopping with Metals

The impact of metals addition as doping agents on IZM-5's interaction with UV-Vis radiation was additionally evaluated. For that, small amounts of copper, iron, nickel and cobalt were added onto the initial gel. Three different M/Sn gel molar ratios (M = Cu, Co, Fe, Ni) were tested: 0,1, 0,3 and 0,6. The diffractograms of the different IZM-5 doped samples are present in Figures 5.3 and 5.4.
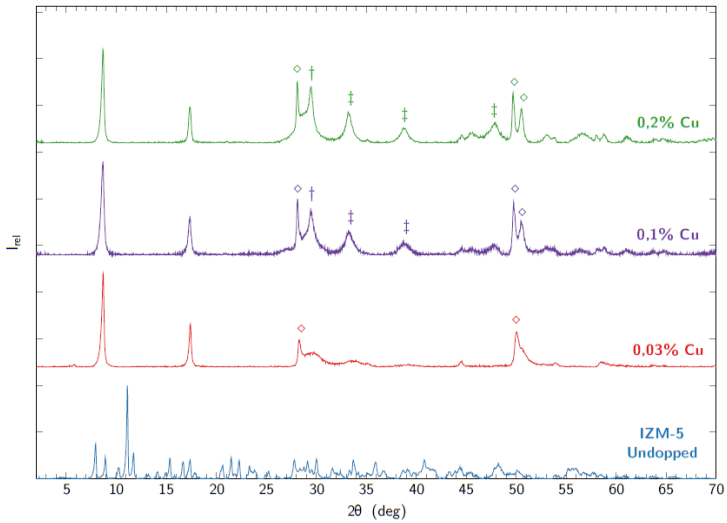
(a)
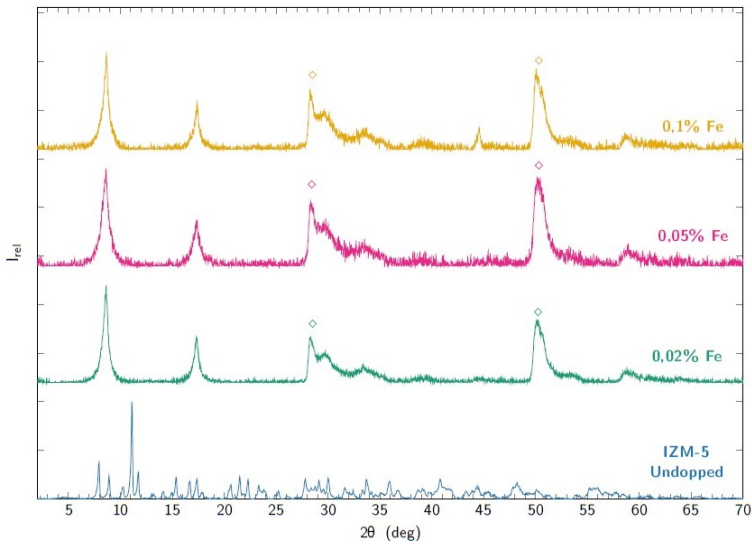
(b)

Figure 5.3: PXRD difractogram of (5.3a) undopped IZM-5 (in blue), ITQ-76 with 0,03% Cu (in red), 0,1% Cu (in purple) and 0,2% Cu (in green), where † denotes a CuS phase, ‡ a Cu_2S phase and ⋄ a ZnS phase; (5.3b) undopped IZM-5 (in blue), ITQ-76 with 0,02% Fe (in green), 0,05% Fe (in pink) and 0,1% Fe (in yellow), where ⋄ denotes a ZnS phase
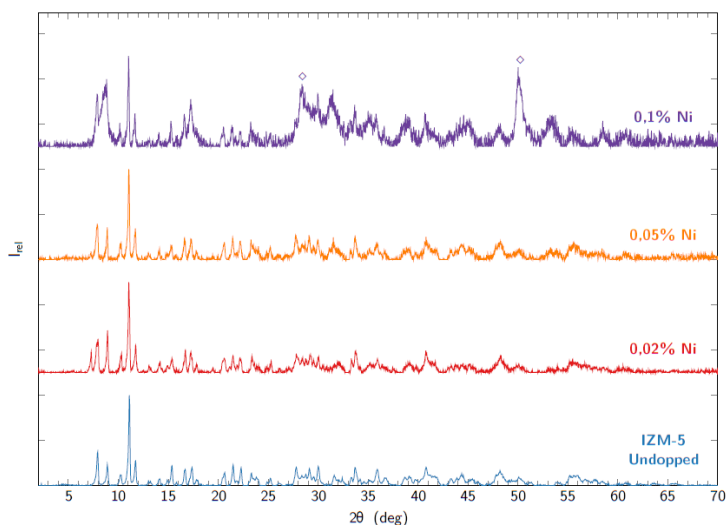
(a)
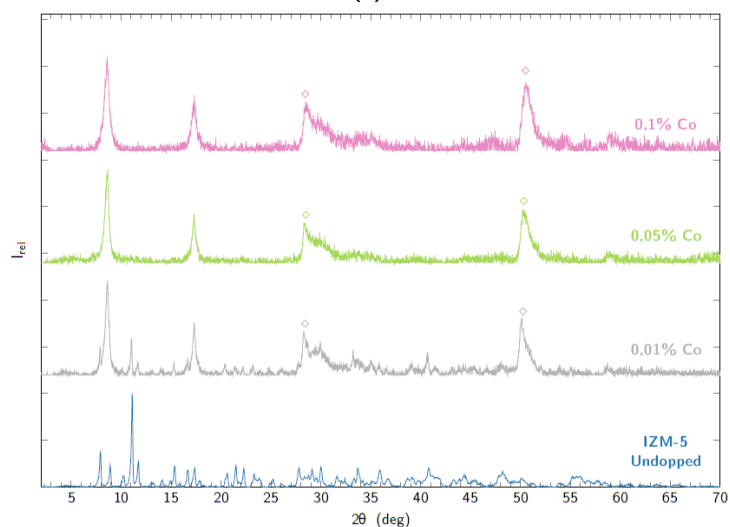
(b)

Figure 5.4: PXRD difractogram of (5.4a) undopped IZM-5 (in blue), IZM-5 with 0,02% Ni (in red), 0,05% Ni (in orange) and 0,1% Ni (in purple), where where ⋄ denotes a ZnS phase; (5.4b) undopped IZM-5 (in blue), ITQ-76 with 0,01% Co (in gray), 0,05% Co (in green) and 0,1% Co (in pink), where ⋄ denotes a ZnS phase

When copper, iron or cobalt is inserted into the synthesis gel, there is a dramatic change in the diffraction pattern obtained. The diffraction pattern obtained is no longer that of IZM-5, but of a new laminar phase. This new laminar phase was named ITQ-76 and is patented by IFPEN, CSIC and UPV [17]. When nickel is inserted into the synthesis gel (see Figure 5.4a), the final material maintains the diffraction pattern of IZM-5 up to a molar concentration on the synthesis gel of 0,05%. When a higher molar concentration of 0,1% is tested, a diffraction pattern that can be seen as combination of IZM-5 ant ITQ-76 diffraction patterns is obtained.

As mentioned beforehand for ITQ-75, the diffraction pattern of ITQ-76 can be associated with a traditional pattern of a laminar material due to the basal distance observed of the first two diffraction peaks [18]. The first diffraction peak is located at 2θ equal to 8,7°, with a basal spacing of 10,1 Å, and the second diffraction peak is located at 2θ equal to 17,4°, with a basal spacing of 5,1 Å. Besides these two diffraction peaks, there are two more stand out, located at 2θ equal to 28,3° and 50,0°, that can be associated with a ZnS phase. Comparing to the ITQ-75 structure (see Figure 5.5), where the main diffraction peaks are located at 2θ equal to 7,5°, 15,2° and 50,2°, the first two diffraction peaks are displaced towards higher angles, implying a more close architecture.
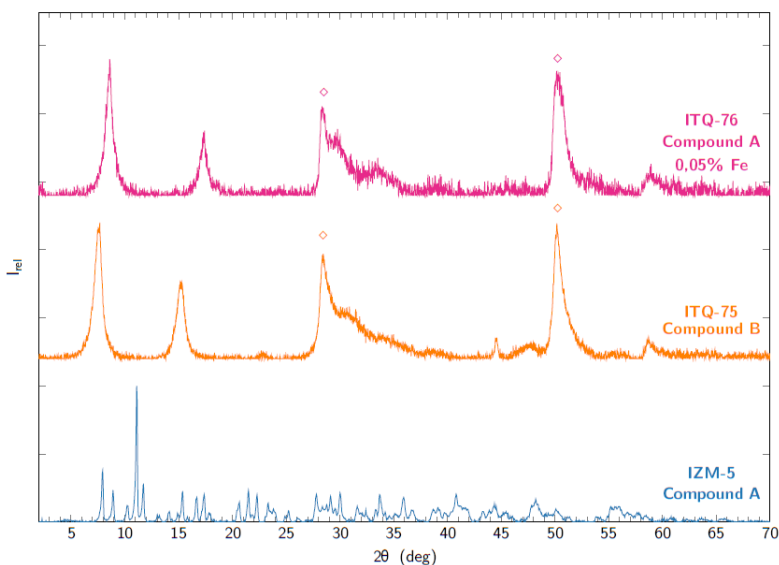
Figure 5.5: PXRD diffractogram of IZM-5, obtained with Compound A as SDA (in blue), ITQ-75, obtained with Compound B as SDA (in orange), and ITQ-76, obtained with Compound A as SDA and with 0,05% Fe (in pink), where ⋄ denotes a ZnS phase

Looking more closely at the behavior of each doping agent, it is observed that the insertion of copper leads to ITQ-76 diffraction pattern and its insertion into the final structure is partially successful (see Figure 5.3a). From a molar concentration of 0,03% Cu, it is possible to see the presence of diffraction peaks that can be associated with CuS and Cu_2S phases. As for the iron insertion onto the ITQ-76 structure (see Figure 5.3b), this seems to be successful, since there are no diffraction peaks that can be associated with a possible Fe extra phase. As mentioned earlier, the behavior at nickel insertion is distinct from the others. Nickel doping is the only doping technique that allows to maintain IZM-5 structure integrity up to a nickel molar concentration on the synthesis gel of 0,05 % (see Figure 5.4a). As for cobalt, the last doping agent tested, it is observed that for the lowest concentration tested there are two diffraction peaks at 2θ equal to 11,0° and 11,7° that can be associated with IZM-5 structure (see Figure 5.4b). For the other two concentrations tested, a similar behavior to Fe-doping is observed, where only ITQ-76 diffraction pattern is obtained without the presence of extra peaks that could be associated with Co extra phase.

Comparing the four metals used as dopants, nickel is the most stable. Thus, and taking into account that this is the only metal that allows to maintain IZM-5

crystalline structure, it is hypothesized that it is not inserted in its framework. As for the other metals, namely copper and iron, these are more easily oxidizable. As such, their insertion into the crystalline structure is facilitated, which would explain the crystalline phase change observed.

In order to confirm the presence of the metals in the final structure, the chemical composition of the studied structures and their molar ratios were determined (see Tables 5.4 and 5.5).

Table 5.4: Chemical composition of the IZM-5 and ITQ-76 ([1] Molar composition (%) on the initial gel. [2]Determined by elemental analysis. [3]Determined by ICP. [4]M represents Cu, Fe, Ni or Co according to the sample)

| SDA	Dopant[1]	Formula	Mass composition (%)						
			N[2]	C[2]	H[2]	S[2]	Sn[3]	Zn[3]	M[4]
	Undoped	$Sn_{3,13}Zn_{1,26}S_8 \cdot C_{15,01}H_{31,49}N_{2,24}$	3,09	17,80	3,11	25,34	36,68	8,12	-
	0,03% Cu	$Sn_{2,97}Zn_{1,30}Cu_{0,21}S_8 \cdot C_{23,39}H_{2,10}N_{39,98}$	2,38	25,50	3,63	23,30	32,04	7,70	1,22
	0,1% Cu	$Sn_{2,57}Zn_{1,08}CuS_8 \cdot C_{10,58}H_{19,17}N_{1,37}$	1,92	12,67	2,10	25,61	30,40	7,03	
	0,2% Cu	$Sn_{2,86}Zn_{1,15}Cu_{2,36}S_8 \cdot C_{8,45}H_{22,64}N_{1,11}$	1,42	9,24	2,06	23,39	30,97	6,83	13,70
	0,02 % Fe	$Sn_{2,91}Zn_{1,31}Fe_{0,63}S_8 \cdot C_{15,25}H_{26,56}N_{1,70}$	2,53	19,42	2,82	27,22	36,72	9,08	3,72
	0,05% Fe	$Sn_{2,16}Zn_{1,05}Fe_{0,74}S_8 \cdot C_{15,61}H_{26,80}N_{1,41}$	2,06	19,58	2,78	26,81	26,76	7,20	4,32
Compound A	0,1% Fe	$Sn_{2,03}Zn_{1,01}Fe_{1,46}S_8 \cdot C_{20,69}H_{35,88}N_{1,72}$	2,06	21,24	3,07	21,95	20,67	5,62	6,99
	0,02 % Ni	$Sn_{2,42}Zn_{1,06}Ni_{0,84}S_8 \cdot C_{13,57}H_{22,76}N_{1,48}$	2,37	18,67	2,61	29,41	32,90	7,91	2,76
	0,05 % Ni	$Sn_{1,89}Zn_{0,93}Ni_{0,64}S_8 \cdot C_{13,57}H_{22,76}N_{1,48}$	2,94	19,62	3,27	28,49	24,86	6,72	4,17
	0,1 % Ni	$Sn_{1,69}Zn_{0,82}Ni_{1,14}S_8 \cdot C_{13,57}H_{22,76}N_{1,48}$	2,41	18,48	3,00	25,88	20,22	5,39	6,76
	0,01 % Co	$Sn_{2,65}Zn_{1,36}Co_{0,35}S_8 \cdot C_{16,95}H_{29,81}N_{1,81}$	2,57	20,67	3,03	26,07	31,93	9,07	2,11
	0,05 % Co	$Sn_{2,11}Zn_{1,16}Co_{0,76}S_8 \cdot C_{22,00}H_{36,37}N_{2,03}$	2,79	25,92	3,57	25,18	24,59	7,43	4,39
	0,1 % Co	$Sn_{1,85}Zn_{0,87}Co_{1,29}S_8 \cdot C_{27,96}H_{43,70}N_{2,50}$	3,22	30,87	4,02	23,30	20,17	5,22	6,99

Table 5.5: Molar ratios of the different IZM-5 metal doped samples on the synthesis gel and on the final structure ([1]M represents Cu, Fe, Ni or Co according to the sample; n.a - not available)

SDA	Dopant[1]	Gel Molar Ratios					Material Molar Ratios				
		Sn/Zn	Sn/S	Sn/M[1]	Zn/M[1]	C/N	Sn/Zn	Sn/S	Sn/M[1]	Zn/M[1]	C/N
	Undoped	3,1	0,2	-	-	6,5	2,5	0,4	-	-	6,7
	0,03% Cu	3,2	0,2	14,1	4,4	6,5	2,3	0,5	14,1	6,2	11,1
	0,1% Cu	3,2	0,2	2,4	0,7	6,5	2,4	0,3	n.a.	n.a.	7,2
	0,2% Cu	3,2	0,2	1,9	0,6	6,5	2,5	0,4	1,2	0,5	7,6
	0,02% Fe	3,1	0,2	6,8	1,0	6,5	2,2	0,4	4,6	0,5	9,0
	0,05% Fe	3,0	0,2	4,4	2,9	6,5	2,0	0,3	2,9	1,4	11,1
Compound A	**0,1% Fe**	2,9	0,2	2,1	1,4	6,5	2,0	0,3	0,7	0,7	12,0
	0,02% Ni	3,2	0,2	7,5	2,3	6,5	2,3	0,3	2,9	1,3	9,2
	0,05% Ni	3,0	0,2	4,1	1,4	6,5	2,0	0,2	3,0	1,4	7,9
	0,1% Ni	3,1	0,2	2,1	0,7	6,5	2,1	0,2	1,5	0,7	8,9
	0,01% Co	3,0	0,2	17,9	6,0	6,5	1,9	0,3	7,5	3,9	9,4
	0,05% Co	2,9	0,2	6,0	2,1	6,5	1,8	0,3	2,8	1,5	10,8
	0,1% Co	2,9	0,2	2,9	1,0	6,5	2,2	0,2	1,4	0,7	11,2

In all doped samples the presence of the metal used as doping agent is always observed in the final material.

With increasing doping agent content on the initial gel there is an increase on its content on the final material and a decrease on Sn and Zn contents. Looking to the molar ratios, these present different behaviors according to the doping agent used. As for the impact of Cu, it is observed that the Sn/Zn molar ratio in the synthesis gel is always higherand the Sn/S molar ratio is always lower than those of the final material. It is thus suggested that there is an excess of the Sn and S precursors in the initial gel. As for the Sn/Cu and Zn/Cu molar ratios, it is observed that with increasing copper content in the initial gel they become similar, so the Cu present on the initial gel is completely present on the final material. Regarding the Fe-doping and Co-doping, they have a similar impact on the Sn/S and Sn/Zn molar ratios. As for the Sn/Dopant and Zn/Dopant molar ratios, it is observed that they are always higher on the initial gel than on the final, so there is an excess of Dopant on the initial gel. Finally, regarding the impact of Ni insertion, it is observed that the Sn/Zn molar ratio has a similar behavior as the other doping methods. As for the behavior of the Sn/S and Zn/Ni molar ratios, it is observed that for the two highest Ni contents the values before and after synthesis are similar.

Regarding the C/N molar ratio, this ratio is always higher on the structure than on the initial gel. The highest increase is observed on the Fe and Co doped structure. This increase might be explain with the possible presence of ethylene glycol onto the final structure, situation previous discussed when the ITQ-75 SDA chemical environment was studied.

Subsequently, the impact of the insertion of the different tested dopants on the optical properties was evaluated. For this, the interaction with UV-Vis radiation was determined (see Figure 5.6) and their optical band gap was determined by the method described by Zanatta [12] (see Table 5.6 and Appendixes D.2.3, D.2.4, D.2.5 and D.2.6 for more information regarding its determination).
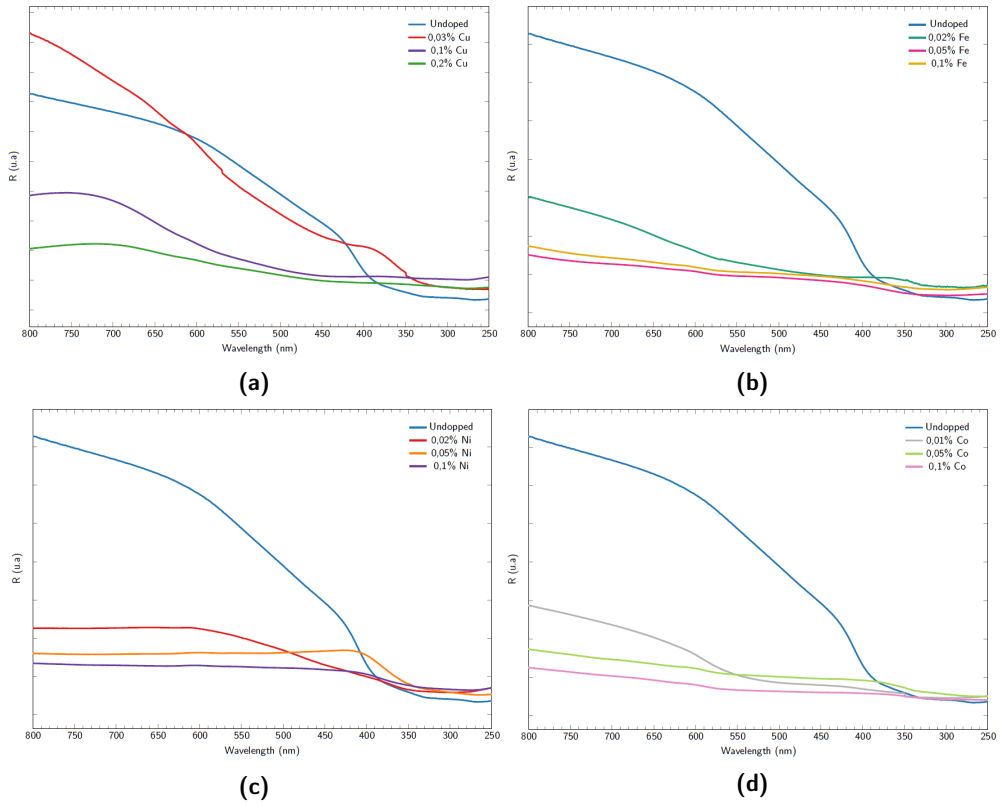
Figure 5.6: UV-Vis spectra of the different materials obtained with Compound A as SDA - (5.6a) Cu-doped materials, (5.6b) Fe-doped samples, (5.6c) Ni-doped samples and (5.6d) Co-doped samples

Table 5.6: Optical band gap values of the different materials obtained with Compound A as SDA - (5.6a) Cu-doped materials, (5.6b) Fe-doped samples, (5.6c) Ni-doped samples and (5.6d) Co-doped samples (n.a. - not available)

(a)

	E_g (eV)
Undoped	3,1
0,03% Cu	2,4
0,1% Cu	2,2
0,2% Cu	2,2

(b)

	E_g (eV)
Undoped	3,1
0,02 % Fe	2,0
0,05 % Fe	n. a.
0,1 % Fe	n. a.

(c)

	E_g (eV)
Undoped	3,1
0,02 % Ni	3,0
0,05 % Ni	3,3
0,1 % Ni	3,2

(d)

	E_g (eV)
Undoped	3,1
0,01 % Co	2,0
0,05 % Co	n. a.
0,1 % Co	n. a.

After the insertion of any of the doping agents under study, regardless of their amount, changes in their reflectance spectrum are observed.

For IZM-5 without any doping agent, the reflectance edge is at 432 nm. After doping with Cu, there is a shift on its edge. For a Cu molar content equal to 0,03%, this edge moves towards lower wavelength, to 393 nm. Albeit this blue shift, there is a decrease on the calculated optical band gap value (see Table 5.6a). For the other two Cu doping contents tested, there is a red shift on the reflectance edge, from to 432 nm to 716 nm, on the sample with 0,1% Cu, and 700 nm, on the sample with 0,2% Cu. As for their optical band gap value, with Cu presence there is a decrease on its value, somethings according to what is described in the literature (see Section 2.4.1).

Regarding the Fe-dopped samples, there is a red shift on the reflectance edge on all three tested Fe contents, from 368 nm to 432 nm (sample with 0,02% Fe), 443 nm (sample with 0,05% Fe) and 447 nm (sample with 0,1% Fe). With this red shift comes along a reduction on the optical band gap value, from 3,1 eV to 2,0 eV (see Table 5.6b). However, it was not possible to determinte the optical band gap value of the samples with 0,05% Fe and 0,1% Fe contents since it was not possible to fit a sigmoidal curve to the experimental data (see Figures D.16 and D.17). Studies on Fe-doped SnS thin films [19], DFT calculations on Fe-doped SnS$_2$ [20], Fe-doped ZnS macrospheres [21] and Fe-doped ZnS nanospheres [22]

show that, after Fe doping there is a reduction on the optical band gap. Therefore, the results present here are according to literature.

As for the effect of doping with nickel (see Figure 5.6c), this is distinguished from that previously observed with Cu or Fe doped samples. After the insertion of 0,02% Ni, a red shift is observed at the edge of the reflectance, from 432 nm to 612 nm. This redshift is accompanied by a reduction of the optical band gap value, from 3,1 eV to 3,0 eV (see Table 5.6c). As the Ni doping concentration increases to 0,05% or 0,1%, the reflectance edge shifts to 426 nm or 477 nm, respectively. With this blue shift is observed an increase in the value of the optical band gap, from 3,1 eV to 3,3 eV or 3,2 eV. Kurnia et al. [23], through first principles calculations, observed that by doping ZnS with Ni, the band gap of the final structure is reduced. These results were confirmed by Kudo et al. [24], which incorporated 0,1% Ni in ZnS, leading to a band gap reduction. For the lowest Ni concentration tested it is possible to observe the reduction of the calculated optical band gap value. However, for the higher concentrations tested the opposite is observed, i.e ., there is an increase in the optical band gap value. A similar situation was observed by Singh et al. [25], where they justified this behavior by the presence of Ni clusters rather than the insertion of Ni into the structure.

Finally, the consequences of Co-doping are similar to those of Fe-doping. After the addition of 0,01% Co there is a redshift of the reflectance edge towards 614 nm, leading to a band gap reduction to 2,0 eV. As for the remaining two Co doping concentrations tested, similarly to the Fe-doped samples, it was not possible to fit a sigmoidal curve to the experimental data (see Figures D.22 and D.23). This situation highlights the limitations of this methodology for the optical band gap determination. When the material presents low reflectance values, which will translate into transitions in the visible-NIR region, it becomes difficult to fit a sigmoidal curve to the experimental data. Comparing to what is reported in the literature, the consequences of Co-doping on the optical properties of the final structure are mixed. Salem et al. [26] studied the introduction of increasing Co contents on ZnS nanoparticles. With increasing Co contents there was a blue shift of the absorption edge, leading to a higher optical bad gap value. Such trend was reported earlier by Sambasivam et al . [27] and Liu et al. [28]. However, when Rahman et al. [29] doped MoS_2 nanosheets with different Co contents there was a decrease on the optical band gap value and only for the higher Co contents there was an increase. According to the authors this behavior is due to the Moss–Burstein effect [30, 31, 32]. When higher amounts of dopant are present, defects start to appear on the conduction band. As such, the absoprtion edge is pushed towards higher energy values, leading to an increase in the optical band gap value.

5.1.1.3   Ru-complex Insertion

The use of a Ru complex had as main objective the increase of light harvesting capabilities of the final structure. Two complex contents were tested in the synthesis gel - the absence of Compound A as SDA (Ru complex/SDA A - ∞) and putting together the two compounds (Ru complex/ SDA - 0,1 and 0,01). The diffractograms of these samples are shown in Figure 5.7.
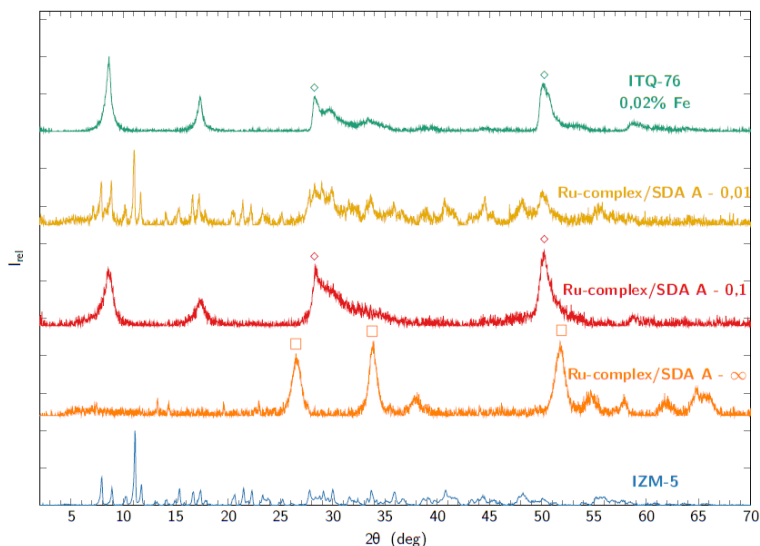
Figure 5.7: PXRD difractogram of undopped IZM-5 (in blue), material obtained using the Ru-complex as SDA (in orange), ITQ-76 with Ru-complex as coSDA, with a Ru-complex/SDA A molar ratio equal to 0,1 (in red) and to 0,01 (in yellow) and ITQ-76 with 0,02% Fe (in green), where □ denotes a SnO_2 phase and ◇ a ZnS phase

As one can see from the Figure 5.7, Compound A is required to obtain a crystalline structure. Otherwise, the diffraction pattern obtained can be associated with SnO_2 diffraction pattern, although this compound is not used as a Sn precursor. When Compound A is present, a crystalline phase is present. Depending on the Ru-complex/SDA A molar ratio, ITQ-76, the structure previously studied when metals were added to the IZM-5's synthesis gel, or purely IZM-5's phase were obtained.

Subsequently, and in order to confirm the presence of the ruthenium complex, the chemical composition (see Table 5.7 and 5.8) and the ^{13}C NMR of the samples with Ru-complex/SDA A molar ratio equal to 0,1 or 0,01 were determined.

Table 5.7: Chemical composition of the IZM-5 and ITQ-76 with Ru-complex ([1] Molar composition (%) on the initial gel. [2]Determined by elemental analysis. [3]Determined by ICP)

SDA	Modification[1]	Formula	Mass composition (%)						
			N[2]	C[2]	H[2]	S[2]	Sn[3]	Zn[3]	Ru[3]
	Undoped	$Sn_{3,13}Zn_{1,26}S_8 \cdot C_{15,01}H_{31,49}N_{2,24}$	3,09	17,80	3,11	25,34	36,68	8,12	-
Compound A	Ru-complex/SDA A - 0,1	$Sn_{1,94}Zn_{0,93}S_8Ru_{1,00} \cdot C_{28,31}H_{43,25}N_{3,01}$	3,69	29,73	3,78	22,44	20,13	5,33	8,82
	Ru-complex/SDA A - 0,01	$Sn_{2,57}Zn_{1,22}S_8Ru_{0,13} \cdot C_{20,47}H_{35,05}N_{2,01}$	2,86	24,46	3,49	25,24	30,3	8,0	1,3

Table 5.8: Molar ratios of the different samples with Ru-Complex on the synthesis gel and on the final structure

SDA	Modification[1]	Gel Molar Ratios					Material Molar Ratios				
		Sn/Zn	Sn/S	Sn/Ru	Zn/Ru	C/N	Sn/Zn	Sn/S	Sn/Ru	Zn/Ru	C/N
	Undoped	3,1	0,2	-	-	6,5	2,5	0,4	-	-	6,7
Compound A	Ru-complex/SDA A - 0,1	3,1	0,2	2,0	0,6	6,2	2,1	0,2	1,9	0,9	9,4
	Ru-complex/SDA A - 0,01	3,2	0,2	15,2	4,8	6,5	2,1	0,3	19,5	9,3	10,0

As for the chemical composition of the sample obtained with the Ru-complex, this element is present in the final sample. As for the C/N molar ratio, there is an increase from 6,7 to 9,4, thus increasing the carbon content compared to IZM-5.

Next, ^{13}C NMR was performed to ensure that the structure of the Ru-complex is not destroyed during synthesis process (see Figure 5.8).
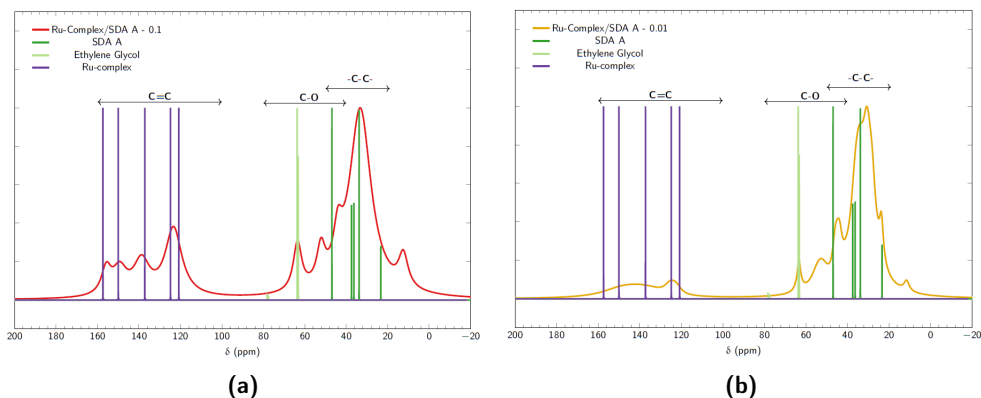
Figure 5.8: ^{13}C NMR spectra of the samples obtained with different Ru-complex/SDA A molar ratios - (5.8a) 0,1 (in red) and (5.8b) 0,01 (in mustard yellow) - and SDA A (in green), ethylene glycol (in bright red) and the Ru-complex (in purple)

Figure 5.8 shows that for the two Ru-complex/SDA molar ratios tested, both Ru-complex and SDA structure's is maintained. It can also be seen that the relative

intensity of the bands associated with the presence of double bonded carbons changes with the different Ru-complex/SDA molar ratios. Finally, both structures show a band at a chemical shift equal to 60 ppm that could be associated with the presence of ethylene glycol, a situation previously observed for ITQ-75 structures.

Finally, the interaction with UV-Vis radiation (see Figure 5.9) and the impact that the presence of this complex has on the optical band gap value (see Table 5.9) was determined.
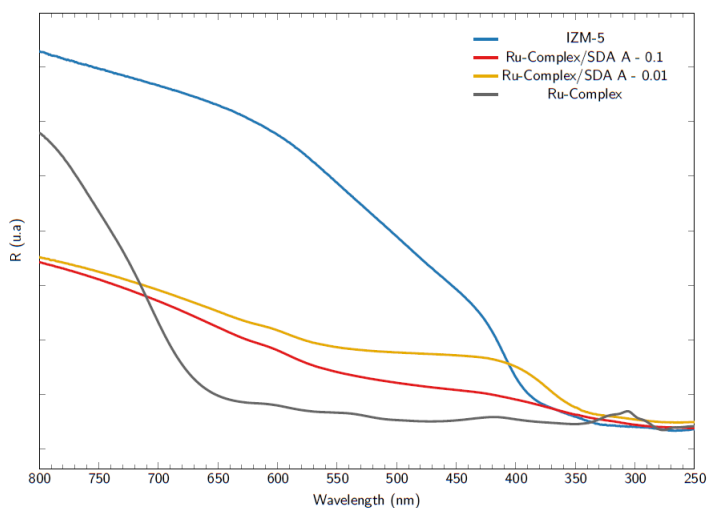
Figure 5.9: UV-Vis spectra of IZM-5 (in blue), with Ru-complex/SDA A molar ratio equal to 0,1 (in blue) and 0,01 (in yellow) and Ru-complex (in grey)
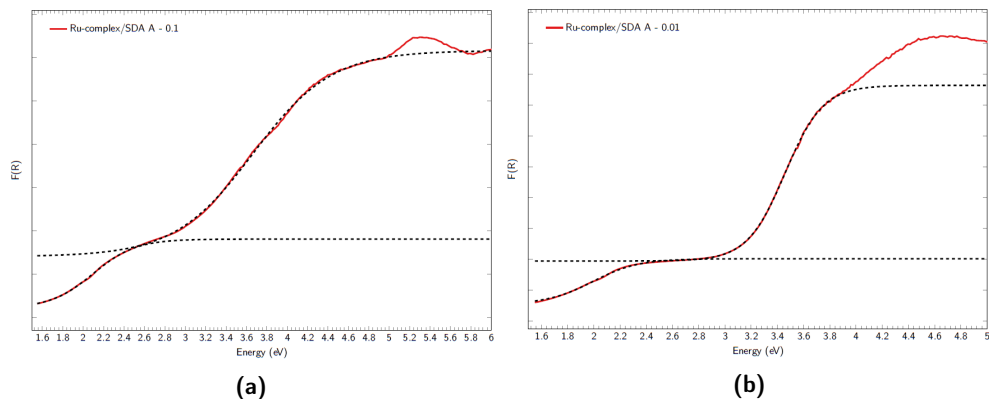
Figure 5.10: Kubelka-Munk function of the structures obtained with Ru-complex/SDA A molar ratios equal to (5.10b) 0,1 and (5.10b) 0,01

As can be seen in Figure 5.9, the structures obtained with the Ru-complex have a distinct reflectance profile from IZM-5, presenting a redshift of the reflectance edge. However, it is not possible to say that this difference is only due to the presence of the Ru-complex, since the materials in question have a distinct crystal structure and this influences the electronic properties of the final structure. Comparing the reflectance profile with that of the isolated Ru-complex, it can be seen that they are quite different. Thus, the UV-Vis interaction of the structures obtained with the Ru-complex is not only due to the presence of this compound, but also due to material's inorganic structure.

Looking at Figure 5.10, one way to observe that it is possible to fit two sigmoidal curves to the structure's Kubelka-Munk function, a situation similar to the one observed previously for IZM-5 with zinc (see Figure 4.12). Due to the observed double contribution, it is possible to determine two values for the optical band gap (see Table 5.9).

Table 5.9: Optical band gap (E_g) of materials obtained with the Ru-complex

Material	E_g (eV)
IZM-5	3,1 & 3,6
Ru-complex/SDA A - 0,1	2,0 & 3,5
Ru-complex/SDA A - 0,01	1,9 & 3,4

After the insertion of the Ru-complex the optic band gap value associated with the first transition decreases, from 3,0 eV to 2.0 eV (for Ru-complex/SDA A - 0,1) or 1.9 eV (for Ru-complex/SDA A - 0,01). Regarding the second transition, the value of the optic band gap does not undergo a large variation.

5.1.1.4 Final Considerations

In order to modulate IZM-5 electronic properties and, as a consequence, its optical band gap value, towards the desired application, two modifications on the synthesis gel were employed - insertion of doping agents or insertion of complexes with light-harvesting properties.

Regarding the different doping agents evaluated, two classes of elements were tested: the insertion of a chalcogenide, namely Se, or metals, in particular copper, iron, nickel, and cobalt.

As for the insertion of Se into IZM-5 crystal lattice, this seems successful, since when evaluating the diffractograms of these materials (see Figure 5.1) they do not show any diffraction peaks that could be associated with a Se extra phase. Evaluating the chemical composition of the different Se-doped IZM-5 samples (see Table 5.1), it is observed that with increasing Se content the S content decreases, which seems to suggest a replacement of S by Se. This is as expected, since S is the only element present with the same valence as Se. As for the impact the presence of Se has on the optical band gap value, it is observed that for the smallest concentrations tested, it increases. It is only observed a decrease for the higher Se content tested, from 3,1 eV to 2,9 eV. This goes against what has been previously described in the literature for this class of materials, as one would expect a decrease in the band gap value for any of the concentrations tested (see Section 2.4.1). Several hypotheses can be thought of to justify this deviation from the literature. The first is the methodology employed to determine the optical band gap value and the assumption of a direct transition between the valence and the conduction bands. This is a matter that is used by most authors but, since it is a new structure and its band structure is not known, it is not clear what kind of transition exists, which can lead to miscalculations in determining the value of this parameter. The second possible hypothesis that could explain the deviation from the literature is the position that the Se occupies in the crystal lattice. As observed in [14, 15], in addition to the chemical nature of the dopant, the position it occupies will also influence the final electronic properties of the structure.

Next, the impact of inserting different metals as doping agents was studied. Starting with copper, it was observed that for any of the molar concentrations tested,

it is not possible to obtain the diffraction pattern of IZM-5. The diffraction pattern obtained can be associated with a new laminar structure, confirmed by XRD study and the position of the first two diffraction peaks, and it was entitled ITQ-76 [17]. The copper insertion is partially successful, since for the highest Cu contents evaluated, the presence of diffraction peaks that can be associated with Cu extra phases is observed. After the insertion of copper there is a decrease in the optical band gap value, from 3,1 eV to 2,2 eV, which is in agreement with the reviewed literature. Next, the impact that iron doping has on the IZM-5 electronic properties was evaluated. As previously observed with copper doping, the presence of iron has a similar impact, that is, there is a change in the crystalline phase obtained. When iron is present, it is not possible to obtain IZM-5 diffraction pattern, only the ITQ-76 difraction pattern. In this situation, no diffraction peaks are present that could be associated with a Fe extra phase. Therefore, for the tested Fe contents the insertion of iron seems to be successful. With the presence of iron, it is possible to decrease the optical band gap value from 3,1 eV to 2,0 eV, which is in agreement with the literature reviewed. The third metal tested was nickel. This was the only metal that allowed to maintain IZM-5 crystalline structure integrity. It is observed that, for the highest nickel concentration tested, the diffraction pattern obtained results from the presence of two crystalline phases, IZM-5 and ITQ-76. Regarding the optical band gap values, for the lowest Ni concentration it decreases, something that is in agreement with the literature. However, for the remaining two concentrations their optical band gap value increase. This situation was observed previously and was justified by the presence of Ni clusters on the surface of the material. The last metal tested was cobalt. As with the presence of copper or iron, when cobalt is present it is only possible to obtain ITQ-76 diffraction pattern. With the presence of cobalt it is possible to reduce the optical band gap value from 3,1 eV to 2,0 eV. Thus, only the addition of copper, iron or cobalt as dopings agents allows the reduction of the optical band gap value. However, none of these dopants allows the integrity of IZM-5 to be maintained, having a crystalline phase change to a new laminar structure, entitled ITQ-76.

5.1.2   ITQ-75 Electronic Structure Tunning

A similar doping strategy for ITQ-75's structure was followed. Again, the insertion of two classes of doping agents, selenium, the chalcogenide next to sulfur in the periodic table, and metals, namely copper, iron, nickel and cobalt, were studied.

Since it is possible to obtain the structure of ITQ-75 with different SDAs, the addition of doping agents was studied in structures obtained with two SDAs - Compounds B and C. In this way, the impact of dopants insertion in structures where the delocalization of electrons along the organic component occurs (as is

the case of ITQ-75 obtained with Compound C as SDA) and does not occur (as in the case of ITQ-75 obtained with Compound B) is evaluated.

5.1.2.1 Dopping with Selenium

For ITQ-75 structure two different molar concentrations of Se in the synthesis gel were studied: 0,1% (Se/S molar ratio equal to 0,03) and 0,2% (Se/S molar ratio equal to 0,09) Se content. The diffractograms of the different samples obtained are shown in Figure 5.11.

(a)   **(b)**
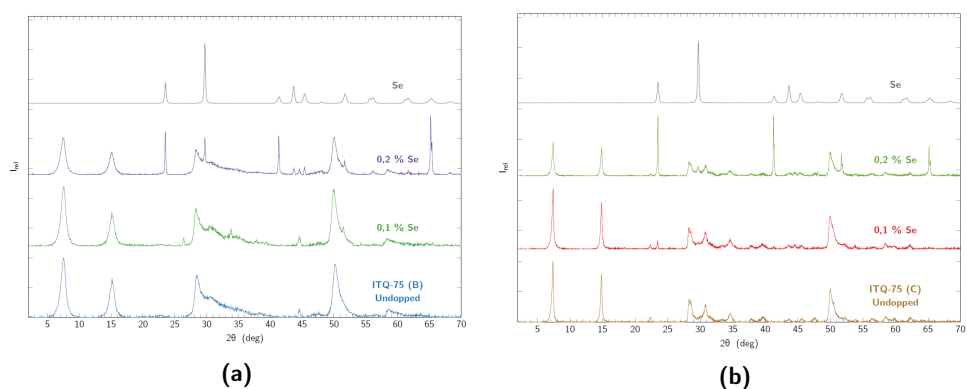
Figure 5.11: PXRD difractogram of (5.11a) undopped ITQ-75 obtained with Compound B as SDA (in blue), doped with 0,1% (in green) and 0,2% Se (in purple); (5.12b) undopped ITQ-75 obtained with Compound C as SDA (in brown), doped with 0,1% (in red) and 0,2% Se (in green) and Se (in grey)

As can be seen in Figure 5.11, the insertion of Se into this structure is partially successful.

In both situations, ITQ-75 obtained with Compound B as SDA (see Figure 5.11a) and Compound C as SDA (see Figure 5.12b), the insertion of 0,1% Se into the structure seems to be successful, since no peaks are present in the diffractogram that could be associated with a possible Se extra phase. However, when selenium molar concentration is increased in the synthesis gel to 0,2% both diffraction patterns show peaks, at 2θ equal to 23,6°, 29,9°, 42,0° and 65,6°, which can be associated with an extra Se phase. It can be seen that ITQ-75 does not allow a Se insertion as freely as the one observed in IZM-5, where an insertion of up to 0,4% Se was observed without visible changes in the diffraction pattern (see Figure 5.1).

Next, the chemical composition of the Se-doped ITQ-75 samples was determined (see Tables 5.10 and 5.11).

Table 5.10: Chemical composition of the ITQ-75 Se-doped samples ([1] Molar composition (%) on the initial gel. [2]Determined by elemental analysis. [3]Determined by ICP)

SDA	Dopant[1]	Formula	Mass composition (%)						
			N[2]	C[2]	H[2]	S[2]	Sn[3]	Zn[3]	Se[3]
Compound B	Undoped	$Sn_{3,52}Zn_{1,27}S_8 \cdot C_{10,59}H_{12,24}N_{1,68}$	2,33	12,57	1,21	25,36	41,50	8,83	-
	0,1% Se	$Sn_{3,30}Zn_{1,32}S_{7,28}Se_{0,72} \cdot C_{13,61}H_{14,94}N_{2,00}$	2,34	15,99	1,46	22,86	38,41	8,46	5,56
	0,2% Se	$Sn_{3,90}Zn_{1,55}S_8Se_{1,92} \cdot C_{23,43}H_{48,49}N_{3,55}$	3,66	14,81	1,31	21,41	32,02	8,88	16,23
Compound C	Undoped	$Sn_{3,05}Zn_{1,33}S_8 \cdot C_{11,54}H_{9,97}N_{2,24}$	2,81	12,41	0,89	22,95	32,41	7,78	-
	0,1% Se	$Sn_{2,52}Zn_{1,01}S_8Se_{1,19} \cdot C_{11,07}H_{10,15}N_{1,92}$	3,17	15,71	1,20	25,81	35,43	7,90	11,12
	0,2% Se	$Sn_{2,80}Zn_{1,17}S_8Se_{1,32} \cdot C_{10,54}H_{9,55}N_{1,83}$	2,76	13,65	1,03	23,12	35,91	8,25	11,21

Table 5.11: Molar ratios of the different ITQ-75 selenium doped samples on the synthesis gel and on the final structure ([1] Molar composition (%) on the initial gel)

SDA	Dopant[1]	Gel Molar Ratios					Material Molar Ratios				
		Sn/Zn	Sn/S	Zn/S	Se/S	C/N	Sn/Zn	Sn/S	Zn/S	Se/S	C/N
Compound B	**Undoped**	3,2	0,2	0,1	-	6,5	2,6	0,4	0,2	-	6,3
	0,1% Se	3,2	0,2	0,1	0,02	6,5	2,5	0,5	0,1	0,1	8,0
	0,2% Se	3,1	0,2	0,1	0,09	6,5	2,5	0,5	0,2	0,2	6,6
Compound C	**Undoped**	3,0	0,2	0,1	-	5,0	2,6	0,4	0,2	-	5,2
	0,1% Se	3,2	0,2	0,1	0,04	5,0	2,5	0,4	0,2	0,2	5,8
	0,2% Se	3,1	0,2	0,1	0,09	5,0	2,4	0,4	0,2	0,2	5,8

After the chemical composition of the different Se doped samples has been determined, this element is detected in the final structure, confirming the presence of Se in the final material. With increase Se content there is a decrease in the Sn/Zn molar ratio, from 3,2 to 2,5, and an increase in the Sn/S molar ratio, from 0,2 to 0,5. With increasing Se content in the initial gel synthesis an increase in the Se/S molar ratio is observed. Thus, and taking into account that the only element with the same valence as Se is S, these experimental data suggest that Se is replacing S in the final structure.

Next, the interaction of the Se-doped samples with UV-Vis radiation was evaluated (see Figure 5.12) and their optical band gap was determined (see Table 5.12).
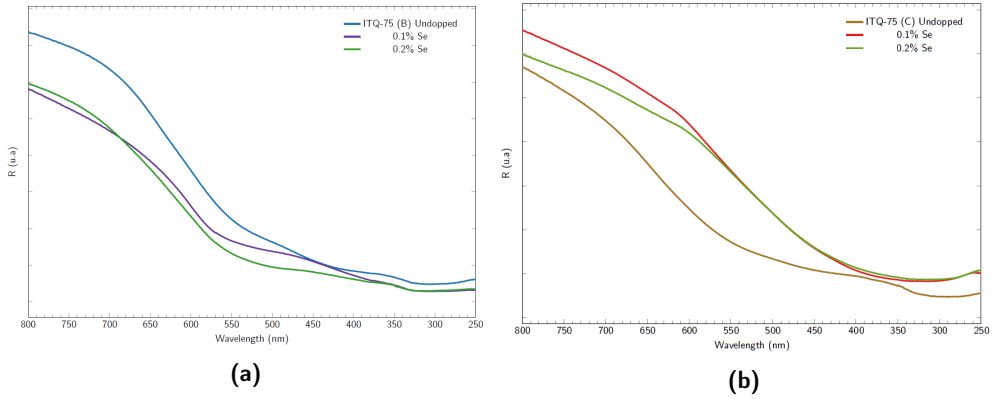
Figure 5.12: (5.12a) UV-Vis spectra of ITQ-75 with Compound B as SDA (in blue) and Se-doped ITQ-75 samples with different Se contents - 0,1% (in purple) and 0,2% (in green); (5.12b) UV-Vis spectra of ITQ-75 with Compound C as SDA (in brown) and Se-doped ITQ-75 samples with different Se contents - 0,1% (in red) and 0,2% (in green)

Table 5.12: Bandgap (E_g) of Se-doped ITQ-75 samples, obtained with (5.12a) Compound B or (5.12b) Compound C as SDA

(a)		(b)	
	E_g (eV)		E_g (eV)
ITQ-75 (B) Undopped	2,7	**ITQ-75 (C) Undopped**	2,2
0,1% Se	2,1	**0,1% Se**	2,8
0,2% Se	2,2	**0,2% Se**	2,7

Observing the behavior of the reflectance profile of the two set of samples, those obtained with Compound B as SDA and those obtained with Compound C as SDA, a different behavior is observed upon insertion of Se into the structure.

When Se is inserted into the structures obtained with Compound B as SDA, there is a red shift on the "reflectance edge" (see Figure 5.12a). For ITQ-75 obtained with Compound B without any doping agent its reflectance edge is at 787 nm. After doping it moves to 799 nm, for 0,1% Se, and 797 nm, for 0,2% Se. This redshift is reflected in the value of the optical band gap, with a reduction in its value (see Table 5.12a). After the addition of Se it is possible to decrease the value of the optical band gap from 2,7 eV to 2,1 eV, in accordance with the literature previous reviewed (see Section 2.4.1) [10, 11].

The opposite is true for the samples obtained with Compound C as SDA. When Se is inserted into the structure, there is a blue shift on the reflectance edge (see Figure 5.12b), from 789 nm to 602 nm, for the sample doped with 0,1% Se, or 580 nm, for the sample doped with 0,2% Se. Consequently, its optical band gap value increases up to 2,8 eV (see Table 5.12b), a situation similar to that previously observed of IZM-5 doped with Se. As mentioned before, there are several hypotheses that justifies such discordance with the literature. The first is associated with the calculation method used to determine the optical band gap value. This was done by using the method presented by Zanata [12], based on fiting a sigmoidal curve to the experimental data. Although it is a method that is meant to solve the disadvantages of using the Tauc plot method [13], it requires the fitting of a sigmoidal curve, which sometimes may not be the most appropriate for the given situation. It is also necessary to know whether the material has a direct or indirect band gap. As this information is not known, since it is a new structure, it is assumed that the structure under study presents a direct band gap. This assumption could be wrong and therefore add a possible error to the value. Another possible hypothesis would be the position that the dopant occupies in the crystal lattice. According to Chen et al. [16], besides the chemical nature of the doping agent, the place where it is inserted in the structure will influence the observed shift in the final band gap value. Since this is a new structure and the location of the inserted dopant in the structure is unknown, this hypothesis cannot be ruled out.

5.1.2.2 Dopping with Metals

As was previously done for IZM-5, small amounts of different metals (copper, iron, nickel and cobalt) were inserted into the synthesis gel and their impact on the electronic properties of the material, namely the optical band gap, was evaluated.

Figure 5.13 shows the ITQ-75 diffractograms obtained with Compound B or C as SDA and with different copper contents.

(a)   **(b)**
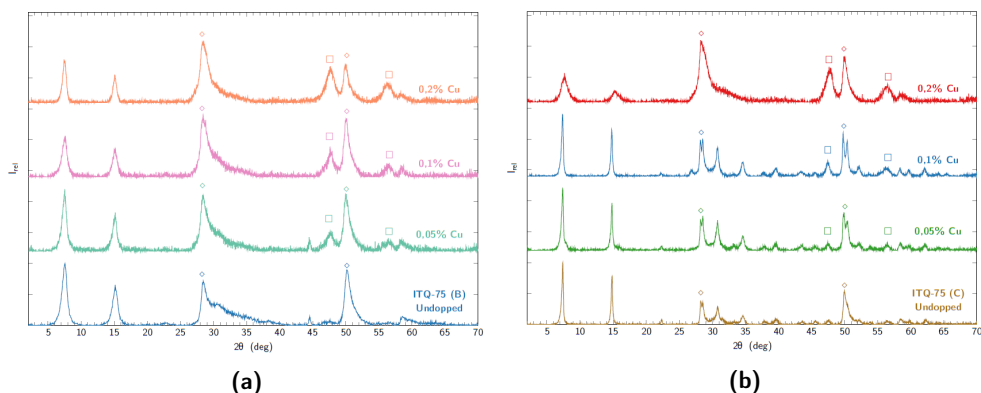
Figure 5.13: PXRD difractogram of (5.13a) undopped ITQ-75 obtained with Compound B as SDA (in blue), doped with 0,05% (in green), 0,1% (in purple) and 0,2% Cu (in orange); (5.14b) undopped ITQ-75 obtained with Compound C as SDA (in brown), doped with 0,05% (in green), 0,1% (in blue) and 0,2% Cu (in red), where $\diamond$ denotes a ZnS phase and $\square$ a Cu_2SnS_3 phase

Looking at Figure 5.13a, it can be seen that the insertion of copper into ITQ-75 obtained with Compound B as SDA is not entirely successful. Although the intensity and position of the first two diffraction peaks remain, it is observed that even for the lowest copper content tested a peak at 2θ equal to 47,8°, which can be associated with an extra Cu_2SnS_3 phase, is present. The intensity of such a peak increases with increasing concentration of copper precursor in the initial gel.

In order to confirm the presence of copper in the final material, as well as the impact that the possible presence of this element has on the others, the chemical composition of the Cu-doped ITQ-75 samples was determined (see Tables 5.13 and 5.14).

Table 5.13: Chemical composition of the ITQ-75 Cu-doped samples ([1] Molar composition (%) on the initial gel. [2]Determined by elemental analysis. [3]Determined by ICP)

SDA	Dopant[1]	Formula	Mass composition (%)						
			N[2]	C[2]	H[2]	S[2]	Sn[3]	Zn[3]	Cu[3]
Compound B	Undoped	$Sn_{3,52}Zn_{1,27}S_8 \cdot C_{10,59}H_{12,24}N_{1,68}$	2,33	12,57	1,21	25,36	41,50	8,83	-
	0,05% Cu	$Sn_{2,62}Zn_{1,27}Cu_{0,65}S_8 \cdot C_{13,77}H_{14,87}N_{1,74}$	2,55	17,34	1,56	26,91	32,62	8,74	4,31
	0,1% Cu	$Sn_{1,72}Zn_{0,70}Cu_{1,70}S_8 \cdot C_{10,14}H_{11,13}N_{1,53}$	2,64	16,18	1,52	25,43	28,12	6,64	7,39
	0,2% Cu	$Sn_{2,47}Zn_{1,02}Cu_{1,17}S_8 \cdot C_{13,58}H_{15,28}N_{1,90}$	2,22	12,61	1,15	26,52	21,16	4,72	11,20
Compound C	Undoped	$Sn_{3,05}Zn_{1,33}S_8 \cdot C_{11,54}H_{9,97}N_{2,24}$	2,81	12,41	0,89	22,95	32,41	7,78	-
	0,05% Cu	$Sn_{3,16}Zn_{1,66}Cu_{0,52}S_8 \cdot C_{10,86}H_{9,86}N_{1,99}$	3,17	14,81	1,12	29,14	42,57	12,36	3,75
	0,1% Cu	$Sn_{3,19}Zn_{1,33}Cu_{1,74}S_8 \cdot C_{13,05}H_{13,35}N_{1,79}$	2,50	15,66	1,34	25,60	37,88	8,70	11,08
	0,2% Cu	$Sn_{2,39}Zn_{1,06}Cu_{2,46}S_8 \cdot C_{10,32}H_{10,32}N_{1,35}$	1,56	10,28	0,86	21,22	23,55	5,76	12,95

Table 5.14: Molar ratios of the different ITQ-75 copper doped samples on the synthesis gel and on the final structure

SDA	Dopant[1]	Gel Molar Ratios					Material Molar Ratios				
		Sn/Zn	Sn/S	Cu/Sn	Cu/Zn	C/N	Sn/Zn	Sn/S	Cu/Sn	Cu/Zn	C/N
Compound B	Undoped	3,2	0,2	-	-	6,5	2,6	0,4	-	-	6,3
	0,05% Cu	3,1	0,2	0,2	0,6	6,5	2,1	0,3	0,3	0,5	7,9
	0,1% Cu	3,3	0,2	0,3	1,1	6,5	2,4	0,3	0,5	1,1	7,2
	0,2% Cu	3,1	0,2	0,7	2,1	6,5	2,5	0,2	1,0	2,4	6,6
Compound C	Undoped	3,0	0,2	-	-	5,0	2,6	0,4	-	-	5,2
	0,05% Cu	2,9	0,2	0,1	0,2	5,0	1,9	0,4	0,2	0,3	5,5
	0,1% Cu	3,1	0,2	0,3	1,0	5,0	2,4	0,4	0,5	1,3	7,3
	0,2% Cu	3,1	0,2	0,6	2,0	5,0	2,3	0,3	1,0	2,3	7,7

Copper is detected in all materials, which confirms the presence of this dopant in the final structure. It is also observed that with the increase of the copper content in the initial gel, its content in the final structure increases. It can also be seen that with increasing copper content, the Sn and Zn contents decrease. For the different molar ratios evaluated, an increase in Sn/S and Sn/Cu and a decrease in Sn/Zn are observed after the synthesis. In addition, Zn/Cu remains similar when Compound B is used as SDA and increases after the synthesis when Compound C is used as SDA. In relation to the C/N molar ratio, this remains similar, which could indicate the maintenance of the SDA structure.

Once the presence of copper in the final material was confirmed, the interaction of the copper-containing materials with UV-Vis radiation (see Figure 5.14) and their optical band gap value (see Table 5.15) were determined.

(a)   (b)
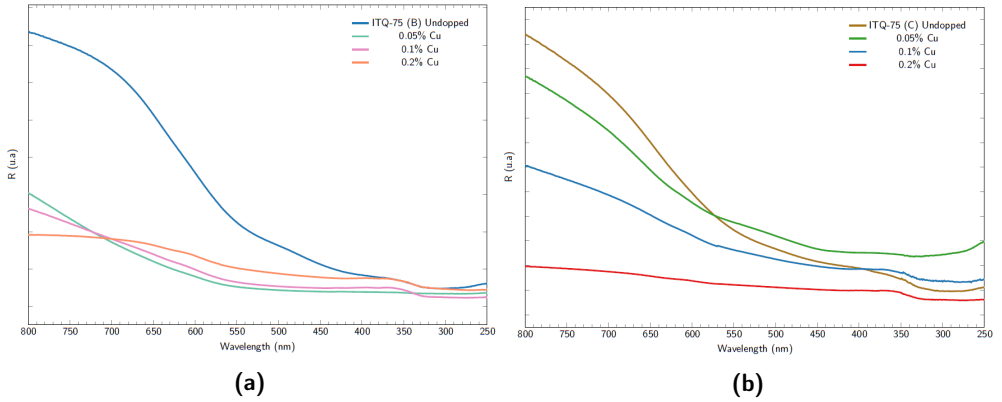
Figure 5.14: (5.14a) UV-Vis spectra of ITQ-75 with Compound B as SDA (in blue) and Cu-dopped ITQ-75 samples with different Cu contents - 0,05% (in green), 0,1% (in purple) and 0,2% (in orange); (5.14b) UV-Vis spectra of ITQ-75 with Compound C as SDA (in brown) and Cu-dopped ITQ-75 samples with different Cu contents - 0,05% (in green), 0,1% (in blue) and 0,2% (in red)

Table 5.15: Band gap (E_g) of Cu-doped ITQ-75 samples, obtained with (5.15a) Compound B or (5.15b) Compound C as SDA

	(a) E_g (eV)		(b) E_g (eV)
ITQ-75 (B) Undopped	2,7	ITQ-75 (C) Undopped	2,2
0,05% Cu	2,3	0,05% Cu	2,0
0,1% Cu	2,1	0,1% Cu	2,0
0,2% Cu	2,2	0,2% Cu	2,0

Starting with the ITQ-75 samples obtained with Compound B (see Figure 5.14a), after the addition of copper, a reduction of the maximum reflectance is observed. For the Cu doped samples it was not possible to determine the reflectance edge, which suggests that it is in the IR region. Observing the optical band gap values of the Cu doped samples (see Table 5.15a), it is reduced up to 2,1 eV. Regarding the ITQ-75 samples obtained with Compound C as SDA, they have a similar behavior to those obtained with Compound B as SDA. The maximum reflectance value decreases, until an almost flat profile is reached when the Cu content is equal to 0,2 % (see Figure 5.14b). This behavior is accompanied with a a decrease in the optical band gap value up to 2,0 eV (see Table 5.15b). The consequences of adding

copper to the samples are in accordance with the previously reviewed literature (see Section 2.4.1).

After evaluating the impact of copper insertion as a doping agent in the ITQ-75 structure, the impact of iron insertion was also evaluated. The diffractograms of ITQ-75 doped with different iron contents are shown in Figure 5.15.

(a)   (b)
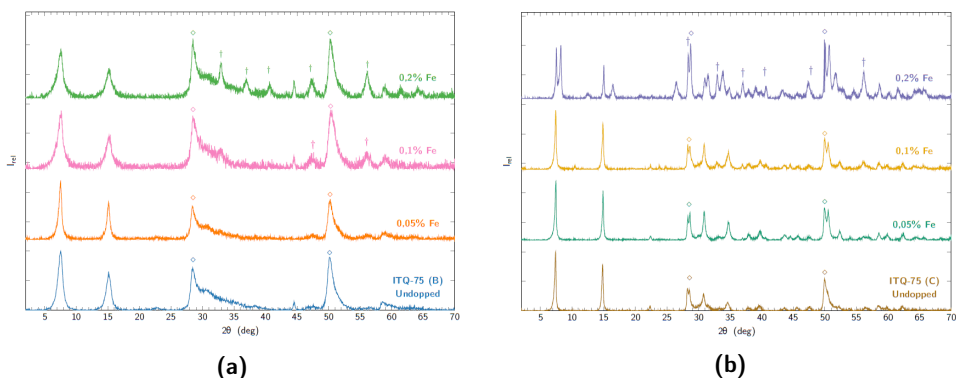
Figure 5.15: PXRD difractograms of (5.15a) undopped ITQ-75 obtained with Compound B as SDA (in blue), doped with 0,05% (in orange), 0,1% (in pink) and 0,2% Fe (in green); (5.17b) undopped ITQ-75 obtained with Compound C as SDA (in brown), doped with 0,05% (in green), 0,1% (in yellow) and 0,2% Fe (in purple). † denotes the FeS_2 diffraction peaks and ◇ a ZnS phase

Looking at Figure 5.15 it can be seen that the iron insertion into ITQ-75 is apparently successful up to a certain content.

In ITQ-75 obtained with Compound B as SDA (see Figure 5.15a) up to a 0,1% iron content extra diffraction peaks were observed. When the iron concentration in the initial gel is increased to 0,2% the diffraction pattern shows extra diffraction peaks that can be associated with a FeS_2 phase. It is interesting to note that the iron goes through a reduction process, since the iron precursor used was $Fe(NO_3)_3$, with an oxidation number of +3, and the extra phase observed, FeS_2, has an oxidation number of +2.

As for the ITQ-75 obtained with Compound C (see Figure 5.17b), it has a similar behavior to ITQ-75 obtained with Compound B. Up to a content an iron content of 0,1%, the presence of extra peaks is not observed. When the iron concentration is increased to 0,2%, there is the appearance of a diffraction peak at 2θ equal to 8,2° that may be associated with a possible laminar phase that is in competition with the known phase. To gain further insight, a kinetic study was performed,

analyzing the consequences of changing the synthesis time from six days to three and nine days. The diffractograms of ITQ-75 obtained with Compound C as SDA, doped with 0,2% iron and with different synthesis times are shown in Figure 5.16.
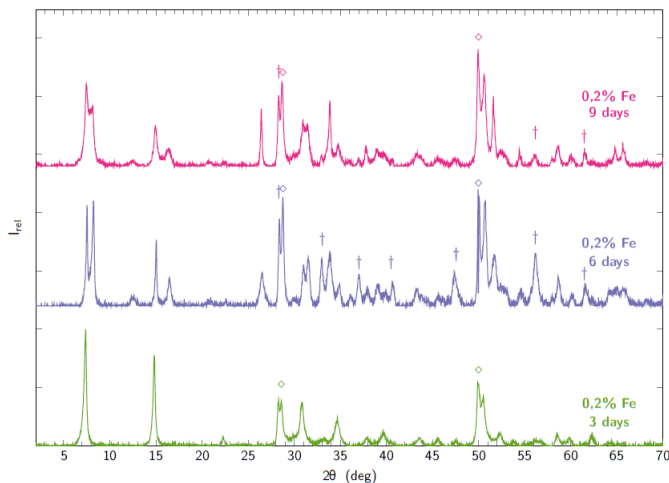
Figure 5.16: PXRD difractograms of ITQ-75 obtained with Compound C as SDA, dopped with 0,2% Fe and with different synthesis times - 3 days (in green), 6 days (in purple) and 9 days (in pink). † denotes the FeS$_2$ diffraction peaks and ◇ a ZnS phase

For three days as synthesis time the unfolding of the first diffraction peak at 2θ equal to 7,5° is not observed. This unfolding only starts to appear after six days of synthesis and is maintained when the synthesis time of the sample is equal to nine days. The extra FeS$_2$ phase is not observed when the synthesis time is equal to three days. Its presence becomes visible only when the synthesis time is increased to six or nine days. Hence, it seems that in order to obtain a structure without the presence of peaks that could be associated with an extra FeS$_2$ phase or an unknown laminar phase, it is necessary to reduce the synthesis time to three days. When the synthesis time is increased to nine days, the peaks that could be associated with an extra FeS$_2$ phase reduce their intensity. This may mean that with increasing synthesis time the structure obtained evolves towards greater thermodynamic stability, i.e., the segregation of the iron from ITQ-75 and its re-insertion into another unknown ITQ-75 like structure.

In order to confirm the presence of iron in the final structure, the chemical composition of the different doped samples was determined (see Tables 5.16 and 5.17).

Table 5.16: Chemical composition of the ITQ-75 Fe-doped samples ([1] Molar composition (%) on the initial gel. [2]Determined by elemental analysis. [3]Determined by ICP)

SDA	Dopant[1]	Formula	Mass composition (%)						
			N[2]	C[2]	H[2]	S[2]	Sn[3]	Zn[3]	Fe[3]
Compound B	Undoped	$Sn_{3,52}Zn_{1,27}S_8 \cdot C_{10,59}H_{12,24}N_{1,68}$	2,33	12,57	1,21	25,36	41,50	8,83	-
	0,05% Fe	$Sn_{2,74}Zn_{1,32}Fe_{0,63}S_8 \cdot C_{12,69}H_{13,04}N_{1,71}$	2,73	17,37	1,49	29,19	37,10	9,86	4,04
	0,1% Fe	$Sn_{2,15}Zn_{1,04}Fe_{1,00}S_8 \cdot C_{20,80}H_{21,52}N_{2,64}$	3,45	23,21	2,01	23,96	23,79	6,37	5,22
	0,2% Fe	$Sn_{1,79}Zn_{0,80}Fe_{1,68}S_8 \cdot C_{22,88}H_{14,63}N_{1,48}$	2,23	29,47	1,57	27,53	22,76	5,63	10,05
Compound C	Undoped	$Sn_{3,05}Zn_{1,33}S_8 \cdot C_{11,54}H_{9,97}N_{2,24}$	2,81	12,41	0,89	22,95	32,41	7,78	-
	0,05% Fe	$Sn_{2,84}Zn_{1,16}Fe_{0,58}S_8 \cdot C_{10,77}H_{9,69}N_{1,99}$	3,28	15,19	1,14	30,10	39,68	8,92	3,83
	0,1% Fe	$Sn_{2,68}Zn_{1,07}Fe_{1,08}S_8 \cdot C_{11,38}H_{10,56}N_{1,94}$	3,17	15,90	1,23	29,88	37,06	8,18	7,05
	0,2% Fe	$Sn_{1,89}Zn_{0,79}Fe_{1,97}S_8 \cdot C_{6,75}H_{15,05}N_{0,92}$	1,21	7,59	1,41	24,03	21,70	4,83	10,32

Table 5.17: Molar ratios of the different ITQ-75 iron doped samples on the synthesis gel and on the final structure

SDA	Dopant[1]	Gel Molar Ratios					Material Molar Ratios				
		Sn/Zn	Sn/S	Fe/Sn	Fe/Zn	C/N	Sn/Zn	Sn/S	Fe/Sn	Fe/Zn	C/N
Compound B	Undoped	3,2	0,2	-	-	6,5	2,6	0,4	-	-	6,3
	0,05% Fe	3,1	0,2	0,2	0,3	6,5	2,1	0,3	0,2	0,5	7,4
	0,1% Fe	3,2	0,2	0,3	0,5	6,5	2,1	0,3	0,5	1,0	7,9
	0,2% Fe	3,4	0,2	0,6	1,1	6,5	2,2	0,2	0,9	2,1	
Compound C	Undoped	3,0	0,2	-	-	5,0	2,6	0,4	-	-	5,2
	0,05% Fe	3,1	0,2	0,2	0,3	5,0	2,5	0,4	0,5	0,5	5,4
	0,1% Fe	3,1	0,2	0,3	0,5	5,0	2,5	0,3	0,4	1,0	5,9
	0,2% Fe	3,2	0,2	0,7	1,0	5,0	2,4	0,2	1,0	2,5	7,3

By looking at Table 5.16 it can be seen that all Fe-doped samples present this element. With the increase of iron content in the initial gel it also increases on the final structure. As it was already observed for the Cu-doped samples, when the iron content increases, the tin and zinc contents decrease. As for the different molar ratios (see Table 5.17), it is observed that the Sn/S, Zn/Fe and Sn/Fe molar ratios are higher in the final material than in the synthesis gel. However, when looking at the Sn/Zn molar ratio, it decreases after synthesis.

After the chemical composition of the iron-doped samples was determined, their UV-Vis spectra (see Figure 5.17) and consequent optical band gap value (see Table 5.18) were determined.
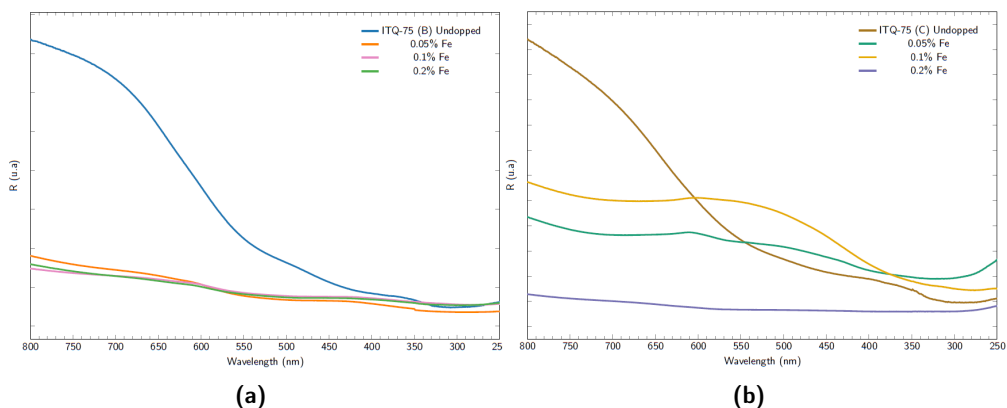
Figure 5.17: (5.17a) UV-Vis spectra of ITQ-75 with Compound B as SDA (in blue) and Fe-dopped ITQ-75 samples with different Fe contents - 0,05% (in yellow), 0,1% (in pink) and 0,2% (in green); (5.17b) UV-Vis spectra of ITQ-75 with Compound C as SDA (in brown) and Fe-dopped ITQ-75 samples with different Fe contents - 0,05% (in green), 0,1% (in yellow) and 0,2% (in purple), where n.a. stqnds for not available

Table 5.18: Band gap (E_g) of Fe-doped ITQ-75 samples, obtained with (5.18a) Compound B or (5.18b) Compound C as SDA (n. a. - not available)

(a)		(b)	
	E_g **(eV)**		E_g **(eV)**
ITQ-75 (B) Undopped	2,7	**ITQ-75 (C) Undopped**	2,2
0,05% Fe	2,1	**0,05% Fe**	n.a
0,1% Fe	2,1	**0,1% Fe**	3,1
0,2% Fe	2,1	**0,2% Fe**	1,9

After doping the ITQ-75 obtained with Compound B with iron it is observed that, regardless of the doping content present, the different reflectance profiles are similar (see Figure 5.17a), which translates into the same optical band gap values (see Table 5.18a). By adding iron to ITQ-75's synthesis gel it is possible to reduce its optical band gap value from 2,7 eV to 2,1 eV.

Looking now at the behavior of the Fe-doped ITQ-75, obtained with Compound C as SDA, samples, these have a somewhat distinct behavior from those discussed earlier (see Figure 5.17b). When the iron content is equal to 0,05% or 0,1%, the reflectance profile shows its edge at a wavelength equal to 605 nm. When

the iron content is increased to 0,2%, the reflectance profile becomes flat. This behavior has been observed previously by Boyle et al. [33]. According to these authors, this behavior is due to the presence of a FeS phase (also confirmed by DRX patterns) that, due to the presence of paramagnetic species, present low fluorescence. Regarding the different optical band gap values after iron doping, unfortunately it was not possible to fit a sigmoidal curve to the sample with 0,05% Fe (see Figure D.43). When the iron content is increased to 0,1%, the optical band gap value increases from 2,2 eV to 3,1 eV. Finally, when the iron content is equal to 0,2% the optical band gap value decreases, from 2,2 eV to 1,9 eV. When comparing to the ITQ-76 samples with Fe (see Figure 5.6b), ITQ-75's samples obtained with Compound B as SDA show a similar behavior. In both situations, the Fe doping allows the reduction of the optical band gap value, something that is according to the literature [19, 20, 21, 22]. However, when ITQ-75 obtained with Compound C as SDA is doped with 0,1% Fe an increase in the optical band gap is observed. As mentioned previously, one cannot eliminate the hypothesis associated with the error committed in the determination of this parameter. It is also interesting to note that, in previously studies done, it was observed that when ZnS nanoparticles are doped with Fe it is possible to observe a small increase in the optical band gap value [34, 35, 36]. According to Kumar et al. [36] this blue shift is due to quantum confinement effects, since Fe^{2+} ions are smaller than Zn^{2+} ions.

After testing copper and iron as doping agents, nickel was evaluated as a doping agent for the ITQ-75 structure. Figure 5.18 shows the diffractograms of different ITQ-75 samples, obtained with Compounds B or C as SDAs, doped with different Ni contents.

(a)   (b)
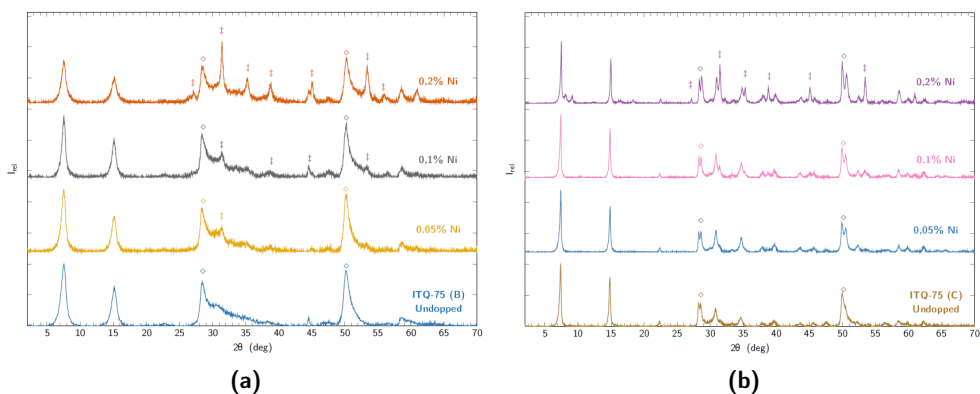
Figure 5.18: PXRD difractograms of (5.18a) undopped ITQ-75 obtained with Compound B as SDA (in blue), doped with 0,05% (in grey), 0,1% (in yellow) and 0,2% Ni (in orange); (5.19b) undopped ITQ-75 obtained with Compound C as SDA (in brown), doped with 0,05% (in blue), 0,1% (in pink) and 0,2% Ni (in purple). ‡ denotes the NiS diffraction peaks and ◇ a ZnS phase

Ni-doping diffractogram results seem to be similar to the Fe-doping ones, as it seems to be successful up to a certain content of the doping agent under study. In the ITQ-75 samples obtained with Compound B as SDA (see Figure 5.18a), only the sample doped with 0,05% Ni shows only one diffraction peak that could be associated with a possible NiS extra phase. As for the samples obtained with Compound C as SDA (see Figure 5.19b), up to 0,1% Ni there are no diffraction peaks that can be associated with a NiS phase.

Afterwards, in order to confirm the presence of nickel, the chemical composition of the samples was determined (see Tables 5.19 and 5.20).

Table 5.19: Chemical composition of the ITQ-75 Ni-doped samples ([1] Molar composition (%) on the initial gel. [2]Determined by elemental analysis. [3]Determined by ICP)

SDA	Dopant[1]	Formula	Mass composition (%)						
			N[2]	C[2]	H[2]	S[2]	Sn[3]	Zn[3]	Ni[3]
Compound B	Undoped	$Sn_{3,52}Zn_{1,27}S_8 \cdot C_{10,59}H_{12,24}N_{1,68}$	2,33	12,57	1,21	25,36	41,50	8,83	-
	0,05% Ni	$Sn_{4,42}Zn_{2,00}Ni_{0,88}S_8 \cdot C_{11,25}H_{12,66}N_{1,60}$	2,18	13,12	1,23	24,87	51,00	12,68	5,00
	0,1% Ni	$Sn_{2,12}Zn_{2,12}Ni_{0,91}S_8 \cdot C_{11,30}H_{23,31}N_{1,36}$	1,81	12,36	2,21	24,32	23,84	6,17	5,10
	0,2% Ni	$Sn_{1,85}Zn_{0,84}Ni_{1,70}S_8 \cdot C_{7,31}H_{30,33}N_{0,88}$	1,05	7,46	2,58	21,82	18,67	4,69	8,46
Compound C	Undoped	$Sn_{3,05}Zn_{1,33}S_8 \cdot C_{11,54}H_{9,97}N_{2,24}$	2,81	12,41	0,89	22,95	32,41	7,78	-
	0,05% Ni	$Sn_{2,77}Zn_{1,22}Ni_{0,67}S_8 \cdot C_{10,10}H_{9,30}N_{1,87}$	3,11	14,35	1,10	30,32	38,98	9,45	4,65
	0,1% Ni	$Sn_{2,30}Zn_{0,83}Ni_{1,08}S_8 \cdot C_{9,77}H_{16,56}N_{1,69}$	2,53	12,53	1,77	27,42	29,13	5,79	6,79
	0,2% Ni	$Sn_{1,70}Zn_{0,50}Ni_{1,67}S_8 \cdot C_{6,80}H_{30,19}N_{1,05}$	1,29	7,14	2,64	22,43	17,64	2,87	8,58

Table 5.20: Molar ratios of the different ITQ-75 nickel doped samples on the synthesis gel and on the final structure

SDA	Dopant[1]	Gel Molar Ratios					Material Molar Ratios				
		Sn/Zn	Sn/S	Ni/Sn	Ni/Zn	C/N	Sn/Zn	Sn/S	Ni/Sn	Ni/Zn	C/N
Compound B	Undoped	3,2	0,2	-	-	6,5	2,6	0,4	-	-	6,3
	0,05% Ni	3,1	0,2	0,2	0,5	6,5	2,1	0,6	0,2	0,4	7,0
	0,1% Ni	3,1	0,2	0,3	1,0	6,5	2,1	0,3	0,4	0,9	8,3
	0,2% Ni	3,2	0,2	0,6	2,0	6,5	2,2	0,2	0,9	2,0	8,3
Compound C	Undoped	3,0	0,2	-	-	5,0	2,6	0,4	-	-	5,2
	0,05% Ni	3,1	0,2	0,2	0,5	5,0	2,3	0,2	0,2	0,5	5,4
	0,1% Ni	3,2	0,2	0,3	1,0	5,0	2,8	0,3	0,5	1,3	5,8
	0,2% Ni	3,2	0,2	0,7	2,1	5,0	3,4	0,2	1,0	3,3	6,5

Evaluating Table 5.19 it can be seen that all Ni-doped samples present this element at their final chemical composition. With the increase of nickel content in the initial gel it also increases on the final structure. As it was already observed for the Cu- and Fe-doped samples, when the nickel content increases, the tin and zinc contents decrease. As for the different molar ratios (see Table 5.20), it is observed that their behavior depends on the SDA used during the synthesis procedure. When Compound B is used as SDA, Sn/S and Sn/Ni molar ratios are higher in the final material than in the synthesis gel. However, when looking at the Sn/Zn molar ratio, it decrease after the synthesis. As for Compound C as SDA, Sn/S, Ni/Zn and Ni/Sn molar ratios increase after the synthesis procedure. As for Sn/Zn molar ratio, it decreases after the synthesis.

Subsequently, the UV-Vis spectra were determined (see Figure 5.19) and the optical band gap value of the different nickel-doped samples were calculated (see Table 5.21).
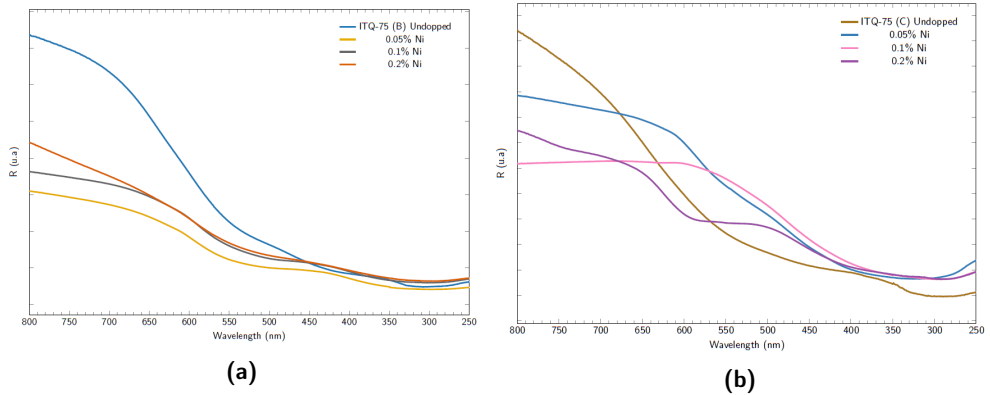
Figure 5.19: (5.19a) UV-Vis spectra of ITQ-75 with Compound B as SDA (in blue) and Ni-doped ITQ-75 samples with different Ni contents - 0,05% (in grey), 0,1% (in yellow) and 0,2% (in orange); (5.19b) UV-Vis spectra of ITQ-75 with Compound C as SDA (in brown) and Ni-doped ITQ-75 samples with different Ni contents - 0,05% (in blue), 0,1% (in pink) and 0,2% (in purple)

Table 5.21: Band gap (E_g) of Ni-doped ITQ-75 samples, obtained with (5.21a) Compound B or (5.21b) Compound C as SDA

<table>
<tr><td align="center">(a)</td><td align="center">(b)</td></tr>
</table>

	E_g (eV)		E_g (eV)
ITQ-75 (B) Undopped	2,7	**ITQ-75 (C) Undopped**	2,2
0,05% Ni	2,1	**0,05% Ni**	2,7
0,1% Ni	2,2	**0,1% Ni**	2,8
0,2% Ni	2,2	**0,2% Ni**	2,0

Observing Figure 5.19, it can be seen that the behavior of the ITQ-75 materials to Ni doping depends on the SDA used. Observing first the ITQ-75 obtained with Compound B as SDA (see Figure 5.19a), it can be seen that after the insertion of Ni its reflectance profile reduces its maximum value, translating into a optical band gap value reduction (see Table 5.21a). This behavior is according to the literature previously reported [23, 24].

As for the behavior of the ITQ-75 samples obtained with Compound C as SDA (see Figure 5.19b), it is somewhat different from those observed previously for the samples studied. For the first two Ni concentrations studied, 0,05% and 0,1%, there is a blue shit on the reflectance edge, from 789 nm to 612 nm (sample

with 0,05% Ni) or 606 nm (sample with 0,1% Ni). This blue shift is followed by an increase in the optical band gap value (see Table 5.21b). When the highest concentration of Ni, 0,2%, is tested, two reflectance edges can be seen. The first one at 740 nm, which means there is a red shift when compared with the undoped sample, and a second transition at 518 nm. ITQ-75 obtained with Compound C and with a nickel content equal to 0,2% presents a reduction of the optical band gap value, from 2,2 eV to 2,0 eV.

The last metal to be tested as a doping agent was cobalt. Figure 5.20 shows the different diffractograms of the different Co-doped ITQ-75 samples.

(a)   (b)
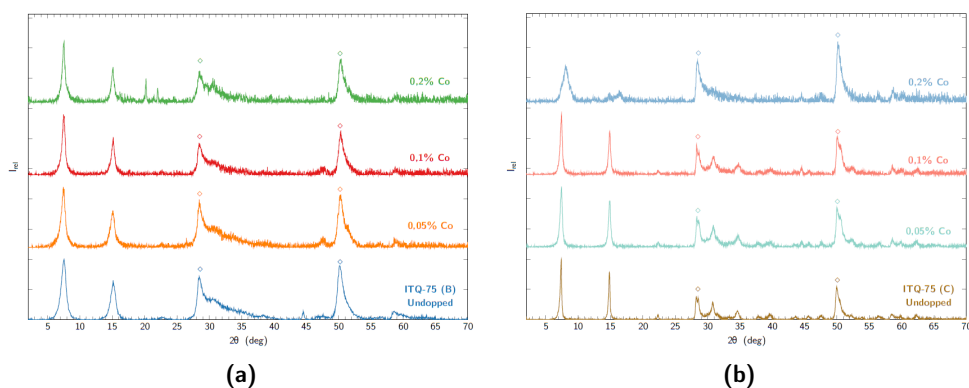
Figure 5.20: PXRD difractograms of (5.20a) undopped ITQ-75 obtained with Compound B as SDA (in blue), doped with 0,05% (in orange), 0,1% (in red) and 0,2% Co (in green); (5.21b) undopped ITQ-75 obtained with Compound C as SDA (in brown), doped with 0,05% (in green), 0,1% (in red) and 0,2% Co (in blue). ⋄ denotes a ZnS phase

The insertion of cobalt into the ITQ-75 structure seems to be partly successful. For the ITQ-75 samples obtained with Compound B as SDA it is observed that up to a cobalt concentration of 0,1% there are no substantial changes in the diffraction pattern. However, when the cobalt concentration increases to 0,2% a diffraction peak appears at 2θ equal to 20,3°. As for ITQ-75 obtained with Compound C as SDA it is observed that up to a cobalt concentration equal to 0,1% there are no significant changes. However, when the cobalt content is equal to 0,2% the intensity of the second diffraction peak at 2θ equal to 15,2° is drastically reduced, affecting the lamellar order and cristallinity of ITQ-75 materials.

Subsequently, in order to confirm the presence of cobalt, the chemical composition of the samples was determined (see Tables 5.22 and 5.23).

Table 5.22: Chemical composition of the ITQ-75 Co-doped samples ([1] Molar composition (%) on the initial gel. [2]Determined by elemental analysis. [3]Determined by ICP)

SDA	Dopant[1]	Formula	Mass composition (%)						
			N[2]	C[2]	H[2]	S[2]	Sn[3]	Zn[3]	Co[3]
Compound B	Undoped	$Sn_{3,52}Zn_{1,27}S_8 \cdot C_{10,59}H_{12,24}N_{1,68}$	2,33	12,57	1,21	25,36	41,50	8,83	-
	0,05% Co	$Sn_{2,82}Zn_{1,48}Co_{0,31}S_8 \cdot C_{13,41}H_{14,85}N_{1,71}$	2,31	15,50	1,43	24,71	32,25	9,33	1,76
	0,1% Co	$Sn_{1,91}Zn_{0,89}Co_{0,77}S_8 \cdot C_{12,83}H_{15,98}N_{1,53}$	2,49	17,92	1,86	29,85	26,32	6,75	5,25
	0,2% Co	$Sn_{2,25}Zn_{0,94}Co_{1,41}S_8 \cdot C_{12,07}H_{21,42}N_{1,53}$	2,03	13,73	2,03	24,31	25,32	5,81	7,89
Compound C	Undoped	$Sn_{3,05}Zn_{1,33}S_8 \cdot C_{11,54}H_{9,97}N_{2,24}$	2,81	12,41	0,89	22,95	32,41	7,78	-
	0,05% Co	$Sn_{3,11}Zn_{1,30}Co_{0,45}S_8 \cdot C_{12,94}H_{14,03}N_{2,08}$	3,09	16,49	1,49	27,25	39,16	9,01	2,80
	0,1% Co	$Sn_{2,03}Zn_{0,55}Co_{1,05}S_8 \cdot C_{10,62}H_{20,28}N_{1,72}$	2,47	13,07	2,08	26,31	24,71	3,72	6,34
	0,2% Co	$Sn_{1,81}Zn_{0,86}Co_{1,36}S_8 \cdot C_{14,35}H_{25,59}N_{2,09}$	2,52	14,80	2,20	22,05	18,45	4,85	6,88

Table 5.23: Molar ratios of the different ITQ-75 cobalt doped samples on the synthesis gel and on the final structure

SDA	Dopant[1]	Gel Molar Ratios					Material Molar Ratios				
		Sn/Zn	Sn/S	Co/Sn	Co/Zn	C/N	Sn/Zn	Sn/S	Co/Sn	Co/Zn	C/N
Compound B	**Undoped**	3,2	0,2	-	-	6,5	2,6	0,4	-	-	6,3
	0,05% Co	3,1	0,2	0,1	0,2	6,5	1,9	0,4	0,1	0,2	7,8
	0,1% Co	3,1	0,2	0,2	0,7	6,5	2,2	0,2	0,4	0,9	8,4
	0,2% Co	3,0	0,2	0,5	1,5	6,5	2,4	0,3	1,6	1,5	7,9
Compound C	**Undoped**	3,0	0,2	-	-	5,0	2,6	0,4	-	-	5,2
	0,05% Co	3,1	0,2	0,1	0,3	5,0	2,4	0,4	0,1	0,3	6,2
	0,1% Co	3,1	0,2	0,3	1,0	5,0	3,7	0,3	0,5	1,9	6,2
	0,2% Co	3,1	0,2	0,5	1,5	5,0	2,1	0,2	0,8	1,6	6,9

After determining the chemical composition of the cobalt-doped samples and confirming the presence of this element in the final structure, the impact that this element has on the interaction with UV-Vis radiation (see Figure 5.21) and on their optical band gap value (see Table 5.24) was evaluated.
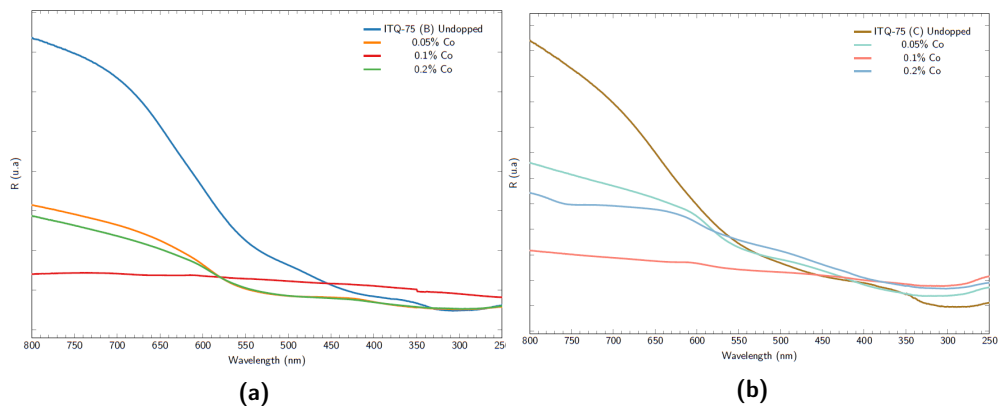
Figure 5.21: (5.21a) UV-Vis spectra of ITQ-75 with Compound B as SDA (in blue) and Co-doped ITQ-75 samples with different Co contents - 0,05% (in orange), 0,1% (in red) and 0,2% (in green); (5.21b) UV-Vis spectra of ITQ-75 with Compound C as SDA (in brown) and Co-doped ITQ-75 samples with different Co contents - 0,05% (in green), 0,1% (in red) and 0,2% (in blue)

Table 5.24: Band gap (E_g) of Co-doped ITQ-75 samples, obtained with (5.24a) Compound B or (5.24b) Compound C as SDA, where n.a stands for not available

(a)	E_g (eV)	(b)	E_g (eV)
ITQ-75 (B) Undopped	2,7	ITQ-75 (C) Undopped	2,2
0,05% Co	2,1	0,05% Co	2,1
0,1% Co	n.a	0,1% Co	n.a
0,2% Co	2,1	0,2% Co	2,1

With the presence of cobalt into the synthesis gel a change in the reflectance profile is observed. Something interesting to note is that for the intermediate cobalt concentration tested, 0,1% Co, the reflectance profile becames flat, something similar to what was observed previously for the ITQ-75 sample obtained with Compound C as SDA and doped with 0,2% iron (see Figure 5.17b). Because of this, it is impossible to determine the value of the optical band gap, since it is not possible to fit a sigmoidal curve to the experimental data (see Figures D.53 and D.56). For the remaining cobalt concentrations tested, regardless of the compound used as SDA, a reduction of the optical band gap value to 2,1 eV is observed (see Table 5.24).

5.1.2.3   Final Considerations

In order to modulate the electronic properties of ITQ-75 a similar methodology as the one followed previously for the structure of IZM-5 was used. To do so, doping agents were added to the synthesis gel, which can be divided in two classes - chalcogenide doping agent, namely selenium, and metal doping agents, namely copper, iron, nickel and cobalt.

The maximum doping content allowed for ITQ-75 crystal structure is 0,1%, except for copper and nickel. When copper is used, diffraction peaks associated with an extra copper-rich phase are always detected. Nickel, on the other hand, has been detected as an extra phase at the lowest concentration tested for ITQ-75 obtained with Compound B as SDA. However, for the intermediate Ni content it was not a detected an extra crystalline phase. Hence, it is suggested that there may have been problems in the solubilization of the nickel precursor during the synthesis procedure. Regarding the electronic propriertes, namely the optical band gap value, the behavior of ITQ-75 obtained with the two Compounds, B or C, as SDA is distinct to the different doping agents employed.

When ITQ-75 obtained with Compound B is doped with any of the doping agents under study, it is possible to reduce the optical band gap value from 2,7 eV to 2,1 eV. The behavior of ITQ-75 obtained with Compound C as SDA is more variable. When it is doped with selenium, an increase in the optical band gap value is observed, from 2,2 eV to 2,8 eV. Doping with copper allows the value of this parameter to decrease from 2,2 eV to 2,0 eV. As for the presence of iron, for the lowest concentration tested the optical band gap increases from 2,2 eV to 3,1 eV. When the highest concentration of iron was tested the optical band gap decreases, from 2,2 eV to 1,9 eV. The behavior towards Ni insertion is similar to that of iron. For the lower concentrations there is an increase in the value of the optical band gap, from 2,2 to 2,7 eV, and for the higher content of this dopant agent it decreases, from 2,2 eV to 2,0 eV. Therefore, in this class of materials only copper and cobalt allow the value of the optical band gap to be reduced, regardless of the compound used as the SDA. For the remaining doping agents tested, i.e. selenium, nickel and iron, the band gap variation apparently depends on the compound used as the SDA.

Several hypotheses can be considered that can explain the behavior of ITQ-75 obtained with Compound C after doping. The first hypothesis is based on the calculation method used to determine the optical band gap value. Besides the error associated with the methodology used, there is the inherent limitation of the method. If the material has a flat reflectance profile, which makes it impossible to fit a sigmoidal curve, it is not possible to determine the optical band gap value,

something that happened in several samples. Another possible justification is the position that the dopants occupy in the structure. As has been shown by other authors [14, 15, 16], this parameter influences the impact it has on the material's band structure and, as a consequence, on the final optical band gap value. Finally, and looking specifically at the ITQ-75 samples obtained with Compound C as SDA and doped with iron or nickel, a possible hypothesis to explain their behavior could be a combination between the Moss–Burstein effect [30, 31, 32] and the presence of multiple crystalline phases. It is possible that the lowest concentrations of iron or nickel tested are already high for the structure in question, which leads to the appearance of defects on the conduction band, causing an increase in the optical band gap value. When testing the highest dopant concentration, diffraction peaks appear that can be associated with an extra-crystalline phase rich in the dopant in question. Thus, the determined optical band gap may be due to the presence of the extra crystalline phase, something already discussed earlier by Boyle et al. [33].

5.1.3 Final Considerations

Optical band gap tunning is not a trivial task. The insertion of different doping agents in the two crystalline structures discussed in the previous chapter, IZM-5 and ITQ-75, was studied. The consequences of the different doping agents were diverse (see Figure 5.22).
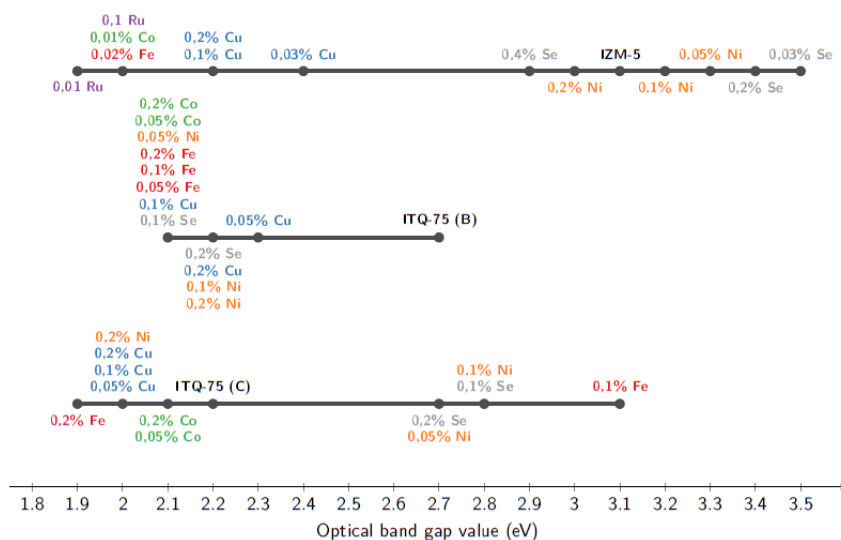
Figure 5.22: Consequences of dopping on the optical band gap value over the different crystalline structures under study

The presence of copper and cobalt allowed, for the different concentrations tested, to observe a red shift in the optical band gap. By using either of these two metals as doping agents, it is possible to obtain materials with an optical band gap equal to 2,0 eV.

Regarding the remaining doping agents studied, the consequences are not so simple to review. Looking first at ITQ-75 obtained with Compound B, it appears that for any of the doping agents there is a decrease in the optical band gap, making it possible to reduce the value of this parameter from 2,7 eV to 2,1 eV. However, this behavior is not translated to the other crystalline structures. For example, with the same iron concentration in the initial gel, an increase in the band gap value is observed for the ITQ-75 obtained with Compound C. This example illustrates that there are factors other than the chemical nature of the dopant that will impact the band structure of the final structure, and, as consequence, its optical band gap. Characteristics such as the dopant concentration, the crystalline structure of the material to be doped and the doping method are some of the examples that are known to influence the band structure modification after doping. Hence, depending on the crystalline structure in question, or the organic agent used as SDA to obtain it, it is possible to obtain different variations on the optical band gap value.

211

Taking into account that the desired application for the materials under study are solar-driven processes, any of the samples doped with copper or cobalt or doped ITQ-75 obtained with Compound B as SDA are promising candidates. As for the ITQ-75 obtained with Compound C, it has an optical band gap value equal to 2,2 eV, which already makes it a very promising material for solar-driven applications. After doping it is possible to decrease this value to 1,9 eV. The insertion of dopants might cause the appearance of defects in the crystal lattice, which might act as charge sinkholes, reducing charge mobility. So it would be interesting to check the gain in charge generation properties due to the presence of the dopant versus the possible change in charge mobility and the impact this will have on the photocatalytic activity of the final material.

5.2 Accessibility Increase

As presented above in Chapter 2, besides the electronic properties being extremely important for a photocatalyst to show superior photocatalytic activity, its textural properties are also important, since a material with a more open architecture allows for the reduction of the average charge carriers mean-path and, as such, reduces the probability of recombination [37]. Chen et al. [38] further observed that for structures with similar band structure, and consequently similar optical band gap value, the one with higher accessibility shows higher photocatalytic activity. Furthermore, theoretically for an open microporus material there is a reduction on the need for charge carriers as each structure atom is accessible within the microporus structure.

The two structures studied, IZM-5 and ITQ-75, exhibit low accessibility with reduced specific surface area. Looking more closely at their isotherms (see Figure 5.23) and textural properties (see Table 5.25) it can be verified that the as-synthesized materials under study present a minimal available microporous area and that the low available accessible surface is due to the external area.
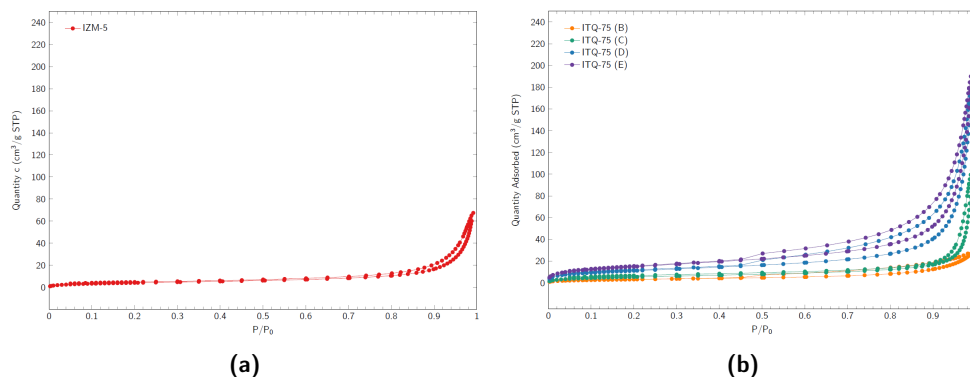
Figure 5.23: (5.23a) IZM-5 and (5.23b) ITQ-75 N_2 adsorption-desorption isotherms

Table 5.25: IZM-5 and ITQ-75 textural properties (n.a. - not available. [1]Determined by FESEM (see Appendix F)

	Pore Volume (cm³/g)	BET surface area (m²/g)	t-plot Micropore Area (m²/g)	t-plot External Surface Area (m²/g)	Crystal Size (μm)[1]
IZM-5	0,092	15,1	n.a	15,4	
ITQ-75 (B)	n.a	11,9	0,5	11,4	1,4 ±0,5
ITQ-75 (C)	0,140	20,2	2,9	17,3	1,8 ±0,6
ITQ-75 (D)	0,255	40,5	3,3	37,2	1,6 ±0,6
ITQ-75 (E)	0,277	54,6	4,6	49,9	1,4 ±0,5

Thus, in order to increase the accessibility of the materials, two different strategies were tested, namely modifications to the synthesis process, with the addition of coSDAs or the modification of the viscosity of the gel, and post-synthesis modifications, by trying to eliminate the organic component (by thermal treatment, ionic exchange, acid washing or photodegradation) or by using methods that do not eliminate this component (by butyl-lithium treatment or ball mill).

5.2.1 Modifications to the Synthesis Procedure

In order to increase the accessibility of the materials under study, the composition of the synthesis gel was modified in two different ways.

The first one is based on the addition of coSDAs, namely fructose and sucrose. These saccharides were previously used as mesopore-directing agent in obtaining hierarchical SAPOs and AlPOs [39, 40]. Furthermore, these compounds are low

cost, abundant and sustainable, and thus in line with the achievement of a more sustainable synthesis route followed during the global development of this work.

The second alteration to the synthesis methodology employed to increase accessibility was to modify the gel viscosity. By increasing its viscosity, the mobility of the crystallization nuclei is reduced and, as such, their probability of aggregation decreases, resulting in smaller crystals. Thus, increasing the viscosity of the gel reduces the particle size, with a consequent increase in the external surface area.

5.2.1.1   Addition of coSDAs - Fructose and Sucrose

The usage of fructose and sucrose as mesopore-directing agent was evaluated in the two families of materials under study, IZM-5 and ITQ-75. For each of these structures, four possible Saccharies/SDA molar ratios were tested - 0.3, 1, 3 and ∞.

i. IZM-5

Figure 5.24 shows the diffractograms IZM-5 samples with different fructose or sucrose contents.

(a)   **(b)**
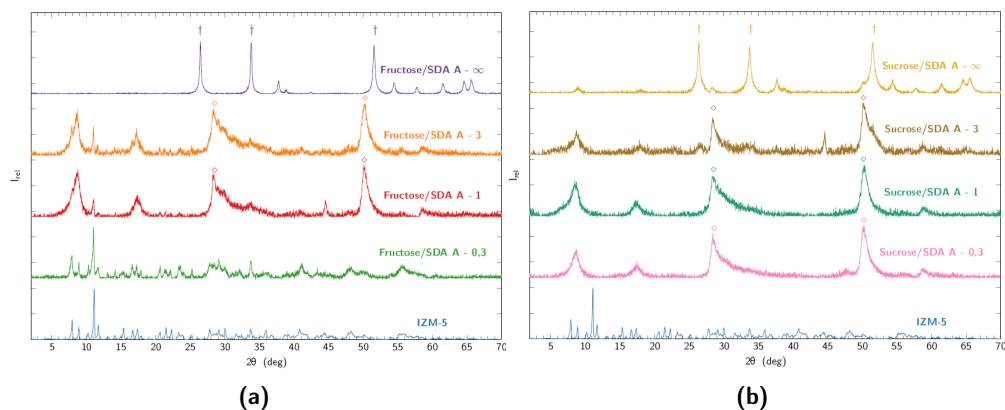
Figure 5.24: PXRD patterns of IZM-5 (in blue), with different (5.24a) fructose contents - Fructose/SDA A - 0,3 (in green), Fructose/SDA A - 1 (in red), Fructose/SDA A - 3 (in orange) and Fructose/SDA A - ∞ (in purple) - and with different (5.24b) sucrose contents - Sucrose/SDA A - 0,3 (in pink), Sucrose/SDA A - 1 (in green); Sucrose/SDA A - 3 (in brown) and Sucrose/SDA A - ∞ (in yellow). † denotes the SnO_2 diffraction peaks and ⋄ a ZnS phase

Starting by evaluating the impact of the fructose presence in the synthesis gel (see Figure 5.24a), it is observed that there is a coexistence of two phases depending on the fructose concentration in the synthesis gel. When the Fructose/SDA A molar ratio is equal to 0,3 no changes to the IZM-5's diffraction pattern are observed. When the molar ratio increases, there is a change in the observed diffraction pattern. The presence of the two main diffraction ITQ-76's peaks at 2θ equal to 8,8° and 17,3° and an extra diffraction peak at 2θ equal to 11,1°, at a diffraction angle equal to the most intense diffraction peak of IZM-5. Hence there seems to be a cohesion between the two crystalline phases, IZM-5 ans ITQ-76 lamellar phase. When only fructose is present in the synthesis gel, only the SnO_2 diffraction pattern is obtained.

When using sucrose as saccharide (see Figure 5.24b) and in the presence of Compound A as SDA, regardless of the concentration used, the diffraction pattern of IZM-5 was no longer obtained, but that of ITQ-76's instead. With increasing Sucrose/SDA A molar ratio the intensity of the two main diffraction peaks decreases. When the Sucrose/SDA A ratio is equal to 3 the intensity of the second diffraction peak is so low that this peak is almost non-existent. When only sucrose is present, only the SnO_2 diffraction pattern is obtained, a situation similar to that already observed when fructose is used. Hence, the presence of saccharide as coSDAs favours the formation of lamellar phase similar to ITQ-76 type materials.

Subsequently, the textural properties of the samples under studied were determined by nitrogen adsorption-desorption (see Figure 5.25 and Table 5.26).

(a)   **(b)**
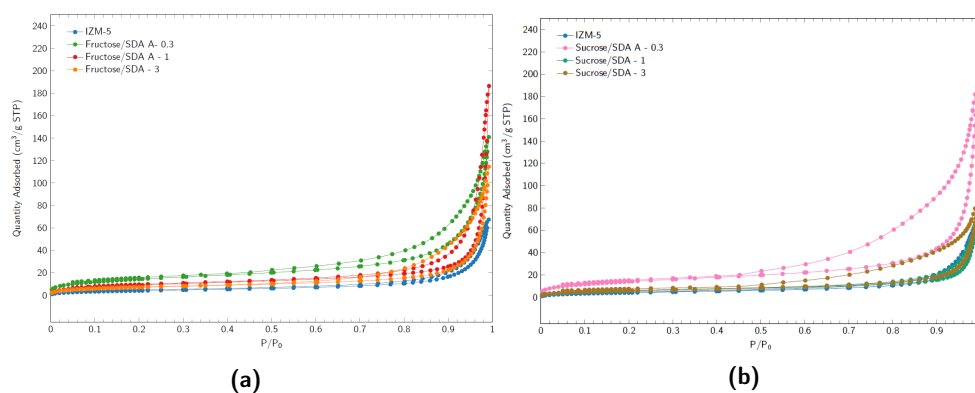
Figure 5.25: N_2 adsorption-desorption isotherms of structures obtained with Compound A as SDA and the different saccharides under study - IZM-5 (in blue), (5.25a) with different fructose contents, Fructose/SDA A equal to 0,3 (in green), 1 (in red) or 3 (in orange); (5.25b) with different sucrose contents, Sucrose/SDA A equal to 0,3 (in pink), 1 (in green) or 3 (in brown)

Table 5.26: IZM-5's and ITQ-76's with saccharides textural properties (n.a. - not available)

	Pore Volume (cm³/g)	BET surface area (m²/g)	t-plot Micropore Area (m²/g)	t-plot External Surface Area (m²/g)
IZM-5	0,092	15,1	n.a	15,4
Fructose/SDA A - 0,3	n.a	7,6	0,9	6,8
Fructose/SDA A - 1	0,248	33,4	8,0	25,5
Fructose/SDA A - 3	0,149	26,0	6,4	19,6
Sucrose/SDA A - 0,3	0,259	51,3	12,2	39,1
Sucrose/SDA A - 1	n.a	21,3	5,9	15,4
Sucrose/SDA A - 3	n.a	21,6	4,5	17,1

After saccharide insertion a general increase in the total volume of adsorbed gas is observed. The largest increase, with an almost tripling of the total adsorbed volume, is seen when the molar ratio Fructose/SDA A is equal to 1 or Sucrose/ SDA is equal to 0,3. Regarding the type of isotherm, and according to the IUPAC classification [41], IZM-5 and saccharide-derived materials have a type III isotherm. This type of isotherm is associated with nonporous or macroporous structures that have a weak adsorbent-adsorbate interaction. As for the hysteresis of the isotherms under study, IZM-5 presents a practically non-existent hysteresis. The same cannot be said of the materials obtained with saccharides. These present a hysteresis of the H3 type [41]. This type of hysteresis is associated with non-rigid laminar structures. It is found that the accessibility of the samples is due to their external surface area, according to the shape of the isotherm and the t-plot method. Comparing the impact that the two types of saccharides had on the textural properties, it can be seen that when the Sucrose/SDA A ratio is equal to 0,3 the greatest increase in external surface area is obtained, from 15,1 m²/g to 51,3 m²/g. However, such a comparison should be made with caution, as two structures with different diffraction patterns are being comparing .

Since the thermal degradation temperature of the different isolated organic compounds is quite different, the thermogravimetry of the saccharides-rich samples was determined in order to check whether there was any change in the thermal degradation profile. Figure 5.26 shows the thermogravimetry profiles of the different samples under study and in Tables 5.27 and 5.28 the chemical composition of such samples.
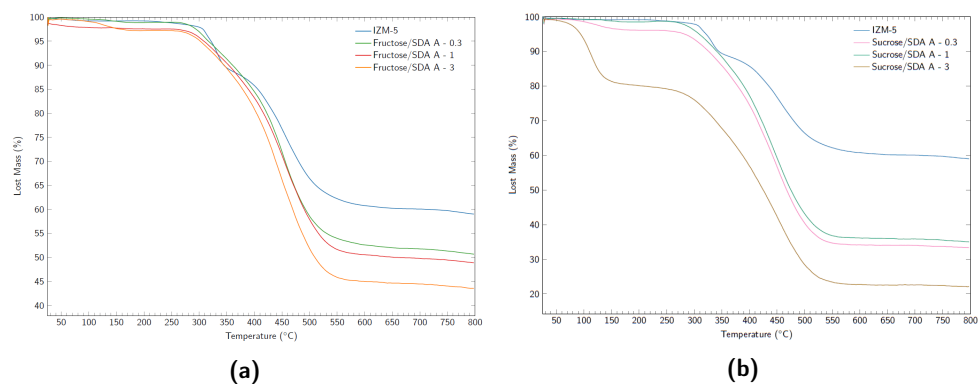
Figure 5.26: Thermogravimetry profiles of structures obtained with Compound A as SDA and the different saccharides under study - IZM-5 (in blue), (5.26a) with different fructose contents, Fructose/SDA A equal to 0,3 (in green), 1 (in red) or 3 (in orange); (5.26b) with different sucrose contents, Sucrose/SDA A equal to 0,3 (in pink), 1 (in green) and 3 (in brown)

Table 5.27: Chemical composition of the synthesized structures obtained with Compound A as SDA and the different saccharides under study ([1]Determined by elemental analysis. [2]Determined by ICP. [3]Determined by TG.)

SDA	Modification	Formula	Mass composition (%)					
			N[1]	C[1]	H[1]	S[1]	Sn[2]	Zn[2]
Compound A	IZM-5	$Sn_{3,13}Zn_{1,26}S_8 \cdot C_{15,01}H_{31,49}N_{2,24}$	3,09	17,80	3,11	25,34	36,68	8,12
	Fructose/SDA A - 0,3	$Sn_{2,89}Zn_{1,46}S_8 \cdot C_{23,98}H_{39,46}N_{2,61}$	3,47	27,33	3,75	24,35	32,59	9,07
	Fructose/SDA A - 1	$Sn_{1,84}Zn_{0,99}S_8 \cdot C_{28,14}H_{37,82}N_{2,46}$	3,21	31,41	3,52	23,86	20,29	6,00
	Fructose/SDA A - 3	$Sn_{2,13}Zn_{1,03}S_8 \cdot C_{33,01}H_{41,03}N_{2,47}$	2,96	33,99	3,52	22,01	21,69	5,79
	Sucrose/SDA A - 0,3	$Sn_{1,61}Zn_{0,68}S_8 \cdot C_{37,02}H_{34,51}N_{1,47}$	1,80	38,84	3,02	22,43	16,68	3,89
	Sucrose/SDA A - 1	$Sn_{2,12}Zn_{0,90}S_8 \cdot C_{35,99}H_{38,59}N_{1,76}$	2,21	38,72	3,46	23,00	22,58	5,27
	Sucrose/SDA A - 3	$Sn_{1,48}Zn_{0,70}S_8 \cdot C_{72,39}H_{75,21}N_{0,97}$	0,76	48,63	4,21	14,36	9,80	2,56

Table 5.28: Molar ratios of the synthesized structures obtained with Compound A as SDA and the different saccharides under study ([1]Determined by elemental analysis. [2]Determined by TG)

SDA	Modification	Gel Molar Ratios			Material Molar Ratios			Material Organic Content (%)	
		Sn/Zn	Sn/S	C/N	Sn/Zn	Sn/S	C/N	CNHS[1]	TG[2]
Compound A	IZM-5	3,2	0,2	6,5	2,6	0,4	6,3	49,3	41,0
	Fructose/SDA A - 0,3	3,1	0,2	7,5	2,0	0,4	9,2	58,9	49,3
	Fructose/SDA A - 1	3,0	0,2	9,4	1,9	0,2	11,4	62,0	50,1
	Fructose/SDA A - 3	3,1	0,2	15,3	2,1	0,3	13,4	62,5	56,5
	Sucrose/SDA A - 0,3	3,3	0,2	8,5	2,4	0,2	25,1	66,1	66,7
	Sucrose/SDA A - 1	2,8	0,2	12,1	2,4	0,3	20,4	67,4	65,0
	Sucrose/SDA A - 3	3,2	0,2	24,3	2,1	0,2	74,7	68,0	77,8

Observing the different thermogravimetry profiles (see Figure 5.26), it can be seen that with the insertion of fructose or sucrose there some are changes in the degradation profile. IZM-5 has three temperatures at which there is the most mass variation, 312°C, 333°C, and 455°C (see Figure E.1 for more information regarding IZM-5's DTG). When fructose is inserted, with a Fructose/SDA A molar ratio equal to 0,3, only the mass variations at 310°C and 450 °C are observed. For the remaining Fructose/SDA A molar ratios evaluated, only two peaks at 333°C and 455°C are verified. As for the samples with Sucrose, they only show the peak of mass change at 455°C.

Concerning the organic content determined by thermogravimetry, it is in agreement with the one determined by elemental analysis (see Table 5.28). It is also verified that with the increase saccharedeo content on the synthesis gel, the final carbon content also increases.

ii. ITQ-75

After the study of fructose or sucrose insertion in IZM-5, a similar approach was done in ITQ-75 structure. Such study was done using ITQ-75 obtained with two SDAs, Compounds B and C. ITQ-75 diffractograms obtained with the different saccharides contents and the two SDAs under study are shown in Figures 5.27 and 5.28.
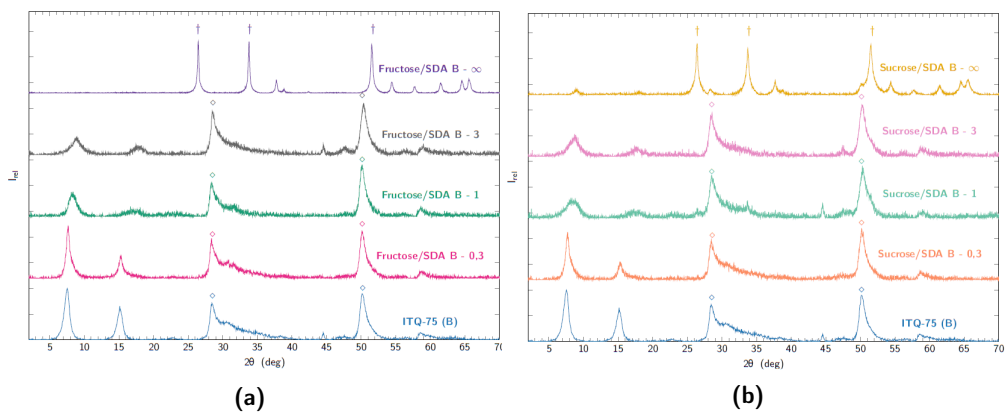
Figure 5.27: PXRD patterns of ITQ-75 obtained with Compound B as SDA (in blue), with different (5.27a) fructose contents - Fructose/SDA B - 0,3 (in pink), Fructose/SDA B - 1 (in green), Fructose/SDA B - 3 (in grey) and Fructose/SDA B - ∞ (in purple) - and with different (5.27b) sucrose contents - Sucrose/SDA B - 0,3 (in orange), Sucrose/SDA B - 1 (in green); Sucrose/SDA B - 3 (in pink) and Sucrose/SDA B - ∞ (in yellow). † denotes the SnO_2 diffraction peaks and ⋄ a ZnS phase
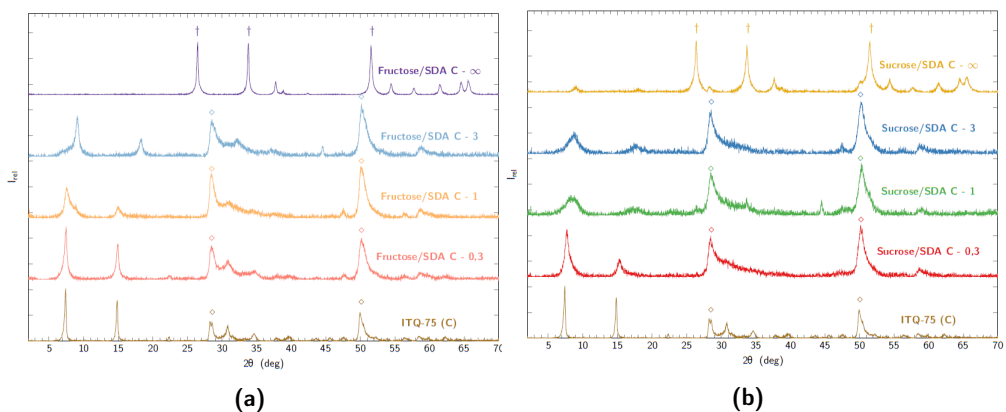
Figure 5.28: PXRD patterns of ITQ-75 obtained with Compound C as SDA (in brown), with different (5.28a) fructose contents - Fructose/SDA C - 0,3 (in pink), Fructose/SDA C - 1 (in orange), Fructose/SDA C - 3 (in blue) and Fructose/SDA C - ∞ (in purple) - and with different (5.28b) sucrose contents - Sucrose/SDA C - 0,3 (in red), Sucrose/SDA C - 1 (in green); Sucrose/SDA C - 3 (in blue) and Sucrose/SDA C - ∞ (in yellow). † denotes the SnO_2 diffraction peaks and ⋄ a ZnS phase

It can be seen that with the insertion of any of the saccharides under study there is no change in the crystalline phase obtained, something that was observed previously for IZM-5.

Starting with ITQ-75 obtained with Compound B as SDA (see Figure 5.27), it is observed that with increasing fructose or sucrose content up to a molar ratio of Saccharide/SDA B equal to 3, the intensity of the first two diffraction peaks, corresponding to lamellar order, decreases. As for the position of the peaks, a shift towards larger angles is observed with increasing saccharide content. This matter could be associated to lower separation between consecutive layers, generating closed and more compacted solids. As for the full width at half maximum (FWHM), this variation is not so linear. When the Saccharide/SDA B ratio is equal to 0,3, the FWHM value decreases in relation to the sample without saccharide. When the Saccharide/SDA B ratio value is increased to 1 or 3, the first two diffraction peaks become wider with respect to the initial sample. Given Scherrer's law [42], when the peaks are broader, i.e., when the peak FWHM increases, the crystal size decreases.

For the ITQ-75 samples obtained with Compound C as SDA (see Figure 5.28) similar observations can be made. With increasing saccharide content there is a decrease in the intensity of the first diffraction peaks, the displacement of these two peaks towards greater angles and their broadening.

In order to verify possible changes to the laminar planes observed by PXRD, HRTEM was performed on the saccharedeo-rich samples. It was chosen two samples, ITQ-75 with a Fructose/SDA B molar ratio equal to 3 (see Figure 5.29) and ITQ-75 with a Fructose/SDA C molar ratio equal to 1 (see Figure 5.30).

(a)   (b)
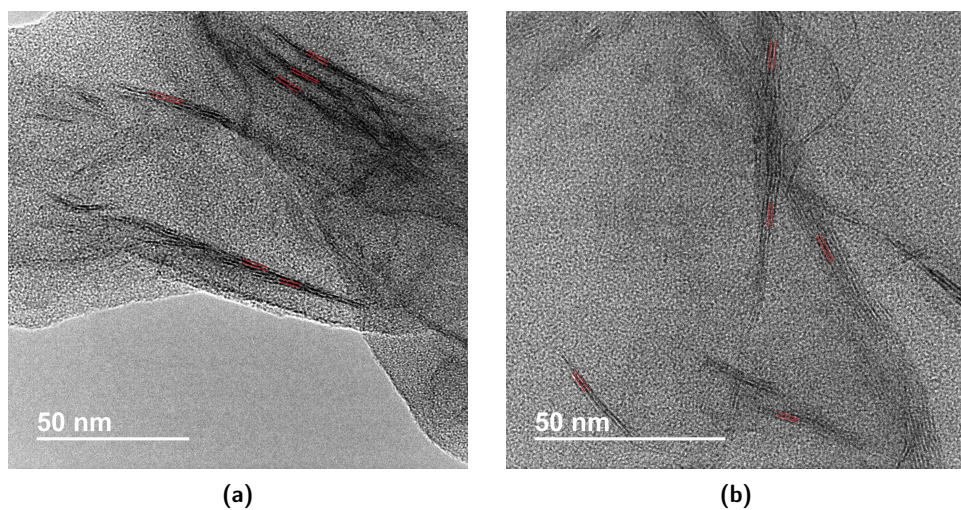
Figure 5.29: ITQ-75, obtained with Compound B as SDA and with a Fructose/SDA B molar ratio equal to 3, HRTEM images, where (5.29a) and (5.29b) highlights the laminar planes, marked in red
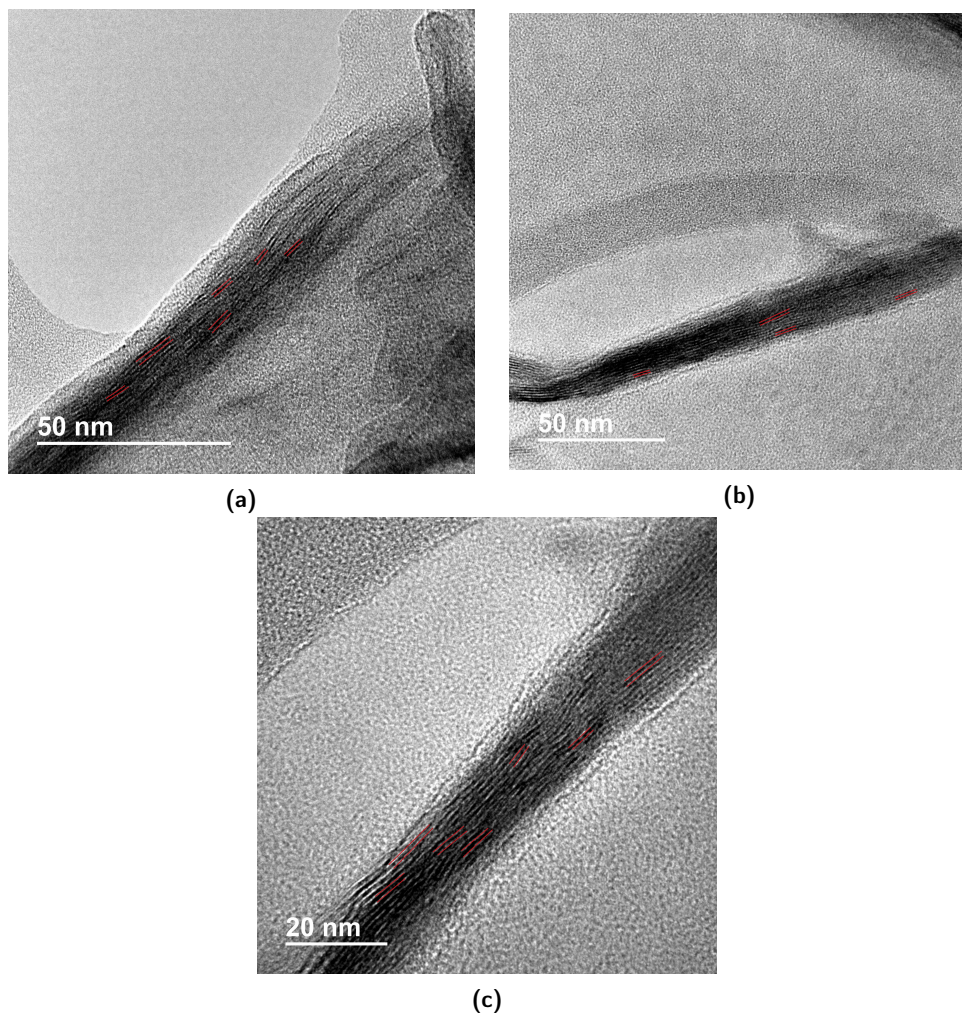
Figure 5.30: ITQ-75, obtained with Compound C as SDA and with a Fructose/SDA B molar ratio equal to 1, HRTEM images, where (5.30a), (5.30b) and (5.30c) highlights the laminar planes, marked in red

As it is possible to observe from Figures 5.29 and 5.30, after the addition of fructose, the ITQ-75 laminar profile is maintained. As for the distance between consecutive individual sheets, there is a decrease in it when compared to the un-modified structure. After the addition of fructose the distance between consecutive layers decreases from 1,1 $\pm$0,2 nm to 0,8 $\pm$0,1 nm, for a Fructose/SDA B molar

ratio equal to 3, or 0,7 ±0,1 nm, for a Fructose/SDA C molar ratio equal to 1. Thereby, with the presence of fructose a more compact structure is obtained, as was suggested earlier by PXRD.

According to the PXRD results previously analyzed, in addition to the impact that the insertion of the saccharides had on the distance between consecutive laminae, it was also hypothesized that it affected the crystal size. In order to confirm such hypothesis, FESEM was performed (see Figure 5.31).
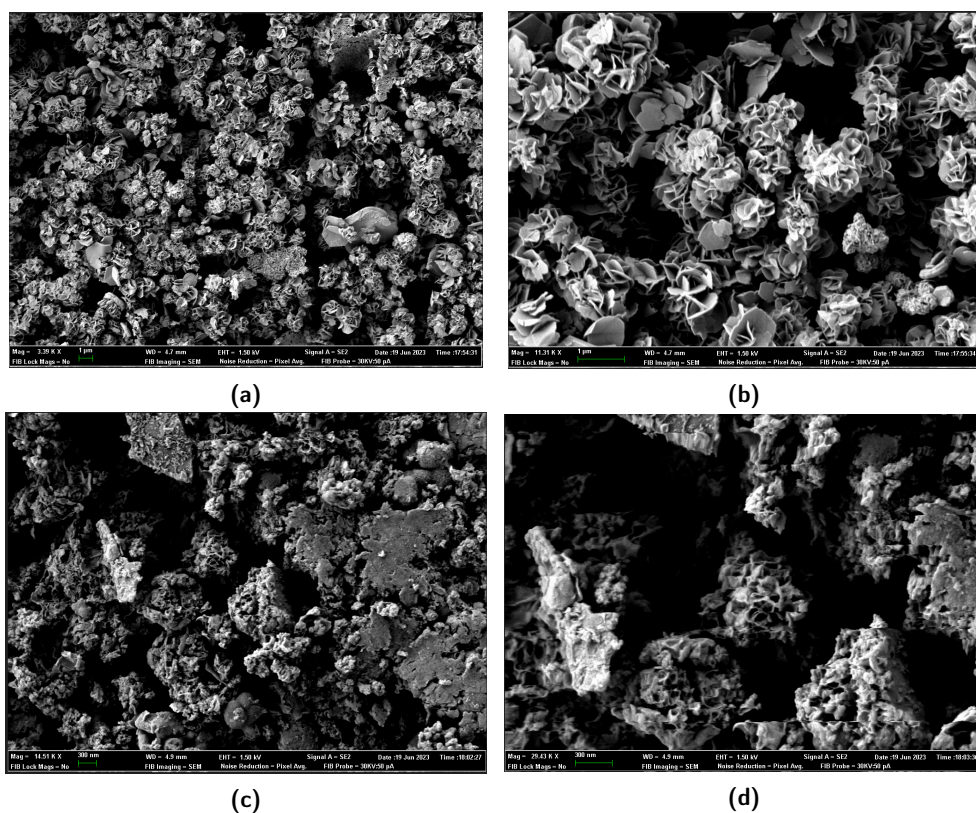
Figure 5.31: FESEM images of ITQ-75 (5.31a and 5.31b) obtained with Compound B or (5.31c and 5.31d) Compound C as SDAs, with a Fructose/SDA molar ratio equal to 1

After the insertion of fructose into the samples, no changes in the crystal morphology are observed, and the presence of flower-like arrangements with the different laminae is present. ITQ-75 obtained with Compound B as SDA and with a Fructose/SDA B molar ratio equal to 1 has a crystal size equal to 1,1 ±0,3 μm. Since

ITQ-75 obtained with Compound B as a crystal size equal to 1,4 ±0,5 μm, there is a crystal size reduction, confirming the results prior obtained with PXRD. Regarding ITQ-75 obtained with Compound C as SDA and with a Fructose/ SDA C molar ratio equal to 1, there is also a crystal size reduction, from 1,8 ±0,6 μm to 1,4 ±0,4 μm.

Subsequently, the N_2 absorption isotherms and textural properties of the saccharedeo-rich ITQ-75 samples obtained with Compound B as SDA (see Figure 5.32 and Table 5.29) or with Compound C as SDA (see Figure 5.33 and Table 5.30) were determined.

(a) (b)
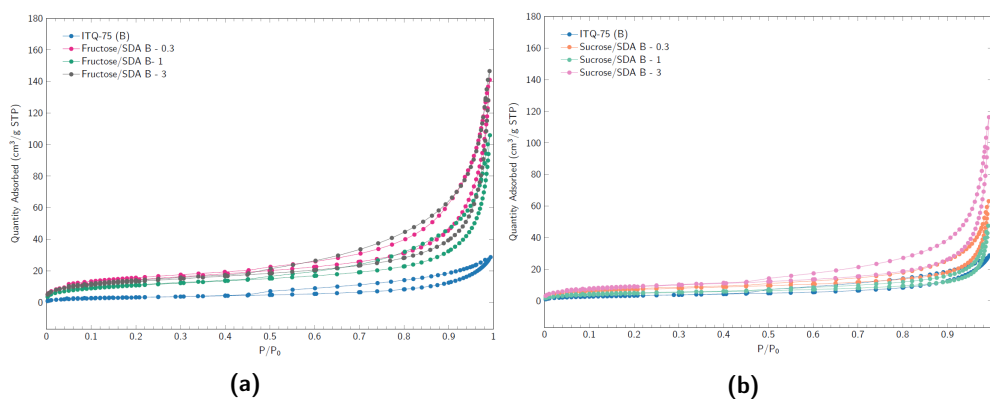
Figure 5.32: N_2 adsorption-desorption isotherms of structures obtained with Compound B as SDA and the different saccharides under study - ITQ-75 (in blue), (5.32a) with different fructose contents, Fructose/SDA B equal to 0,3 (in pink), 1 (in green) or 3 (in grey) and (5.32b) with different sucrose contents, Sucrose/SDA B equal to 0,3 (in orange), 1 (in green) and 3 (in pink)

Table 5.29: ITQ-75's (obtained with Compound B as SDA) with saccharides textural properties (n.a. - not available)

	Pore Volume (cm³/g)	BET surface area (m²/g)	t-plot Micropore Area (m²/g)	t-plot External Surface Area (m²/g)
ITQ-75 (B)	n.a.	11,9	0,5	11,4
Fructose/SDA B - 0,3	0,198	52,6	13,0	39,6
Fructose/SDA B - 1	n.a.	39,5	10,5	29,0
Fructose/SDA B - 3	0,200	47,9	12,9	35,0
Sucrose/SDA B - 0,3	0,081	25,5	9,3	16,2
Sucrose/SDA B - 1	n.a.	16,9	5,3	11,6
Sucrose/SDA B - 3	n.a.	32,0	9,1	22,9

(a)   (b)
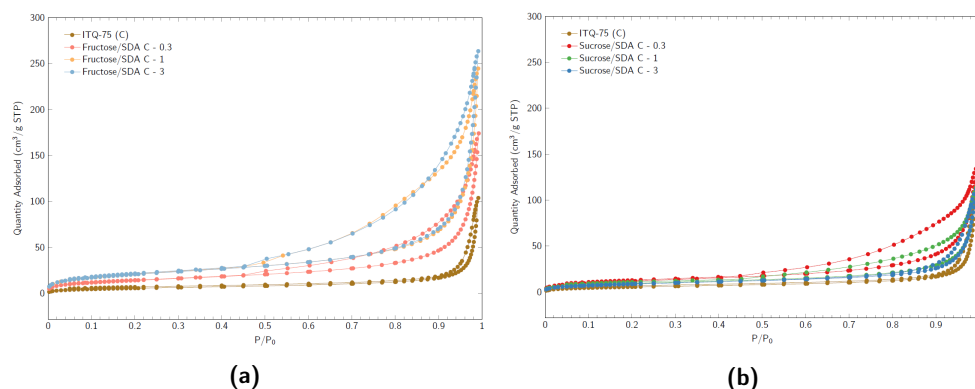
Figure 5.33: N_2 adsorption-desorption isotherms of structures obtained with Compound C as SDA and the different saccharides under study - ITQ-75 (in brown), (5.33a) with different fructose contents, Fructose/SDA C equal to 0,3 (in pink), 1 (in yellow) or 3 (in grey) and (5.33b) with different sucrose contents, Sucrose/SDA C equal to 0,3 (in red), 1 (in green) and 3 (in blue)

Table 5.30: ITQ-75's (obtained with Compound C as SDA) with saccharides textural properties (n.a. - not available)

	Pore Volume (cm³/g)	BET surface area (m²/g)	t-plot Micropore Area (m²/g)	t-plot External Surface Area (m²/g)
ITQ-75 (C)	0,140	20,2	2,9	17,3
Fructose/SDA C - 0.3	0,241	51,2	4,8	46,4
Fructose/SDA C - 1	0,351	75,8	8,8	67,0
Fructose/SDA C - 3	0,379	75,5	8,7	66,8
Sucrose/SDA C - 0.3	0,186	43,3	1,8	41,4
Sucrose/SDA C - 1	0,152	34,1	5,7	28,3
Sucrose/SDA C - 3	n.a.	32,2	7,8	24,3

Any of the saccharides under study were successful in increasing the total adsorbed volume. Looking more closely at the samples obtained with Compound B as SDA, ITQ-75 without any change has a type III isotherm and a small hysteresis of type H3 according to the IUPAC classification [41]. After the addition of fructose or sucrose it is observed that the isothermal type is maintained, as well as the hysteresis type, although this becomes more marked with increasing saccharides content. Fructose is more successful than sucrose in increasing the accessibility of the sample. When the Fructose/ SDA B ratio is equal to 0,3 there is an increase in the total adsorbed volume up to five times. This increase in accessibility is mainly due to the increase of the external surface area. A small increase in the micropore area is observed, from almost 0,5 to 13 m²/g. In respect to the external surface area, there is an

increase of up to four times in relation to ITQ-75 without modification, from 11,4 m²/g to 40 m²/g.

For the samples obtained using Compound C as SDA (see Figure 5.33 and Table 5.30), it is observed that after the insertion of fructose it is possible to obtain the sample with the highest total adsorbed volume of 264 cm³/g STP. As observed previously for ITQ-75 obtained with Compound B as SDA, fructose is more effective in increasing the accessibility of the sample. When the molar ratio Fructose/SDA C is equal to 1 or 3, there is an increase up to three times on the total adsorbed volume. As for the increase of the external surface area, this is up to four times from 17,3 m²/g to   67 m²/g.

According to the literature, the insertion of these components should allow the creation of a secondary porous system [39, 40]. As can be seen from the isotherms obtained previously, both for IZM-5 (see Figure 5.25) and ITQ-75 (see Figures 5.32 and 5.33 for structures obtained with Compound B and C, respectively), the materials obtained with the different types and contents of saccharides do not present a mesoporous system. The observed increase in accessibility is due to the increase in the external surface area, probably associated to smallest crystal size.

As was done previously for IZM-5, the thermogravimetric profile of the differente ITQ-75 samples was determined in order to ascertain the impact that the presence of the different saccharides on the thermal degradation of the final structure. The degradation profiles of ITQ-75 samples obtained with Compound B or C as SDA, as well as its chemical composition, are present in Figure 5.34 and 5.35, respectively, and Tables 5.31, 5.32, 5.33 and 5.34.
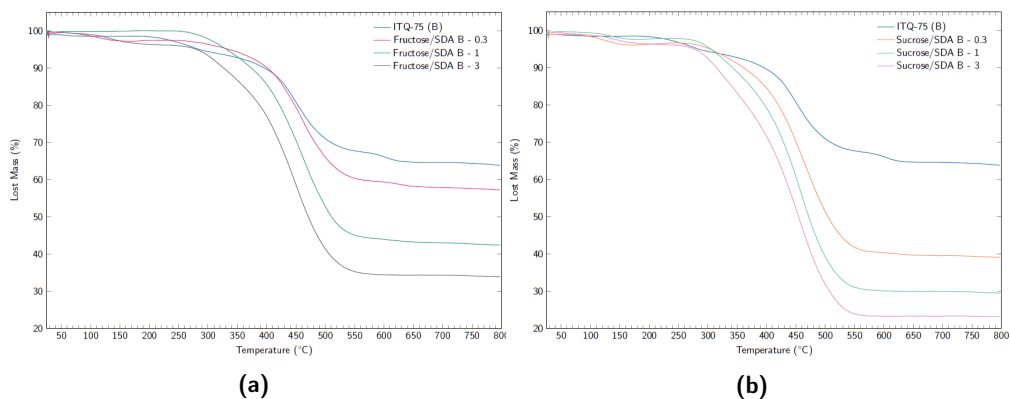
Figure 5.34: TG of ITQ-75 obtained with Compound B as SDA (in blue) and with different (5.34a) Fructose/SDA B molar ratios - 0,3 (in pink), 1 (in green) and 3 (in grey) - and (5.34b) Sucrose/SDA B molar ratios - 0,3 (in orange), 1 (in green) and 3 (in pink)

Table 5.31: Chemical composition of ITQ-75 obtained with different saccharedeos contents ([1]Determined by elemental analysis. [2]Determined by ICP)

Material	Modification	Formula	Mass composition (%)					
			N^1	C^1	H^1	S^1	Sn^2	Zn^2
Compound B	ITQ-75 (B)	$Sn_{3,52}Zn_{1,27}S_8 \cdot C_{10,59}H_{12,24}N_{1,68}$	2,33	12,57	1,21	25,36	41,50	8,83
	Fructose/SDA B - 0.3	$Sn_{3,50}Zn_{0,51}S_8 \cdot C_{18,61}H_{17,50}N_{1,67}$	2,42	23,02	1,81	26,44	18,31	3,46
	Fructose/SDA B - 1	$Sn_{3,17}Zn_{1,67}S_8 \cdot C_{40,56}H_{61,73}N_{1,98}$	1,80	31,68	4,02	16,70	24,46	7,11
	Fructose/SDA B - 3	$Sn_{2,04}Zn_{1,04}S_8 \cdot C_{38,59}H_{32,90}N_{1,64}$	1,90	37,67	2,70	21,03	19,90	5,59
	Sucrose/SDA B - 0.3	$Sn_{2,50}Zn_{1,14}S_8 \cdot C_{48,20}H_{41,22}N_{3,25}$	3,30	42,02	3,00	18,64	21,61	5,42
	Sucrose/SDA B - 1	$Sn_{2,49}Zn_{1,50}S_8 \cdot C_{55,99}H_{46,44}N_{2,82}$	2,68	45,50	3,15	17,37	20,05	6,63
	Sucrose/SDA B - 3	$Sn_{1,48}Zn_{0,63}S_8 \cdot C_{51,39}H_{43,09}N_{1,74}$	1,73	43,83	3,06	18,23	12,48	2,90

Table 5.32: Molar ratios of ITQ-75 obtained with different saccharedeos contents ([1]Determined by elemental analysis. [2]Determined by TG)

SDA	Modification	Gel Molar Ratios			Material Molar Ratios			Material Organic Content (%)	
		Sn/Zn	Sn/S	C/N	Sn/Zn	Sn/S	C/N	CHNS[1]	TG[2]
Compound B	Undoped	3,2	0,2	6,5	2,6	0,4	6,3	41,5	36,1
	Fructose/SDA B - 0.3	3,2	0,2	7,5	2,9	0,2	11,1	53,7	42,8
	Fructose/SDA B - 1	2,9	0,2	9,5	1,9	0,4	20,5	54,2	57,4
	Fructose/SDA B - 3	2,8	0,2	8,5	2,0	0,3	23,5	63,6	66,1
	Sucrose/SDA B - 0.3	3,2	0,2	8,5	2,2	0,3	14,8	67,0	60,9
	Sucrose/SDA B - 1	2,9	0,2	12,2	1,7	0,3	19,8	68,7	70,5
	Sucrose/SDA B - 3	2,9	0,2	24,1	2,4	0,2	29,5	66,8	76,6
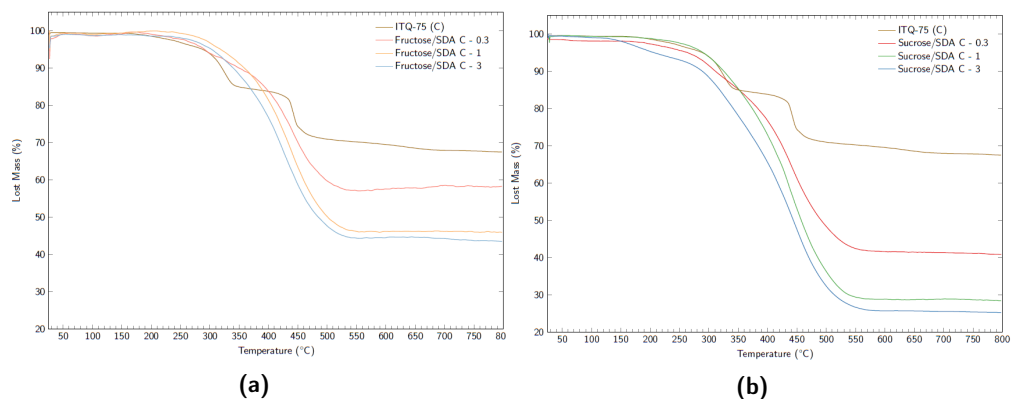
Figure 5.35: TG of ITQ-75 obtained with Compound C as SDA (in brown) and with different (5.35a) Fructose/SDA C molar ratios - 0,3 (in red), 1 (in orange) and 3 (in blue) - and (5.35b) Sucrose/SDA C molar ratios - 0,3 (in red), 1 (in green) and 3 (in blue)

Table 5.33: Chemical composition of ITQ-75 obtained with different saccharedeos contents ([1]Determined by elemental analysis. [2]Determined by ICP)

Material	Modification	Formula	Mass composition (%)					
			N[1]	C[1]	H[1]	S[1]	Sn[2]	Zn[2]
Compound C	ITQ-75 (C)	$Sn_{3,05}Zn_{1,33}S_8 \cdot C_{11,54}H_{9,97}N_{2,24}$	2,81	12,41	0,89	22,95	32,41	7,78
	Fructose/SDA C - 0,3	$Sn_{2,69}Zn_{0,73}S_8 \cdot C_{20,29}H_{14,52}N_{1,90}$	2,85	26,07	1,56	27,46	34,2	5,08
	Fructose/SDA C - 1	$Sn_{1,07}Zn_{0,35}S_8 \cdot C_{25,64}H_{18,23}N_{1,33}$	1,92	31,57	1,87	26,32	13,01	2,33
	Fructose/SDA C - 3	$Sn_{2,35}Zn_{0,60}S_8 \cdot C_{29,70}H_{22,16}N_{1,02}$	1,37	33,93	2,11	24,42	26,59	3,76
	Sucrose/SDA C - 0,3	$Sn_{1,95}Zn_{0,81}S_8 \cdot C_{27,70}H_{18,83}N_{1,86}$	2,65	33,85	1,92	26,13	23,63	5,42
	Sucrose/SDA C - 1	$Sn_{1,53}Zn_{0,64}S_8 \cdot C_{39,59}H_{28,63}N_{1,53}$	1,86	41,11	2,48	22,20	15,70	3,61
	Sucrose/SDA C - 3	$Sn_{1,81}Zn_{0,55}S_8 \cdot C_{56,64}H_{48,08}N_{1,30}$	1,22	45,60	3,23	17,21	14,45	2,41

Table 5.34: Molar ratios of ITQ-75 obtained with different saccharedeos contents ([1]Determined by elemental analysis. [2]Determined by TG)

SDA	Modification	Gel Molar Ratios			Material Molar Ratios			Material Organic Content (%)	
		Sn/Zn	Sn/S	C/N	Sn/Zn	Sn/S	C/N	CHNS[1]	TG[2]
Compound C	ITQ-75 (C)	3,0	0,2	5,0	2,6	0,4	5,2	39,1	31,9
	Fructose/SDA C - 0,3	3,3	0,2	5,6	3,7	0,3	10,7	57,9	41,7
	Fructose/SDA C - 1	3,1	0,2	8,0	3,1	0,1	19,2	61,7	54,0
	Fructose/SDA C - 3	3,0	0,2	13,9	3,9	0,3	29,0	61,8	52,3
	Sucrose/SDA C - 0,3	3,2	0,2	7,0	2,4	0,2	14,9	64,5	57,5
	Sucrose/SDA C - 1	3,0	0,2	10,8	2,4	0,7	25,8	67,6	70,6
	Sucrose/SDA C - 3	3,1	0,2	22,6	3,3	0,3	43,6	67,3	74,7

As can be seen in Figures 5.34 and 5.35, there are small changes on the thermodegradation profile after the saccharide insertion. ITQ-75 obtained with Compound

B as SDA has two major degradation peaks at 279 °C and 455°C (see Figure E.8 for more information regarding the DTG of this sample). With the presence of fructose the first degradation peak disappears, having only one major peak at 455°C. As for the changes in thermal stability after sucrose presence, it is observed that, except for the first Sucrose/SDA B molar ratio tested, the peak at 455°C is maintained. For the sample with a Sucrose/SDA B molar ratio of 0,3, this peak moves to a higher temperature of 473°C. On the other hand, ITQ-75 obtained with Compound C has two major degradation peaks at 327°C and 441°C. When any of tested saccharide are present, there is only one major peak at 441°C.

It can be seen that with increasing saccharide content the organic content of the sample increases, which is in agreement with the data obtained from elemental analysis (see Tables 5.32 and 5.34). Of the different molar ratios determined, Sn/Zn, Sn/S, and C/N, the one that varies the most is the C/N molar ratio. This increases as the saccharide content in the synthesis gel increases. Therefore, the presence of saccharide, as well as the increase of its content as it increases in the synthesis gel, seems to be confirmed.

5.2.1.2 Modification of gel's viscosity

The second methodology used during the materials synthesis process to increase its accessibility was the modification of the gel's viscosity. A more viscous synthesis gel does not allow for such easy mobility of the formed nuclei, and as such, the likelihood of them meeting and increasing in size is reduced. Therefore, smaller crystal sizes should be obtained [43].

During the synthesis process two solvents are used, water and ethylene glycol, with a molar ratio EG/H_2O equal to 0,96. Since ethylene glycol is more viscous than water, with a viscosity equal to 18,4 cP versus 1 cP of water, its content was increased, i.e. the EG/H_2O molar ratio was increased. Six distinct EG/H_2O molar ratios, 1,25, 1,5, 2, 2,5, 3 and 3,5 were tested. The diffractograms of the ITQ-75 samples obtained with Compound B as SDA and with the different EG/H_2O tested molar ratios are present in Figure 5.36.
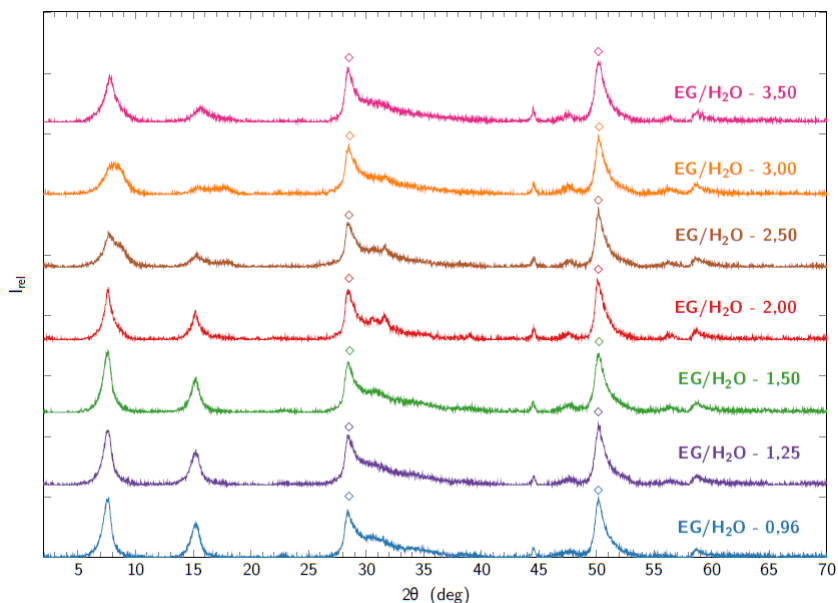
Figure 5.36: PXRD patterns of ITQ-75 obtained with Compound B as SDA (in blue) and with different EG/H_2O molar ratios - 1,25 (in purple), 1,50 (in green), 2,00 (in red), 2,50 (in brown), 3,00 (in orange) and 3,50 (in pink), where ⋄ denotes a ZnS phase

With increasing EG/H_2O molar ratio, a maintenance of the diffraction pattern is observed but a change in the position and shape of the first two diffraction peaks, corresponding to lamellar order, is present. From an EG/H_2O molar ratio equal to 2,5, a change in the position of the first two diffraction peaks towards higher angles is observed. Therefore, a structure with a slightly more closed architecture is obtained. With respect to their shape, as the ethylene glycol content increases, the diffraction peaks become flatter, with a consequent increase in FWHM value. Therefore, a decrease in crystal size according to Scheer's [42] law is thus observed.

In order to confirm the impact that changing the EG/H_2O ratio had on the samples accessibility, the textural properties were determined by determining the N_2 adsorption-desorption isotherms (see Figure 5.37 and Table 5.35).
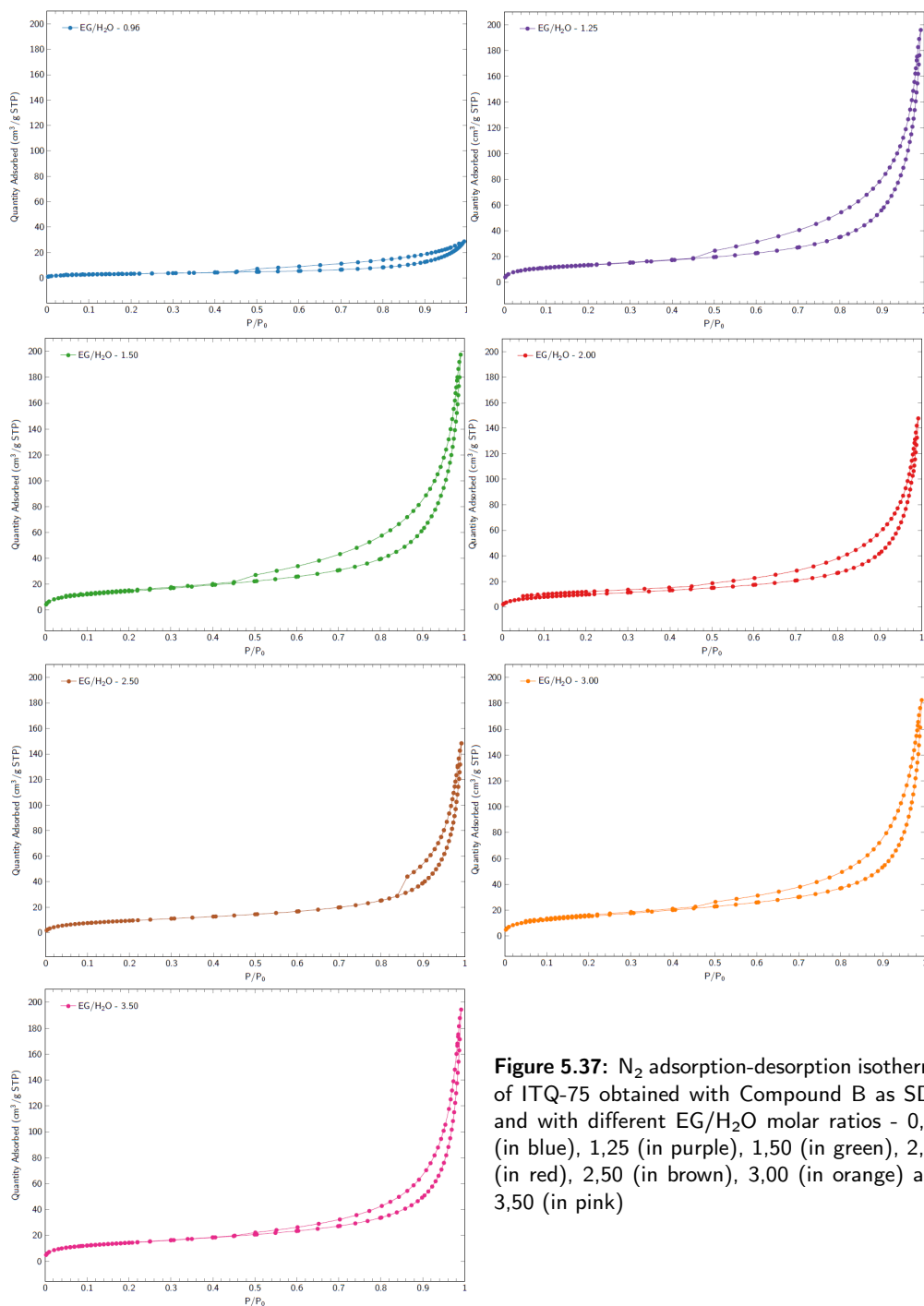
Figure 5.37: N$_2$ adsorption-desorption isotherms of ITQ-75 obtained with Compound B as SDA and with different EG/H$_2$O molar ratios - 0,96 (in blue), 1,25 (in purple), 1,50 (in green), 2,00 (in red), 2,50 (in brown), 3,00 (in orange) and 3,50 (in pink)

Table 5.35: Textural properties of ITQ-75 obtained with Compound B as SDA and with different EG/H_2O molar ratios (n.a. - not available)

	Pore Volume (cm³/g)	BET surface area (m²/g)	t-plot Micropore Area (m²/g)	t-plot External Surface Area (m²/g)
EG/H_2O - 0,96	n.a.	11,9	0,5	11,4
EG/H_2O - 1,25	0,271	48,2	n.a.	49,8
EG/H_2O - 1,50	0,279	53,8	n.a.	58,4
EG/H_2O - 2,00	n.a.	36,4	n.a.	39,6
EG/H_2O - 2,50	0,202	35,6	n.a.	37,1
EG/H_2O - 3,00	n.a.	56,4	3,1	53,3
EG/H_2O - 3,50	0,268	51,2	5,2	46,0

As can be seen in Figure 5.37 and Table 5.35, by changing the EG/H_2O molar ratio it is possible to change the accessibility of the samples. It can be seen that the change in accessibility after modifying the EG/H_2O molar ratio is mainly due to the external surface area, something similar to what was found with the saccharides-rich samples. Regarding the type of isotherm and hysteresis, the samples with increased EG/H_2O molar ratio have a type III isotherm and a hysteresis of type H3 according to the IUPAC classification [41]. When the EG/H_2O molar ratio is increased, the external surface area is increased up to five times, probably associated to the existence of sample formed by smaller crystals. In order to confirm this hypothesis, a FESEM analysis was performed on ITQ-75 sample with a EG/H_2O molar ratio equal to 3 (see Figure 5.38).

(a)

(b)
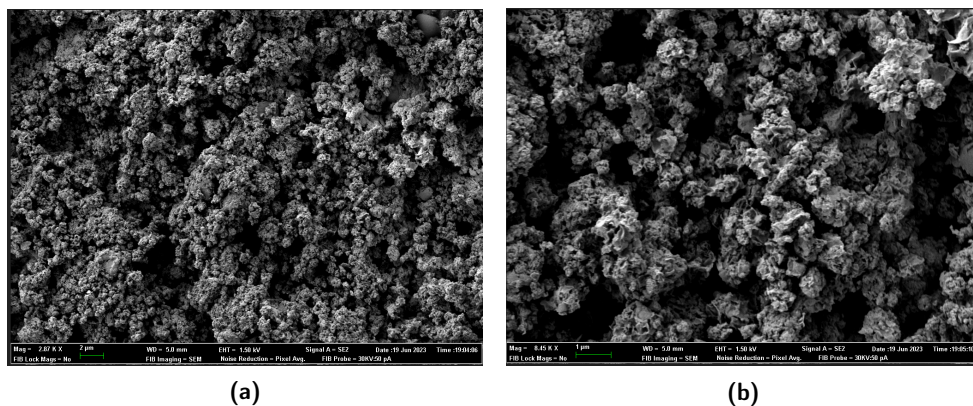
Figure 5.38: FESEM images of ITQ-75, obtained with Compound B as SDA, with a EG/H_2O molar ratio equal to 3

Looking at Figure 5.38 it can be seen that after increasing the gel viscosity the crystals can be seen as an accumulation of laminae with different orientations. As for their dimension, they have a crystal size equal to 1,2 ±0,7 μm. Since the ITQ-75 obtained with Compound B prior to any modification has a crystal size equal to 1,4 ±0,5 μm, by increasing the gel viscosity, its crystal size decreases.

Since when the EG/H_2O ratio is increased to 3,00 the greatest increase in ITQ-75's accessibility is observed, the consequences of increasing such ratio on the other two structures under study, IZM-5 and ITQ-75 obtained with Compound C as SDA, were tested. The diffractograms obtained after modifying such parameter are shown in the Figure 5.39.

(a)   **(b)**
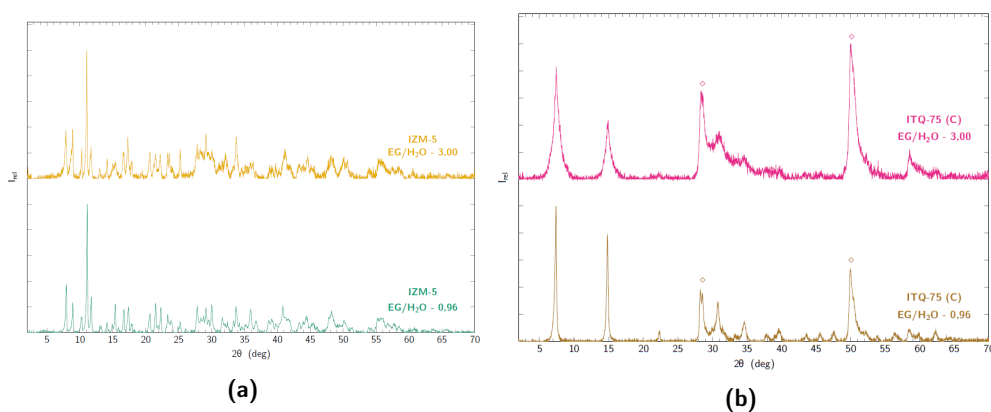
Figure 5.39: PXRD diffractograms of (5.39a) IZM-5 with a EG/H_2O ratio equal to 0,96 (in green) and 3,00 (in yellow) and (5.39b) ITQ-75 obtained with Compound C as SDA with a EG/H_2O ratio equal to 0,96 (in brown) and 3,00 (in pink)

After increasing the ethylene glycol content, the diffraction pattern of IZM-5 is maintained (see Figure 5.39a), something that did not always occur when fructose or sucrose was added to its synthesis gel (see Figure 5.24).

Regarding the EG/H_2O ratio modification in ITQ-75 obtained with Compound C as SDA (see Figure 5.39b), a similar behavior to the one observed in ITQ-75 obtained with Compound B as SDA is detected. A displacement of the diffraction peaks towards higher angles and an increase in the FWHM of the first two diffraction peaks are observed, thus translating into a more close architecture and smaller crystal size.

Afterwards, the textural properties of IZM-5 and ITQ-75 obtained with Compound C as SDA were determined in order to assess the impact of EG/H_2O ratio increasing (see Figure 5.40 and Table 5.36).

(a) (b)
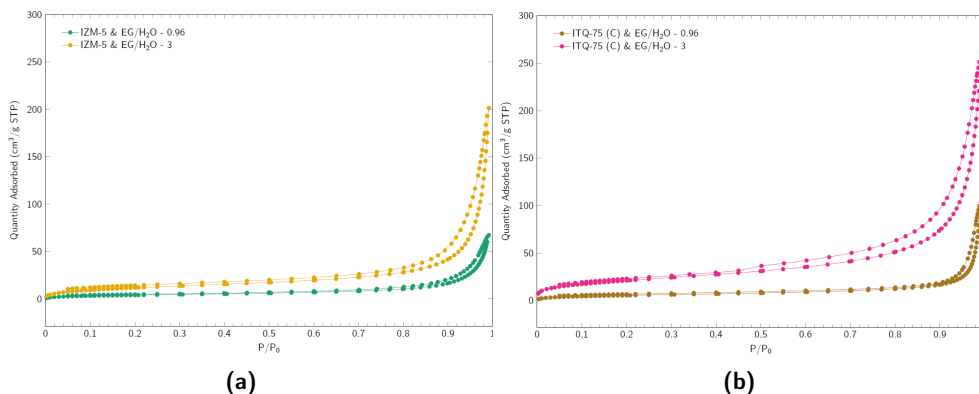
Figure 5.40: N_2 adsorption-desoption isotherms of (5.40a) IZM-5 with a EG/H_2O ratio equal to 0,96 (in green) and 3,00 (in yellow) and (5.40b) ITQ-75 obtained with Compound C as SDA with a EG/H_2O ratio equal to 0,96 (in brown) and 3,00 (in pink)

Table 5.36: Textural properties of IZM-5 and ITQ-75 obtained with Compound C as SDA with increase EG/H_2O molar ratio (n.a. - not available)

	Pore Volume (cm³/g)	BET surface area (m²/g)	t-plot Micropore Area (m²/g)	t-plot External Surface Area (m²/g)
IZM-5 & EG/H₂O - 0,96	0,092	15,1	n.a.	15,4
IZM-5 & EG/H₂O - 3,00	0,271	41,4	5,8	38,6
ITQ-75 (C) & EG/H₂O - 0,96	0,140	20,2	2,9	17,3
ITQ-75 (C) & EG/H₂O - 3,00	n.a.	77,8	5,8	72,0

It can be seen that increasing the ethylene glycol content on the synthesis gel had a positive impact on increasing the accessibility of the structures under study. In both cases it is observed that the increase of the total adsorbed volume is due to the increase of the external surface area, a situation analogous to that already observed for ITQ-75 obtained with Compound B as SDA. In IZM-5, by increasing the EG/H_2O molar ratio, it is possible to increase the BET surface area from 15,1 m²/g to 41,4 m²/g. Regarding ITQ-75 obtained with Compound C as SDA, its BET surface area is increased from 20,2 m²/g to 77,8 m²/g.

5.2.1.3   Addition of coSDAS & Modification of Gel's Viscosity

Two changes to the synthesis gel chemical composition in order to increase the material's accessibility were tested - the insertion of saccharedeos together with increasing the viscosity of the gel. The results obtanied showed that both modifications were successful, with up to a sixfold increase in the external surface area. Thus, for each of the structures studied, a combination of both methods was tested. Regarding the first method, the use fructose as a saccharide and two concentrations, Fructose/SDA ratio equals to 0,3 and 1, were selected since they were the ones that guaranteed greater accessibility. Regarding the increase in gel's viscosity, the EG/H$_2$O molar ratio is increased to 3 because it was the one that facilitated the highest accessibility.

Starting with ITQ-75 obtained with Compound B as SDA, the diffractograms of the materials obtained with the two Fructose/SDA B ratios tested and the EG/H$_2$O molar ratio increased to 3 are present in Figure 5.41.
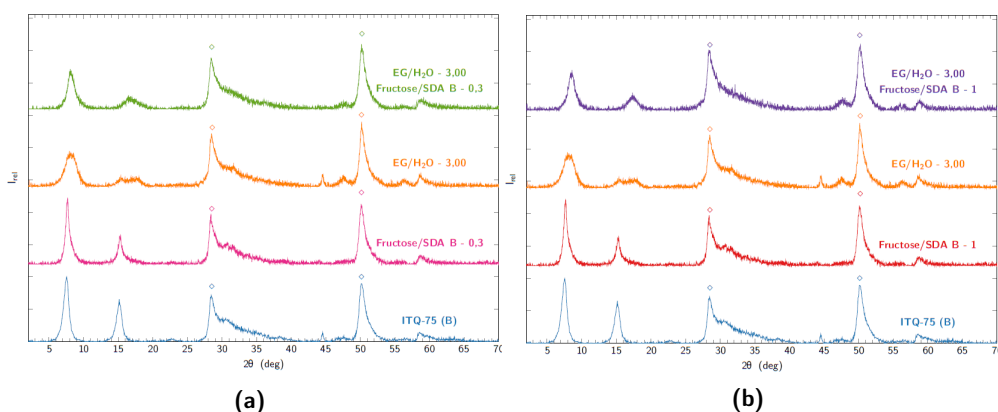
Figure 5.41: PXRD diffractograms of ITQ-75 obtanied with Compound B as SDA (in blue), with a EG/H$_2$O molar ratio equal to 3 (in orange), (5.42a) a Fructose/SDA B ratio equal to 0,3 (in pink), a EG/H$_2$O molar ratio equal to 3 and a Fructose/SDA B ratio equal to 0,3 (in green), (5.42b) a Fructose/SDA B ratio equal to 1 (in red) and a EG/H$_2$O molar ratio equal to 3 and a Fructose/SDA B ratio equal to 1 (in purple), where ◇ denotes a ZnS phase

When the two modifications to the synthesis gel are combined, the greatest shift of the first two diffraction peaks toward higher angle values is observed. It can be seen that the first diffraction peak is displaced by about 1° and the second diffraction peak by about 2°. As for the broadening of the diffraction peaks, this is similar to that observed when fructose is added to the synthesis gel, generating

materials with the individual layers close between them and crystals with smaller dimensions.

In order to evaluate the impact on the textural proprieties, the N_2 adsorption-desorption isotherms were determined (see Figure 5.42 and Table 5.37).
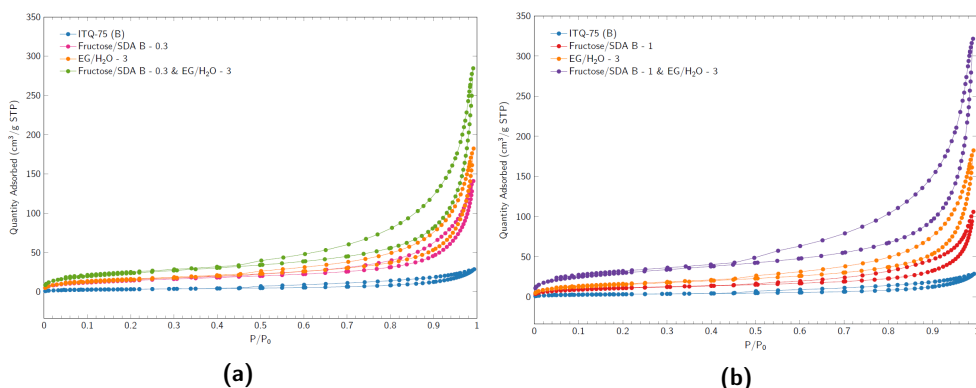
Figure 5.42: N_2 adsorption-desoption isotherms of ITQ-75 obtanied with Compound B as SDA (in blue), with a EG/H_2O molar ratio equal to 3 (in orange), (5.42a) a Fructose/SDA B ratio equal to 0,3 (in pink), a EG/H_2O molar ratio equal to 3 and a Fructose/SDA B ratio equal to 0,3 (in green), (5.42b) a Fructose/SDA B ratio equal to 1 (in red) and a EG/H_2O molar ratio equal to 3 and a Fructose/SDA B ratio equal to 1 (in purple)

Table 5.37: Textural properties of ITQ-75 obtained with Compound B as SDA with increase EG/H_2O molar ratio combined with different Fructose/SDA B ratios (n.a. - not available)

	Pore Volume (cm³/g)	BET surface area (m²/g)	t-plot Micropore Area (m²/g)	t-plot External Surface Area (m²/g)
ITQ-75 (B)	n.a.	11,9	0,5	11,4
EG/H₂O - 3,00	n.a.	77,82	5,83	71,99
Fructose/SDA B - 0,3	0,241	52,6	13,0	39,6
Fructose/SDA B - 1	0,351	39,5	10,5	29,0
EG/H₂O - 3,00 Fructose/SDA B - 0.3	0,403	86,5	11,4	75,4
EG/H₂O - 3,00 Fructose/SDA B - 1	0,471	108,5	18,9	89,7

When combining both modifications an increase in accessibility is observed. The sample with the highest accessibility is obtained when combining the increased

ethylene glycol content and the Fructose/SDA B ratio is equal to 1 (purple isotherm at Figure 5.42b). Such a sample has a total adsorbed volume equal to 321,5 cm³/g STP, about 12 times higher than the value of ITQ-75 without modifications, and an external surface area equal to 89,7 m²/g, about eight times higher than the sample without modifications.

5.2.1.4 Final Considerations

As shown earlier, besides the importance of the electronic properties to obtain samples with a high photo-activity, the textural properties are equally important [37, 38]. The structures under study, IZM-5 and ITQ-75, present low accessibility, which may limit their photocatalytic performance. Thus, in order to increase their accessibility, two modifications to their synthesis process were studied.

First the insertion of saccharides, namely fructose and sucrose, as coSDAs was studied, since these compounds were previously used as mesoporous agents and, due to their low degradation temperature, could be eliminated later by a thermal process. This technique was successful in increasing the accessibility of the samples under study. However, it is observed that the increased accessibility is due to the increase of the external surface area. The presence of these compounds hardly affects the microporous area nor does it lead to the formation of a mesoporous system, probably due to the reduction of crystal size. Regarding the thermal stability of the samples, with the insertion of saccharides there are some modifications in it. However, these changes do not suggest a decrease in the degradation temperature of the organic component present. Looking more closely at the behavior of the structures, it can be seen that with the insertion of the saccharides under study in the IZM-5 synthesis gel there are changes in the diffraction pattern of the material obtained. With the presence of Fructose, the final diffraction pattern can be seen as a combination of IZM-5 and ITQ-76 diffraction patterns, thus having a coexistence between these two crystalline phases. When sucrose is used, only the diffraction pattern of ITQ-76 is obtained. When using a Sucrose/SDA A molar ratio equal to 0,3, the greatest increase in the external surface area is verified, from 15,4 m²/g to 39,1 m²/g. As for ITQ-75, when the saccharides are inserted into its synthesis gel, its diffraction pattern is maintained. However, changes occur in the peaks associated with the ITQ-75 laminar phase that suggest that a more compact structure is obtained, that is, with less distance between consecutive laminar planes. This hypothesis is latter confirmed by HRTEM. Fructose is the most successful in increasing ITQ-75 external surface area. When using a Fructose/SDA B molar ratio equal to 0,3 the external surface area increases from 11,4 m²/g to 39,6 m²/g. As for ITQ-75 obtained with Compound C as SDA, it is possible,

by using a Fructose/SDA C molar ratio equal to 1 or 3, to increase the external surface area from 17,3 m²/g to approximately 67,0 m²/g.

The second methodology tested to increase accessibility is based on modifying the viscosity of the synthesis gel. By increasing the synthesis gel viscosity, the mobility of the nuclei formed is reduced and, as such, smaller crystals will be obtained, avoiding their agglomeration. Since ethylene glycol is more viscous than water, the two solvents used during the synthesis process, it was decided to increase the content of the organic solvent. By increasing the molar ratio EG/H_2O from 0,96 to 3 it was possible to increase the accessibility of the structures. Similar to what was seen for the saccharide-rich samples, the increased accessibility is due to the external surface area. By increasing the ethylene glycol content in the synthesis gel it was possible to increase the external surface area of IZM-5 from 15,1 m²/g to 41,4 m²/g. Something important to mention is that with this modification there were no changes to IZM-5 diffraction pattern, something that was not possible with the first methodology tested. Regarding ITQ-75, it was possible to increase its external surface area from 11,9 m²/g to 56,4 m²/g, when ITQ-75 is obtained with Compound B as SDA, or from 20,2 m²/g to 77,8 m²/g, when ITQ-75 is obtained with Compound C as SDA.

Since the two methodologies were successful in improving the textural properties of the structures under study, they were combined. By increasing the EG/H_2O molar ratio from 0,96 to 3 and by adding fructose, with a Fructose/SDA B equal to 1, it is possible to increase ITQ-75, obtained with Compound B as SDA, external surface area from 11,4 m²/g to 89,7 m²/g.

5.2.2 Post Synthesis Modifications

Besides the modification of the synthesis parameters to increase the accessibility of the samples under study, the possibility of post synthesis modifications to increase this parameter has been evaluated. These modifications can be divided into two, those that involve the elimination of SDA, such as thermal treatment, ion exchange, acid washing and photodegradation, and those that modify directly the laminar structure obtained, such as n-butyllithium and ball mill treatments.

5.2.2.1   SDA Elimination Methods

i. Thermal Treatment

The thermal treatment was carried out in the presence of a nitrogen atmosphere rather than air. This atmosphere was chosen in order to maintain the carbon, since it would help to avoid the structure collapse and at the same time to create a junction between the two materials (inorganic and organic components), improving the charge separation properties of the final structure.

In order to determine the temperature at which the thermal treatment would be carried out, XRD in situ was performed under nitrogen atmosphere in order to evaluate the evolution of the crystalline phase with increasing temperature (see Figures 5.43 and 5.45 for both IZM-5 and ITQ-75 structures, respectively).
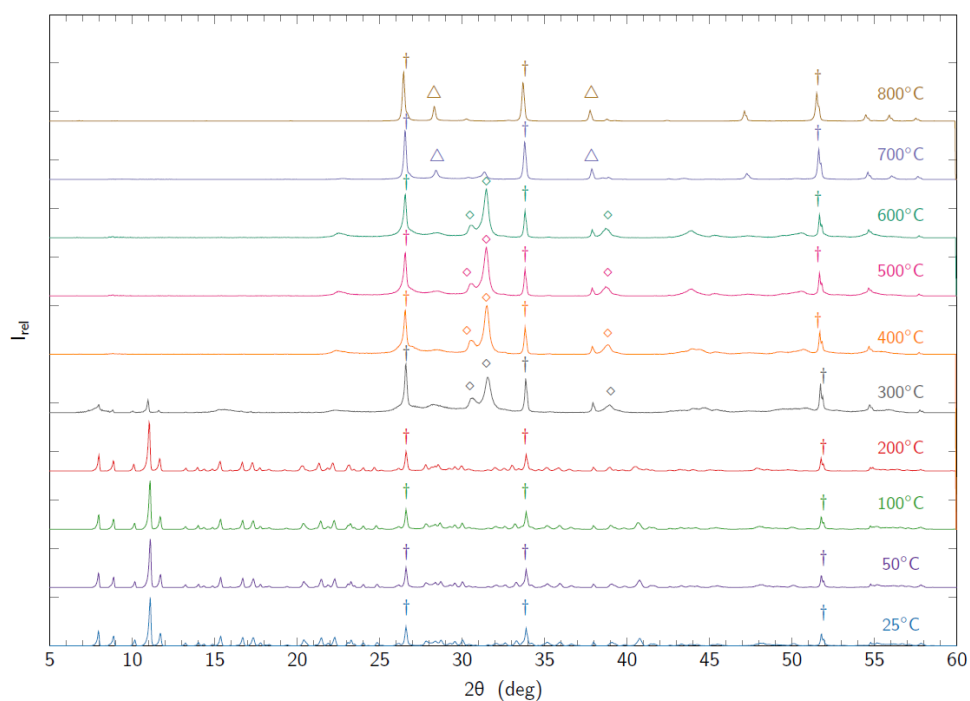
Figure 5.43: XRD in situ of IZM-5 under nitrogen atmosphere at 25°C (in blue), 50°C (in purple), 100°C (in green), 200°C (in red), 300°C (in gray), 400°C (in orange), 500°C (in pink), 600°C (dark green), 700°C (in dark purple) and 800°C (in brown). †denotes a SnO_2 phase, ◊ a SnS phase and △ a Sn^0 phase

By looking at Figure 5.43 it can be seen that up to 200°C there is no variation in the diffraction pattern. When 300°C is reached there is a reduction in intensity of the diffraction peaks associated with IZM-5 and a new crystalline phase appears. This phase can be associated with SnS. From 400°C on, the IZM-5 diffraction pattern is no longer detected. The diffraction pattern obtained at 400°C remains stable until 600°C. From 700°C the diffraction peaks associated with SnS decrease their intensity and diffraction peaks that can be associated with Sn^0 appear. At 800°C only the Sn^0 and SnO_2 diffraction peaks are detected. Therefore, a thermal treatment under nitrogen atmosphere at 350°C was chosen. The resulting diffractogram is represented in red in Figure 5.44.
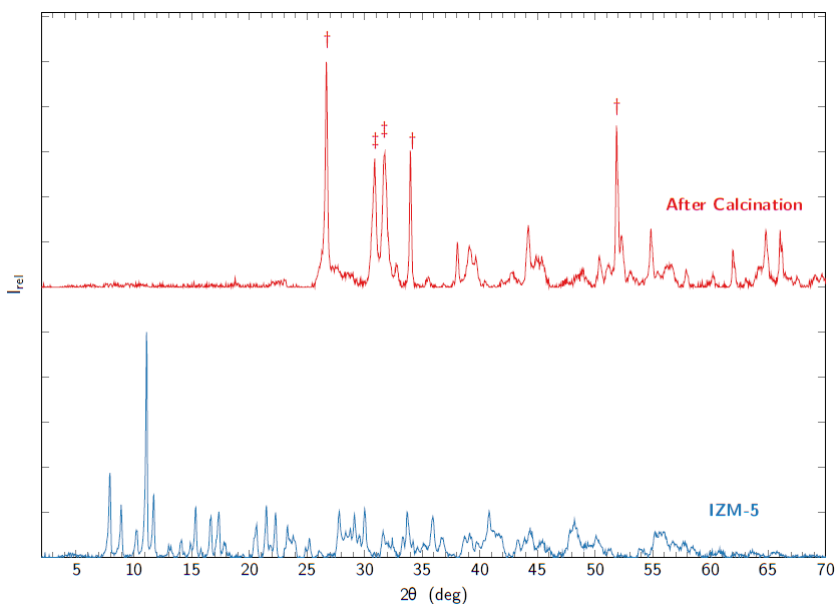
Figure 5.44: PXRD patterns of IZM-5 before (in blue) and after the thermal treatment under nitrogen atmosphere at 350°C (in red), where † denotes a SnO_2 and ‡ a SnO phase

As can be seen in the previous figure, such thermal treatment led to the disappearance of the diffraction peaks associated with IZM-5, so this thermal treatment was not successful in maintaining its structure, after the degradation of the internal organic template.

Subsequently, ITQ-75 XRD in situ was performed under nitrogen atmosphere in order to evaluate the evolution of the different crystalline phases present (see Figure 5.45).
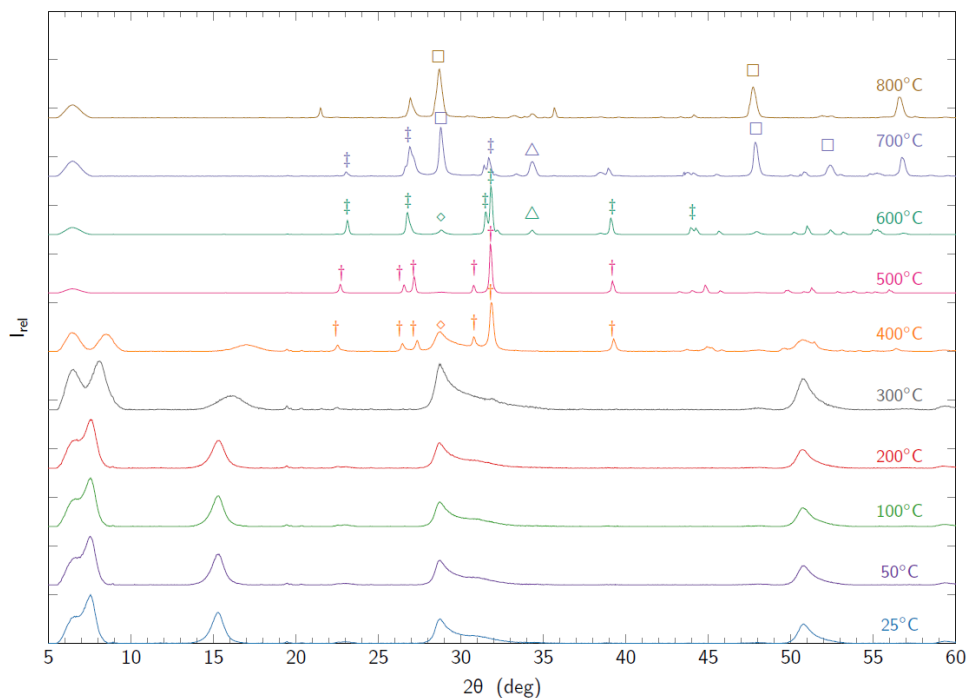
Figure 5.45: XRD in situ of ITQ-75 under nitrogen atmosphere at 25°C (in blue), 50°C (in purple), 100°C (in green), 200°C (in red), 300°C (in gray), 400°C (in orange), 500°C (in pink), 600°C (dark green), 700°C (in dark purple) and 800°C (in brown). † denotes a SnS orthorhombic phase, ◇ a ZnS rhombohedral phase, △ a α-SnS phase, ‡ a SnO_2 phase and □ $Zn_{0,94}Sn_{0,06}O$ phase

By observing Figure 5.45 one can see that up to 200°C no variations in the diffraction pattern are observed. At 300°C the diffraction peaks up to 2θ equal to 20°. It is observed that the first diffraction peak is split in two peaks and the intensity of the second peak is reduced. At 400°C diffraction peaks appear that can be associated with the orthorhombic structure of SnS and the rhombohedral structure of ZnS. At 600°C the SnS phase evolves into an α-SnS phase. The ZnS phase remains and a diffraction pattern emerges that can be associated with SnO_2. At 700°C the presence of α-SnS is reduced. The SnO_2 and ZnS phases are maintained. At 800°C most diffraction peaks are related to the ZnS phase. The remaining less

241

intense peaks may correspond to Sn^0, a mixed oxide with the chemical formula $Zn_{0.94}Sn_{0.06}O$ and traces of SnO_2.

Since IZM-5 and ITQ-75 show similar thermal stability, i.e. are stable up to $200°C$, it was decided to perform a calcination at low temperatures and over a long period of time in order to find out if it would be possible to eliminate part of the organic content and avoid the collapse of the structure. Thus, ITQ-75 calcined in a nitrogen atmosphere at $150°C$ for a period of 24 hours was performed. The diffractogram resulting from low temperature calcination is represented in orange in Figure 5.44.
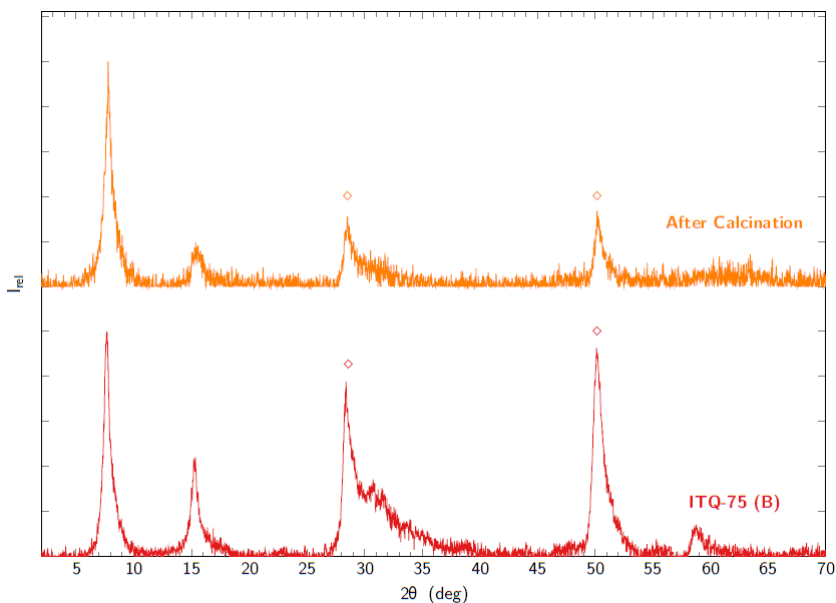
Figure 5.46: PXRD patterns of ITQ-75 before (in red) and after the thermal treatment under nitrogen atmosphere at $150°C$ for 24 hours (in orange), where $\diamond$ denotes a ZnS phase

Observing the previous figure, it can be seen that after the thermal treatment the diffraction peaks maintain their position but their intensity is reduced. Thus, its carbon content was determined through elemental analysis to verify if there was any change in the chemical composition (see Table 5.38).

Table 5.38: Chemical composition (% w/w), determined by elemental analysis, of ITQ-75 before and after the thermal treatment

	Chemical Composition (% w/w)			
	N	C	H	S
Before Calcination	2,42	23,02	1,80	26,44
After Calcination	2,49	23,49	1,58	25,30

As can be seen from Table 5.38, there were no significant changes to the chemical composition of the sample. Thus, although there were changes in the diffraction pattern, these have not translated into significant variations in the chemical composition.

These results shows that with the thermal treatments tested it is not possible to maintain the crystalline structure of the materials under study if the organic counterpart is degradated or eliminated, at least, partially. Thus, these results seems to suggest that the presence of SDA is fundamental for the materials to have their crystalline structure.

ii. Ionic Exchange

The second post-synthesis modification to increase the accessibility of the materials was ionic exchange (IE). This method is the most widely used by the various authors who have studied this class of materials to reduce the organic content and increase the accessibility of the materials [44], overall, in the case of lamellar materials. The ionic exchange is carried out with CsCl, since Cs^+ has a relatively large ionic radius, allowing to easily replace the internal organic counterpart without changing the overall crystalline stricture.

The methodology followed by Lin et al. [44] was used. As such, multiple ionic exchanges with CsCl were performed and the chemical composition was determined via elemental analysis between exchanges.

Starting with the IZM-5' structure, its diffractograms after the different ionic permutations, as well as their chemical composition, are shown in Figure 5.47 and Table 5.39, respectively.
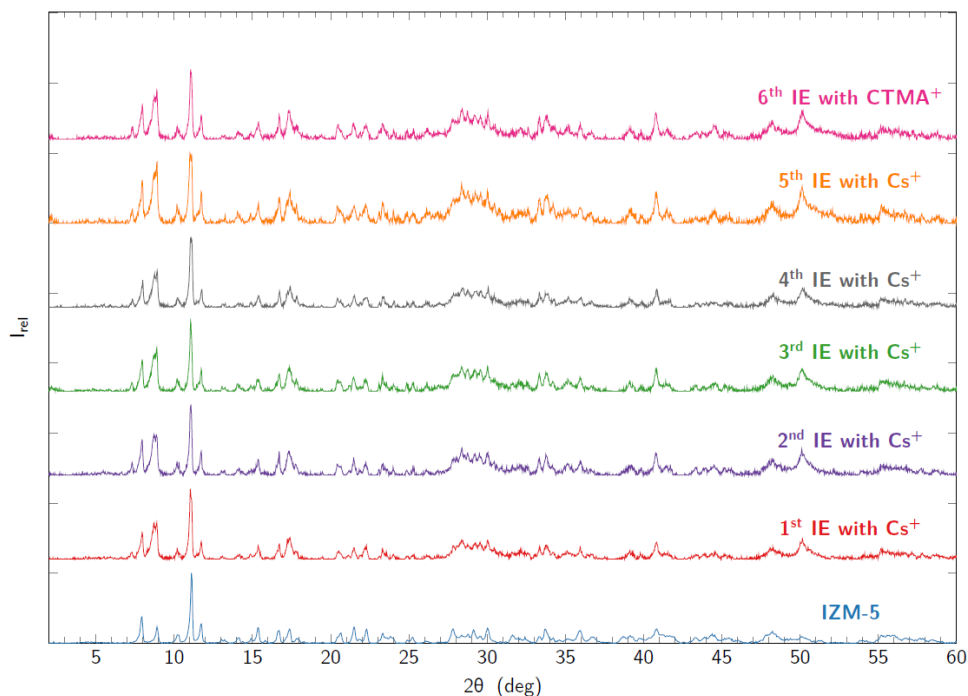
Figure 5.47: PXRD patterns of IZM-5 before ionic exchange (in blue), after one (in red), two (in purple), three (in green), four (in gray) and five (in orange) ionic exchanges with CsCl and after one ionic exchange with CTMABr (in pink)

Table 5.39: Chemical composition (% w/w), determined by elemental analysis, of IZM-5 before and after the several ionic exchanges

IZM-5	Chemical Composition (% w/w)			
	N	C	H	S
Before IE	3,09	17,80	3,11	25,34
After 1st IE with Cs+	2,61	17,91	2,95	26,18
After 2nd IE with Cs+	2,60	17,68	2,88	26,59
After 3rd IE with Cs+	2,49	17,42	2,87	24,07
After 4th IE with Cs+	2,48	17,28	2,81	25,33
After 5th IE with Cs+	2,47	16,97	2,66	25,70
After 6th IE with CTMA+	2,35	18,63	2,98	20,60

After the five exchanges with CsCl it is observed that there was a small variation in the carbon content. According to [44], in the structure studied after the five CsCl permutations the carbon content was reduced to residual values, something that did not occur in IZM-5. Thus, this method is not the most suitable for reducing the carbon content. This confirms the absence of ionic species and the strong interaction between the SDA and the inorganic part of the material.

In order to assess whether the size of the ion to be exchanged has an impact on the ease with which the structure is exchanged, cetyltrimethylammonium bromide (CTMABr) was used instead of CsCl, i. e., a long chain cationic surfactant with capabilities as swelling agent. The diffractogram obtained after the exchange with $CTMA^+$ is shown in pink in Figure 5.47 and its chemical composition in Table 5.39. After the exchange with $CTMA^+$ there is no dramatic change in the diffraction pattern. Regarding its carbon content, it is slightly increased. Since the increase is small, this method was considered not effective on the IZM-5 structure.

Then the possibility of performing a similar procedure on the ITQ-75 structure was evaluated. Thus, it was first performed the five ionic exchanges with CsCl to the ITQ-75 obtained with Compound B as SDA. The different diffractograms obtained, as well as their chemical composition, are shown in Figure 5.48 and Table 5.40, respectively.
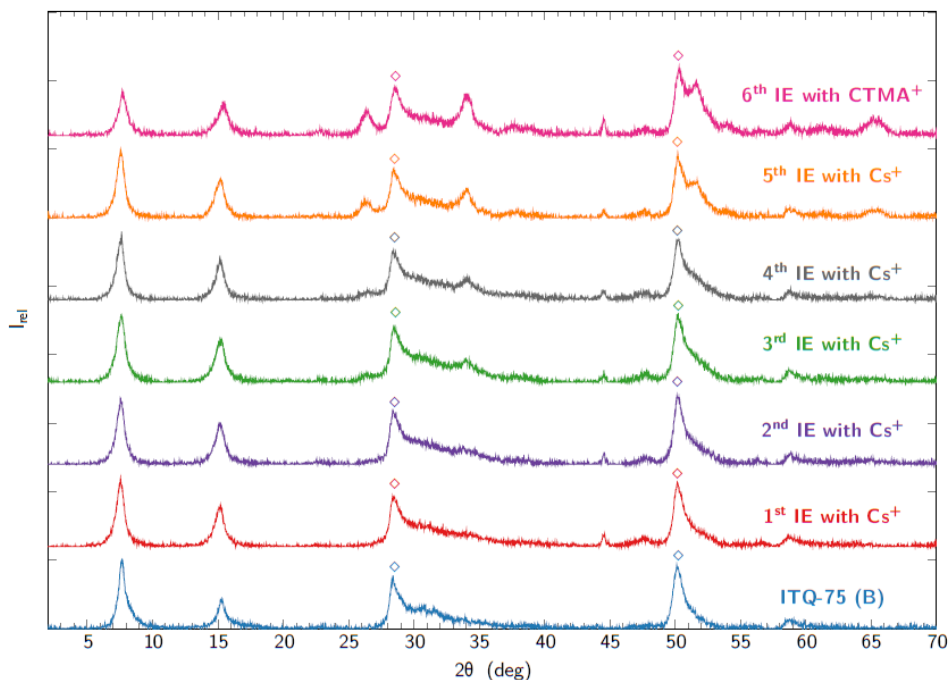
Figure 5.48: PXRD patterns of ITQ-75 before ionic exchange (in blue), after one (in red), two (in purple), three (in green), four (in gray) and five (in orange) ionic exchanges with CsCl and after one ionic exchange with CTMABr (in pink), where ◇ denotes a ZnS phase

Table 5.40: Chemical composition (% w/w), determined by elemental analysis, of ITQ-75 before and after the several ionic exchanges (n.a. - not available)

ITQ-75	Chemical Composition (% w/w)			
	N	C	H	S
Before Ionic Exchange	2,33	12,57	1,21	25,36
After 1st IE with Cs+	2,19	13,61	1,17	26,59
After 2nd IE with Cs+	2,16	13,31	1,17	24,67
After 3rd IE with Cs+	n.a.	n.a.	n.a.	n.a.
After 4th IE with Cs+	1,99	12,64	1,17	23,17
After 5th IE with Cs+	1,97	11,84	1,14	26,11
After 6th IE with CTMA+	1,57	13,15	1,61	21,53

After the five ionic exchanges with CsCl a small reduction in carbon content is observed, similar to the situation observed previously for IZM-5. Thus, for similar reasons, ITQ-75 was exchanged with CTMABr. It can be seen that after the exchange with CTMABr the carbon content is slightly increased (see Table 5.40). Thus, the structure of ITQ-75 is not exchangeable with the selected ions.

Given the experimental results presented above, the reduction of the carbon content through an ionic exchange is not a successful method to increase the accessibility of the structures under study.

iii. Acid Washing

The third method to be studied for reducing the carbon content of the samples was acid washing to liberate internal volume and increase the acessability of the materials. It was chosen to use a low concentration of HCl in order to perform a gentle washing that attacks only the organic part, without affecting the metals present in the structure. This method was tested on two samples, IZM-5 and on ITQ-75 obtained with Compound B as SDA. Their diffractograms, as well as their chemical composition, are shown in Figure 5.49 and Table 5.41, respectively.

(a)   (b)
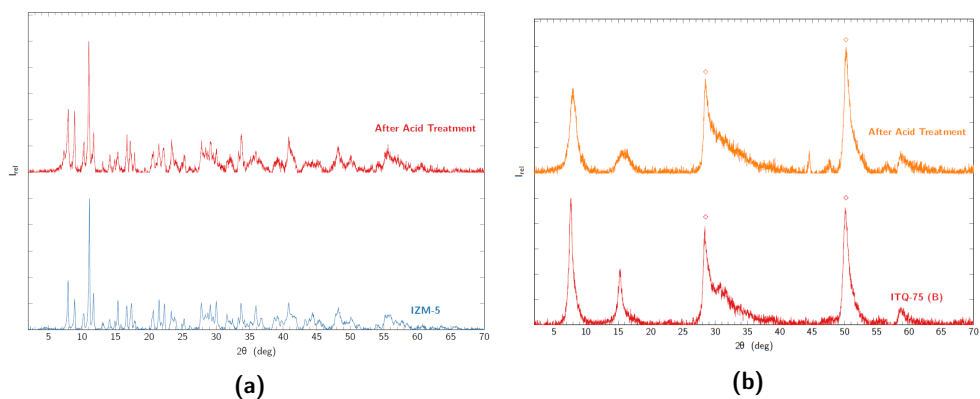
Figure 5.49: PXRD patterns of (5.49a) IZM-5 before (in blue) and after (in red) acid washing and (5.49b) ITQ-75 before (in red) and after (in orange) acid washing, where ⋄ denotes a ZnS phase

Table 5.41: Chemical composition (% w/w), determined by elemental analysis, of IZM-5 and ITQ-75 before and after acid washing

IZM-5	Chemical Composition (% w/w)			
	N	C	H	S
Before Acid Treatment	3,09	17,80	3,11	25,34
After Acid Treatment	3,05	18,55	3,17	26,09
ITQ-75	Chemical Composition (% w/w)			
	N	C	H	S
Before Acid Treatment	2,33	12,57	1,21	25,36
After Acid Treatment	2,17	12,99	1,10	26,91

After the acid treatment the diffraction pattern of the two structures is maintained, but the intensity of some diffraction peaks is modified. Looking first at IZM-5 (see Figure 5.49a), it can be seen that after the HCl treatment the first two diffraction peaks become more intense. For ITQ-75 obtained with Compound B as SDA (see Figure 5.49b), a reduction of the intensity of the first two diffraction peaks is observed.

Evaluating now the chemical composition and comparing the values before and after the acid treatment, unfortunately no significant changes are observed in the carbon content. Thus, this method was not successful in reducing the organic content of the targeted samples.

iv. SDA Photodegradation

The last post-modification method involving the organic content elimination tested was through the SDA photodegradation. This method uses a light source, in the presence or absence of an oxidizing agent, to degrade the organic components present. Two degradation times, four and six hours, and three concentrations of oxidants, 0%, 5% and 10%, were evaluated. Note that the percentage of oxidant present is in relation to the molar carbon content of the original sample. The first structure to be tested on this methodology was the ITQ-75 obtained with Compound B as SDA. The different diffractograms, as well as the chemical compositions, are present in Figure 5.50 and Table 5.42, respectively.
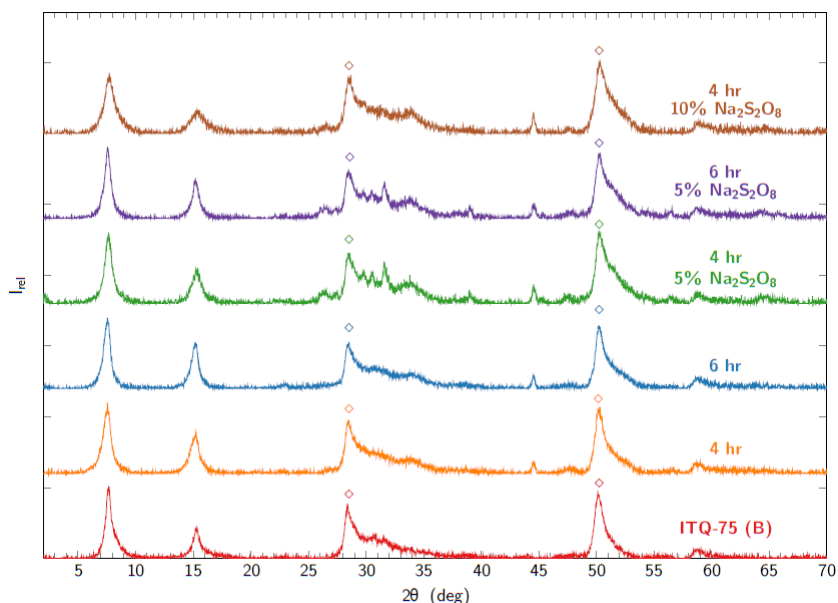
Figure 5.50: PXRD patterns of ITQ-75 before photodegradation (in red), after 4 hours under radiation (in orange), after 6 hours under radiation (in blue), after 4 hours under radiation and with 5% $Na_2S_2O_8$ (in green), after 6 hours under radiation and with 5% $Na_2S_2O_8$ (in purple) and after 4 hours under radiation and with 10% $Na_2S_2O_8$ (in brown), where $\diamond$ denotes a ZnS phase

Table 5.42: Chemical composition (% w/w), determined by elemental analysis, of ITQ-75 before and after the different photodegradation experiments

ITQ-75	Chemical Composition (% w/w)			
	N	C	H	S
Before Photodegradation	2,33	12,57	1,21	25,36
4 hours	2,05	13,39	1,31	23,87
6 hours	2,26	13,48	1,25	27,36
4 hours with 5% $Na_2S_2O_8$	1,91	11,93	1,28	27,28
6 hours with 5% $Na_2S_2O_8$	2,05	13,35	1,34	24,67
4 hours with 10% $Na_2S_2O_8$	1,83	13,68	1,48	24,08

Looking at the diffractograms after the different tests (see Figure 5.50), it can be seen that after the presence of the oxidant $Na_2S_2O_8$, the broad peak located at 2θ equal to 28,7° changes. The same cannot be said of the remaining tests, since

249

no changes in the diffraction pattern are observed. Analyzing now the chemical composition (see Table 5.42), it appears that there are no significant changes in carbon content, so this method was not successful.

Next, and using the highest concentration of oxidant, this method of SDA photodegradation was tested on the IZM-5 structure. The difractograms, as well as the chemical composition of the samples in question, are shown in Figure 5.51 and Table 5.43.
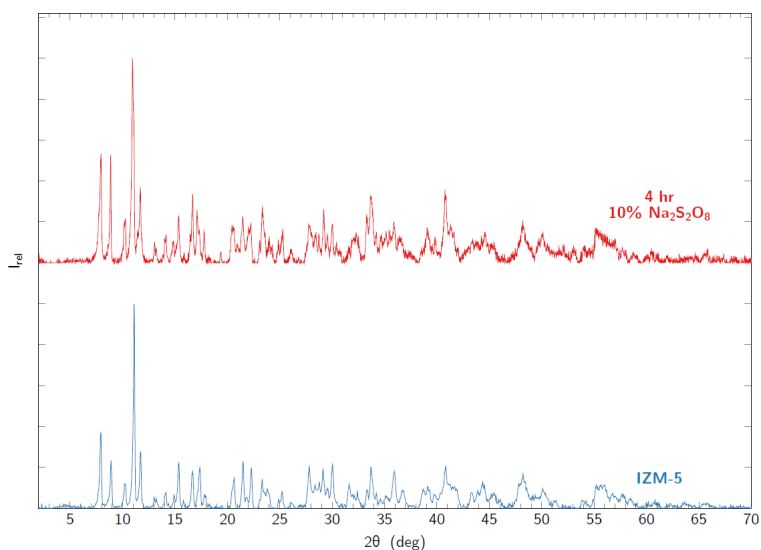
Figure 5.51: PXRD patterns of IZM-5 before photodegradation (in blue) and after 4 hours under radiation and with 10% $Na_2S_2O_8$ (in red)

Table 5.43: Chemical composition (% w/w), determined by elemental analysis, of IZM-5 before and after photodegradation

IZM-5	Chemical Composition (% w/w)			
	N	C	H	S
Before Photodegradation	3,09	17,80	3,11	25,34
4 hours with 10% $Na_2S_2O_8$	3,07	17,67	3,21	25,84

Although some changes in the diffraction pattern of IZM-5 are observed, namely the increase in intensity of the first two diffraction peaks, the reduction in carbon content after the process is minimal.

Hence, it can be concluded that photodegradation is not an effective method that allows the reduction of the carbon content of the samples and, thus, increasing their accessibility.

5.2.2.2   Structure Modification Methods

In order to increase the accessibility of the samples, they were modified post synthesis. As shown previously, methods involving the elimination of the SDA used during synthesis were not successful. Thus, two methodologies that modify the crystals obtained were tested, namely n-butyllithium and ball mill treatments.

i. n-Butyllithium Treatment

According to the reviewed literature, the treatment with n-butyllithium allows the chemical exfoliation of a laminar material, obtaining single sheets or crystals with fewer sheets [45, 46, 47, 48, 49]. By this method is possible to produce transitional metal chalcogenides nanosheets by a ultrasound-promoted hydration of lithium-intercalated compounds, becoming the most effective method to do such [48].

This treatment was applied to ITQ-75 obtained with Compound C as SDA. After the n-butyllithium treatment two solids were recovered. A first one, referred to as pellet, results from the solid recovered after the first centrifugation cycle. The second one, referred to as supernatant, is the solid recovered by precipitation, due to the addition of HCl, from the supernatant recovered after the first centrifugation cycle (see Appendix A for more details). The resulting diffractograms are shown in Figure 5.52.
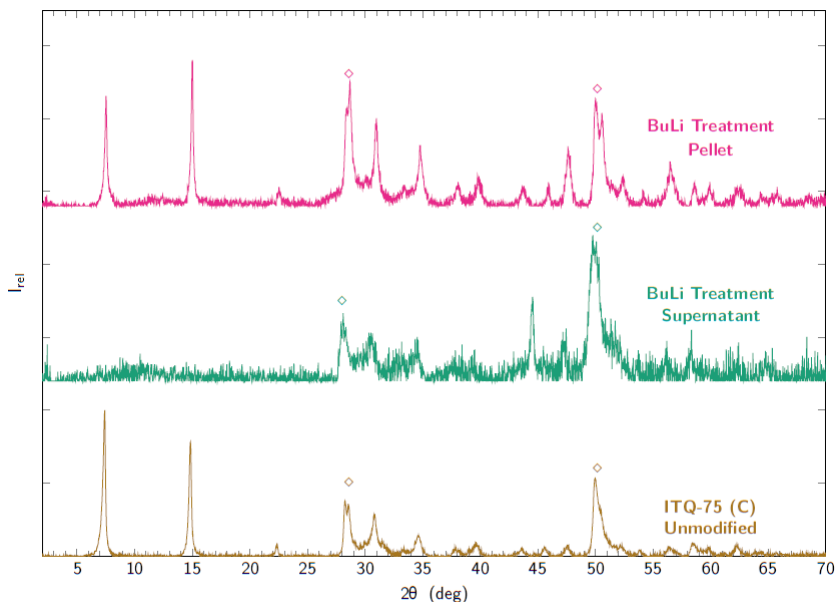
Figure 5.52: PXRD diffraction patterns of ITQ-75, obtained with Compound C as SDA, and after the BuLi treatment, the supernatant (in green) and the pellet (in pink) recovered after centrifuging, where $\diamond$ denotes a ZnS phase

Looking at Figure 5.52, it can be seen that both solids recovered after the butyl lithium treatment undergo changes in their diffraction pattern. The first two diffraction peaks, associated with the laminar phase, disappear from the diffraction pattern of the solid entitled supernatant. This solid, being the one present in the recovered colloid after the first centrifugation cycle, is expected to be the most delaminated. As for the pellet recovered after the first centrifugation cycle, its diffraction pattern shows changes from its original pattern. First, a change in the relative intensity of the diffraction peaks is observed. In the original structure the first diffraction peak is more intense than the second. In the recovered pellet, the most intense diffraction peak becomes the second one. The first two diffraction peaks, associated with the laminar phase, of the as-synthesized structure are located at 2θ equal to 7,4° and 14,8° and have a FWHM equal to 0,27 and 0,25, respectively. After treatment with butyllithium, the recovered pellet difraction peaks are slightly displaced towards larger angles and become thinner. The first diffraction peak is located at 2θ equal to 7,5, with a FWHM equal to 0,25, and the second diffraction peak is located at 2θ equal 15,0°, with a FWHM equal to 0,20. These results thus suggest that this structure is a material that has suffered

a partial attack by butyllithium, since the changes in its diffraction pattern are minimal.

To verify the changes in laminar profile and morphology, HRTEM (see Figures 5.53 and 5.54) was performed on the different samples resulting from the treatment with butyllithium.
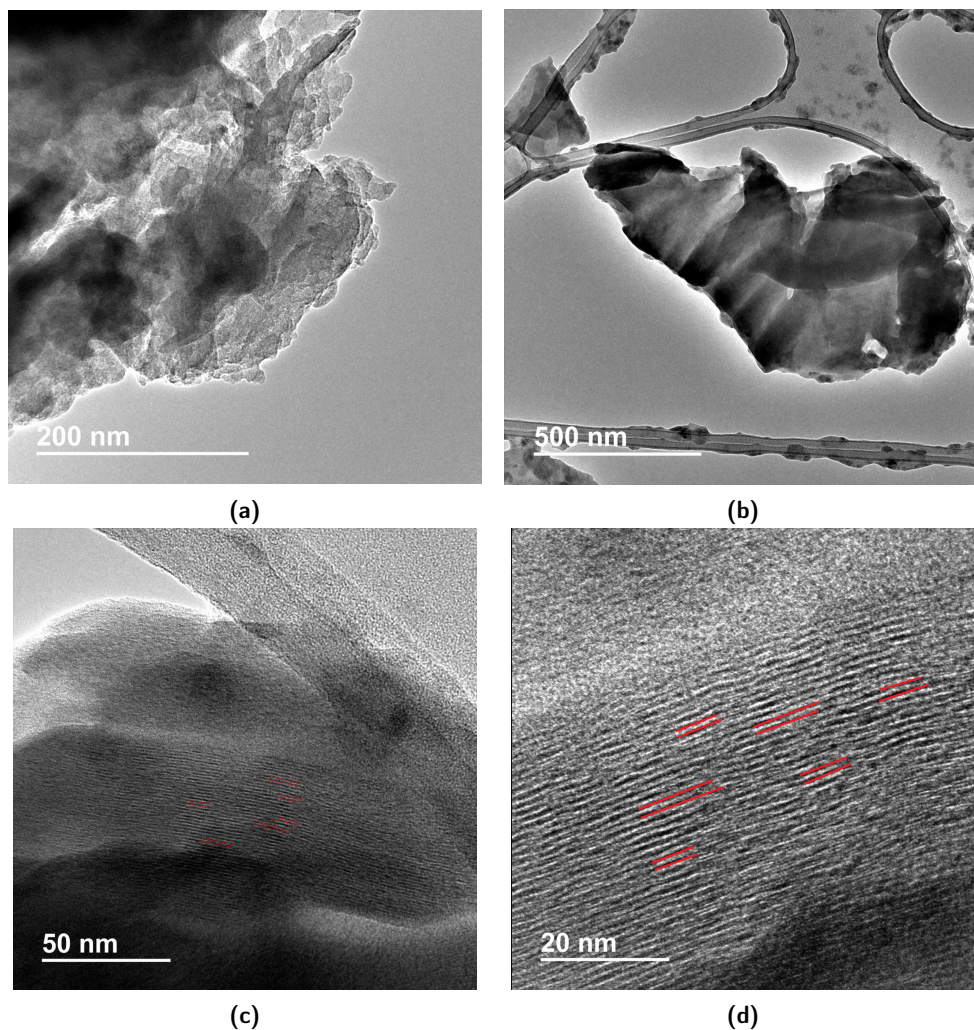
Figure 5.53: ITQ-75' BuLi Supernatant HRTEM images, obtained with Compound C as SDA after, where (5.53a) and (5.53b) highlights its morphology and (5.53c) and (5.53d) the laminar planes, marked in red

253
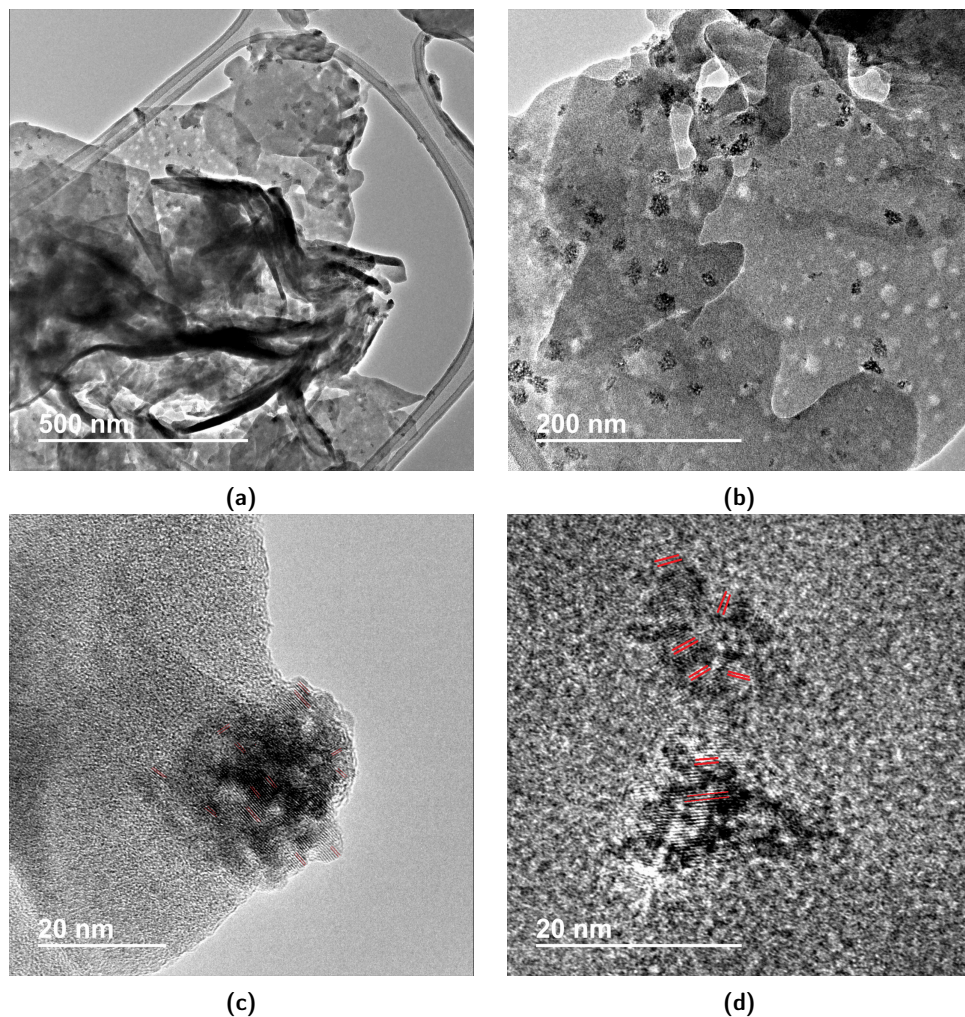
Figure 5.54: ITQ-75' BuLi Pellet HRTEM images, obtained with Compound C as SDA after, where (5.54a) and (5.54b) highlights its morphology and (5.54c) and (5.54d) the laminar planes, marked in red

Looking at Figure 5.53 it can be seen that after the treatment with butyllithium ITQ-75 maintains its laminar profile. The fiber-like particles organized into a ball, previously observed on ITQ-75 as-synthesized, are no longer observable. Only the presence of overlapping laminae with different dimensions is visible. The intercalary laminae are 0,7 $\pm$0,09 nm apart, representing a closer structure when compared

to the original structure. Observing now Figure 5.54, it is verified that the pellet recovered after treatment with BuLi presents an intermediate morphology, between ITQ-75 as-synthesized and the sample obtained after the complete BuLi treatment. The pellet still presents some fiber-like particles, something that was not observed in the sample that undergoes the full treatment with BuLi, but also some isolated laminae, something hardly present in the ITQ-75 as synthesized. It can also be observe the presence of holes and accumulations of small portions of laminae with different orientations on the surface of the crystal (see Figure 5.54b and 5.54c).

Next, to verify the impact that this treatment has on textural properties, N_2 adsorption-desoprtion isotherm was performed (see Figure 5.55 and Table 5.44).
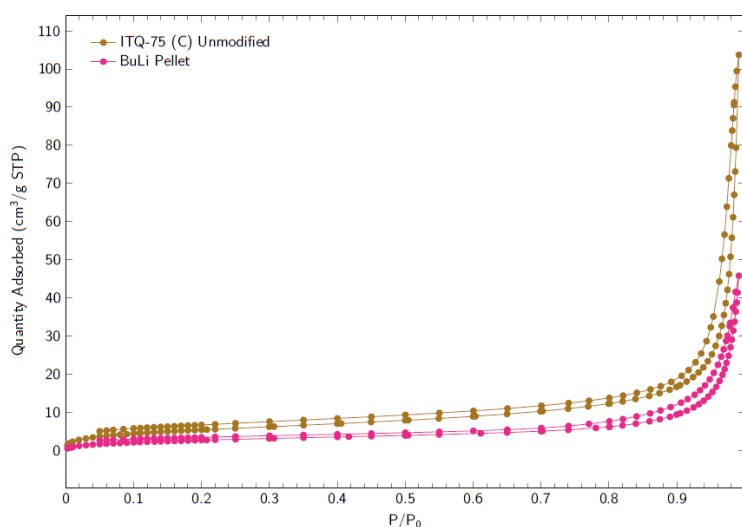
Figure 5.55: N_2 adsorption-desoprtion isotherms of ITQ-75, obtained with Compound C as SDA, before (in brown) and after (in pink) the BuLi treatment

Table 5.44: Textural properties of ITQ-75 obtained with Compound C as SDA before and after the BuLi treatment (n.a. - not available)

	Pore Volume (cm³/g)	BET surface area (m²/g)	t-plot Micropore Area (m²/g)	t-plot External Surface Area (m²/g)
ITQ-75 (C)	0,140	20,2	2,9	17,3
BuLi Pellet	n.a.	10,5	2,5	7,9

Unfortunately, there was not enough mass to perform the analysis of the textural properties of the supernatant recovered after the BuLi treatment. Observing the textural properties of the pellet recovered, it can be seen that it has a lower external surface area. Since it was observed earlier that the first two diffraction peaks of this sample have become thinner after the treatment, it can be hypothesized that this decrease in the external surface area is due to the increase in crystal size. In order to confirm this hypothesis, FESEM was performed (see Figure 5.56).

(a)   (b)
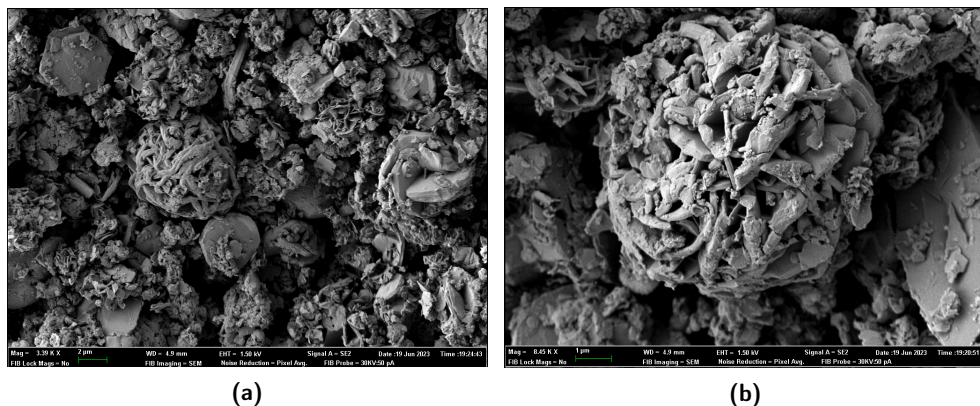
Figure 5.56: FESEM images of the pellet recovred after the BuLi treatment

Observing Figure 5.56, it can be seen that, although the crystal morphology continues to resemble that of a flower, it is possible to find between the different lamina the presence of some kind of "debris". Since this structure is an intermediate stage of the delamination process, it is possible that the "debris" between the laminae is already at a more advanced stage of delamination than the flower-like structures. As for the crystal size of the crystals, it is equal 5 ± 1 µm, confirming the increasing on crystal size when compared to ITQ-75 as synthesized.

ii. Ball Mill Treatment

The second methodology used to increase the samples accessibility by modifying its crystals was through a ball mill treatment. This method has been used previously to reduce the size of crystallites of various materials [50, 51, 52, 53] and is seen as a sustainable process, since it is environmentally-friendly, cost-effective technique [54, 55].

This methodology was applied to ITQ-75 obtained with Compound C as SDA. Different milling times were tested - 30, 90 and 210 minutes. The diffractograms of the different milled samples are present in Figure 5.57 (see Appendix A for more details).
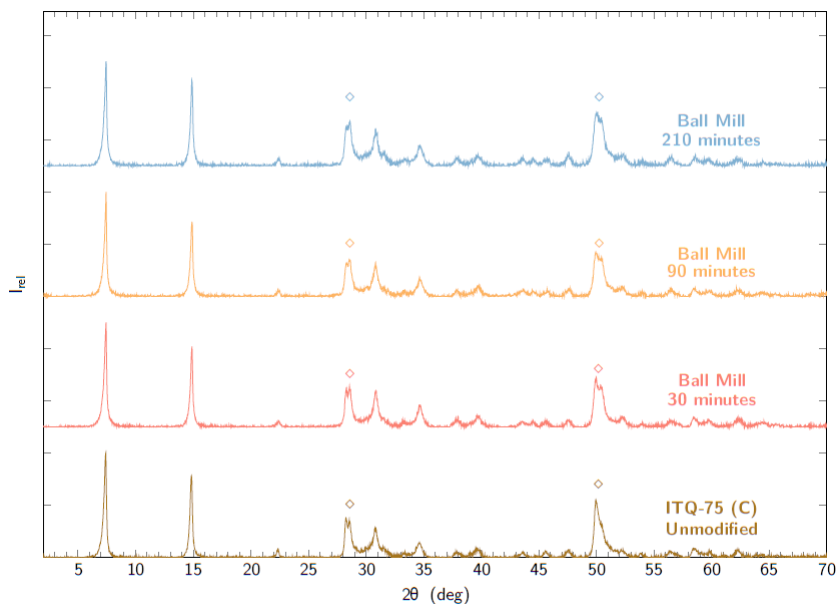
Figure 5.57: PXRD diffraction patterns of ITQ-75, obtained with Compound C as SDA, unmodified (in brown), after 30 minutes (in red), 90 minutes (in orange) and 210 minutes (in blue) of ball mill treatment, where ◇ denotes a ZnS phase

Looking at Figure 5.57, it can be seen that the impact of the different milling times tested was minimum on the diffraction pattern. Looking the the position and the broadening of the first two diffraction peaks, associated with the laminar phase, there are minimum changes after milling. On the as-synthesized structure, the peaks are located at 2θ equal to 7,4° and 14,8° and have a FWHM equal to 0,27 and 0,25, respectively. After milling their position does not change. However, there is a small broadening with increasing milling time.

Afterwards, in order to evaluate the impact that milling had on textural properties, N_2 adsorption-desoprtion isotherms (see Figure 5.58 and Table 5.45) was performed.
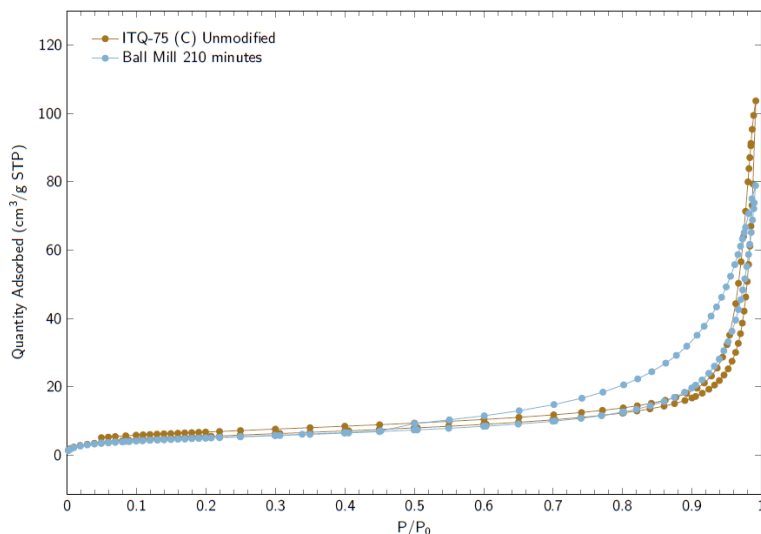
Figure 5.58: N$_2$ adsorption-desoprtion isotherms of ITQ-75, obtained with Compound C as SDA, before (in brown) and after (in blue) milling

Table 5.45: Textural properties of ITQ-75 obtained with Compound C as SDA before and after milling (n.a. - not available)

	Pore Volume (cm³/g)	BET surface area (m²/g)	t-plot Micropore Area (m²/g)	t-plot External Surface Area (m²/g)
ITQ-75 (C)	0,140	20,2	2,9	17,3
Ball Mill 210 minutes	n.a.	18,2	0,1	18,1

Observing Figure 5.58 it can be seen that after the milling treatment the total adsorbed volume decreases and the hysteresis becomes more marked. This shows that the external surface area value was barely affected by this experimental methodology.

5.2.2.3   Final Considerations

In order to increase the accessibility of the structures under study, different methodologies were tested.

The first one is based on the SDA elimination used during the synthesis procedure, through thermal treatment, ionic exchange (with Cs^+ or $CTMA^+$), acid washing or by photodegradation (in the absence or presence of an oxidizing agent). All these methodologies have proven to be ineffective, as they either lead to the collapse of crystal structure or no change in the carbon content. These results show that the presence of SDA is critical for the structures under study to maintain their crystallinity.

As such, methodologies have been tested that allow increasing their accessibility without having to eliminate the SDA present onto the structures. These are based on modifying the crystals, namely reducing their size. Two post-synthesis strategies were tested for this - n-butyllithium and ball mill treatments. With these two methodologies modifications in the textural properties of the materials occur, however it did not translate into an increase in accessibility.

As a result, none of the methodologies tested in this section were successful in increasing the accessibility of the materials.

5.3   Conclusions

The samples synthesized in the previous chapter were modified in order to increase their interaction with UV-Vis radiation - through the addition of dopants - or their accessibility - through modifications to the synthesis process or post synthesis modifications.

Different metals and a Ru-complex were used to modify the electronic structure. The most successful metals were Cu and Co. With the insertion of these metals it was possible to reduce the optical band gap to values equal to 2,0 eV, a very interesting value in view of the final application.

Regarding the methodologies used to increase accessibility, either modification of the synthesis process or post-synthesis methodologies were used. As for modifications to the synthesis process, the insertion of saccharides as coSDA, namely fructose and sucrose, and the modification of the gel viscosity by increasing the EG/H_2O molar ratio were tested. For both methodologies it was found that the main change was in the external surface area. None of the methodologies was successful in increasing the pore volume of the materials under study. By inserting

saccharides into the synthesis gel it is possible to increase the external surface area up to 75,5 m^2/g. As for the increase in gel viscosity by increasing the ethylene glycol content, it was again found that the increase in accessibility is mostly due to the increase in external surface area. With this methodology it is possible to obtain samples with an external surface area up to 77,8 m^2/g. Both methodologies were successful in increasing the external surface area but not in releasing the microporous volume. Finally, since both methodologies allowed to increase the accessibility of the material surface, they were combined. By inserting fructose as coSDA and increasing the gel viscosity, it is possible to obtain samples with an external surface area equal to 108,5 m^2/g.

Regarding the post-synthesis modifications used to increase the accessibility of the materials, these can be divided into two classes, those that would eliminate the SDA present or that would reduce the crystal size. As for the former, none have been successful in maintaining the crystal structure or modifying the organic content. As for the latter, although modifications to textural properties were observed, none translated into an increase in accessibility. Thus, the post-synthesis modifications tested were not successful in increasing the accessibility of the materials under study.

References

[1] Don L. Anderson. "Chemical composition of the mantle". In: *Journal of Geophysical Research: Solid Earth* 88.S01 (1983), B41–B52. DOI: `https://doi.org/10.1029/JB088iS01p00B41`.

[2] Pingwu Du and Richard Eisenberg. "Catalysts made of earth-abundant elements (Co, Ni, Fe) for water splitting: Recent progress and future challenges". In: *Energy Environ. Sci.* 5 (3 2012), pp. 6012–6021. DOI: `10.1039/C2EE03250C`.

[3] P. Sutra and A. Igau. "Emerging Earth-abundant (Fe, Co, Ni, Cu) molecular complexes for solar fuel catalysis". In: *Current Opinion in Green and Sustainable Chemistry* 10 (2018). Green Catalysis, pp. 60–67. ISSN: 2452-2236. DOI: `https://doi.org/10.1016/j.cogsc.2018.03.004`.

[4] Jingjing Wang et al. "Nanostructured Metal Sulfides: Classification, Modification Strategy, and Solar-Driven CO$_2$ Reduction Application". In: *Advanced Functional Materials* (), p. 2008008. DOI: `https://doi.org/10.1002/adfm.202008008`.

[5]   Gaofei Xue et al. "Recent advances in various applications of nickel cobalt sulfide-based materials". In: *J. Mater. Chem. A* 10 (15 2022), pp. 8087–8106. DOI: 10.1039/D2TA00305H.

[6]   Frédérique Loiseau et al. "An artificial antenna complex containing four Ru(bpy)$^{32+}$-type chromophores as light-harvesting components and a Ru(bpy)(CN)$_{42}$ subunit as the energy trap. A structural motif which resembles the natural photosynthetic systems". In: *Chem. Commun.* (2 2003), pp. 286–287. DOI: 10.1039/B211122E.

[7]   Daibin Kuang et al. "High Molar Extinction Coefficient Heteroleptic Ruthenium Complexes for Thin Film Dye-Sensitized Solar Cells". In: *Journal of the American Chemical Society* 128.12 (2006), pp. 4146–4154. DOI: 10.1021/ja058540p.

[8]   C.-Y. Chen et al. "A New Route to Enhance the Light-Harvesting Capability of Ruthenium Complexes for Dye-Sensitized Solar Cells". In: *Advanced Materials* 19.22 (2007), pp. 3888–3891. DOI: https://doi.org/10.1002/adma.200701111.

[9]   Georgios C. Vougioukalakis et al. "A Ruthenium-Based Light-Harvesting Antenna Bearing an Anthracene Moiety in Dye-Sensitized Solar Cells". In: *Asian Journal of Organic Chemistry* 3.9 (2014), pp. 953–962. DOI: https://doi.org/10.1002/ajoc.201402096.

[10]   Tao Wu et al. "Phase Selection and Site-Selective Distribution by Tin and Sulfur in Supertetrahedral Zinc Gallium Selenides". In: *Journal of the American Chemical Society* 133.24 (2011), pp. 9616–9625. DOI: https://doi.org/10.1021/ja203143q.

[11]   Nan-Nan Shen et al. "Discrete Supertetrahedral T3 InQ Clusters (Q = S, S/Se, Se, Se/Te): Ionothermal Syntheses and Tunable Optical and Photodegradation Properties". In: *Crystal Growth & Design* 18.2 (2018), pp. 962–968. DOI: https://doi.org/10.1021/acs.cgd.7b01437.

[12]   A. R. Zanatta. "Revisiting the optical bandgap of semiconductors and the proposal of a unified methodology to its determination". In: *Scientific Reports* 9 (2019), p. 11225. DOI: 10.1038/s41598-019-47670-y.

[13]   J. Tauc, R. Grigorovici, and A. Vancu. "Optical Properties and Electronic Structure of Amorphous Germanium". In: *physica status solidi (b)* 15.2 (1966), pp. 627–637. DOI: https://doi.org/10.1002/pssb.19660150224.

[14]   Takahiro Shinada et al. "Enhancing semiconductor device performance using ordered dopant arrays". In: *Nature Letters* 437 (2005), pp. 1128–1131. DOI: https://doi.org/10.1038/nature04086.

[15] Baotao Kang et al. "Importance of doping site of B, N, and O in tuning electronic structure of graphynes". In: *Carbon* 105 (2016), pp. 156–162. ISSN: 0008-6223. DOI: `https://doi.org/10.1016/j.carbon.2016.04.032`.

[16] Xitong Chen et al. "Charge- and Size-Complementary Multimetal-Induced Morphology and Phase Control in Zeolite-Type Metal Chalcogenides". In: *Chemistry – A European Journal* 24.42 (July 2018), pp. 10812–10819. DOI: `https://doi.org/10.1002/chem.201801571`.

[17] Beatriz Silva Gaspar et al. "ITQ-76 Crystallised Solid and Method for Preparing Same". December 15, 2022, WO/2022/258473.

[18] José María Moreno et al. "Single-Layered Hybrid Materials Based on 1D Associated Metalorganic Nanoribbons for Controlled Release of Pheromones". In: *Angewandte Chemie International Edition* 55.37 (2016), pp. 11026–11030. DOI: `https://doi.org/10.1002/anie.201602215`.

[19] S. Sebastian et al. "Investigations on Fe doped SnS thin films by nebulizer spray pyrolysis technique for solar cell applications". In: *Journal of Materials Science: Materials in Electronics* 30 (2019), pp. 8024–8034. DOI: `10.1007/s10854-019-01124-3`.

[20] Lili Sun et al. "Electronic structure and optical properties of Fe-doped SnS_2 from first-principle calculations". In: *RSC Adv.* 6 (5 2016), pp. 3480–3486. DOI: `10.1039/C5RA20980C`.

[21] Saima Zafar et al. "Effect of Fe doping on the structural and optical properties of ZnS macro-spheres". In: *Optik* 262 (2022), p. 169342. ISSN: 0030-4026. DOI: `https://doi.org/10.1016/j.ijleo.2022.169342`.

[22] T.V. Vineeshkumar et al. "Fe induced optical limiting properties of $Zn_{1x}Fe_xS$ nanospheres". In: *Optics Laser Technology* 99 (2018), pp. 220–229. ISSN: 0030-3992. DOI: `https://doi.org/10.1016/j.optlastec.2017.09.006`.

[23] Fran Kurnia and Judy N. Hart. "Band-Gap Control of Zinc Sulfide: Towards an Efficient Visible-Light-Sensitive Photocatalyst". In: *ChemPhysChem* 16.11 (2015), pp. 2397–2402. DOI: `https://doi.org/10.1002/cphc.201500264`.

[24] Akihiko Kudo and Masahiko Sekizawa. "Photocatalytic H_2 evolution under visible light irradiation on Ni-doped ZnS photocatalyst". In: *Chem. Commun.* (15 2000), pp. 1371–1372. DOI: `10.1039/B003297M`.

[25] Archana Kumari Singh, Satya Pal Singh, and Priya Yadav. "Synthesis and Characterization of Structural and Optical Properties of Ni-doped Zinc Sulphide Nanoparticles". In: *Journal of Advanced Scientific Research* (13 2022), pp. 87–93.

[26] Jamil K. Salem et al. "Structural and Optical Properties of Co-doped ZnS Nanoparticles Synthesized by a Capping Agent". In: *Journal of Materials Science: Materials in Electronics* (25 2014), pp. 2177–2182.

[27] S. Sambasivam et al. "Doping induced magnetism in Co–ZnS nanoparticles". In: *Journal of Solid State Chemistry* 182.10 (2009), pp. 2598–2601. ISSN: 0022-4596. DOI: https://doi.org/10.1016/j.jssc.2009.07.015.

[28] Lingyun Liu et al. "Optical properties of water-soluble Co^{2+}:ZnS semiconductor nanocrystals synthesized by a hydrothermal process". In: *Materials Letters* 66.1 (2012), pp. 121–124. ISSN: 0167-577X. DOI: https://doi.org/10.1016/j.matlet.2011.08.025.

[29] Rosy Rahman et al. "Tuning of structural and optical properties with enhanced catalytic activity in chemically synthesized Co-doped MoS_2 nanosheets". In: *RSC Adv.* 11 (3 2021), pp. 1303–1319. DOI: 10.1039/D0RA08229E.

[30] T S Moss. "The Interpretation of the Properties of Indium Antimonide". In: *Proceedings of the Physical Society. Section B* 67.10 (Oct. 1954), p. 775. DOI: 10.1088/0370-1301/67/10/306.

[31] Elias Burstein. "Anomalous Optical Absorption Limit in InSb". In: *Phys. Rev.* 93 (3 Feb. 1954), pp. 632–633. DOI: 10.1103/PhysRev.93.632.

[32] Soniya Gahlawat et al. "Exploring Burstein–Moss type effects in nickel doped hematite dendrite nanostructures for enhanced photo-electrochemical water splitting". In: *Phys. Chem. Chem. Phys.* 21 (36 2019), pp. 20463–20477. DOI: 10.1039/C9CP04132J.

[33] Timothy J. Boyle et al. "Synthesis and optical properties of naturally occurring fluorescent mineral, ferroan sphalerite, inspired (Fe,Zn)S nanoparticles". In: *Journal of Materials Science* 42 (2007), pp. 2792–2795.

[34] S. Sambasivam et al. "Optical and ESR studies on Fe doped ZnS nanocrystals". In: *Physics Letters A* 373.16 (2009), pp. 1465–1468. ISSN: 0375-9601. DOI: https://doi.org/10.1016/j.physleta.2009.02.032.

[35] Yanan Li, Chuanbao Cao, and Zhuo Chen. "Magnetic and optical properties of Fe doped ZnS nanoparticles synthesized by microemulsion method". In: *Chemical Physics Letters* 517.1 (2011), pp. 55–58. ISSN: 0009-2614. DOI: https://doi.org/10.1016/j.cplett.2011.09.048.

[36] Sunil Kumar and N. K. Verma. "Structural, optical and magnetic investigations on Fe-doped ZnS nanoparticles". In: *Journal of Materials Science: Materials in Electronics* 26 (2015), pp. 2754–2759. DOI: 10.1039/D0RA08229E.

[37] Minting Hao et al. "Soluble Supertetrahedral Chalcogenido T4 Clusters: High Stability and Enhanced Hydrogen Evolution Activities". In: *Inorganic Chemistry* 58.8 (2019), pp. 5126–5133. DOI: https://doi.org/10.1021/acs.inorgchem.9b00207.

[38] Xitong Chen et al. "Selective Ion Exchange and Photocatalysis by Zeolite-Like Semiconducting Chalcogenide". In: *Chemistry – A European Journal* 23.49 (Sept. 2017), pp. 11913–11919. DOI: https://doi.org/10.1002/chem.201702418.

[39] Xiaomei Yang et al. "Synthesis of hierarchical AlPO-n molecular sieves templated by saccharides". In: *Microporous and Mesoporous Materials* 144.1 (2011), pp. 176–182. ISSN: 1387-1811. DOI: https://doi.org/10.1016/j.micromeso.2011.04.011.

[40] Ivana Miletto et al. "Hierarchical SAPO-34 Architectures with Tailored Acid Sites using Sustainable Sugar Templates". In: *ChemistryOpen* 7.4 (2018), pp. 297–301. DOI: https://doi.org/10.1002/open.201800001.

[41] Matthias Thommes et al. In: *Pure and Applied Chemistry* 87.9-10 (2015), pp. 1051–1069. DOI: doi:10.1515/pac-2014-1117.

[42] P. Scherrer. "Bestimmung der Größe und der inneren Struktur von Kolloidteilchen mittels Röntgenstrahlen". In: *Nachrichten von der Gesellschaft der Wissenschaften zu Göttingen, Mathematisch-Physikalische Klasse* 1918 (1918), pp. 98–100.

[43] A. R. Patel and A. Venkateswara Rao. "Crystal growth in gel media". In: *Bulletin of Materials Science* 4 (1982), pp. 527–548. DOI: 10.1007/BF02824961.

[44] Qipu Lin et al. "Mimicking High-Silica Zeolites: Highly Stable Germanium- and Tin-Rich Zeolite-Type Chalcogenides". In: *Journal of the American Chemical Society* 137.19 (2015), pp. 6184–6187. DOI: https://doi.org/10.1021/jacs.5b03550.

[45] E Benavente et al. "Intercalation chemistry of molybdenum disulfide". In: *Coordination Chemistry Reviews* 224.1 (2002), pp. 87–109. ISSN: 0010-8545. DOI: https://doi.org/10.1016/S0010-8545(01)00392-7.

[46] Luwei Sun, Hubiao Huang, and Xinsheng Peng. "Laminar MoS_2 membranes for molecule separation". In: *Chem. Commun.* 49 (91 2013), pp. 10718–10720. DOI: 10.1039/C3CC46136J.

[47]   Mark A. Lukowski et al. "Enhanced Hydrogen Evolution Catalysis from Chemically Exfoliated Metallic MoS_2 Nanosheets". In: *Journal of the American Chemical Society* 135.28 (2013), pp. 10274–10277. DOI: 10.1021/ja404523s.

[48]   Manish Chhowalla et al. "The chemistry of two-dimensional layered transition metal dichalcogenide nanosheets". In: *Nature Chemistry* 5 (2013), pp. 263–275. DOI: 10.1038/nchem.1589.

[49]   Guoliang Liu et al. "MoS_2 monolayer catalyst doped with isolated Co atoms for the hydrodeoxygenation reaction". In: *Nature Chemistry* 9 (2017), pp. 810–816. DOI: 10.1038/nchem.2740.

[50]   Neeraj Sharma, Tilak Raj, and Kamal Kumar Jangra. "Microstructural Evaluation of NiTi-powder, Steatite, and Steel Balls After Different Milling Conditions". In: *Materials and Manufacturing Processes* 31.5 (2016), pp. 628–632. DOI: 10.1080/10426914.2015.1004710.

[51]   Peng Lv et al. "Effect of ball milling and cryomilling on the microstructure and first hydrogenation properties of TiFe+4wt.% Zr alloy". In: *Journal of Materials Research and Technology* 8.2 (2019), pp. 1828–1834. ISSN: 2238-7854. DOI: https://doi.org/10.1016/j.jmrt.2018.12.013.

[52]   F.N. Tenorio Gonzalez et al. "Reducing the crystallite and particle size of $SrFe_{12}O_{19}$ with PVA by high energy ball milling". In: *Journal of Alloys and Compounds* 771 (2019), pp. 464–470. ISSN: 0925-8388. DOI: https://doi.org/10.1016/j.jallcom.2018.08.297.

[53]   Ardhy Purwo Nugroho, Masruroh, and Setyawan P. Sakti. "The design and optimization process of ball mill to reduce particle size of calcium carbonate materials". In: *AIP Conference Proceedings* 2296.1 (2020), p. 020112. DOI: 10.1063/5.0030531.

[54]   Carmen C. Piras, Susana Fernández-Prieto, and Wim M. De Borggraeve. "Ball milling: a green technology for the preparation and functionalisation of nanocellulose derivatives". In: *Nanoscale Adv.* 1 (3 2019), pp. 937–947. DOI: 10.1039/C8NA00238J.

[55]   Charitha Thambiliyagodage and Ramanee Wijesekera. "Ball milling – A green and sustainable technique for the preparation of titanium based materials from ilmenite". In: *Current Research in Green and Sustainable Chemistry* 5 (2022), p. 100236. ISSN: 2666-0865. DOI: https://doi.org/10.1016/j.crgsc.2021.100236.

Photocatalytic Performance

Chapters 5 and 6 were devoted to the synthesis and characterization of IZM-5, ITQ-75 and ITQ-76 structures and to their modification, namely their electronic structure and surface accessibility. These modifications were performed in order to develop materials with characteristics that would best fit the desired final application. As such, the optical band gap value was adjusted to be more in line with the solar spectrum and the external surface area was increased to facilitate surface exchanges.

Hence, after obtaining and studying the different materials and taking into account the social context presented in Chapter 1, it was decided to evaluate their photocatalytic performance with the CO$_2$ photoreduction reaction.

6.1   CO$_2$ Photoreduction Reaction

The reaction chosen to evaluate the photocatalytic performance of the different samples was the CO$_2$ photoreduction. Apart from the high social and economic interest associated with this reaction as shown in Chapter 1, the use of these materials as photocatalysts in this reaction has been little studied, as seen in Chapter 2.

After testing the different materials (IZM-5 and ITQ-75 modified samples) under the experimental conditions given in Section A.5 no carbon based products were detected, only H$_2$. In order to verify that everything was working correctly with the unit, P25 and P25 with 1wt.% Pt photodeposited were tested, whose behaviors are well described in the literature [1]. However, both materials show no production of carbon products, only H$_2$ production.

Comparing the experimental conditions used with those reported in the literature for CO$_2$ photoreduction batch mode in a gas-solid system, they start at a pressure of 71 kPa [1], 150 kPa [2] or 172 kPa [3], pressures well above those used in this study of 10 kPa. Due to the installed pressure relief valve, which is set to 60 kPa for safety reasons, it was not possible to test the experimental conditions reported in the literature with the unit available. Thompson et al. [4] reviewed and analyze the different factors influencing the CO$_2$ photoreduction kinetics. Light transport, reactor geometry, temperature and pressure impact the photocatalyts performance. However, according to the Langmuir-Hinshelwood type kinetic model proposed by Tahir and Amin [5], for a low H$_2$O/CO$_2$ ratio the pressure effect on the reaction rate can be negligible [2]. However, the major difference between the experimental conditions used and those described in the literature [1, 2, 3] was the initial pressure used. Thus, although pressure does not appear to be a major factor influencing

reactivity at the given H_2O/CO_2 ratio, higher initial pressures would have to be tested to verify this hypothesis.

Taking into account the experimental results obtained, the photocatalytic performance of the synthesized materials was inconclusive, so nothing can be said about the possible use of these materials in the CO_2 photoreduction.

6.2 Photocatalytic Water Splitting

Considering the results obtained in the previous reaction, it was decided to evaluate the photocatalytic performance of the materials under study in the water splitting process. This reaction, as shown in Chapters 1 and 2, is of high interest considering the final product obtained and the system simplicity.

Due to the high versatility of the experimental points taken, it was necessary to model the results obtained. Such modeling procedure is detailed in Appendix G. In addition, modeling ensures that the materials were compared at the same reaction time, namely at their initial performance. This is significant because the different materials could present different deactivation rates and mechanisms, thus making it quite complicate to compare the different observable performances. It is important to highlight that such modeling was solely based on mathematical considerations, by fitting the shape of a curve with the experimental points and to get the better mathematical description possible, with no typical kinetic law to be found relevant. Thus, and since no thermodynamic equilibrium considerations were not taken into account, the model obtained is a pseudo kinetic model, including the constants derive from the modeling.
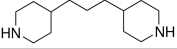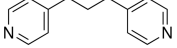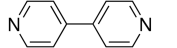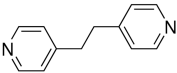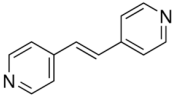
Three paramaters were used to evaluate the photocatalytic performance. The first parameter, the initial H_2 rate, allowed to evaluate the H_2 productivity. The second parameter, the initial apparent quantum yield, allowed to assess the generation, separation and transport of charge carries, electrons e^- and holes h^+, towards the surface and the chemical species involved in the desired reaction. As for the last parameter, the initial solar to fuel yield, it allows the evaluation of the global energetic yield of the reaction under study.

In order to compare the different materials under study, firstly a comparison between the materials without any modification will be done. After that, the impact that the different modifications previously done to improve the material's reactivity, have on the photocatalytic performance.

270

6.2.1 Unmodified materials - IZM-5 and ITQ-75

The photocatalytic performance evaluation is going to be started with the comparison between the different structures under study, IZM-5 and ITQ-75, without any modification. The purpose is to evaluate the impact that the different crystal structures and the different SDAs present have on the photocatalytic performance. Their main characteristics are systematized in the Table 6.1.

Table 6.1: Unmodified IZM-5 and ITQ-75 main features

Structure	SDA	Reference	Chemical Formula	Chemical Representation	Area (m²/g)		E_g (eV)
					S_μ	S_{ext}	
IZM-5	1,3-Bis(4-piperidyl)propane	Compound A	$C_{13}H_{26}N_2$		0,0	15,1	3,1
ITQ-75	1,3-Bis(4-pyridyl)propane	Compound B	$C_{13}H_{14}N_2$		0,5	11,4	2,7
	4,4'-Dipyridyl	Compound C	$C_{10}H_8N_2$		2,9	17,3	2,2
	1,2-Bis(4-pirydyl)ethane	Compound D	$C_{12}H_{12}N_2$		3,3	37,2	2,5
	1,2-Di(4-pyridyl)ethylene	Compound E	$C_{12}H_{10}N_2$		4,6	49,9	2,2

The initial H_2 rate, apparent quantum yield and solar to fuel yield of the different materials under study are represent, according to their optical band gap value E_g and external surface area S_{ext}, on Figures 6.1, 6.2 and 6.3, respectively.
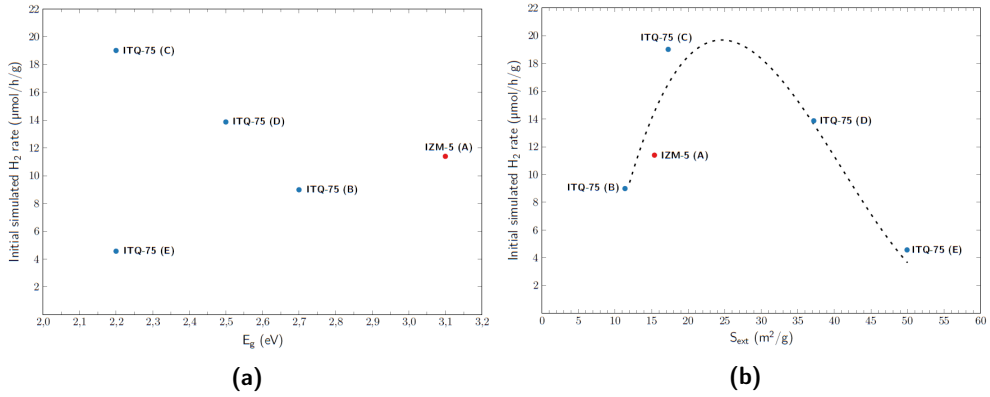
Figure 6.1: Initial simulated H_2 rate of IZM-5 (in red) and ITQ-75 series (in blue) according to (6.1a) their optical band gap value E_g and (6.1b) their external surface area area S_{ext}
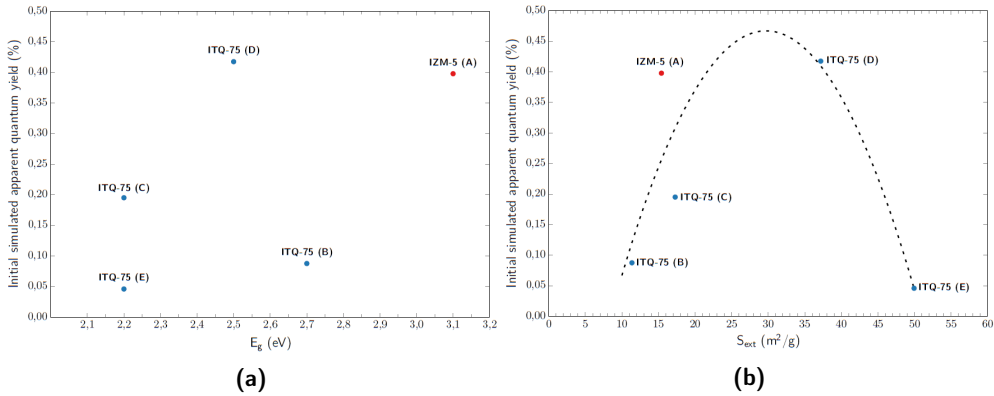
Figure 6.2: Initial simulated apparent quantum yield of IZM-5 (in red) and ITQ-75 series (in blue) according to (6.2a) their optical band gap value E_g and (6.2b) their external surface area area S_{ext}

(a) (b)
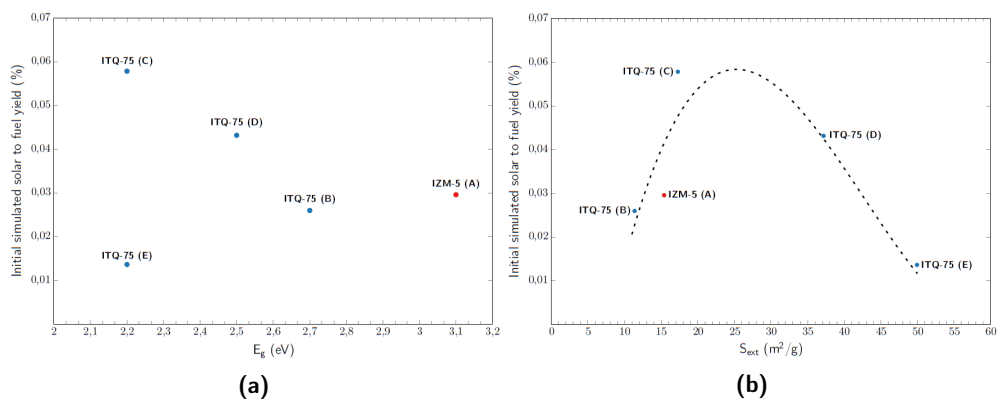
Figure 6.3: Initial simulated solar to fuel yield of IZM-5 (in red) and ITQ-75 series (in blue) according to (6.3a) their optical band gap value E_g and (6.3b) their external surface area S_{ext}

Looking at the productivity of the different samples (see Figure 6.1), it can be seen that the sample with the highest productivity is ITQ-75 obtained with Compound C as SDA, with a H_2 production equal to 19,0 μmol/h/g. Regarding the relation between the material's characteristics, namely its optical band gap value E_g or its external surface area S_{ext}, and their productivity it is observed that with the E_g there is no observable correlation between it and the observed productivity (see Figure 6.1a). As for the external surface area S_{ext}, a volcano-like curve can be used to correlate the S_{ext} with the observed productivity.

In relation to the apparent quantum yield (see Figure 6.2), it can be noticed that the structures with the highest apparent quantum yield are the IZM-5, obtained with Compound A as SDA, or the ITQ-75 obtained with Compound D as SDA, with a value equal to 0,40%. As with the H_2 productivity, only the external surface area seems to be correlated with the apparent quantum yield, with a volcano-like curve (see Figure 6.3b).

Finally, concerning the global energetic yield of the process (see Figure 6.3), as was previously observed for the productivity, the material which presents the highest solar to fuel yield is ITQ-75 obtained with Compound C as SDA, with a value equal to 0,06%. This parameter has a similar behavior to that previously observed for the H_2 productivity, with a similar relationship between the external surface area and its energetic yield. It is possible to observe that when the optical band gap is decreased to 2,2 eV the solar to fuel yield increases. This possible trend however does not apply to ITQ-75 obtained with Compound E as SDA.

Therefore, it is verified that for the unmodified structures the optical band gap value does not allow to correlate with the three parameters used to evaluate the photocatalytic performance.

By looking at the two materials with the lower optical band gap value, i. e. ITQ-75 obtained with Compounds C and E as SDA, it is verified that the one obtained with Compound C as SDA presents the highest productivity and the highest energy yield, although the one obtained with Compound E as SDA presents the highest external surface area. Hence, besides the interaction with radiation and the ability to produce charge carriers, there are other parameters that interfere with the final photocatalytic performance. As noted earlier (see Chapter 2), and although there is still some controversy about this [6], it is desirable to obtain materials with high crystallinity, since the defects and the boundaries in the crystalline framework act as traps, thus facilitating the charge recombination [7, 8]. As for the influence of surface area, a high surface area is desirable, as it allows for a greater number active sites to be available. However, a high surface area also implies a higher number of surface defect sites [9]. Lukic et al. [10], by studying the influence that the degree of crystallinity and the specific surface area have on the photocatalytic performance, concluded that the highest overall water splitting activity is obtained when an optimum ratio between a high degree of crystallinity and specific surface area is verified. This information serves as a possible explanation to the apparent correlation found between the external surface area and the different parameters used to quantify the photocatalytic performance. The volcano-type curve evidences the presence of an optimum value for it. Therefore, a higher external surface area leads to a higher number of defects, which has as a possible consequence a lower photocatalytic reactivity. Furthermore, it would allow to explain the different solar to fuel yields of the ITQ-75 samples obtained with Compound C and E as SDAs.
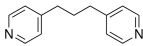
These results highlight the possible importance that crystallinity has on photocatalytic performance. It is also shown that it is likely that, for the same structure, the different SDAs used impact the final crystallinity.

6.2.2 Doped Structures

6.2.2.1 ITQ-75 obtained with Compound B as SDA

After evaluating the photocatalytic performance of the different unmodified materials, the performance of the materials doped with different metals will be assessed. Firstly, the impact of different doping agents on ITQ-75 obtained with Compound B as SDA is evaluated. The main characteristics of these materials are systematized in the Table 6.2.

Table 6.2: Metal-doped ITQ-75, obtained with Compound B as SDA, main characteristicas (n.a. - not available)

Structure	SDA	Reference	Chemical Representation	Doping	Formula	Area (m²/g)		E_g (eV)
						S_μ	S_{ext}	
				-	$Sn_{3,52}Zn_{1,27}S_8 \cdot C_{10,59}H_{12,24}N_{1,68}$	0,5	11,4	2,7
				0,1 % Cu	$Sn_{1,72}Zn_{0,70}Cu_{1,70}S_8 \cdot C_{10,14}H_{11,13}N_{1,53}$	0	95,8	2,3
				0,2% Cu	$Sn_{2,47}Zn_{1,02}Cu_{1,17}S_8 \cdot C_{13,58}H_{15,28}N_{1,90}$	5,9	72,7	2,1
ITQ-75	1,3-Bis(4-pyridyl)propane	Compound B		0,1 % Fe	$Sn_{2,19}Zn_{1,04}Fe_{1,00}S_8 \cdot C_{20,80}H_{21,52}N_{2,64}$	3,1	39,2	2,1
				0,05% Ni	$Sn_{4,42}Zn_{2,00}Ni_{0,88}S_8 \cdot C_{11,25}H_{12,66}N_{1,60}$	0	20,3	2,1
				0,05% Co	$Sn_{2,82}Zn_{1,48}Co_{0,31}S_8 \cdot C_{13,41}H_{14,85}N_{1,71}$	0	49,4	2,1
				0,1% Co	$Sn_{1,91}Zn_{0,89}Co_{0,77}S_8 \cdot C_{12,83}H_{15,98}N_{1,53}$	0	31,8	n.a.
				0,2% Co	$Sn_{2,25}Zn_{0,94}Co_{1,41}S_8 \cdot C_{12,07}H_{21,42}N_{1,53}$	1,8	14,1	2,1

The H_2 productivity of the different samples presented in Table 6.2 are represented in Figure 6.4, as well as their apparent quantum and energetic yields in Figures 6.5 and 6.6, respectively.

(a)

(b)
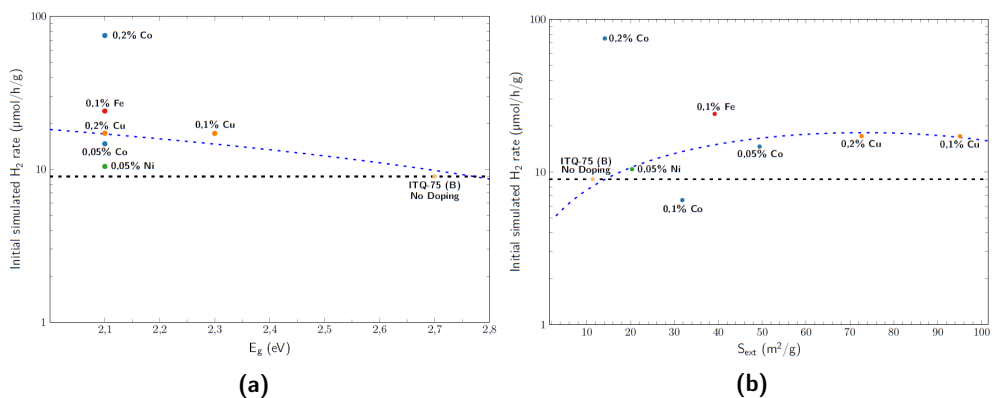
Figure 6.4: Initial simulated H_2 rate of undoped ITQ-75 obtained with Compound B as SDA (in yellow), doped with iron (in red), with copper (in orange), with nickel (green) and with cobalt (in blue), according to (6.4a) their optical band gap value E_g and (6.4b) their external surface area S_{ext}
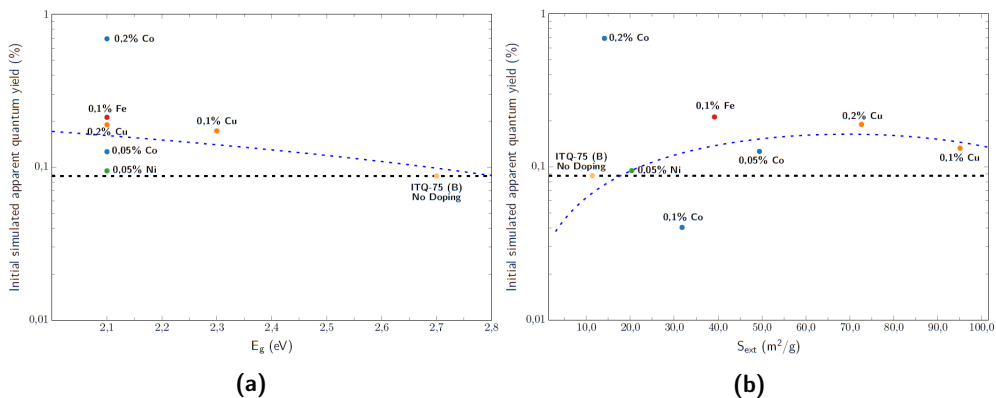
Figure 6.5: Initial simulated apparent quantum yield of undoped ITQ-75 obtained with Compound B as SDA (in yellow), doped with iron (in red), with copper (in orange), with nickel (green) and with cobalt (in blue), according to (6.5a) their optical band gap value E_g and (6.5b) their external surface area area S_{ext}
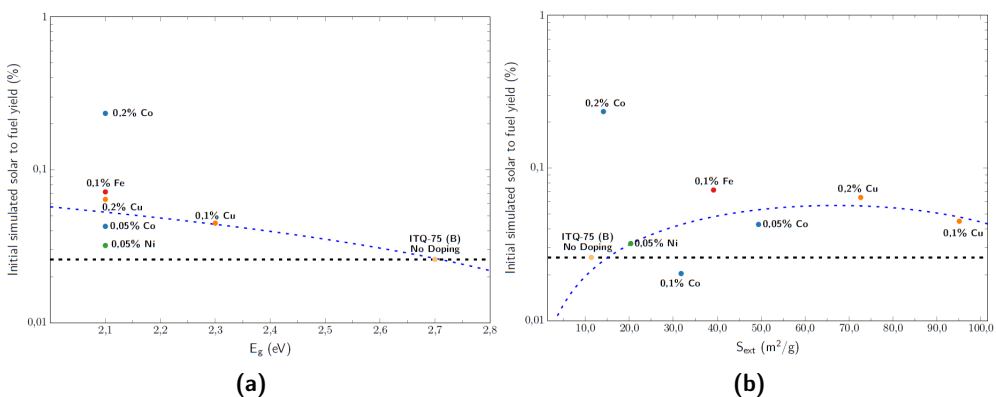
Figure 6.6: Initial simulated solar to fuel yield of undoped ITQ-75 obtained with Compound B as SDA (in yellow), doped with iron (in red), with copper (in orange), with nickel (green) and with cobalt (in blue), according to (6.6a) their optical band gap value E_g and (6.6b) their external surface area S_{ext}

By observing Figure 6.4 it can be seen that the sample with the highest H_2 productivity is the one doped with 0,2% Co, presenting a H_2 productivity equal to 75,1 µmol/h/g, representing an eight-fold increase over the unmodified material. However, the consequences of cobalt doping are not linear. When ITQ-75 obtained with Compound B is doped with 0,05% Co, there is an increase in H_2 productivity,

from 9,0 to 14,7 μmol/h/g. When the amount of cobalt increases to 0,1%, the H_2 productivity remains similar to the undoped sample. Regarding the consequences of the copper presence as a dopant, regardless of the concentration tested, there is an increase in H_2 productivity, from 9,0 to 17,2 μmol/h/g. As for the only sample doped with iron, by adding 0,1% to the ITQ-75 obtained with Compound B as SDA, it was possible to increase the H_2 productivity about three times, from 9,0 to 24,1 μmol/h/g. Concerning the presence of nickel, it was observed that for the only concentration tested, it had little impact on the H_2 productivity observed.

As for the impact that the dopants had on the apparent quantum yield (see Figure 6.5), it can be seen that the sample with the highest H_2 productivity is the one with the highest apparent quantum yield. By doping ITQ-75 obtained with Compound B as SDA with 0,2% Co, it is possible to increase the apparent quantum yield from 0,09% to 0,69%. Although doping allows to decrease the optical band gap value E_g for all the tested samples, such decrease does not directly translate into an increase on the apparent quantum yield (see Figure 6.5a). By looking at the Cu-doped samples, it is possible to see that, although they present different E_g values, both present similar apparent quantum yields. Looking at samples with E_g values equal to 2,1 eV, it is possible to see that they present different apparent quantum yields. Therefore, solely the optical band gap value E_g does not explain the behavior observed for the apparent quantum yield. Therefore, as was seen earlier with the unmodified samples, the material performances cannot be explained by electronic effects alone.

Finally, regarding the global energetic yield (see Figure 6.6), this presents a behavior similar to what was previously observed for the H_2 productivity. The sample with the highest global energetic yield is the one doped with 0,2% Co. By adding 0,2% Co as doping agent it is possible to increase the solar to fuel yield nine times, from 0,03% to 0,23%.

Comparing the different parameters used to evaluate the photocatalysts performance of the doped structures with their optical band gap value and their external surface area, it is possible to trace a linear and a volcano-type curve correlation between them, respectively. As discussed previously for the unmodified materials, the observed relationship between the photocatalytic performance and the external surface area can be explained as an optimal balance between external surface accessibility and a high crystallinity [10]. Regarding the relationship between the optical band gap value and the observed photocatalytic performance, it is necessary to recall the fundamental characteristics of a semiconductor to carry out the reaction under study [11, 12]. For a semiconductor to be photo-active in the overall water splitting it is necessary that the conduction and the valence edge potentials to be align with the potentials of the species involved, the optical band

gap value to be smaller than 3,0 eV to take advantage of the solar spectrum and to be physicochemically stable during the photocatalytic reaction. The standard free energy for overall water splitting is 1,23 eV. However, according to Gerischer [13], in order to overcome the overpotential associated with water oxidation and proton reduction, it is necessary for the semiconductor to generate a potential much greater than 1,23 eV, suggesting that the band gap value should not be bellow 2,3 eV. Therefore, a compromise regarding the optical band gap value has to be reached. On the one hand, it is necessary that the material exhibits an optical band gap below 3 eV, in order to take maximum advantage of the solar spectrum, but high enough to overcome the overpotential associated with the water oxidation and proton reduction [12]. Acar et al. [14] evaluated the photocatalytic performance of 49 different materials and concluded that the ideal range of values for the optical band gap is between 1,9 eV and 2,4 eV. With the addition of doping agents it is possible to obtain materials with optical band gap values within the optimal range observed by Acar et al. [14]. Thus, the addition of doping agents in ITQ-75 obtained with Compound B as SDA appears to allow to increase the photocatalytic performance.

Besides considering the optical band gap value and the external surface area to correlate with the photocatalytic performance, the dopant/Sn molar ratio was used in order to evaluate the impact of the chemical composition (see Figure 6.7).

(a)

(b)

(c)
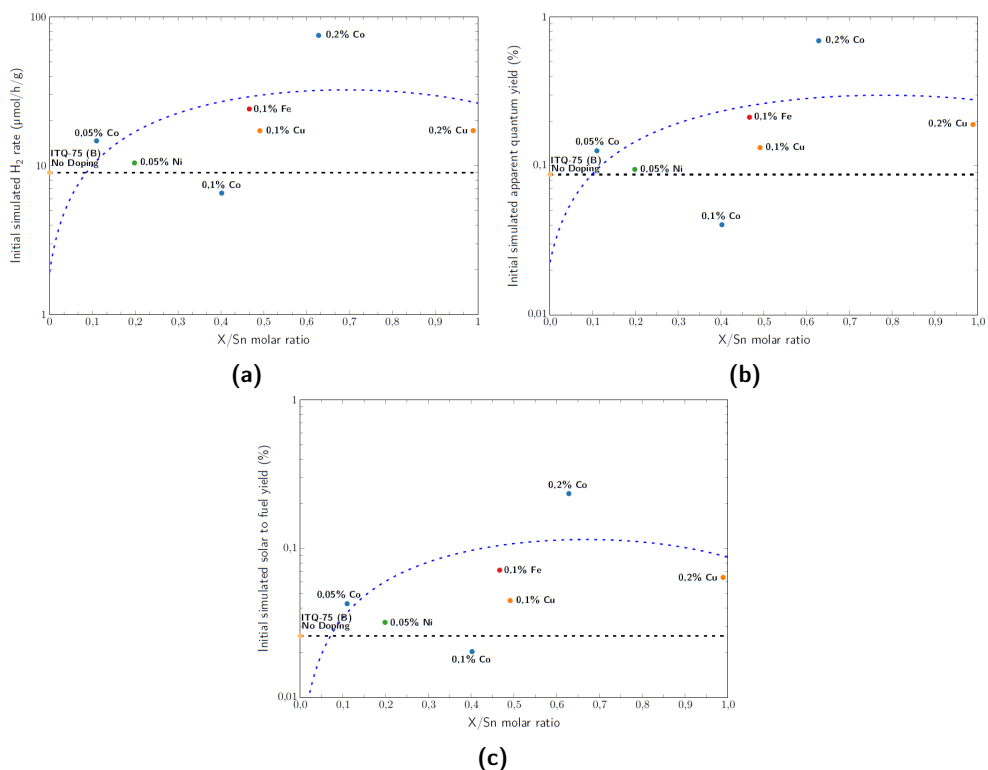
Figure 6.7: (6.7a) Initial simulated H_2 rate, (6.7b) initial simulated apparent quantum yield and (6.7c) maximum simulated solar to fuel yield of undoped ITQ-75 obtained with Compound B as SDA (in yellow), doped with iron (in red), with copper (in orange), with nickel (green) and with cobalt (in blue), according to their X/Sn molar ratio (X - Fe, Cu, Ni, Co)

As can be seen in Figure 6.7, regardless of the parameter used to evaluate the photocatalytic performance, there is an improvement in performance at low doping values and a stabilization at higher doping contents. Moreover, it can be seen that the sample doped with 0,1% Co does not follow the same trend as the others. Thus, and taking into account the behavior previously observed, it is possible that such sample is a result of an overlayer and it would be necessary to redo its test.
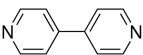
By adding the different doping agents, defects are inserted into the crystal lattice [15] and the interaction with the radiation is altered, something evident with the modification of the optical band gap value. Due to the presence of dopants, defects are inserted into the crystalline lattice which, as previously discussed, (their impact is still controversial [6]) may act as charge recombination centers [7, 8],

but allow to reduce the optical band gap value, increasing the interaction with the solar spectrum. Therefore, similarly to the existing balance between crystallinity and surface accessibility [10], there seems to exist an equilibrium between the performance gains due to the reduction of the optical band gap value and the presence of defects.

6.2.2.2 ITQ-75 obtained with Compound C as SDA

After the evaluation of the photocatalytic performance of the different doped ITQ-75's samples, obtained with Compound B as SDA, a similar approach was carried out for ITQ-75 doped samples obtained with Compound C as SDA. Their main characteristics are summarize at Table 6.3.

Table 6.3: Metal-doped ITQ-75, obtained with Compound C as SDA, main features (n.a. - not available)

Structure	SDA	Reference	Chemical Representation	Doping	Formula	Area (m²/g)		E_g (eV)
						S_μ	S_{ext}	
ITQ-75	4,4'-Dipyridyl	Compound C		-	$Sn_{3,05}Zn_{1,33}S_8 \cdot C_{11,54}H_{9,97}N_{2,24}$	2,9	17,3	2,2
				0,1 % Cu	$Sn_{3,19}Zn_{1,33}Cu_{1,74}S_8 \cdot C_{13,05}H_{13,35}N_{1,79}$	3,5	30,4	2,0
				0,2% Cu	$Sn_{2,39}Zn_{1,06}Cu_{2,46}S_8 \cdot C_{10,32}H_{10,32}N_{1,35}$	1,8	12,7	2,0
				0,05% Co	$Sn_{3,11}Zn_{1,30}Co_{0,45}S_8 \cdot C_{12,94}H_{14,03}N_{2,08}$	1,1	5,9	2,1
				0,1% Co	$Sn_{2,03}Zn_{0,55}Co_{1,05}S_8 \cdot C_{10,62}H_{20,28}N_{1,72}$	0,9	26,3	n.a.
				0,2% Co	$Sn_{1,81}Zn_{0,86}Co_{1,36}S_8 \cdot C_{14,35}H_{25,59}N_{2,09}$	5,3	32,7	2,1

The H_2 productivity of the different doped ITQ-75 samples presented in Table 6.3 are represented in Figure 6.8, as well as their apparent quantum and energetic yields in Figures 6.9 and 6.10, respectively.
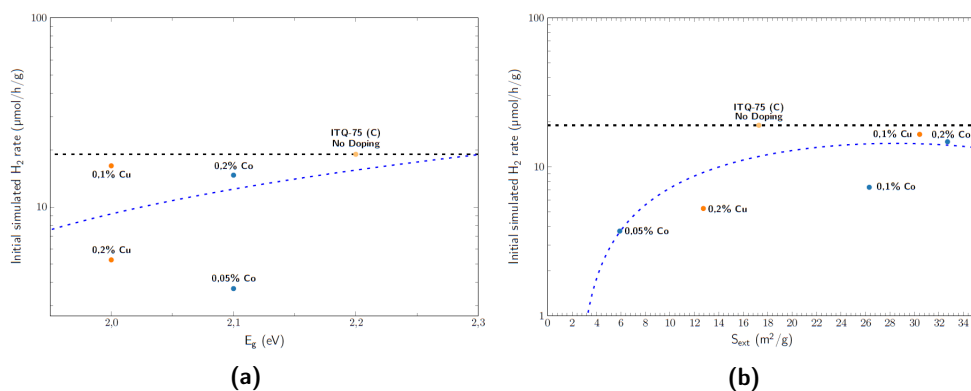
Figure 6.8: Initial simulated H_2 rate of undoped ITQ-75 obtained with Compound C as SDA (in yellow), doped with copper (in orange) and with cobalt (in blue), according to (6.8a) their optical band gap value E_g and (6.8b) their external surface area S_{ext}
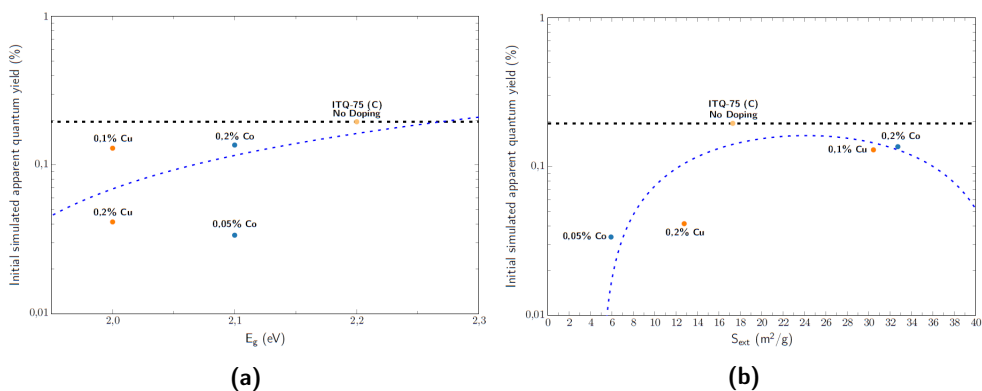
Figure 6.9: Initial simulated apparent quantum yield of undoped ITQ-75 obtained with Compound C as SDA (in yellow), doped with copper (in orange) and with cobalt (in blue), according to (6.9a) their optical band gap value E_g and (6.9b) their external surface area S_{ext}
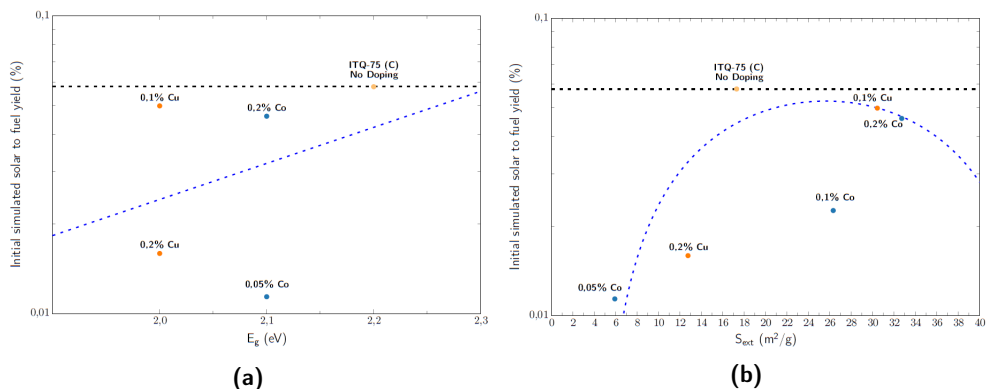
Figure 6.10: Initial simulated solar to fuel yield of undoped ITQ-75 obtained with Compound C as SDA (in yellow), doped with copper (in orange) and with cobalt (in blue), according to (6.10a) their optical band gap value E_g and (6.10b) their external surface area S_{ext}

As can be seen in the previous figures, after the insertion of any of the dopants under study, the photocatalytic performance of the final material decreases, something contrary to what was observed for some doped samples of ITQ-75 obtained with Compound B as SDA. After the insertion of copper there is a decrease in H_2 productivity from 19,0 to 5,3 µmol/h/g, and a reduction in apparent quantum yield from 0,20 % to 0,04% (for the sample doped with 0,2% Cu). For colbalt doping, there is a reduction in H_2 productivity from 19,0 to 3,7 µmol/h/g and a reduction in apparent quantum yield from 0,2% to 0,03% (for the sample doped with 0,05% Co).

Several hypotheses can be given to try to explain these results. ITQ-75 obtained with Compound C as SDA presents an optical band gap value equal to 2,2 eV, a value within the optical band gap range presented by Acar et al [14]. When the different dopants are added, there is a reduction of this parameter up to 1,9 eV, i.e. the limit of the range of optical band gap values. Hence, the doped materials may already have a low optical band gap for the reaction under study, not being able to conduct it.

With the insertion of the different dopants defects in the crystal lattice are inserted. Thus, it is hypothesized that the gain obtained with the reduction of the optical band gap value is lost due to the increase of defects in the crystalline framework. However, in order to verify this hypothesis it would be necessary to quantify the defects in the crystal lattice and the capacity for separation, diffusion and transfer of the photo-generated charge carriers towards the chemical species at the sur-

face in order to fully understand the impact that doping has on the photocatalitc performance.

That being stated, and following the methodology followed applied for the ITQ-75 doped samples obtained with Compound B as SDA, the dopant/Sn molar ratio was compared with the different parameters used to evaluate the photocatalytic performance (see Figure 6.11).

(a)

(b)

(c)
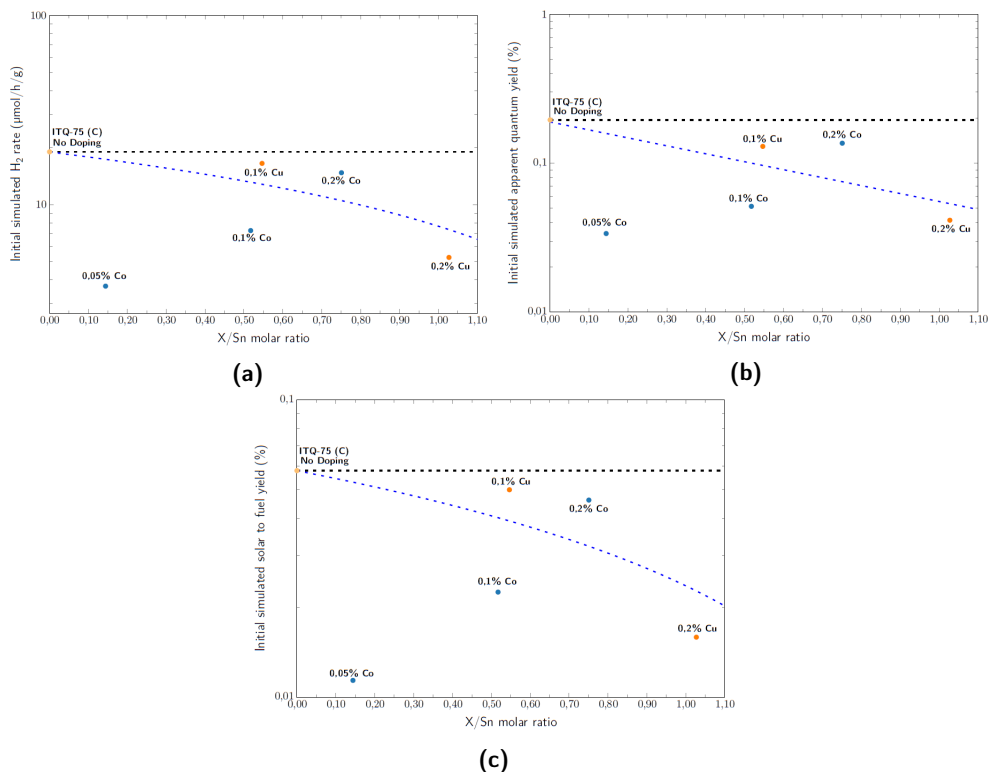
Figure 6.11: (6.11a) Initial simulated H_2 rate, (6.11b) initial simulated apparent quantum yield and (6.11c) maximum simulated solar to fuel yield of undoped ITQ-75 obtained with Compound C as SDA (in yellow), doped with copper (in orange) and with cobalt (in blue), according to their X/Sn molar ratio (X - Cu, Co)

As can be seen in the previous figure, with increasing dopant/Sn molar ratio there is a general reduction in the photocatalytic performance. Observing the sample with higher dopant content, there is a reduction in the H_2 productivity from 19,0 to 5,3 μmol/h/g and a reduction in apparent quantum yield from 0,2% to 0,04% (for the

283

sample doped with 0,2% Cu). It can be seen that the higher the dopant content, there is a general tendency for a decrease in the photocatalytic performance. As previously stated, the addition of dopants has as a consequence the decrease of the optical band gap value but it seems to lead to an increase of defects in the crystalline framework. Thus, these results seem to show that, for this set of samples, the gain associated with the reduction of the optical band gap is lost with the increase of the defects in the crystalline framework. It is important to note that the defects after the addition of dopants have not been quantified in our study and, as such, the increase of defects in the crystalline lattice is a hypothesis and based on the literature consulted.

6.2.2.3   Comparison

After evaluating the doping effects in each individual structure, a comparison of performances between all ITQ-75 doped structures is followed. Figures 6.12, 6.13 and 6.14 show the different parameters used to evaluate the photocatalytic performance as a function of the optical band gap value or the external surface area.
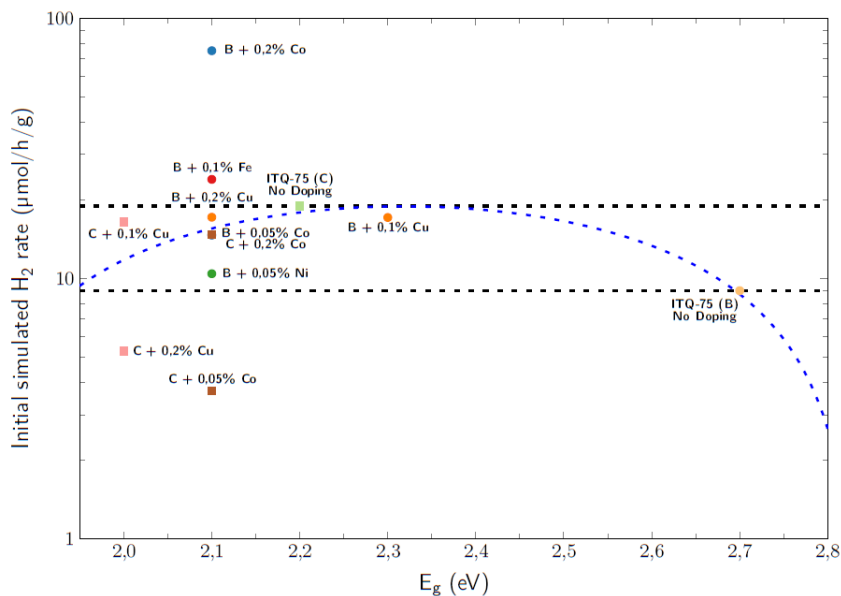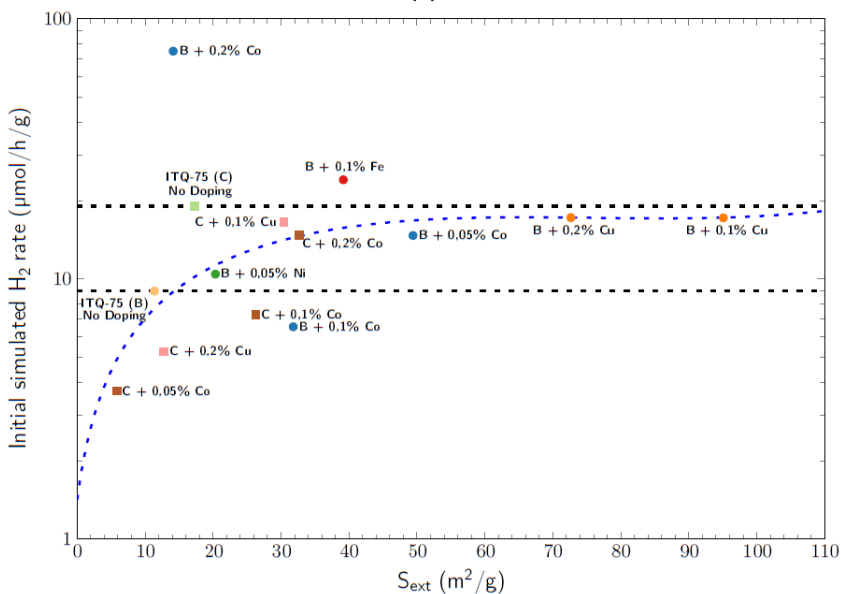
Figure 6.12: Initial simulated H$_2$ rate of undoped ITQ-75 obtained with Compound B as SDA (in yellow), doped with iron (in red), with copper (in orange), with nickel (green) and with cobalt (in blue); undoped ITQ-75 obtained with Compound C as SDA (in light green), doped with copper (in pink) and with cobalt (in brown), according to (6.12a) their optical band gap value E$_g$ and (6.12b) their external surface area S$_{ext}$

285
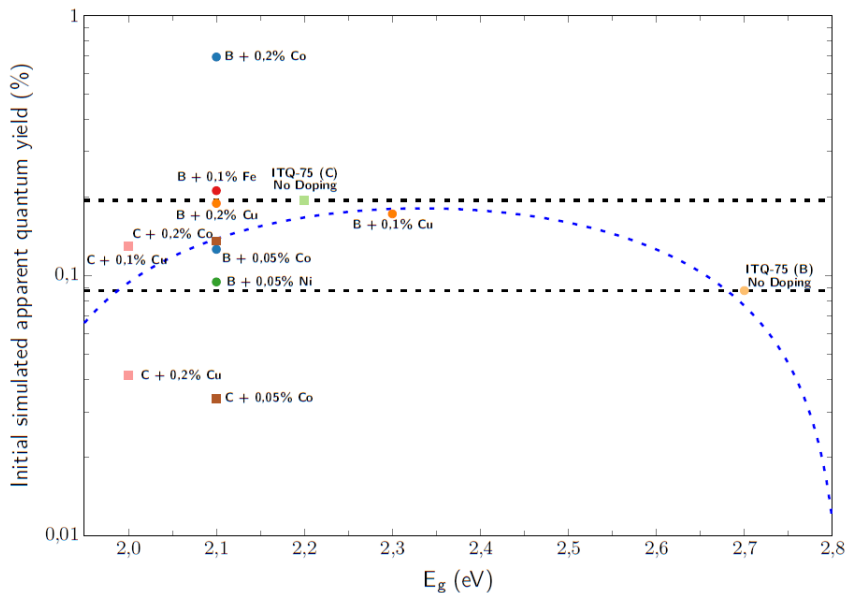
(a)
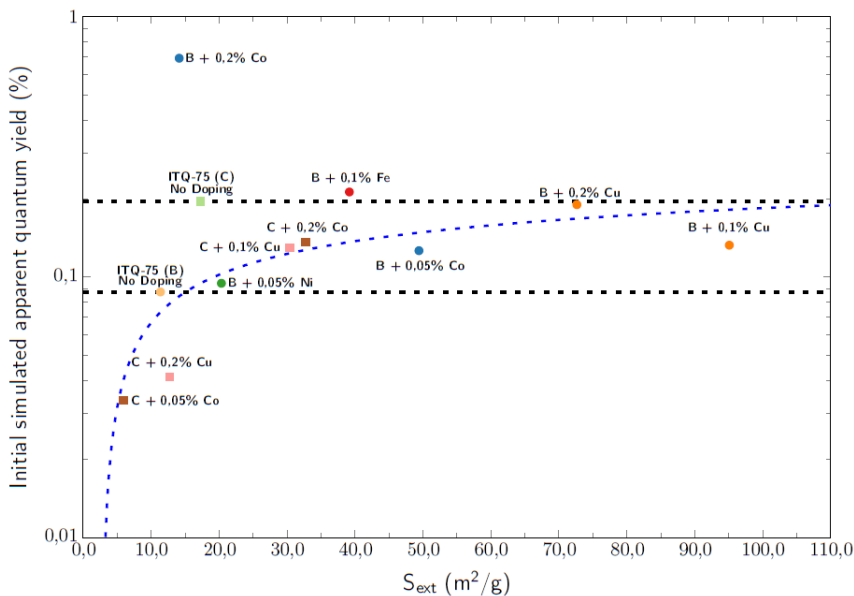
(b)

Figure 6.13: Initial simulated apparent quantum yield of undoped ITQ-75 obtained with Compound B as SDA (in yellow), doped with iron (in red), with copper (in orange), with nickel (green) and with cobalt (in blue); undoped ITQ-75 obtained with Compound C as SDA (in light green), doped with copper (in pink) and with cobalt (in brown), according to (6.13a) their optical band gap value E_g and (6.13b) their external surface area S_{ext}
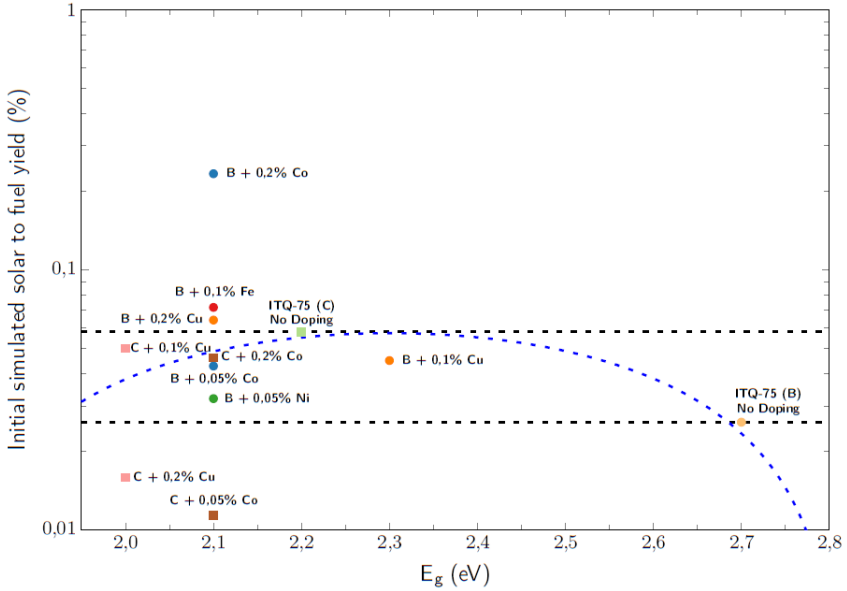
(a)
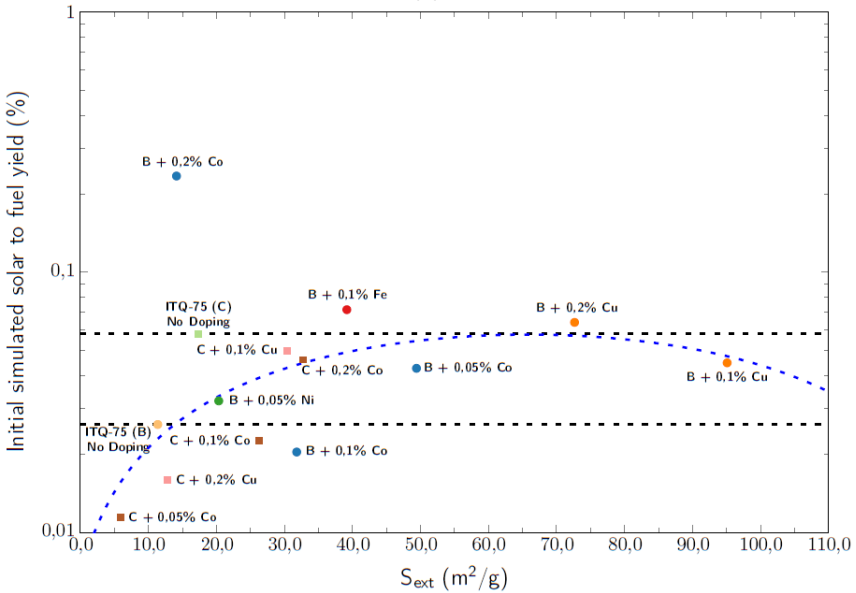
(b)

Figure 6.14: Initial simulated solar to fuel yield of undoped ITQ-75 obtained with Compound B as SDA (in yellow), doped with iron (in red), with copper (in orange), with nickel (green) and with cobalt (in blue); undoped ITQ-75 obtained with Compound C as SDA (in light green), doped with copper (in pink) and with cobalt (in brown), according to (6.14a) their optical band gap value E_g and (6.14b) their external surface area S_{ext}

287

Starting first with the H_2 productivity (see Figure 6.12), it can be seen that the sample with the highest H_2 productivity is ITQ-75 obtained with Compound B as SDA and doped with 0,2% Co, with a productivity equal to 75,1 μmol/h/g. Observing how the H_2 productivity relates to the optical band gap value (see Figure 6.12a), it can be seen that there is a volcano-type relationship. By reducing the optical band gap value to 2,1 eV there is a general improvement in H_2 productivity. For most samples with a lower optical band gap value, it is observed that their H_2 productivity starts to decrease. These observations are in line with the findings of Acar et al [14], which have been discussed earlier in relation to the existence of an optimal range of band gap values. Regarding the relationship between H_2 productivity and external surface area (see Figure 6.12b), it can be seen that up to an external surface area of 50 m^2/g there is an increase in H_2 productivity, after which it stabilizes. It can be hypothesized that from these values on, the gains associated with increasing the external surface accessibility are lost due to the defects created on the surface.

It is also interesting to note that, regardless of the characteristics of the material used, and excluding the sample with the highest H_2 productivity, the performance of ITQ-75 obtained with Compound C as SDA works as a maximum for the remaining samples. When the optical band gap value is reduced to 2,1 eV the samples tend to have a H_2 productivity similar to that of ITQ-75 obtained with Compound C as SDA, and when the external surface area is increased the productivity tends to that of ITQ-75 obtained with Compound C as SDA. Recalling the characterization performed on ITQ-75 obtained with Compound C as SDA (see Chapter 5), this is the only material of the ITQ-75 series that does not present ethylene glycol in its structure. Although the function of ethylene glycol in the structure is not known, it cannot be ruled out that its presence may create defects in the crystal lattice. Moreover, this material prior to any modification has an optical band gap equal to 2,2 eV and an external surface area equal to 17,3 m^2/g. Thus, and assuming that the presence of ethylene glycol has as a consequence the formation of defects, this material combines a higher crystallinity than the others and, low optical band gap value and an optimal external surface area, which could explain why it presents a photocatalytic performance superior to the other materials.

Looking now at the other parameters used to evaluate the photocatalytic performance, the apparent quantum (see Figure 6.13) and the solar to fuel (see Figure 6.14) yields, the sample with the best performance is ITQ-75 obtained with Compound B as SDA doped with 0,2% Co, with an apparent quantum yield equal to 0,69% and a solar to fuel yield equal to 0,23%. The remaining samples seem to follow the behavior observed earlier for the H_2 productivity. By looking at how the optical band gap value correlates with the apparent quantum yield (see Figure

6.13a) or the solar to fuel yield (see Figure 6.14a), it can be seen that there is an increase in performance with the reduction of the optical band gap value, up to values of about 2,1 eV. For lower values the performance seems to decrease. As for the external surface area (see Figures 6.13b and 6.14b), there is an improvement until an external surface area equal to 50 m^2/g and a subsequent stabilization. For both parameters, and excluding the sample with the highest performance, the ITQ-75 obtained with Compound C as SDA seems to act as a maximum expected performance something that was previously observed for the H_2 productivity.

In this case, the doping with 0,2 wt.% Co is particularly beneficial to increase the photocatalytic performance for the water splitting process. However this performance seems to be out of range and trends of all the reaming materials. In order to confirm that the performance is accurate and that the presented result is reproducible, it would be necessary to repeat the test twice. With the current results, doping with 0,2% Co seems to be an interesting and promising technique to increase the photocatalytic performance, but it does not allow to discharge the possibility of an overlayer. It was not possible to repeat the tests with such samples due to the low synthesis yield for each material, thus not having enough materials to perform several tests.
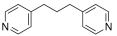
6.2.3 Accessibility Modified Samples

After evaluating the impact that doping shown on photocatalytic activity, the evaluation of the different techniques used to increase accessibility on photocatalytic performance will be indicated. As before, firstly such evaluation will be done on the ITQ-75 structures obtained with Compounds B or C as SDA separately. After it, both series of materials will be compared together.

6.2.3.1 ITQ-75 obtained with Compound B as SDA

The different ITQ-75 samples obtained with Compound B as SDA evaluated, as well as their main characteristics, are systematized in Table 6.4. It was choosen to study the photocatalytic performance of two samples whose accessibility was increased due to the presence of a saccharide (ITQ-75 obtained with a Fructose/SDA B or Sucrose/SDA B molar ratios equal to 1), due to the increased gel viscosity (ITQ-75 obtained with a EG/H_2O molar ratio equal to 3) and combination of both techniques (ITQ-75 obtained with a EG/H_2O molar ratio equal to 3 and a Fructose/SDA B molar ratio equal to 1).

Table 6.4: ITQ-75, obtained with Compound B as SDA, with increase accessibility main features (n.a. - not available; [1] determined by FESEM)

Structure	SDA	Reference	Chemical Representation	Modification	Formula	Area (m²/g) S_μ	S_{ext}	E_g (eV)	Crystal Size (μm)[1]
ITQ-75	1,3-Bis(4-pyridyl)propane	Compound B		-	$Sn_{3.52}Zn_{1.27}S_8 \cdot C_{10.59}H_{12.24}N_{1.68}$	0,5	11,4	2,7	1,4 ±0,5
				Fructose/SDA B - 1	$Sn_{3.17}Zn_{1.67}S_8 \cdot C_{40.56}H_{61.73}N_{1.98}$	10,5	29,0	1,9	1,1 ±0,3
				EG/H₂O - 3	$Sn_{3.39}Zn_{1.55}S_8 \cdot C_{10.68}H_{13.46}N_{1.28}$	3,1	53,3	2,1	1,2 ±0,7
				Sucrose/SDA B - 1	$Sn_{2.49}Zn_{1.50}S_8 \cdot C_{55.99}H_{46.44}N_{2.82}$	5,3	11,6	n.a.	1,2 ±0,4
				Fructose/SDA B - 1 & EG/H₂O - 3	$Sn_{2.15}Zn_{0.87}S_8 \cdot C_{21.70}H_{17.33}N_{1.63}$	18,9	89,7	3,1	0,6 ±0,2

The H_2 productivity of the different ITQ-75 samples presented in Table 6.4 are represented in Figure 6.15, as well as their apparent quantum and energetic yields in Figures 6.16 and 6.17, respectively. It is important to note that due to the Kubelka-Monk shape of the sample obtained with Sucrose, it was not possible to determine the optical band gap value (see Figure D.61). As such, it was not possible to calculate the apparent quantum yield or to use this material characteristic to relate to its photocatalytic performance.

(a)   (b)
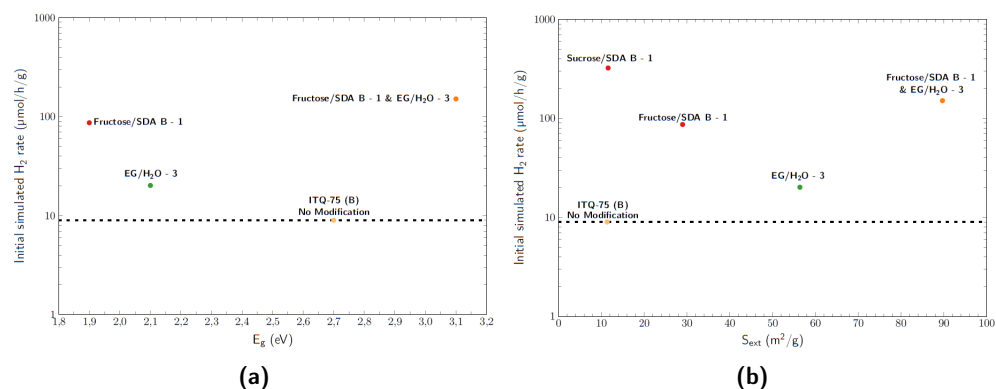
Figure 6.15: Initial simulated H_2 rate of unmodified ITQ-75 obtained with Compound B as SDA (in yellow), modified with saccharadeos (in red), with increased gel viscosity (in green) and modified with fructose and increased gel viscosity (orange), according to (6.15a) their optical band gap value E_g and (6.15b) their external surface area S_{ext}
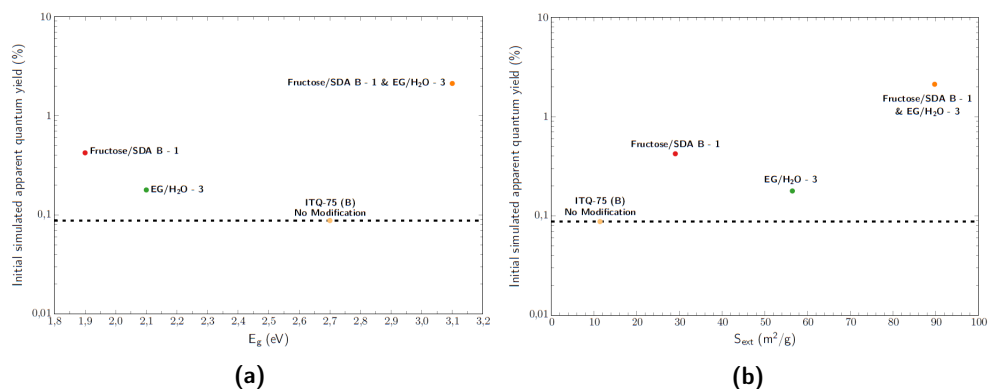
Figure 6.16: Initial simulated apparent quantum yield of unmodified ITQ-75 obtained with Compound B as SDA (in yellow), modified with saccharadeos (in red), with increased gel viscosity (in green) and modified with fructose and increased gel viscosity (orange), according to (6.15a) their optical band gap value E_g and (6.15b) their external surface area S_{ext}
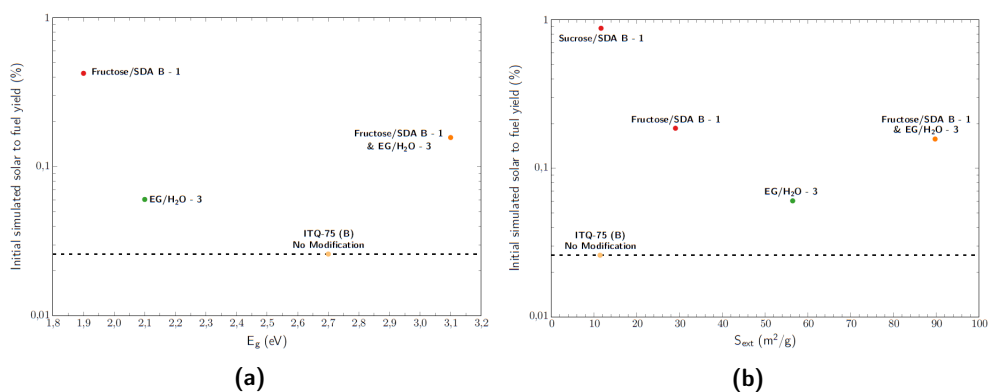
Figure 6.17: Initial simulated solar to fuel yield of unmodified ITQ-75 obtained with Compound B as SDA (in yellow), modified with saccharadeos (in red), with increased gel viscosity (in green) and modified with fructose and increased gel viscosity (orange), according to (6.17a) their optical band gap value E_g and (6.17b) their external surface area S_{ext}

Starting first with the H_2 productivity evaluation (see Figure 6.15), it can be seen that the sample with the highest H_2 productivity is the one with sucrose in its composition. By inserting sucrose it is possible to increase the H_2 productivity about 36 times, from 9,0 to 323,1 μmol/h/g. This sample also presents the largest increase in the solar to fuel yield (see Figure 6.17), from 0,03% to 0,9%.

Regarding the relationship between the different parameters used to evaluate the photocatalytic performance and the characteristics of the materials under study, it is observed that it was not possible to trace a correlation between such parameters and the the optical band gap value or the external surface area.

Two techniques were used to increase the material's accessibility - the insertion of a coSDA and increasing the viscosity of the synthesis gel. The first, according to the reviewed literature [16, 17], would create a mesoporous system. This did not occur, and it was hypothesized, and later confirm by microscopy, that the presence of the saccharides decreased the crystal size, since the major change in the textural properties was in the external surface area. Another major change observed was the increase in the organic content. When sucrose or fructose is inserted, there is an increase in the C/N molar ratio, from 6,3 to 20,5 and 19,8, respectively. Thus, in view of this information, it was checked how the C/N molar ratio relates to photocatalytic activity (see Figure 6.18).
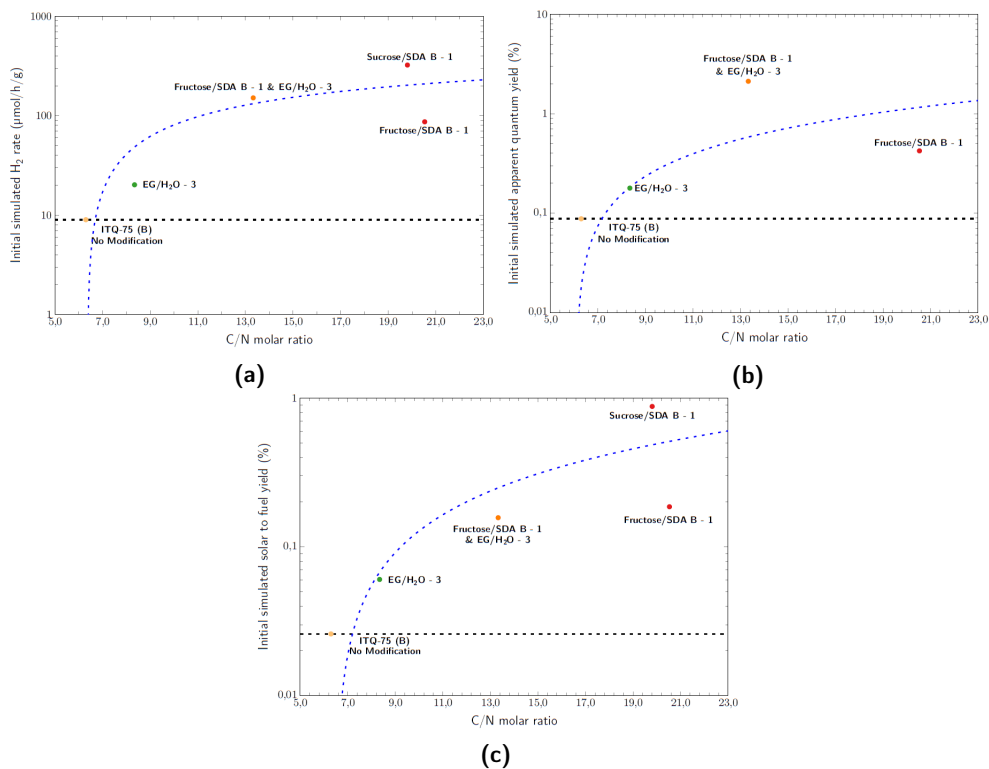
Figure 6.18: (6.18a) Initial simulated H$_2$ rate, (6.18b) initial simulated apparent quantum yield and (6.18c) maximum simulated solar to fuel yield of unmodified ITQ-75 obtained with Compound B as SDA (in yellow), modified with saccharadeos (in red), with increased gel viscosity (in green) and modified with fructose and increased gel viscosity (orange), according to their C/N molar ratio

As can be seen in the previous figure, for any of the parameters used to evaluate photocatalytic performance, there seems to exist a logarithmic relationship between the organic content and the photocatalytic performance. Thus, increasing the organic content seems to have a positive impact on the photocatalytic performance.
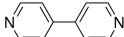
As discussed earlier (see Chapter 2), one of the main reasons associated with the low photocatalyitc yields is the rapid charge recombination. Several methodologies to minimize this effect have been investigated, namely the construction of hetero-junctions, which would allow to improved charge separation efficiency. According to the band arrangement of the semiconductors involved, the heterojuctions can be p-n, Schottky, conventional type II, Z-scheme, S-scheme and hybrid organic-inorganic

[18, 19, 20]. More recently the latter type of heterojunction is being further investigated, as the synergy created between the organic and inorganic components may offer new electronic properties. By increasing the organic content of the samples, through the insertion during synthesis of fructose or sucrose, it is possible to increase the photocatalytic performance. Since the chemical environment of the saccharides and their structure after synthesis is not known, the creation of a heterojunction between these compounds and the inorganic component cannot be ruled out. Such possible formation of a hybrid heterojunction could explain why a high photocatalytic performance is observed and how such performance is obtained even in the presence of a low optical band gap value. Given the results obtained, a more detailed characterization of these materials would be necessary to better understand the environment in which the saccharides are located after the synthesis (as well as their chemical structure) and their influence on the ability to separate and transport photogenerated charge carriers.

6.2.3.2   ITQ-75 obtained with Compound C as SDA

After the evaluating of the performance of ITQ-75 samples obtained with Compound B as SDA with increase accessibility, the assessment of the analogous samples obtained with Compound C as SDA follows. The main characteristics of those samples are systematized in the Table 6.5. It was decided to evaluate the performance of the samples obtained with different saccharide (ITQ-75 obtained with a Fructose/SDA C or Sucrose/SDA C molar ratios equal to 1), and post modified by Ball Mill or BuLi treatments (discussed in Chapter 5). Although these treatments were not successful in increasing the accessibility of the samples, they did result in an increase in the optical band gap and, as such, it is intended to assess what impact such modifications might have on photocatalytic performance.

Table 6.5: ITQ-75, obtained with Compound C as SDA, with increase accessibility main features (n.a. - not available)

Structure	SDA	Reference	Chemical Representation	Doping	Formula	Area (m²/g) S_μ	Area (m²/g) S_{ext}	E_g (eV)	Crystal Size (μm)
ITQ-75	4,4'-Dipyridyl	Compound C		-	$Sn_{3.05}Zn_{1.33}S_8 \cdot C_{11.54}H_{9.97}N_{2.24}$	2,9	17,3	2,2	1,8 ±0,6
				Fructose/SDA C - 1	$SnZnS_8 \cdot C_{23.64}H_{18.23}N_{1.33}$	8,8	67,0	n.a.	1,4 ±0,4
				Sucrose/SDA C - 1	$Sn_{1.53}Zn_{0.64}S_8 \cdot C_{39.59}H_{28.63}N_{1.53}$	5,7	28,3	n.a.	1,0 ±0,4
				Ball Mill	$Sn_{3.10}Zn_{1.63}S_8 \cdot C_{10.80}H_{9.97}N_{2.01}$	0,1	18,1	2,7	1,3 ±0,5
				BuLi Treatment	$Sn_{2.39}Zn_{2.42}S_8 \cdot C_{13.38}H_{15.12}N_{1.92}$	2,5	7,9	2,9	5 ±1

The H$_2$ rate, the apparent quantum yield and the solar to fuel yield of the different samples present on the previous table can be found in Figures 6.19, 6.20 and 6.21, respectively. Since it is not possible to determine the optical band gap value due to the Kubelka-Munk shape of the samples with saccharides (see Figure D.59 and

D.61), it is not possible to calculate the apparent quantum yield value or use this characteristic to relate to their reactivity.

(a)   **(b)**
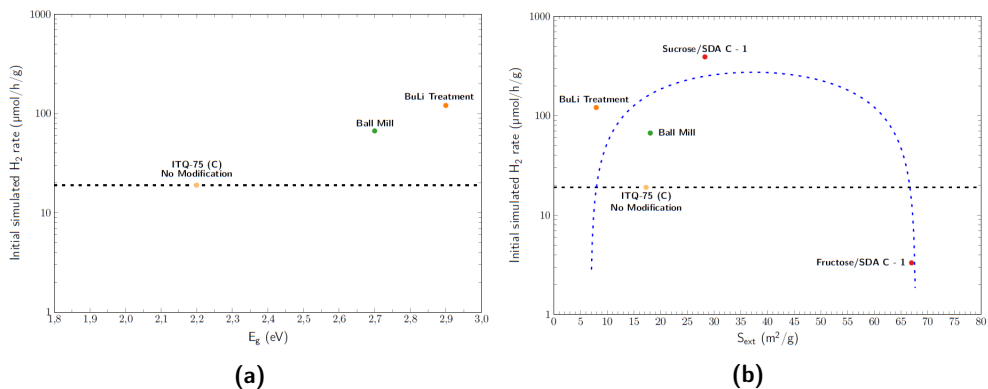
Figure 6.19: Initial simulated H_2 rate of unmodified ITQ-75 obtained with Compound C as SDA (in yellow), modified with saccharadeos (in red), after ball mill (in green) and BuLi post treatments (orange), according to (6.19a) their optical band gap value E_g and (6.19b) their external surface area S_{ext}

(a)   **(b)**
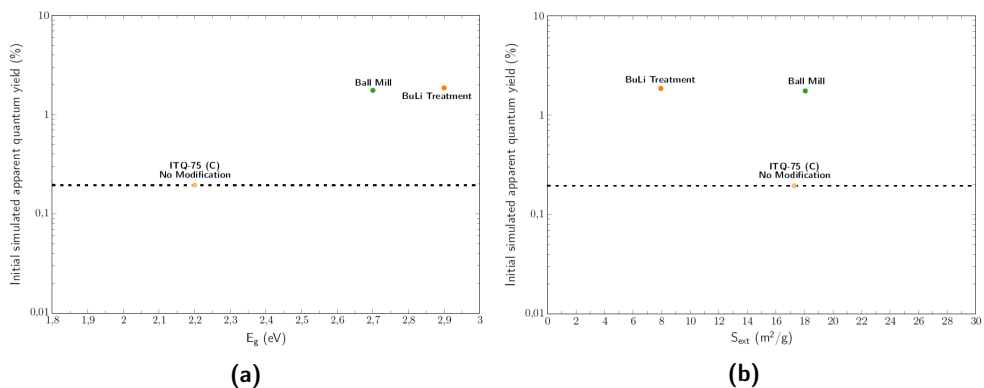
Figure 6.20: Initial simulated apparent quantum yield of unmodified ITQ-75 obtained with Compound C as SDA (in yellow), modified with saccharadeos (in red), after ball mill (in green) and BuLi post treatments (orange), according to (6.20a) their optical band gap value E_g and (6.20b) their external surface area S_{ext}
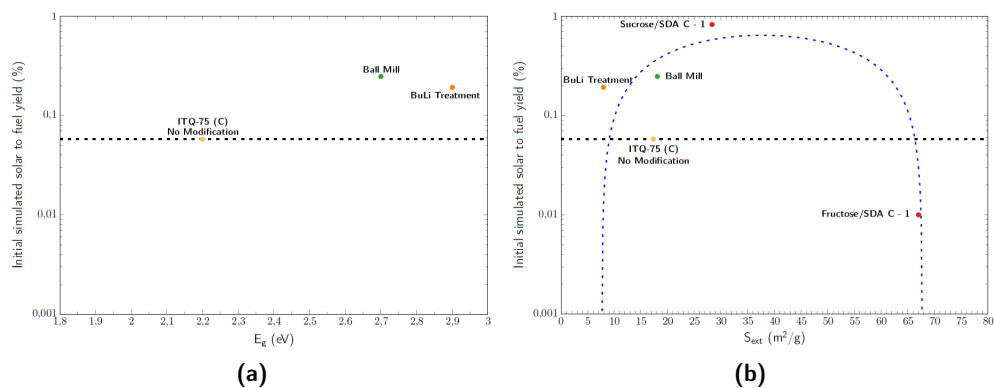
Figure 6.21: Initial simulated solar to fuel yield of unmodified ITQ-75 obtained with Compound C as SDA (in yellow), modified with saccharadeos (in red), after ball mill (in green) and BuLi post treatments (orange), according to (6.21a) their optical band gap value E_g and (6.21b) their external surface area S_{ext}

After observing the different figures above, it can be seen that the sample with the best performance is the one modified with Sucrose. With the presence of Sucrose at a Sucrose/SDA C molar ratio equal to 1 the H_2 rate is increased from 19,0 µmol/h/g, for the unmodified material, to 390,5 µmol/h/g (see Figure 6.19). Regarding the solar to fuel yield, it also increases, from 0,06% to 0,8% (see Figure 6.21).

Concerning the correlation between the different photocatalytic performances and the external surface area (see Figures 6.19b, 6.20a and 6.21a), it can be seen that there is again a volcano type correlation between them. Regarding the relationship between the external surface area and the H_2 productivity (see Figure 6.19b), it can be seen that by increasing the external surface area there is an increase in productivity but, for external surface areas above 30m²/g, such reactivity decreases. This observation is in line with what was described previously in the literature [9, 10]. With the increase of the external surface area there is an increase on the active sites, translating into a higher reactivity. However, by increasing the external surface area, the number of surface defects also increases, acting as possible charge recombination centers. Hence, there is a balance between external accessibility and defects, highlighted by the volcano-type correlation.

Regarding the relation between the optical band gap value and the apparent quantum or the solar to fuel yields (see Figures 6.20a and 6.21a respectively), unfortunately it was not possible to determine this parameter for the saccharide-rich samples due to the shape of their Kubelka-Munk function. For the remaining two

samples it is possible to observe that, although there was an increase in the optical band gap value, the apparent quantum yield increases, from 0,2 % to almost 1,8%. Regarding their solar to fuel yield, similar considerations can be observed. After the different post-treatments test, their solar to fuel yields increases to almost 1 %. Such fact means that, although there is a smaller number of absorb photons, the charge carriers produce by it are better employed on the desired process.

As it was previously done for the ITQ-75 samples obtained with Compound B as SDA with increase accessibility, the relationship between the observed photocatalytic performance and the C/N molar ratio was verified (see Figure 6.22).

(a)

(b)

(c)
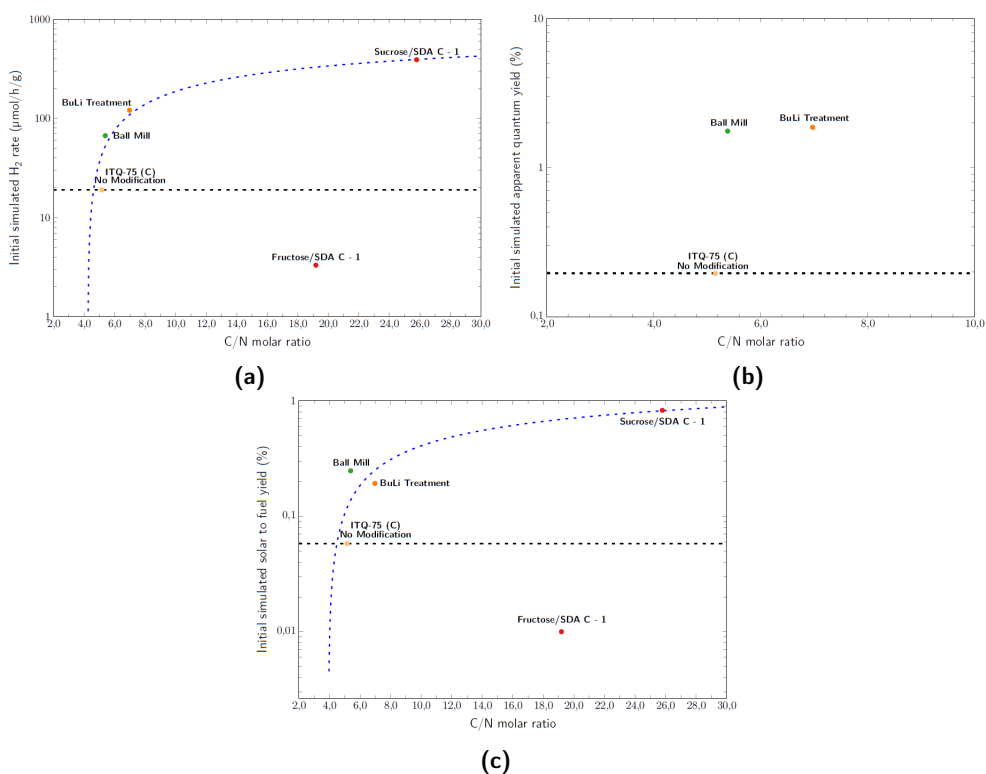
Figure 6.22: (6.22a) Initial simulated H_2 rate, (6.22b) initial simulated apparent quantum yield and (6.22c) maximum simulated solar to fuel yield of unmodified ITQ-75 obtained with Compound C as SDA (in yellow), modified with saccharadeos (in red), after ball mill (in green) and BuLi post treatments (orange), according to their C/N molar ratio

There is a similar trend as previously observed for the ITQ-75, obtained with Compound B as SDA, samples with increased accessibility. Except the sample obtained with fructose, a possible increase in photocatalytic performance with increasing carbon content can thus be observed.

In this set of samples, besides the sucrose-rich sample, the performance of two samples to which no organic compound was added during the synthesis process is evaluated. These two samples underwent two different post-synthesis treatments that resulted in not only changes in their morphology and optical band gap values, but also an increase in their molar C/N ratio. This shows the importance of the organic content in the final material on the observed photocatalytic performance. To evaluate the true importance of the organic content in the final reactivity it would be necessary to perform a deeper electrochemical characterization of these materials.

6.2.3.3   Comparison

After evaluating the impact that the different methodologies used to increase accessibility have on ITQ-75's photocatalytic performance, a comparison between the different structures obtained with Compounds B or C as SDA is followed. Figures 6.23, 6.24 and 6.25 show the H_2 rate, the apparent quantum yield and the solar to fuel yield, respectively, of the different ITQ-75 accessibility modified samples, which are evaluated.
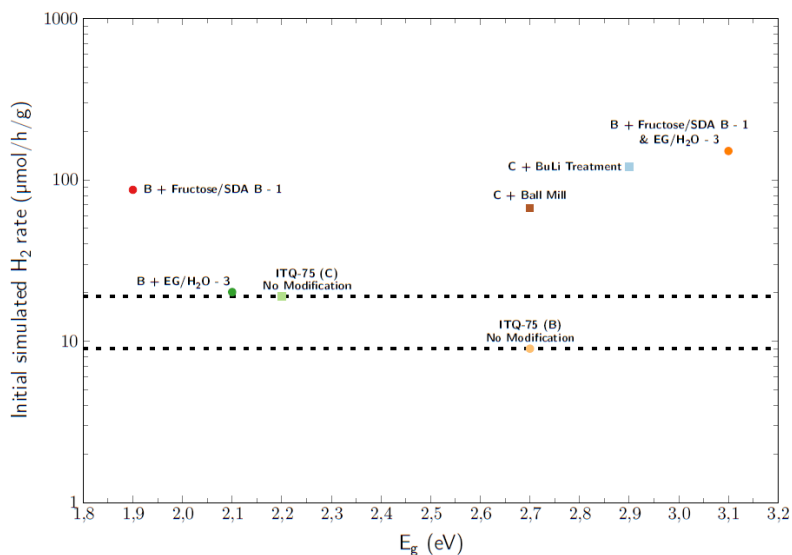
(a)
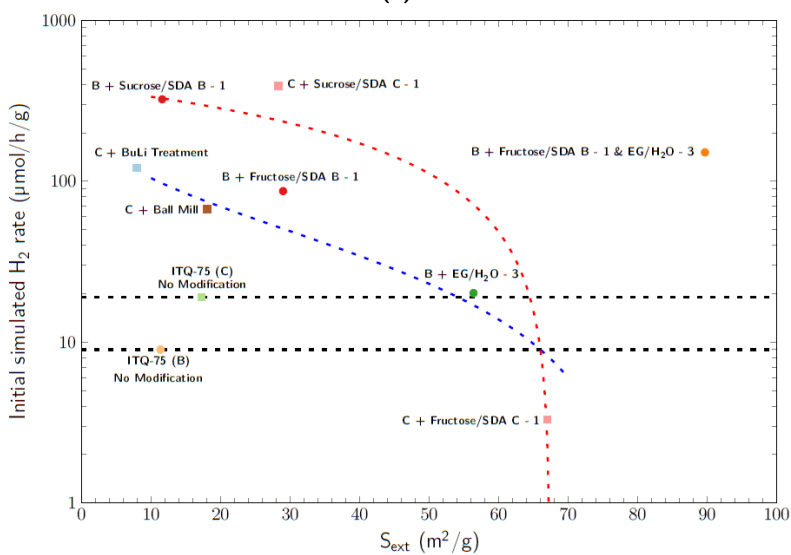
(b)

Figure 6.23: Initial simulated H_2 rate of undoped ITQ-75 obtained with Compound B as SDA (in yellow), modified with saccharides (in red), with increased EG/H_2O molar ratio (green) and with fructose and increased EG/H_2O molar ratio (in orange); undoped ITQ-75 obtained with Compound C as SDA (in light green), modified with saccharides (in pink) and with cobalt (in brown), according to (6.23a) their optical band gap value E_g and (6.23b) their external surface area S_{ext}
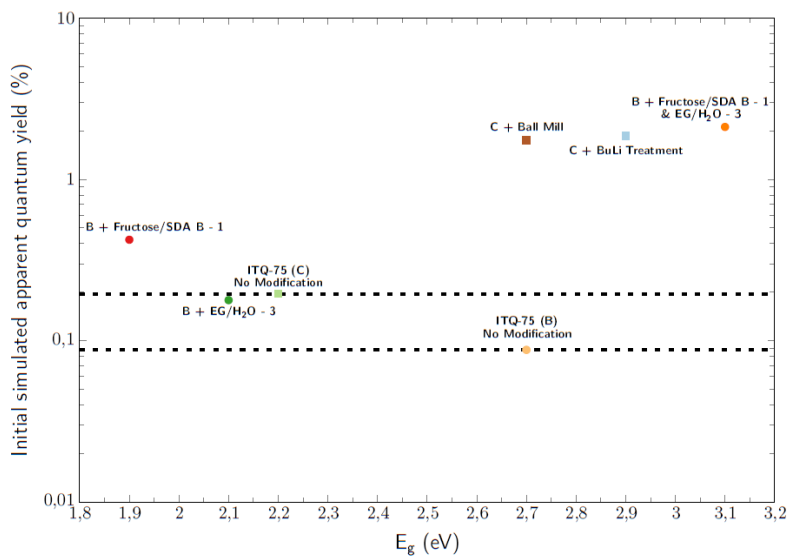
(a)
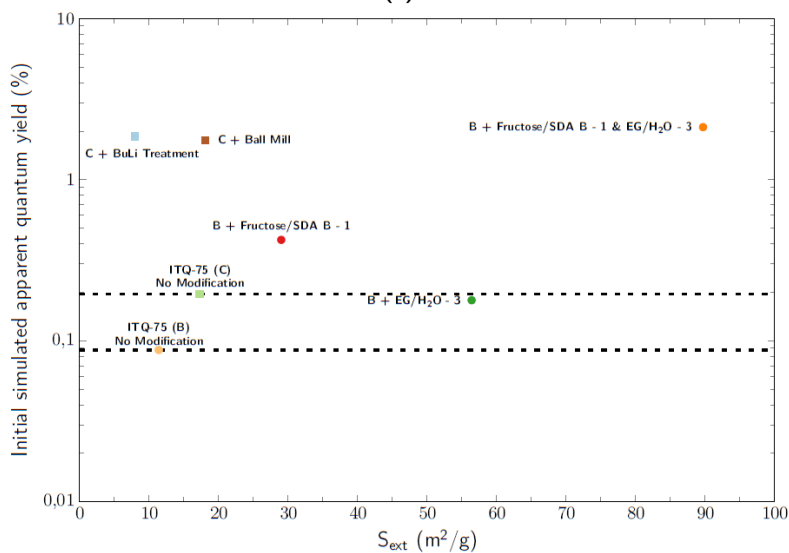
(b)

Figure 6.24: Initial simulated apparent quantum yield (%) of undoped ITQ-75 obtained with Compound B as SDA (in yellow), modified with saccharides (in red), with increased EG/H_2O molar ratio (green) and with fructose and increased EG/H_2O molar ratio (in orange); undoped ITQ-75 obtained with Compound C as SDA (in light green), modified with saccharides (in pink) and with cobalt (in brown), according to (6.24a) their optical band gap value E_g and (6.24b) their external surface area S_{ext}
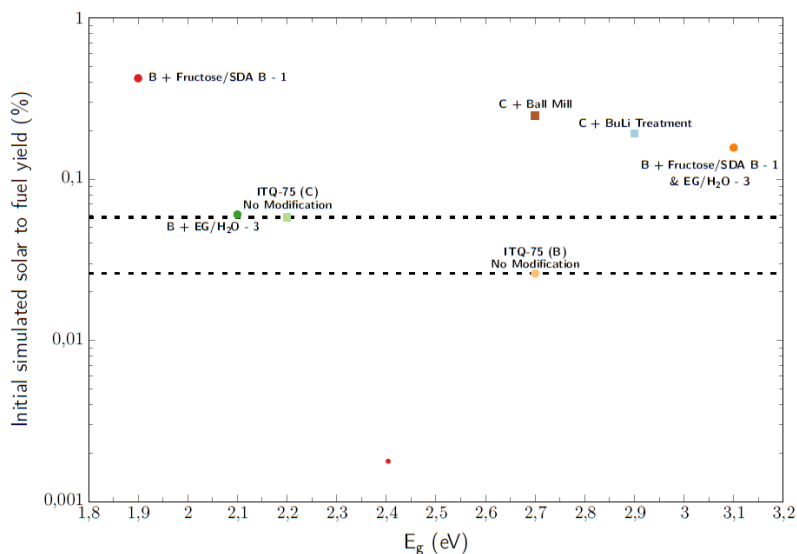
(a)
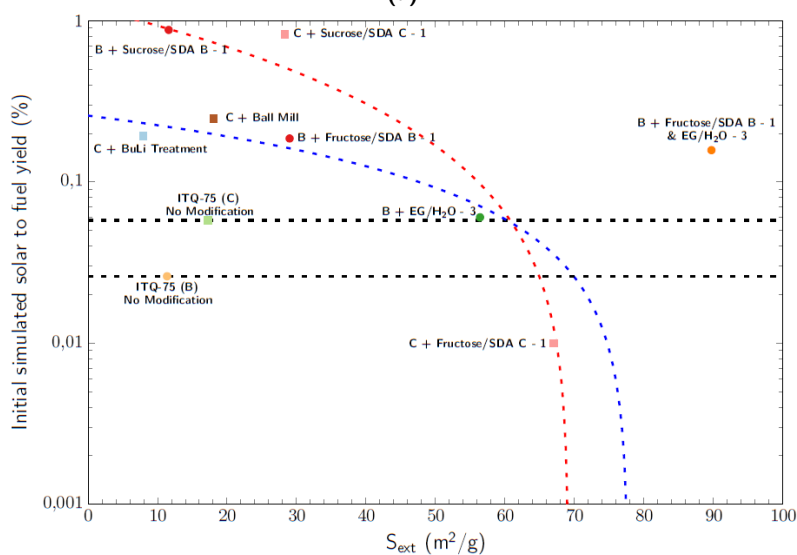
(b)

Figure 6.25: Initial simulated solar to fuel yield (%) of undoped ITQ-75 obtained with Compound B as SDA (in yellow), modified with saccharides (in red), with increased EG/H$_2$O molar ratio (green) and with fructose and increased EG/H$_2$O molar ratio (in orange); undoped ITQ-75 obtained with Compound C as SDA (in light green), modified with saccharides (in pink) and with cobalt (in brown), according to (6.25a) their optical band gap value E$_g$ and (6.25b) their external surface area S$_{ext}$

The samples that present the best H_2 productivity are the ones obtained with sucrose and it is independent of the Compound used as SDA, making this modification the most promising one. Although after the sucrose insertion both structures obtained with Compound B or C and SDA show similar performances, the highest increase of performance is observed in the ITQ-75 obtained with Compound B as SDA. After the sucrose insertion the H_2 rate increases up to 36 times, from 9,0 μmol/h/g to 323,1 μmol/h/g, and the solar to fuel yield 34 times, from 0,03% to 0,9%.

Earlier, when comparing the different doped ITQ-75 samples, it was observed that ITQ-75 obtained with Compound C as SDA without any modification seemed to behave as a reactivity maximum. This does not occur in the samples with increase their accessibility. Except the sample of ITQ-75 obtained with Compound C as SDA with a Fructose/SDA C molar ratio equal to 1, the remaining samples have a photocatalytic performance similar or above the one that the unmodified ITQ-75 obtained with Compound C as SDA. Hence, the different methodologies used to increase accessibility seem to be more successful in increasing photocatlytic performance than the metal insertion.

Evaluating now how the different material's characteristics relate to their photocatalytic performance, it is observed that it is not possible to trace a correlation between the different parameters used and the optical band gap value (see Figures 6.23a, 6.24a and 6.25a).

Regarding the relation between the photocatalytic performance and the external surface area (see Figures 6.23b, 6.24b and 6.25b), it was chosen to correlate the different samples with the type of modification used in order to make it easier to compare different samples but under the same type of modification. Thus, the samples modified by saccharide insertion were correlated with their performance through the blue curve and the remaining modifications with a red curve. In both cases it was found that the larger the external surface area, the lower the photocatalytic performance, regardless of the parameter used to evaluate it.
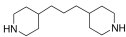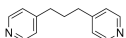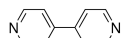
It is therefore observed that, regardless of the SDA used, there is an improvement in ITQ-75 photocatalytic performance with the insertion of saccharide. However, how these saccharide influence the photocatalytic performance is unknown. The presence of these components can act in different steps of the photocatalytic process. They may act on the reactant adsorption, protons reservoir or on the electronic structure. Since the final chemical structure of the sugars is unknown, one cannot ignore the possible presence of hydroxyl groups that can be oxidized to carbonyls (ketone or aldehydes), being a source of H^+. This would require checking the chemical environment (e.g. by IR or ^{13}C NMR) before and after the reaction to

see if there has been any modification to the organic component present. Another consequence of the presence of sugars may be the alteration of the electronic structure of the material. This would require a more in-depth electrochemical characterization, for example by impedance spectroscopy, which would allow the generation, transport and transfer of charge carriers to be assessed.

6.2.4 Materials with similar optical band gap values

After analyzing the consequences that doping or accessibility increasing have on the photocatalytic performance, it was possible to verify that there were samples within the same range of optical band gap value that present a distinct performance. Therefore, in this section, it is intended to explore the photocatalytic behavior of samples that, although present the similar optical band gap value, show different performances. To this end, and taking into account the samples evaluated, the samples with an optical band gap values between 1,9 eV and 2,1 eV will be further analyzed (see Table 6.6). How these relate to their external surface area value according to the different parameters used to evaluate photocatalytic performance is shown in Figures 6.26 and 6.27.

Table 6.6: Structures with an optical band gap value between 1,9 eV and 2,1 eV main features (n.a. - not available; [1] see Appendix B.2 for more information regarding these samples)

Structure	SDA	Reference	Chemical Representation	Modification	Formula	Area (m²/g)		E_g (eV)
						S_μ	S_{ext}	
ITQ-76	1,3-Bis(4-piperidyl)propane	Compound A		Ru-Complex/SDA A - 0,1	$Sn_{1.94}Zn_{0.93}S_8Ru_{1.00} \cdot C_{28.31}H_{43.25}N_{3.01}$	7,4	28,7	2,0
ITQ-75	1,3-Bis(4-pyridyl)propane	Compound B		EG/H$_2$O - 3	$Sn_{3.39}Zn_{1.55}S_8 \cdot C_{10.68}H_{13.46}N_{1.28}$	3,1	53,3	2,1
				0,1 % Fe	$Sn_{2.15}Zn_{1.04}Fe_{1.00}S_8 \cdot C_{20.80}H_{21.52}N_{2.64}$	3,1	39,2	2,1
				0,05% Ni	$Sn_{4.42}Zn_{2.00}Ni_{0.88}S_8 \cdot C_{11.25}H_{12.66}N_{1.60}$	0	20,3	2,1
				0,05% Co	$Sn_{2.82}Zn_{1.48}Co_{0.31}S_8 \cdot C_{13.41}H_{14.85}N_{1.71}$	0	49,4	2,1
				Fructose/SDA B - 1 & 0,1% Co[1]	n.a	5,2	28,6	1,9
				Fructose/SDA B - 1 & 0,1% Cu[1]	n.a	17,9	51,2	2,0
ITQ-75	4,4'-Dipyridyl	Compound C		0,1 % Cu	$Sn_{3.19}Zn_{1.33}Cu_{1.74}S_8 \cdot C_{13.05}H_{13.35}N_{1.79}$	3,5	30,4	2,0
				0,2% Cu	$Sn_{2.39}Zn_{1.06}Cu_{2.46}S_8 \cdot C_{10.32}H_{10.32}N_{1.35}$	1,8	12,7	2,0
				0,05% Co	$Sn_{3.11}Zn_{1.30}Co_{0.45}S_8 \cdot C_{12.94}H_{14.03}N_{2.08}$	1,1	5,9	2,1
				0,2% Co	$Sn_{1.81}Zn_{0.86}Co_{1.36}S_8 \cdot C_{14.35}H_{25.59}N_{2.09}$	5,3	32,7	2,1
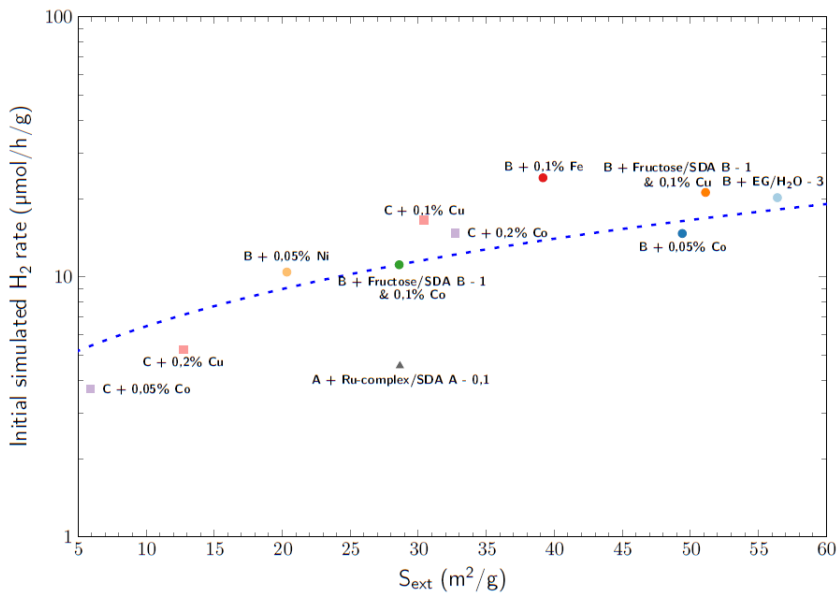
(a)
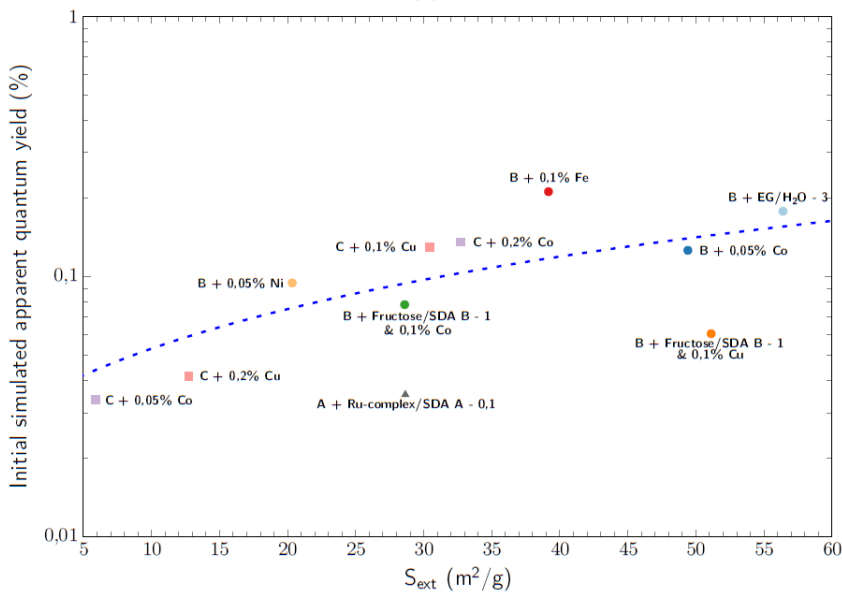
(b)

Figure 6.26: (6.26a) Initial simulated H_2 rate and (6.26b) initial apparent quantum yield of samples within the same optical band gap range (1,9 eV - 2,1 eV)
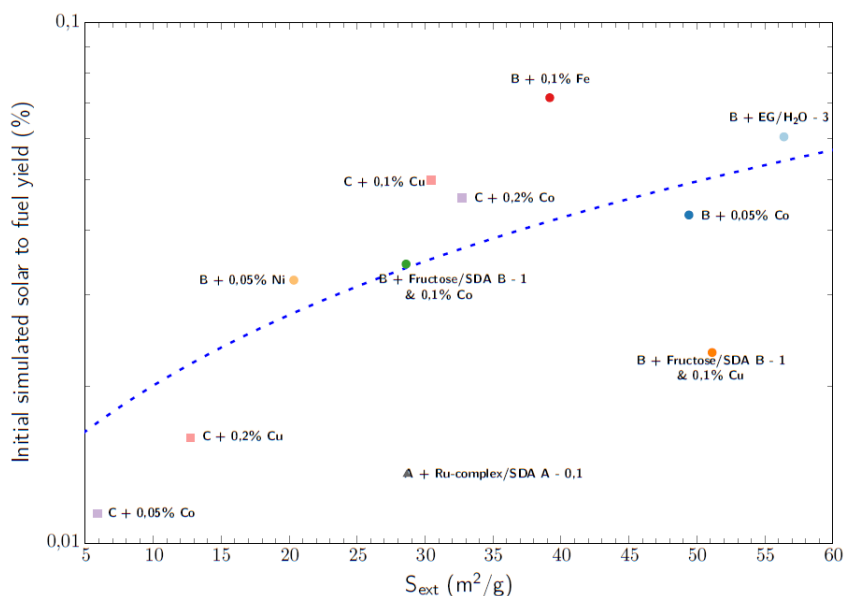
Figure 6.27: Initial simulated solar to fuel yield of samples within the same optical band gap range (1,9 eV - 2,1 eV)

By observing Figures 6.26 and 6.27 it is possible to see that, for the samples with an optical band gap value between 1,9 eV and 2,1 eV, there is a linear relationship between the external surface area and the photocatalytic performance. By linear increasing the external surface area, there is a linear increase in the H_2 productivity, apparent quantum or solar to fuel yields.

As it was presented on Chapter 2, the overall water splitting can be divided into two reactions - the hydrogen evolution reaction (HER) - see Equation 6.1 - and the oxygen evolution reaction (OER) - see Equation 6.2.

$$4H^+ + 4e^- \rightarrow 2H_2 \qquad (6.1)$$

$$2\,H_2O + 4\,h^+ \rightarrow O_2 + 4\,H^+ \qquad (6.2)$$
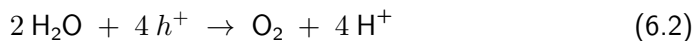
The OER is considered to be the rate-determining step in the whole reaction [21]. According to computational results performed at Nørskov group [22, 23, 24], OER involves four elementary steps, each step involving the electron transfer coupled

305

with electron removal (see Equations 6.3, 6.4, 6.5 and 6.6 where $*$ represents a surface cite and Y^* an attached Y intermediate on the surface). It was also found that the water chemisorbetion or the O^* formation could be the limiting step (see Equation 6.3 and 6.5).

$$H_2O + * \rightarrow HO^* + H^+ + e^- \tag{6.3}$$

$$HO^* \rightarrow O^* + H^+ + e^- \tag{6.4}$$

$$O^* + H_2O \rightarrow HOO^* + H^+ + e^- \tag{6.5}$$

$$HOO^* \rightarrow * + O_2 + H^+ + e^- \tag{6.6}$$
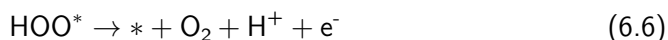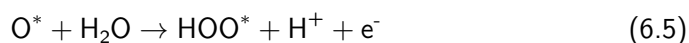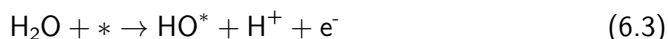
Dionigi et al. [25] related the photocatalytic hydrogen production rate with the chemisorbed water coverage. It was also observed that the initial reaction rate is higher at the beginning of the reaction, something similar observed by Shearer et al. [26]. As the reaction proceeds, the water coverage is reduced compared to the initial one and, therefore, the reaction rate also decreases. Eventually the initial excess of water is consumed and the reaction rate is limited by the rate of chemisorb water, with this step expected to be the rate limiting one, thus being in agreement with the computational results [22, 23, 24]. Taking into account the information presented, it can be hypothesized that, for a given range of external surface area values, it would be expected that by increasing this parameter, the water coverage would also increase and, therefore, an increase on the the chemisorbed water would be observed.

For any of the parameters used to evaluate the photocatalytic performance, a linear increase in performance is observed with increasing external surface area, for a given range. Hence, and taking into account the literature reviewed, this correlation between the reactivity and the external surface area can be explained by taking into account the water coverage and chemisorption, highlighting the possibility that this step could be the rate limiting one of the process under study.

6.2.5 State of the Art Comparison

Table 6.7 systematizes the most promising photocatalytic results discussed throughout this chapter, as well as the performances found in the literature.

Table 6.7: Summary of the photocatalytic performances of the materials under study, TiO_2 and materials reported in the literature in gas-phase

Photocatalyst	Feed	Light	Reactor	H_2 rate (μmol/h/g)	Ref.
ITQ-75 (B) & 0,2% Co	Pure Water	UV-Visible	Batch	75	This thesis
ITQ-75 (B) & Fructose/SDA B - 1	Pure Water	UV-Visible	Batch	87	This thesis
ITQ-75 (C) & BuLi Treatment	Pure Water	UV-Visible	Batch	121	This thesis
ITQ-75 (B) & Fructose/SDA B - 1 & EG/H_2O – 3	Pure Water	UV-Visible	Batch	151	This thesis
ITQ-75 (B) & Sucrose/SDA B – 1	Pure Water	UV-Visible	Batch	323	This thesis
ITQ-75 (C) & Sucrose/SDA C – 1	Pure Water	UV-Visible	Batch	391	This thesis
TiO_2	Pure Water	UV-Visible	Batch	5	This thesis
Au/TiO_2	Ethanol and Water	UV-Visible	Continuous - Micro reactor	1800	[27]
Ag-Mt/pCN-TiO_2	Methanol and Water	UV	Continuous - Fixed Bed	6087	[28]
Ag-Mt/pCN-TiO_2	Methanol and Water	UV	Continuous - Monolith	11735	[28]
N-doped TiO_2 aerogels/Pd	Methanol and Water	Visible	Continuous - Fixed Bed	3100	[29]

Comparing the results obtained with those in the literature, it can be seen that the performances obtained are lower than those previously reported. However, looking at the experimental conditions, they are quite different from those used. The performances previously reported were with materials that have noble metals in their composition, a sacrificial agent was used, a different radiation and a different reactor set up were used. These experimental conditions are quite different from those used, since no noble metals were used, only pure water was used as a reactant and the tests were carried out in batch mode. It is therefore quite challenging to compare the performances of the different samples, something previously pointed out by Kwon et al. [29]. Unfortunately, it was not possible to find reported in the literature results with more similar experimental conditions to the ones used for the photocatalytic water splitting in gas phase.

However, in order to compare the performance of the different materials under study with a reference material, it was decided to test TiO_2 under the same experimental conditions. Due to its physical and chemical properties, TiO_2 is one of the most widely used materials as a photocatalyst [30]. Using the same experimental conditions employed throughout this thesis, it can be seen that TiO_2 as a H_2 rate equal to 5 μmol/h/g (see Table 6.7). When comparing TiO_2 performance with the different materials under study, it is possible to observed that the last ones have a higher photocalytic performance. For the samples with saccharedeos on their composition such increase in performance is about two orders of magnitude. In the light of these results, the materials under study can be seen as promising photocatalysts for the reaction under study.

6.3 Conclusions

The photocatalytic performance of the different materials under study was assessed following two reactions with high social and economic interest - the CO_2 photoreduction and water splitting.

The results of CO_2 photoreduction were not conclusive, since even using widely studied reference materials it was not possible to obtain carbon products, only H_2. Thus, there was some problem in the experimental unit or in the experimental conditions used that was not detected by us. As such, it is not known whether the newly synthesized materials are active in the CO_2 photoreduction reaction or not.

Taking into account the previous results, the photocatalytic activity of the materials using the water splitting reaction was studied. In addition to evaluating the performance of the unmodified materials, the impact of the two types of modification - metal doping and accessibility modifications - was also evaluated.

For the unmodified materials, IZM-5 and ITQ-75, it was observed that only the external surface area presents an aparent correlation with the different parameters used to evaluate the photocatalytic performance. A possible volcano-like relationship was observed between the photocatalytic performance and the external surface area. According to the literature, this relationship can be explained by the balance between a higher surface accessibility of the active centers and the presence of defects in the crystal lattice.

As for the metal-doped samples, a similar behavior is observed regarding the relationship between the observed photocatalytic performance and the external surface area. In respect to the optical band gap, it is verified that with the decrease of this parameter there is an apparent increase of the photocatalytic performance. This increase can be explained by the fact that by decreasing the optical band gap to a certain point, the interaction between the incident radiation and the material increases, and still allowing to produce charge carriers with sufficient potential to carry out the desired reaction. It was also verified how the Dopant/Sn molar ratio is related to the photocatalytic performance. A volcano-like behavior was found between the Dopant/Sn molar ratio and the photocatalytic performance. By inserting dopants in the material, according to the literature, defects in the crystal lattice are inserted. Thus, there is a balance between the gains associated with the presence of the dopants (which has as a consequence the modification of the interaction with the incident radiation) and the losses associated with a possible increase of the defects in the crystalline lattice. It is worth noting the apparent interesting behavior of ITQ-75 obtained with Compound C as SDA. This material, prior to any modification, presents an optical band gap equal to 2,2 eV, a value

within the optical range of optical band gaps according to the literature consulted. Taking into account the behavior of this sample, and comparing it with the other doped samples, it seems to act as a maximum reachable performance. Hence, it seems that ITQ-75 obtained with Compound C as SDA prior to any modification presents an optimum external surface area value and optical band gap value for the reaction under study.

As for the different techniques used to increase accessibility, the most promising one seems to be the addition of saccharides, namely sucrose. By adding sucrose during synthesis it is possible to increase the photocatalytic performance about 36 times, from 9,0 µmol/h/g to 323,1 µmol/h/g (for ITQ-75 obtained with Compound B as SDA) or from 19,0 µmol/h/g to 390,5 µmol/h/g (for ITQ-75 obtained with Compound C). In order to better understand the influence of saccharides on the photocatalytic performance, a more in-depth study of this would be required. It would be necessary to understand the chemical environment in which they are inserted and their influence on the electronic structure of the material, as well as their role in the generation, transport and transfer of photogenerated charges. It would also be important to know whether their presence could be a possible source of H^+ and whether the organic phase is subject to modifications during the photochemical reaction. It is also interesting to note that although the samples post-modified with the ball mill or the butyl lithium treatments do not show improvements in their textural properties, they possible influence their electronic properties. After the post treatments, it was found that there was an increase in the optical band gap, that leads to less photons being absorbed. However, the apparent quantum yield increased from 0,2% to almost 1,8%. Thus, although the samples absorb less photons, these are better utilized in the reaction. It is thus concluded that, although these treatments were not successful in increasing accessibility, they apparently modify their electronic properties, which seems to benefit their photocatalytic performance.

Finally, samples with a similar optical band gap, i.e. between 1,9 eV and 2,1 eV, were grouped and it was verified how the different parameters used to evaluate the photocatalytic performance relate to their external surface area. It was found that, for samples within this band gap range (which have a maximum external surface area of 60 m^2/g), there is an apparent linear relationship between the external surface area and the observed performance. According to the mechanism proposed in the literature, the limiting step is the chemisorption of water. Thus, the observed apparent relationship could be explained by the limiting step of the photocatalytic process. By increasing the external surface area, the water coverage is increased and, as such, the water chemisorption is also increased. In order to confirm this hypothesis it would be necessary to evaluate the water adsorption by the samples

and verify if indeed with the increase of the external surface area the chemisorption increases.

In view of the interesting results obtained for the water splitting reaction, it would be worthwhile to evaluate the stability and performance of the different materials in liquid phase for the same reaction.

References

[1] Zhuo Xiong et al. "CO$_2$ photocatalytic reduction over Pt deposited TiO$_2$ nanocrystals with coexposed 101 and 001 facets: Effect of deposition method and Pt precursors". In: *Catalysis Communications* 96 (2017), pp. 1–5. ISSN: 1566-7367. DOI: https://doi.org/10.1016/j.catcom.2017.03.013.

[2] Alberto Olivo et al. "Investigation of process parameters assessment via design of experiments for CO$_2$ photoreduction in two photoreactors". In: *Journal of CO2 Utilization* 36 (2020), pp. 25–32. ISSN: 2212-9820. DOI: https://doi.org/10.1016/j.jcou.2019.10.009.

[3] Ștefan Neațu et al. "Gold–Copper Nanoalloys Supported on TiO$_2$ as Photocatalysts for CO$_2$ Reduction by Water". In: *Journal of the American Chemical Society* 136.45 (2014), pp. 15969–15976. DOI: 10.1021/ja506433k.

[4] Warren Athol Thompson, Eva Sanchez Fernandez, and M. Mercedes Maroto-Valer. "Review and Analysis of CO$_2$ Photoreduction Kinetics". In: *ACS Sustainable Chemistry & Engineering* 8.12 (2020), pp. 4677–4692. DOI: 10.1021/acssuschemeng.9b06170.

[5] Muhammad Tahir and NorAishah Saidina Amin. "Photocatalytic CO$_2$ reduction with H$_2$O vapors using montmorillonite/TiO$_2$ supported microchannel monolith photoreactor". In: *Chemical Engineering Journal* 230 (2013), pp. 314–327. ISSN: 1385-8947. DOI: https://doi.org/10.1016/j.cej.2013.06.055.

[6] Zaiba Zafar et al. "Recent Development in Defects Engineered Photocatalysts: An Overview of the Experimental and Theoretical Strategies". In: *Energy & Environmental Materials* 5.1 (2022), pp. 68–114. DOI: https://doi.org/10.1002/eem2.12171.

[7] Takashi Hisatomi, Tsutomu Minegishi, and Kazunari Domen. "Kinetic Assessment and Numerical Modeling of Photocatalytic Water Splitting toward Efficient Solar Hydrogen Production". In: *Bulletin of the Chemical Society of Japan* 85.6 (2012), pp. 647–655. DOI: 10.1246/bcsj.20120058.

[8] Dan Kong et al. "Recent advances in visible light-driven water oxidation and reduction in suspension systems". In: *Materials Today* 21.8 (2018), pp. 897–924. DOI: https://doi.org/10.1016/j.mattod.2018.04.009.

[9] Frank E. Osterloh. "Nanoscale Effects in Water Splitting Photocatalysis". In: *Solar Energy for Fuels*. Ed. by Harun Tüysüz and Candace K. Chan. Cham: Springer International Publishing, 2016, pp. 105–142. ISBN: 978-3-319-23099-3. DOI: 10.1007/128_2015_633.

[10] Sasa Lukic et al. "Decoupling the Effects of High Crystallinity and Surface Area on the Photocatalytic Overall Water Splitting over β-Ga$_2$O$_3$ Nanoparticles by Chemical Vapor Synthesis". In: *ChemSusChem* 10.21 (2017), pp. 4190–4197. DOI: https://doi.org/10.1002/cssc.201701309.

[11] Conrado Martinez Suarez, Simelys Hernández, and Nunzio Russo. "BiVO$_4$ as photocatalyst for solar fuels production through water splitting: A short review". In: *Applied Catalysis A: General* 504 (2015). Nanocatalysis Science: Preparation, Characterization and Reactivity, dedicated to the scientific work of Jacques C. Vedrine., pp. 158–170. ISSN: 0926-860X. DOI: https://doi.org/10.1016/j.apcata.2014.11.044.

[12] Nick Serpone et al. "Why do Hydrogen and Oxygen Yields from Semiconductor-Based Photocatalyzed Water Splitting Remain Disappointingly Low? Intrinsic and Extrinsic Factors Impacting Surface Redox Reactions". In: *ACS Energy Letters* 1.5 (2016), pp. 931–948. DOI: 10.1021/acsenergylett.6b00391.

[13] Heinz Gerischer. "Semiconductor Electrodes and Their Interaction with Light". In: *Photoelectrochemistry, Photocatalysis and Photoreactors: Fundamentals and Developments*. Ed. by Mario Schiavello. Dordrecht: Springer Netherlands, 1985, pp. 39–106. ISBN: 978-94-015-7725-0. DOI: 10.1007/978-94-015-7725-0_2.

[14] Canan Acar, Ibrahim Dincer, and Greg F. Naterer. "Review of photocatalytic water-splitting methods for sustainable hydrogen production". In: *International Journal of Energy Research* 40.11 (2016), pp. 1449–1473. DOI: https://doi.org/10.1002/er.3549.

[15] H.Philipp Ebert. "Imaging defects and dopants". In: *Materials Today* 6.6 (2003), pp. 36–43. ISSN: 1369-7021. DOI: https://doi.org/10.1016/S1369-7021(03)00632-1.

[16] Xiaomei Yang et al. "Synthesis of hierarchical AlPO-n molecular sieves templated by saccharides". In: *Microporous and Mesoporous Materials* 144.1 (2011), pp. 176–182. ISSN: 1387-1811. DOI: https://doi.org/10.1016/j.micromeso.2011.04.011.

[17]   Ivana Miletto et al. "Hierarchical SAPO-34 Architectures with Tailored Acid Sites using Sustainable Sugar Templates". In: *ChemistryOpen* 7.4 (2018), pp. 297–301. DOI: `https://doi.org/10.1002/open.201800001`.

[18]   Qian Su et al. "Heterojunction Photocatalysts Based on 2D Materials: The Role of Configuration". In: *Advanced Sustainable Systems* 4.9 (2020), p. 2000130. DOI: `https://doi.org/10.1002/adsu.202000130`.

[19]   Simrjit Singh et al. "Hybrid Organic–Inorganic Materials and Composites for Photoelectrochemical Water Splitting". In: *ACS Energy Letters* 5.5 (2020), pp. 1487–1497. DOI: `10.1021/acsenergylett.0c00327`.

[20]   Baoqian Ye et al. "Organic-inorganic heterojunction photocatalysts: From organic molecules to frameworks". In: *Materials Science in Semiconductor Processing* 164 (2023), p. 107623. ISSN: 1369-8001. DOI: `https://doi.org/10.1016/j.mssp.2023.107623`.

[21]   Yidan Wang et al. "Unraveling the Mechanism of Photocatalytic Water Splitting in α-Ga_2O_3 Loaded with a Nickel Oxide Cocatalyst: A First-Principles Investigation". In: *The Journal of Physical Chemistry C* 123.14 (2019), pp. 8990–9000. DOI: `10.1021/acs.jpcc.9b00047`.

[22]   J. Rossmeisl et al. "Electrolysis of water on oxide surfaces". In: *Journal of Electroanalytical Chemistry* 607.1 (2007). Theoretical and Computational Electrochemistry, pp. 83–89. DOI: `https://doi.org/10.1016/j.jelechem.2006.11.008`.

[23]   Á. Valdés et al. "Oxidation and Photo-Oxidation of Water on TiO_2 Surface". In: *The Journal of Physical Chemistry C* 112.26 (2008), pp. 9872–9879. DOI: `10.1021/jp711929d`.

[24]   Isabela C. Man et al. "Universality in Oxygen Evolution Electrocatalysis on Oxide Surfaces". In: *ChemCatChem* 3.7 (2011), pp. 1159–1165. DOI: `https://doi.org/10.1002/cctc.201000397`.

[25]   Fabio Dionigi et al. "Gas phase photocatalytic water splitting with $Rh_{2y}CryO_3$/GaN:ZnO in μ-reactors". In: *Energy Environ. Sci.* 4 (8 2011), pp. 2937–2942. DOI: `10.1039/C1EE01242H`.

[26]   Cameron J. Shearer et al. "Gas phase photocatalytic water splitting of moisture in ambient air: Toward reagent-free hydrogen production". In: *Journal of Photochemistry and Photobiology A: Chemistry* 401 (2020), p. 112757. DOI: `https://doi.org/10.1016/j.jphotochem.2020.112757`.

[27]   Alejandra Castedo et al. "Effect of temperature on the gas-phase photocatalytic H_2 generation using microreactors under UVA and sunlight irradiation". In: *Fuel* 222 (2018), pp. 327–333. ISSN: 0016-2361. DOI: `https://doi.org/10.1016/j.fuel.2018.02.128`.

[28] Nur Fajrina and Muhammad Tahir. "Monolithic Ag-Mt dispersed Z-scheme pCN-TiO$_2$ heterojunction for dynamic photocatalytic H$_2$ evolution using liquid and gas phase photoreactors". In: *International Journal of Hydrogen Energy* 45.7 (2020), pp. 4355–4375. ISSN: 0360-3199. DOI: `https://doi.org/10.1016/j.ijhydene.2019.11.194`.

[29] Junggou Kwon et al. "Gas-Phase Nitrogen Doping of Monolithic TiO$_2$ Nanoparticle-Based Aerogels for Efficient Visible Light-Driven Photocatalytic H$_2$ Production". In: *ACS Applied Materials & Interfaces* 13.45 (2021), pp. 53691–53701. DOI: `10.1021/acsami.1c12579`.

[30] Muhammad Rafique et al. "Hydrogen Production Using TiO$_2$-Based Photocatalysts: A Comprehensive Review". In: *ACS Omega* 8.29 (2023), pp. 25640–25648. DOI: `10.1021/acsomega.3c00963`.

Chapter 7

General Conclusions and Future Perspectives

In all affairs it's a healthy thing now and then to hang a question mark on the things you have long taken for granted.

Bertrand Russel

The objective of this doctoral thesis was to develop open framework chalcogenide materials with suitable characteristics to be used as photocatalyits for solar fuels production. Although the objective have been partially achieved, new structures have been extensively studied, opening doors for future research.

Throughout this doctoral thesis, three materials were studied. IZM-5, recently patented by IFPEN, ITQ-75 and ITQ-76 which were developed and patented throughout the development of this thesis. IZM-5, according to SCXRD, can be seen as a laminar structure with a semicube as building unit. Regarding ITQ-75 and ITQ-76, unfortunately their structure could not be solved due to low crystallinity and small particle size, but according to the information obtained by PXRD and HRTEM, the materials seem to have a laminar profile as well.

When these materials are synthesized they present an optical band gap between 2,2 eV and 3,6 eV and a low accessibility. Thus, in order to adapt their characteristics to the final application, they were modified. The first modification studied was the insertion of doping agents or a Ru complex in order to modify their electronic structure or radiation absorption capabilities, respectively. Several metals, such

as cobalt, copper, iron and nickel, and a chalcogenide, such as selenium, were tested as doping agents. The consequences of these doping agents were diverse. The use of copper and cobalt allowed to obtain materials with an optical band gap value equal to 2,0 eV, resulting in structures with optical band gap in the ideal range of values for the final application. For the other doping agents, the behavior was not so linear. It is thus shown that besides the chemical nature of the doping agent used, other factors such as the crystal structure of the material to be doped, the SDA present in it or the concentration of the doping agent used are important factors to be taken into account. Hence, it is possible to obtain different consequences to the present of the doping agent on the final optical band gap value.

Regarding the materials accessibility, when they are obtained they present a low accessibility, which according to the literature reviewed, it might jeopardize their photocatalytic performance. Therefore, different methodologies, from the alteration of the synthesis gel composition to post synthesis modifications were tested in order to improve their textural properties. Regarding the modifications to the synthesis gel, two methodologies were tested: the insertion of coSDAs previously known to create a secondary porous system and with reduced thermal degradation temperature, namely fructose or sucrose, and the increase of the gel viscosity, by raising the ethylene glycol content, in order to obtain crystals with reduced dimensions. As for the addition of fructose or sucrose, it was found that there is not the formation of a secondary porous system and the final thermal stability was not altered. However, there was an increase in the accessibility of the samples due to the increase in the external surface area, later confirmed by FESEM that it was due to the reduction of crystal size. With the insertion of these compounds it was possible to obtain structures with an external surface area around to 75 m^2/g. However, the chemical environment where the resulting fructose or sucrose compound is located is unknown, as well as its influence on the electronic structure. Therefore, a deeper study of these structures is needed to understand what kind of organic structure is found in the final material as well as a more detailed electrochemical characterization to understand the real impact it had on the band structure as well as on the ability to generate, transport and transfer photogenerated charges. Regarding the second modification on the synthesis gel studied, it was found that by increasing the ethylene glycol content, its external surface area increases due to a decrease in crystal size. Thus, although these methodologies did not allow obtaining samples with a reasonable porous volume, their external accessibility was improved. The combination of these two methodologies allows to further increase the external surface area up to 108 m^2/g.

With the addition of doping agents, namely copper and cobalt, it was possible to reduce the optical band gap value to values suitable for the production of solar fuels but it was not possible to obtain structures with appreciable microporous volume. However, by using coSDAs and increasing gel viscosity, it allowed to improve the accessibility of the surface, due to the reduction of the crystals size. Taking into consideration the vast industrial applications of microporous crystalline structures, it is still desirable to obtain stable chalcogenide-based materials with an open microporosity. To this end, it is suggested to study and develop SDAs without a possible valency with the inorganic structure or that are easily degradable, for example thermally.

That said, the photocatalytic performance of the different materials was evaluated. It was started by evaluating their photocatalytic performance using the direct CO_2 photoreduction reaction, whose reaction products have a high social and economic interest and the usage of this class of materials in such reaction is reduced. Unfortunately, the results were not conclusive. Using as reference materials TiO_2 and TiO_2 with photodeposited Pt, photocatalysts widely studied in the literature for the reaction in question, it was not possible to obtain carbon products, only H_2. Thus, there was a problem in the experimental conditions or in the experimental unit used that did not allow to draw conclusions on the photocalytic performance of the materials under study. Therefore, in order to draw such conclusions, more tests need to be carried out. It is therefore suggested to adapt the system used and to test other experimental conditions before being able to draw conclusions about these structures performance. Other experimental conditions suggested to test can be performing the photocatalytic tests the continuous mode rather than the batch mode, with higher pressures, evaluating the performance in liquid phase by dissolving the CO_2 in an appropriate solvent and using a sacrificial agent to overcome the CO_2/H_2O balance limitations.

In view of the results obtained, it was decided to study the photocatalytic performance of the materials under study by using the water splitting reaction, whose reaction product is also of a high social and economic interest and could be used for indirect solar valorization of CO_2.

Due to the diversity of the results obtained, in order to better compare the samples, a modeling was performed. This modeling allowed to compare the different materials at the same reaction time, i.e. at the initial reaction time, thus allowing to rule out possible deactivation effects. The model made was based only on mathematical considerations, being a pseudo-kinetic model, as well as the parameters derived therefrom. With the different results obtained it was possible to verify that there are several characteristics of the materials that influence the observed photocatalytic performance. It was tried to correlate the value of the optical band

gap, a characteristic related to the capacity of photogeneration of charges, and the external surface area, since this is the textural property that predominates in the samples under study and is related to the surface accessibility. Regarding the relationship between the optical band gap value and the photocatalytic performance, it was found that by decreasing the optical band gap value there is an apparent improvement in performance. By reducing its value, the ability to produce photogenerated charges increases, since the interaction with the incident radiation increases. However, this improvement is verified up to a certain point, since from a certain value of band gap the photogenerated charges no longer have sufficient potential to participate in the reaction under study. Thus, there is a balance between the ability of the material to absorb photons and to photogenerate charges and the charges desired potential for the reaction under study. Regarding the correlation between external surface area and the photocatalytic performance, there seems to be a volcano-like relationship between the two. By increasing the external surface area up to a certain value there is an apparent improvement in photocatalytic performance. This improvement can be explained, according to the literature reviewed, by the increased interaction between the external surface and the substrate. However, from a certain value of external surface, there is a decrease in photocatalytic performance. Although there is still some difficulty in explaining the influence that defects have, there are several studies that show that with their increase the charge transport capacity of a given material decreases. Thus, by increasing the external surface area, the number of defects on the surface increases, which could explain why the performance decreases for higher external surface area values. Finally, the samples that showed the most promising performances were those modified with sucrose. With these samples it was possible to obtain H_2 rates up to 390 µmol/h/g and energetic yields close to 1%. However, given the limited information on the role of sucrose in the electronic properties, a more in-depth study, including electrochemical characterization, would be required. The stability of these compositions during the photocatalytic process would also need to be assessed, since the possibility of the organic component undergoing oxidation, and as such being an proton donor, cannot be ruled out with the information available. If the presence of a hybrid junction of the organic/inorganic type is indeed confirmed, the possibility of creating other junctions could be studied, by using for example organic or carbonitride semiconductors coupled with the chalcogenides structures under study. It is thus concluded that some of the developed materials present characteristics and preliminary results that make them promising candidates as photocatalysts in the water splitting reaction.

This thesis has only studied one of the three possible configurations, electrochemical, photoelectrochemical and photocatalytic powder dispersion, for the production of solar fuels. Therefore, and given the high social, environmental and economic

interests associated with the solar fuels production, it would be of the utmost interest to evaluate the performance of the new structures in the two remaining configurations. In addition, other photocatalytic reactions could be explored in which these new materials could be used as photocatalysts. These include the CO_2 hydrogenation, an indirect route to value CO_2, degradation of organic compounds, such as VOCs or other polluting compounds, or organic synthesis, thus enabling the production of organic compounds with great industrial interest, for example for the pharmaceutical sector.

Appendix A

Experimental Methodology

In this Chapter the experimental methodology used to obtain the results present in this thesis is presented. It will be divided into four sections. On the first section a summary of all the reagents used is presented. Subsequently, the synthesis of the different structures, as well as the modifications to the initial methodology, are described. On the second section the different characterization techniques employed are introduced. Finally, the photocatalytic tests, namely a description of the unit and the procedure used, are described.

A.1   Reagents

This section summarizes the different reagents used throughout this thesis. The different reagents were used as they came, with no extra purification procedures. These are divided into different tables according to their classification: inorganic solids (see Table A.1), SDAs (see Table A.2), co-SDAs (see Table A.3), liquids (see Table A.4), and gases (see Table A.5). The reagents were used as received, without any further purification process.

Table A.1: Different inorganic solids used

Solid	Supplier	Chemical Formula
Tin Oxide	Sigma-Aldrich	SnO_2
Tin Chloride	Sigma-Aldrich	$SnCl_2$
Sulfur	JT Baker	S
Zinc Nitrate	Alfa Aesar	$Zn(NO_3)_2 \cdot 6\,H_2O$
Selenium	Panreac	Se
Copper Nitrate	Sigma-Aldrich	$Cu(NO_3)_2 \cdot 3\,H_2O$
Iron Nitrate	Sigma-Aldrich	$Fe(NO_3)_3 \cdot 9\,H_2O$
Cobalt Nitrate	Sigma-Aldrich	$Co(NO_3)_2 \cdot 6\,H_2O$
Nickel Nitrate	Sigma-Aldrich	$Ni(NO_3)_2 \cdot 6\,H_2O$
Cesium Chloride	Sigma-Aldrich	CsCl
Cetyltrimethylammonium Bromide (CTMABr)	Sigma-Aldrich	$C_{19}H_{42}BrN$
Sodium Persulfate	Sigma-Aldrich	$Na_2S_2O_8$
Sodium Nitrate	Sigma-Aldrich	$NaNO_3$

Table A.2: Different SDAs used
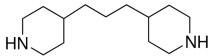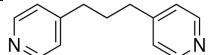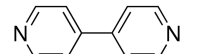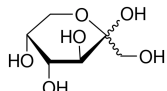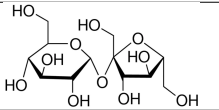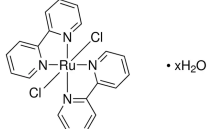
SDA	Reference	Supplier	Chemical Formula	Chemical Representation
1,3-Bis(4-piperidyl)propane	Compound A	Sigma-Aldrich	$C_{13}H_{26}H_2$	
1,3-Bis(4-pyridyl)propane	Compound B	Sigma-Aldrich	$C_{13}H_{14}H_2$	
4,4'-Dipyridyl	Compound C	Sigma-Aldrich	$C_{10}H_8N_2$	
1,2-Bis(4-pirydyl)ethane	Compound D	Sigma-Aldrich	$C_{12}H_{12}N_2$	
1,2-Di(4-pyridyl)ethylene	Compound E	Sigma-Aldrich	$C_{12}H_{10}N_2$	

Table A.3: Different coSDAs used

coSDA	Supplier	Chemical Formula	Chemical Representation
Fructose	Sigma-Aldrich	$C_6H_{12}O_6$	
Sucrose	Sigma-Aldrich	$C_{12}H_{22}O_{11}$	
cis-Dichlorobis(2,2-bipyridine)ruthenium(II)	Sigma-Aldrich	$C_{20}H_{16}Cl_2N_4Ru \cdot x\ H_2O$	

Table A.4: Different liquids used

Liquid	Supplier	Chemical Formula
Distilled Water		H_2O
Milli-Q Water		H_2O
Ethylene glycol	Scharlab	$(CH_2OH)_2$
Ethanol	Scharlab	C_2H_6O
Acetone	Scharlab	$(CH_3)_2CO$

Table A.5: Different gases used

Liquid	Supplier	Chemical Formula
Nitrogen	Air Liquide	N_2
Carbon Dioxide	Air Liquide	CO_2
Helium	Air Liquide	He

A.2   Material Synthesis

The initial methodology for obtaining the material consists on mixing SnO_2, $Zn(NO_3)_2$ · $6 H_2O$, S, SDA, ethylene glycol and deionized water in a flask for 1 hour, at room temperature. The final gel has a molar composition of 1 SnO_2 : 0,32 $Zn(NO_3)_2$: 5,72 S : 6,29 SDA : 132,64 $C_2H_6O_2$: 138,08 H_2O. The gel is then transferred to a Teflon vessel in an autoclave, and placed inside an oven for 12 days at 190°C. At the end of the synthesis period, the autoclave is cooled quickly, using water and ice, and the sample is recovered through filtration, ethanol washed and placed to dry at 100°C overnight.

A.2.1 Screening Different Synthesis Conditions

Since there is no information on how the parameters of synthesis influence the final material obtained, several conditions of synthesis were tested. All changes to the initial methodology assessed are schematized in the Figure .

In order to evaluate the impact that different organic compounds have on the final crystalline structure, the different compounds shown in the Table A.2 were evaluated as SDA. As for the Sn source, two compounds, SnO_2 and $SnCl$, were evaluated as possible Sn sources. Regarding the synthesis time, it was checked if it was possible to reduce it. For this, the synthesis time was reduced to 1, 2, 3, 6, 8 and 10 days. Finally, the impact that the cooling method of the autoclaves has on the final structure was evaluated. Room temperature cooling and fast cooling, using dry ice and acetone, were tested.

As for the gel composition, the influence of Sn, SDA and solvent contents were evaluated. The Sn content was reduced by 10%, 20% and 30%. As for the SDA content, it was increased and decreased by 20%. Regarding the EG/H_2O ratio, it was modified from 0,96 to 0,57 and 0,32. Finally, the H_2O/Sn ratio was changed from 139 to 200 and 300 while keeping the EG/H_2O equal to 0,96. The different molar compositions tested are systematized in the Table A.6.

Table A.6: Different gel's molar compositions evaluated

	Gel Molar Composition							
	Sn	Zn	S	SDA	EG	H_2O	EG/H_2O	H_2O/Sn
Original	1	0,32	5,72	6,29	132,64	138,08	0,96	138,08
-10% Sn Content	0,9	0,32	5,72	6,29	132,64	138,08	0,96	153,42
-20% Sn Content	0,8	0,32	5,72	6,29	132,64	138,08	0,96	172,60
-30% Sn Content	0,7	0,32	5,72	6,29	132,64	138,08	0,96	197,26
+20% SDA Content	1	0,32	5,72	7,55	132,64	138,08	0,96	138,08
-20% SDA Content	1	0,32	5,72	5,03	132,64	138,08	0,96	138,08
0,57 EG/H_2O	1	0,32	5,72	6,29	78,71	138,08	0,57	138,08
0,32 EG/H_2O	1	0,32	5,72	6,29	44,19	138,08	0,32	138,08
200 H_2O/Sn	1	0,32	5,72	6,29	192,00	200,00	0,96	200,00
300 H_2O/Sn	1	0,32	5,72	6,29	288,00	300,00	0,96	300,00

The possibility of obtaining the material without the use of an SDA was also evaluated. For this, the SDA was replaced by seeds or $NaNO_3$. To evaluate the impact that the presence of Na^+ cations would have on the final structure, three different S/Na^+ ratios were tested: 1,02, 1,25 and 0,84. As for the use of seeds,

it was decided to reduce the synthesis time to one day, and 10% w/w of the Sn present in the gel came from the seeds.

A.2.2 Materials modification during synthesis

Considering the final application of the materials, their synthesis procedure was altered in order to change the interaction with the radiation and its porous system.

To modify the interaction with radiation doping with different elements, such as selenium, copper, cobalt, iron and nickel, were used (see Table A.1). Different concentrations of these dopants were used. For selenium three different Se/S molar ratios were tested: 0,01, 0,1 and 0,2. For the remaining metals, three M/Sn molar ratios (M = Cu, Co, Fe, Ni) were tested: 0,1, 0,3 and 0,6.

Regarding the radiation absorption capability, a Ru-based complex was used in the synthesis gel (see Table A.3). Three conditions were tested, the use of the Ru-complex as the SDA or use it combined with the SDA present on the original methodology (Ru-complex/SDA molar ratio equal to 0,1 or o,01).

The porous system was altered by using co-SDAs, namely fructose and sucrose, as mesoporous agents (see Table A.3). Three Sugar/SDA ratios were tested: 0,33, 1, and 3. The impact that the gel's viscosity would have on the particle size and, as a consequence, on the accessibility of the material was also evaluated. To do this, the EG/H_2O ratio was increased from 0,96 to 3,5.

A.3 Material's Post-Modification

To increase the accessibility of the synthesized materials, different methodologies post-synthesis were tested. These can be divided into methods that involve the elimination of the SDA, such as a thermal treatment or ionic exchange, or the non-elimination of the organic component (see Figure A.1).
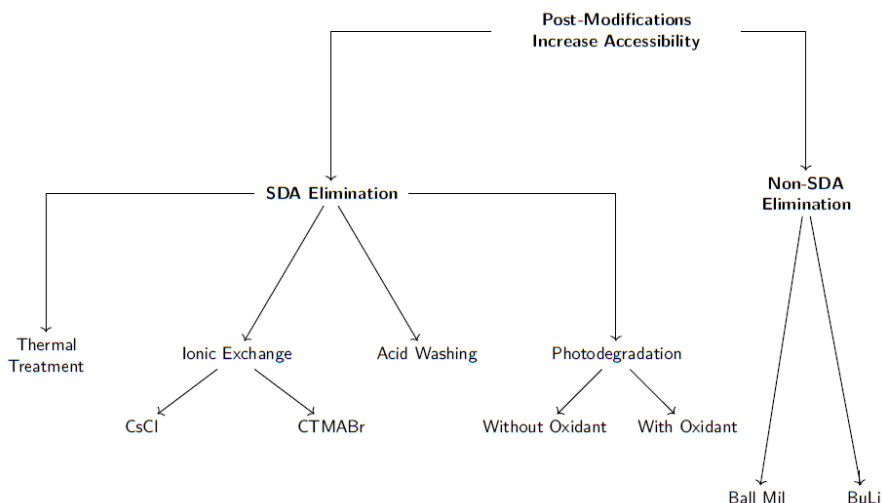
Figure A.1: Scheme of the different methodologies used to increase the accessibility of the synthesized materials

A.3.1 Increasing accessibility by SDA elimination

A.3.1.1 Thermal Treatment

To eliminate the SDA present in the samples, a thermal treatment under nitrogen, with a flow of 2,5 mL/s, was performed under the conditions presented at Figure A.2.
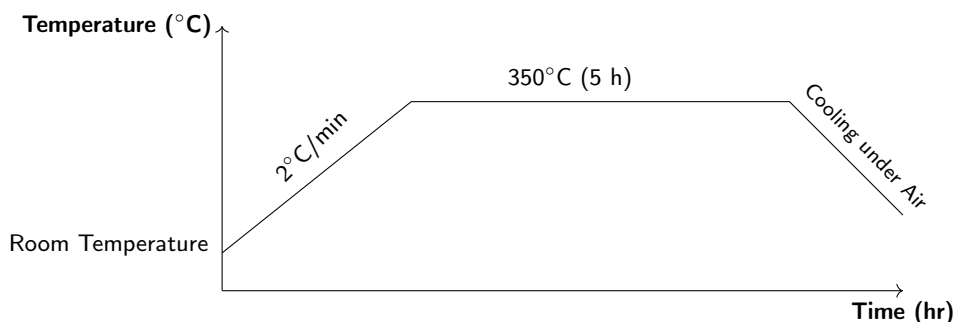
Figure A.2: Thermal treatment conditions

329

A.3.1.2   Ionic Exchange

To try to exchange the SDA present with other species, Cs^+ and $CTMA^+$ were used. These species were used in the form of CsCl and CTMABr respectively.

A certain quantity of the solid to be exchanged was suspended in a solution containing the species to be exchanged (0,01 M), so that the ratio of solid to solution was 15 mg of solid per mL of solution. The suspension was kept under strong stirring under reflux. The CsCl exchange was performed using two different experimental conditions. The first set of consitions consisted on keeping the suspension under reflux at a temperature of 80°C for 5 hours. This process was repeated five times. As for the second set of experimental conditions, it consisted on maintaining the suspension at a temperature of 100°C for 24 hours. Regarding the CTMABr exchange, the suspension was kept under strong striring for 24 hours at 100°C. After the ionic exchange, the solid was filtered and washed with abundant water in order to eliminate residual cations and placed to dry at 100°C overnight.

A.3.1.3   Acid Washing

To try to degraded the SDA present, a soft acid treatment with HCl was performed.

A certain quantity of the solid to be washed was suspended in an ethanolic solution containing HCl (0,05 M), so that the ratio of solid to solution was 20 mg of solid per mL of solution. The suspension was kept under strong stirring for 16 hours, at a temperature of 80°C under reflux. After the acid washing, the solid was filtered and washed with abundant water in order to eliminate residual acid and placed to dry at 100°C overnight.

A.3.1.4   SDA Photodegradation

In order to degrade the SDA present, a photodegradation process was employed in the presence or absence of an oxidant.

A certain quantity of the solid to be photodegradated was sonicated for ten minutes in deionized water, so that the ratio of solid to water was 2 mg of solid per mL of solution. The suspension was kept under strong stirring for four or six hours, at room temperature under a 1000 W Xe lamp. To the suspension was also added $Na_2S_2O_8$ in order to accelerate the degradation process. The amount added depends on the carbon content of the starting material. Two concentrations were tested, 5 and 10% (molar percentage) of the carbon initially present. After the

photodegradation, the solid was filtered and washed with abundant water and placed to dry at 100°C overnight.

A.3.2 Increasing accessibility by non-SDA elimination

A.3.2.1 n-Butyllithium Treatment

In order to reduce the number of lamellars per stack, the structures were subjected to a treatment with n-butyllithium, following the experimental procedure in [1].

One gram of as-synthesized material was placed in 8 mL of 1,6 M n-butyllithium/ hexane for 48 hours under a nitrogen atmosphere. The material was then recovered and washed by filtration with hexane to remove excess n-butyllithium and dried under nitrogen atmosphere for 24 hours. Subsequently, the resulting powder was immersed in 500 mL of deionized water and the suspension was sonicated for 30 minutes. The dispersion was centrifuged at 5000 rpm for 15 minutes and the supernatant was recovered with a pipette. The recovered supernatant will have a basic pH due to the presence of lithium hydroxide traces. In order to recover the material present in the colloid, HCl was added dropwise to reach a pH of 3. The precipitate was washed and recovered by centrifugation several times until a neutral pH was reached. Finally, the material was dried at 60°C overnight.

A.3.2.2 Ball Mill Treatment

Ball milling allows to grind powders into fine particles and blend materials and it is widely known to reduce crystallite size [2].

A certain quantity of solid to be milled was mixed with Zr balls (with a diameter equal to 2mm), so that the ratio solid:balls was 1:5. The mixture was milled in a tumbler ball mill for different periods of time and at a rotation equal to 50 rpm.

A.4   Material Characterization

A.4.1   *Chemical Composition*

Two different techniques, elemental analysis and atomic absorption, were used to determine the chemical composition of the final samples obtained.

A.4.1.1   *Elemental Analysis*

This technique allows, from the combustion of the sample, to determine the content of C, H, N and S. After the sample combustion, the gases formed (CO_2, H_2O, N_2 and SOx) are carried away by a He flux and separated by a chromatographic column, which allows their quantification. For this purpose, a Carlo Erba 1106 elemental analyzer was used.

A.4.1.2   *Inductively Coupled Plasma - Optical Emission Spectrometry (ICP-OES)*

The inductively coupled plasma, together with a optical emission spectrometry, allows to determine the chemical composition of a solid or a liquid sample.

A Spectra AA 10 Plus, Varian was used to determine the inorganic chemical content. Since the samples were on solid state, it was necessary to mineralise them first. Normally, samples are mineralised in acid medium (HNO_3/HF/HCl in a volumetric proportion of 1:1:3) for 24 hours. However, this methodology does not work for the samples under study. It was found that for a correct mineralization it is first necessary to dissolve 20 mg of the sample to be analyzed in 20 mL of aqua regia and 10 mL of deonized water. The sample is then transferred to a Teflon vessel in a microwave autoclave and put it under the following program:

- First stage - 3 minutes, 900 W, T_{max} – 180°C, T_{min} – 120°C, 70% agitation;

- Second stage - 2 hours, 600 W, T_{max} – 180°C, T_{min} – 120°C, 70% agitation;

- Third stage – cooling to room temperature.

A.4.2 Powder X-ray Diffraction (PXRD)

X-ray diffraction (XRD), a widely used technique, is based on the interaction of monochromatic X radiation with a crystalline structure. This interaction causes constructive interference and diffracted rays, which are detected and processed, originating a unique diffraction pattern for each crystalline structure. When the incident radiation has a wavelength λ comparable to atomic space, it can suffer a regular reflection and create a constructive interference with the atoms of the crystalline system (see Figure A.3) [3, 4].
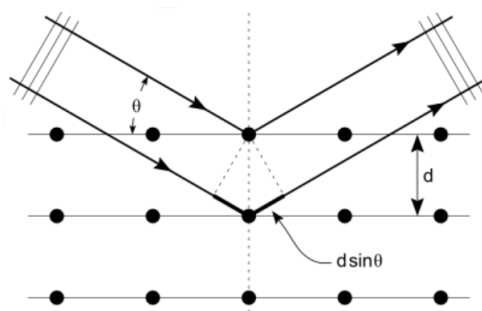
Figure A.3: Bragg's diffraction scheme (adapted from [3, 4])

When the phenomenon described in the Figure A.3 occurs, it is said to be in the presence of Bragg diffraction and the Equation A.1 is valid. On Equation A.1 n represents the diffraction order, λ the radiation wavelength, d the distance between successive layers of atoms and θ the glancing angle [3, 4].

$$n\lambda = 2d\sin\theta \qquad (A.1)$$

XRD was used for the determination of crystalline phases on the sample. This analysis was carried out with a Philips X'PERT diffractometer equipped with a proportional detector and a secondary graphite monochromator. Data were collected stepwise over the angle range of $2° \leq 2\theta \leq 70°$ in steps of 0,02° (2θ) with an accumulation time of 20 s per step using Cu Kα ($\lambda=$ 1,54178 Å) radiation.

In order to evaluate the thermal stability of the crystalline structure under different temperatures and atmospheres, XRD in situ was used. It is thus possible to obtain the diffraction pattern under different temperatures and different atmospheres.

XRD in situ analysis was performed with a PANalytical X'Pert Pro with a Bragg-Brentano geometry. Data were collected stepwise over the angle range of $5° \leq 2\theta \leq 60°$ in steps of $0,033°$ (2θ) with an accumulation time of 200 s per step using Cu Kα ($\lambda= 1,5406$ Å) radiation. As for in situ treatment conditions, both tests were performed with 100% N_2 or 100% air and with a flow rate of 1 L/h. Regarding temperature, both tests were performed between 25°C and 800°C and with a temperature increase of 5°C/min.

A.4.3   Thermal gravimetric analysis and differential thermal analyses (TGA-DTA)

This characterization technique is based on recording the mass of the sample over time with a change in temperature. It is therefore possible to obtain information regarding thermal decompositions, namely the thermal decomposition of the SDA present in the sample, as well as quantifying the organic and water contents.

Thermal gravimetric analysis and differential thermal analyses (TGA-DTA) were conducted in an air or nitrogen streams with a Mettler Toledo TGA/SDTA 851E analyzer.

A.4.4 N_2 adsorption-desorption isotherm

N_2 physisorption is one of the most common techniques used to characterize a meso and microporous solid. From the N_2 physical adsorption-desorption on the surface of a solid it is possible to calculate its specific surface area or the size distribution of meso and micropores.

From the Brunauer-Emmett-Teller (BET) theory that explains the physical adsorption of gas molecules on a surface of a solid, it is possible to determine the specific area of a material.

The BET equation in its linear form (see equation A.2) [5] was applied to the N_2 isotherm to calculate the specific area of the material S_{BET}. In equation A.2 P/P_0 represents the relative pressure, V_A the adsorbed volume of N_2 at pressure P, V_M the volume of the monolayer and c is associated with the adsorption heat of the first layer and the condensation heat. In order to calculate the volume of the monolayer V_M, $(P/P_0)/(V_A(1 - P/P_0))$ was represented in function of P/P_0 for $0 < P/P_0 < 0,35$, obtaining a straight line with slope $\alpha= (c-1)/V_M$ and y-intercept $i = 1/V_M c$. Thus, $V_M = 1/(\alpha + i)$ [6].

$$\frac{\frac{P}{P_0}}{V_A(1 - \frac{P}{P_0})} = \frac{1}{V_M\, c} + \frac{c-1}{V_M\, c}\frac{P}{P_0} \tag{A.2}$$

Knowing the volume of the monolayer V_M, the specific area S_{BET} is given by the expression A.3 [5], where σ represents the area occupied by an adsorbate molecule, N_A the number of Avogadro, m the weight of the adsorbate and V_0 the molar volume of the gas [6].

$$S_{BET} = \frac{V_M\, \sigma\, N_A}{m\, V_0} \tag{A.3}$$

According to the BET theory, the value of the specific area corresponds only to multilayer adsorption. For a more detailed textural analysis, methods based on the standard isotherm will be used [6].

For a given gas adsorbed in a series of non-porous materials with similar characteristics it is to be expected that the shape of the isothermal will not vary greatly. By normalizing the amount adsorbed, the different isotherms can overlap, resulting in a standard isotherm. For this purpose, the parameter t (parameter that transforms the adsorbed quantity into an average film thickness of the adsorbed material) is represented as a function of the relative pressure P/P_0 [6]. To convert the relative pressure P/P_0 into adsorbate film thickness t the Harkins-Jura expression was used (see equation A.4) [7].

$$t = \left(\frac{13,99}{-\log\frac{P}{P_0} + 0,034}\right)^{1/2} \tag{A.4}$$

The t-method is based on comparing the experimental isotherm with the respective standard isotherm. For this purpose, the adsorbed volume as a function of t is graphically represented. If the experimental isotherm is equal to the standard isotherm, a straight line that passes at the origin is obtained. Otherwise, if the material presents micropores, it is verified that for low pressures the adsorbed quantity is higher than expected. From the moment that the micropores become saturated, only adsorption in multilayers is verified, defining a linear zone in the graphic.

The y-intercept of this straight line corresponds to the microporous volume [6]. From the slope m_t from the straight line the external and mesoporous areas S_t can

be calculated using the expression A.5. The microporous area S_μ is given by the difference between the S_{BET} and the S_t (see equation A.6).

$$S_t = 1,5468 \cdot m_t \tag{A.5}$$

$$S_\mu = S_{BET} - S_t \tag{A.6}$$

Nitrogen adsorption-desorption isotherms were measured at 77 K with a Micromeritics ASAP 2010 volumetric analyzer. Before the measurement, the samples were outgassed for 12 hours at 80°C. The BET specific surface area was calculated from the nitrogen adsorption data in the relative pressure range from 0,04 to 0,2. The total pore volume was obtained from the amount of N_2 adsorbed at a relative pressure of about 0,99.

A.4.5 Electronic Microscopy

Electronic microscopy is a microscopic technique which allows high resolution images of a material to be obtained. These images are obtained due to the interaction between and electron beam and the sample. Since the electrons have a much shorter wavelength than the photons of the visible spectrum, it is possible to obtain a higher resolving power than a light microscope.

A.4.5.1 Field-emission scanning electron microscopy (FE-SEM)

Scanning electron microscopy (SEM) is a microscopy technique where images of the sample are produced by scanning the solid surface with a focused beam of electrons. Through the interaction of the electrons with the sample, it is possible to collect information about the solid topography and composition. This microscopic technique was used to evaluate the surface morphology of the samples.

Field-emission scanning electron microscopy (FE-SEM), a high resolution SEM, micrographs were recorded on a ZEISS Ultra 55 microscope operating at 2 kV, with a 2×10^{-9} A beam current and 2,5 mm as the working distance.

A.4.5.2 High Resolution Transmission Electron Microscopy (HR-TEM)

Transmission electron microscopy (TEM) is a microscopy technique based on the transmission of an electron beam through the sample to create an image. This microscopy techniwue allowed to determine the interlaminar space of the samples studied.

For this technique to be performed it is required that the sample presents an ultrathin section, less than 100 nm thick. For that, it was necessary do grind, disperse in dimethylformamide (DMF) and sonify for 30 minutes. After, the sample was deposited on carbon copper grids. High resolution transmission electron microscopy (HR-TEM) micrographs were obtained with a JEOL JEM2100F electron microscope operating at 200 keV.

A.4.6 Spectroscopy

Spectroscopy is the study of the interaction of electromagentic radiation with matter. This technique, by measuring the spectra of electromagnetic radiation as a function of its wavelength or frequency, allows to obtain information concerning the structure and properties of matter.

Different spectroscopic techniques exist, depending on the electromagnetic radiation used.

A.4.6.1 X-ray Photoelectron Spectroscopy (XPS)

X-ray Photoelectron Spectroscopy (XPS) is a spectroscopy based on the photoelectric effect that allows to identify and quantify chemical elements and its chemical state.

The XPS spectra were measured in a SPECS spectrometer equipped with a Phoibos 9MCD multichannel and a dual X-ray radiation source of Al Kα(1483,6 eV) and Mg Kα(1253,6 eV). The electron binding energy was determinate with a precision of $\pm$ 0,1 eV. For correction of the spectra obtained the C1s signal (284,6 eV) was used through the CasaXPS software.

A.4.6.2 UV–Vis Diffuse Reflectance Spectroscopy (DRS)

UV–Vis Diffuse Reflectance Spectroscopy (DRS) is a spectroscopy technique based on the measurement of UV–Vis radiation absorbed by the interaction with a sample. This technique is commonly used to determine the band gap value of a semiconductor. For this, it is necessary to resort to the Kubelka-Munk theory [8, 9], one the main theories to explain the behavior of a light flux through a homogeneous media [10].

According to this theory, the diffuse reflectance, R, can be related to the absorption, k, and the scattering coefficient, s, through the Kubelka-Munk function $F(R)$ (see Equation A.7).

$$\frac{(1 - R)^2}{2R} = \frac{k}{s} = F(R) \tag{A.7}$$

The band gap value, E_g, can be related to the absorption coefficient through the Tauc equation (see Equation A.8), where α is the linear absorption coefficient, h is the Planck Constant, υ is the light frequency, A is a proportionality constant and n is equal to $1/2$ for direct band gap materials [11, 12].

$$\alpha h \upsilon = A \left(h \upsilon - E_g \right)^n \tag{A.8}$$

When the incident radiation scatters in a perfect diffuse manner and considering s constant along the wavelenght:

$$k = 2\alpha \Leftrightarrow [F(R)h\upsilon]^2 = A \left(h\upsilon - E_g \right) \tag{A.9}$$

The band gap value E_g can be then determined. For that, $[F(R)h\upsilon]^2$ is plotted as a function of $h\upsilon$ and then extrapolate the linear part to $[F(R)h\upsilon]^2 = 0$.

However, this method, although widely used in the scientific community, may not be the most appropriate. According to Zanatta [13], this method is strongly conditioned by data processing, due to the need to extrapolate the linear least squares fit of the equation to zero, being highly susceptible to the operator's intervention. Furthermore, it is also stated that this method should only be used on amorphous or glassy materials. Thus, a method was developed based on fitting a sigmoidal function (see Equation A.10) to the experimental data of F(R) vs Energy.

$$\alpha(E) = \alpha_{max} + \frac{\alpha_{min} - \alpha_{max}}{1 + \exp\left(\frac{\mathsf{E} - \mathsf{E}^{\mathbf{Boltz}}}{\delta\mathsf{E}}\right)} \tag{A.10}$$

In the previous equation α_{max} and α_{min} stands for maximum and minimum absorption coefficient, respectively, $\mathsf{E}^{\text{Boltz}}$ the energy coordinate which corresponds halfways between α_{max} and α_{min} and $\delta\mathsf{E}$ is associated with the slope of the sigmoidal curve.

After studying various semiconductor materials, it was observed that the band gap of the material E_g can be be calculated by Equation A.11, where $\mathsf{n}^{\text{Boltz}}$ is an empiracal value, that can be 0,3 for direct band gap and 4,3 for indirect band gap.

$$\mathsf{E}_g = \mathsf{E}^{\text{Boltz}} - \mathsf{n}^{\text{Boltz}} \times \delta\mathsf{E} \tag{A.11}$$

A Cary 5 spectrometer equipped with a Diffuse Reflectance accessory was used to perform the UV-Vis measurements.

A.4.6.3   Infrared Spectroscopy (IR)

Infrared spectroscopy (IR) allows to study and identify chemical substances, organic compounds or functional groups. In this study this technique was used to study the interaction between the SDA and the structure.

IR spectra were obtained in a ThermoOptek Nicolet spectrometer (4 cm^{-1} resolution) equipped with a DTGS detector and using a Golden-Gate diamond tip. Wafers of 10 mg cm^{-2} were outgassed at $100°$C overnight.

A.4.6.4   Nuclear Magnetic Ressonance Spectroscopy (NMR)

Nuclear magnetic resonance spectroscopy (NMR) is a technique that allows to evaluate the chemical environmental of the atoms present by applying a magnetic field to it.

Liquid state ^{13}C NMR spectra were recorded at 75 MHz using a Bruker AMX300 spectrometer. The chemical shifts are reported in ppm and are referened to the appropiate residual solvent peak.

Solid state ^{13}C NMR spectra were recorded at room temperature using a Bruker AV-400 spectrometer. The spectra were recorded with a 7 mm Bruker BL-7 probe, at a sample spinning rate of 5 kHz and referred to adamantine.

A.5   Photocatalytic Tests

In order to evaluate the photocatalytic performance of the synthesized materials, several photocatalytic tests were performed. Two photocatalytic reactions were studied, the H_2 production by water splitting and CO_2 photoreduction.

A.5.1   Equipment Description

The equipment used to carry out the tests can be divided into three essential pieces of equipment: the reactor, the solar simulator and the system for analyzing the products obtained.

The reactor (see Figure A.4) can be seen as a sealed quartz cylinder, with an interior diameter of 55,5 cm and 110,3 cm as length, and equipped with a pressure indicator, a pressure relief valve to avoid overpressure, and a feed valve which allows the reactor to be fed with the desired gases or samples to be taken when required. Inside the quartz cylinder there is a thermostated plate where the photocatalyst can be placed. In order to ensure that the irradiated area is constant, the photocatalyst is placed on the thermostated plate in a Teflon ring with an interior diameter of 32,4 mm. A thermocouple, equipped with a temperature indicator, was also placed on the surface of the photocatalyst.

| (a) | (b) |
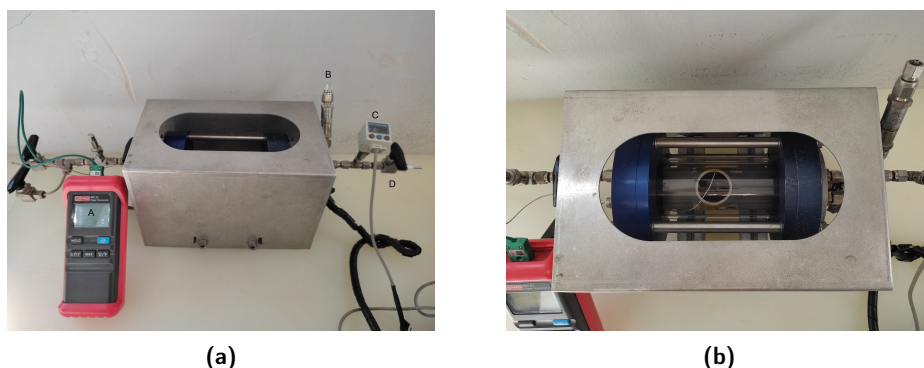
Figure A.4: Pictures of the reactor ((A.4a) lateral and (A.4b) top views) used to perform the photocatalytic tests

A Newport arc lamp housing equipped with a 1000 W Xe Ozone-free lamp with two filters, a AM 1,5G filter to mimic the solar spectrum and a IR filter to eliminate the photocatalysts heating, was used as a solar simulator. More information regarding this equipment, namely the irradiance spectrum of the lamp, can be found in Appendix A.5.3.1.

To analyze the reaction gases a gas chromatograph (GC) Bruker 450GC Rapid Refinery Gas Analyzer was used. The GC was equipped with two thermal conductivity detectors (TCD) and one flame ionization detector (FID). The first TCD channel used N_2 has carrier gas and was equipped with a Hayesep Q 80/100 Mesh 1.5m x 1/16'' x 1mm Ultimetal CP1305 column. Regarding the second TCD channel, this was equipped with a Molesieve 5[a] 80/100 Mesh 1.5m x 1/16'' x 1mm Ultimetal CP1306 colum and used He as carrier gas.

A.5.2   Experimental Standard Procedure

The photocatalytic tests were carried out in batch mode, in a solido-gas system and under atmospheric pressure. The plate where the photocatalyst is placed is thermostated at a temperature of 25°C. As for the composition of the reaction gases, the reactor is loaded with a gas stream of N_2 or CO_2, depending on the reaction to be performed, saturated with 6% (molar composition) of H_2O.

A photocatalytic test comprises the following steps:

1. Photocatalystis pre-treatment - to ensure the elimination of ethanol used during filtration and washing of the samples, the photocatalyst must be dried overnight at 125°C and under vacuum prior to testing;

2. Reactor loading - the required amount of photocatalyst is weighed (0,150 g per test was used) and placed on the reactor's plate within the Teflon ring. The photocatalyst is well dispersed in the Teflon ring to ensure that all tests are performed with the same irradiated area ($30,3 \cdot 10^{-3} m^2$);

3. Proof of the absence of leaks - after the photocatalyst loading, the reactor is sealed and brought to a relative pressure of -100 kPa to ensure that there are no leaks;

4. Reactor purge - after verifying that there are no leaks, the reactor is subjected to five purging cycles in order to reduce the oxygen content;

5. Photocatalytic test - after performing the purging cycles, the reactor is loaded with the appropriate gases until it reaches a pressure equal to 10 kPa and placed under the solar simulator. The distance between the photocatalyst

and the solar simulator was kept constant and equal to 12 cm. Samples are taken at constant times (0, 0,5, 1 and 4 hours) and immediately injected in the GC. In the first TCD channel H_2 is read, in the second TCD channel CO_2, O_2, N_2, CH_4 and CO and in the FID the remaining hydrocarbons;

6. Photocatalytic test termination - after the test time, the solar simulator is switched off and it is checked that the photocatalyst's crystallinity remains unchanged by performing PXRD measurements. This allow to assess whether there has been any SDA degradation, since it is closely linked to the inorganic structure.

A.5.3 Data Treatment

The chromatograms obtained allow to quantity a particular chemical species present in the sample. For that, it is first necessary to determine the relation between the area of the peak associated with the chemical species and its quantity in the mixture.

In order to quantify a particular chemical species it was first necessary to produce a calibration curve for each of the species of interest: H_2, CO, CH_4, O_2, C_2H_4, C_2H_6, C_3H_6 and C_3H_8. The calibration curve for each of the species was produced by injecting mixtures with known compositions into the GC. This procedure allowed to relate the area obtained with the composition. Three compositions (0,5%, 1% and 2% molar composition) were selected for each gas, which allowed a calibration curve with three points to be obtained.

With the calibration curve for species i, it is possible to calculate its molar quantity at time t and the theoretical conversion of H_2O. This parameter is calculated by knowing the amount of H_2O needed to reduce the species i (see Table A.7) and the H_2O content at initial time $H_2O_{t=0}$ (see Equation A.12).

$$\text{Theoretical Water Conversation (\%)} = \frac{\sum \text{Molar Quantity}_i \cdot H_2O_{\text{Reduce Species}_i}}{H_2O_{t=0}} \cdot 100$$

$$(\text{A.12})$$

Table A.7: Calorific Power, water and charge carriers necessary to reduce the species involved in the photocatalytc processes under study

Species$_i$	H$_2$O necessary to reduce	H$^+$ and e^- necessary to reduce	Calorific Power (J/mol)
H$_2$	1	2	286000
CO	1	2	283240
CH$_4$	2	8	889000

The proton selectivity for the species i can be calculated by knowing the protons required to reduce it (see Table A.7 and Equation A.13).

$$\text{Proton Selectivity Species}_i(\%) = \frac{\text{Molar Quantity}_i \cdot \text{H}^+_{\text{Reduce Species}_i}}{\sum \text{Molar Quantity}_i \cdot \text{H}^+_{\text{Reduce Species}_i}} \cdot 100 \quad \text{(A.13)}$$

Another important parameter that can be calculated is the instantaneous productivity per mass of photocatalyst (see Equation A.14) or per irradiated surface (see Equation A.15) per unit of time.

$$\text{Instantaneous Productivity}_i \left(\frac{\text{mol}}{\text{g h}}\right) = \frac{\text{Molar Quantity}_i}{\text{Mass Photocatalyts} \cdot \text{Time}} \quad \text{(A.14)}$$

$$\text{Instantaneous Productivity}_i \left(\frac{\text{mol}}{\text{m}^2\text{h}}\right) = \frac{\text{Molar Quantity}_i}{\text{Irradiated Surface} \cdot \text{Time}} \quad \text{(A.15)}$$

It is possible to convert Accumulated Productivity$_i$ to the total e^- necessary to produce the specifies present (see Equation A.16).

$$\text{Accumulated Productivity}_{e^-} = \sum \text{Accumulated Productivity}_i \cdot e^-_{\text{Reduce Species}_i} \quad \text{(A.16)}$$

The two following parameters allow to determine the performance of the photocatalyst: the global energy efficiency and the apparent quantum yield. The global energy efficiency compares the energy produced by the photocatalytic process with the energy supplied by the solar simulator at a given time t (see Equation A.17).

$$\text{Global Energy Efficiency (\%)} = \frac{\sum \text{Accumulated Productivity}_i \cdot \text{Calorific Power}_i}{t \cdot \text{Total Lamp Irradiance}} \cdot 100 \quad \text{(A.17)}$$

The apparent quantum yield ϕ assumes that one absorbed photon produces one electron. Therefore, the apparent quantum yield compares the electrons that are actually produced with the photons emitted by the solar simulator at a given time t (see Equation A.18).

$$\phi(\%) = \frac{\text{Accumulated Productivity}_{e^-}}{t \cdot \text{Cumulative Photon Flux of Absorbable Photons}} \cdot 100 \qquad \text{(A.18)}$$

To determine the total lamp irradiance and the cumulative photon flux it is necessary to look into detail the light source used.

A.5.3.1   Solar Simulator Characteristics

As a solar simulator a Newport High Power Xenon Light Source was used. This equipment is composed by a lamp power supply and an arc lamp housing, where the 1000 W Xe ozone free lamp is placed.

i. Lamp Characteristics

The arc lamp housing was equipped with a 1000 W Xe ozone-free lamp (model number 6271) with the irradiance spectrum present on Figure A.5.
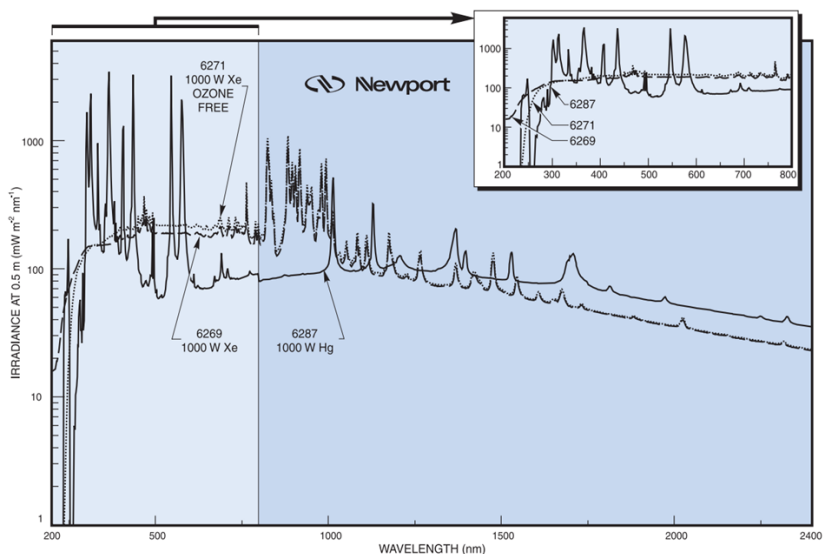
Figure A.5: Irradiance spectrum of the Newport 1000 W Xe ozone-free lamp (model number 6271)

Two filters were place on the filter holder present on the arc lamp. The first one, an AM 1,5 filter, allows to correct the lamp output to better match the total spectrum when the sun is at a zenith angle equal to $37°$. The second filter allow to cut wavelengths above 760 nm in order to avoid the sample heating due to the IR presence.

In order to determinate the Total Lamp Irradiance it was first necessary to manual fit data points to the irradance spectrum (see Figure A.5) since it was the only information public available by the supplier. After it, the filters and the luxmeter's detection limits were taking into consideration when transforming the theoretical spectrum to the real one. Finally, the irradiance measurement performed with a luxmeter was used to convert the theoretical spectrum to the actual spectrum. By summing the the actual irradiance values per wavelength value it is possible to determine the total lamp irradiance.

To determine the Cumulative Photon Flux first it is necessary to know the band gap value of the photocatalyts (determine previously by DRS). Since the material can only absorb photons with an energy higher than its band gap value, it will only be considered for the cumulative photon flux such photons. Firstly, it is necessary to know the number of photons associated with each wavelength. For that, the

actual irradiance values per wavelength are divided by the energy associate with the wavelength. The cumulative photon flux will be given by the sum of the photons with an energy higher than the material's band gap.

References

[1] Guoliang Liu et al. "MoS$_2$ monolayer catalyst doped with isolated Co atoms for the hydrodeoxygenation reaction". In: *Nature Chemistry* 9 (2017), pp. 810–816. DOI: 10.1038/nchem.2740.

[2] Charitha Thambiliyagodage and Ramanee Wijesekera. "Ball milling – A green and sustainable technique for the preparation of titanium based materials from ilmenite". In: *Current Research in Green and Sustainable Chemistry* 5 (2022), p. 100236. ISSN: 2666-0865. DOI: https://doi.org/10.1016/j.crgsc.2021.100236.

[3] William Henry Bragg and William Lawrence Bragg. "The reflection of X-rays by crystals". In: *Proceedings of the Royal Society of London. Series A, Containing Papers of a Mathematical and Physical Character* 88.605 (1913), pp. 428–438. DOI: 10.1098/rspa.1913.0040.

[4] William Henry Bragg and William Lawrence Bragg. *X Rays and Crystal Structure*. G. Bell and Sons, LTD., 1915.

[5] Stephen Brunauer, P. H. Emmett, and Edward Teller. "Adsorption of Gases in Multimolecular Layers". In: *J. Am. Chem. Soc* 2 (1938), pp. 309–319. DOI: https://doi.org/10.1021/ja01269a023.

[6] Jose Luis Figueiredo and Fernando Ramoa Ribeiro. *Catalise Heterogenea*. 3rd. Fundaçao Calouste Gulbenkian, 2015.

[7] William D. Harkins and Geroge Jura. "A Vapor Adsorption Method for the Determination of the Area of a Solid without the Assumption of a Molecular Area, and the Areas Occupied by Nitrogen and Other Molecules on the Surface of a Solid". In: *J. Am. Chem. Soc* 68 (1944), pp. 1366–1373.

[8] Paul Kubelka. "New Contributions to the Optics of Intensely Light-Scattering Materials. Part I". In: *J. Opt. Soc. Am.* 38.5 (May 1948), pp. 448–457. DOI: 10.1364/JOSA.38.000448.

[9] Paul Kubelka. "New Contributions to the Optics of Intensely Light-Scattering Materials. Part II: Nonhomogeneous Layers*". In: *J. Opt. Soc. Am.* 44.4 (Apr. 1954), pp. 330–335. DOI: 10.1364/JOSA.44.000330.

[10] R. Alcaraz De La Osa et al. "The extended Kubelka–Munk theory and its application to spectroscopy". In: *ChemTexts* 6.6 (2020). DOI: https://doi.org/10.1007/s40828-019-0097-0.

[11]   J. Tauc, R. Grigorovici, and A. Vancu. "Optical Properties and Electronic Structure of Amorphous Germanium". In: *physica status solidi (b)* 15.2 (1966), pp. 627–637. DOI: https://doi.org/10.1002/pssb.19660150224.

[12]   G P Joshi et al. "Band gap determination of Ni-Zn ferrites". In: *Bulletin of Materials Science* 26.4 (2003), pp. 387–389. DOI: 10.1007/bf02711181.

[13]   A. R. Zanatta. "Revisiting the optical bandgap of semiconductors and the proposal of a unified methodology to its determination". In: *Scientific Reports* 9 (2019), p. 11225. DOI: 10.1038/s41598-019-47670-y.

Appendix B

Material Synthesis

B.1 Modifications to the initial procedure evaluated

The initial methodology for obtaining the material consists on mixing SnO_2 (Sigma-Aldrich), $Zn(NO_3)_2 \cdot 6\,H_2O$ (Alfa Aesar), S (JT Baker), structure directing agent (SDA), ethylene glycol (Scharlab) and deonized water in a flask for 1 hour at room temperature. Then, the gel was transfer to a Teflon vessel in an autoclave and put it in a oven for 12 days at 190°C. After the synthesis time the autoclave is cooled quickly, using water and ice, and the sample is recovered through filtration, washed with ethanol and placed to dry at 100°C overnight.

Five different compounds were used as SDA (see Figure B.1).
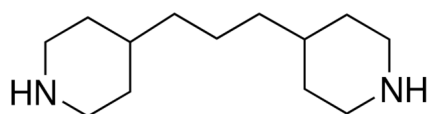
(a) 1,3-Bis(4-piperidyl)propane (CAS: 16898-52-5) - Compound A
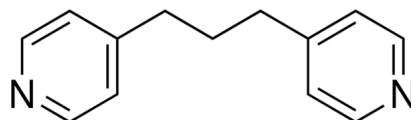
(b) 1,3-Bis(4-pyridyl)propane (CAS: 17252-51-6) - Compound B
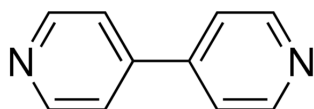
(c) 4,4'-Dipyridyl (CAS: 553-26-4) - Compound C
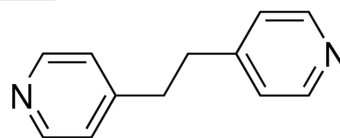
(d) 1,2-Bis(4-pirydyl)ethane (CAS: 4916-57-8) - Compound D
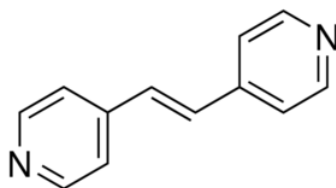
(e) 1,2-Di(4-pyridyl)ethylene (CAS: 13362-78-2) - Compound E

Figure B.1: The five different SDA's used

The presence of an extra phase associated with SnO_2 was observed via PXRD. In order to try to eliminate this phase, the following changes were made to the initial gel composition gel:

- Reducing the Sn amount in 10%, 20% and 40%;
- Substitution of SnO_2 for $SnCl_2$;

- Changing the EG/H_2O ratio from 0,96 to 0,57 and 0,32;

- Changing the H_2O/Sn ratio from 139 to 200 and 300 while keeping the EG/H_2O ratio equal to 0,96;

- Changing the amount of SDA used by +/- 20%.

A kinetic study was also performed, reducing the synthesis time to 1, 2, 3, 6, 9 and 11 days, in order to see if it was possible to reduce the synthesis time.

Three ways of cooling the autoclaves were evaluated after the days of synthesis: very fast, with dry ice and acetone, fast, with ice and water, and at room temperature.

B.1.1 PXRD Patterns

B.1.1.1 SnO_2 vs. $SnCl_2$ and Sn content reduction

Figure B.2 shows the diffractograms of the samples synthesized with the same time of synthesis, 6 days, but different Sn sources and Sn contents.
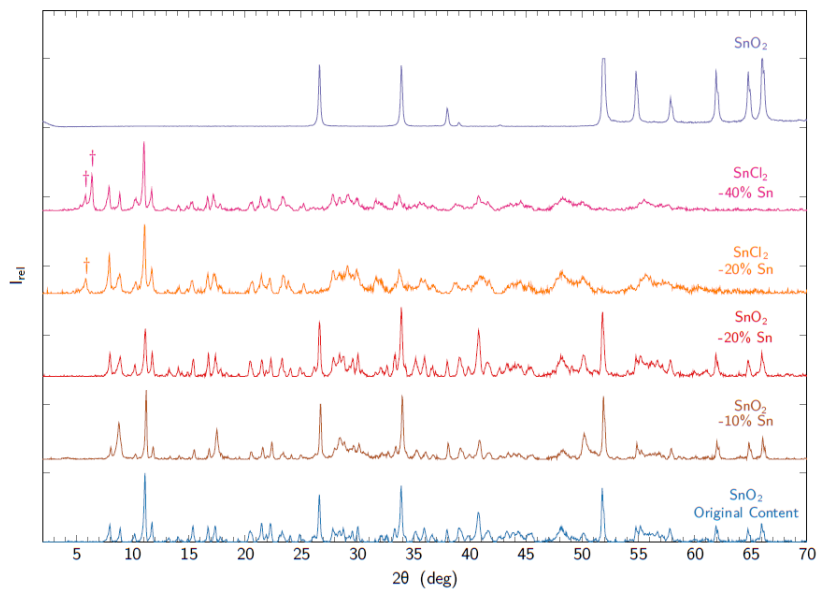
Figure B.2: PXRD patterns of IZM-5 with the original SnO_2 content (in blue), with the SnO_2 molar content reduced by 10% (in brown) and by 20% (in red), with the $SnCl_2$ molar content reduced by 20% (in orange) and by 40% (in pink) and SnO_2 (in purple), where † denotes an unknown phase

B.1.1.2 Solvent Composition

Figure B.3 shows the diffractograms of the samples synthesized with the same time of synthesis, 6 days, but different solvent composition.
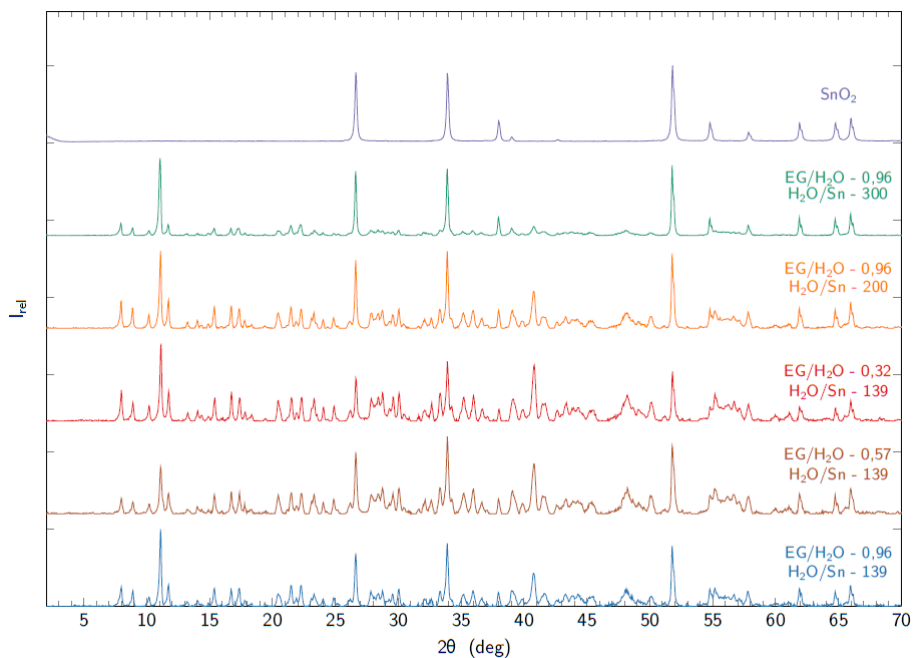
Figure B.3: PXRD patterns of IZM-5 with the original gel composition (in blue), with reduced EG/H$_2$O molar ratio, from 0,96 to 0,57 (in brown) and 0,32 (in red), while maintaining the H$_2$O/Sn molar ratio equal to 139, with increased H$_2$O/Sn molar ratio, from 139 to 200 (in orange) and 300 (in green), while maintaining the EG/H$_2$O molar ratio equal to 0,96, and SnO$_2$ (in purple)

Looking at Figure B.3, it is easy to assess that the composition of the solvent used has little influence on the relative intensity of the peaks associated with the SnO$_2$ phase. However, when a H$_2$O/Sn ratio of 300 is used, the peaks associated with impurities decrease their intensity.

353

B.1.1.3 SDA content

Figure B.4 shows the diffractograms of the samples synthesized with different SDA contents.
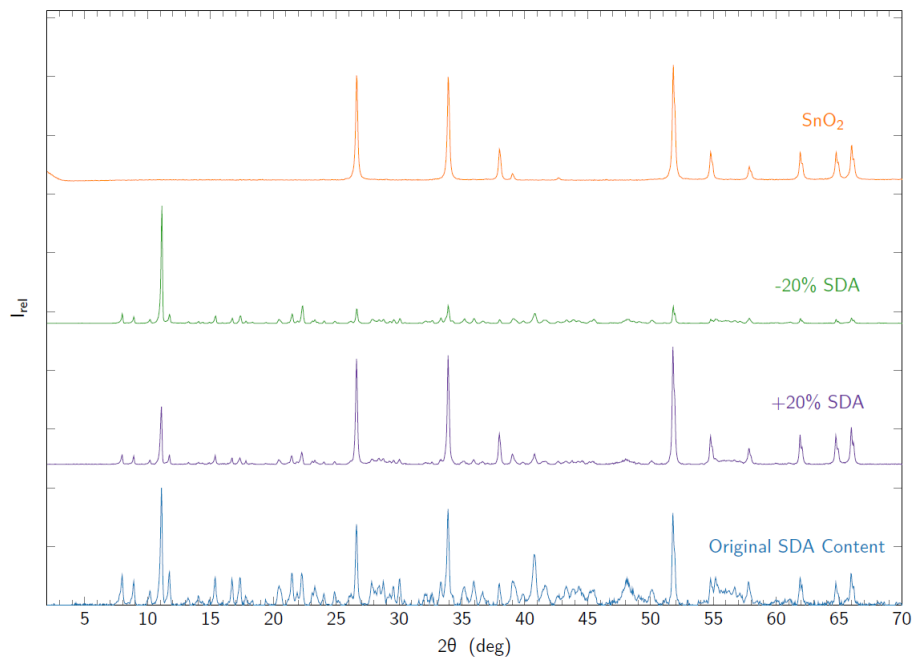
Figure B.4: PXRD patterns IZM-5 with the original gel composition (in blue), with increased SDA molar content by 20% (in purple), with reduced SDA molar content by 20% (in green) and SnO_2 (in orange)

Looking at the Figure B.4, it is easy to conclude that the SDA content in the gel has a great influence on the SnO_2 extra phase. The 20% reduction in SDA content leads to a drastic reduction in the relative intensity of SnO_2 peaks while a 20% increase leads to a reduction in the intensity of the peaks associated with IZM-5 phase.

B.1.1.4 Combination of different experimental variables

After the analysis of isolated variables, the ones that most strongly affect the formation of the SnO_2 extra phase and other impurities were selected. Taking into account the diffractograms previously presented, the variables selected were the Sn source, the Sn and SDA contents in the gel and the solvent composition. All samples, whose diffractograms are shown in Figure B.5, were obtained with 6 days as synthesis time and with a fast cooling (ice and water).

Figure B.5: PXRD patterns of IZM-5 with a reduced $SnCl_2$ molar content by 20% (in blue), with SnO_2 and Sn source and increased H_2O/Sn molar ratio to 300 (in purple), with a reduced $SnCl_2$ molar content by 20% and increased H_2O/Sn molar ratio to 300 (in green), with a reduced $SnCl_2$ molar content by 20%, increased H_2O/Sn molar ratio to 300 and reduced SDA molar content by 20% (in red), with a reduced SnO_2 molar content by 20%, increased H_2O/Sn molar ratio to 300 and reduced SDA molar content by 20% (in grey), with a reduced SnO_2 molar content by 40%, increased H_2O/Sn molar ratio to 300 and reduced SDA molar content by 40% (in brown), with a reduced $SnCl_2$ molar content by 40%, increased H_2O/Sn molar ratio to 300 and reduced SDA molar content by 40% (in pink) and with a reduced $SnCl_2$ molar content by 40% and increased H_2O/Sn molar ratio to 300 (in orange)

Evaluating the difratograms present in Figure B.5, the combination that ensures the lowest presence of impurities and the elimination of the SnO_2 extra phase is when using $SnCl_2$ as a Sn source, a 20% reduction in the content of Sn and SDA in the gel and a H_2O/Sn ratio equal to 300, while keeping the EG/H_2O ratio equal to 0,96.

B.2 Addiction of Saccharide and Dopants

After studying the modifications to the initial gel, the insertion of dopants and different saccharides was studied in order to alter the accessibility of the samples. These results and their discussion can be found throughout the Chapter 5. After it, samples combining the presence of dopants and saccharides were synthesized.

Using Compound B as the SDA and fructose as the saccharide, with the molar ratio Fructose/SDA B equal to 1, two metals were added as dopants: copper and cobalt, with a molar content in the gel equal to 0,1%. The gel molar composition of the material containing fructose and copper was 1,00 SnO_2 : 0,32 ZnO : 5,66 S : 2,56 SDA B : 226,38 EG : 237,27 H_2O : 0,25 CuO : 2,50 Fructose (see Figure B.6 for the PXRD patterns). The gel molar composition of the material containing fructose and cobalt was 1,00 SnO_2 : 0,32 ZnO : 5,66 S : 2,56 SDA B : 226,86 EG : 238,74 H_2O : 0,30 CoO : 2,50 Fructose (see Figure B.7 for the PXRD patterns).
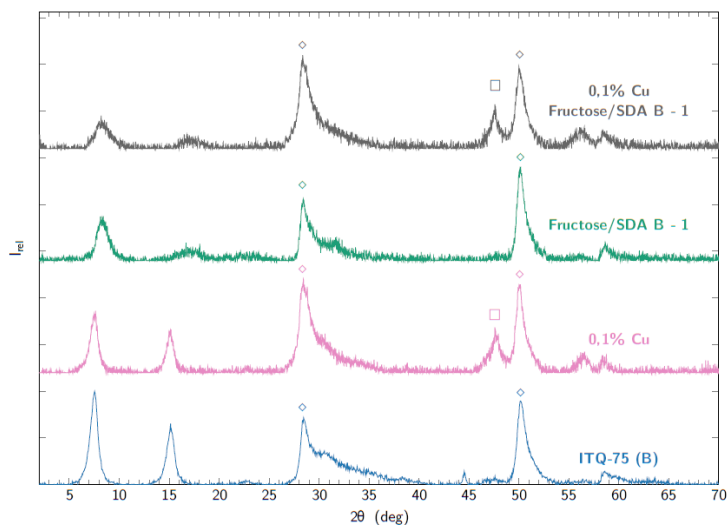
Figure B.6: PXRD patterns of ITQ-75 obtained with Compound B as SDA (in blue), doped with 0,1% Cu (in pink), with a Fructose/SDA B equal to 1 (in green) and with 0,1% Cu and Fructose/SDA B equal to 1 (in gray), where $\diamond$ denotes a ZnS phase and $\square$ a Cu_2SnS_3 phase
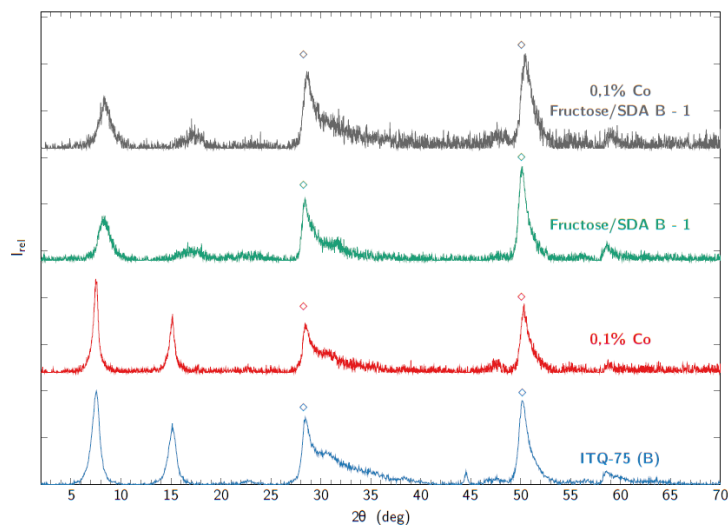
Figure B.7: PXRD patterns of ITQ-75 obtained with Compound B as SDA (in blue), doped with 0,1% Co (in red), with a Fructose/SDA B equal to 1 (in green) and with 0,1% Co and Fructose/SDA B equal to 1 (in gray), where $\diamond$ denotes a ZnS phase

Appendix C

IZM-5 Diffraction Pattern

Table C.1: Diffraction peaks of the

h	k	l	Simulated 2θ (deg)	d (Å)	I rel (%)	Experimental 2θ (deg)	d (Å)	I rel (%)
1	1	0	7,96	11,10	65,5	7,94	11,14	37,4
1	1	0	7,98	11,10	32,6			
1	1	-1	8,35	10,59	2,3			
1	1	-1	8,37	10,59	1,1			
2	0	0	8,89	9,93	41,8			
2	0	0	8,92	9,93	20,8	8,93	9,91	21,3
2	0	-2	10,22	8,65	26,0			
2	0	-2	10,24	8,65	12,9	10,26	8,62	11,3
0	0	2	11,16	7,92	100,0	11,11	7,96	100,0
0	0	2	11,19	7,92	49,8			
1	1	-2	11,76	7,52	37,5	11,73	7,55	28,0
1	1	-2	11,79	7,52	18,7			
0	2	0	13,22	6,69	7,9	13,23	6,69	4,6
0	2	0	13,25	6,69	3,9			
3	1	-1	13,37	6,62	1,3			
3	1	-2	14,06	6,29	8,7			
3	1	-2	14,10	6,29	4,4	14,12	6,27	7,5
0	2	1	14,36	6,16	6,6			
0	2	1	14,39	6,16	3,3			
3	1	0	14,91	5,94	3,7	14,92	5,94	6,0
3	1	0	14,95	5,94	1,9			
2	2	-1	15,36	5,76	4,7	15,37	5,77	22,2
2	2	-1	15,40	5,76	2,3			
1	1	2	15,44	5,74	14,8			
1	1	2	15,47	5,74	7,4			
2	2	0	15,96	5,55	2,0			
2	2	0	16,00	5,55	1,0			
1	1	-3	16,44	5,39	1,4			
3	1	-3	16,72	5,30	1,0	16,69	5,31	17,7
2	2	-2	16,74	5,29	18,4			
2	2	-2	16,78	5,29	9,1			
0	2	2	17,33	5,11	5,7			
0	2	2	17,37	5,11	2,8	17,39	5,10	19,5
2	0	2	17,45	5,08	12,0			
2	0	2	17,49	5,08	6,0			
4	0	0	17,84	4,97	5,6			

			Simulated			Experimental		
h	k	l	2θ (deg)	d (Å)	I rel (%)	2θ (deg)	d (Å)	I rel (%)
4	0	0	17,89	4,97	2,8	17,98	4,93	5,7
3	1	1	18,14	4,89	1,9			
2	2	1	18,34	4,83	4,1			
2	2	1	18,38	4,83	2,0			
2	0	-4	19,52	4,54	1,6	19,51	4,55	1,1
1	3	0	20,39	4,35	2,0			
5	1	-2	20,45	4,34	2,5			
5	1	-2	20,50	4,34	1,2			
4	0	-4	20,52	4,33	5,6			
4	0	-4	20,57	4,33	2,8			
3	1	-4	20,62	4,30	4,9			
4	2	-1	20,65	4,30	3,0	20,65	4,30	14,6
3	1	-4	20,67	4,30	2,5			
4	2	-1	20,70	4,30	1,5			
5	1	-1	21,20	4,19	1,1			
5	1	-3	21,22	4,18	1,3			
0	2	3	21,47	4,15	0,2	21,50	4,13	22,6
1	1	-4	21,59	4,11	13,9			
1	1	-4	21,65	4,11	6,9			
4	2	-3	21,86	4,06	0,8	21,85	4,07	5,3
2	2	2	21,95	4,05	4,5			
2	2	2	22,01	4,05	2,2			
4	2	0	22,27	3,99	2,4			
4	2	0	22,33	3,99	1,2	22,30	3,99	19,5
3	1	2	22,36	3,97	3,7			
3	1	2	22,42	3,97	1,9			
0	0	4	22,42	3,96	7,8			
0	0	4	22,48	3,96	3,9			
3	3	-1	23,09	3,85	6,1			
3	3	-1	23,15	3,85	3,1			
6	0	-2	23,35	3,81	10,2	23,31	3,82	13,4
5	1	-4	23,37	3,80	1,4			
6	0	-2	23,41	3,81	5,1			
3	3	-2	23,51	3,78	2,8			
3	3	-2	23,56	3,78	1,4			
3	3	0	24,03	3,70	7,0	23,82	3,74	9,5
3	3	0	24,09	3,70	3,5	24,05	3,70	5,6

Table C.1 continued from previous page

			Simulated			Experimental		
h	k	l	2θ (deg)	d (Å)	I rel (%)	2θ (deg)	d (Å)	I rel (%)
1	3	2	24,37	3,65	1,8			
6	0	-4	24,96	3,56	7,7			
6	0	-4	25,02	3,56	3,8			
3	3	-3	25,22	3,53	1,7	25,23	3,53	8,2
0	2	4	26,12	3,41	1,8	26,05	3,42	2,9
3	3	1	26,20	3,40	4,9			
3	3	1	26,26	3,40	2,4			
2	4	-1	27,78	3,21	3,7			
2	4	-1	27,85	3,21	1,8	27,81	3,21	19,8
5	3	-2	27,87	3,20	2,7			
5	3	-2	27,94	3,20	1,3			
2	0	4	28,09	3,17	1,9			
2	4	0	28,12	3,17	2,9			
2	4	0	28,19	3,17	1,4			
6	2	-4	28,35	3,15	1,0			
7	1	-2	28,37	3,14	1,6			
5	3	-1	28,44	3,14	4,0			
5	3	-3	28,45	3,13	1,9			
5	3	-1	28,51	3,14	2,0			
2	4	-2	28,58	3,12	1,4			
7	1	-4	28,84	3,09	7,9	28,77	3,10	12,4
7	1	-4	28,91	3,09	3,9			
3	3	2	29,33	3,04	3,3	29,14	3,07	18,7
3	3	2	29,40	3,04	1,6			
2	4	1	29,58	3,02	9,1	29,57	3,02	8,9
2	4	1	29,65	3,02	4,5			
6	2	0	30,09	2,97	3,8			
5	3	0	30,09	2,97	5,4			
5	3	-4	30,12	2,96	2,0			
6	2	0	30,16	2,97	1,9			
5	3	0	30,17	2,97	2,7			
2	4	-3	30,45	2,93	2,5			
2	4	-3	30,53	2,93	1,2			
6	0	-6	30,99	2,88	1,8			
0	4	3	31,63	2,83	3,0	31,59	2,83	10,2
0	4	3	31,71	2,83	1,5			
2	4	2	32,01	2,79	3,1			

Table C.1 continued from previous page

Table C.1 continued from previous page

h	k	l	Simulated 2θ (deg)	d (Å)	I rel (%)	Experimental 2θ (deg)	d (Å)	I rel (%)
2	4	2	32,09	2,79	1,6			
7	1	0	32,21	2,78	3,1			
7	1	0	32,29	2,78	1,5			
1	1	-6	32,56	2,75	1,7			
5	3	1	32,69	2,74	6,1			
5	3	-5	32,73	2,73	1,1			
5	3	1	32,77	2,74	3,0			
7	1	-6	33,47	2,68	12,0			
7	1	-6	33,55	2,68	6,0			
1	5	0	33,76	2,65	1,1	33,71	2,66	20,0
6	2	-6	33,82	2,65	3,7			
6	2	-6	33,90	2,65	1,9			
0	0	6	33,91	2,64	1,1			
7	3	-3	33,94	2,64	2,2			
8	2	-3	34,00	2,63	1,1			
7	3	-3	34,02	2,64	1,1			
7	3	-2	34,22	2,62	1,0	34,22	2,62	7,2
4	4	1	34,30	2,61	4,6			
8	2	-4	34,30	2,61	1,2			
4	4	1	34,39	2,61	2,3			
7	3	-4	34,62	2,59	0,0	34,59	2,59	3,9
1	5	1	34,63	2,59	1,2			
8	0	-6	35,08	2,56	2,4			
8	0	-6	35,17	2,56	1,2			
2	4	3	35,23	2,55	9,3			
2	4	3	35,32	2,55	4,6			
7	3	-1	35,44	2,53	1,6			
8	2	-5	35,54	2,52	1,1			
9	1	-4	35,91	2,50	0,8	35,96	2,50	17,6
5	3	2	36,04	2,49	6,8			
5	3	-6	36,09	2,49	2,2			
5	3	2	36,13	2,49	3,4			
5	3	-6	36,18	2,49	1,1			
4	4	-5	36,66	2,45	0,4			
2	4	-5	36,73	2,45	2,3	36,67	2,45	8,7
6	2	2	36,76	2,44	2,3			
2	4	-5	36,82	2,45	1,1			

			Simulated			Experimental		
h	k	l	2θ (deg)	d (Å)	I rel (%)	2θ (deg)	d (Å)	I rel (%)
6	2	2	36,85	2,44	1,1			
4	4	2	37,17	2,42	2,1			
4	4	2	37,26	2,42	1,0			
3	5	1	37,79	2,38	0,2	37,78	2,38	1,0
7	3	-6	38,73	2,33	0,0	38,73	2,33	8,4
0	4	5	39,12	2,30	2,5	39,11	2,30	10,3
0	4	5	39,22	2,30	1,2			
10	0	-4	39,24	2,29	1,0			
7	1	2	39,25	2,29	3,3			
5	5	-1	39,35	2,29	1,5			
7	1	2	39,35	2,29	1,6			
5	5	-3	39,36	2,29	1,5			
5	3	3	39,99	2,25	2,5			

Table C.1 continued from previous page

Appendix D

Optical Band Gap Determination

D.1 Isolated Compounds

Figure D.1: Kubelka-Monk representation of SDA A and its sigmoidal fit (see Equation D.1)

$$F\left(R\right) = 19,79766 + \frac{0,39709 - 19,79766}{1 + \exp\left(\frac{\text{Energy} - 5,69036}{0,09036}\right)} \tag{D.1}$$

Table D.1: Optical band gap, direct and indirect, of SDA A

	Optical band gap (eV)
Direct	5,7
Indirect	5,3
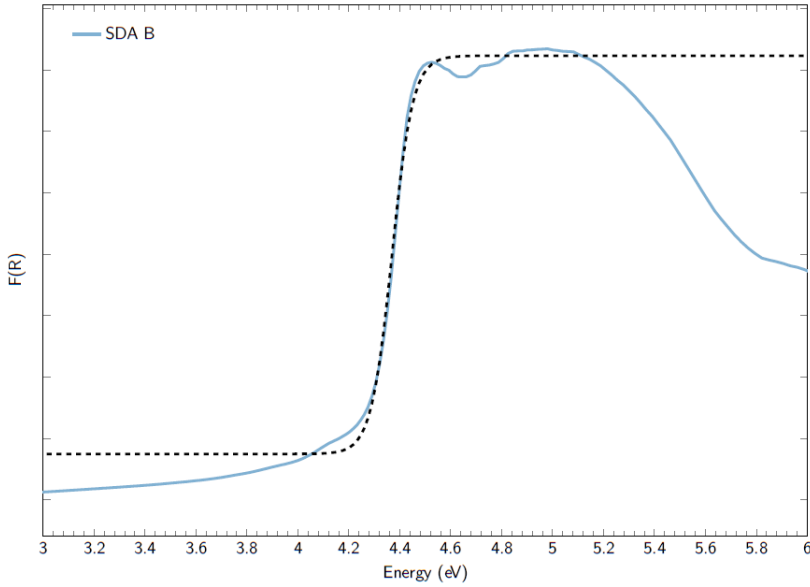
Figure D.2: Kubelka-Monk representation of SDA B and its sigmoidal fit (see Equation D.2)

$$F\left(R\right) = 14,46649 + \frac{1,49419 - 14,46649}{1 + \exp\left(\frac{\text{Energy} - 4,36953}{0,09036}\right)} \tag{D.2}$$

Table D.2: Optical band gap, direct and indirect, of SDA B

	Optical band gap (eV)
Direct	4,4
Indirect	4,2
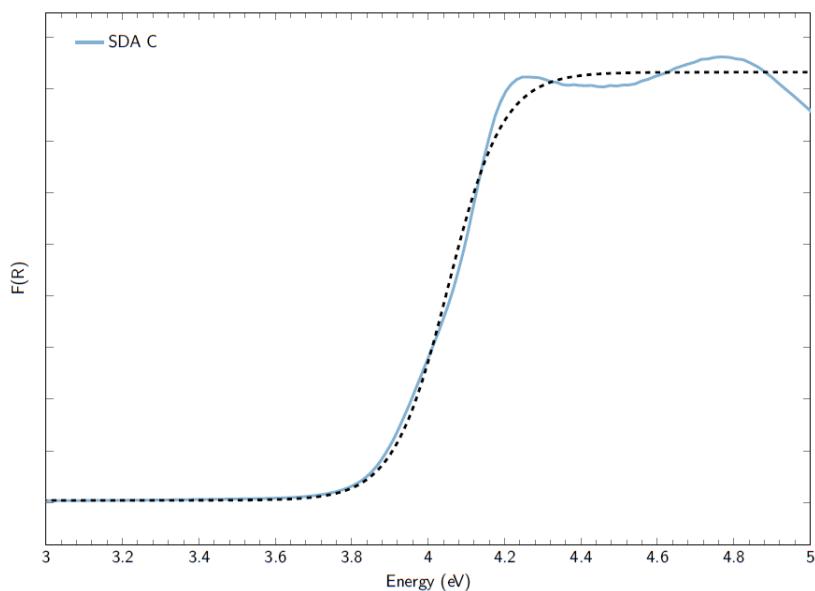
Figure D.3: Kubelka-Monk representation of SDA C and its sigmoidal fit (see Equation D.3)

$$F\left(R\right) = 8,32696 + \frac{0,04039 - 8,32696}{1 + \exp\left(\frac{\text{Energy} - 4,05275}{0,07163}\right)} \tag{D.3}$$

Table D.3: Optical band gap, direct and indirect, of SDA C

	Optical band gap (eV)
Direct	4,0
Indirect	3,7
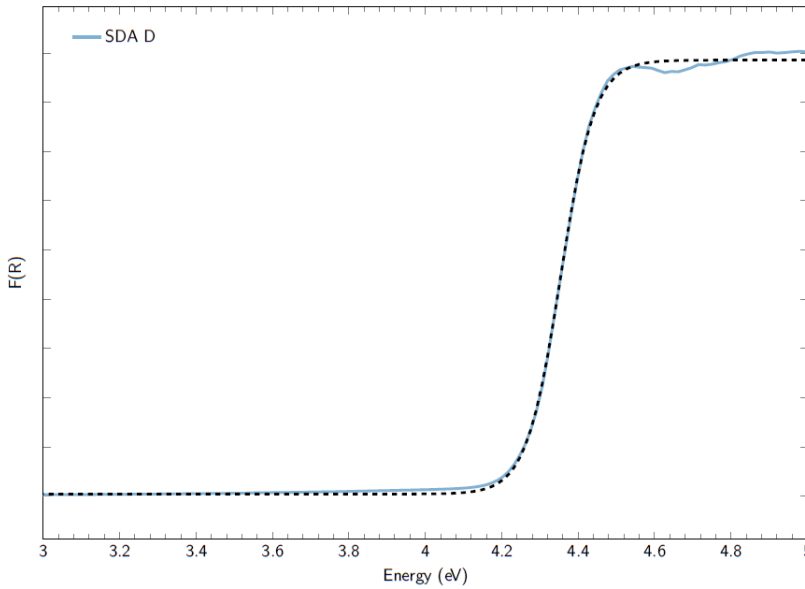
Figure D.4: Kubelka-Monk representation of SDA D and its sigmoidal fit (see Equation D.4)

$$F\left(R\right) = 8,85637 + \frac{0,04709 - 8,85637}{1 + \exp\left(\frac{\text{Energy} - 4,35397}{0,04461}\right)} \tag{D.4}$$

Table D.4: Optical band gap, direct and indirect, of SDA D

	Optical band gap (eV)
Direct	4,3
Indirect	4,2
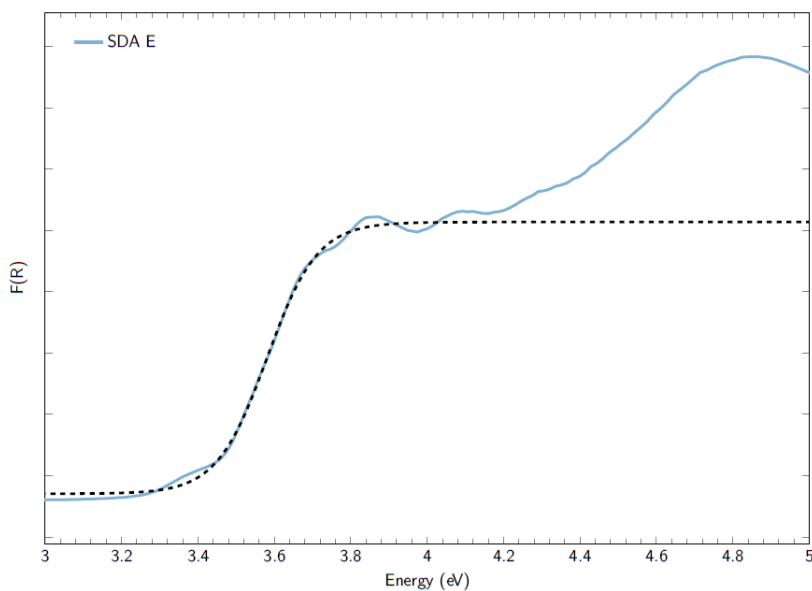
Figure D.5: Kubelka-Monk representation of SDA E and its sigmoidal fit (see Equation D.5)

$$\text{F (R)} = 2,56958 + \frac{0,35288 - 2,56958}{1 + \exp\left(\frac{\text{Energy} - 3,58089}{0,06569}\right)} \tag{D.5}$$

Table D.5: Optical band gap, direct and indirect, of SDA E

	Optical band gap (eV)
Direct	3,6
Indirect	3,3
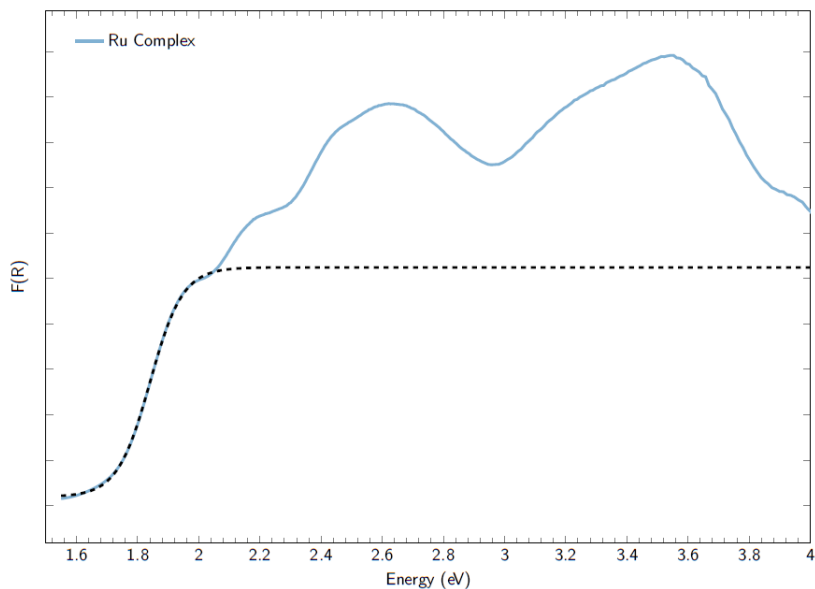
Figure D.6: Kubelka-Monk representation of Ru complex and its sigmoidal fit (see Equation D.6)

$$\text{F}\left(R\right) = 5,24841 + \frac{0,1938 - 5,24841}{1 + \exp\left(\frac{\text{Energy} - 1,84056}{0,05353}\right)} \tag{D.6}$$

Table D.6: Optical band gap, direct and indirect, of Ru Complex

	Optical band gap (eV)
Direct	1,8
Indirect	1,6

D.2 IZM-5 & ITQ-76

D.2.1 Undopped
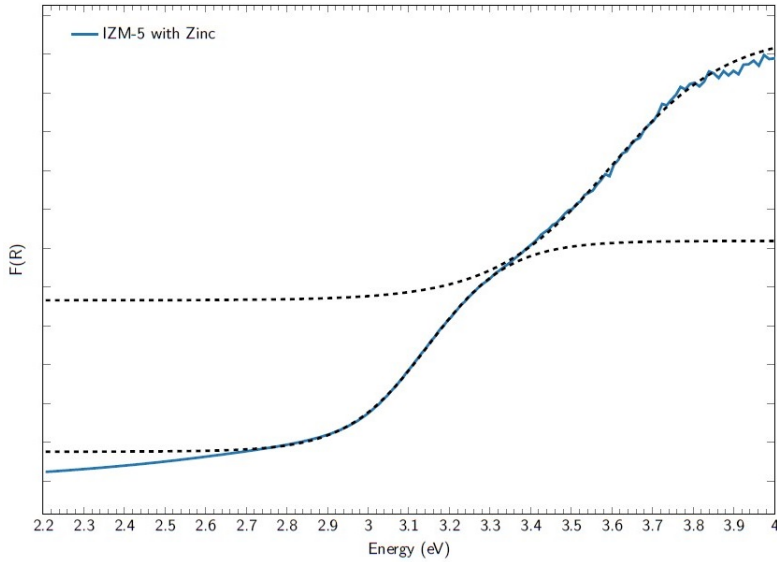
Figure D.7: Kubelka-Monk representation of IZM-5 with zinc and its sigmoidal fit (see Equations D.9 and D.8)

$$F\left(R\right)_{I} = 6,19098 + \frac{0,75663 - 6,19098}{1 + \exp\left(\frac{\text{Energy} - 3,14656}{0,09932}\right)} \tag{D.7}$$

$$F\left(R\right)_{II} = 11,5635 + \frac{4,65984 - 11,5635}{1 + \exp\left(\frac{\text{Energy} - 3,59799}{0,14394}\right)} \tag{D.8}$$

Table D.7: Optical band gap, direct and indirect, of IZM-5 with zinc

	Optical band gap (eV)	
	Transition I	Transition II
Direct	3,1	3,6
Indirect	2,7	3,0
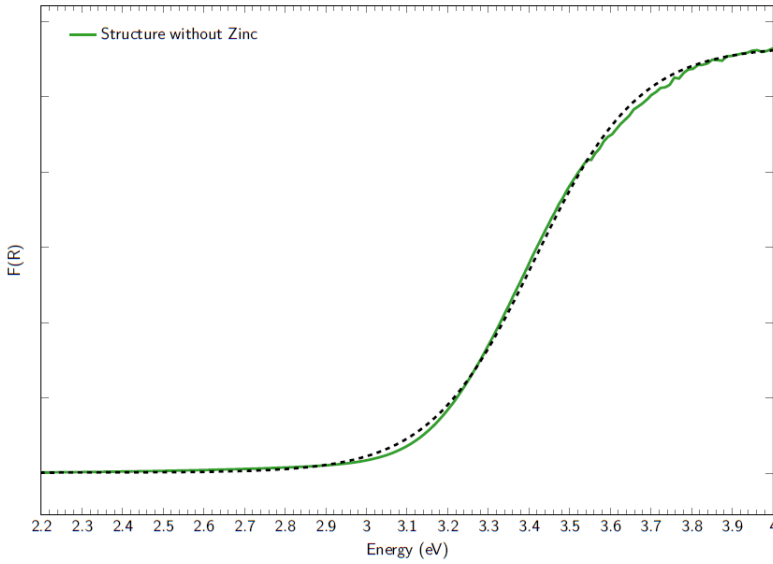
Figure D.8: Kubelka-Monk representation of IZM-5 without zinc and its sigmoidal fit (see Equation D.9)

$$F\left(R\right) = 5,67209 + \frac{0,00856 - 5,67209}{1 + \exp\left(\frac{\text{Energy} - 3,41418}{0,12847}\right)}$$ (D.9)

Table D.8: Optical band gap, direct and indirect, of IZM-5 without zinc

	Optical band gap (eV)
Direct	3,4
Indirect	2,9

D.2.2 Dopped with Se
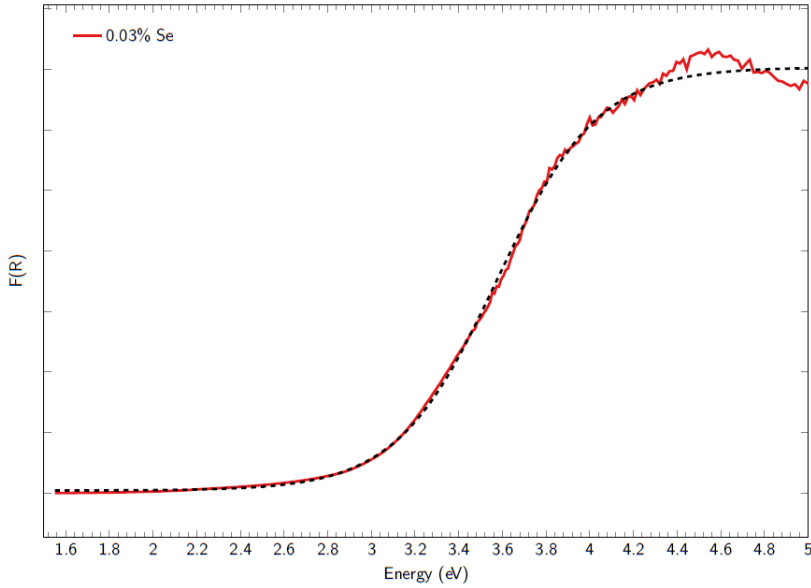
Figure D.9: Kubelka-Monk representation of IZM-5 dopped with 0,03% Se and its sigmoidal fit (see Equation D.10)

$$F\left(R\right) = 14,06381 + \frac{0,08571 - 14,06381}{1 + \exp\left(\frac{\text{Energy} - 3,57745}{0,23032}\right)} \tag{D.10}$$

Table D.9: Optical band gap, direct and indirect, of IZM-5 dopped with 0,03% Se

	Optical band gap (eV)
Direct	3,5
Indirect	2,6
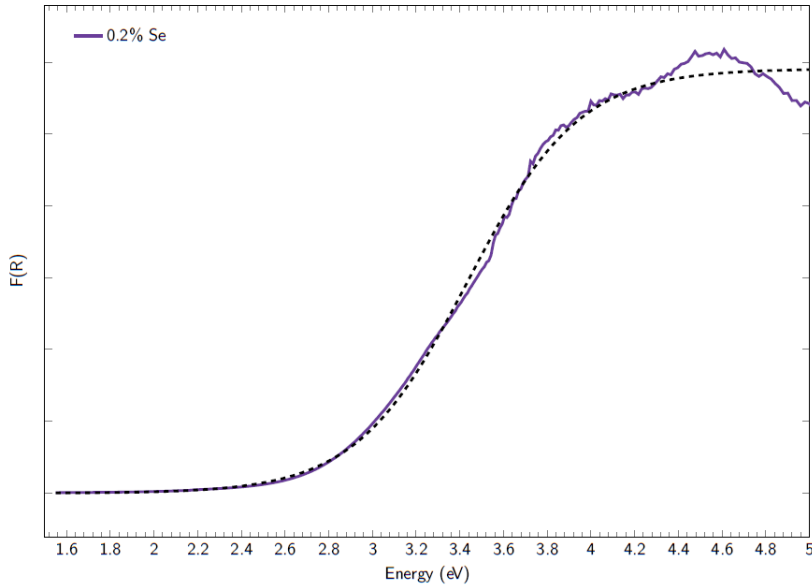
Figure D.10: Kubelka-Monk representation of IZM-5 dopped with 0,2% Se and its sigmoidal fit (see Equation D.11)

$$F\left(R\right) = 11,81858 + \frac{-0,00697 - 11,81858}{1 + \exp\left(\frac{\text{Energy} - 3,43705}{0,25523}\right)} \tag{D.11}$$

Table D.10: Optical band gap, direct and indirect, of IZM-5 dopped with 0,2% Se

	Optical band gap (eV)
Direct	3,4
Indirect	2,4
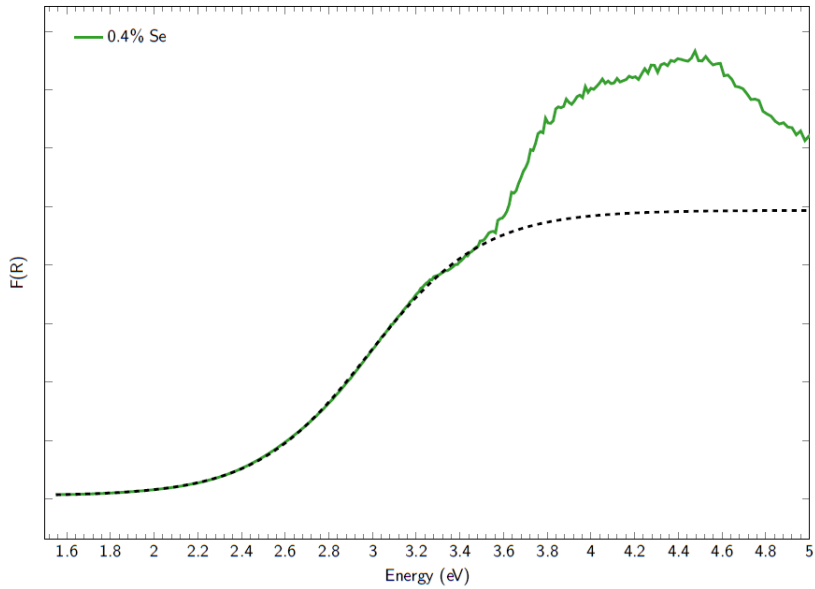
Figure D.11: Kubelka-Monk representation of IZM-5 dopped with 0,4% Se and its sigmoidal fit (see Equation D.12)

$$F\left(R\right) = 9,87553 + \frac{0,10298 - 9,87553}{1 + \exp\left(\frac{\text{Energy} - 2,9852}{0,25968}\right)} \tag{D.12}$$

Table D.11: Optical band gap, direct and indirect, of IZM-5 dopped with 0,4% Se

	Optical band gap (eV)
Direct	2,9
Indirect	1,9

D.2.3 Dopped with Cu
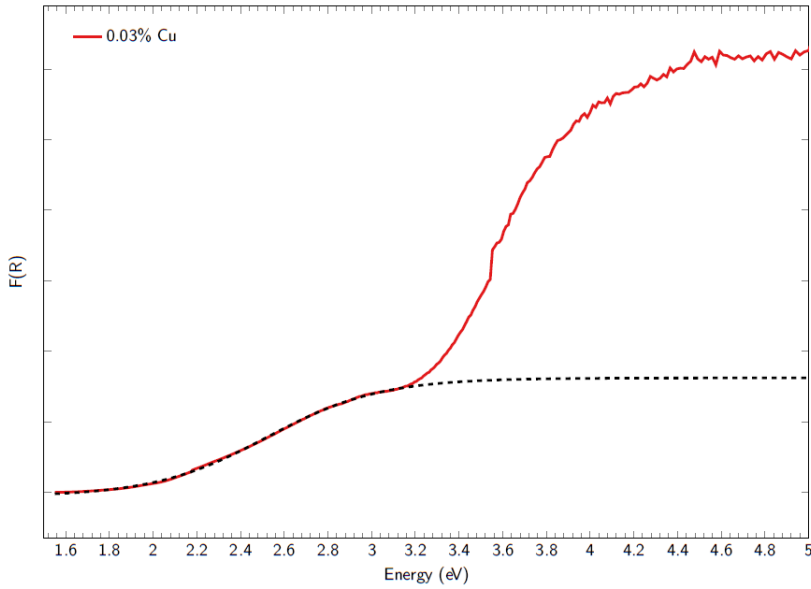
Figure D.12: Kubelka-Monk representation of ITQ-76 dopped with 0,03% Cu and its sigmoidal fit (see Equation D.13)

$$F\left(R\right) = 1,62329 + \frac{-0,05701 - 1,62329}{1 + \exp\left(\frac{\text{Energy} - 2,52079}{0,25964}\right)} \tag{D.13}$$

Table D.12: Optical band gap, direct and indirect, of ITQ-76 dopped with 0,03% Cu

	Optical band gap (eV)
Direct	2,4
Indirect	1,4
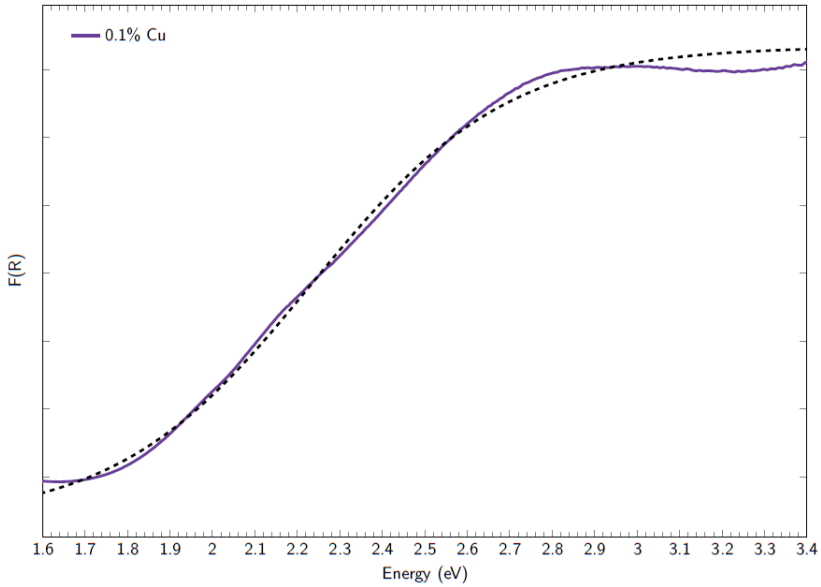
Figure D.13: Kubelka-Monk representation of ITQ-76 dopped with 0,1% Cu and its sigmoidal fit (see Equation D.14)

$$F\left(R\right) = 3,67256 + \frac{0,17507 - 3,67256}{1 + \exp\left(\frac{\text{Energy} - 2,23403}{0,23001}\right)} \tag{D.14}$$

Table D.13: Optical band gap, direct and indirect, of ITQ-76 dopped with 0,1% Cu

	Optical band gap (eV)
Direct	2,2
Indirect	1,2
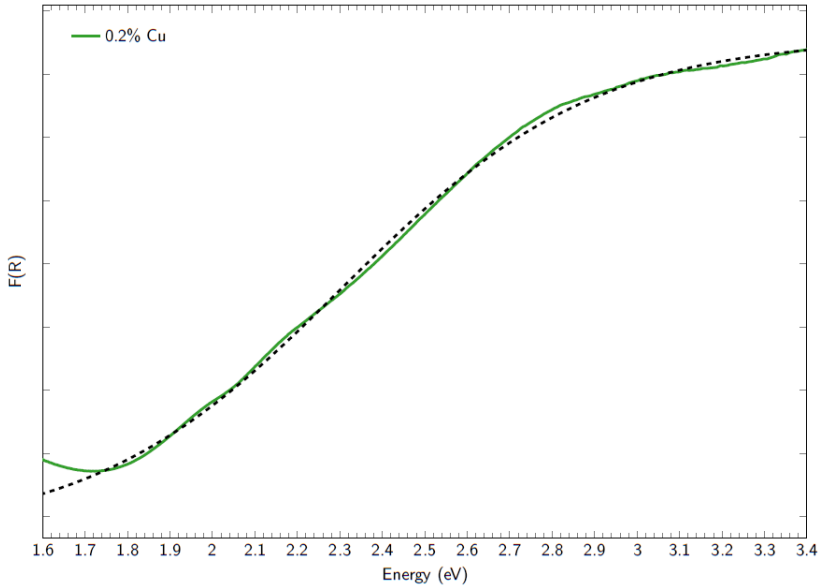
Figure D.14: Kubelka-Monk representation of ITQ-76 dopped with 0,2% Cu and its sigmoidal fit (see Equation D.15)

$$F\left(R\right) = 4,78602 + \frac{0,84881 - 4,78602}{1 + \exp\left(\frac{\text{Energy} - 2,30789}{0,29664}\right)} \tag{D.15}$$

Table D.14: Optical band gap, direct and indirect, of ITQ-76 dopped with 0,2% Cu

	Optical band gap (eV)
Direct	2,2
Indirect	1,0

D.2.4 Dopped with Fe
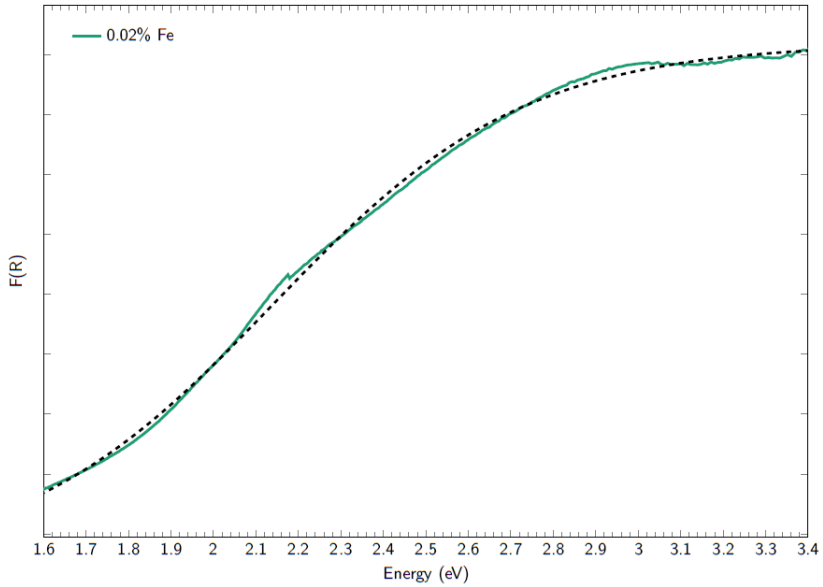
Figure D.15: Kubelka-Monk representation of ITQ-76 dopped with 0,02% Fe and its sigmoidal fit (see Equation D.16)

$$F\left(R\right) = 4,5992 + \frac{0,22851 - 4,5992}{1 + \exp\left(\frac{\text{Energy} - 2,13923}{0,29787}\right)} \tag{D.16}$$

Table D.15: Optical band gap, direct and indirect, of ITQ-76 dopped with 0,02% Fe

	Optical band gap (eV)
Direct	2,0
Indirect	0,9
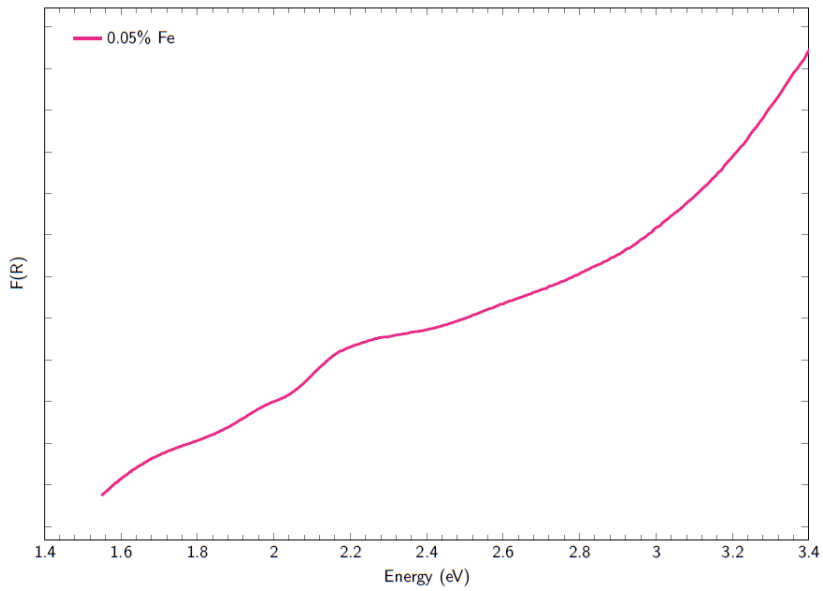
Figure D.16: Kubelka-Monk representation of ITQ-76 dopped with 0,05% Fe
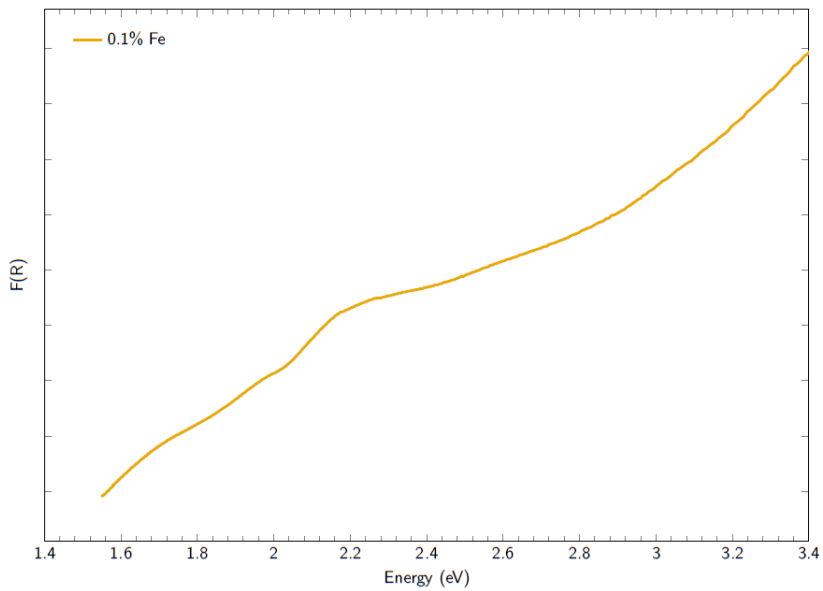
Figure D.17: Kubelka-Monk representation of ITQ-76 dopped with 0,1% Fe

D.2.5 Dopped with Ni
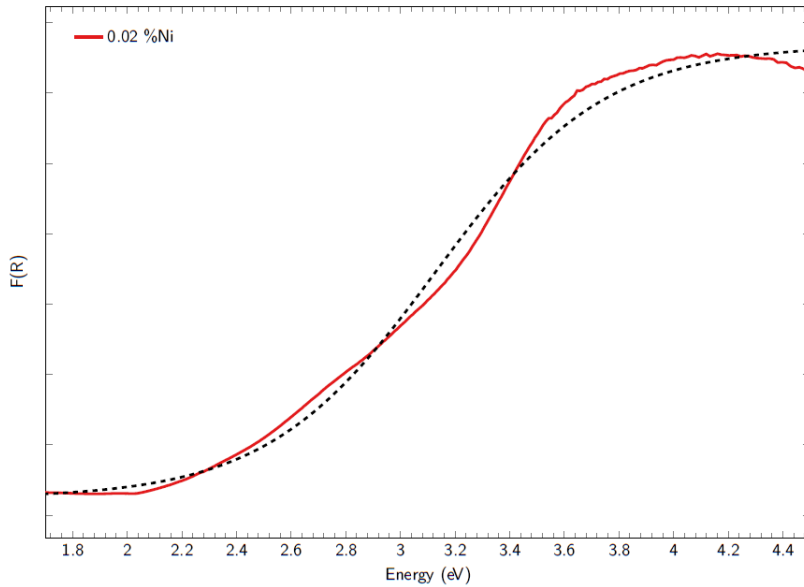
Figure D.18: Kubelka-Monk representation of IZM-5 dopped with 0,02% Ni and its sigmoidal fit (see Equation D.17)

$$F\left(R\right) = 7,6819 + \frac{1,24149 - 7,6819}{1 + \exp\left(\frac{\text{Energy} - 3,12932}{0,30874}\right)} \tag{D.17}$$

Table D.16: Optical band gap, direct and indirect, of IZM-5 dopped with 0,02% Ni

	Optical band gap (eV)
Direct	3,0
Indirect	1,8
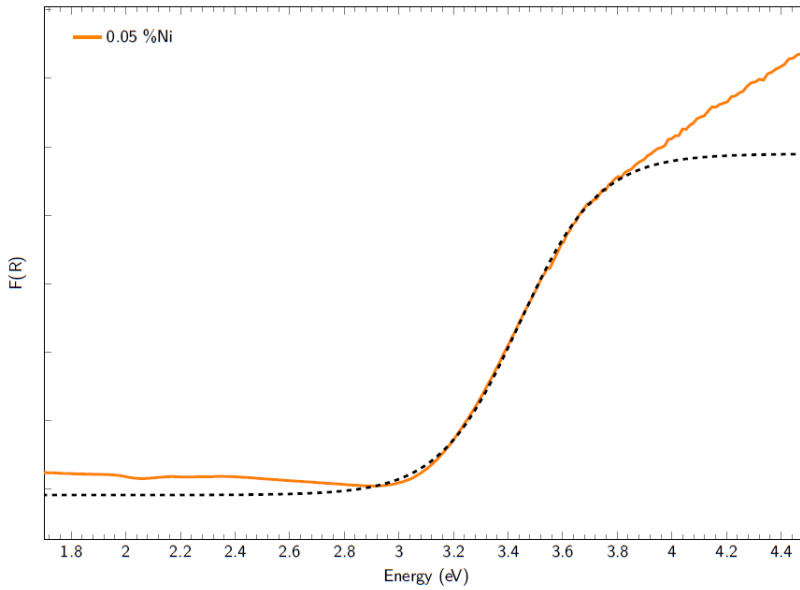
Figure D.19: Kubelka-Monk representation of IZM-5 dopped with 0,05% Ni and its sigmoidal fit (see Equation D.18)

$$F\left(R\right) = 6,89749 + \frac{1,9156 - 6,89749}{1 + \exp\left(\frac{\text{Energy} - 3,44017}{0,14594}\right)} \tag{D.18}$$

Table D.17: Optical band gap, direct and indirect, of IZM-5 dopped with 0,05% Ni

	Optical band gap (eV)
Direct	3,3
Indirect	2,8
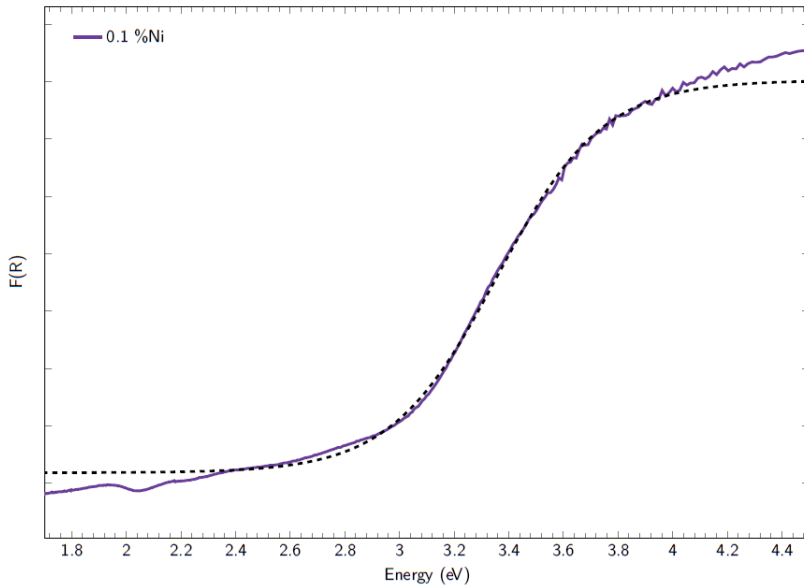
Figure D.20: Kubelka-Monk representation of IZM-5 dopped with 0,1% Ni and its sigmoidal fit (see Equation D.19)

$$F\left(R\right) = 6,5123 + \frac{3,08984 - 6,5123}{1 + \exp\left(\frac{\text{Energy}-3,35732}{0,19402}\right)} \tag{D.19}$$

Table D.18: Optical band gap, direct and indirect, of IZM-5 dopped with 0,1% Ni

	Optical band gap (eV)
Direct	3,2
Indirect	2,5

D.2.6 Dopped with Co
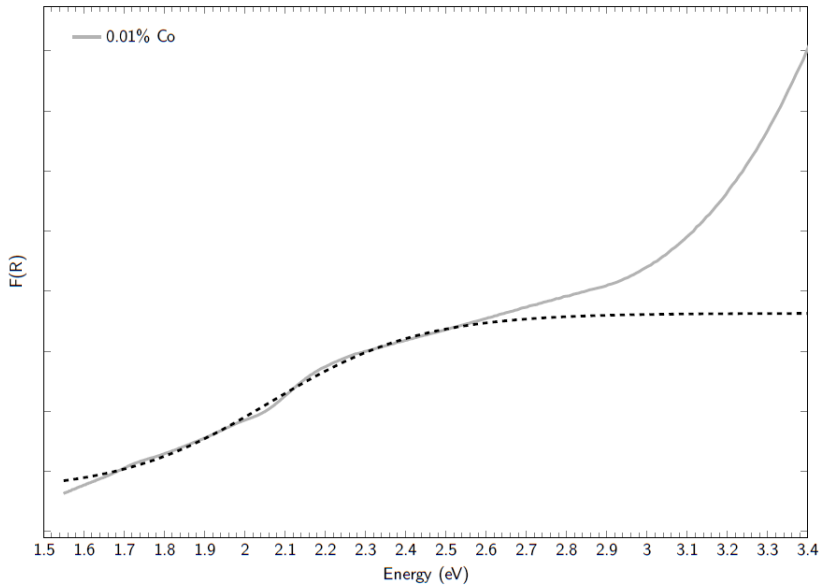
Figure D.21: Kubelka-Monk representation of ITQ-76 dopped with 0,01% Co and its sigmoidal fit (see Equation D.20)

$$F\left(R\right) = 2,31601 + \frac{0,83120 - 2,31601}{1 + \exp\left(\frac{\text{Energy} - 2,06221}{0,1878}\right)} \tag{D.20}$$

Table D.19: Optical band gap, direct and indirect, of ITQ-76 dopped with 0,01% Co

	Optical band gap (eV)
Direct	2,0
Indirect	1,3
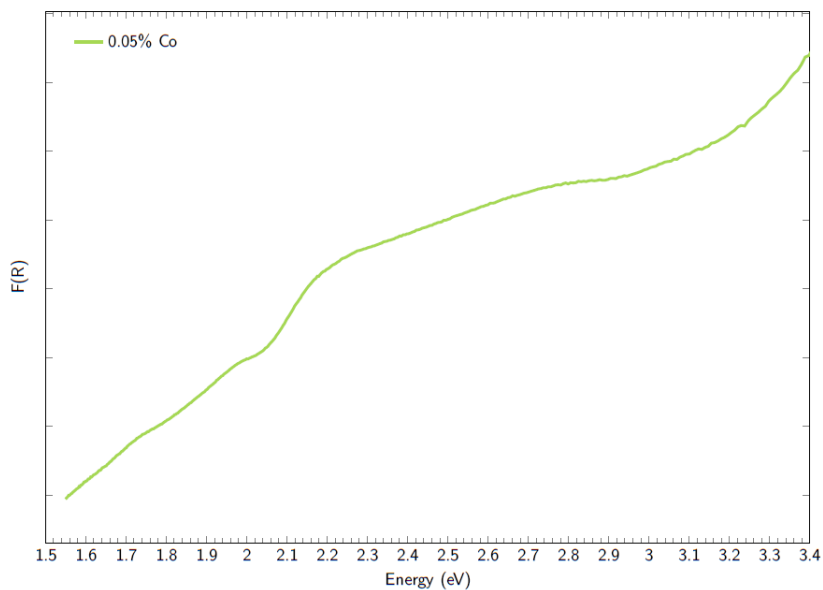
Figure D.22: Kubelka-Monk representation of ITQ-76 dopped with 0,05% Co
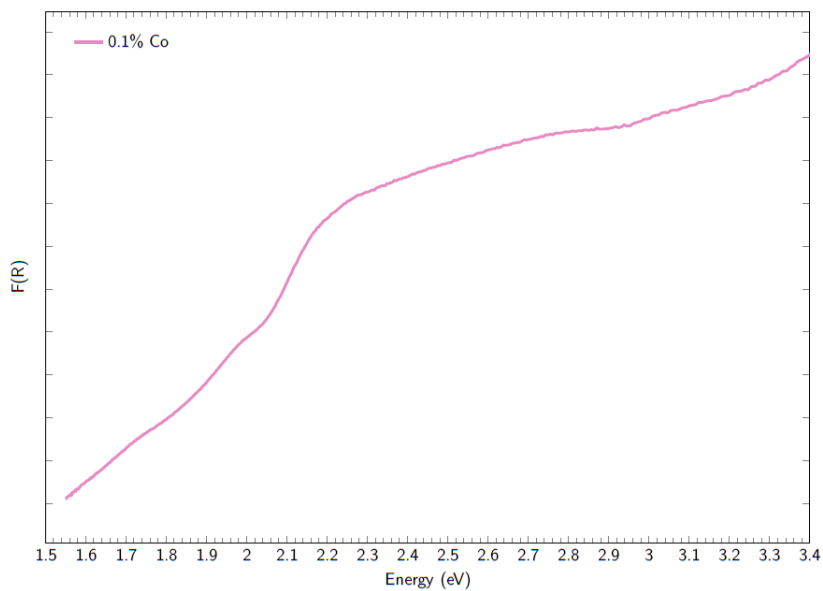
Figure D.23: Kubelka-Monk representation of ITQ-76 dopped with 0,1% Co

D.2.7   Insertion of Ru-Complex
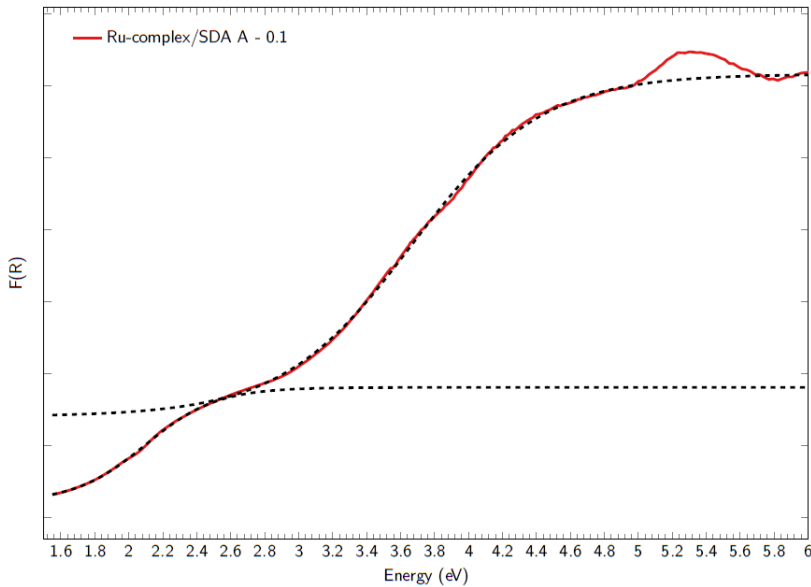
Figure D.24: Kubelka-Monk representation of ITQ-76 with Ru-complex/SDA A - 0,1 and its sigmoidal fit (see Equations D.21 and D.22)

$$F(R)_I = 3,61636 + \frac{0,42414 - 3,61636}{1 + \exp\left(\frac{\text{Energy} - 2,09826}{0,209}\right)} \tag{D.21}$$

$$F(R)_{II} = 12,32884 + \frac{2,80985 - 12,32884}{1 + \exp\left(\frac{\text{Energy} - 3,66422}{0,3857}\right)} \tag{D.22}$$

Table D.20: Optical band gap, direct and indirect, of ITQ-76 with Ru-complex/SDA A - 0,1

	Optical band gap (eV)	
	Transition I	Transition II
Direct	2,0	3,4
Indirect	1,2	2,0
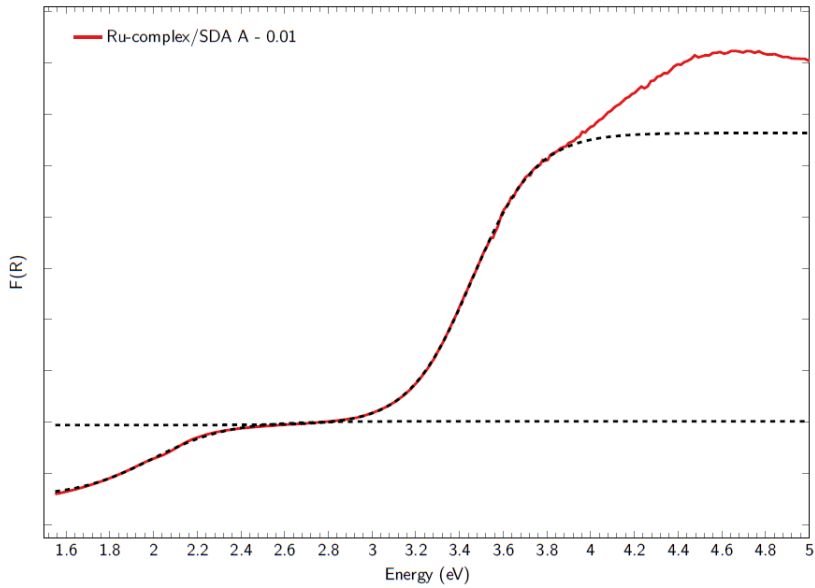
Figure D.25: Kubelka-Monk representation of ITQ-76 with Ru-complex/SDA A - 0,01 and its sigmoidal fit (see Equations D.23 and D.24)

$$\text{F}(\text{R})_I = 2,017 + \frac{0,5389 - 2,017}{1 + \exp\left(\frac{\text{Energy} - 1,9916}{0,1745}\right)} \tag{D.23}$$

$$\text{F}(\text{R})_{II} = 7,6364 + \frac{1,943 - 7,6364}{1 + \exp\left(\frac{\text{Energy} - 3,4585}{0,1449}\right)} \tag{D.24}$$

Table D.21: Optical band gap, direct and indirect, of ITQ-76 with Ru-complex/SDA A - 0,01

	Optical band gap (eV)	
	Transition I	Transition II
Direct	1,9	3,4
Indirect	1,2	2,8

D.3 ITQ-75

D.3.1 Undopped
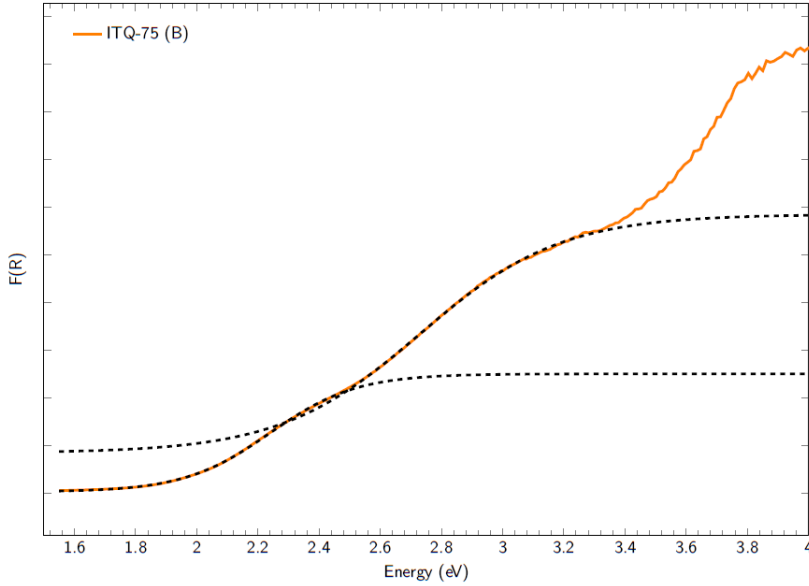
Figure D.26: Kubelka-Monk representation of ITQ-75, obtained with Compound B as SDA, and its sigmoidal fit (see Equations D.25 and D.26)

$$F\left(R\right)_{I} = 2,49866 + \frac{0,01939 - 2,49866}{1 + \exp\left(\frac{\text{Energy} - 2,24007}{0,14093}\right)} \tag{D.25}$$

$$F\left(R\right)_{II} = 5,8462 + \frac{0,83898 - 5,8462}{1 + \exp\left(\frac{\text{Energy} - 2,73092}{0,22951}\right)} \tag{D.26}$$

Table D.22: Optical band gap, direct and indirect, of ITQ-75 obtained with Compound B as SDA

| | Optical band gap (eV) | |
	Transition I	Transition II
Direct	2,2	2,7
Indirect	1,6	1,7
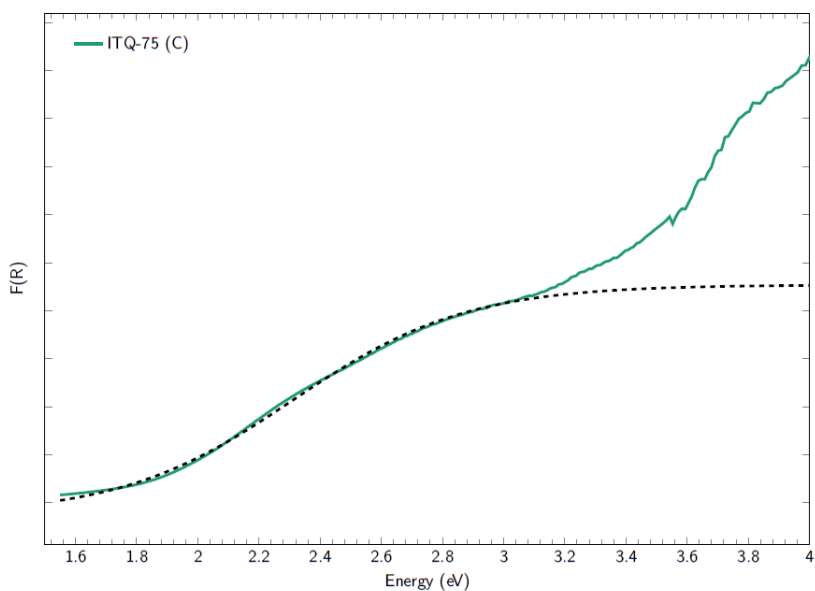
Figure D.27: Kubelka-Monk representation of ITQ-75, obtained with Compound C as SDA, and its sigmoidal fit (see Equation D.27)

$$\text{F (R)} = 4,538 + \frac{-0,25359 - 4,538}{1 + \exp\left(\frac{\text{Energy} - 2,31199}{0,28248}\right)} \tag{D.27}$$

Table D.23: Optical band gap, direct and indirect, of ITQ-75 obtained with Compound C as SDA

	Optical band gap (eV)
Direct	2,2
Indirect	1,1
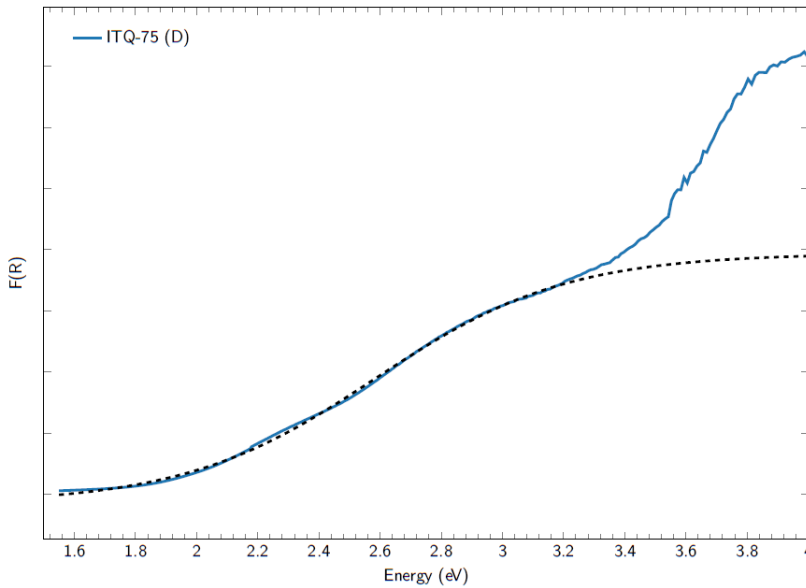
Figure D.28: Kubelka-Monk representation of ITQ-75, obtained with Compound D as SDA, and its sigmoidal fit (see Equation D.28)

$$\text{F (R)} = 3,93786 + \frac{-0,15475 - 3,93786}{1 + \exp\left(\frac{\text{Energy} - 2,58441}{0,31226}\right)} \tag{D.28}$$

Table D.24: Optical band gap, direct and indirect, of ITQ-75 obtained with Compound D as SDA

	Optical band gap (eV)
Direct	2,5
Indirect	1,2
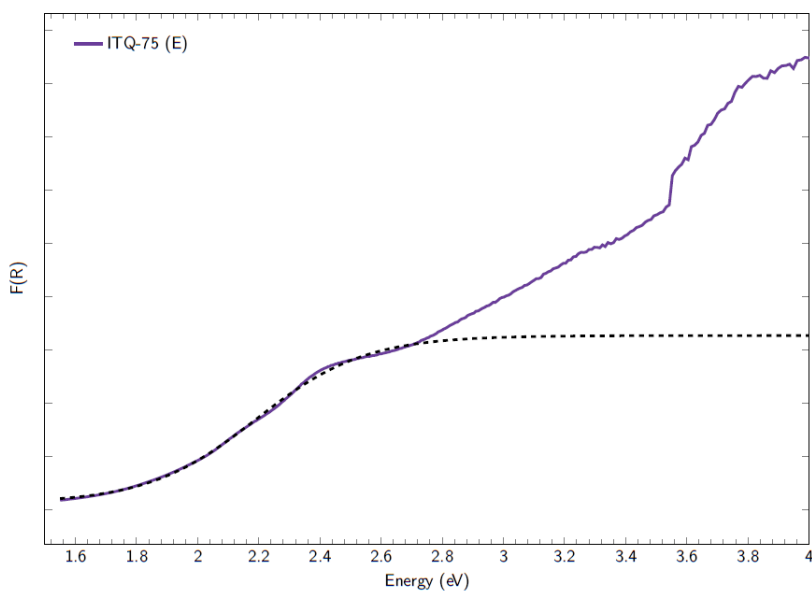
Figure D.29: Kubelka-Monk representation of ITQ-75, obtained with Compound E as SDA, and its sigmoidal fit (see Equation D.29)

$$F\ (R) = 3,27335 + \frac{0,13158 - 3,27335}{1 + \exp\left(\frac{\text{Energy} - 2,19094}{-0,17748}\right)} \tag{D.29}$$

Table D.25: Optical band gap, direct and indirect, of ITQ-75 obtained with Compound E as SDA

	Optical band gap (eV)
Direct	2,2
Indirect	3,0

D.3.2 Dopped with Se
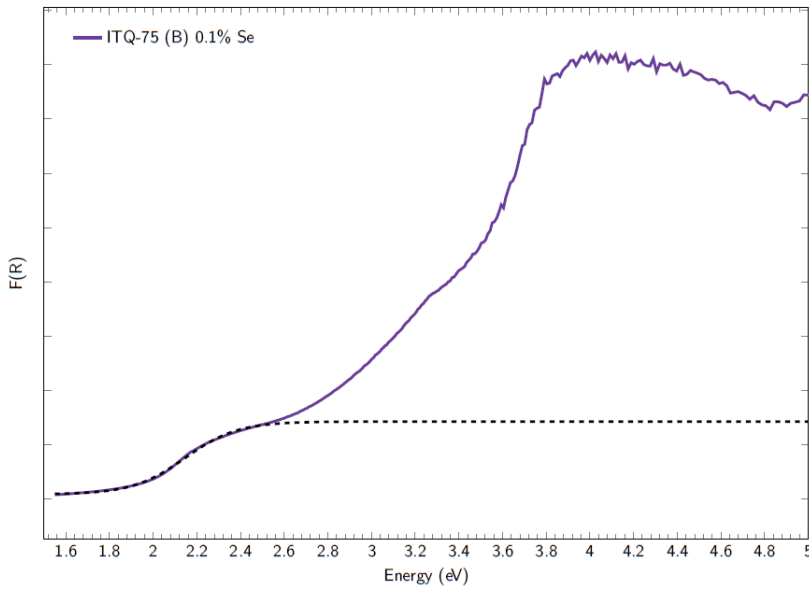
Figure D.30: Kubelka-Monk representation of ITQ-75, obtained with Compound B as SDA, dopped with 0,1% Se and its sigmoidal fit (see Equation D.30)

$$\text{F}\left(R\right) = 2,85198 + \frac{0,16716 - 2,85198}{1 + \exp\left(\frac{\text{Energy} - 2,14655}{0,12021}\right)} \tag{D.30}$$

Table D.26: Optical band gap, direct and indirect, of ITQ-75 obtained with Compound B as SDA dopped with 0,1% Se

	Optical band gap (eV)
Direct	2,1
Indirect	1,6
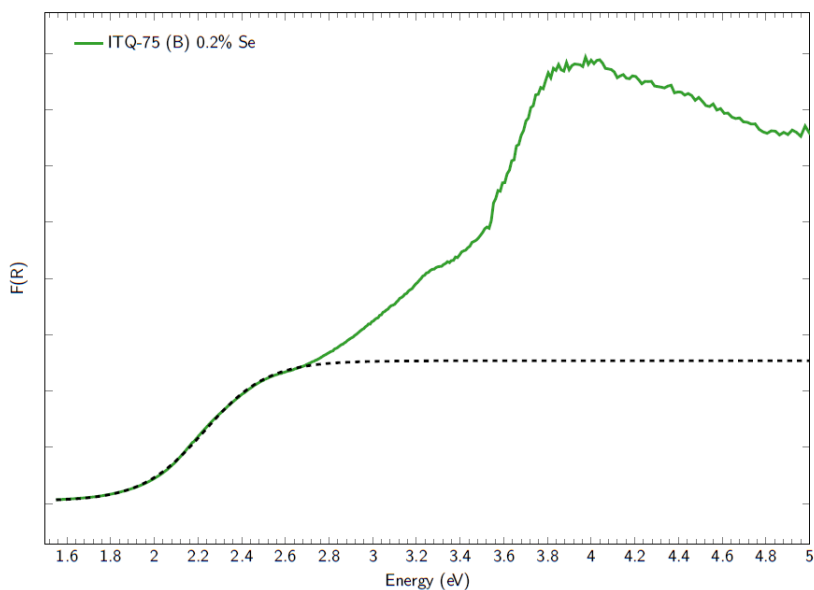
Figure D.31: Kubelka-Monk representation of ITQ-75, obtained with Compound B as SDA, dopped with 0,2% Se and its sigmoidal fit (see Equation D.31)

$$\text{F}(R) = 5,07402 + \frac{0,08788 - 5,07402}{1 + \exp\left(\frac{\text{Energy} - 2,22969}{0,14379}\right)} \tag{D.31}$$

395

Table D.27: Optical band gap, direct and indirect, of ITQ-75 obtained with Compound B as SDA dopped with 0,2% Se

	Optical band gap (eV)
Direct	2,2
Indirect	1,6
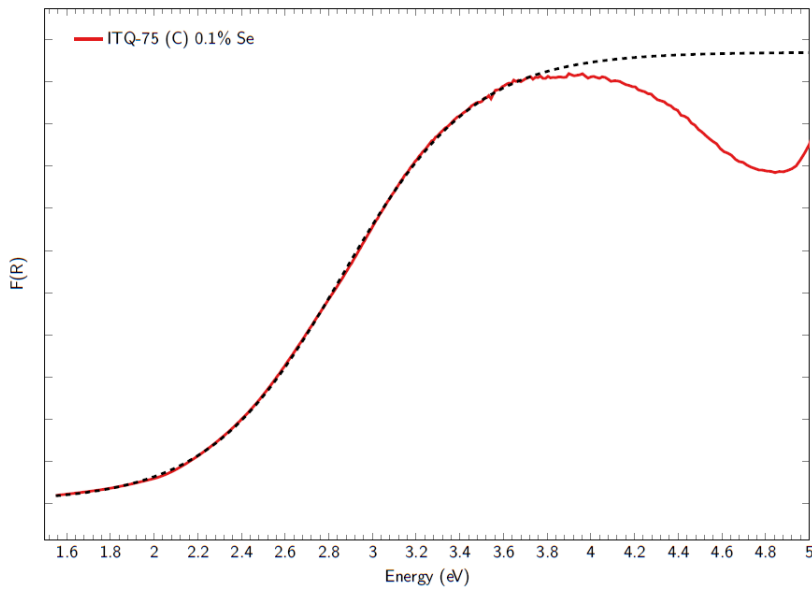
Figure D.32: Kubelka-Monk representation of ITQ-75, obtained with Compound C as SDA, dopped with 0,1% Se and its sigmoidal fit (see Equation D.32)

$$\text{F}(R) = 5,35423 + \frac{0,01619 - 5,35423}{1 + \exp\left(\frac{\text{Energy} - 2,85737}{0,30305}\right)} \tag{D.32}$$

Table D.28: Optical band gap, direct and indirect, of ITQ-75 obtained with Compound C as SDA dopped with 0,1% Se

	Optical band gap (eV)
Direct	2,8
Indirect	1,6
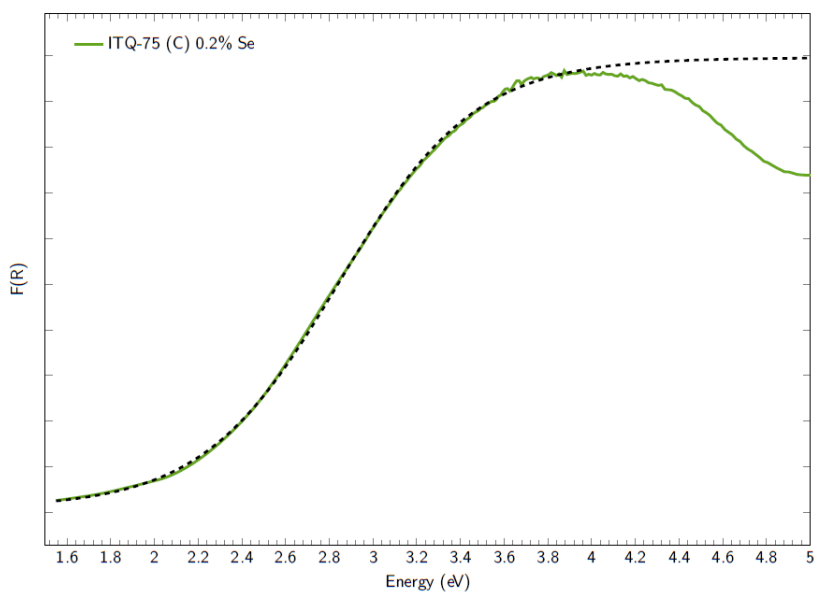
Figure D.33: Kubelka-Monk representation of ITQ-75, obtained with Compound C as SDA, dopped with 0,2% Se and its sigmoidal fit (see Equation D.33)

$$\text{F (R)} = 4,98347 + \frac{0,05415 - 4,98347}{1 + \exp\left(\frac{\text{Energy} - 2,84316}{0,31138}\right)} \tag{D.33}$$

Table D.29: Optical band gap, direct and indirect, of ITQ-75 obtained with Compound C as SDA dopped with 0,2% Se

	Optical band gap (eV)
Direct	2,7
Indirect	1,5

D.3.3 Dopped with Cu
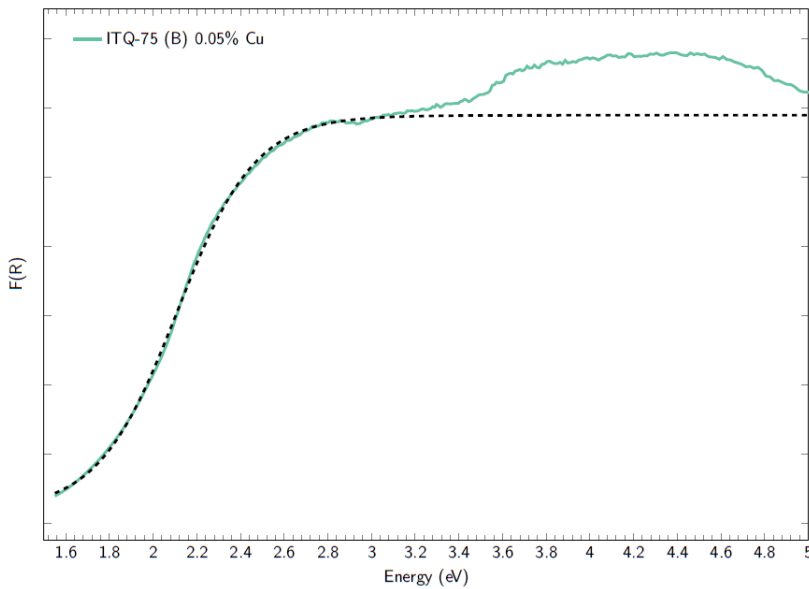
Figure D.34: Kubelka-Monk representation of ITQ-75, obtained with Compound B as SDA, dopped with 0,05% Cu and its sigmoidal fit (see Equation D.34)

$$F\left(R\right) = 11,7864 + \frac{0,3919 - 11,7864}{1 + \exp\left(\frac{\text{Energy} - 2,10825}{0,17982}\right)} \tag{D.34}$$

Table D.30: Optical band gap, direct and indirect, of ITQ-75 obtained with Compound B as SDA dopped with 0,05% Cu

	Optical band gap (eV)
Direct	2,1
Indirect	1,3
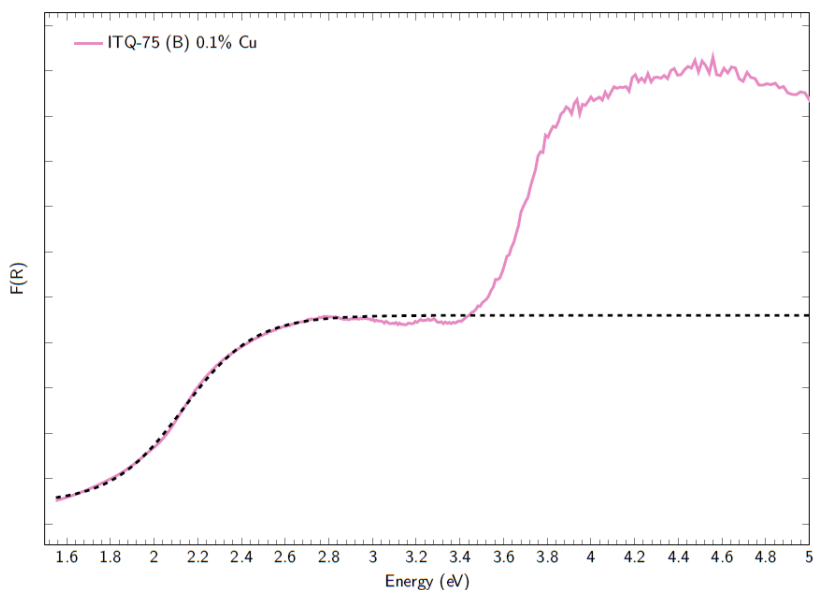
Figure D.35: Kubelka-Monk representation of ITQ-75, obtained with Compound B as SDA, dopped with 0,1% Cu and its sigmoidal fit (see Equation D.35)

$$F(R) = 9,20628 + \frac{0,9398 - 9,20628}{1 + \exp\left(\frac{\text{Energy} - 2,13198}{0,16356}\right)} \tag{D.35}$$

Table D.31: Optical band gap, direct and indirect, of ITQ-75 obtained with Compound B as SDA dopped with 0,1% Cu

	Optical band gap (eV)
Direct	2,1
Indirect	1,4
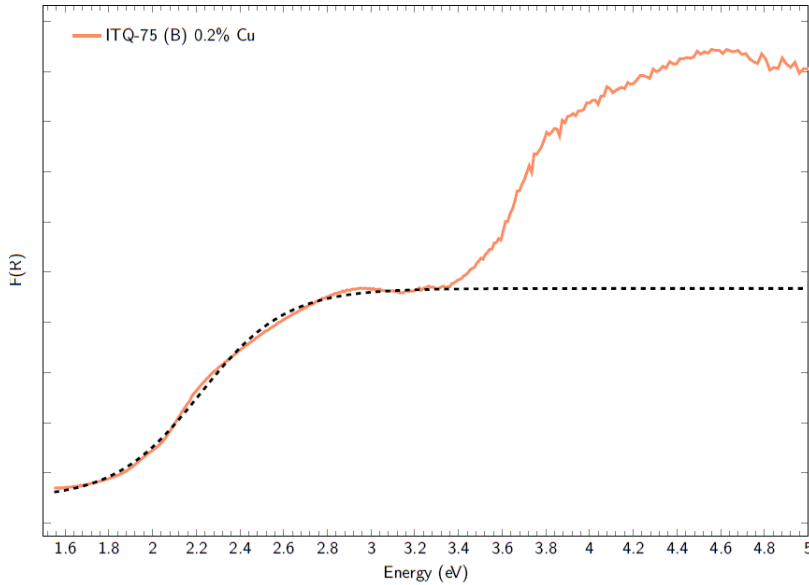
Figure D.36: Kubelka-Monk representation of ITQ-75, obtained with Compound B as SDA, dopped with 0,2% Cu and its sigmoidal fit (see Equation D.36)

$$F\left(R\right) = 1,4876 + \frac{5,67627 - 1,4876}{1 + \exp\left(\frac{\text{Energy} - 2,21876}{-0,1949}\right)} \qquad (D.36)$$

Table D.32: Optical band gap, direct and indirect, of ITQ-75 obtained with Compound B as SDA dopped with 0,2% Cu

	Optical band gap (eV)
Direct	2,3
Indirect	3,1
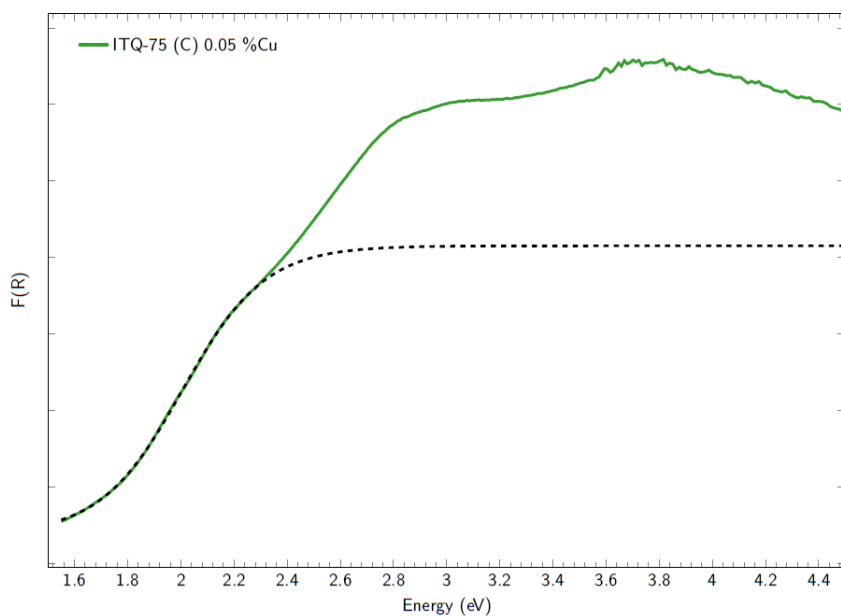
Figure D.37: Kubelka-Monk representation of ITQ-75, obtained with Compound C as SDA, dopped with 0,05% Cu and its sigmoidal fit (see Equation D.37)

$$F\left(R\right) = 2,00636 + \frac{0,19012 - 2,00636}{1 + \exp\left(\frac{\text{Energy} - 2,00636}{0,1545}\right)} \tag{D.37}$$

Table D.33: Optical band gap, direct and indirect, of ITQ-75 obtained with Compound C as SDA dopped with 0,05% Cu

	Optical band gap (eV)
Direct	2,0
Indirect	1,3
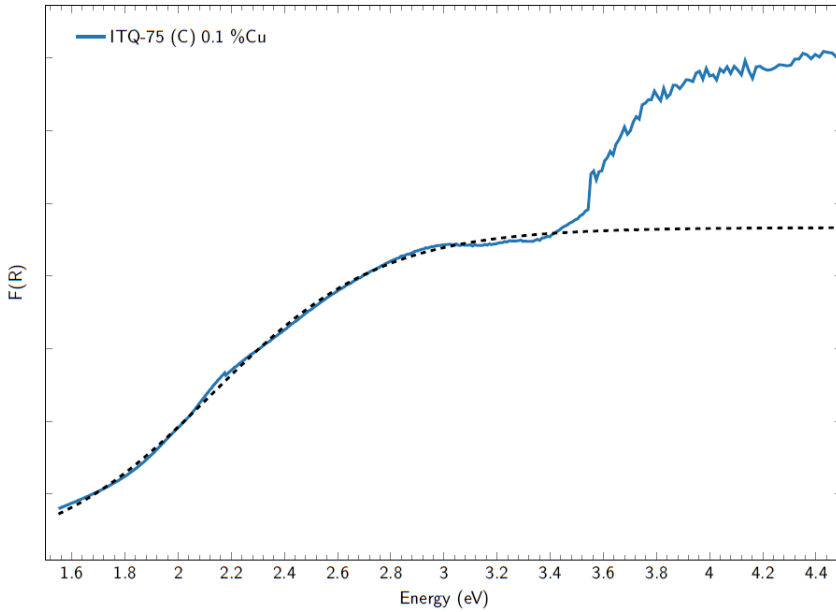
Figure D.38: Kubelka-Monk representation of ITQ-75, obtained with Compound C as SDA, dopped with 0,1% Cu and its sigmoidal fit (see Equation D.38)

$$F\left(R\right) = 4,66552 + \frac{0,08495 - 4,66552}{1 + \exp\left(\frac{\text{Energy} - 2,12744}{0,31736}\right)} \tag{D.38}$$

Table D.34: Optical band gap, direct and indirect, of ITQ-75 obtained with Compound C as SDA dopped with 0,1% Cu

	Optical band gap (eV)
Direct	2,0
Indirect	0,8
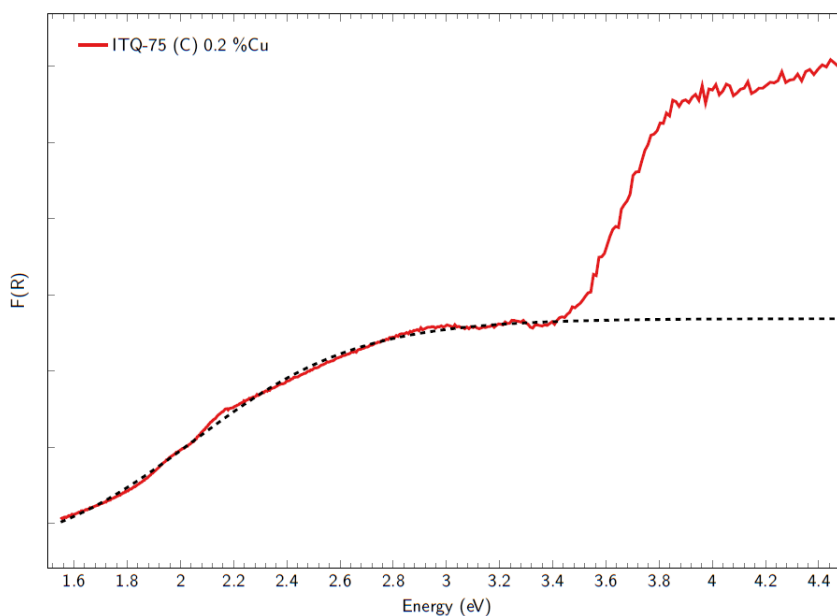
Figure D.39: Kubelka-Monk representation of ITQ-75, obtained with Compound C as SDA, dopped with 0,2% Cu and its sigmoidal fit (see Equation D.39)

$$\mathsf{F}\ (\mathsf{R}) = 9,38063 + \frac{2,98496 - 9,38063}{1 + \mathsf{exp}\left(\frac{\mathsf{Energy} - 2,05171}{0,30919}\right)} \tag{D.39}$$

Table D.35: Optical band gap, direct and indirect, of ITQ-75 obtained with Compound C as SDA dopped with 0,2% Cu

	Optical band gap (eV)
Direct	2,0
Indirect	0,7

D.3.4 Dopped with Fe
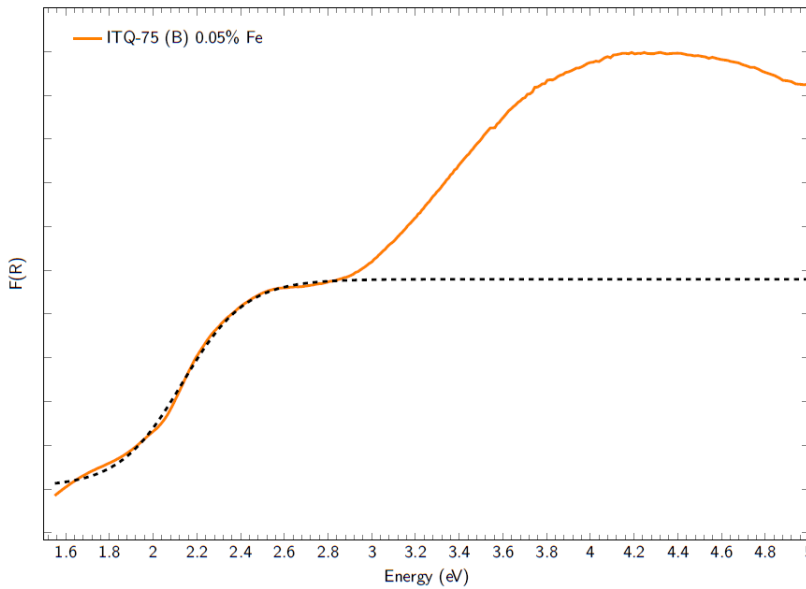
Figure D.40: Kubelka-Monk representation of ITQ-75, obtained with Compound B as SDA, dopped with 0,05 % Fe and its sigmoidal fit (see Equation D.40)

$$\text{F (R)} = 2,33636 + \frac{6,73288 - 2,33636}{1 + \exp\left(\frac{\text{Energy} - 2,11405}{0,124}\right)} \tag{D.40}$$

Table D.36: Optical band gap, direct and indirect, of ITQ-75 obtained with Compound B as SDA dopped with 0,05% Fe

	Optical band gap (eV)
Direct	2,1
Indirect	1,6
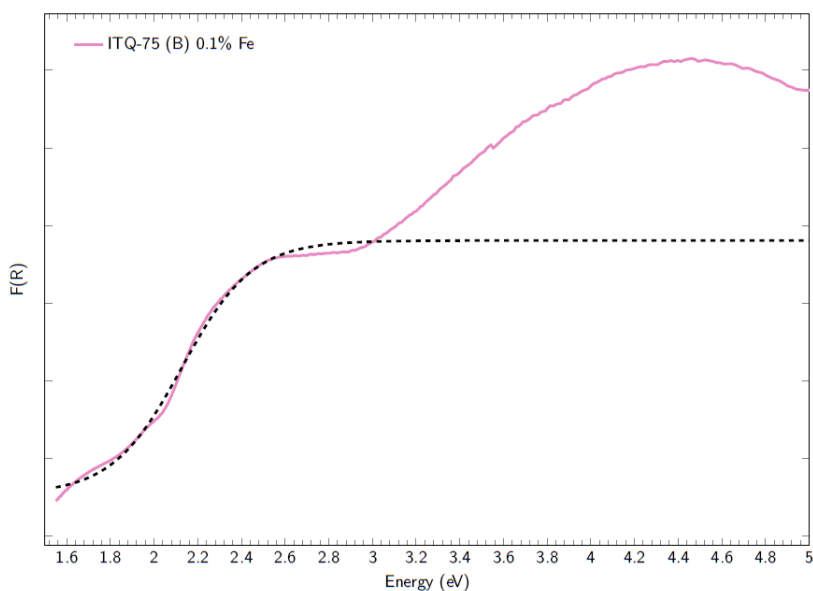
Figure D.41: Kubelka-Monk representation of ITQ-75, obtained with Compound B as SDA, dopped with 0,1% Fe and its sigmoidal fit (see Equation D.41)

$$F(R) = 2,54015 + \frac{5,80621 - 2,54015}{1 + \exp\left(\frac{\text{Energy} - 2,12768}{0,16059}\right)} \tag{D.41}$$

Table D.37: Optical band gap, direct and indirect, of ITQ-75 obtained with Compound B as SDA dopped with 0,1% Fe

	Optical band gap (eV)
Direct	2,1
Indirect	1,4
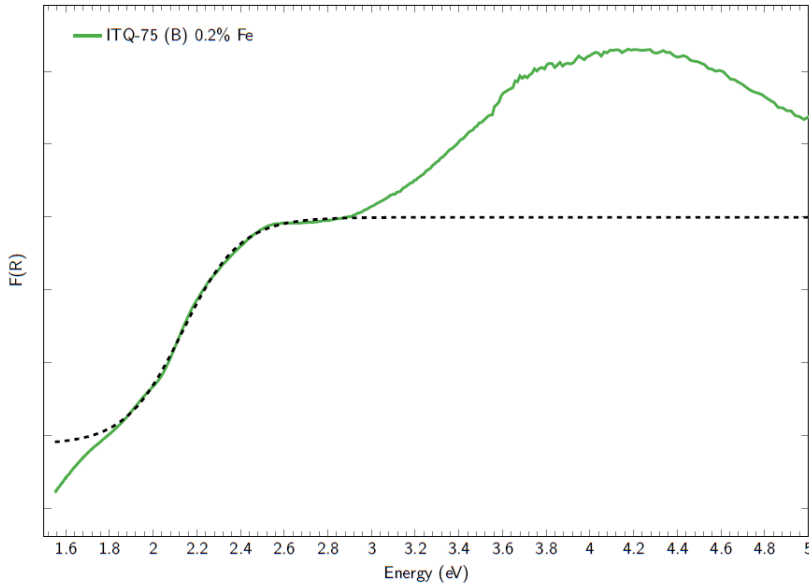
Figure D.42: Kubelka-Monk representation of ITQ-75, obtained with Compound B as SDA, dopped with 0,2% Fe and its sigmoidal fit (see Equation D.42)

$$\text{F (R)} = 5,99657 + \frac{2,87855 - 5,99657}{1 + \exp\left(\frac{\text{Energy} - 2,13567}{0,13068}\right)} \tag{D.42}$$

Table D.38: Optical band gap, direct and indirect, of ITQ-75 obtained with Compound B as SDA dopped with 0,2% Fe

Optical band gap (eV)	
Direct	2,1
Indirect	1,6
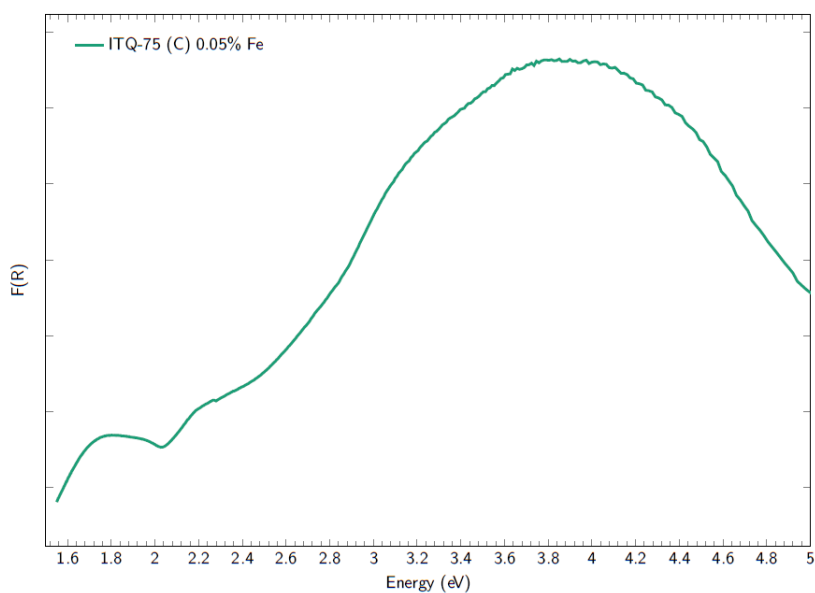
Figure D.43: Kubelka-Monk representation of ITQ-75, obtained with Compound C as SDA, dopped with 0,05% Fe
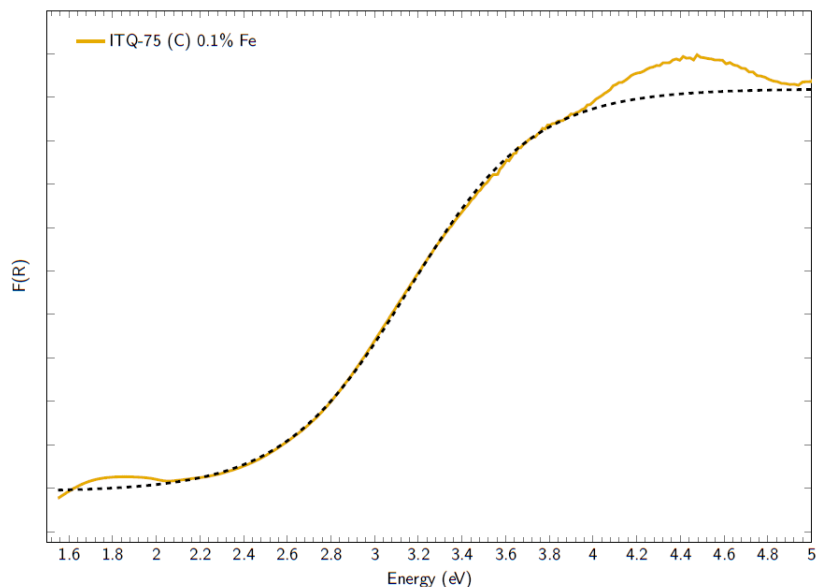
Figure D.44: Kubelka-Monk representation of ITQ-75, obtained with Compound C as SDA, dopped with 0,1% Fe and its sigmoidal fit (see Equation D.43)

$$F\left(R\right) = 5,59681 + \frac{0,96235 - 5,59681}{1 + \exp\left(\frac{\text{Energy} - 3,15414}{0,28626}\right)} \tag{D.43}$$

Table D.39: Optical band gap, direct and indirect, of ITQ-75 obtained with Compound C as SDA dopped with 0,1% Fe

	Optical band gap (eV)
Direct	3,1
Indirect	1,9
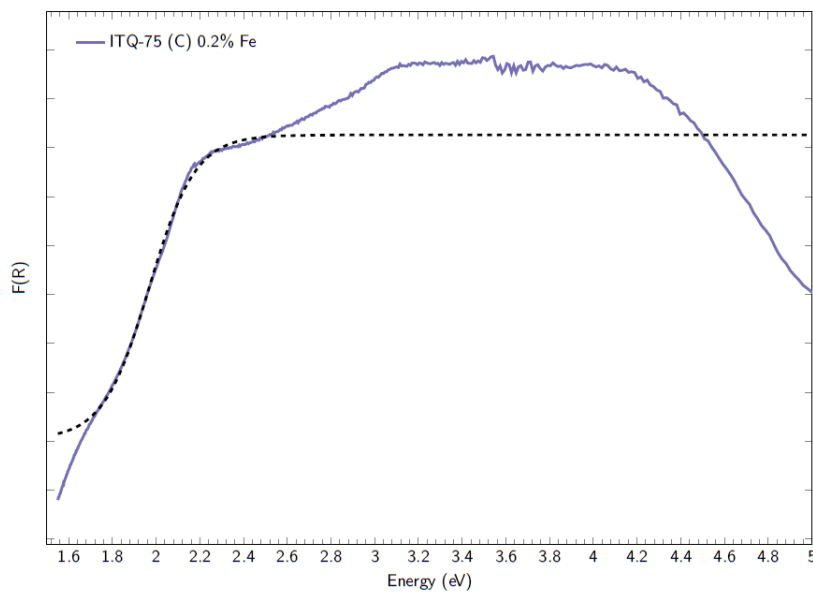
Figure D.45: Kubelka-Monk representation of ITQ-75, obtained with Compound C as SDA, dopped with 0,2% Fe and its sigmoidal fit (see Equation D.44)

$$F\left(R\right) = 14,26134 + \frac{8,03965 - 14,26134}{1 + \exp\left(\frac{\text{Energy} - 1,96863}{0,10533}\right)} \tag{D.44}$$

Table D.40: Optical band gap, direct and indirect, of ITQ-75 obtained with Compound C as SDA dopped with 0,2% Fe

	Optical band gap (eV)
Direct	1,9
Indirect	1,5

D.3.5 Dopped with Ni
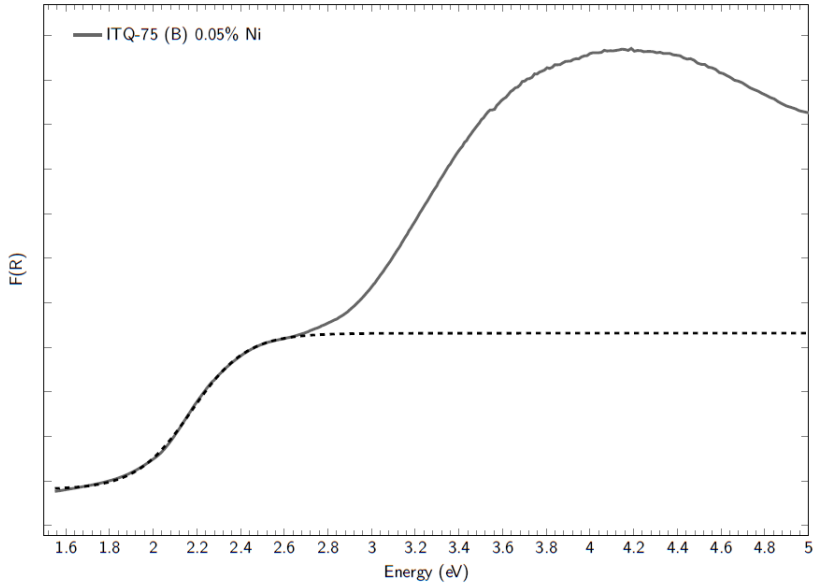
Figure D.46: Kubelka-Monk representation of ITQ-75, obtained with Compound B as SDA, dopped with 0,05% Ni and its sigmoidal fit (see Equation D.45)

$$F\left(R\right) = 4,31648 + \frac{0,81098 - 4,31648}{1 + \exp\left(\frac{\text{Energy} - 2,17385}{0,12564}\right)} \tag{D.45}$$

Table D.41: Optical band gap, direct and indirect, of ITQ-75 obtained with Compound B as SDA dopped with 0,05% Ni

	Optical band gap (eV)
Direct	2,1
Indirect	1,6
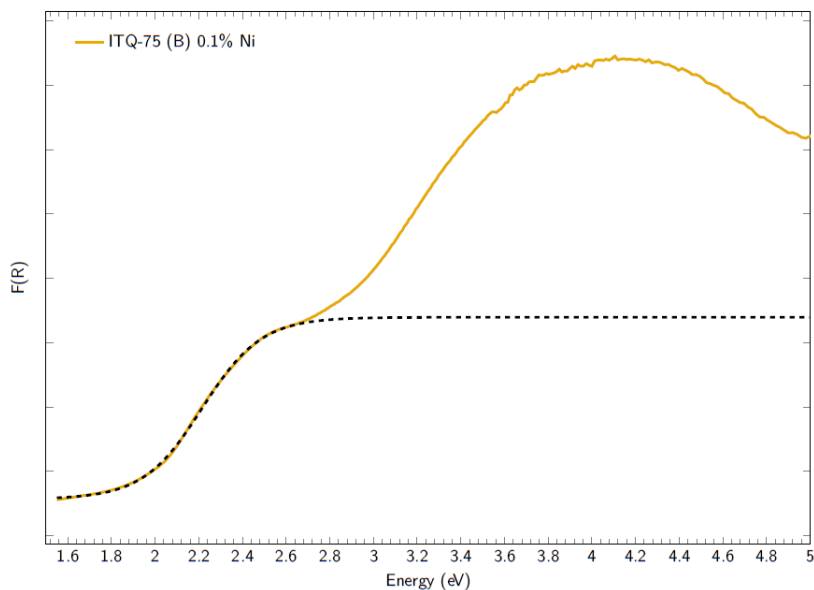
Figure D.47: Kubelka-Monk representation of ITQ-75, obtained with Compound B as SDA, dopped with 0,1% Ni and its sigmoidal fit (see Equation D.46)

$$F\left(R\right) = 3,39357 + \frac{0,56916 - 3,39357}{1 + \exp\left(\frac{\text{Energy} - 2,21545}{0,13555}\right)} \tag{D.46}$$

Table D.42: Optical band gap, direct and indirect, of ITQ-75 obtained with Compound B as SDA dopped with 0,1% Ni

	Optical band gap (eV)
Direct	2,2
Indirect	1,6
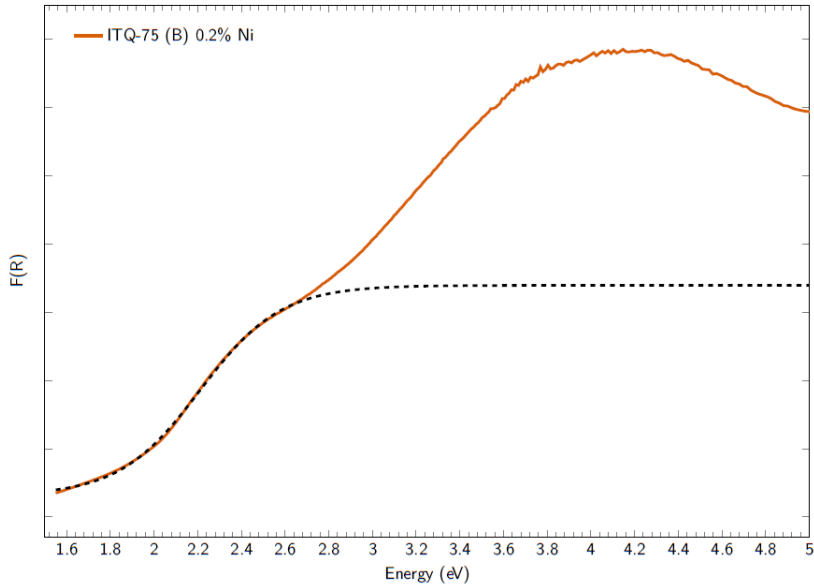
Figure D.48: Kubelka-Monk representation of ITQ-75, obtained with Compound B as SDA, dopped with 0,2% Ni and its sigmoidal fit (see Equation D.47)

$$\text{F (R)} = 3,3938 + \frac{0,31278 - 3,3938}{1 + \exp\left(\frac{\text{Energy} - 2,21005}{0,18511}\right)} \tag{D.47}$$

Table D.43: Optical band gap, direct and indirect, of ITQ-75 obtained with Compound B as SDA dopped with 0,2% Ni

	Optical band gap (eV)
Direct	2,2
Indirect	1,4
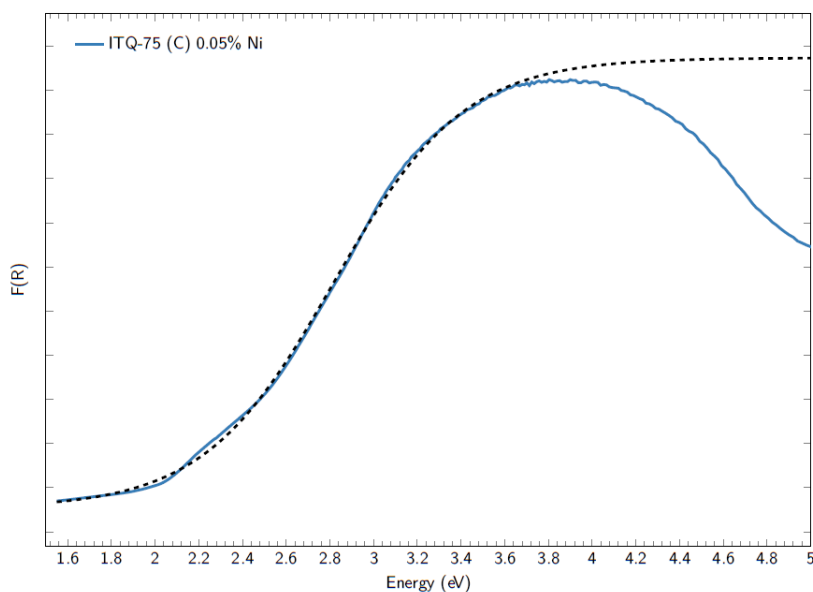
Figure D.49: Kubelka-Monk representation of ITQ-75, obtained with Compound C as SDA, dopped with 0,05% Ni and its sigmoidal fit (see Equation D.48)

$$F\left(R\right) = 5,36819 + \frac{0,2685 - 5,36819}{1 + \exp\left(\frac{\text{Energy} - 2,81616}{0,29709}\right)} \tag{D.48}$$

Table D.44: Optical band gap, direct and indirect, of ITQ-75 obtained with Compound C as SDA dopped with 0,05% Ni

	Optical band gap (eV)
Direct	2,7
Indirect	1,5
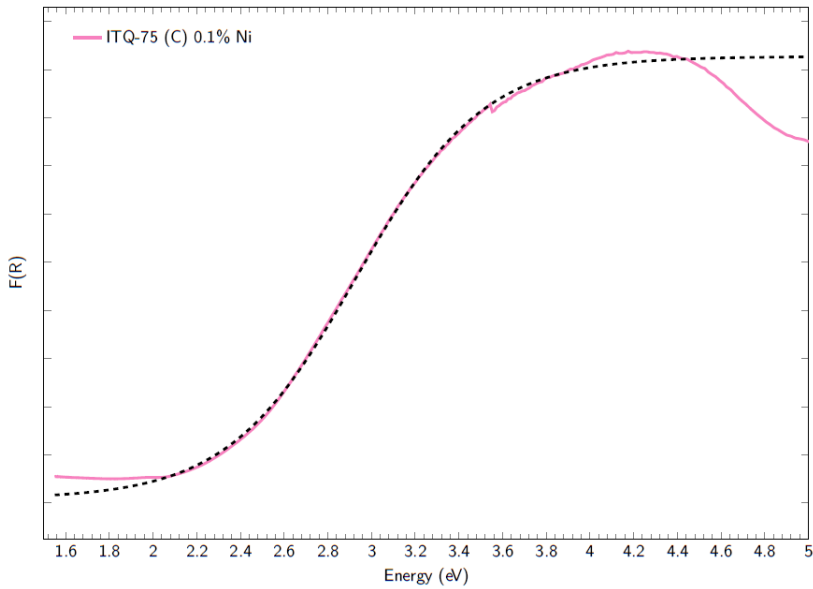
Figure D.50: Kubelka-Monk representation of ITQ-75, obtained with Compound C as SDA, dopped with 0,1% Ni and its sigmoidal fit (see Equation D.49)

$$F(R) = 5,13549 + \frac{0,54243 - 5,13549}{1 + \exp\left(\frac{\text{Energy} - 2,92955}{0,29198}\right)} \tag{D.49}$$

Table D.45: Optical band gap, direct and indirect, of ITQ-75 obtained with Compound C as SDA dopped with 0,1% Ni

	Optical band gap (eV)
Direct	2,8
Indirect	1,7
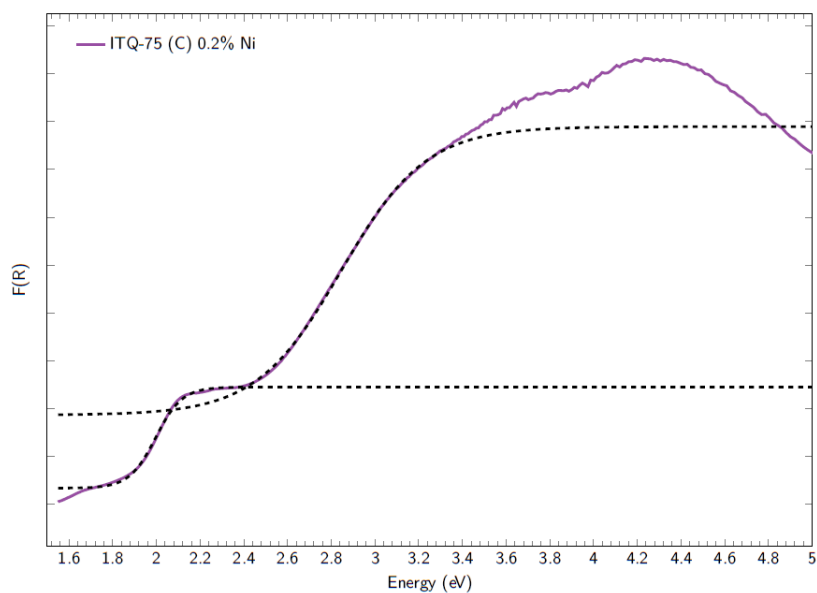
Figure D.51: Kubelka-Monk representation of ITQ-75, obtained with Compound C as SDA, dopped with 0,2% Ni and its sigmoidal fit (see Equations D.50 and D.51)

$$F\left(R\right)_{I} = 1,72392 + \frac{0,66571 - 1,72392}{1 + \exp\left(\frac{\text{Energy} - 1,99661}{0,14093}\right)} \tag{D.50}$$

$$F\left(R\right)_{II} = 4,44773 + \frac{1,43078 - 4,44773}{1 + \exp\left(\frac{\text{Energy} - 2,845}{0,19431}\right)} \tag{D.51}$$

Table D.46: Optical band gap, direct and indirect, of ITQ-75 obtained with Compound C as SDA dopped with 0,2% Ni

	Optical band gap (eV)	
	Transition I	Transition II
Direct	2,0	1,7
Indirect	2,8	2,0

D.3.6 Dopped with Co
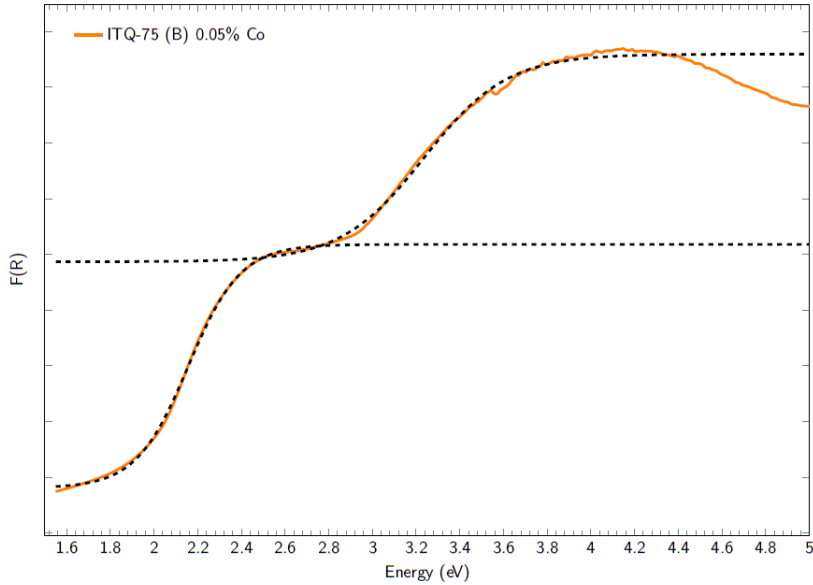
Figure D.52: Kubelka-Monk representation of ITQ-75, obtained with Compound B as SDA, dopped with 0,05% Co and its sigmoidal fit (see Equations D.52 and D.53)

$$F\left(R\right)_I = 5,17893 + \frac{0,80954 - 5,17893}{1 + \exp\left(\frac{\text{Energy} - 2,15681}{0,11958}\right)} \tag{D.52}$$

$$F\left(R\right)_{II} = 8,59307 + \frac{4,86748 - 8,59307}{1 + \exp\left(\frac{\text{Energy} - 3,23564}{0,19053}\right)} \tag{D.53}$$

Table D.47: Optical band gap, direct and indirect, of ITQ-75 obtained with Compound B as SDA dopped with 0,05% Co

	Optical band gap (eV)	
	Transition I	Transition II
Direct	2,1	1,6
Indirect	3,2	2,4
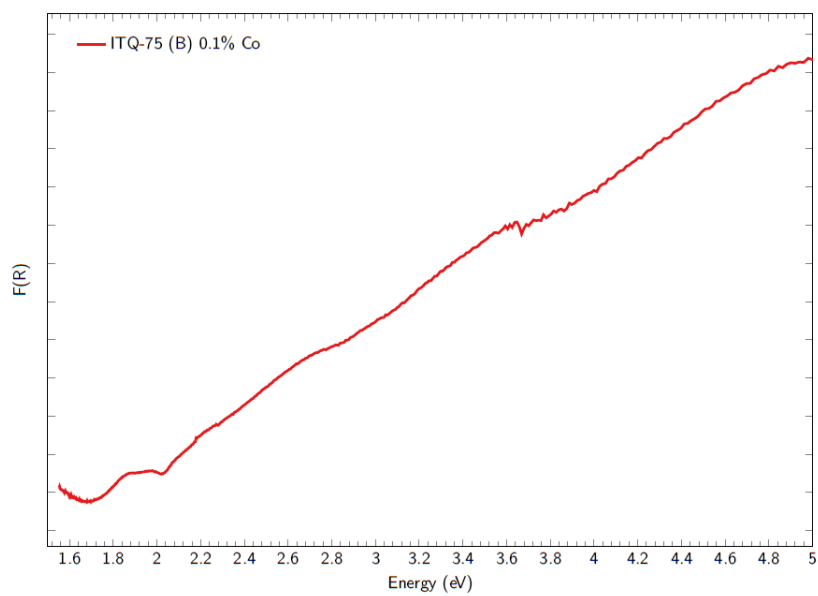
Figure D.53: Kubelka-Monk representation of ITQ-75, obtained with Compound B as SDA, dopped with 0,1% Co
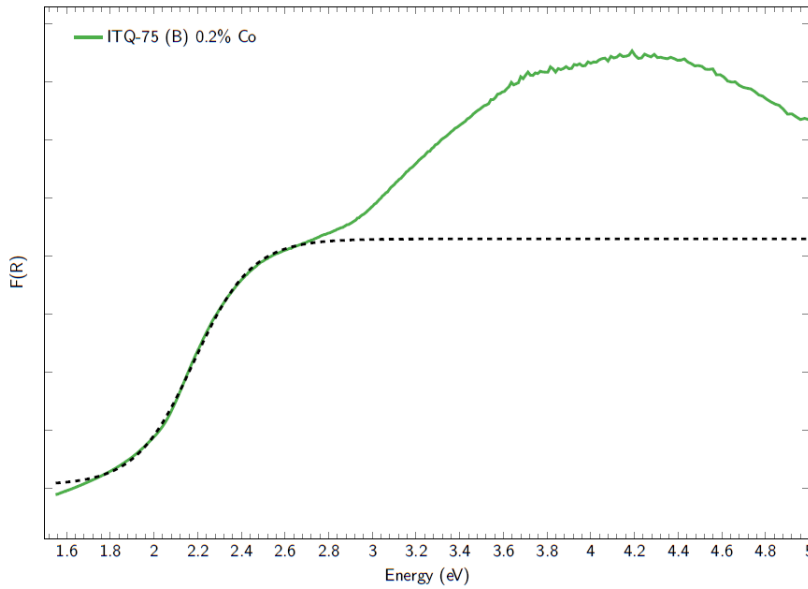
Figure D.54: Kubelka-Monk representation of ITQ-75, obtained with Compound B as SDA, dopped with 0,2% Co (see Equation D.54)

$$F\left(R\right) = 5,29337 + \frac{1,05076 - 5,29337}{1 + \exp\left(\frac{\text{Energy} - 2,18198}{0,1321}\right)} \tag{D.54}$$

Table D.48: Optical band gap, direct and indirect, of ITQ-75 obtained with Compound B as SDA dopped with 0,2% Co

	Optical band gap (eV)
Direct	2,1
Indirect	1,6
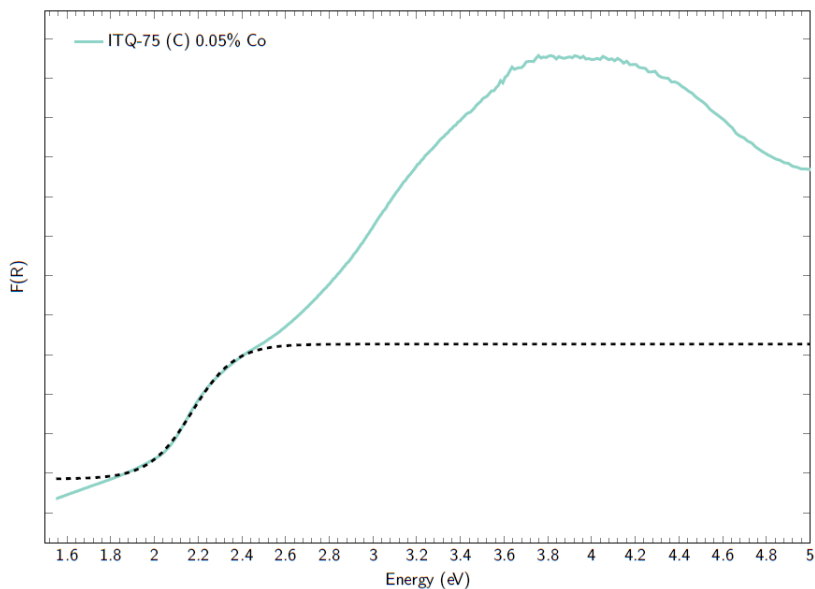
Figure D.55: Kubelka-Monk representation of ITQ-75, obtained with Compound C as SDA, dopped with 0,05% Co (see Equation D.55)

$$F\,(R) = 2,63406 + \frac{0,92738 - 2,63406}{1 + \exp\left(\frac{\text{Energy} - 2,1726}{0,09774}\right)} \tag{D.55}$$

Table D.49: Optical band gap, direct and indirect, of ITQ-75 obtained with Compound C as SDA dopped with 0,05% Co

	Optical band gap (eV)
Direct	2,1
Indirect	1,8
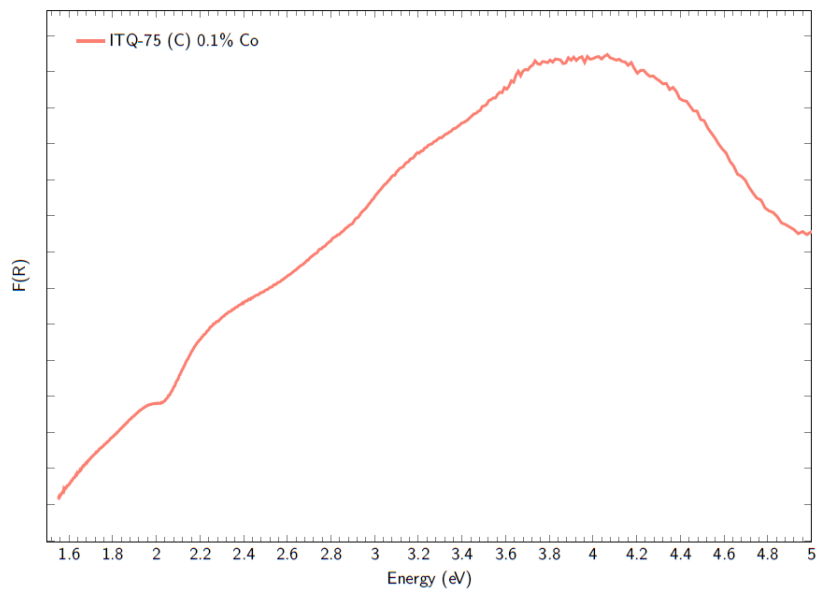
Figure D.56: Kubelka-Monk representation of ITQ-75, obtained with Compound C as SDA, dopped with 0,1% Co
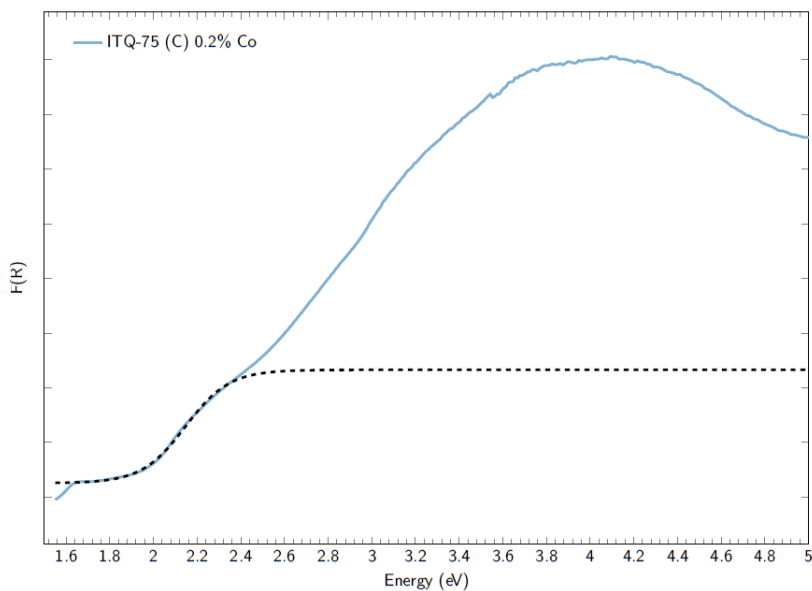
Figure D.57: Kubelka-Monk representation of ITQ-75, obtained with Compound C as SDA, dopped with 0,2% Co (see Equation D.56)

$$F\left(R\right) = 2,16471 + \frac{1,12825 - 2,16471}{1 + \exp\left(\frac{\text{Energy} - 2,14664}{0,10048}\right)} \tag{D.56}$$

Table D.50: Optical band gap, direct and indirect, of ITQ-75 obtained with Compound C as SDA dopped with 0,2% Co

	Optical band gap (eV)
Direct	2,1
Indirect	1,7

421

D.3.7 Saccharide Presence
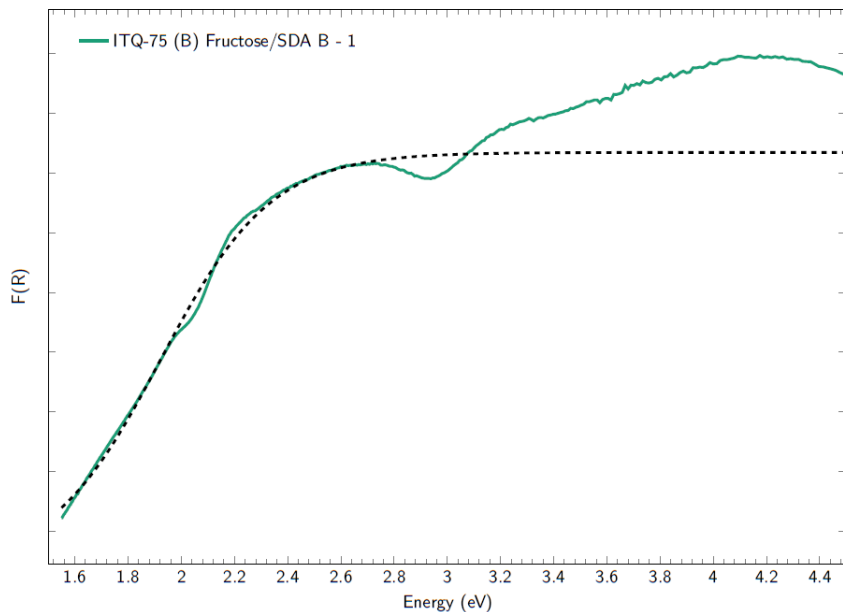
Figure D.58: Kubelka-Monk representation of ITQ-75, obtained with Compound B as SDA, with Fructose/SDA B - 1 (see Equation D.57)

$$\text{F (R)} = 10,40134 + \frac{3,40134 - 10,34464}{1 + \exp\left(\frac{\text{Energy} - 1,92199}{0,20833}\right)} \tag{D.57}$$

Table D.51: Optical band gap, direct and indirect, of ITQ-75 obtained with Compound B as SDA and with Fructose/SDA B - 1

	Optical band gap (eV)
Direct	1,9
Indirect	1,0
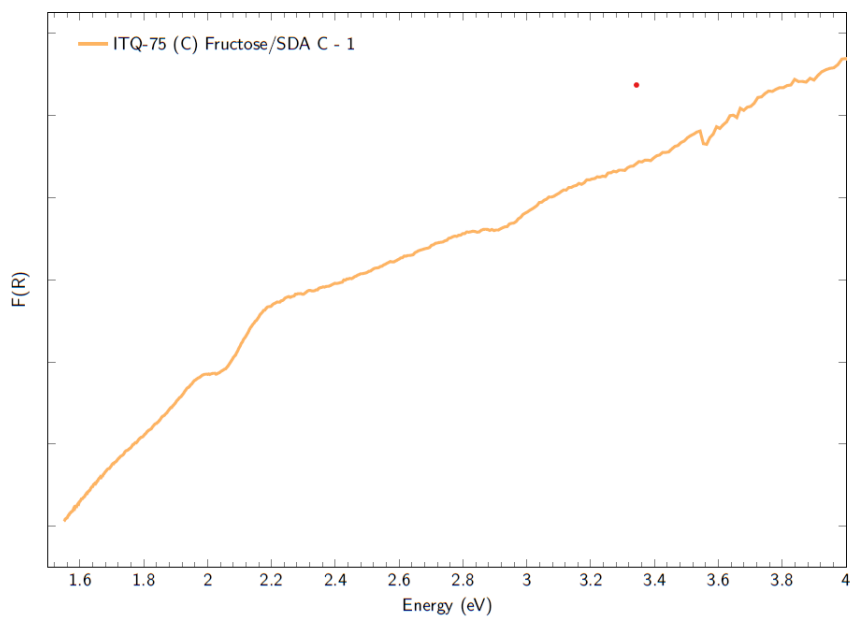
Figure D.59: Kubelka-Monk representation of ITQ-75, obtained with Compound C as SDA, with Fructose/SDA C - 1
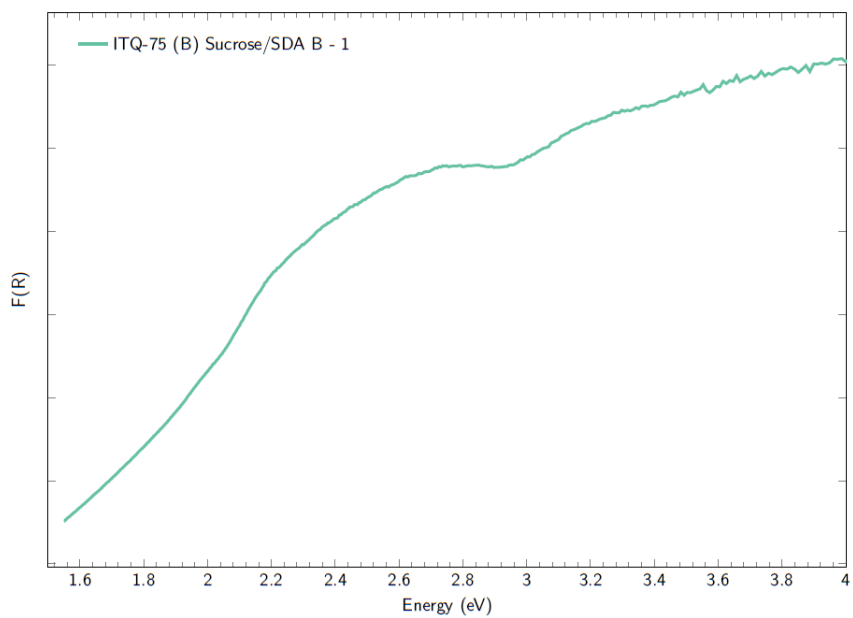
Figure D.60: Kubelka-Monk representation of ITQ-75, obtained with Compound B as SDA, with Sucrose/SDA B - 1
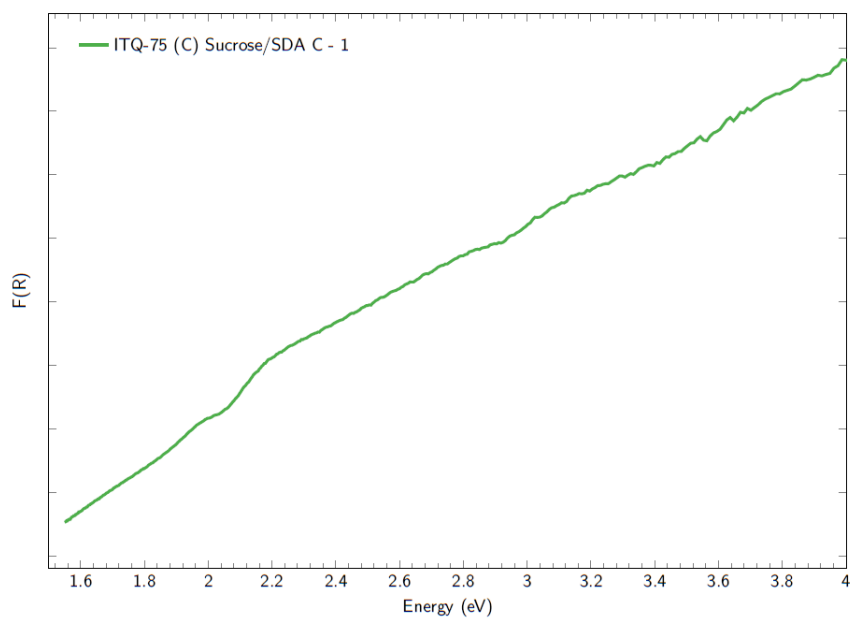
Figure D.61: Kubelka-Monk representation of ITQ-75, obtained with Compound C as SDA, with Sucrose/SDA B - 1

D.3.8 Saccharide and Dopants Presence
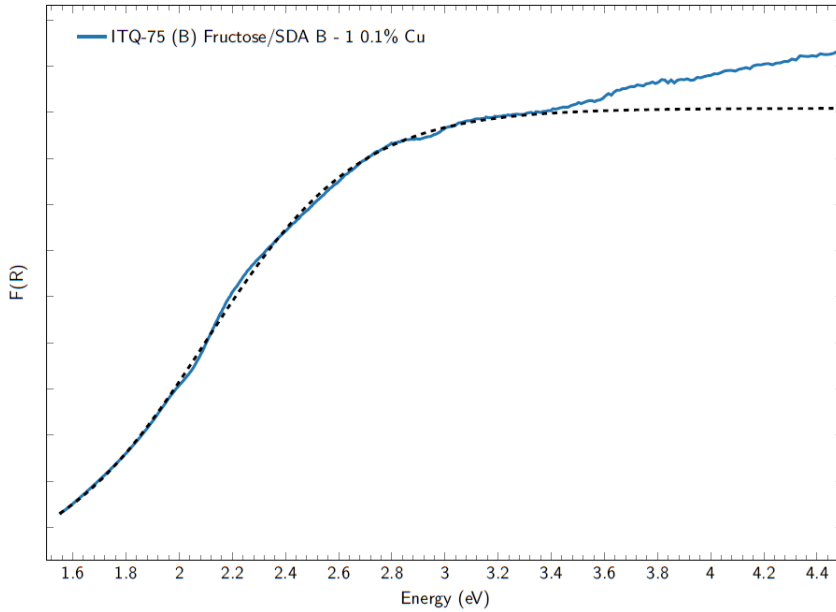
Figure D.62: Kubelka-Monk representation of ITQ-75, obtained with Compound B as SDA, with Fructose/SDA B - 1 and 0,1% Cu (see Equation D.58)

$$\text{F (R)} = 14,86887 + \frac{4,37027 - 14,86887}{1 + \exp\left(\frac{\text{Energy} - 1,94178}{0,180404}\right)} \tag{D.58}$$

Table D.52: Optical band gap, direct and indirect, of ITQ-75 obtained with Compound B as SDA and with Fructose/SDA B - 1 and 0,1% Cu

	Optical band gap (eV)
Direct	2,0
Indirect	0,9
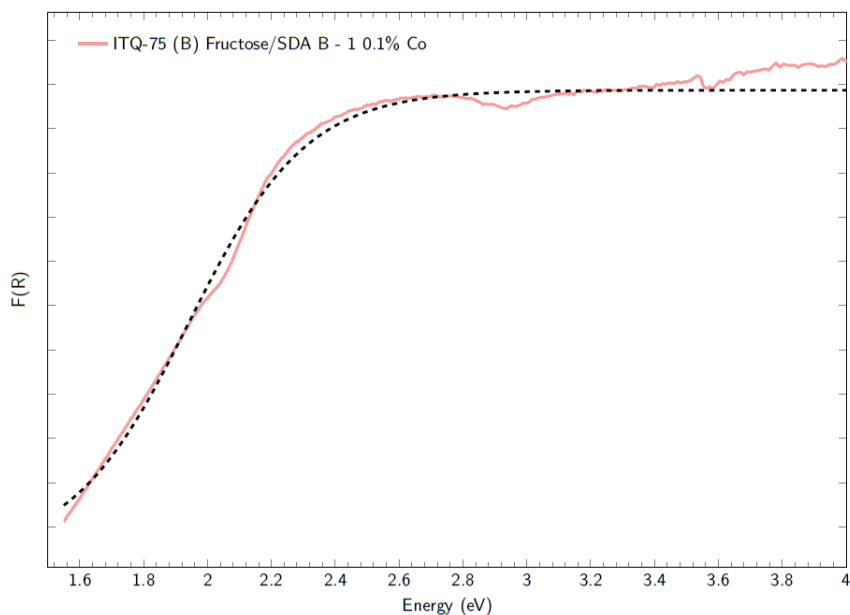
Figure D.63: Kubelka-Monk representation of ITQ-75, obtained with Compound B as SDA, with Fructose/SDA B - 1 and 0,1% Co (see Equation D.59)

$$F\left(R\right) = 11,08466 + \frac{1,04225 - 11,08466}{1 + \exp\left(\frac{\text{Energy} - 2,10395}{0,28523}\right)} \tag{D.59}$$

Table D.53: Optical band gap, direct and indirect, of ITQ-75 obtained with Compound B as SDA and with Fructose/SDA B - 1 and 0,1% Co

	Optical band gap (eV)
Direct	1,9
Indirect	1,2

D.3.9 Gel Viscosity Modification
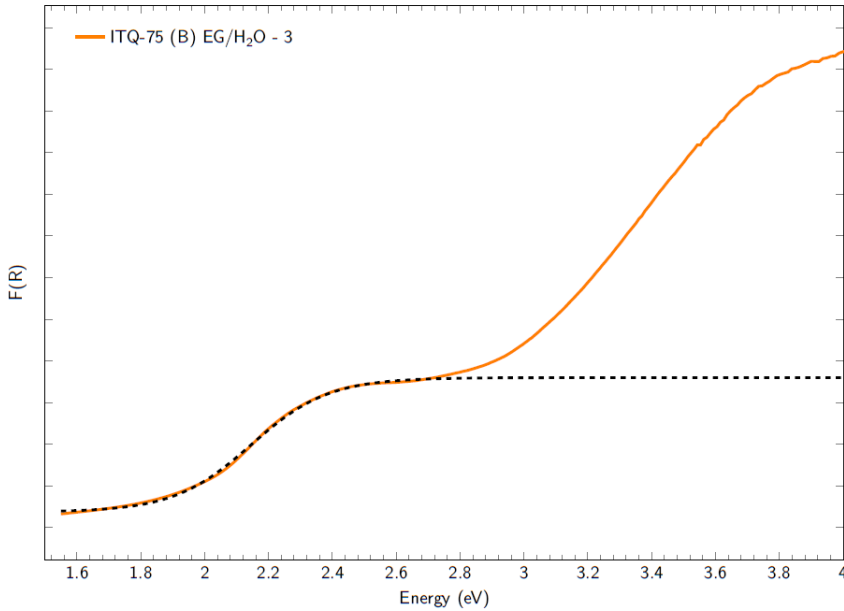
Figure D.64: Kubelka-Monk representation of ITQ-75, obtained with Compound B as SDA, with EG/H$_2$O - 3 (see Equation D.60)

$$F(R) = 3,59944 + \frac{0,375 - 3,59944}{1 + \exp\left(\frac{\text{Energy} - 2,14551}{0,12113}\right)} \tag{D.60}$$

Table D.54: Optical band gap, direct and indirect, of ITQ-75 obtained with Compound B as SDA and with EG/H$_2$O - 3

	Optical band gap (eV)
Direct	2,1
Indirect	1,6

D.3.10 Saccharide Presence and Gel Viscosity Modification
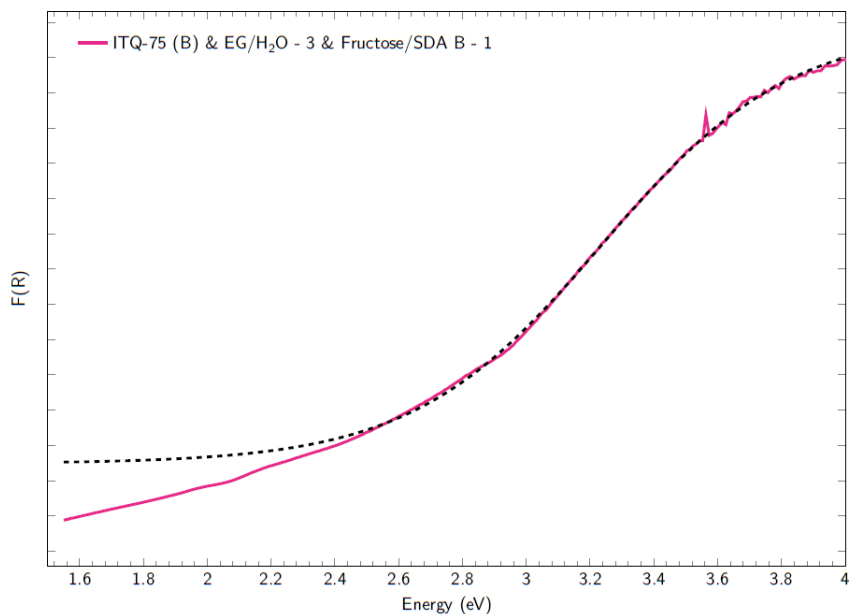
Figure D.65: Kubelka-Monk representation of ITQ-75, obtained with Compound B as SDA, with EG/H$_2$O - 3 and a Fructose/SDA B - 3 (see Equation D.61)

$$F\left(R\right) = 6,96961 + \frac{6,96961 - 31,74717}{1 + \exp\left(\frac{\text{Energy} - 3,2357}{0,2963}\right)} \tag{D.61}$$

Table D.55: Optical band gap, direct and indirect, of ITQ-75 obtained with Compound B as SDA, with EG/H$_2$O - 3 and a Fructose/SDA B - 3

	Optical band gap (eV)
Direct	3,1
Indirect	2,0

Appendix E

Thermogravimetry

E.1 IZM-5 & ITQ-76

E.1.1 Undopped

Figure E.1: TG and DTG of IZM-5

E.1.2 Saccharide as coSDA
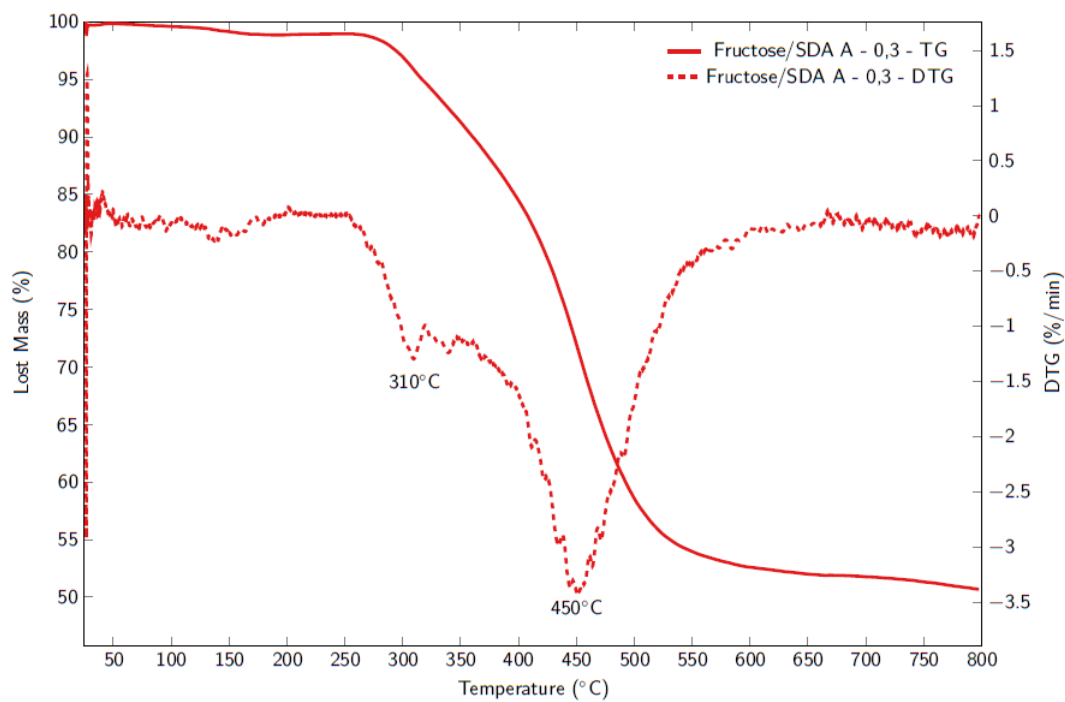
Figure E.2: TG and DTG of IZM-5 with a Fructose/SDA A molar ratio equal to 0,3
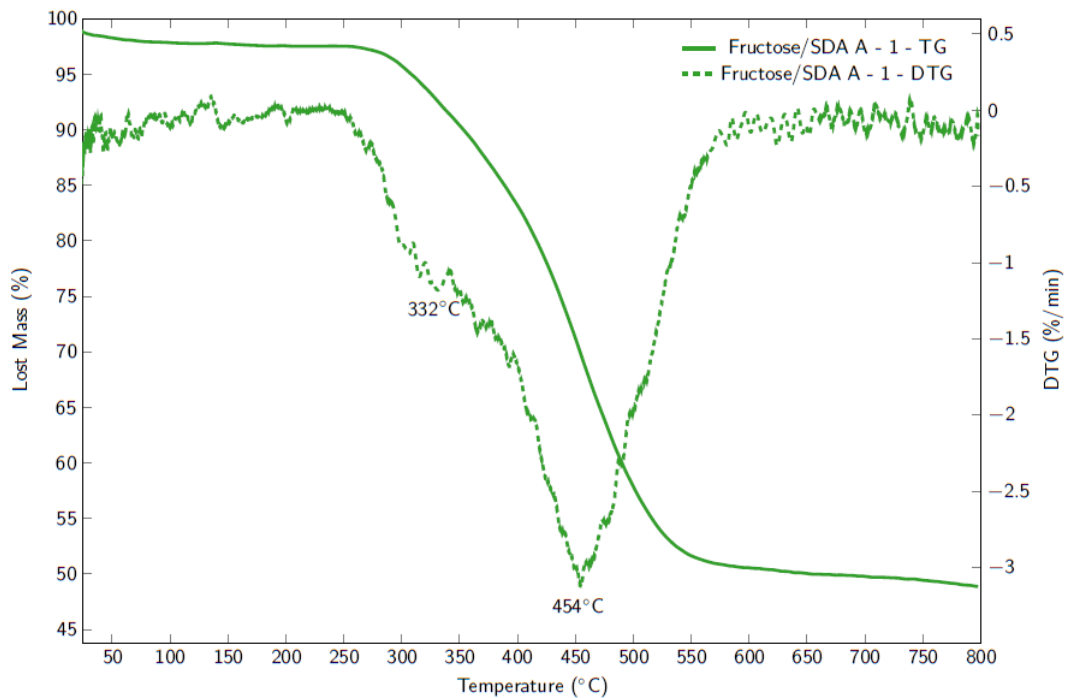
Figure E.3: TG and DTG of ITQ-76 with a Fructose/SDA A molar ratio equal to 1
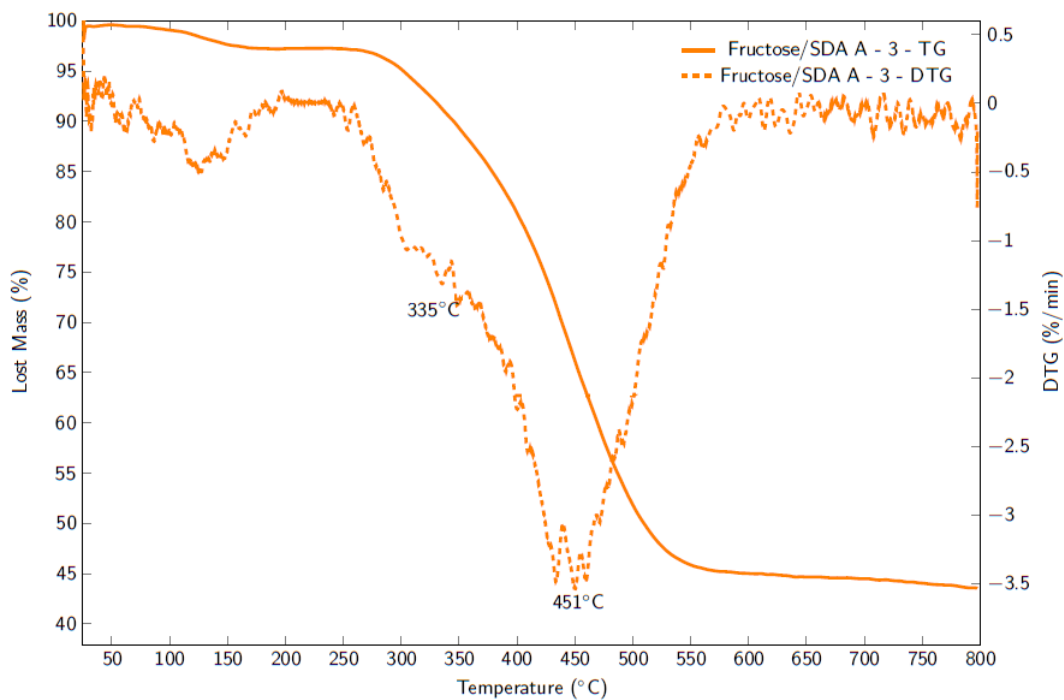
Figure E.4: TG and DTG of ITQ-76 with a Fructose/SDA A molar ratio equal to 3
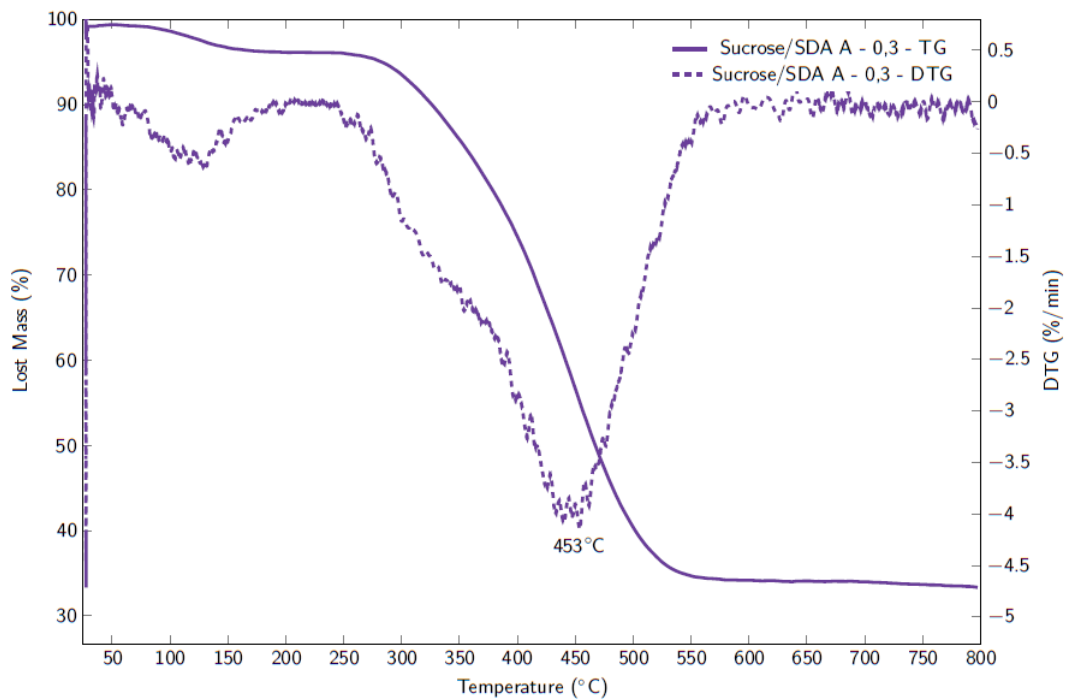
Figure E.5: TG and DTG of ITQ-76 with a Sucrose/SDA A molar ratio equal to 0,3
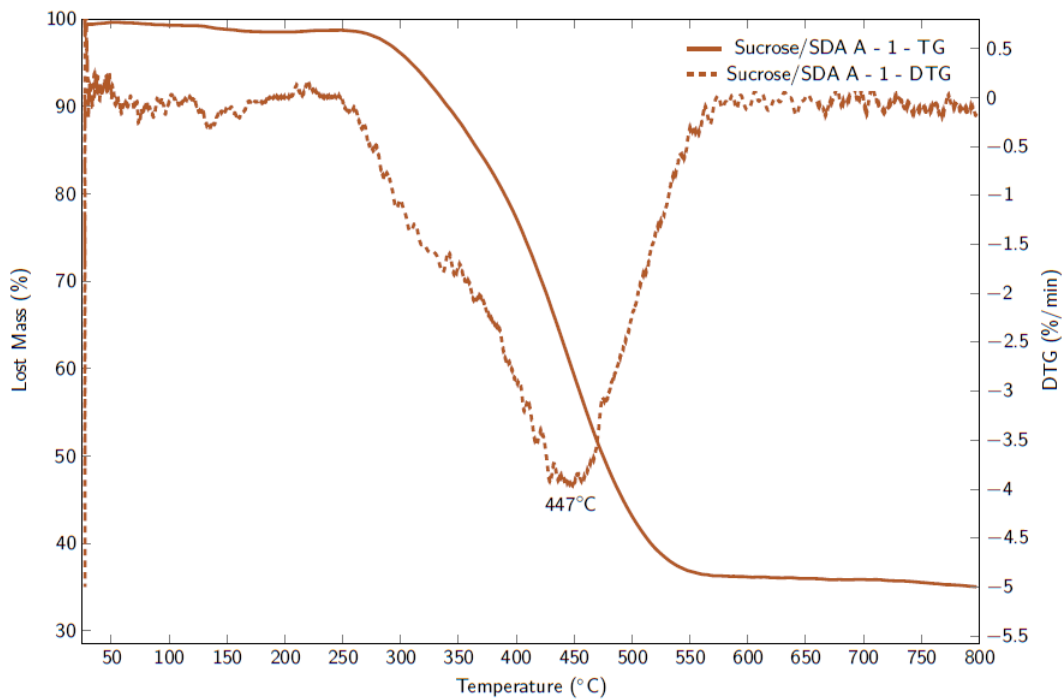
Figure E.6: TG and DTG of ITQ-76 with a Sucrose/SDA A molar ratio equal to 1

Figure E.7: TG and DTG of ITQ-76 with a Sucrose/SDA A molar ratio equal to 3

E.2 ITQ-75

E.2.1 Undopped
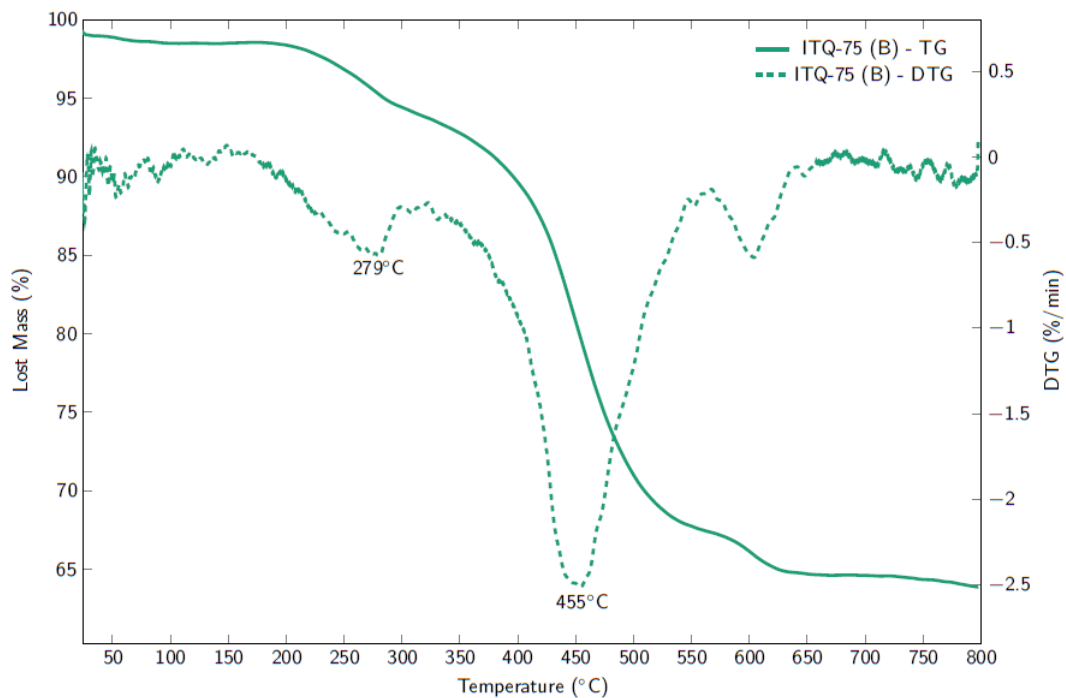
Figure E.8: TG and DTG of ITQ-75 obtained with Compound B as SDA
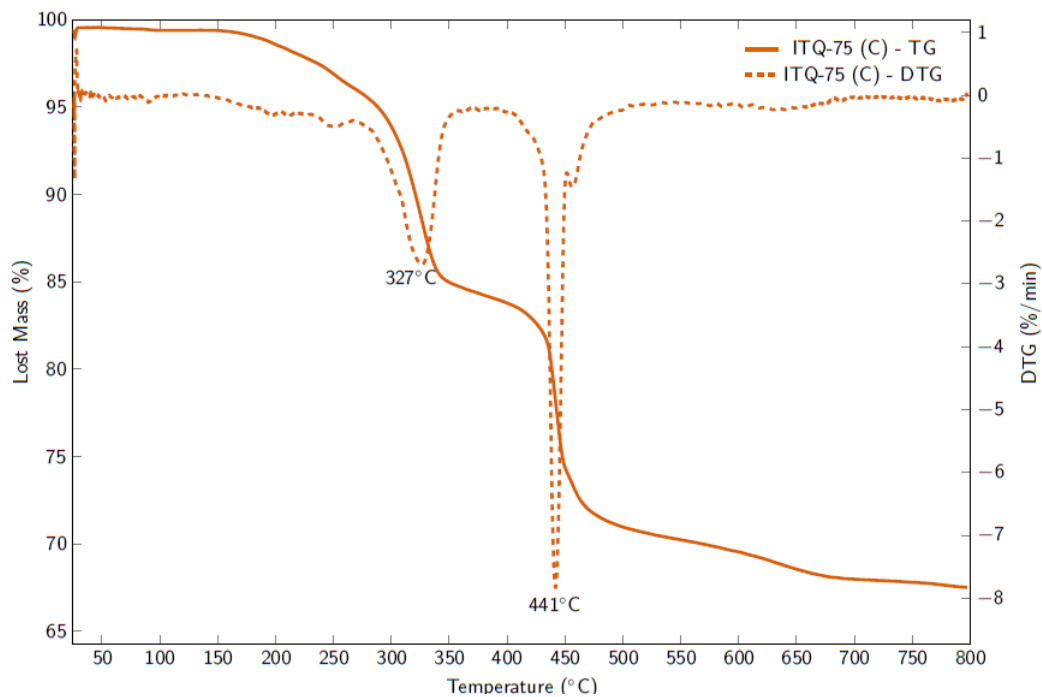
Figure E.9: TG and DTG of ITQ-75 obtained with Compound C as SDA
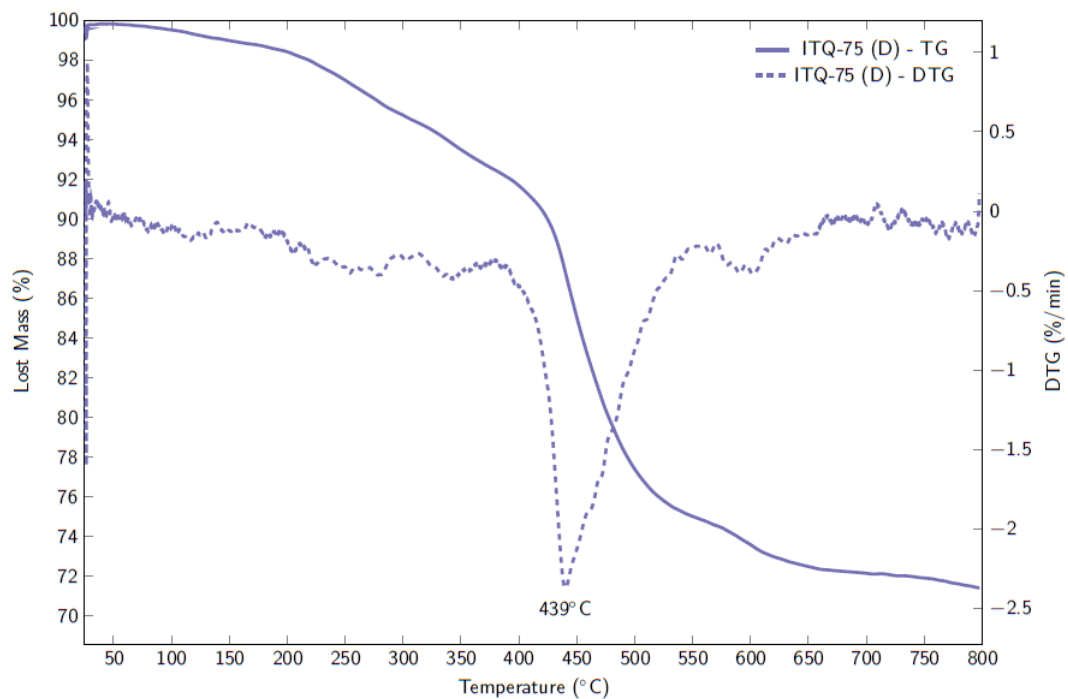
Figure E.10: TG and DTG of ITQ-75 obtained with Compound D as SDA
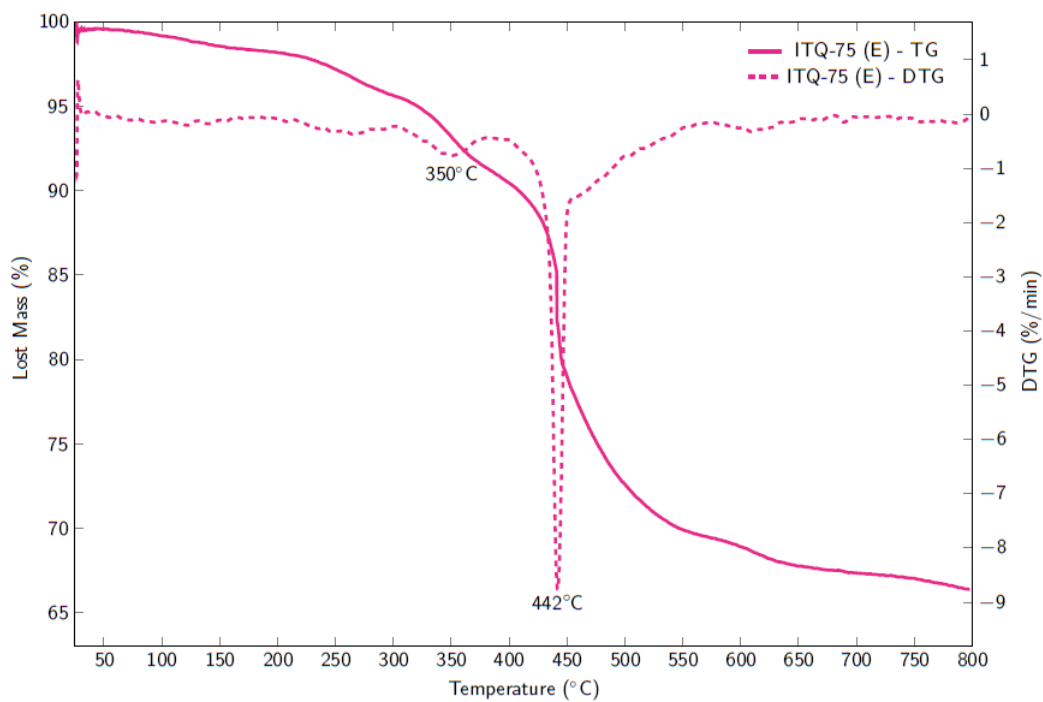
Figure E.11: TG and DTG of ITQ-75 obtained with Compound E as SDA

E.2.2   Saccharide as coSDA

E.2.2.1   SDA B as SDA
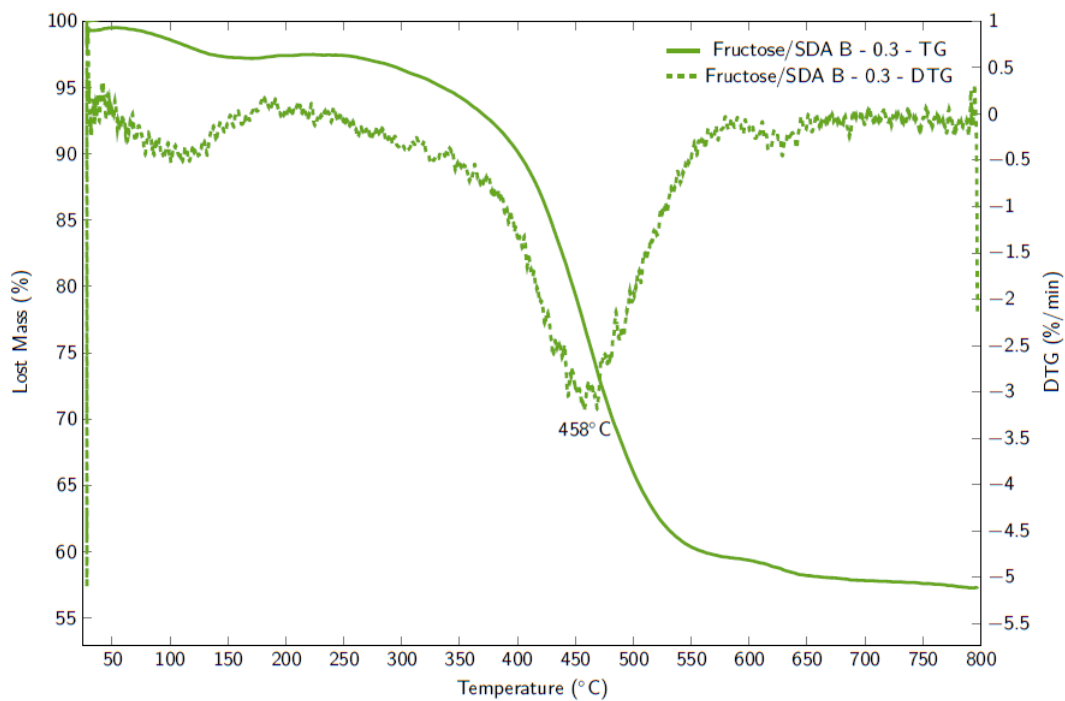
Figure E.12: TG and DTG of ITQ-75 with a Fructose/SDA B molar ratio equal to 0,3
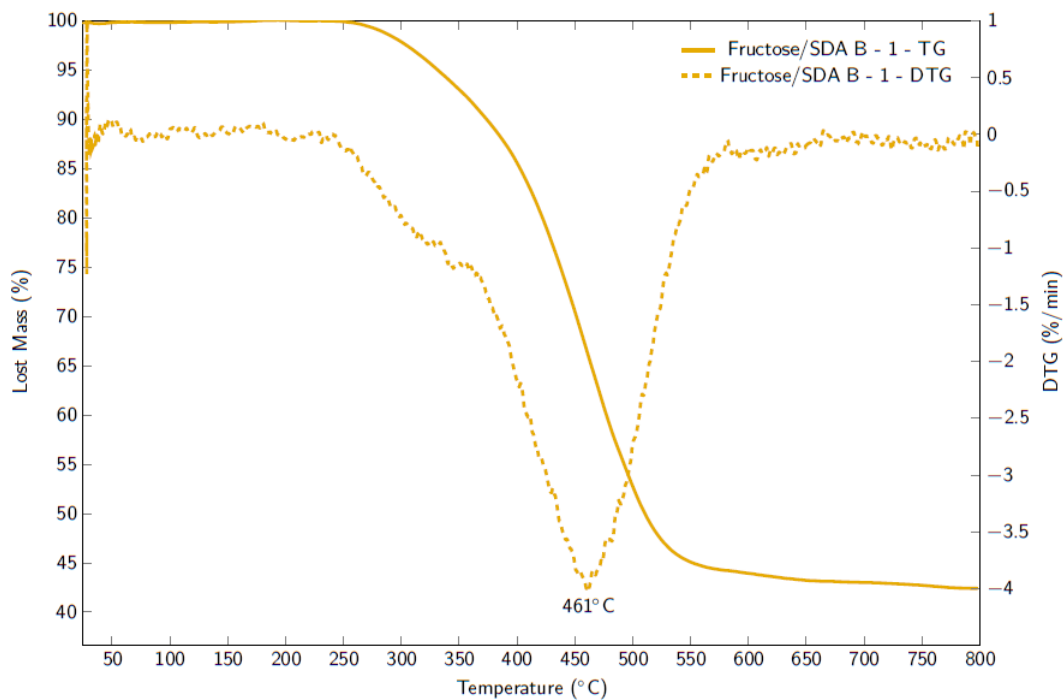
Figure E.13: TG and DTG of ITQ-75 with a Fructose/SDA B molar ratio equal to 1
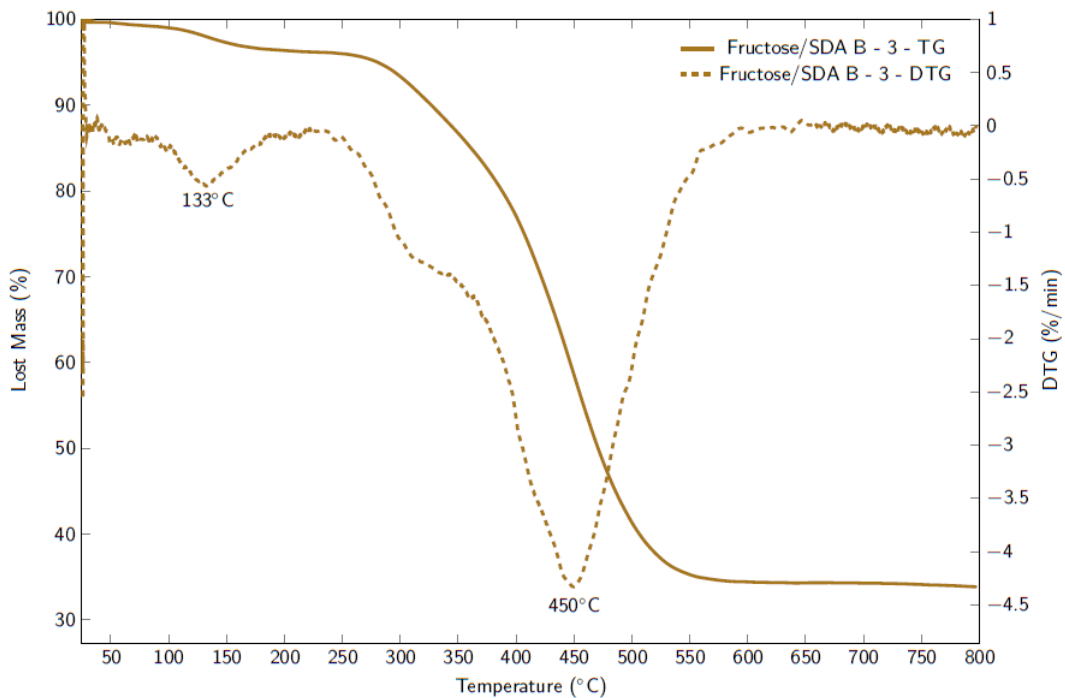
Figure E.14: TG and DTG of ITQ-75 with a Fructose/SDA B molar ratio equal to 3
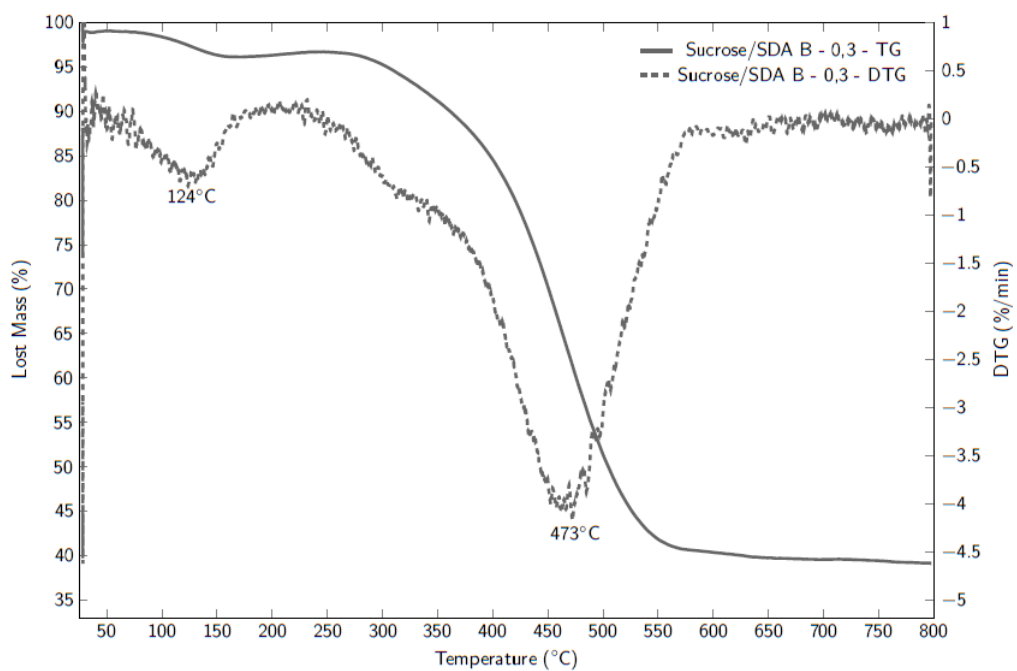
Figure E.15: TG and DTG of ITQ-75 with a Sucrose/SDA B molar ratio equal to 0,3
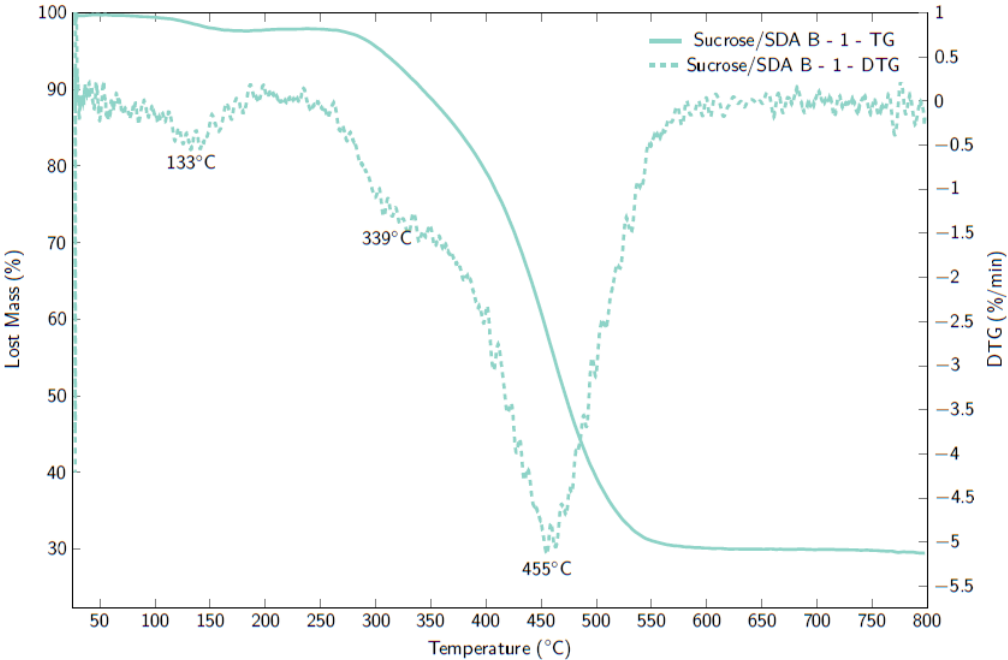
Figure E.16: TG and DTG of ITQ-75 with a Sucrose/SDA B molar ratio equal to 1
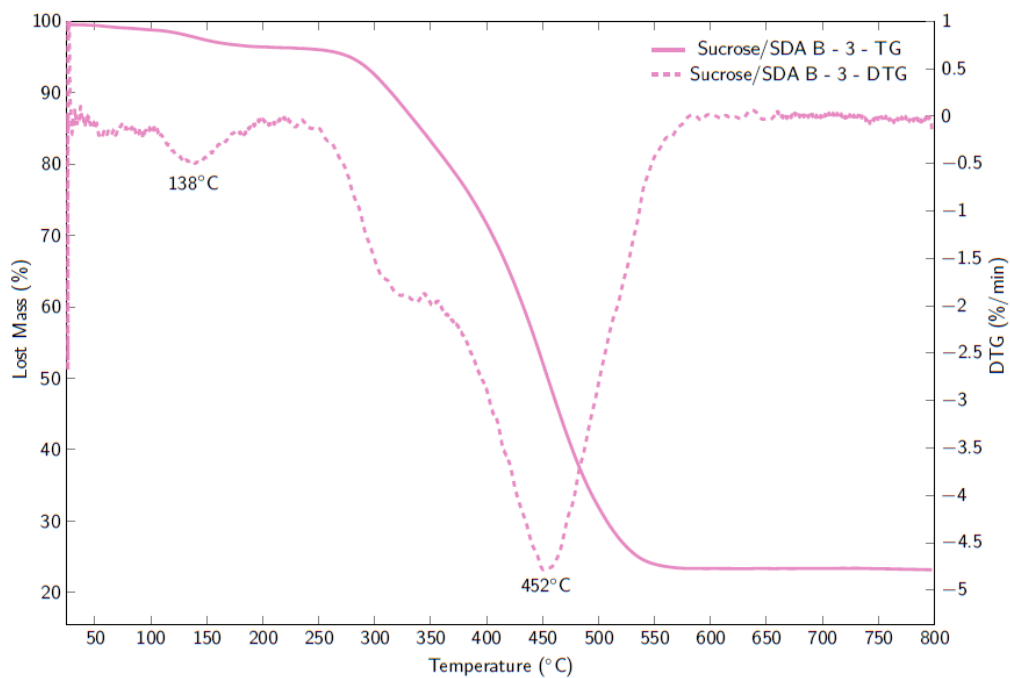
Figure E.17: TG and DTG of ITQ-75 with a Sucrose/SDA B molar ratio equal to 3

E.2.2.2   SDA C as SDA
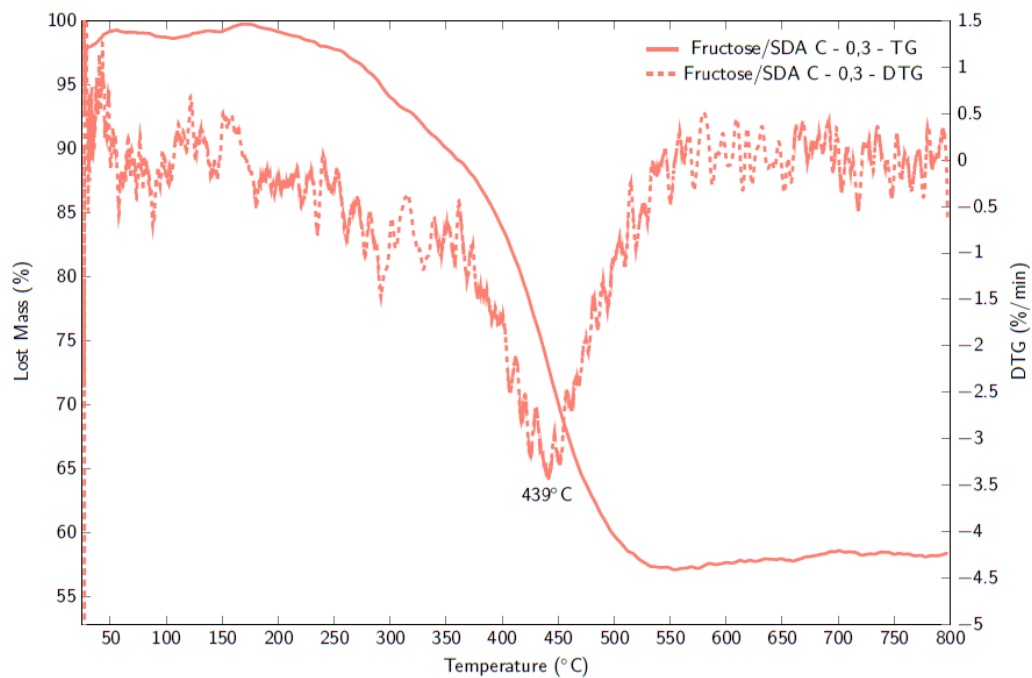
Figure E.18: TG and DTG of ITQ-75 with a Fructose/SDA C molar ratio equal to 0,3
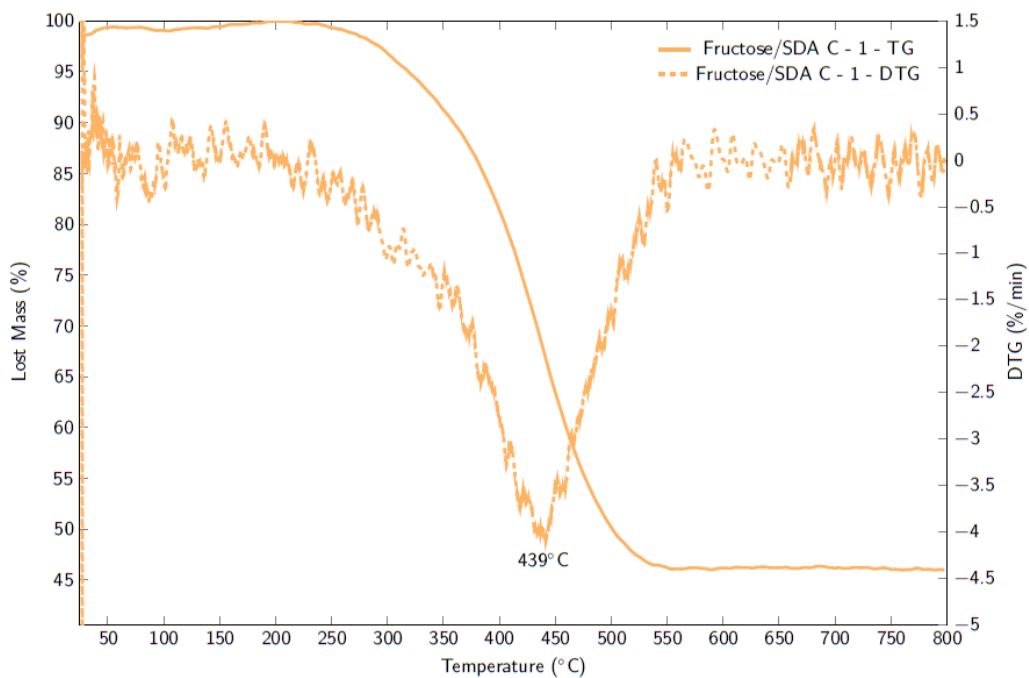
Figure E.19: TG and DTG of ITQ-75 with a Fructose/SDA C molar ratio equal to 1
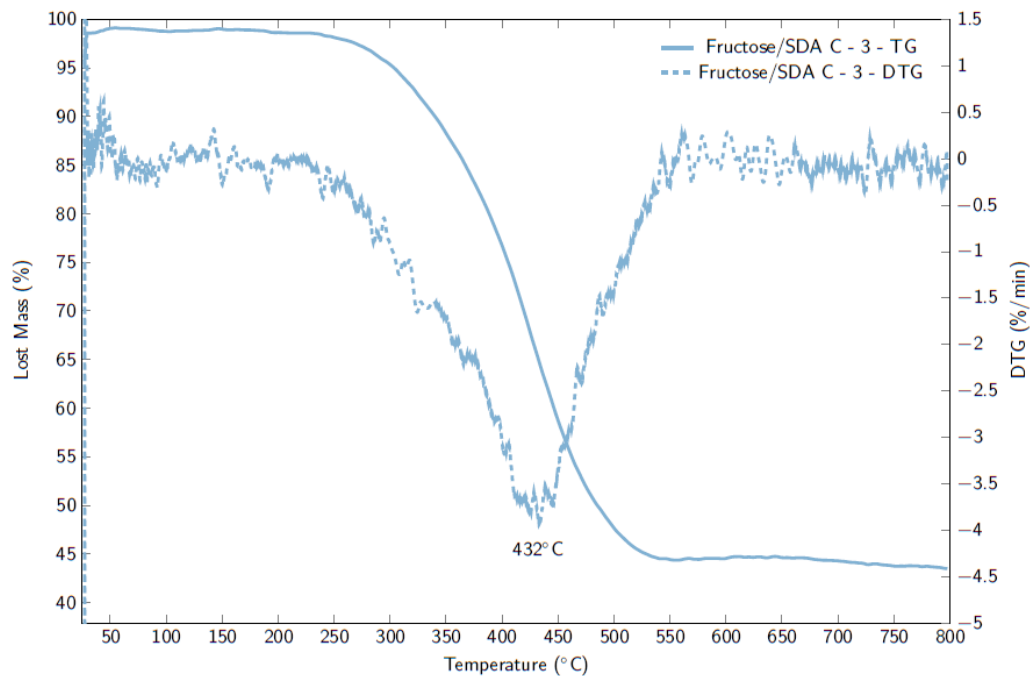
Figure E.20: TG and DTG of ITQ-75 with a Fructose/SDA C molar ratio equal to 3
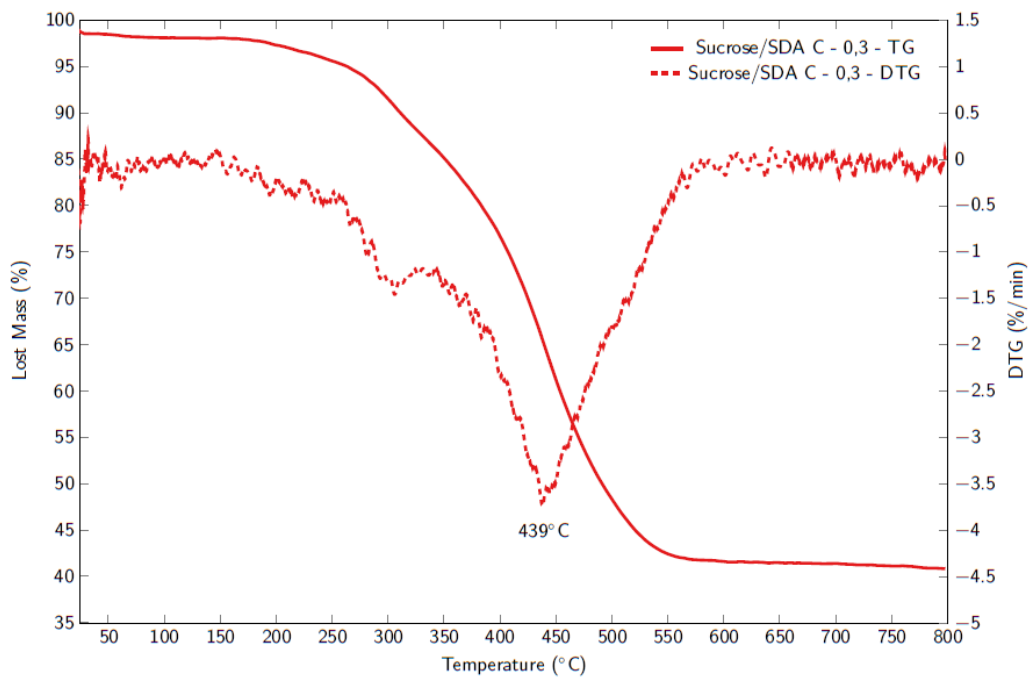
Figure E.21: TG and DTG of ITQ-75 with a Sucrose/SDA C molar ratio equal to 0,3
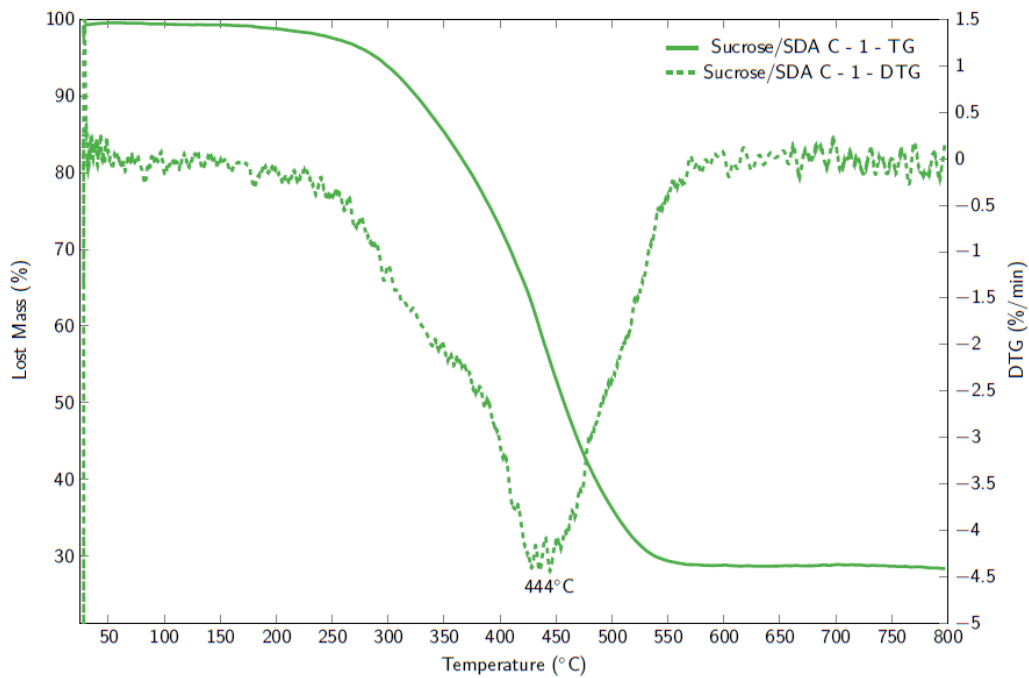
Figure E.22: TG and DTG of ITQ-75 with a Sucrose/SDA C molar ratio equal to 1
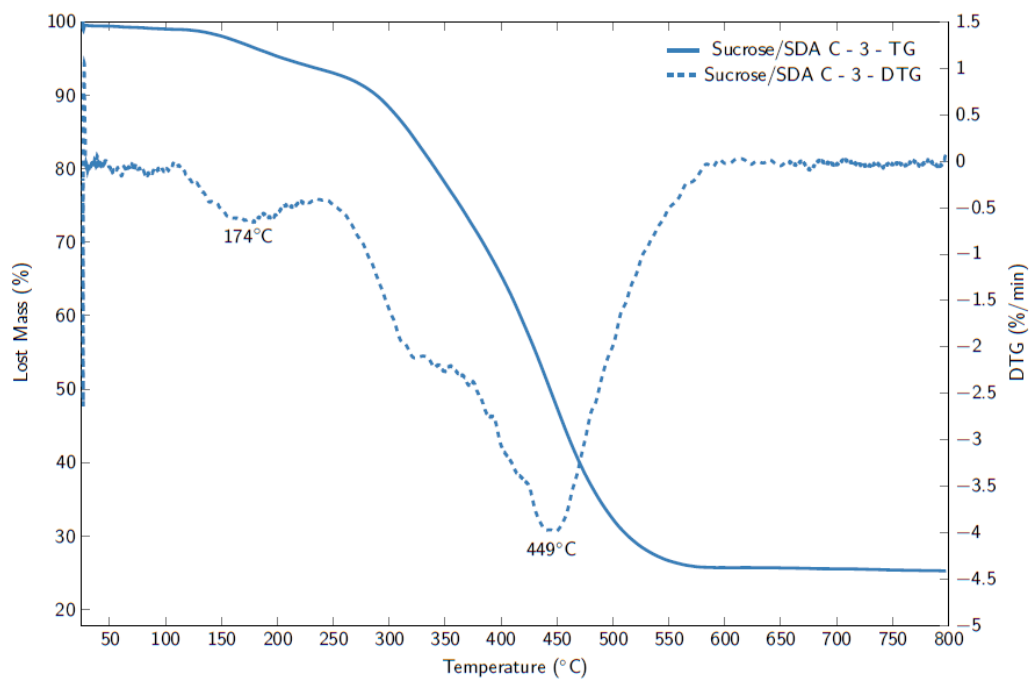
Figure E.23: TG and DTG of ITQ-75 with a Sucrose/SDA C molar ratio equal to 3

Appendix F

FESEM Images and Crystal Size Determination

F.1 ITQ-75

F.1.1 Unmodified

(a)

(b)

(c)

(d)
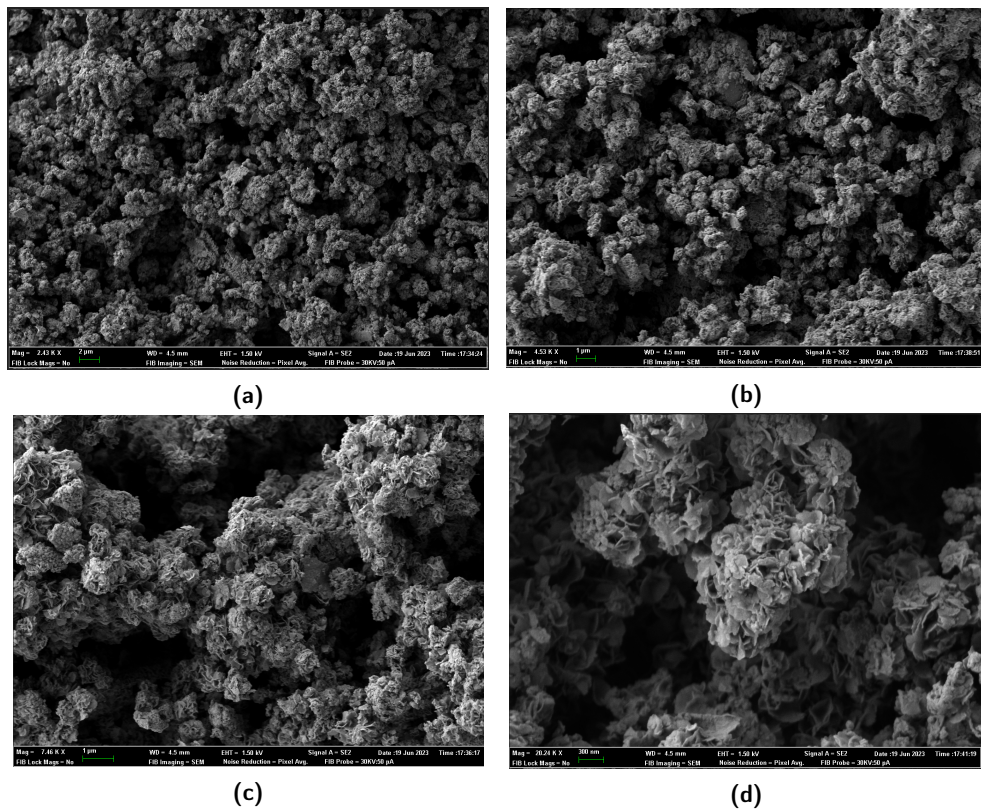
Figure F.1: ITQ-75 FESEM images, obtained with Compound B as SDA
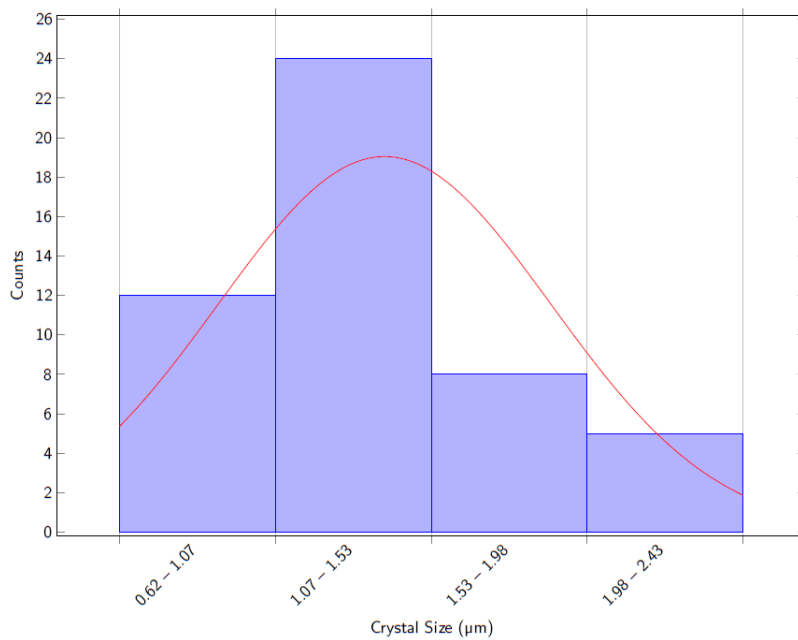
Figure F.2: Crystal Size Distribution of ITQ-75 obtained with Compound B as SDA

457
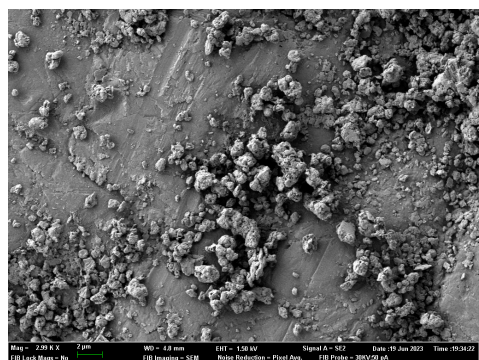
(a)
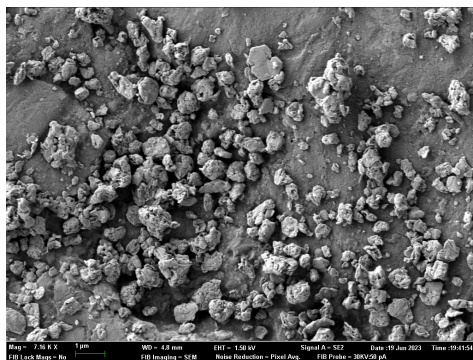
(b)
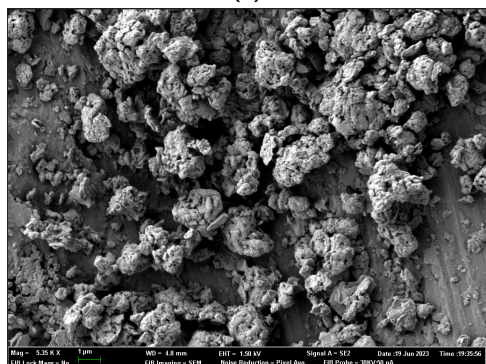
(c)
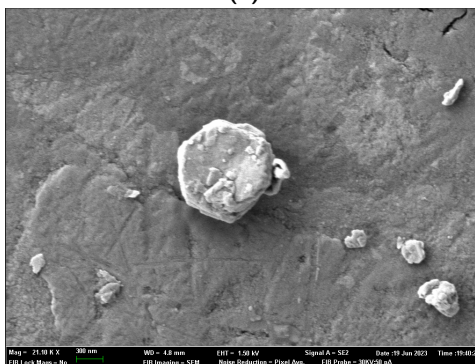
(d)

Figure F.3: ITQ-75 FESEM images, obtained with Compound C as SDA
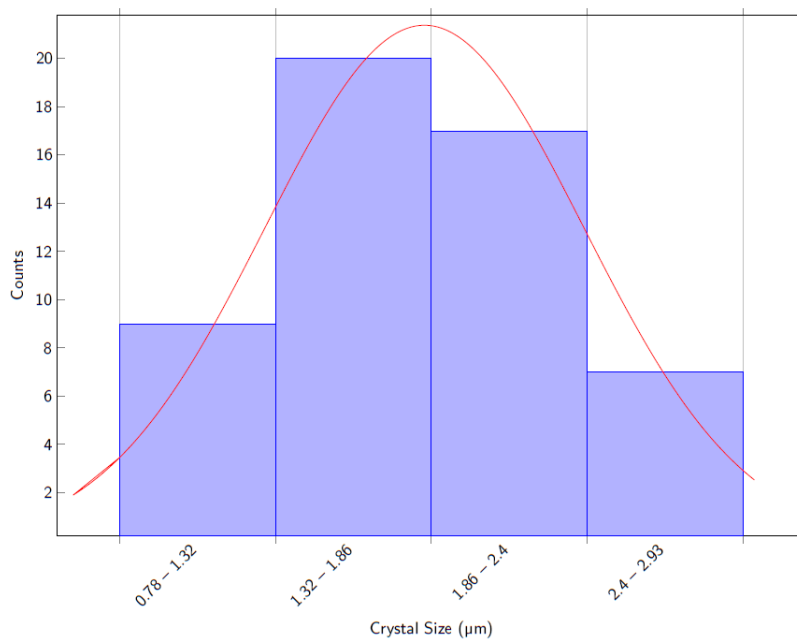
Figure F.4: Crystal Size Distribution of ITQ-75 obtained with Compound C as SDA

(a)

(b)

(c)

(d)
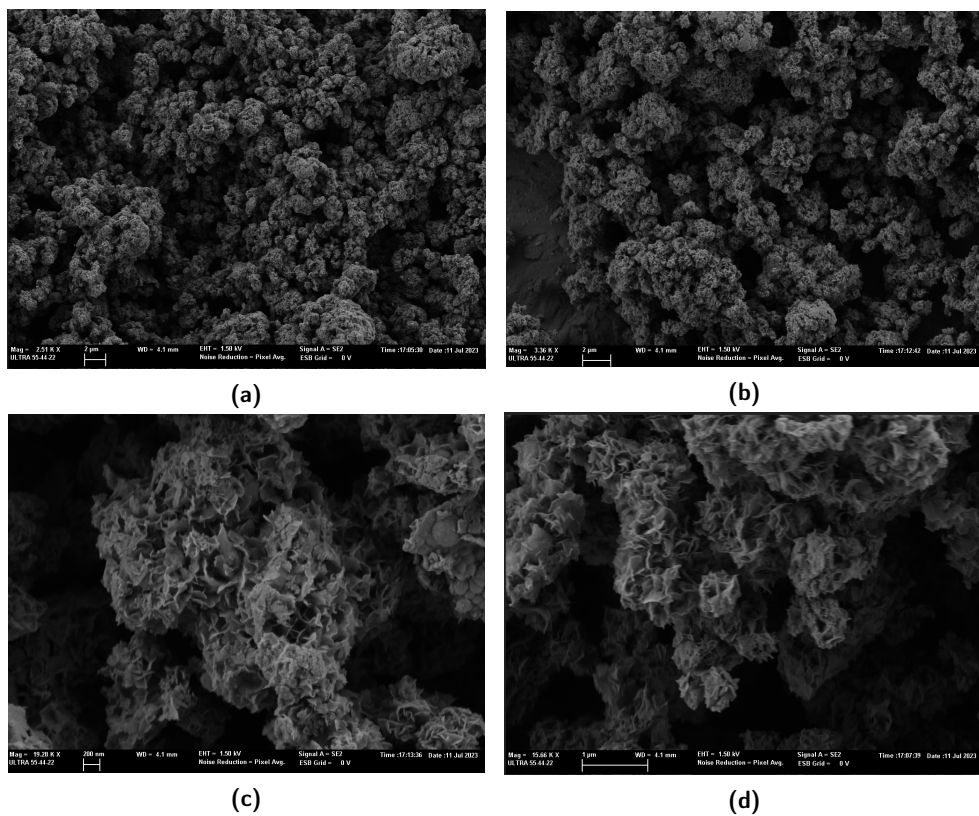
Figure F.5: ITQ-75 FESEM images, obtained with Compound D as SDA
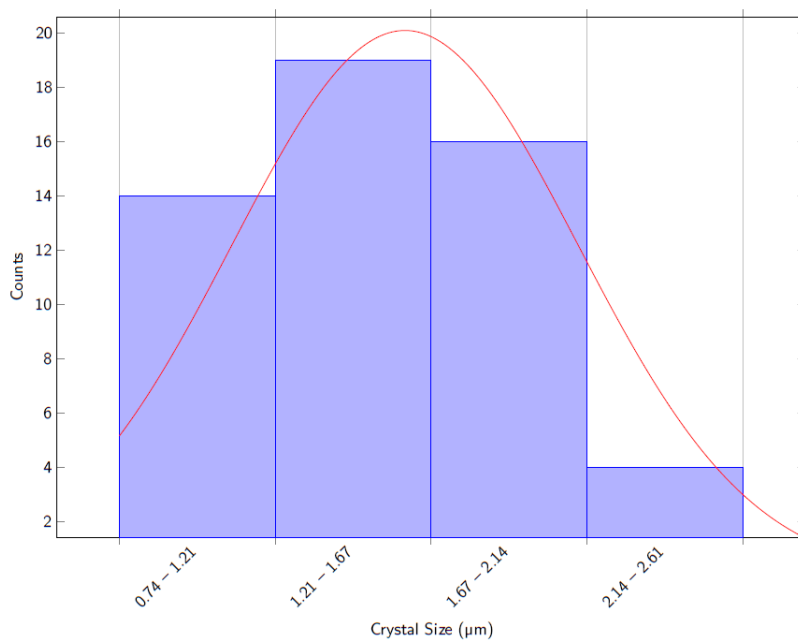
Figure F.6: Crystal Size Distribution of ITQ-75 obtained with Compound D as SDA

(a)

(b)

(c)

(d)
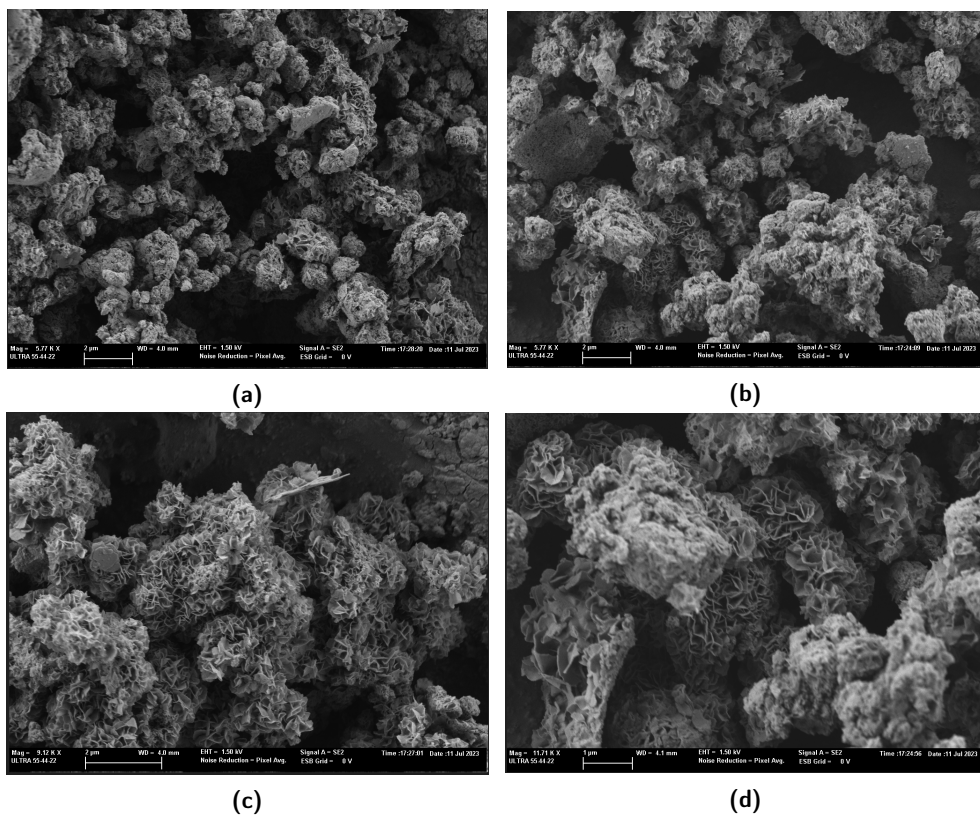
Figure F.7: ITQ-75 FESEM images, obtained with Compound E as SDA
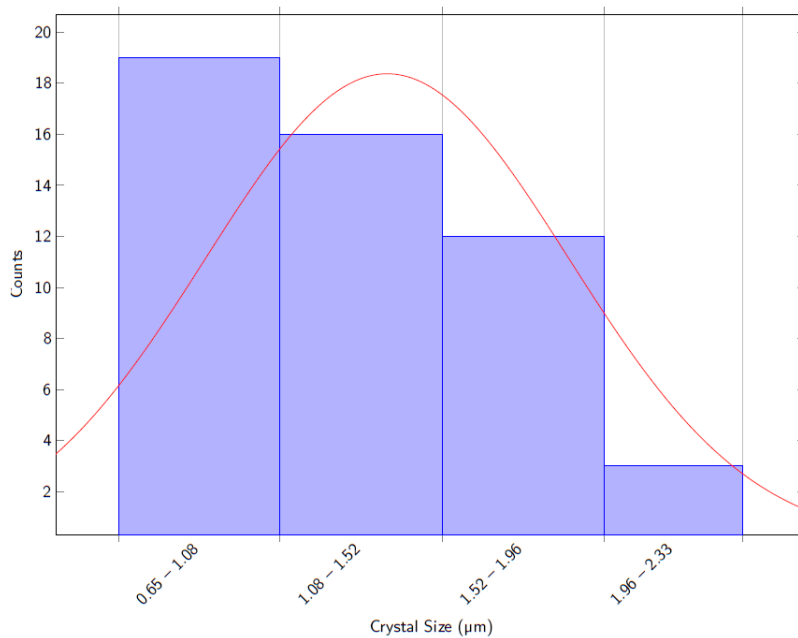
Figure F.8: Crystal Size Distribution of ITQ-75 obtained with Compound E as SDA

F.1.2   Accessibility Modified Samples

(a)

(b)

(c)

(d)
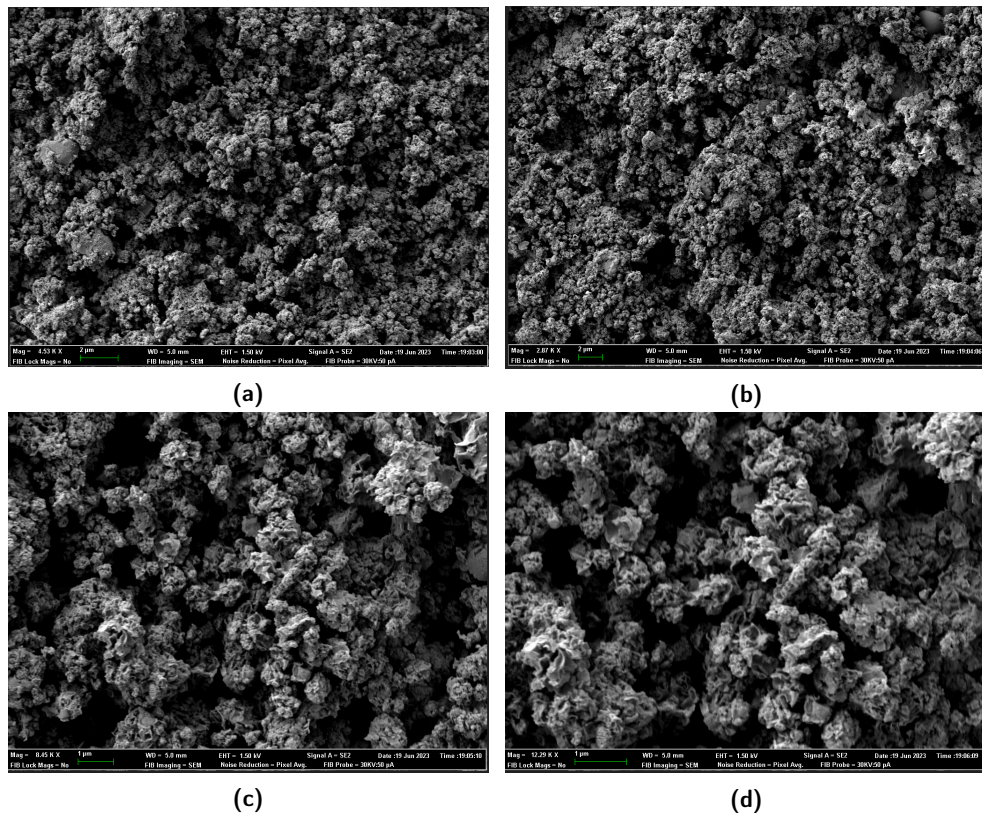
Figure F.9: ITQ-75 FESEM images, obtained with Compound B as SDA, with a EG/H$_2$O molar ratio equal to 3
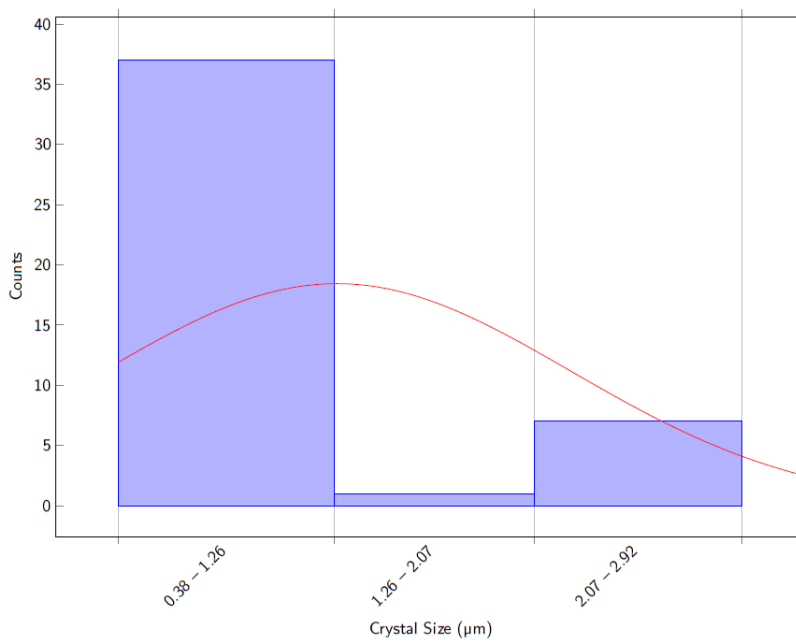
Figure F.10: Crystal Size Distribution of ITQ-75 obtained with Compound B as SDA and with a EG/H$_2$O molar ratio equal to 3

(a)

(b)

(c)

(d)
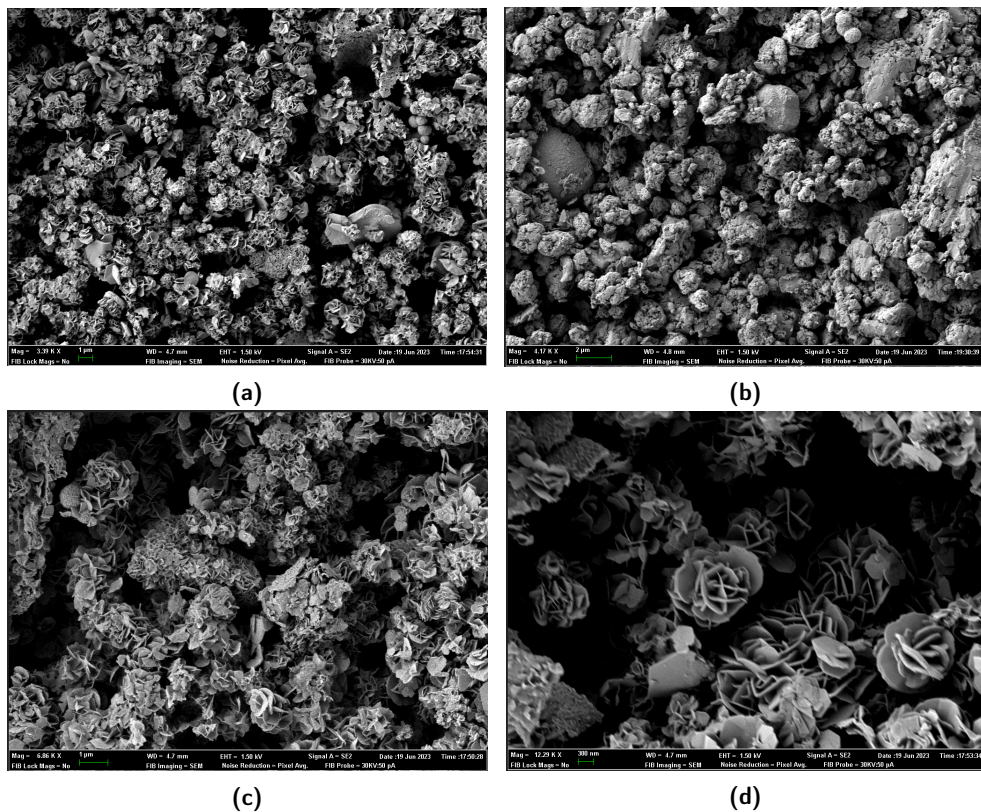
Figure F.11: ITQ-75 FESEM images, obtained with Compound B as SDA, with a Fructose/SDA B molar ratio equal to 1
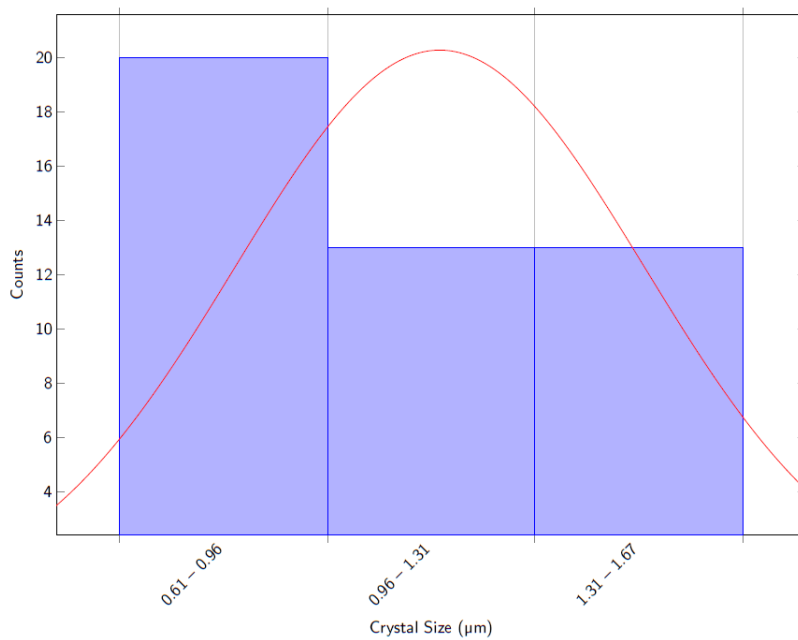
Figure F.12: Crystal Size Distribution of ITQ-75 obtained with Compound B as SDA and with a Fructose/SDA B molar ratio equal to 1

467

(a)

(b)

(c)

(d)
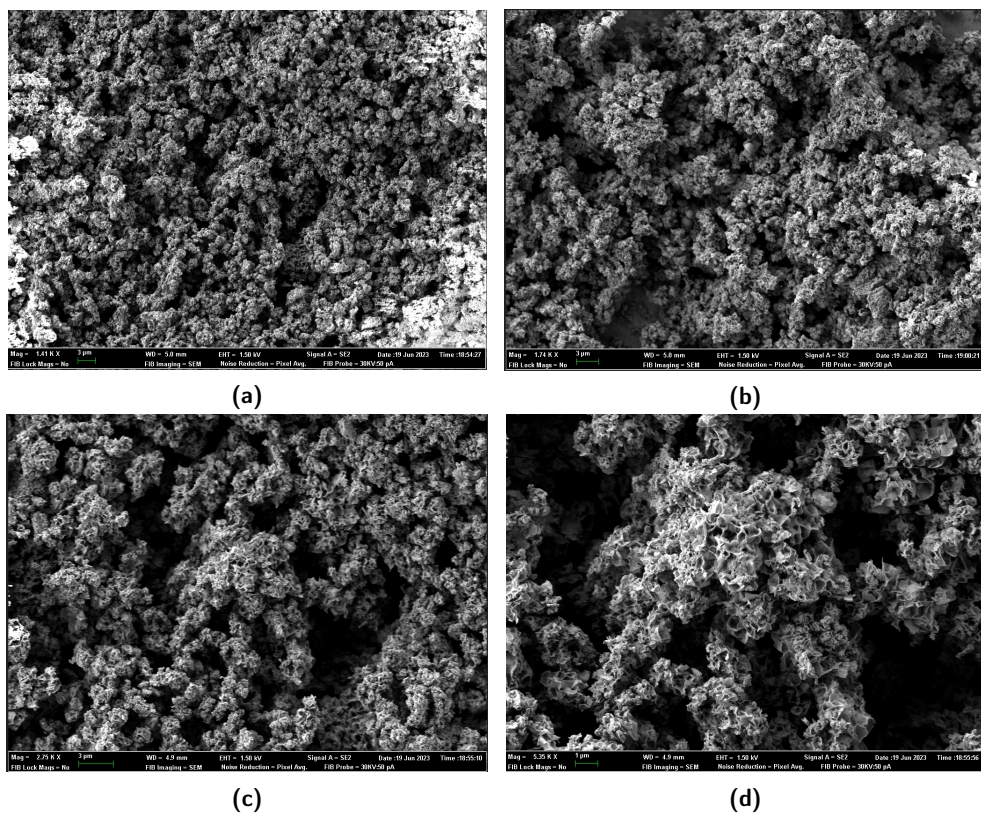
Figure F.13: ITQ-75 FESEM images, obtained with Compound B as SDA, with a Fructose/SDA B molar ratio equal to 1 and a EG/H$_2$O molar ratio equal to 3
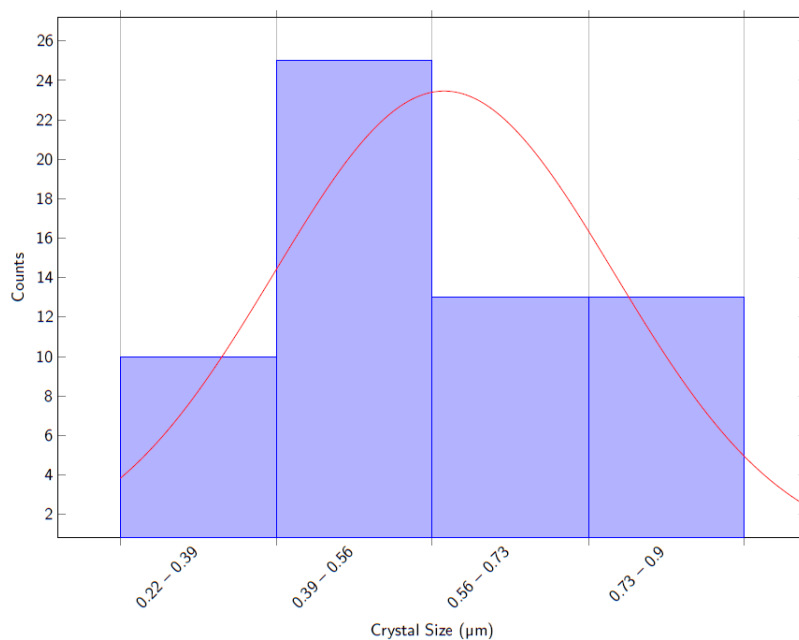
Figure F.14: Crystal Size Distribution of ITQ-75 obtained with Compound B as SDA and with a Fructose/SDA B molar ratio equal to 1 and a EG/H$_2$O molar ratio equal to 3

(a) **(b)**
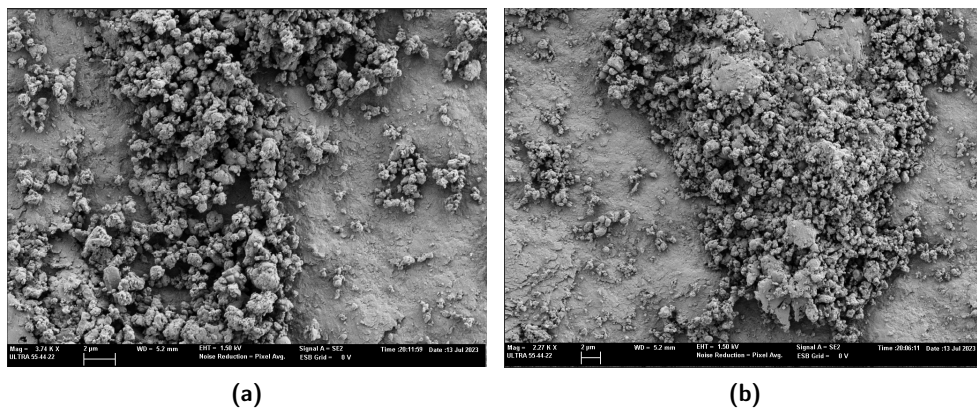
Figure F.15: ITQ-75 FESEM images, obtained with Compound B as SDA, with a Sucrose/SDA B molar ratio equal to 1
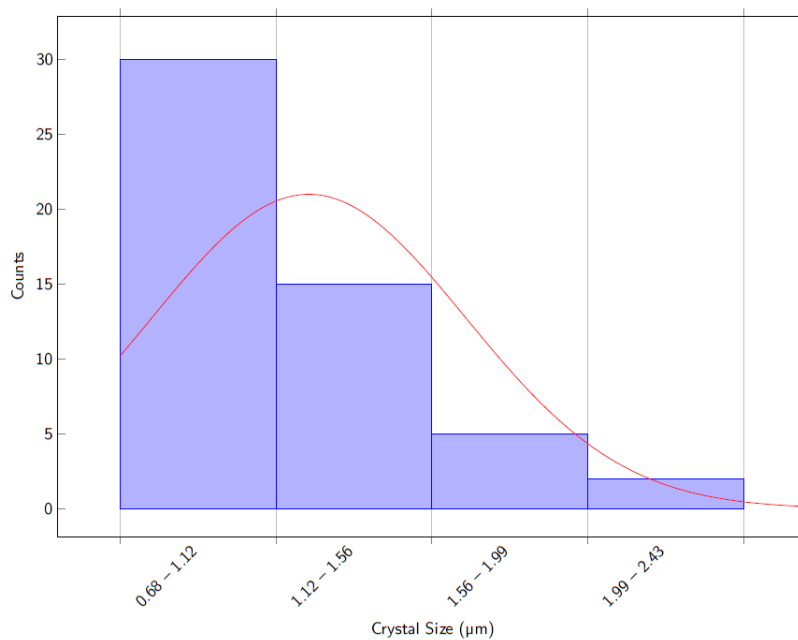
Figure F.16: Crystal Size Distribution of ITQ-75 obtained with Compound B as SDA and with a Sucrose/SDA B molar ratio equal to 1
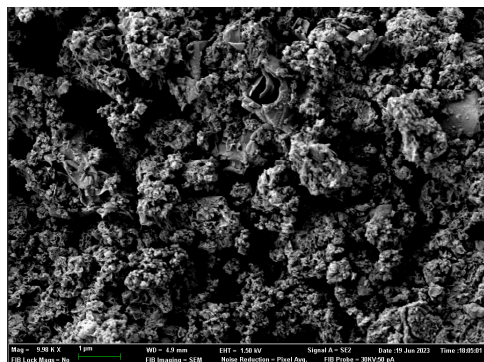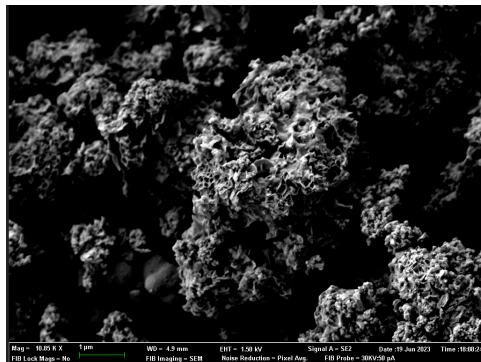
(a)   **(b)**

Figure F.17: ITQ-75 FESEM images, obtained with Compound C as SDA, with a Fructose/SDA C molar ratio equal to 1
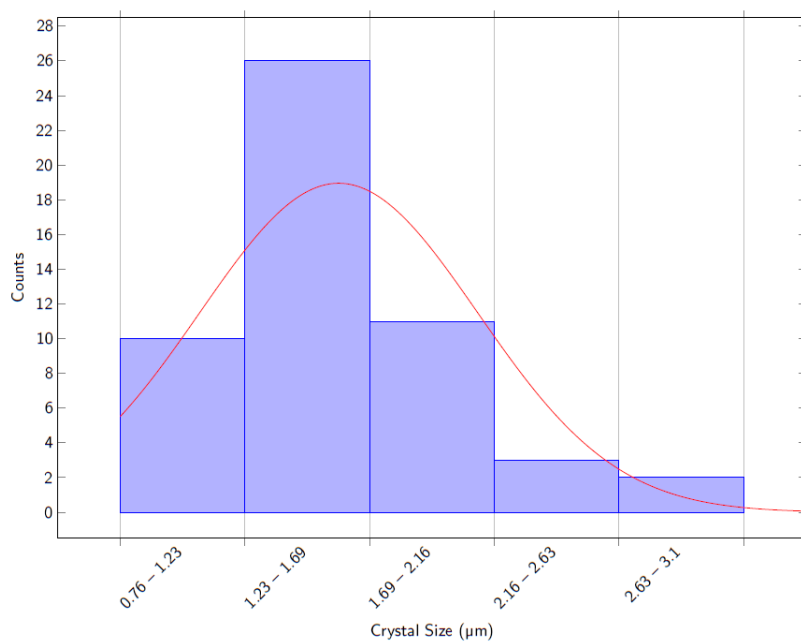
Figure F.18: Crystal Size Distribution of ITQ-75 obtained with Compound C as SDA and with a Fructose/SDA C molar ratio equal to 1

(a)   **(b)**
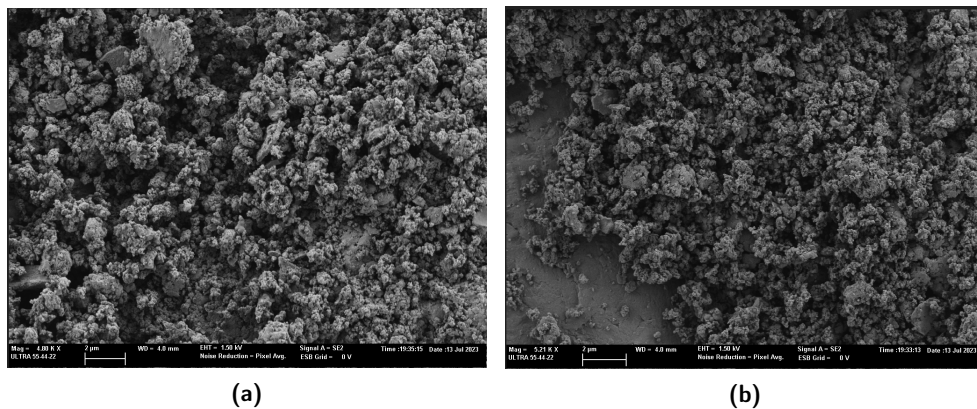
Figure F.19: ITQ-75 FESEM images, obtained with Compound C as SDA, with a Sucrose/SDA C molar ratio equal to 1
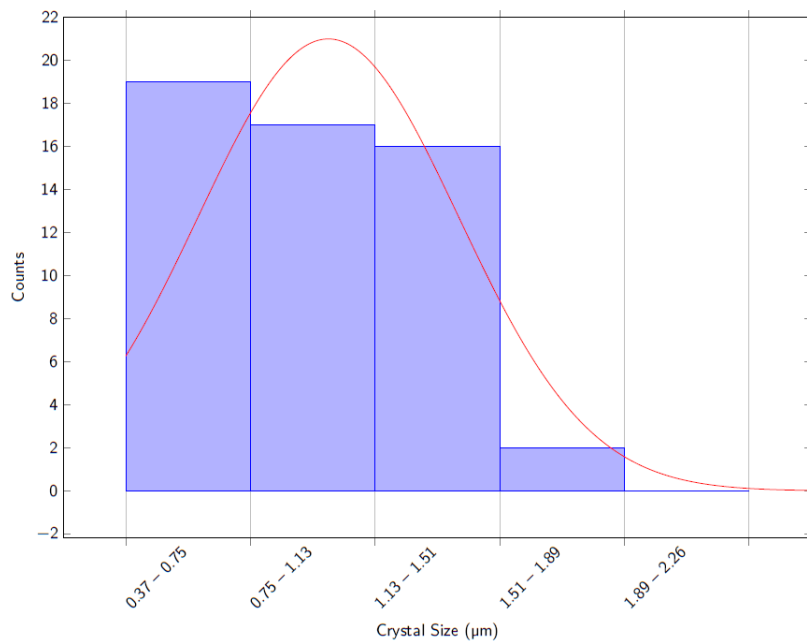
Figure F.20: Crystal Size Distribution of ITQ-75 obtained with Compound C as SDA and with a Sucrose/SDA C molar ratio equal to 1

| (a) | (b) |
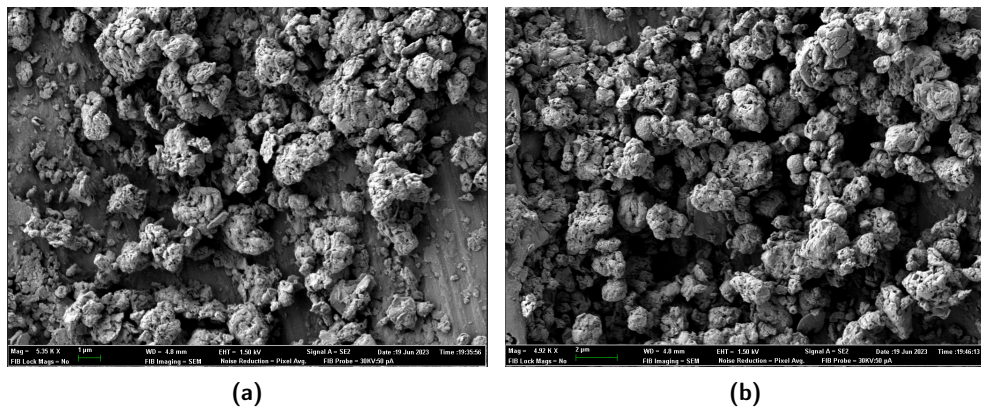
Figure F.21: ITQ-75 FESEM images, obtained with Compound C as SDA, after Ball Mill post treatment
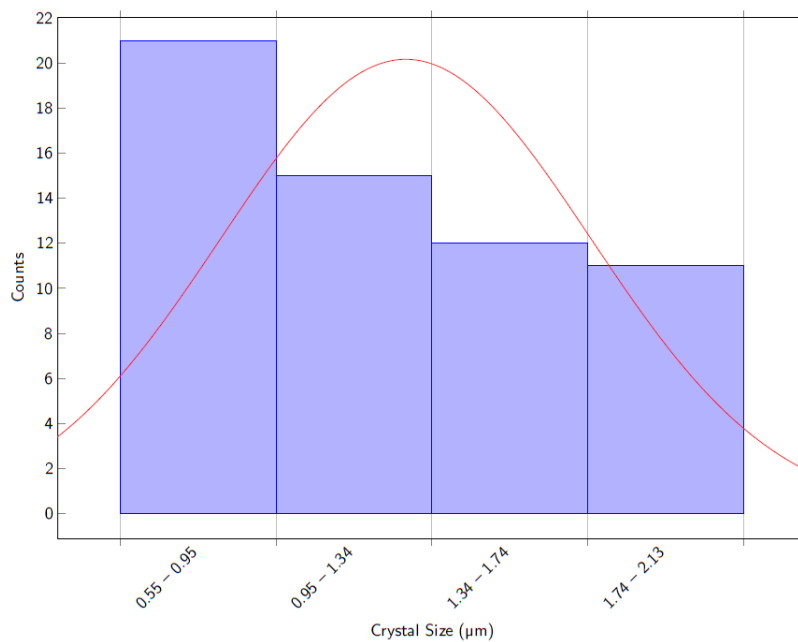
Figure F.22: Crystal Size Distribution of ITQ-75 obtained with Compound C as SDA after Ball Mill post treatment
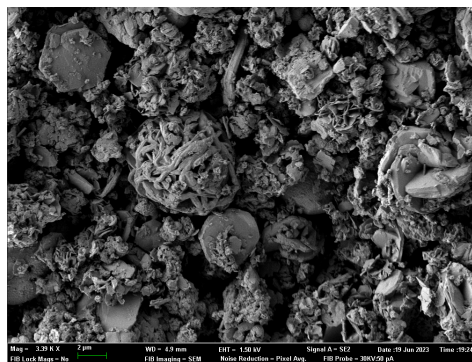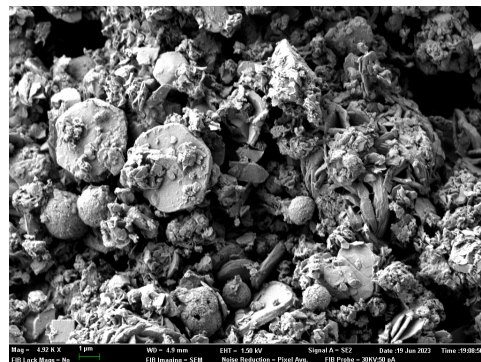
(a)   (b)

Figure F.23: ITQ-75 FESEM images, obtained with Compound C as SDA, after Butyl Lithium post treatment (pellet)
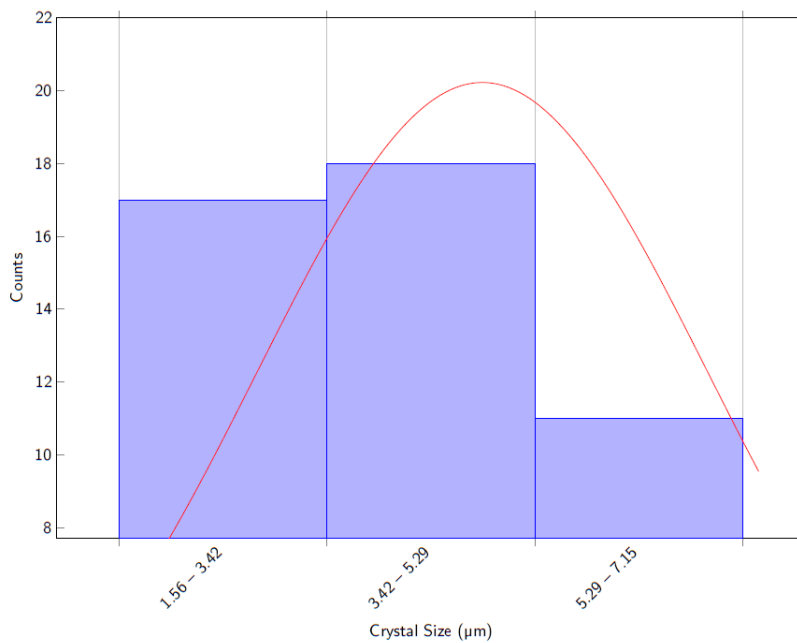
Figure F.24: Crystal Size Distribution of ITQ-75 obtained with Compound C as SDA after Butyl Lithium post treatment (pellet)

Appendix G

Photocatalytic Water Splitting Results

G.1 Modeling Details

When the experimental results started to be obtained, it was possible to see that they were quite diverse. As such, the problem of comparing the photocatalytic performance of the different samples was encountered. Therefore, in order to perform such comparison, the experimental results were modeled. In this way it would be possible to compare the samples at the same reaction time, i.e. at the initial reaction time $t = 0h$. In addition, it allows not to take into account the possible deactivation mechanisms and rates that may be different due to the diversity of samples under study. Furthermore, and taking into consideration the batch mode, the possible back reaction between the O_2 and the H_2 formed to react back into H_2O would not allow for a correct product evaluation.

The modeling was carried out taking into account the experimental results obtained and adapting a curve that best fits these. As such, after trying several curves, it was decided to adapt the Equation G.1, where $[H_2]_t$ represents the H_2 concentration at time t , $[H_2O]_0$ the water concentration at initial time $t = 0h$ and k_1 and k_{-1} the model parameters. These constants, k_1 and k_{-1}, are respectively supposed to characterize the ability of the material the promote H_2O splitting, and to drives back H_2O formation and its possible deactivation.

$$[H_2]_t = [H_2O]_0(1 - e^{(k_1 \cdot t)}) \cdot e^{k_{-1}t} \tag{G.1}$$

As can be seen from Equation G.1, the model results from mathematical considerations solely, not taking into account equilibrium thermodynamic considerations. As such, the model is a pseudo kinetic one and the parameters obtained from it have only mathematical meaning.

In order to determine the parameters of the model it was necessary to fit the curve to the experimental results obtained. For this purpose, the sum of the quadratic error between the model data and the experimental results was minimized using the SOLVER tool present in the MS Office Excel software. In the following sections it is possible to verify the experimental results, the modeled curve as well as the model parameters resulting from such operation.

G.2   Error Determination

In order to determine the experimental error associated with the unit used, it was decided to evaluate multiple times the performance of the P25 Degusa sample, a TiO_2 mixture of anatase and rutile crystalline phases. This material was chosen because it is widely used as a photocatalyst benchmark.

The following figures show the experimental results of the different tests performed with P25 and on Table G.1 all the information is systematized.
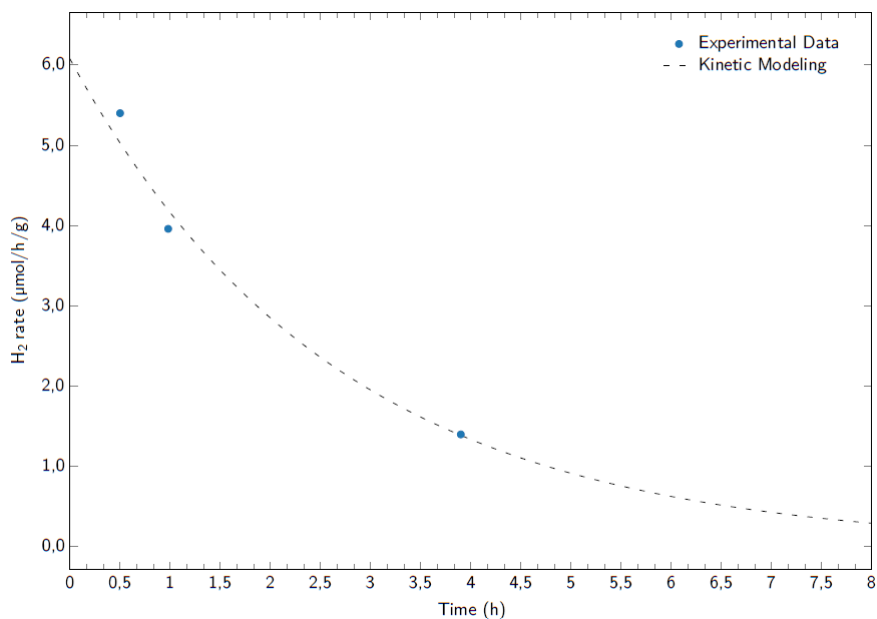
Figure G.1: H_2 rate (µmol/h/g) of P25 (first trial), where the blue dots represent the experimental data and the black dashed line the kinetic modeling
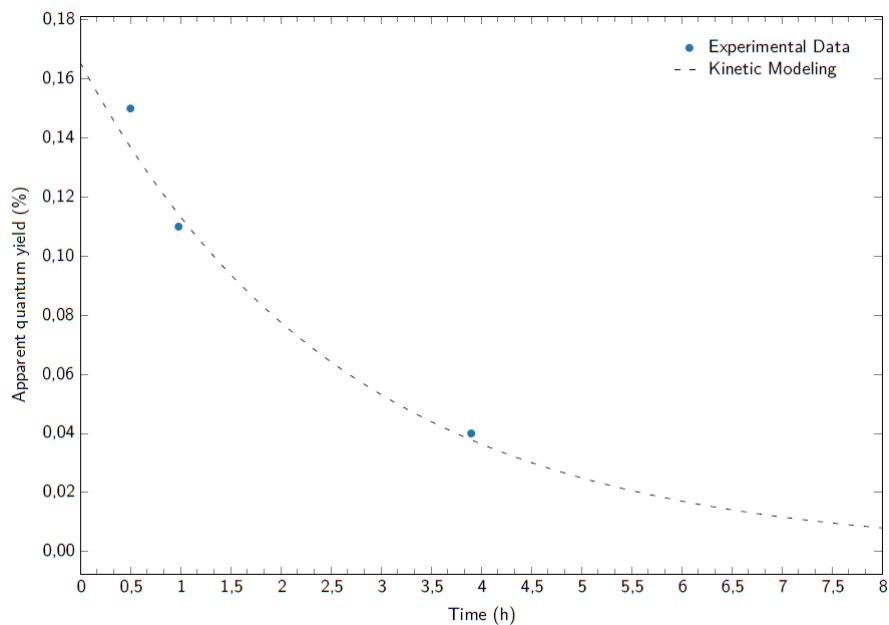
Figure G.2: Apparent quantum yield (%) of P25 (first trial), where the blue dots represent the experimental data and the black dashed line the kinetic modeling
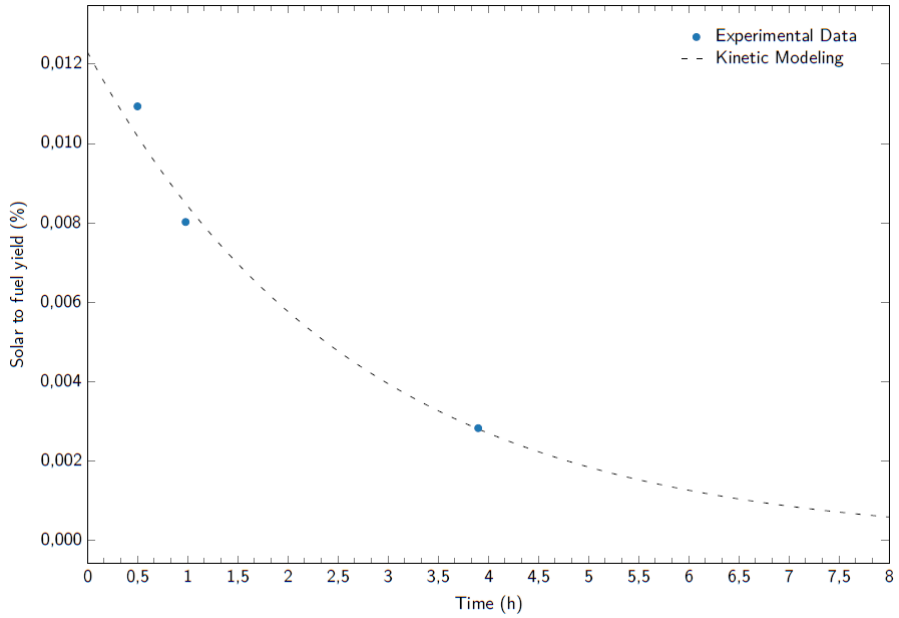
Figure G.3: Solar to fuel yield (%) of P25 (first trial), where the blue dots represent the experimental data and the black dashed line the kinetic modeling
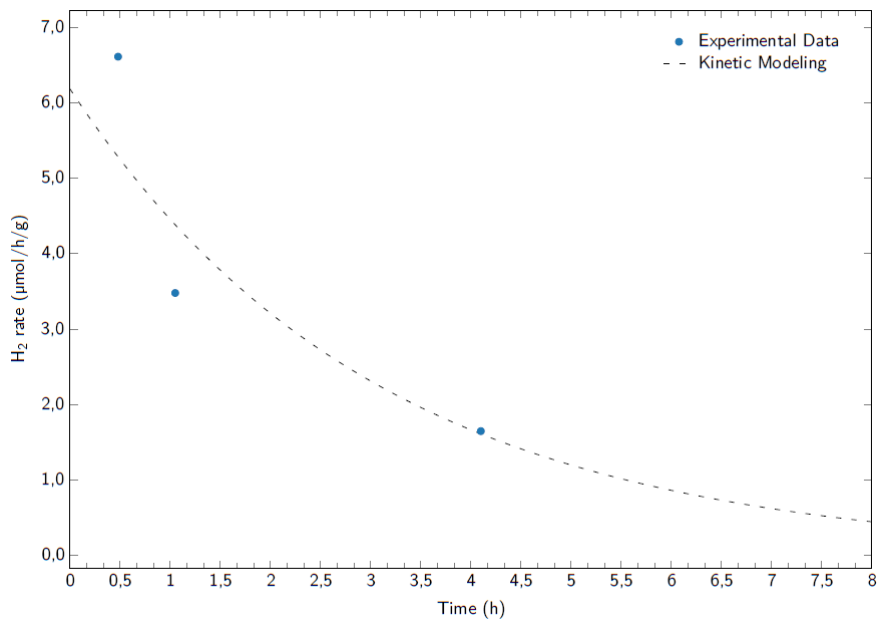
Figure G.4: H$_2$ rate (µmol/h/g) of P25 (second trial), where the blue dots represent the experimental data and the black dashed line the kinetic modeling
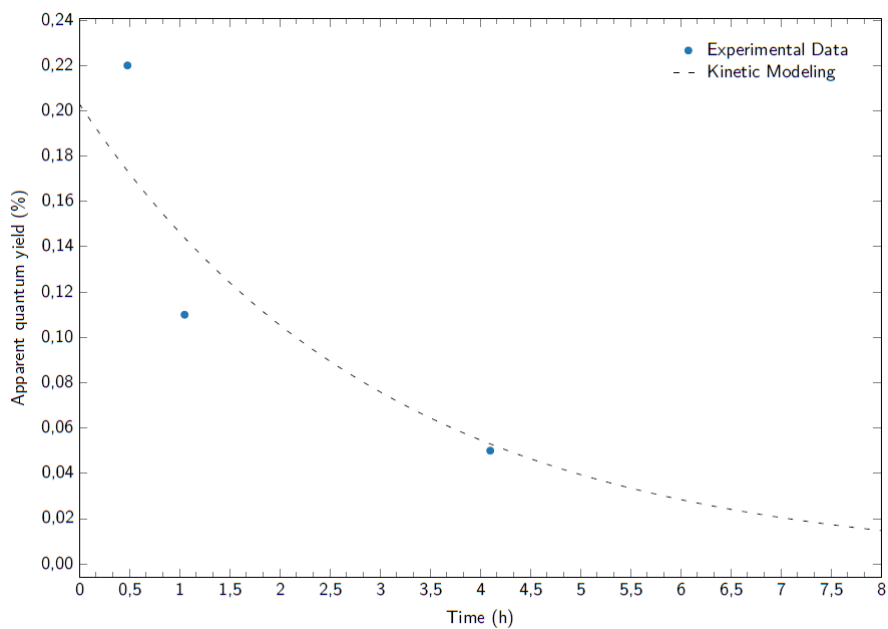
Figure G.5: Apparent quantum yield (%) of P25 (second trial), where the blue dots represent the experimental data and the black dashed line the kinetic modeling
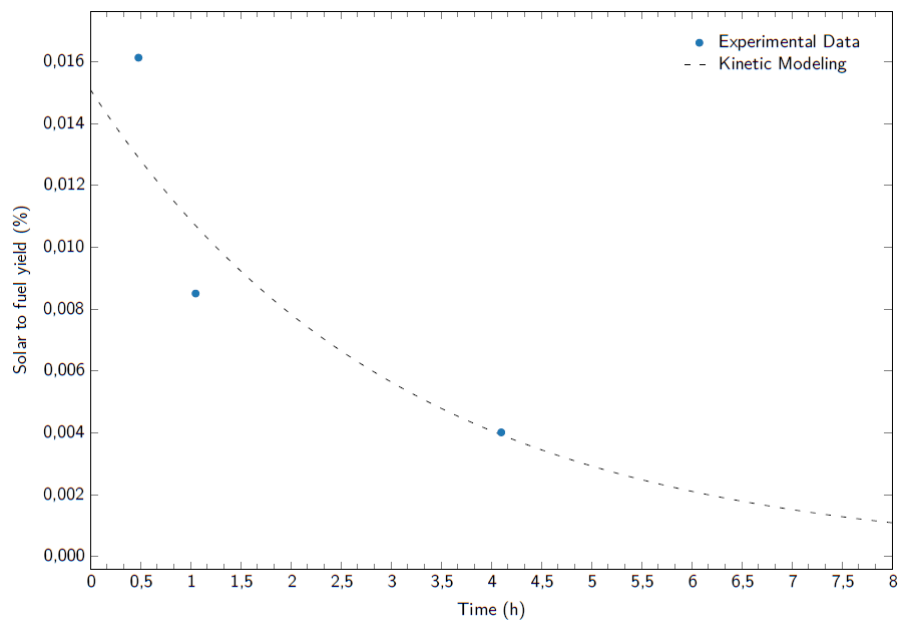
Figure G.6: Solar to fuel yield (%) of P25 (second trial), where the blue dots represent the experimental data and the black dashed line the kinetic modeling
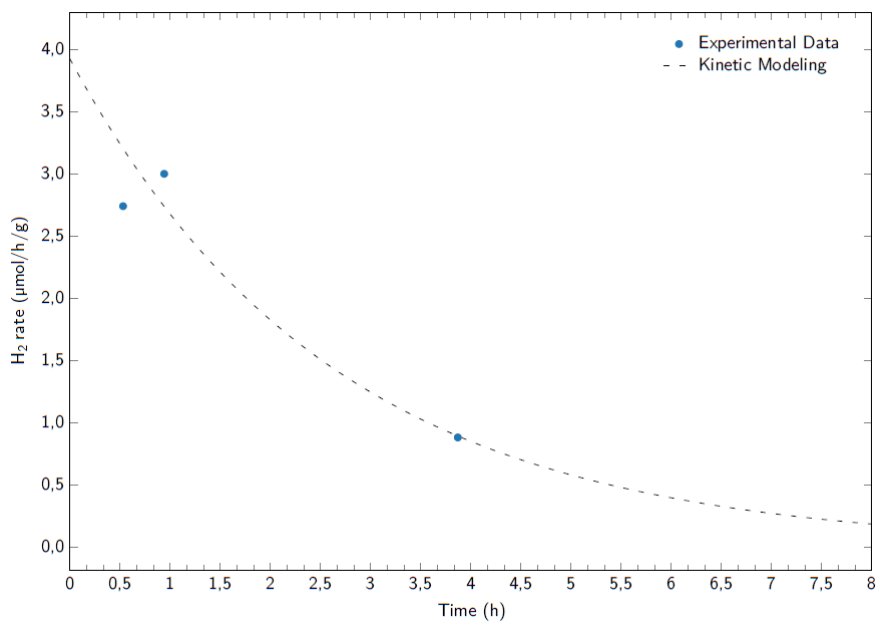
Figure G.7: H_2 rate (µmol/h/g) of P25 (third trial), where the blue dots represent the experimental data and the black dashed line the kinetic modeling
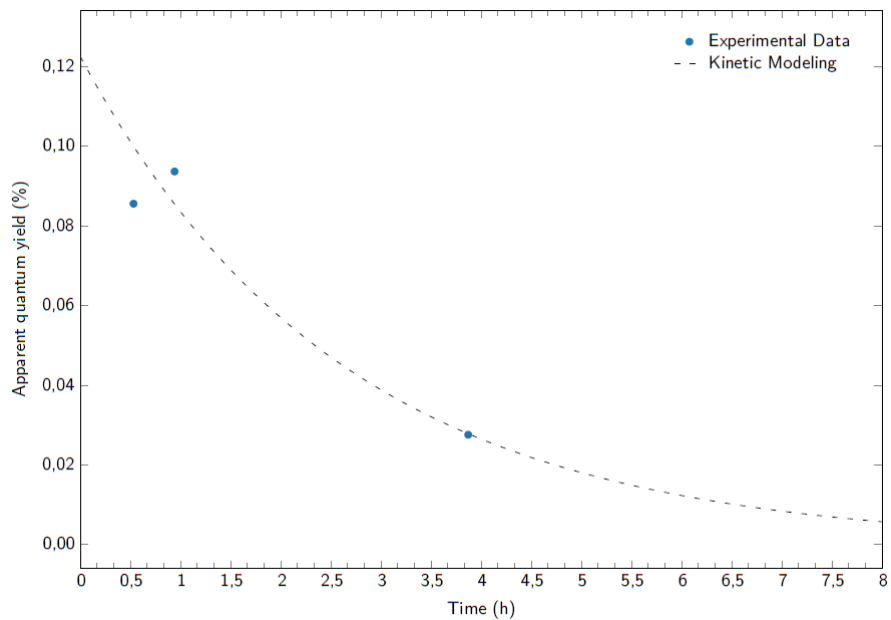
Figure G.8: Apparent quantum yield (%) of P25 (third trial), where the blue dots represent the experimental data and the black dashed line the kinetic modeling
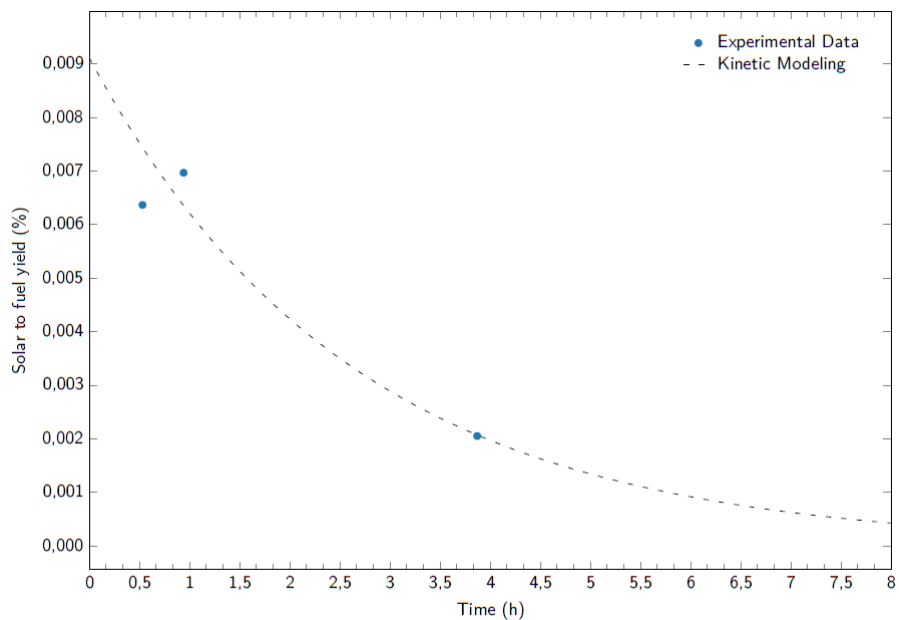
Figure G.9: Solar to fuel yield (%) of P25 (third trial), where the blue dots represent the experimental data and the black dashed line the kinetic modeling

Table G.1: P25 main photocatalytic test results

	1st Trial	2nd Trial	3rd Trial	Average
Initial simulated H_2 rate (µmol/h/g)	6,08	6,18	3,92	5 ± 2
Initial simulated apparent quantum yield (%)	0,17	0,20	0,12	$0,16 \pm 0,06$
Initial simulated solar-to-fuel yield (%)	0,012	0,015	0,009	$0,012 \pm 0,005$
Water splitting apparent kinetic constant k_1 (h^{-1})	$8,86 \cdot 10^{-4}$	$1,09 \cdot 10^{-3}$	$6,75 \cdot 10^{-4}$	$8 \pm 2 \cdot 10^{-4}$
Back reaction apparent kinetic constant k_{-1} (h^{-1})	$3,78 \cdot 10^{-1}$	$3,27 \cdot 10^{-1}$	$3,83 \cdot 10^{-1}$	$3,6 \pm 0,5 \cdot 10^{-1}$

G.3   IZM-5 & ITQ-76

G.3.1   Unmodified Structure
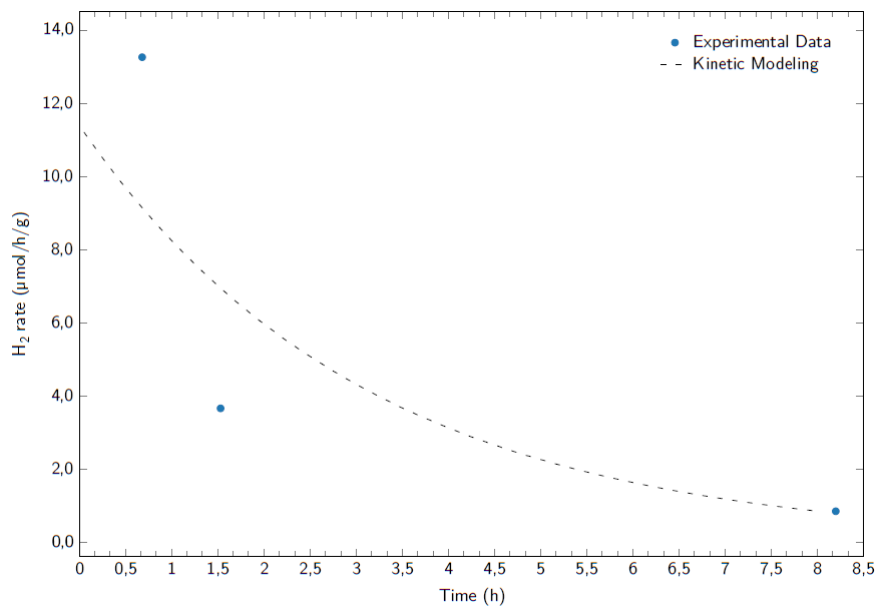
Figure G.10: H_2 rate (µmol/h/g) of IZM-5, where the blue dots represent the experimental data and the black dashed line the kinetic modeling
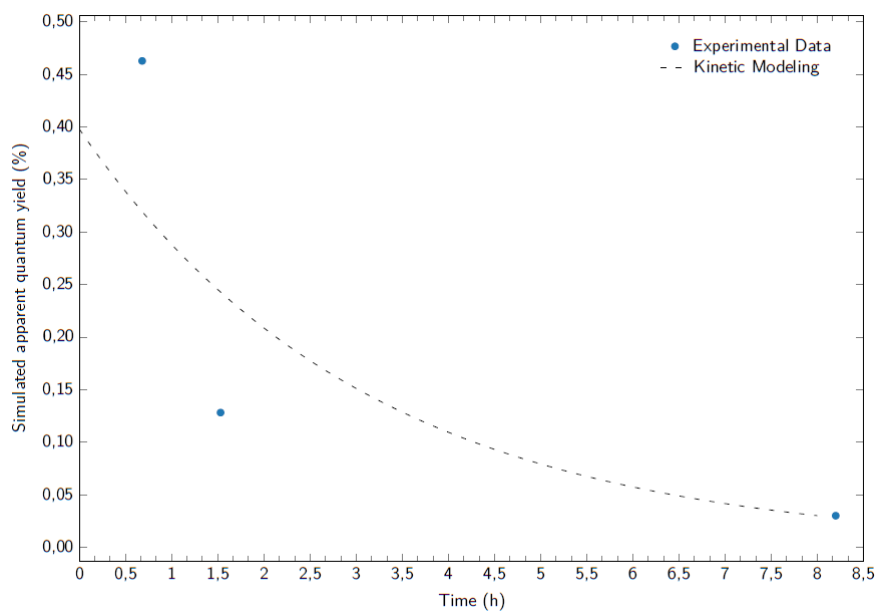
Figure G.11: Apparent quantum yield (%) of IZM-5, where the blue dots represent the experimental data and the black dashed line the kinetic modeling
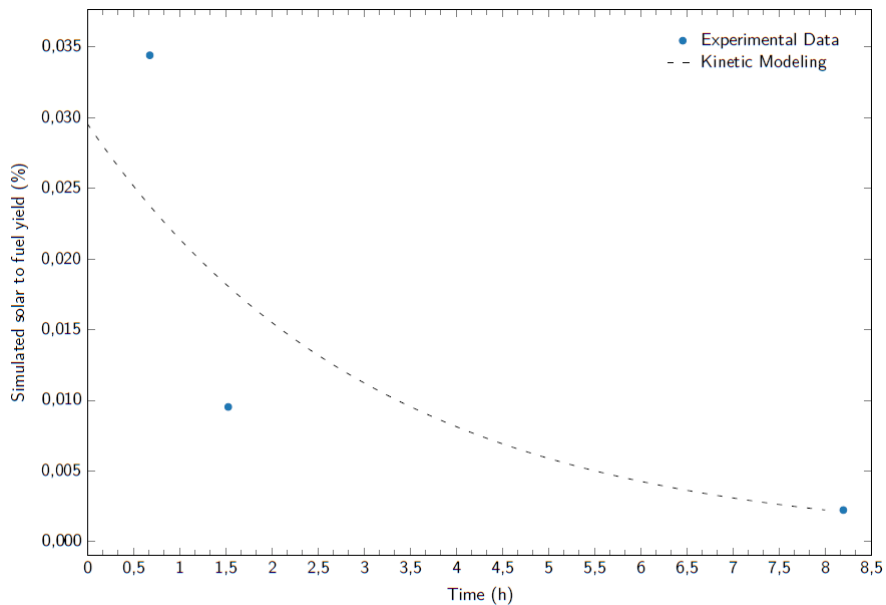
Figure G.12: Solar to fuel yield (%) of IZM-5, where the blue dots represent the experimental data and the black dashed line the kinetic modeling

Table G.2: IZM-5 main photocatalytic test results

Initial simulated H_2 rate (µmol/h/g)	11,39
Initial simulated apparent quantum yield (%)	0,57
Initial simulated solar-to-fuel yield (%)	0,030
Water splitting apparent kinetic constant k_1 (h^{-1})	$2,13 \cdot 10^{-3}$
Back reaction apparent kinetic constant k_{-1} (h^{-1})	$3,21 \cdot 10^{-1}$

G.3.2   With Ru-Complex
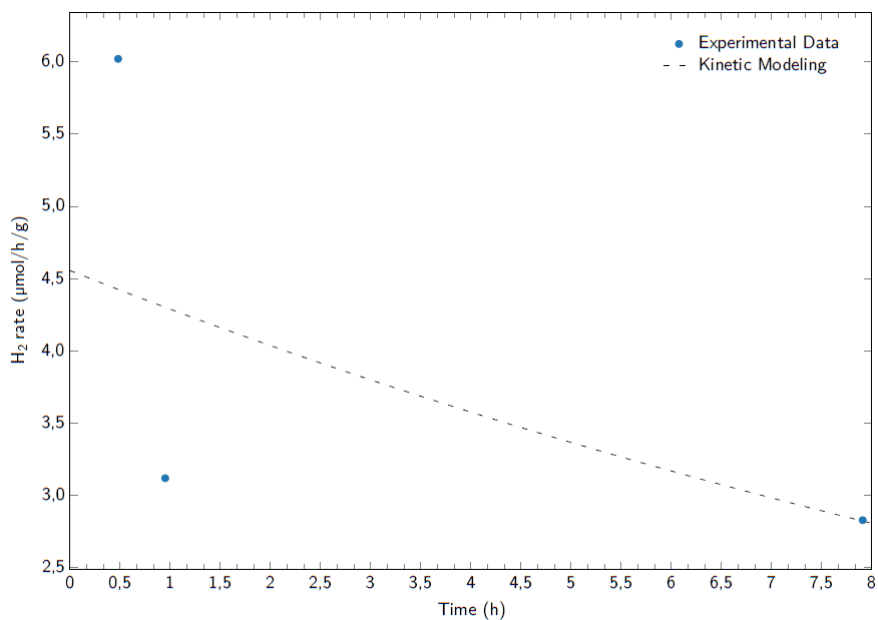
Figure G.13: H$_2$ rate (µmol/h/g) of ITQ-76, with Ru-Complex/SDA A molar ratio equal to 0,1, where the blue dots represent the experimental data and the black dashed line the kinetic modeling
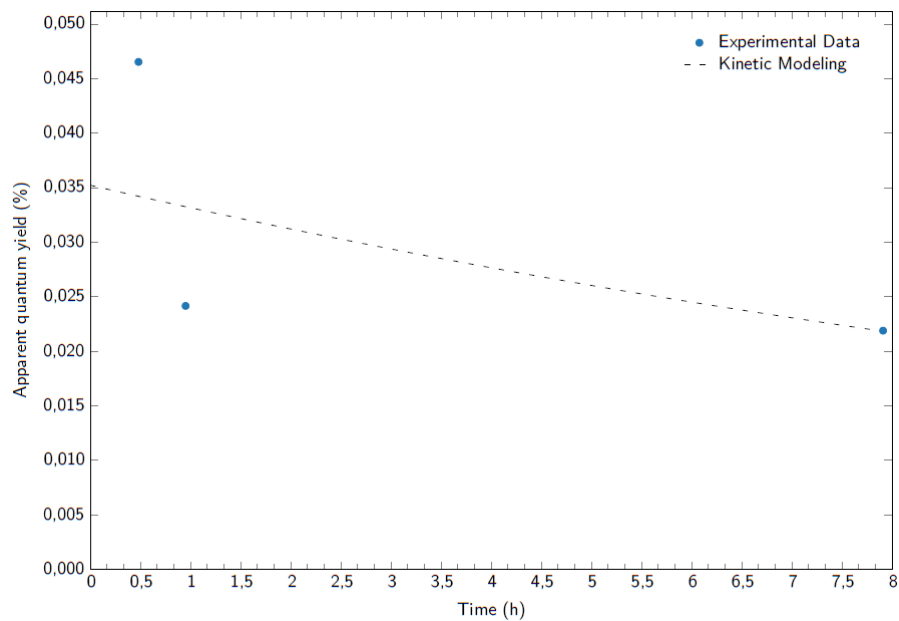
Figure G.14: Apparent quantum yield (%) of ITQ-76, with Ru-Complex/SDA A molar ratio equal to 0,1, where the blue dots represent the experimental data and the black dashed line the kinetic modeling
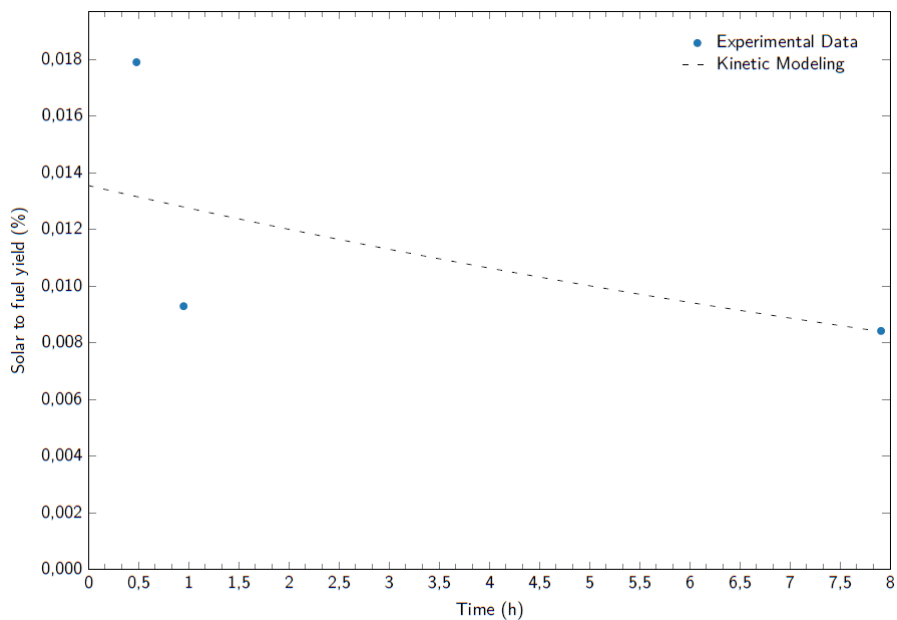
Figure G.15: Solar to fuel yield (%) of ITQ-76, with Ru-Complex/SDA A molar ratio equal to 0,1, where the blue dots represent the experimental data and the black dashed line the kinetic modeling

Table G.3: ITQ-76, with Ru-Complex/SDA A molar ratio equal to 0,1, main photocatalytic test results

Initial simulated H_2 rate (µmol/h/g)	4,56
Initial simulated apparent quantum yield (%)	0,04
Initial simulated solar-to-fuel yield (%)	0,014
Water splitting apparent kinetic constant k_1 (h^{-1})	$9,76 \cdot 10^{-4}$
Back reaction apparent kinetic constant k_{-1} (h^{-1})	$6,00 \cdot 10^{-2}$

G.4 ITQ-75

G.4.1 Unmodified
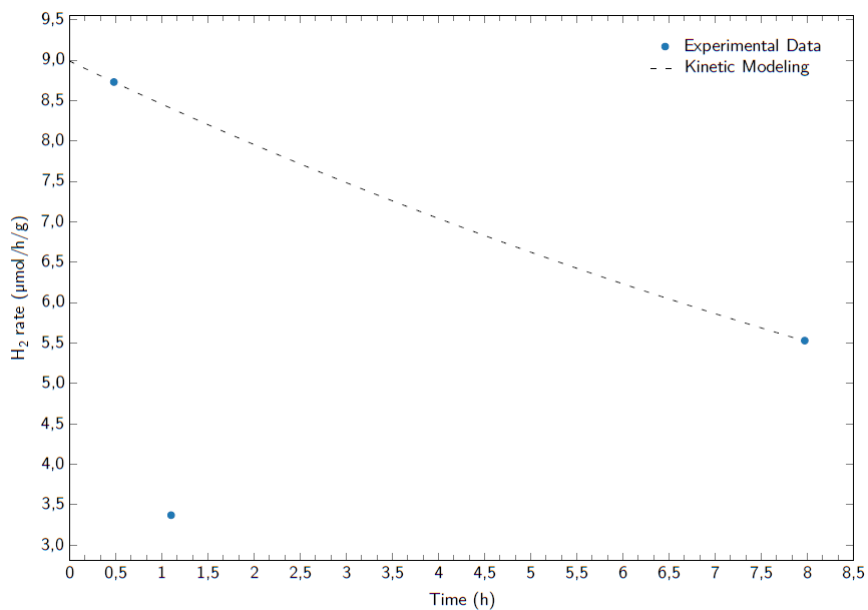
Figure G.16: H_2 rate (μmol/h/g) of ITQ-75, obtained with Compound B as SDA, where the blue dots represent the experimental data and the black dashed line the kinetic modeling
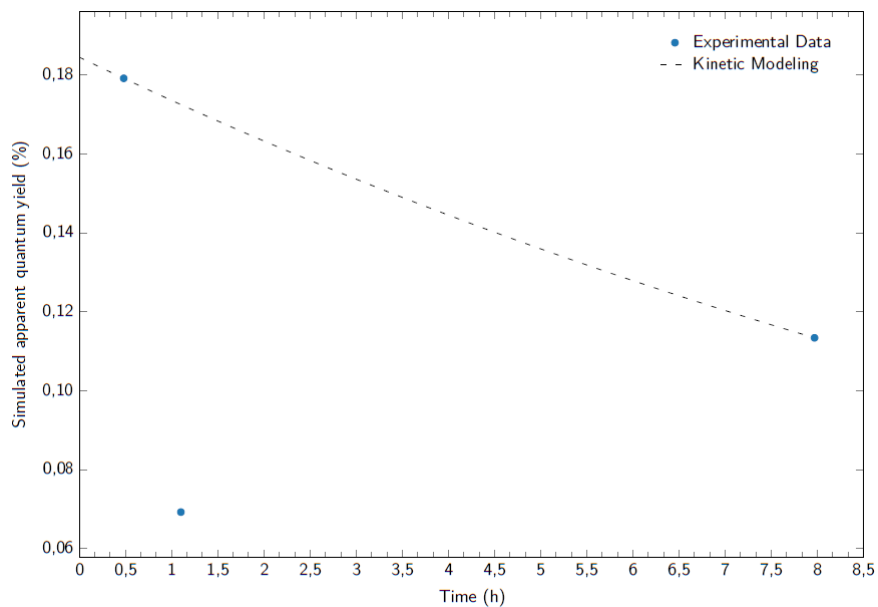
Figure G.17: Apparent quantum yield (%) of ITQ-75, obtained with Compound B as SDA, where the blue dots represent the experimental data and the black dashed line the kinetic modeling
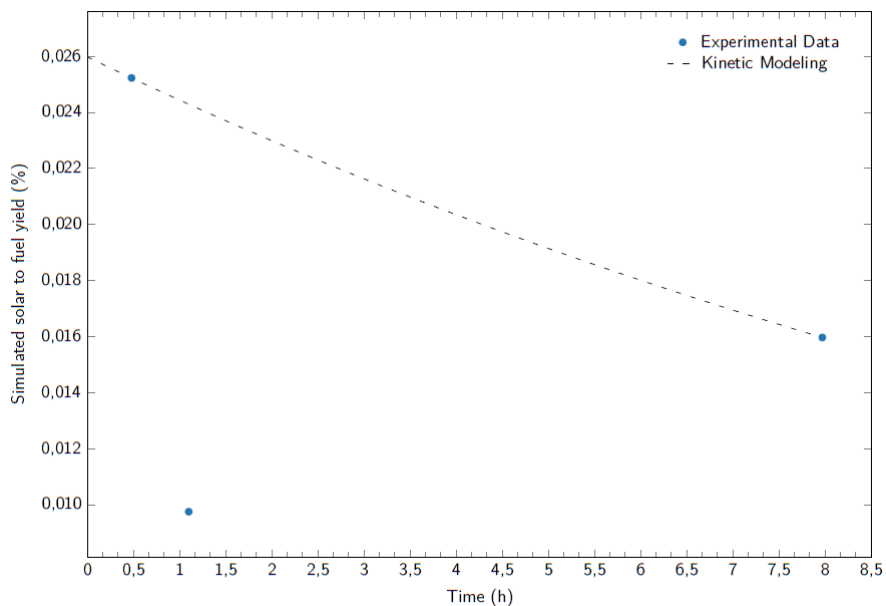
Figure G.18: Solar to fuel yield (%) of ITQ-75, obtained with Compound B as SDA, where the blue dots represent the experimental data and the black dashed line the kinetic modeling

Table G.4: ITQ-75, obtained with Compound B as SDA, main photocatalytic test results

Initial simulated H_2 rate (μmol/h/g)	8,99
Initial simulated apparent quantum yield (%)	0,22
Initial simulated solar-to-fuel yield (%)	0,026
Water splitting apparent kinetic constant k_1 (h^{-1})	$1,87 \cdot 10^{-3}$
Back reaction apparent kinetic constant k_{-1} (h^{-1})	$6,01 \cdot 10^{-2}$
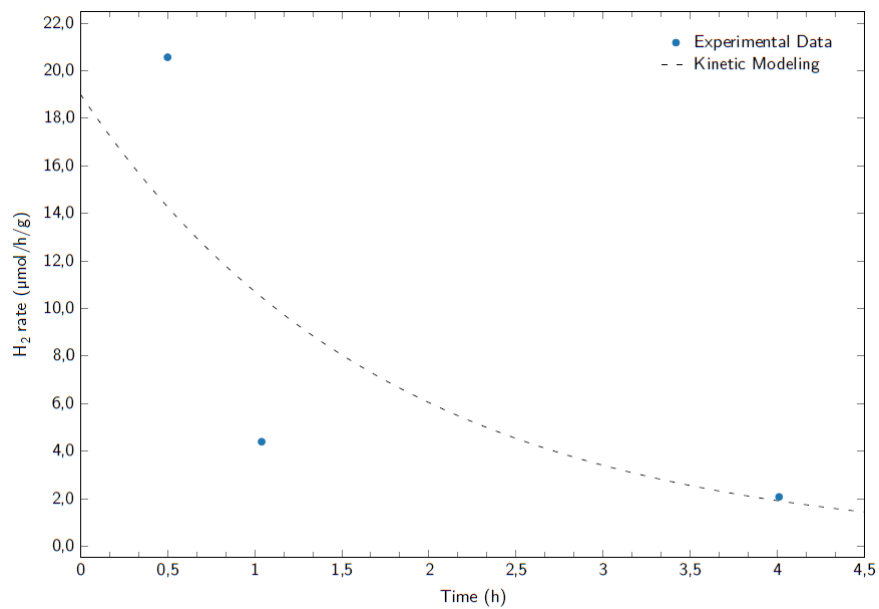
Figure G.19: H_2 rate (µmol/h/g) of ITQ-75, obtained with Compound C as SDA, where the blue dots represent the experimental data and the black dashed line the kinetic modeling
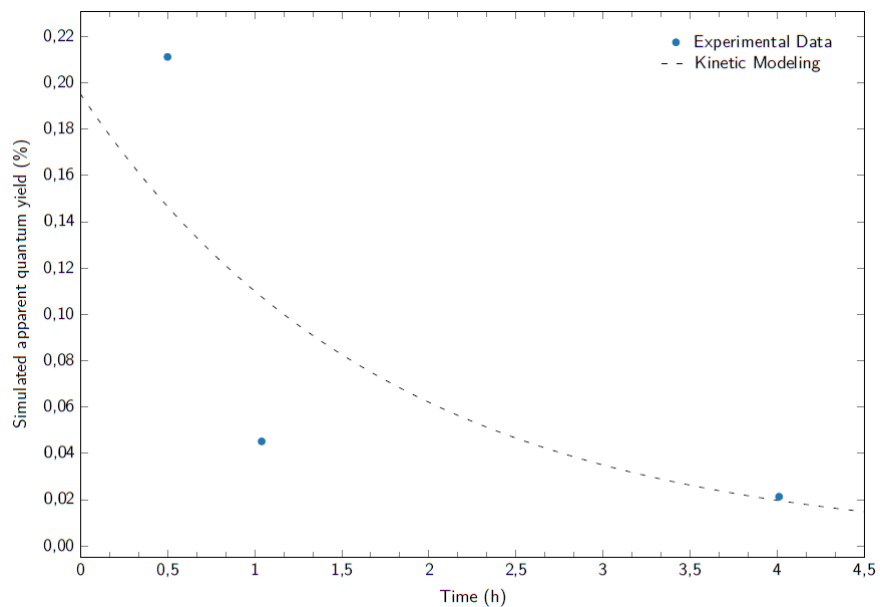
Figure G.20: Apparent quantum yield (%) of ITQ-75, obtained with Compound C as SDA, where the blue dots represent the experimental data and the black dashed line the kinetic modeling
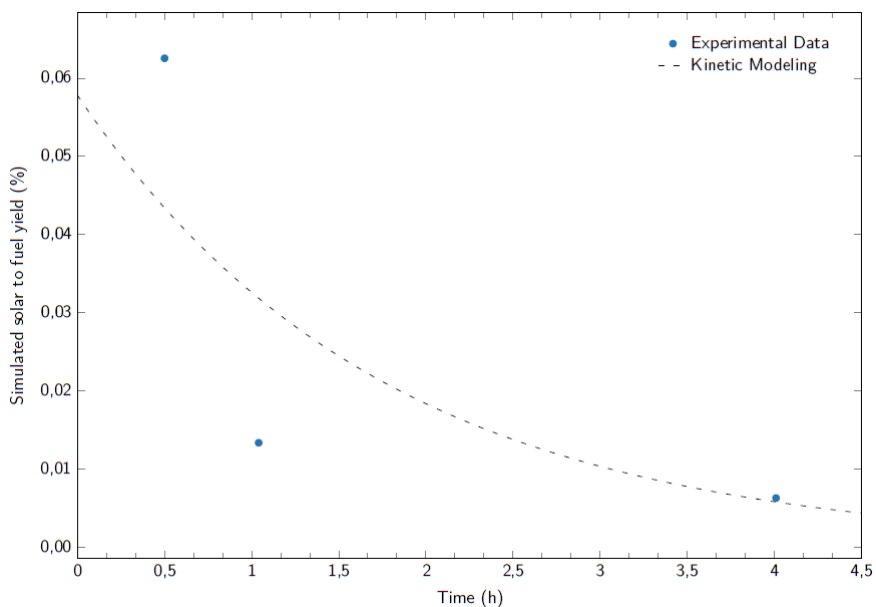
Figure G.21: Solar to fuel yield (%) of ITQ-75, obtained with Compound C as SDA, where the blue dots represent the experimental data and the black dashed line the kinetic modeling

Table G.5: ITQ-75, obtained with Compound C as SDA, main photocatalytic test results

Initial simulated H_2 rate (µmol/h/g)	19,01
Initial simulated apparent quantum yield (%)	0,34
Initial simulated solar-to-fuel yield (%)	0,058
Water splitting apparent kinetic constant k_1 (h^{-1})	$4,17 \cdot 10^{-3}$
Back reaction apparent kinetic constant k_{-1} (h^{-1})	$5,71 \cdot 10^{-1}$
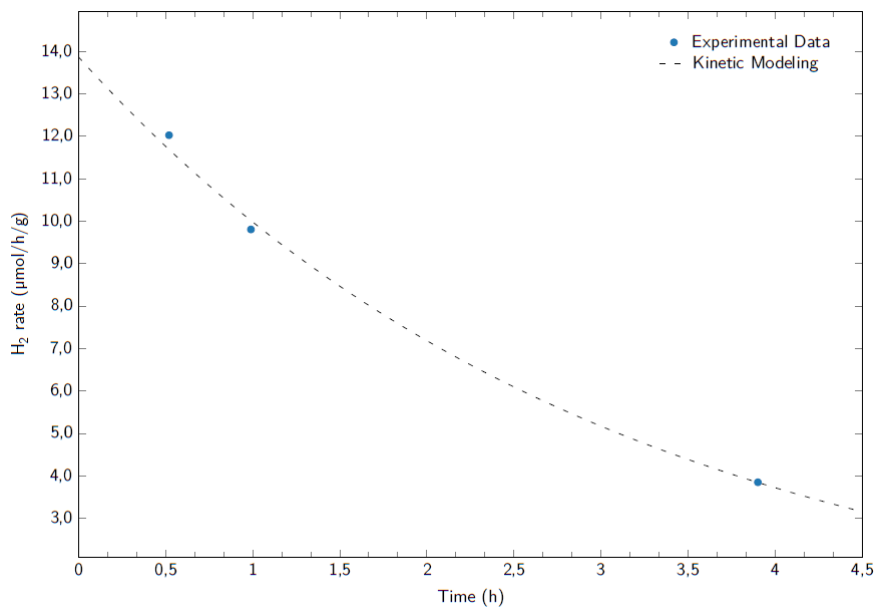
Figure G.22: H_2 rate (µmol/h/g) of ITQ-75, obtained with Compound D as SDA, where the blue dots represent the experimental data and the black dashed line the kinetic modeling
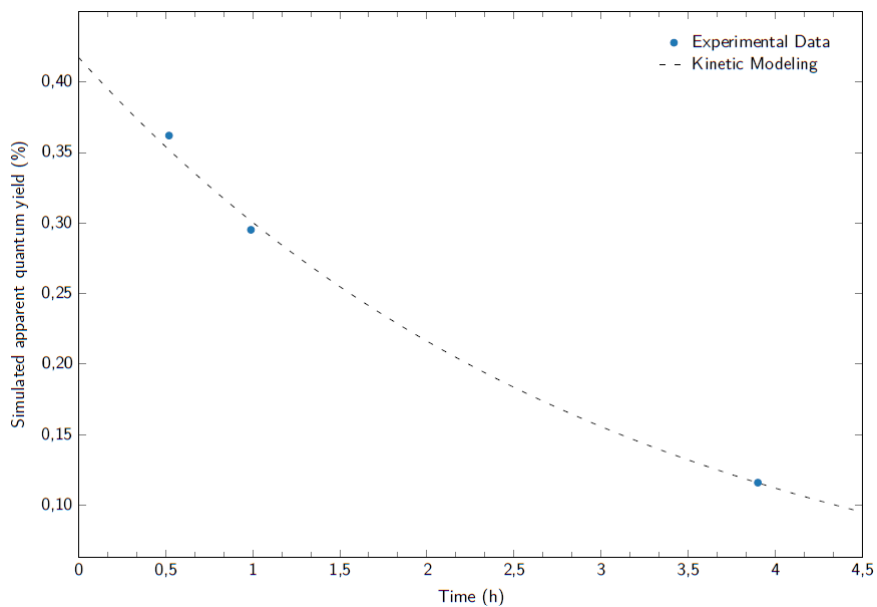
Figure G.23: Apparent quantum yield (%) of ITQ-75, obtained with Compound D as SDA, where the blue dots represent the experimental data and the black dashed line the kinetic modeling
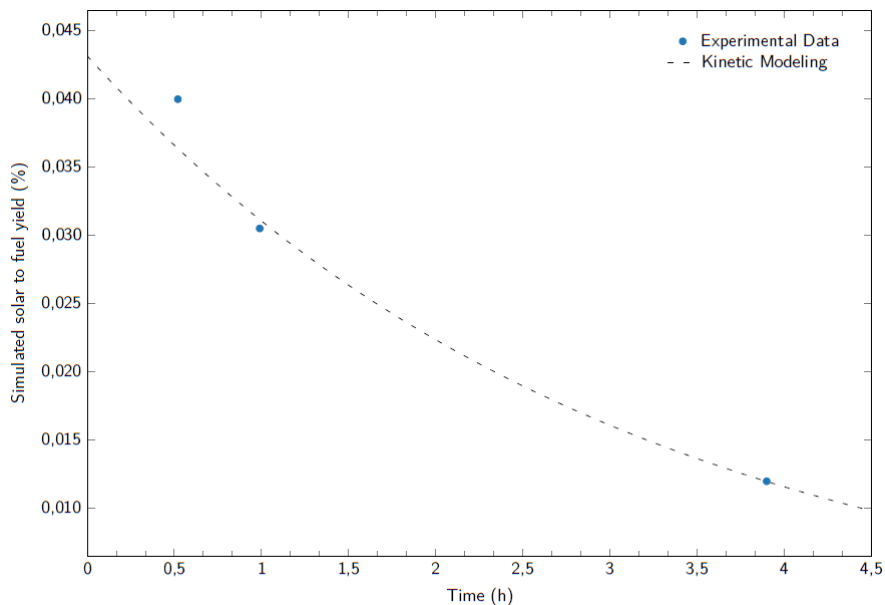
Figure G.24: Solar to fuel yield (%) of ITQ-75, obtained with Compound D as SDA, where the blue dots represent the experimental data and the black dashed line the kinetic modeling

Table G.6: ITQ-75, obtained with Compound D as SDA, main photocatalytic test results

Initial simulated H_2 rate (µmol/h/g)	13,87
Initial simulated apparent quantum yield (%)	0,42
Initial simulated solar-to-fuel yield (%)	0,043
Water splitting apparent kinetic constant k_1 (h^{-1})	$3,11 \cdot 10^{-3}$
Back reaction apparent kinetic constant k_{-1} (h^{-1})	$3,27 \cdot 10^{-1}$
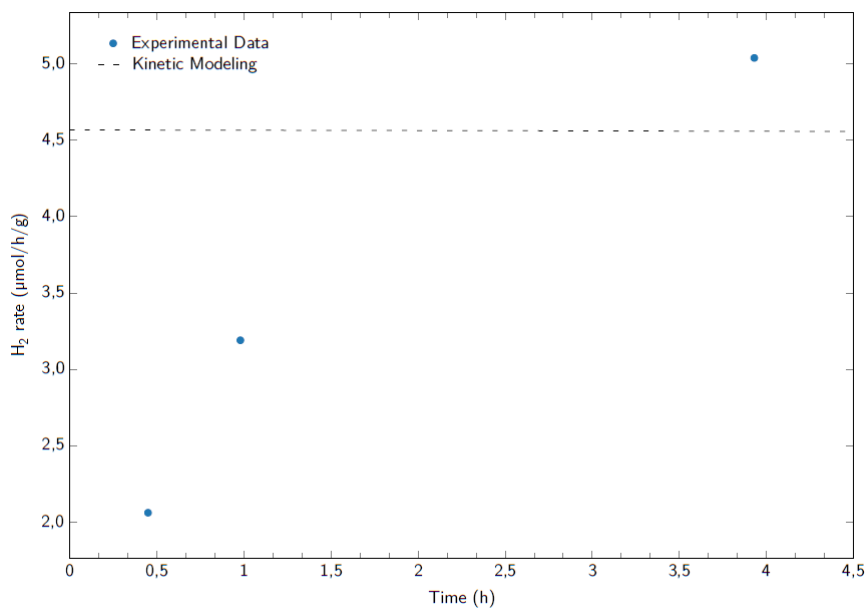
Figure G.25: H$_2$ rate (μmol/h/g) of ITQ-75, obtained with Compound E as SDA, where the blue dots represent the experimental data and the black dashed line the kinetic modeling
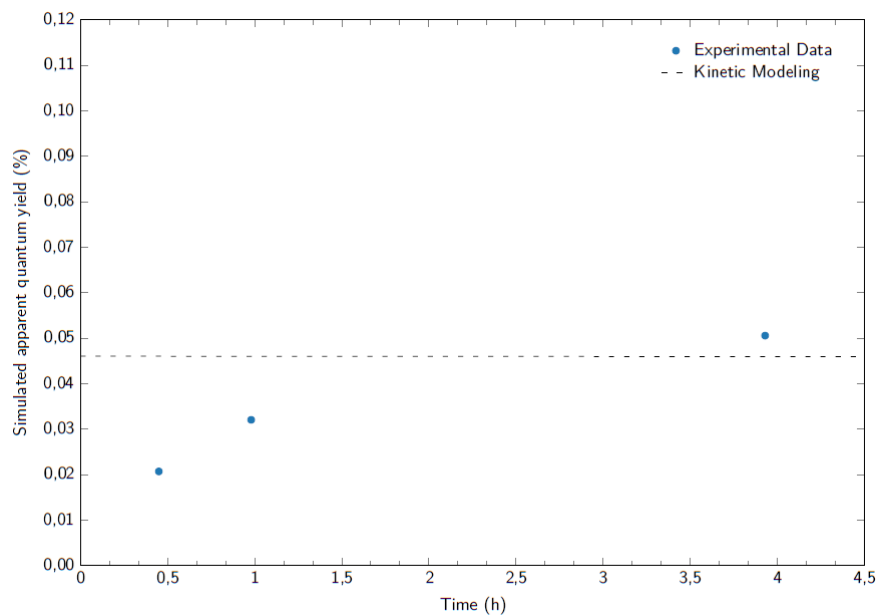
Figure G.26: Apparent quantum yield (%) of ITQ-75, obtained with Compound E as SDA, where the blue dots represent the experimental data and the black dashed line the kinetic modeling
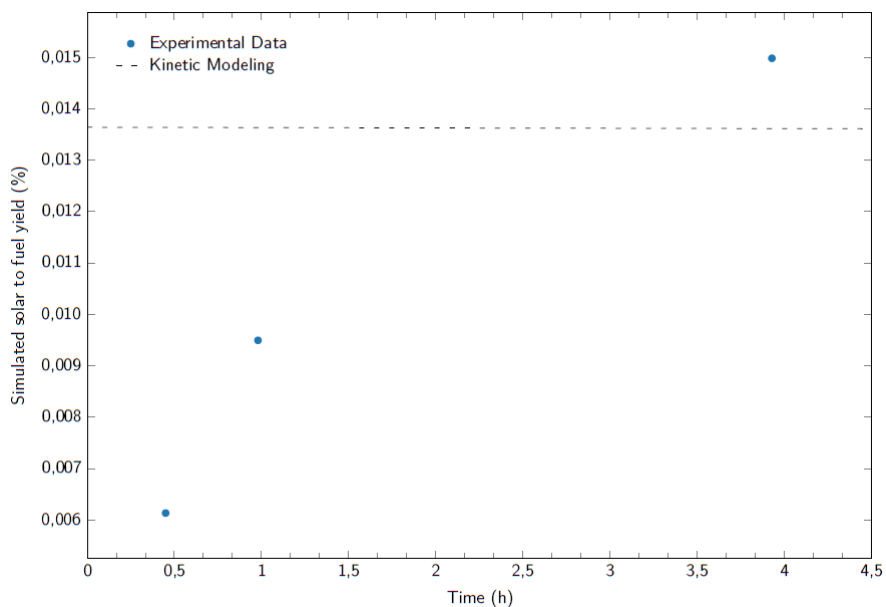
Figure G.27: Solar to fuel yield (%) of ITQ-75, obtained with Compound E as SDA, where the blue dots represent the experimental data and the black dashed line the kinetic modeling

Table G.7: ITQ-75, obtained with Compound E as SDA, main photocatalytic test results ([a] arbitrary value for the fit)

Initial simulated H_2 rate (µmol/h/g)	4,57
Initial simulated apparent quantum yield (%)	0,10
Initial simulated solar-to-fuel yield (%)	0,014
Water splitting apparent kinetic constant k_1 (h^{-1})	$9,83 \cdot 10^{-4}$
Back reaction apparent kinetic constant k_{-1} (h^{-1})	$1,00 \cdot 10^{-10}$ [a]

G.4.2   Doped with Metals
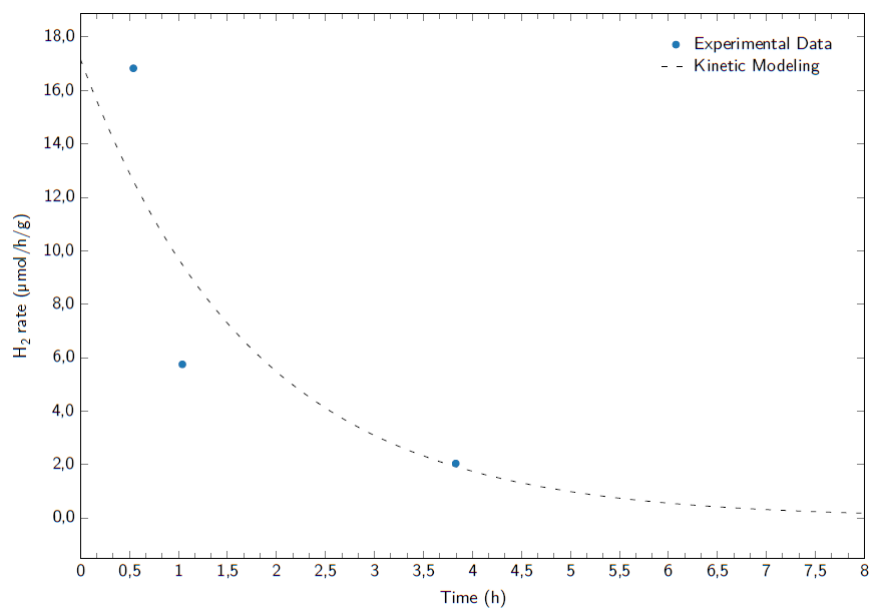
Figure G.28: H_2 rate (μmol/h/g) of ITQ-75, obtained with Compound B as SDA and doped with 0,1wt.% Cu, where the blue dots represent the experimental data and the black dashed line the kinetic modeling
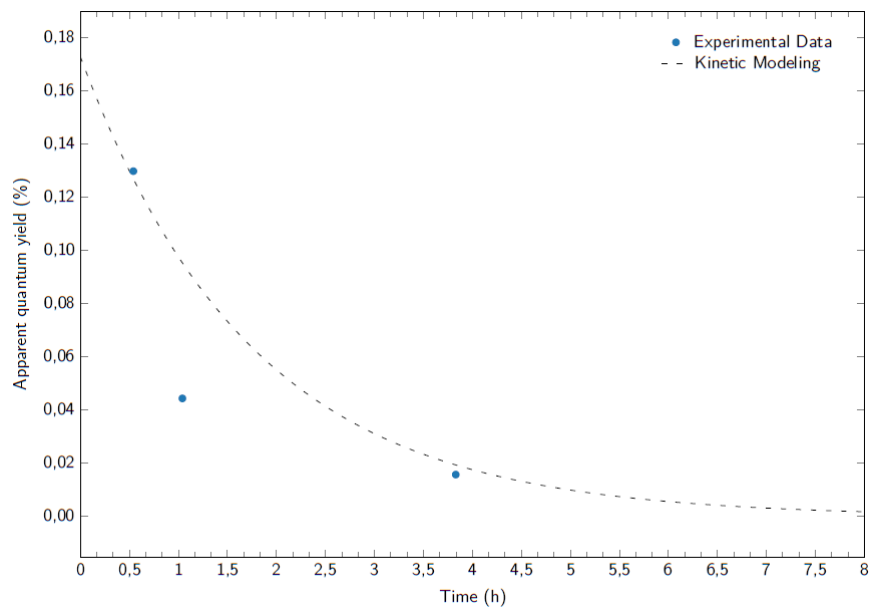
Figure G.29: Apparent quantum yield (%) of ITQ-75, obtained with Compound B as SDA and doped with 0,1wt.% Cu, where the blue dots represent the experimental data and the black dashed line the kinetic modeling
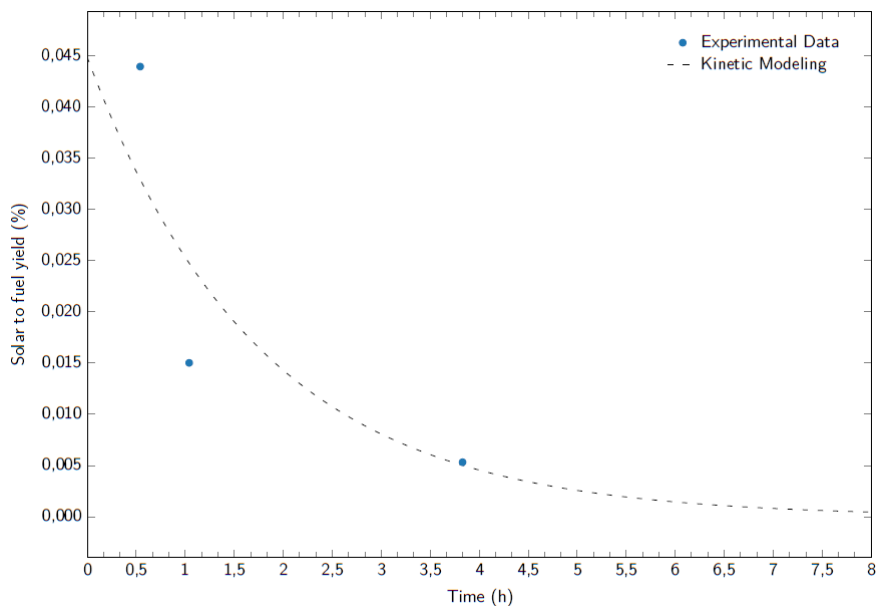
Figure G.30: Solar to fuel yield (%) of ITQ-75, obtained with Compound B as SDA and doped with 0,1wt.% Cu, where the blue dots represent the experimental data and the black dashed line the kinetic modeling

Table G.8: ITQ-75, obtained with Compound B as SDA and doped with 0,1wt.% Cu, main photocatalytic test results

Initial simulated H_2 rate (μmol/h/g)	17,17
Initial simulated apparent quantum yield (%)	0,17
Initial simulated solar-to-fuel yield (%)	0,045
Water splitting apparent kinetic constant k_1 (h^{-1})	$3,23 \cdot 10^{-3}$
Back reaction apparent kinetic constant k_{-1} (h^{-1})	$5,70 \cdot 10^{-1}$
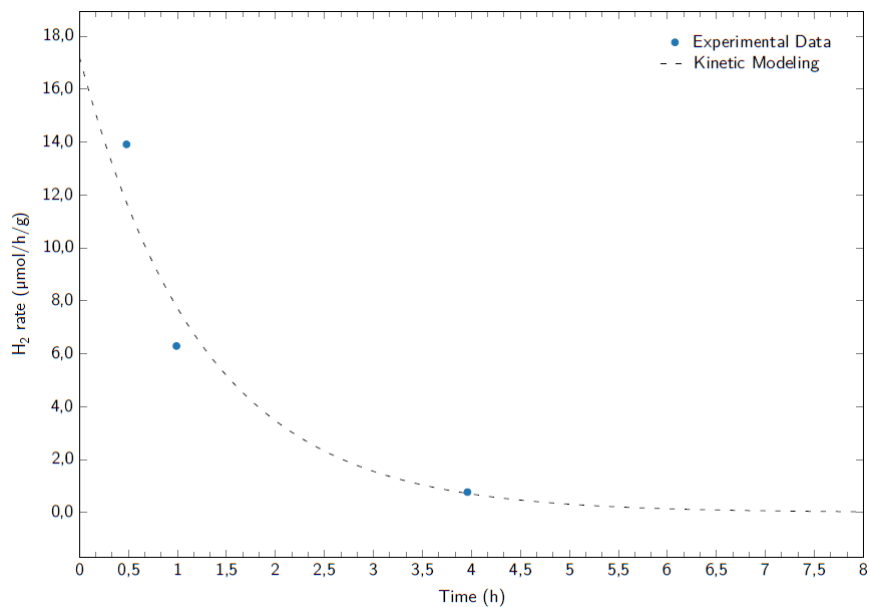
Figure G.31: H$_2$ rate (µmol/h/g) of ITQ-75, obtained with Compound B as SDA and doped with 0,2wt.% Cu, where the blue dots represent the experimental data and the black dashed line the kinetic modeling
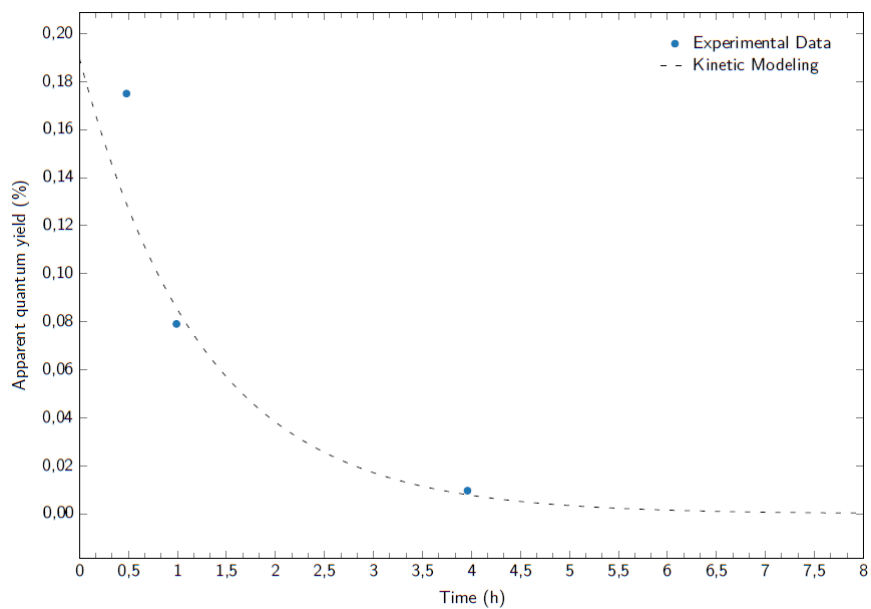
Figure G.32: Apparent quantum yield (%) of ITQ-75, obtained with Compound B as SDA and doped with 0,2wt.% Cu, where the blue dots represent the experimental data and the black dashed line the kinetic modeling
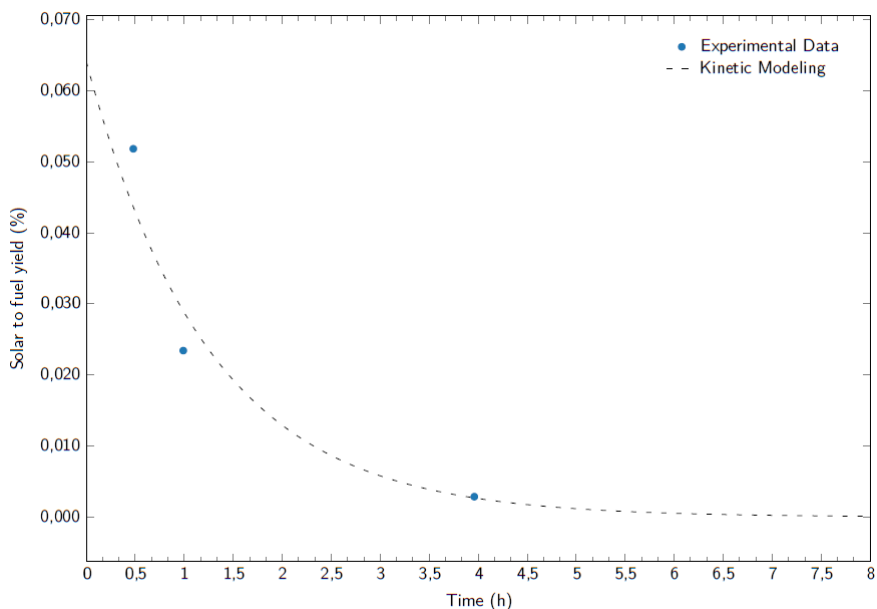
Figure G.33: Solar to fuel yield (%) of ITQ-75, obtained with Compound B as SDA and doped with 0,2wt.% Cu, where the blue dots represent the experimental data and the black dashed line the kinetic modeling

Table G.9: ITQ-75, obtained with Compound B as SDA and doped with 0,2wt.% Cu, main photocatalytic test results

Initial simulated H_2 rate (µmol/h/g)	17,21
Initial simulated apparent quantum yield (%)	0,19
Initial simulated solar-to-fuel yield (%)	0,064
Water splitting apparent kinetic constant k_1 (h^{-1})	$4,62 \cdot 10^{-3}$
Back reaction apparent kinetic constant k_{-1} (h^{-1})	$7,99 \cdot 10^{-1}$
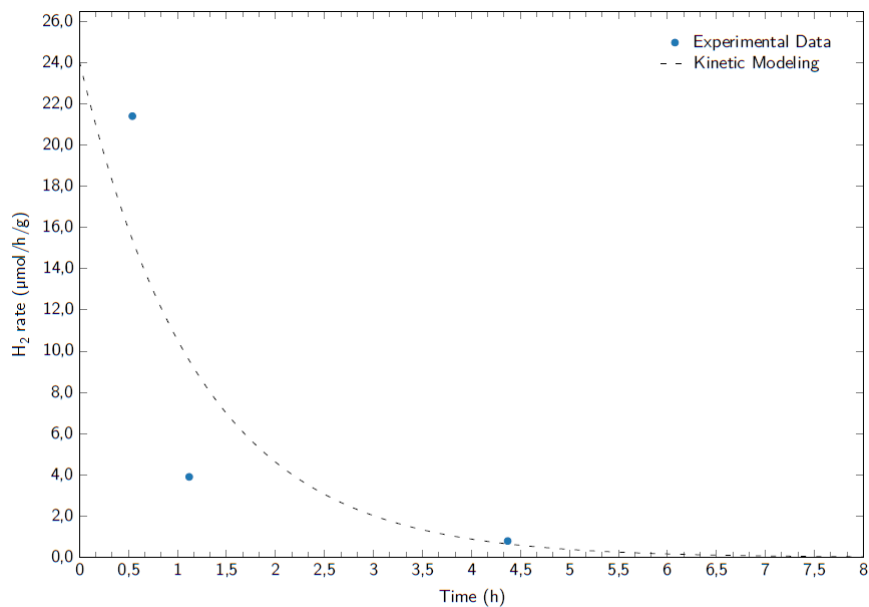
Figure G.34: H_2 rate (µmol/h/g) of ITQ-75, obtained with Compound B as SDA and doped with 0,1wt.% Fe, where the blue dots represent the experimental data and the black dashed line the kinetic modeling
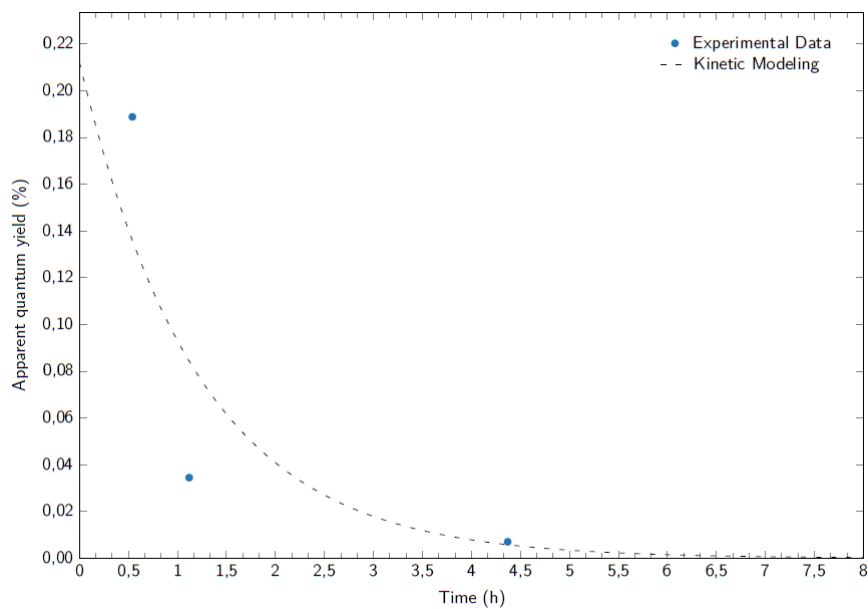
Figure G.35: Apparent quantum yield (%) of ITQ-75, obtained with Compound B as SDA and doped with 0,1wt.% Fe, where the blue dots represent the experimental data and the black dashed line the kinetic modeling
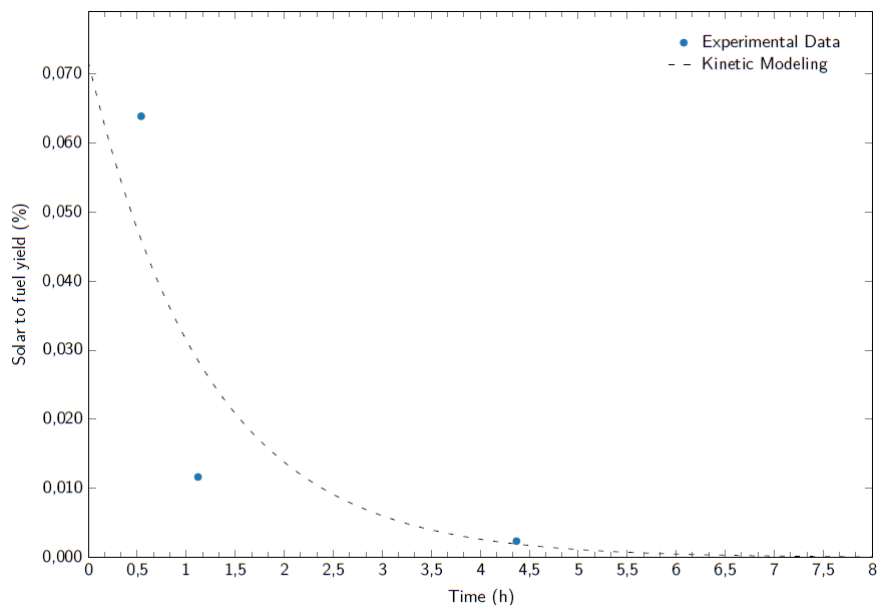
Figure G.36: Solar to fuel yield (%) of ITQ-75, obtained with Compound B as SDA and doped with 0,1wt.% Fe, where the blue dots represent the experimental data and the black dashed line the kinetic modeling

Table G.10: ITQ-75, obtained with Compound B as SDA and doped with 0,1wt.% Fe, main photocatalytic test results

Initial simulated H_2 rate (µmol/h/g)	24,06
Initial simulated apparent quantum yield (%)	0,21
Initial simulated solar-to-fuel yield (%)	0,072
Water splitting apparent kinetic constant k_1 (h^{-1})	$5,17 \cdot 10^{-3}$
Back reaction apparent kinetic constant k_{-1} (h^{-1})	$8,22 \cdot 10^{-1}$
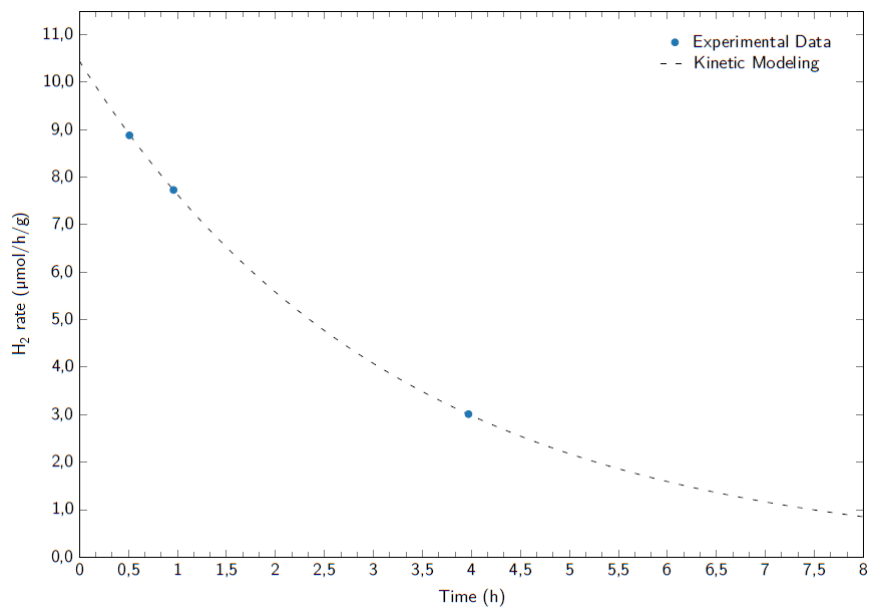
Figure G.37: H$_2$ rate (µmol/h/g) of ITQ-75, obtained with Compound B as SDA and doped with 0,05wt.% Ni, where the blue dots represent the experimental data and the black dashed line the kinetic modeling
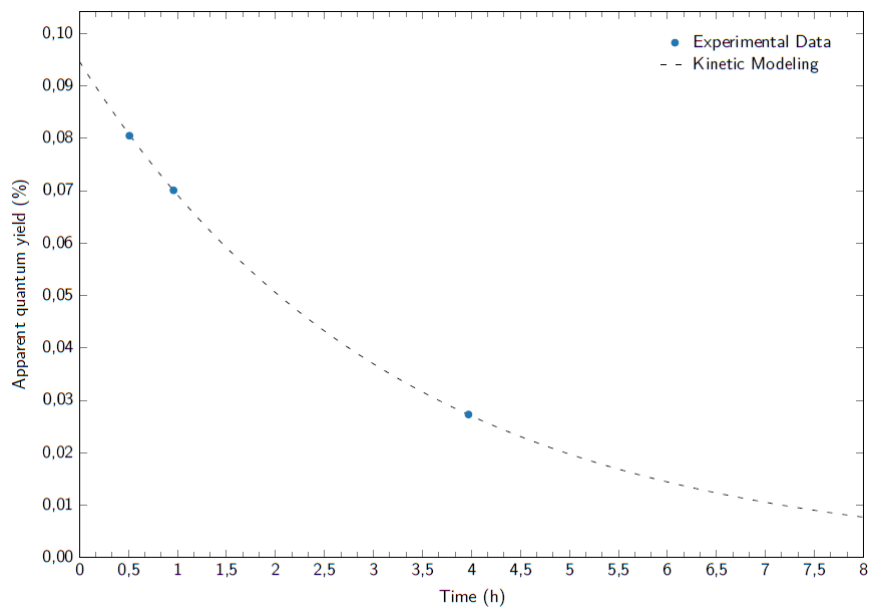
Figure G.38: Apparent quantum yield (%) of ITQ-75, obtained with Compound B as SDA and doped with 0,05wt.% Ni, where the blue dots represent the experimental data and the black dashed line the kinetic modeling
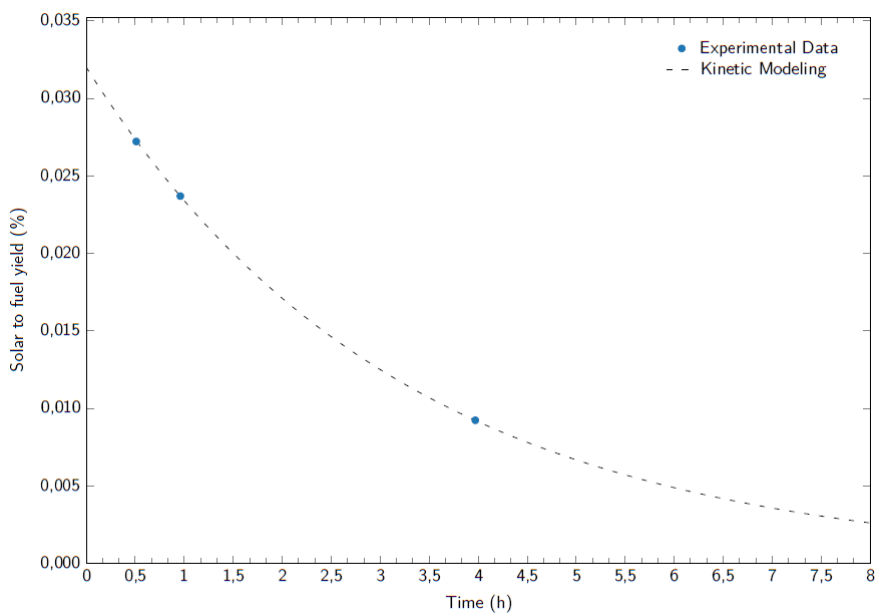
Figure G.39: Solar to fuel yield (%) of ITQ-75, obtained with Compound B as SDA and doped with 0,05wt.% Ni, where the blue dots represent the experimental data and the black dashed line the kinetic modeling

Table G.11: ITQ-75, obtained with Compound B as SDA and doped with 0,05wt.% Ni, main photocatalytic test results

Initial simulated H_2 rate (µmol/h/g)	10,44
Initial simulated apparent quantum yield (%)	0,09
Initial simulated solar-to-fuel yield (%)	0,032
Water splitting apparent kinetic constant k_1 (h^{-1})	$2,31 \cdot 10^{-3}$
Back reaction apparent kinetic constant k_{-1} (h^{-1})	$3,12 \cdot 10^{-1}$
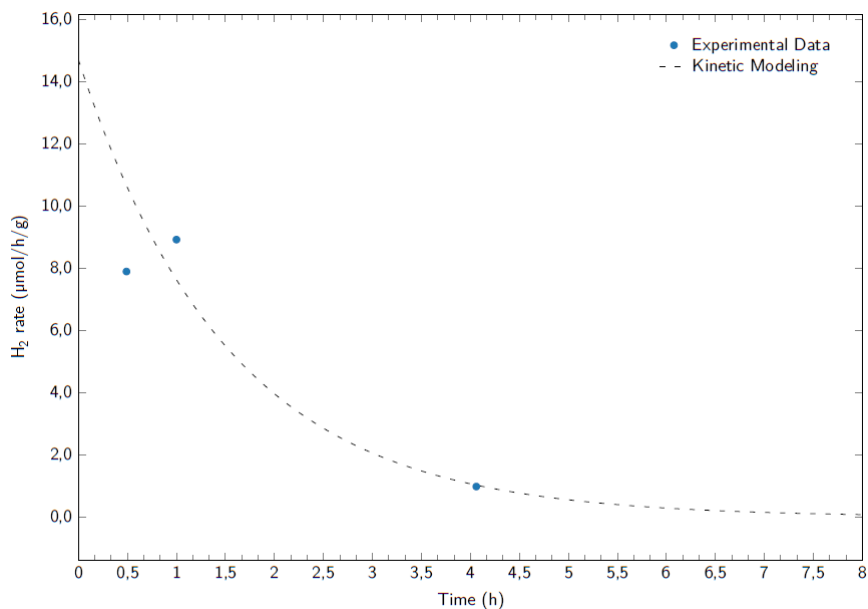
Figure G.40: H$_2$ rate (μmol/h/g) of ITQ-75, obtained with Compound B as SDA and doped with 0,05wt.% Co, where the blue dots represent the experimental data and the black dashed line the kinetic modeling
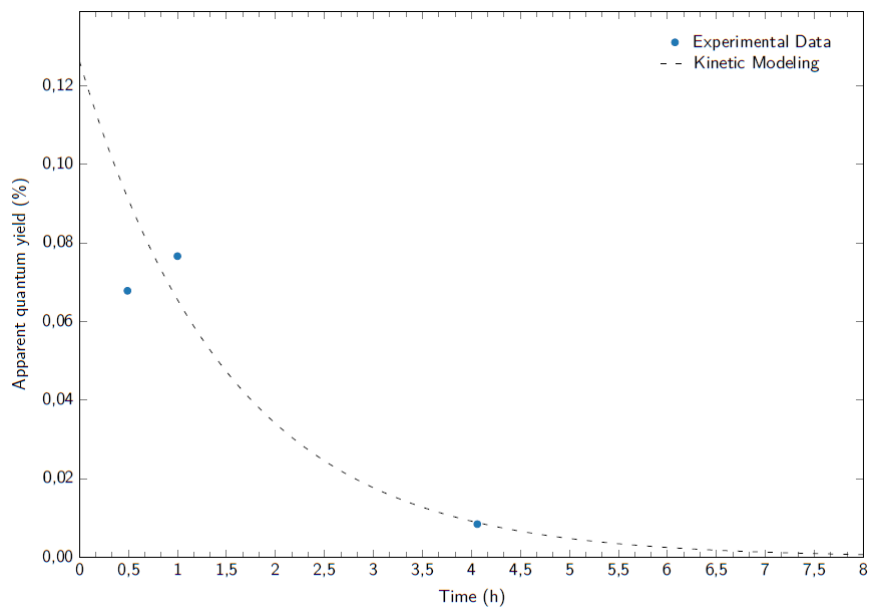
Figure G.41: Apparent quantum yield (%) of ITQ-75, obtained with Compound B as SDA and doped with 0,05wt.% Co, where the blue dots represent the experimental data and the black dashed line the kinetic modeling
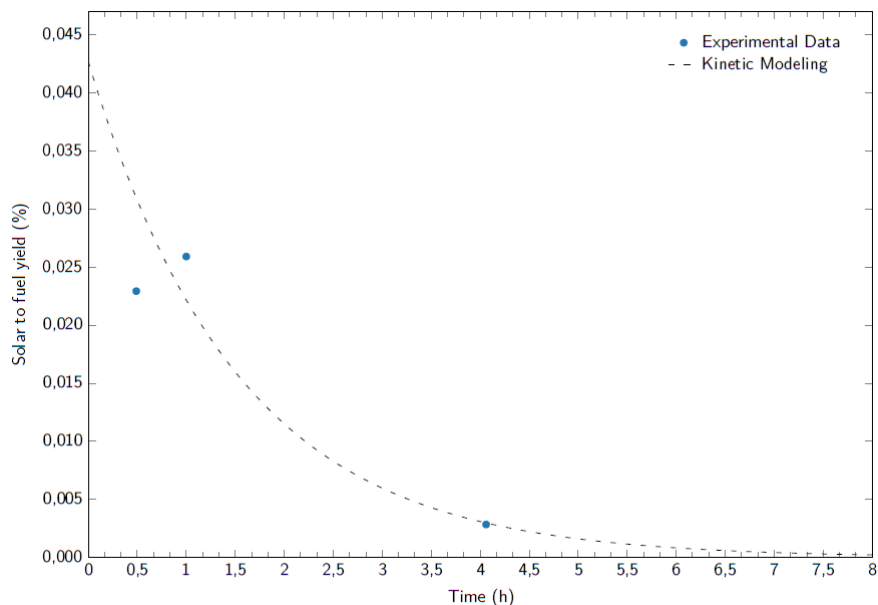
Figure G.42: Solar to fuel yield (%) of ITQ-75, obtained with Compound B as SDA and doped with 0,05wt.% Co, where the blue dots represent the experimental data and the black dashed line the kinetic modeling

Table G.12: ITQ-75, obtained with Compound B as SDA and doped with 0,05wt.% Co, main photocatalytic test results

Initial simulated H_2 rate (μmol/h/g)	10,69
Initial simulated apparent quantum yield (%)	0,13
Initial simulated solar-to-fuel yield (%)	0,043
Water splitting apparent kinetic constant k_1 (h^{-1})	$3,08 \cdot 10^{-3}$
Back reaction apparent kinetic constant k_{-1} (h^{-1})	$6,54 \cdot 10^{-1}$
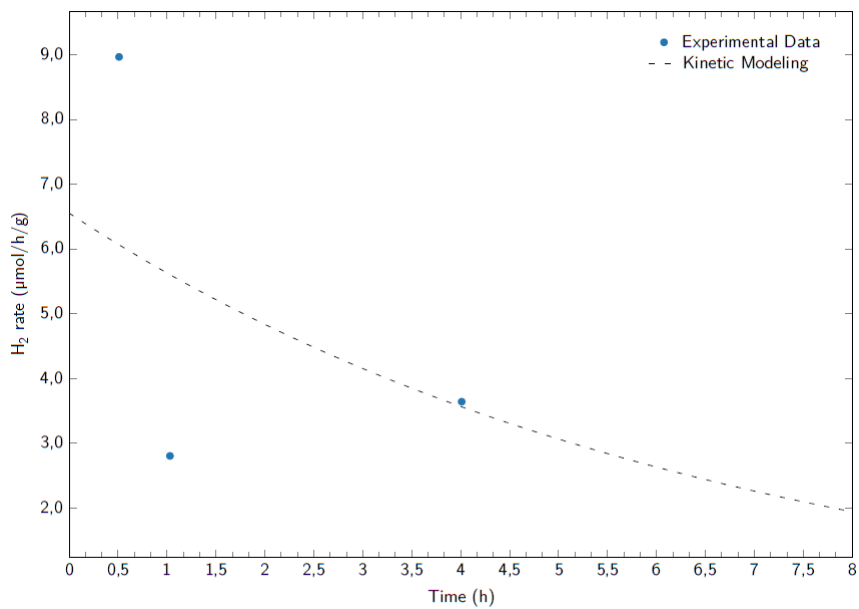
Figure G.43: H$_2$ rate (µmol/h/g) of ITQ-75, obtained with Compound B as SDA and doped with 0,1wt.% Co, where the blue dots represent the experimental data and the black dashed line the kinetic modeling
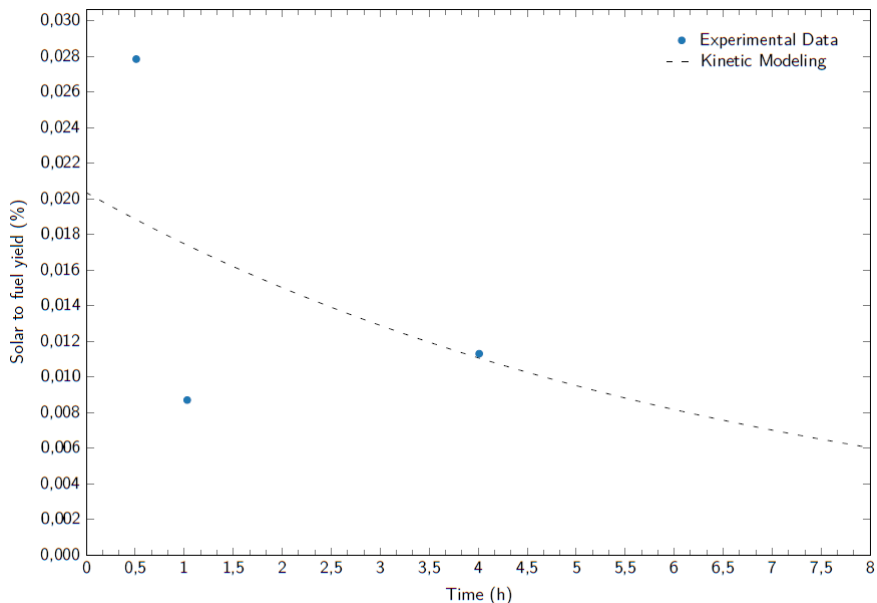
Figure G.44: Solar to fuel yield (%) of ITQ-75, obtained with Compound B as SDA and doped with 0,1wt.% Co, where the blue dots represent the experimental data and the black dashed line the kinetic modeling

Table G.13: ITQ-75, obtained with Compound B as SDA and doped with 0,1wt.% Co, main photocatalytic test results (n.a. - not available)

Initial simulated H_2 rate (µmol/h/g)	6,55
Initial simulated apparent quantum yield (%)	n.a.
Initial simulated solar-to-fuel yield (%)	0,020
Water splitting apparent kinetic constant k_1 (h^{-1})	$1,47 \cdot 10^{-3}$
Back reaction apparent kinetic constant k_{-1} (h^{-1})	$1,51 \cdot 10^{-1}$
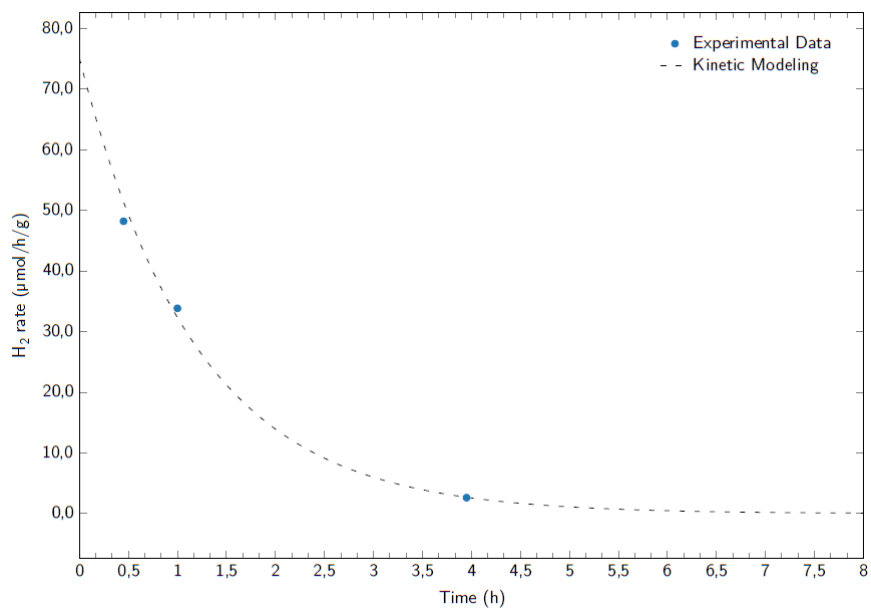
Figure G.45: H_2 rate (μmol/h/g) of ITQ-75, obtained with Compound B as SDA and doped with 0,2wt.% Co, where the blue dots represent the experimental data and the black dashed line the kinetic modeling
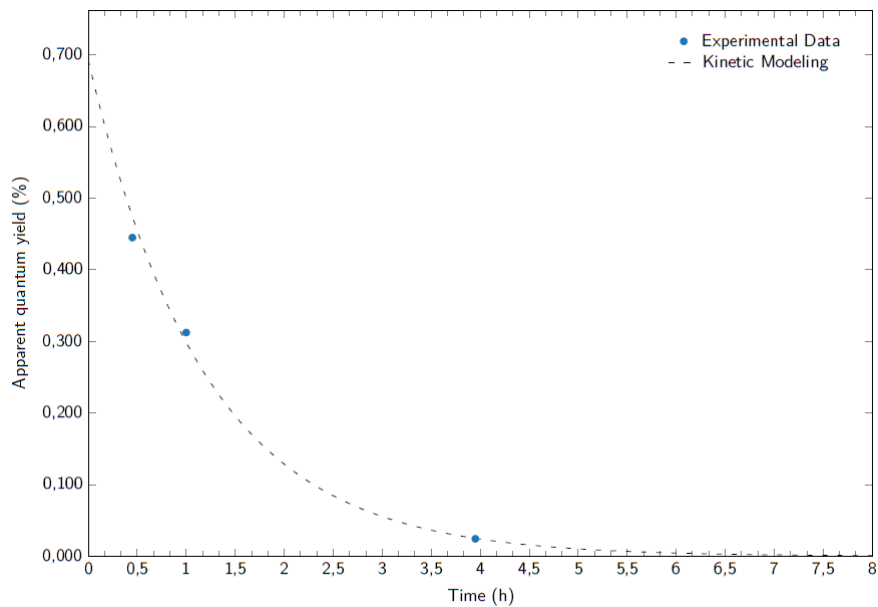
Figure G.46: Apparent quantum yield (%) of ITQ-75, obtained with Compound B as SDA and doped with 0,2wt.% Co, where the blue dots represent the experimental data and the black dashed line the kinetic modeling
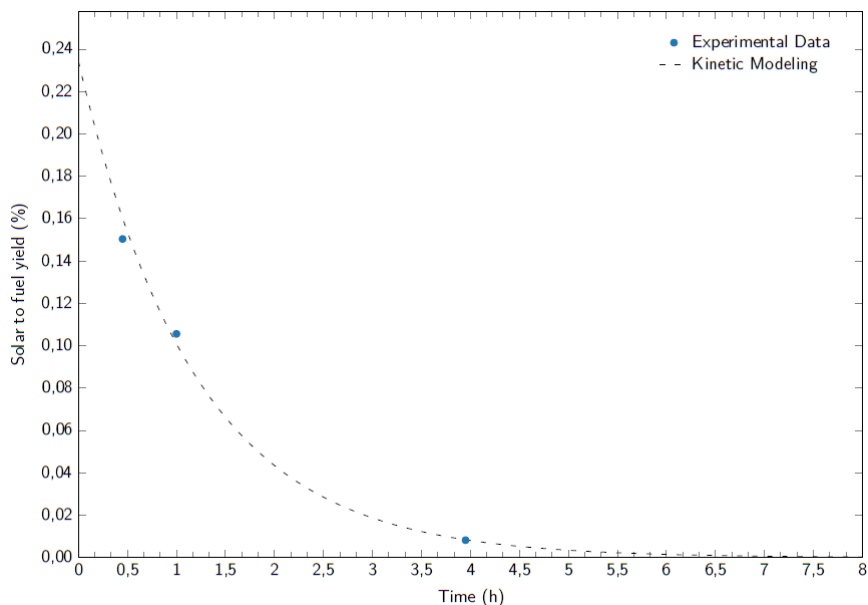
Figure G.47: Solar to fuel yield (%) of ITQ-75, obtained with Compound B as SDA and doped with 0,2wt.% Co, where the blue dots represent the experimental data and the black dashed line the kinetic modeling

Table G.14: ITQ-75, obtained with Compound B as SDA and doped with 0,2wt.% Co, main photocatalytic test results

Initial simulated H_2 rate (μmol/h/g)	75,06
Initial simulated apparent quantum yield (%)	0,69
Initial simulated solar-to-fuel yield (%)	0,23
Water splitting apparent kinetic constant k_1 (h^{-1})	$1,69 \cdot 10^{-2}$
Back reaction apparent kinetic constant k_{-1} (h^{-1})	$8,34 \cdot 10^{-1}$
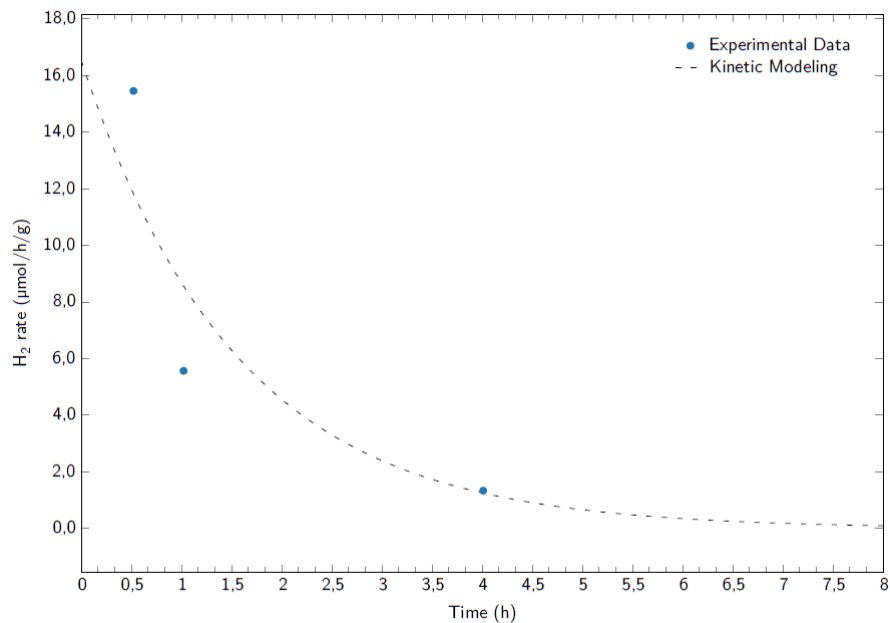
Figure G.48: H_2 rate (µmol/h/g) of ITQ-75, obtained with Compound C as SDA and doped with 0,1wt.% Cu, where the blue dots represent the experimental data and the black dashed line the kinetic modeling
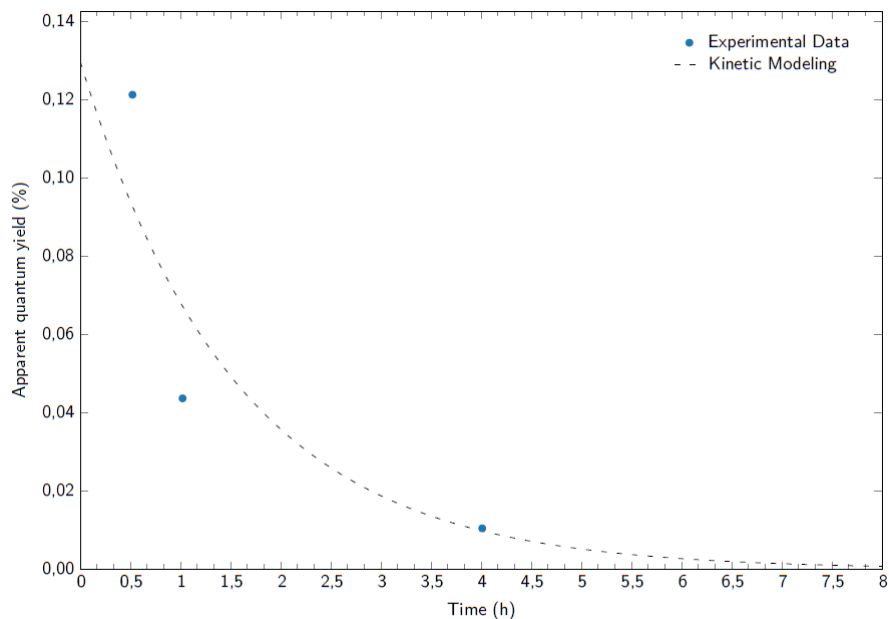
Figure G.49: Apparent quantum yield (%) of ITQ-75, obtained with Compound C as SDA and doped with 0,1wt.% Cu, where the blue dots represent the experimental data and the black dashed line the kinetic modeling
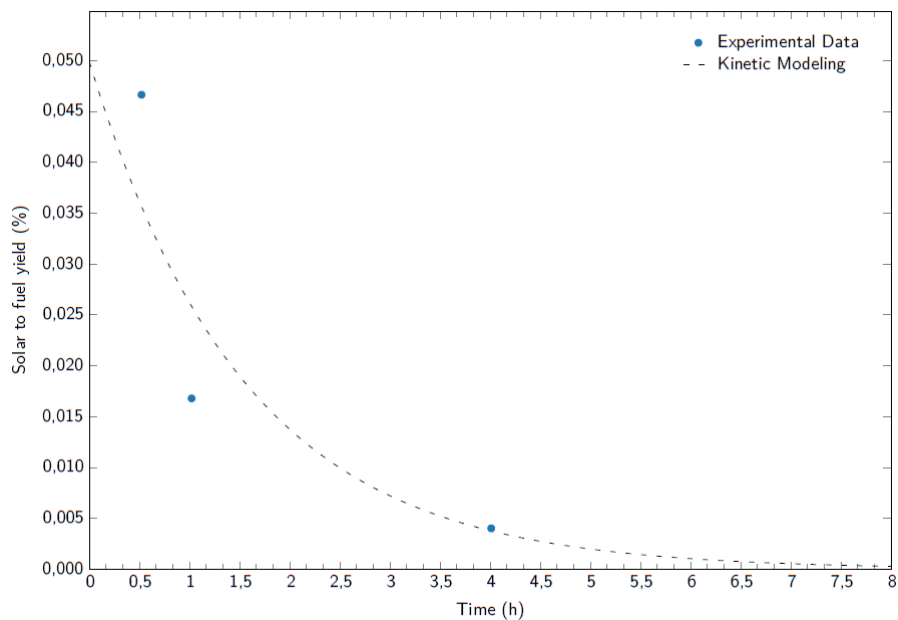
Figure G.50: Solar to fuel yield (%) of ITQ-75, obtained with Compound C as SDA and doped with 0,1wt.% Cu, where the blue dots represent the experimental data and the black dashed line the kinetic modeling

Table G.15: ITQ-75, obtained with Compound C as SDA and doped with 0,1wt.% Cu, main photocatalytic test results

Initial simulated H_2 rate (µmol/h/g)	16,52
Initial simulated apparent quantum yield (%)	0,13
Initial simulated solar-to-fuel yield (%)	0,050
Water splitting apparent kinetic constant k_1 (h^{-1})	$3,59 \cdot 10^{-3}$
Back reaction apparent kinetic constant k_{-1} (h^{-1})	$6,42 \cdot 10^{-1}$
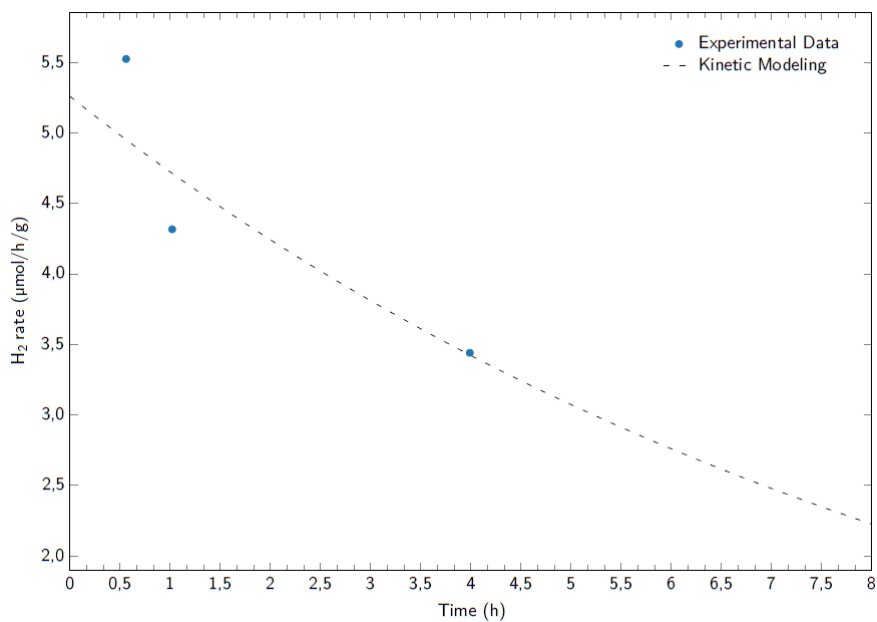
Figure G.51: H$_2$ rate (µmol/h/g) of ITQ-75, obtained with Compound C as SDA and doped with 0,2wt.% Cu, where the blue dots represent the experimental data and the black dashed line the kinetic modeling
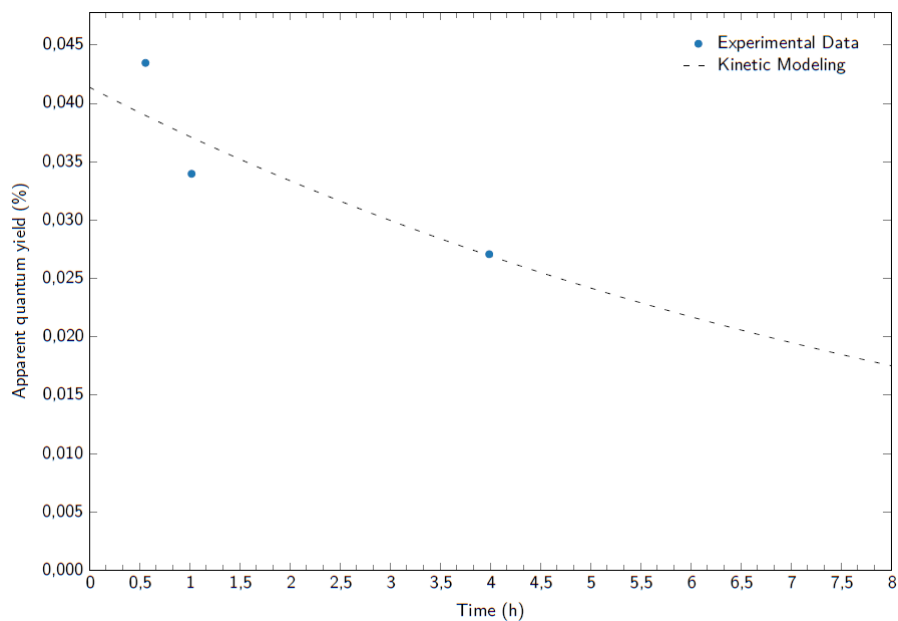
Figure G.52: Apparent quantum yield (%) of ITQ-75, obtained with Compound C as SDA and doped with 0,2wt.% Cu, where the blue dots represent the experimental data and the black dashed line the kinetic modeling
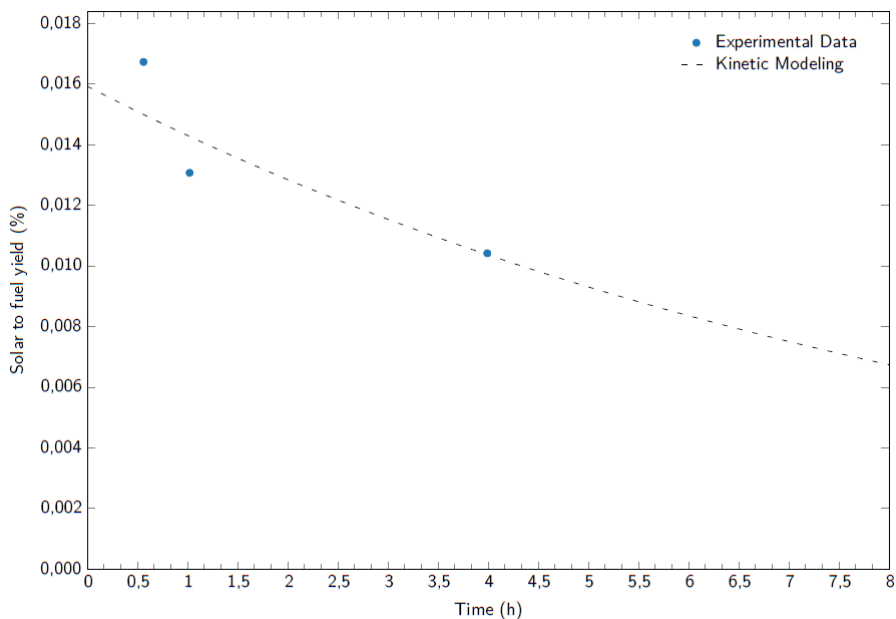
Figure G.53: Solar to fuel yield (%) of ITQ-75, obtained with Compound C as SDA and doped with 0,2wt.% Cu, where the blue dots represent the experimental data and the black dashed line the kinetic modeling

Table G.16: ITQ-75, obtained with Compound C as SDA and doped with 0,2wt.% Cu, main photocatalytic test results

Initial simulated H_2 rate (µmol/h/g)	5,26
Initial simulated apparent quantum yield (%)	0,04
Initial simulated solar-to-fuel yield (%)	0,016
Water splitting apparent kinetic constant k_1 (h^{-1})	$1,15 \cdot 10^{-3}$
Back reaction apparent kinetic constant k_{-1} (h^{-1})	$1,07 \cdot 10^{-1}$
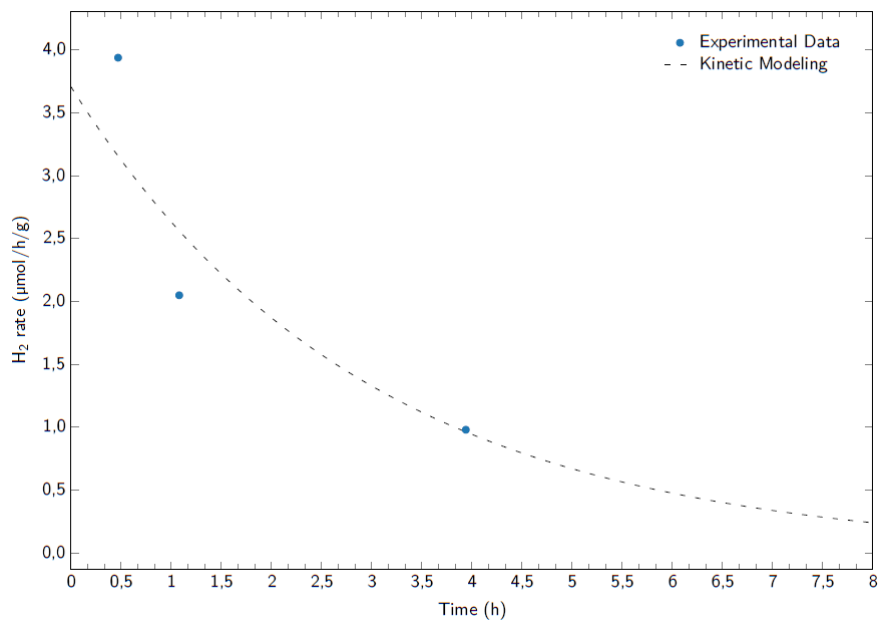
Figure G.54: H_2 rate (µmol/h/g) of ITQ-75, obtained with Compound C as SDA and doped with 0,05wt.% Co, where the blue dots represent the experimental data and the black dashed line the kinetic modeling
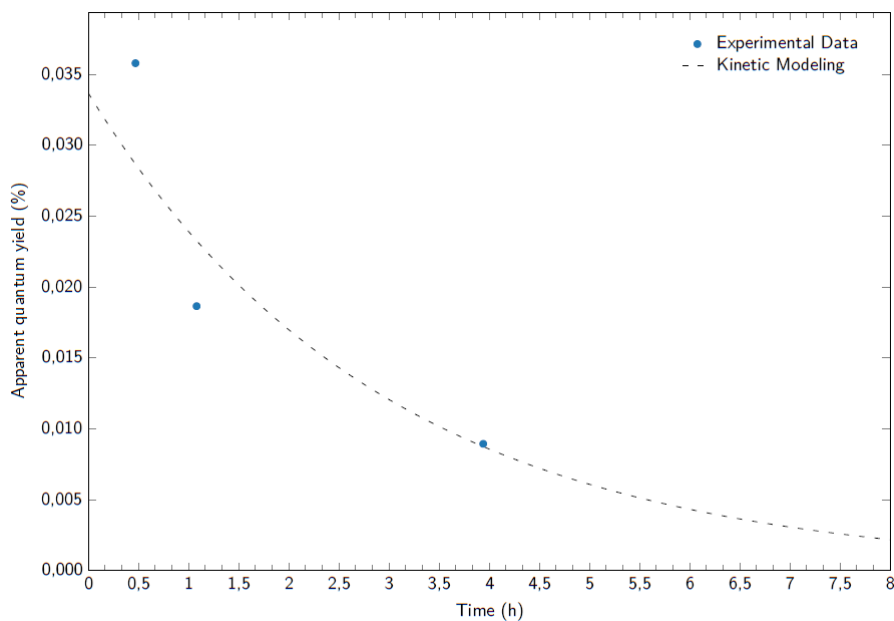
Figure G.55: Apparent quantum yield (%) of ITQ-75, obtained with Compound C as SDA and doped with 0,05wt.% Co, where the blue dots represent the experimental data and the black dashed line the kinetic modeling
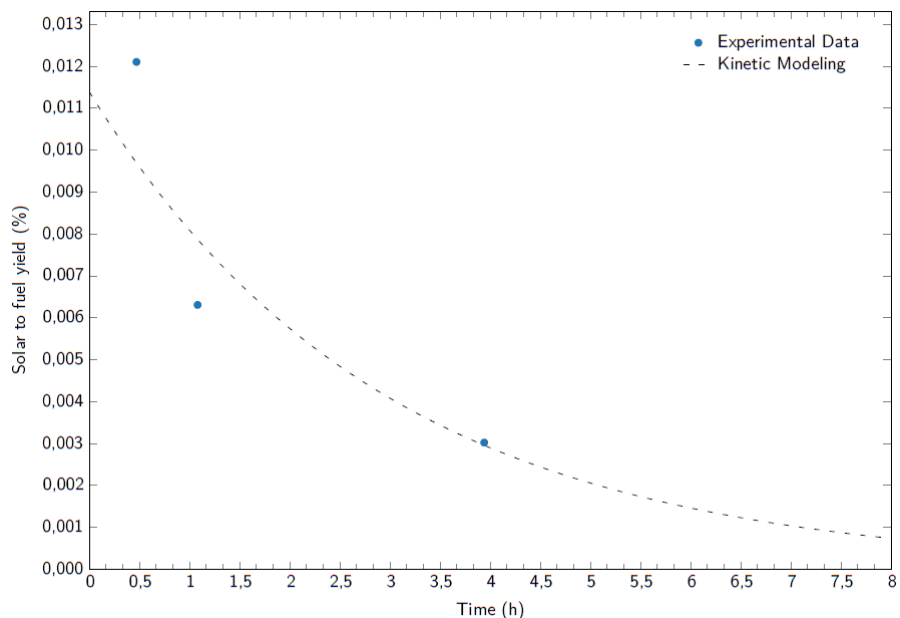
Figure G.56: Solar to fuel yield (%) of ITQ-75, obtained with Compound C as SDA and doped with 0,05wt.% Co, where the blue dots represent the experimental data and the black dashed line the kinetic modeling

Table G.17: ITQ-75, obtained with Compound C as SDA and doped with 0,05wt.% Co, main photocatalytic test results

Initial simulated H_2 rate (µmol/h/g)	3,71
Initial simulated apparent quantum yield (%)	0,03
Initial simulated solar-to-fuel yield (%)	0,011
Water splitting apparent kinetic constant k_1 (h^{-1})	$8,20 \cdot 10^{-4}$
Back reaction apparent kinetic constant k_{-1} (h^{-1})	$3,42 \cdot 10^{-1}$
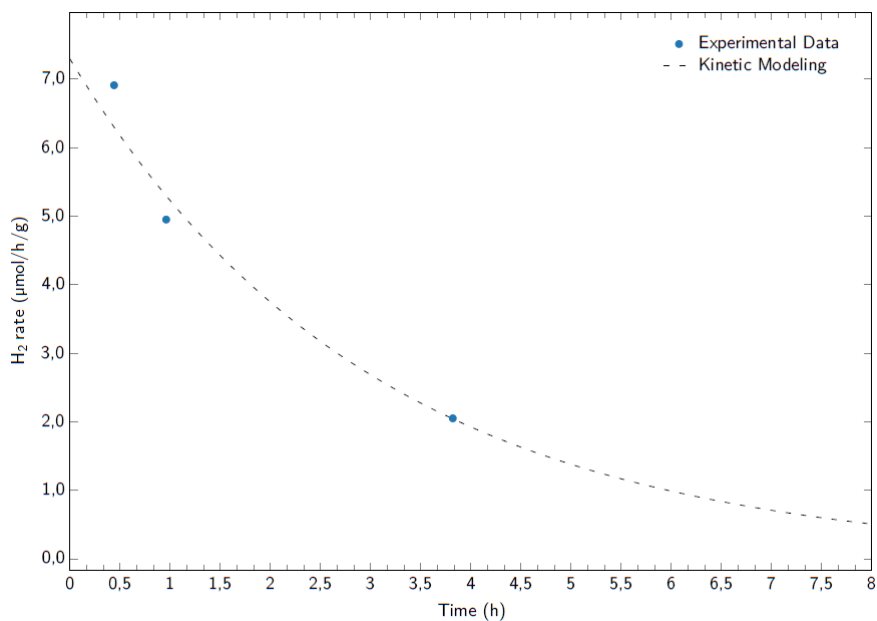
Figure G.57: H$_2$ rate (µmol/h/g) of ITQ-75, obtained with Compound C as SDA and doped with 0,1wt.% Co, where the blue dots represent the experimental data and the black dashed line the kinetic modeling
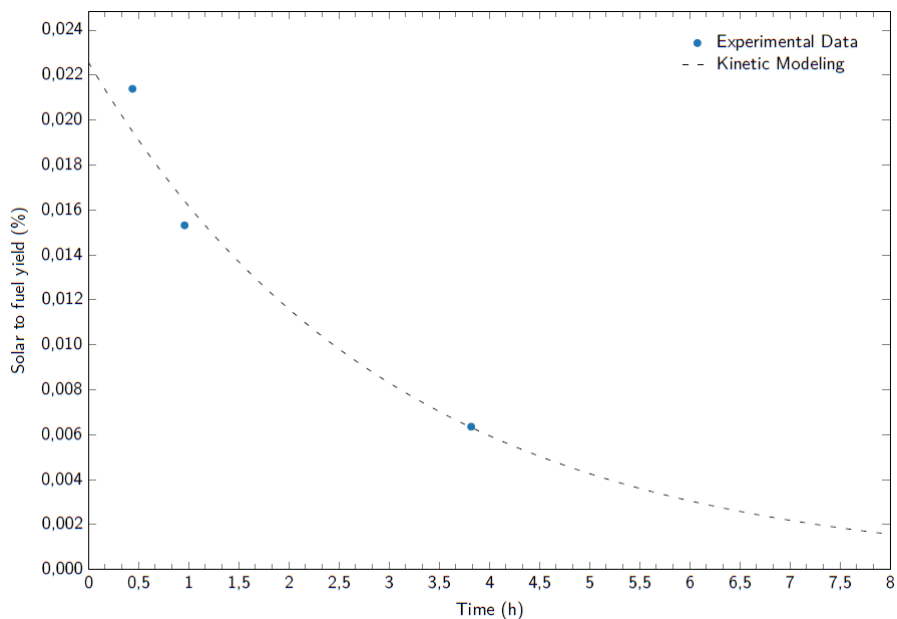
Figure G.58: Solar to fuel yield (%) of ITQ-75, obtained with Compound C as SDA and doped with 0,1wt.% Co, where the blue dots represent the experimental data and the black dashed line the kinetic modeling

Table G.18: ITQ-75, obtained with Compound C as SDA and doped with 0,1wt.% Co, main photocatalytic test results (n.a. - not available)

Initial simulated H_2 rate (µmol/h/g)	7,29
Initial simulated apparent quantum yield (%)	n.a.
Initial simulated solar-to-fuel yield (%)	0,023
Water splitting apparent kinetic constant k_1 (h^{-1})	$1,63 \cdot 10^{-3}$
Back reaction apparent kinetic constant k_{-1} (h^{-1})	$3,32 \cdot 10^{-1}$
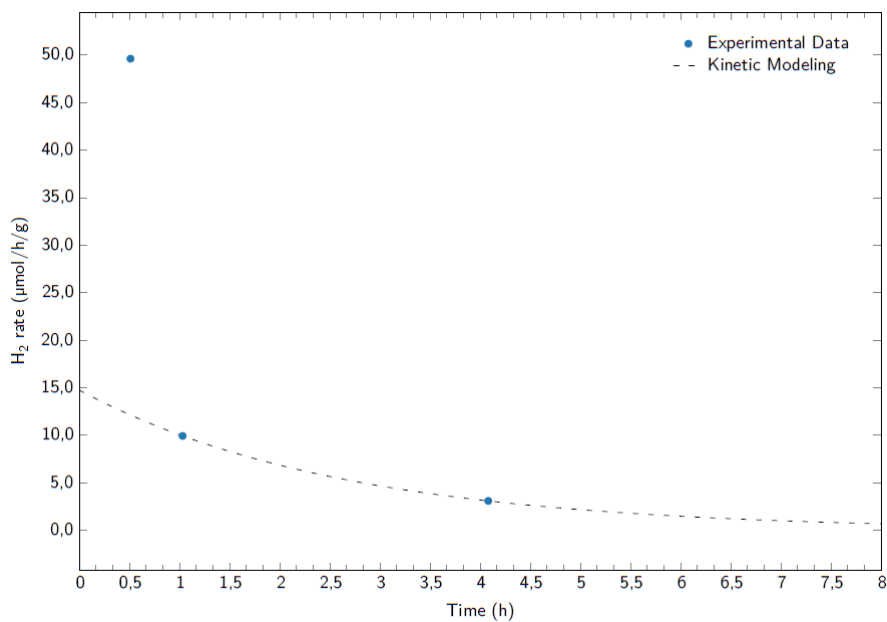
Figure G.59: H$_2$ rate (µmol/h/g) of ITQ-75, obtained with Compound C as SDA and doped with 0,2wt.% Co, where the blue dots represent the experimental data and the black dashed line the kinetic modeling
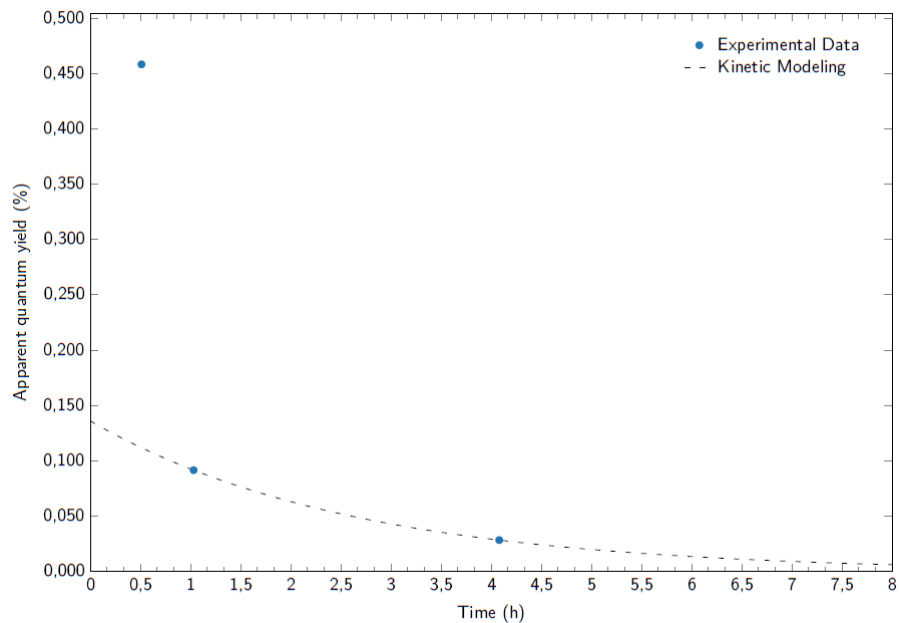
Figure G.60: Apparent quantum yield (%) of ITQ-75, obtained with Compound C as SDA and doped with 0,2wt.% Co, where the blue dots represent the experimental data and the black dashed line the kinetic modeling
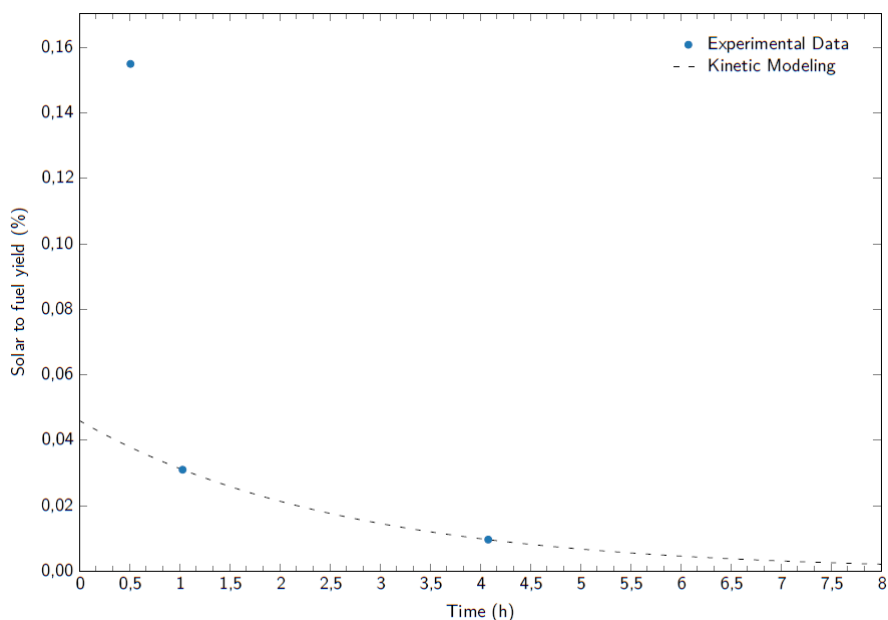
Figure G.61: Solar to fuel yield (%) of ITQ-75, obtained with Compound C as SDA and doped with 0,2wt.% Co, where the blue dots represent the experimental data and the black dashed line the kinetic modeling

Table G.19: ITQ-75, obtained with Compound C as SDA and doped with 0,2wt.% Co, main photocatalytic test results

Initial simulated H_2 rate (µmol/h/g)	14,74
Initial simulated apparent quantum yield (%)	0,14
Initial simulated solar-to-fuel yield (%)	0,046
Water splitting apparent kinetic constant k_1 (h^{-1})	$3,23 \cdot 10^{-3}$
Back reaction apparent kinetic constant k_{-1} (h^{-1})	$3,81 \cdot 10^{-1}$

G.4.3 Accessibility modified samples
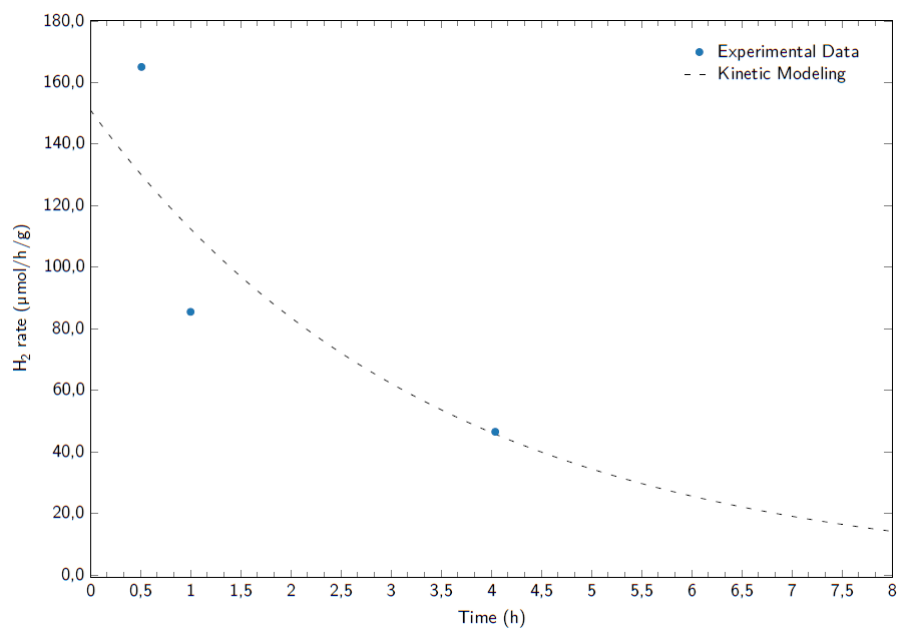
Figure G.62: H_2 rate (µmol/h/g) of ITQ-75, obtained with Compound B as SDA, with a Fructose/SDA B molar ratio equal to 1 and a EG/H_2O molar ratio equal to 3, where the blue dots represent the experimental data and the black dashed line the kinetic modeling
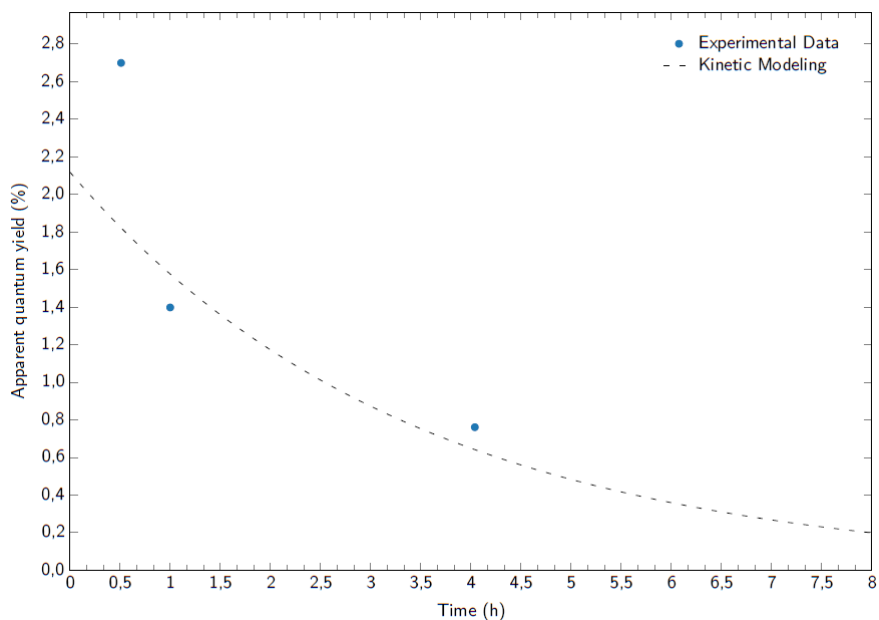
Figure G.63: Apparent quantum yield (%) of ITQ-75, obtained with Compound B as SDA, with a Fructose/SDA B molar ratio equal to 1 and a EG/H_2O molar ratio equal to 3, where the blue dots represent the experimental data and the black dashed line the kinetic modeling
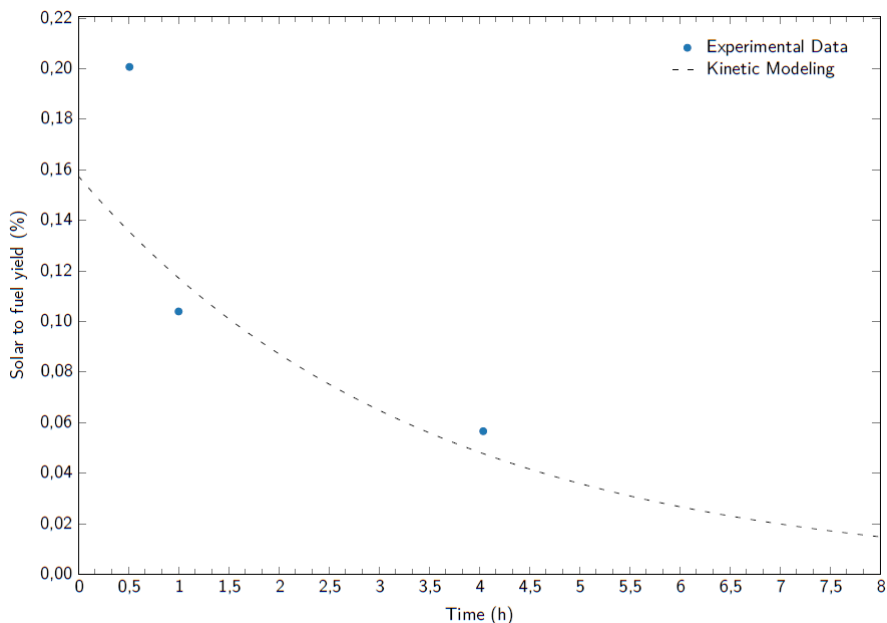
Figure G.64: Solar to fuel yield (%) of ITQ-75, obtained with Compound B as SDA, with a Fructose/SDA B molar ratio equal to 1 and a EG/H$_2$O molar ratio equal to 3, where the blue dots represent the experimental data and the black dashed line the kinetic modeling

Table G.20: ITQ-75, obtained with Compound B as SDA, with a Fructose/SDA B molar ratio equal to 1 and a EG/H$_2$O molar ratio equal to 3, main photocatalytic test results

Initial simulated H$_2$ rate (µmol/h/g)	151,11
Initial simulated apparent quantum yield (%)	2,12
Initial simulated solar-to-fuel yield (%)	0,16
Water splitting apparent kinetic constant k$_1$ (h^{-1})	$1,13 \cdot 10^{-2}$
Back reaction apparent kinetic constant k$_{-1}$ (h^{-1})	$2,90 \cdot 10^{-1}$
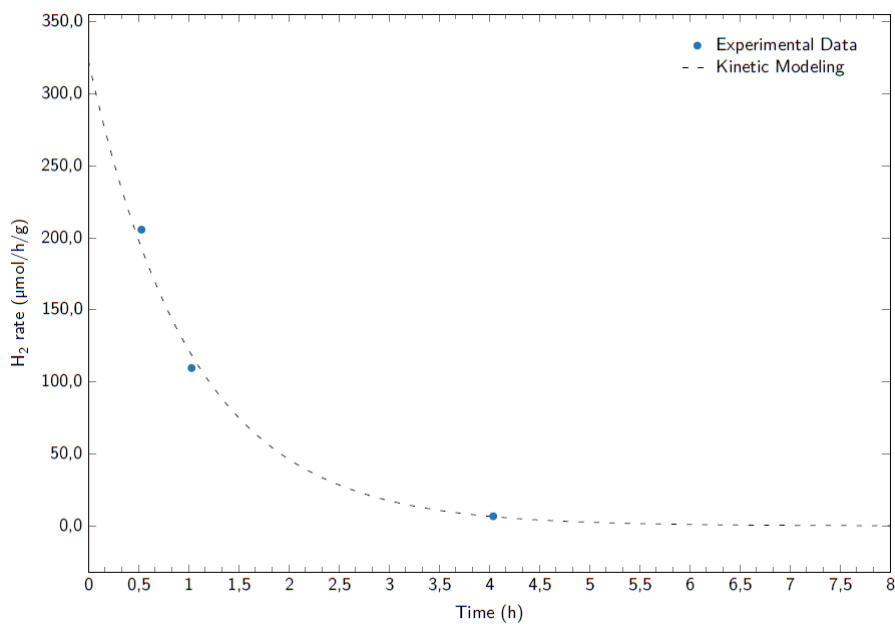
Figure G.65: H$_2$ rate (µmol/h/g) of ITQ-75, obtained with Compound B as SDA and with a Sucrose/SDA B molar ratio equal to 1, where the blue dots represent the experimental data and the black dashed line the kinetic modeling
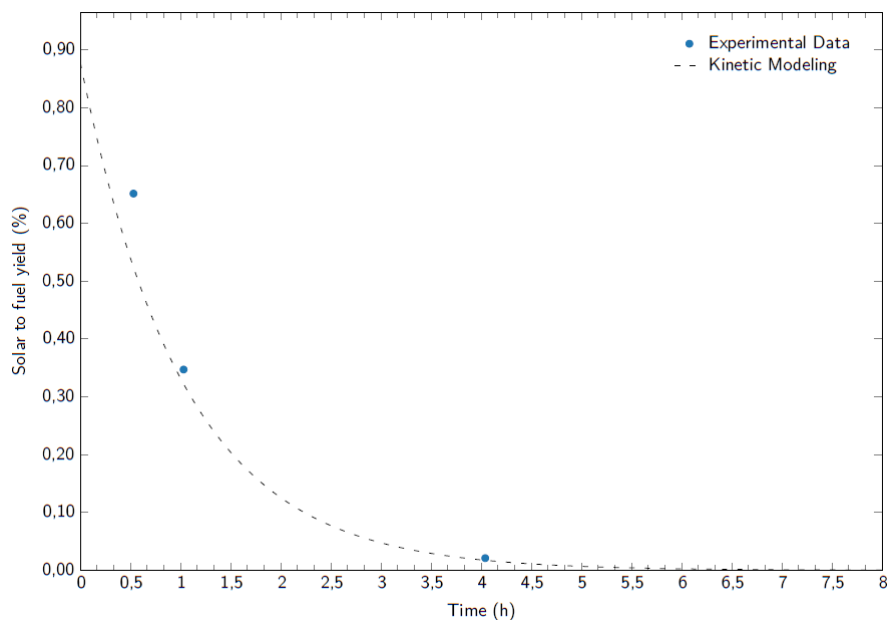
Figure G.66: Solar to fuel yield (%) of ITQ-75, obtained with Compound B as SDA and with a Sucrose/SDA B molar ratio equal to 1, where the blue dots represent the experimental data and the black dashed line the kinetic modeling

Table G.21: ITQ-75, obtained with Compound B as SDA, with a Sucrose/SDA B molar ratio equal to 1, main photocatalytic test results (n.a. - not available)

Initial simulated H$_2$ rate (µmol/h/g)	323,13
Initial simulated apparent quantum yield (%)	n.a.
Initial simulated solar-to-fuel yield (%)	0,88
Water splitting apparent kinetic constant k$_1$ (h^{-1})	$6,32 \cdot 10^{-2}$
Back reaction apparent kinetic constant k$_{-1}$ (h^{-1})	$9,41 \cdot 10^{-1}$
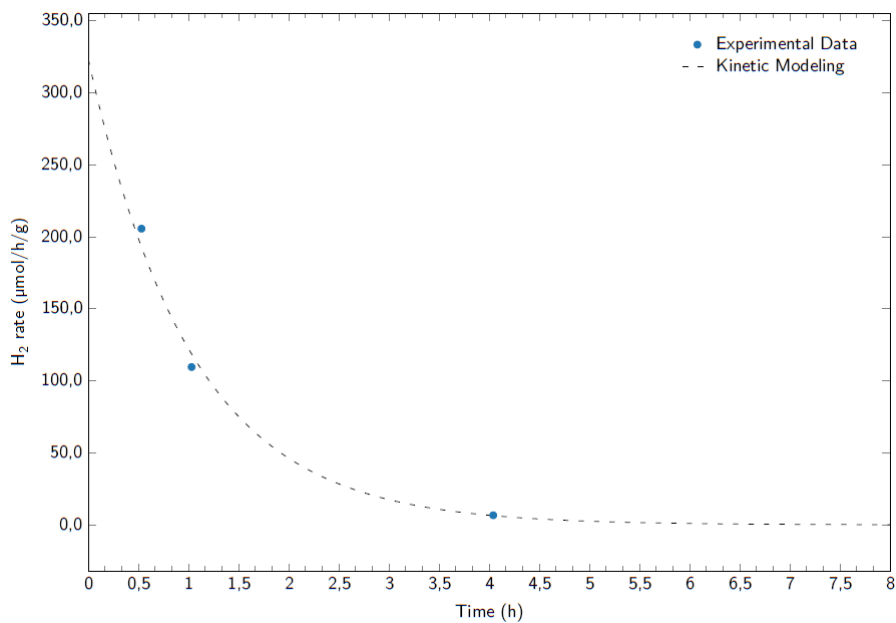
Figure G.67: H$_2$ rate (μmol/h/g) of ITQ-75, obtained with Compound B as SDA and with a Fructose/SDA B molar ratio equal to 1, where the blue dots represent the experimental data and the black dashed line the kinetic modeling
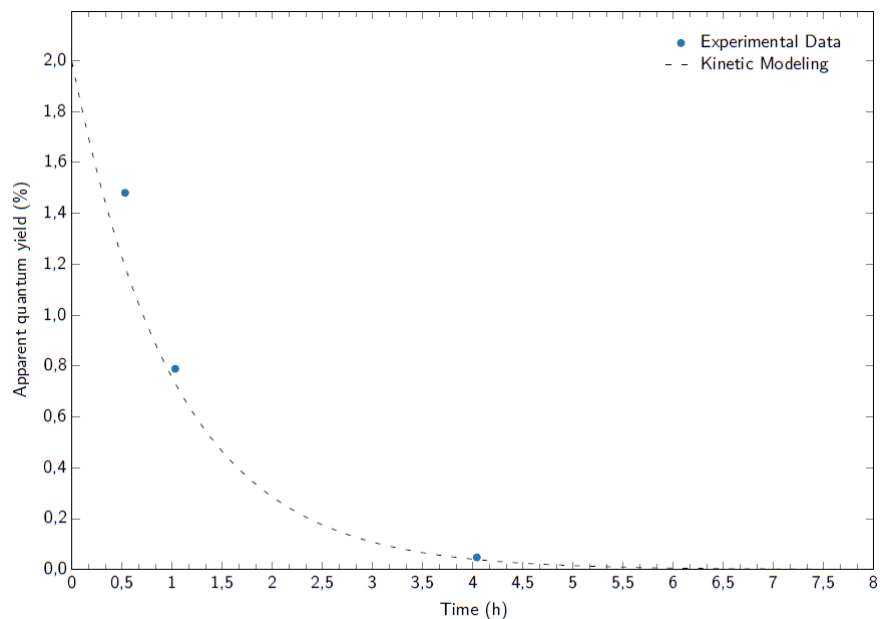
Figure G.68: Apparent quantum yield (%) of ITQ-75, obtained with Compound B as SDA and with a Fructose/SDA B molar ratio equal to 1, where the blue dots represent the experimental data and the black dashed line the kinetic modeling
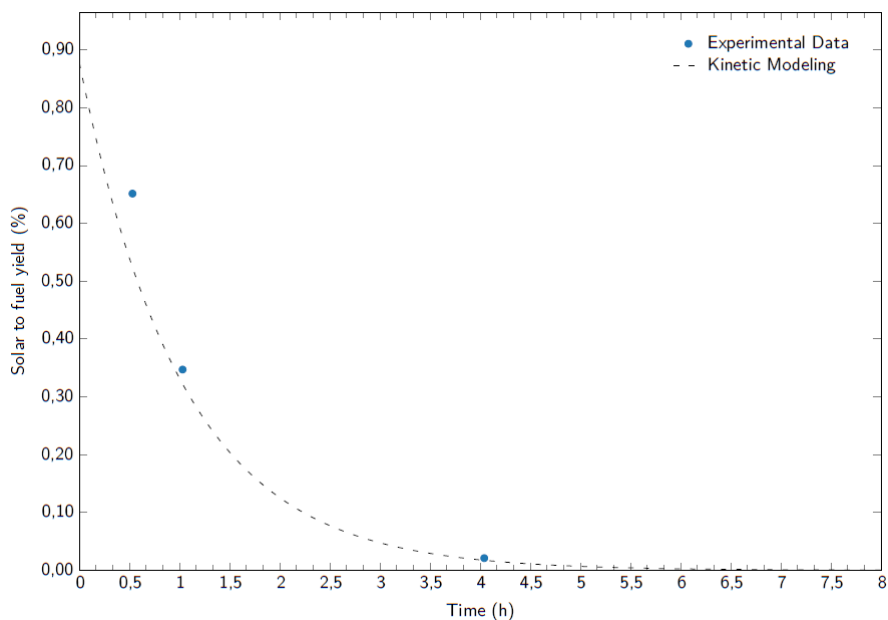
Figure G.69: Solar to fuel yield (%) of ITQ-75, obtained with Compound B as SDA and with a Fructose/SDA B molar ratio equal to 1, where the blue dots represent the experimental data and the black dashed line the kinetic modeling

Table G.22: ITQ-75, obtained with Compound B as SDA, with a Fructose/SDA B molar ratio equal to 1, main photocatalytic test results

Initial simulated H$_2$ rate (µmol/h/g)	86,80
Initial simulated apparent quantum yield (%)	0,42
Initial simulated solar-to-fuel yield (%)	0,19
Water splitting apparent kinetic constant k$_1$ (h^{-1})	$1,34 \cdot 10^{-2}$
Back reaction apparent kinetic constant k$_{-1}$ (h^{-1})	$9,58 \cdot 10^{-1}$
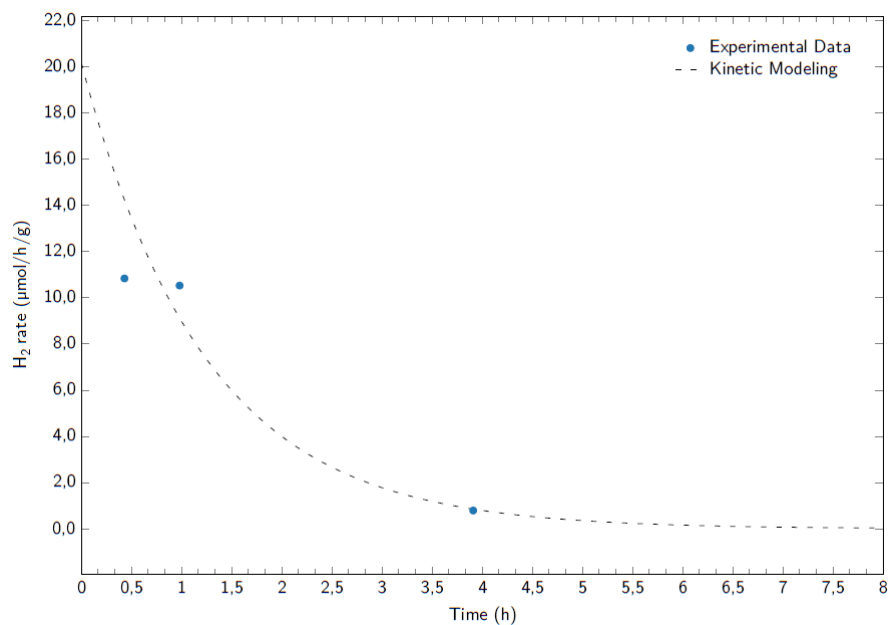
Figure G.70: H_2 rate (μmol/h/g) of ITQ-75, obtained with Compound B as SDA and with a EG/H_2O molar ratio equal to 3, where the blue dots represent the experimental data and the black dashed line the kinetic modeling
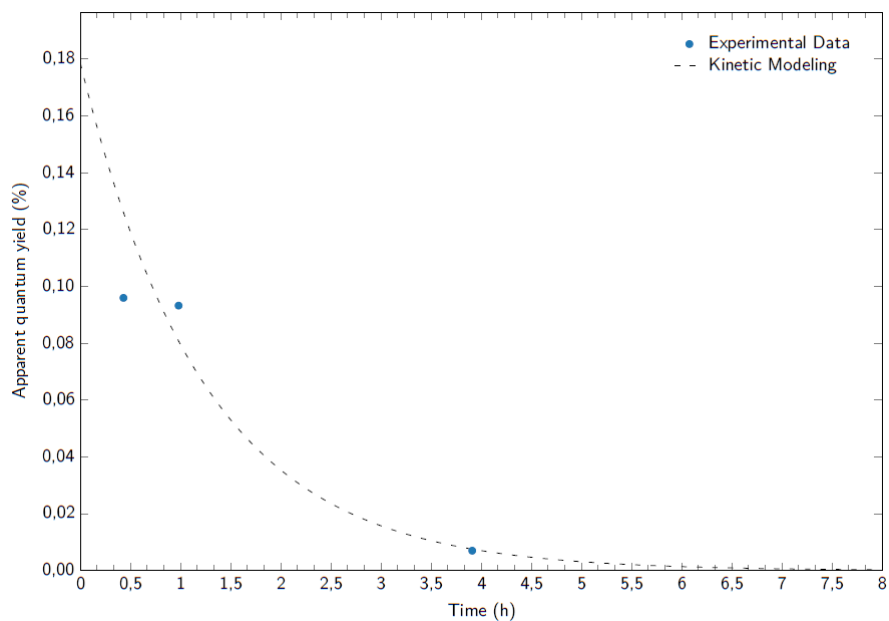
Figure G.71: Apparent quantum yield (%) of ITQ-75, obtained with Compound B as SDA and with a EG/H_2O molar ratio equal to 3, where the blue dots represent the experimental data and the black dashed line the kinetic modeling
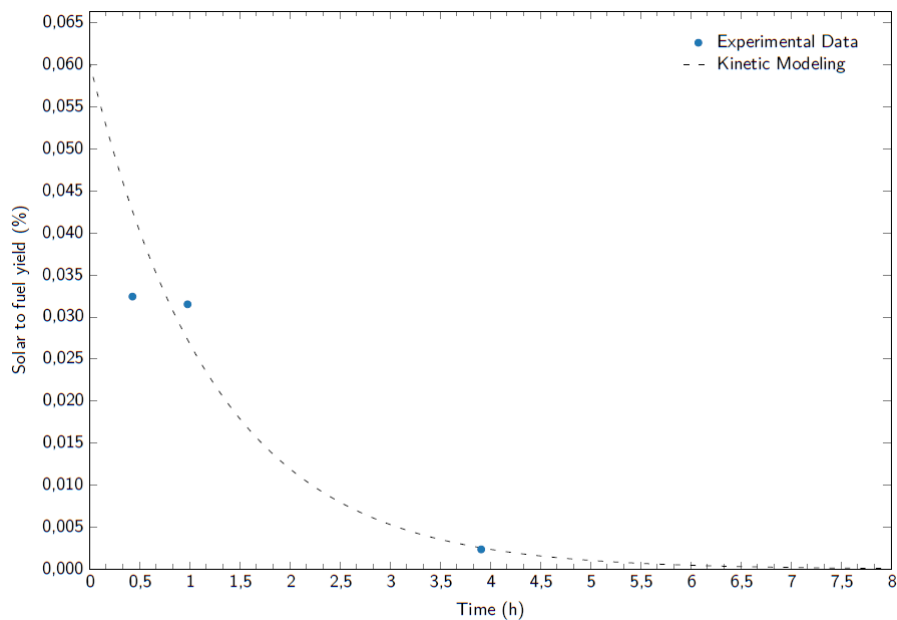
Figure G.72: Solar to fuel yield (%) of ITQ-75, obtained with Compound B as SDA and with a EG/H$_2$O molar ratio equal to 3, where the blue dots represent the experimental data and the black dashed line the kinetic modeling

Table G.23: ITQ-75, obtained with Compound B as SDA and a EG/H$_2$O molar ratio equal to 3, main photocatalytic test results

Initial simulated H$_2$ rate (µmol/h/g)	20,18
Initial simulated apparent quantum yield (%)	0,18
Initial simulated solar-to-fuel yield (%)	0,060
Water splitting apparent kinetic constant k$_1$ (h^{-1})	4,35 · 10^{-3}
Back reaction apparent kinetic constant k$_{-1}$ (h^{-1})	8,07 · 10^{-1}
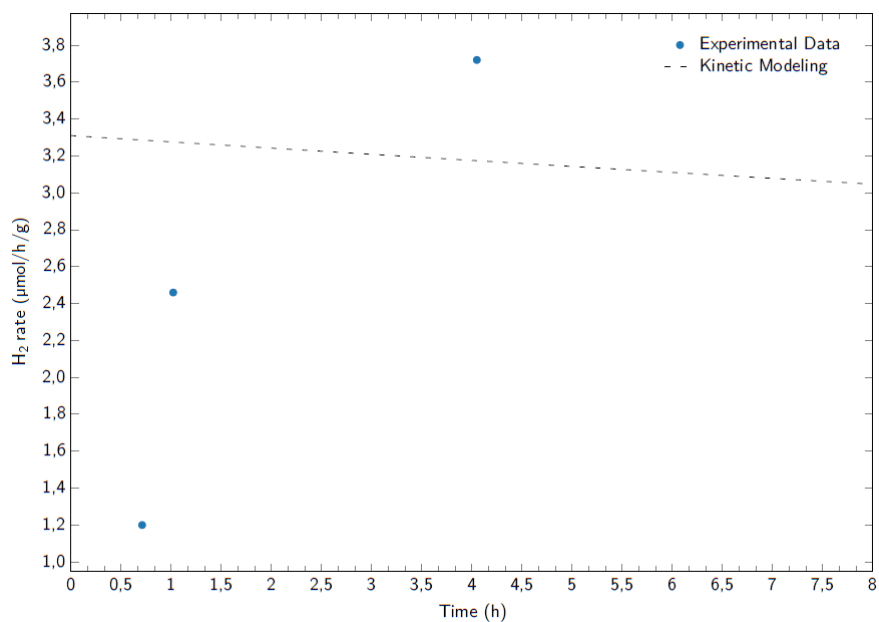
Figure G.73: H_2 rate (µmol/h/g) of ITQ-75, obtained with Compound C as SDA and with a Fructose/SDA B molar ratio equal to 1, where the blue dots represent the experimental data and the black dashed line the kinetic modeling
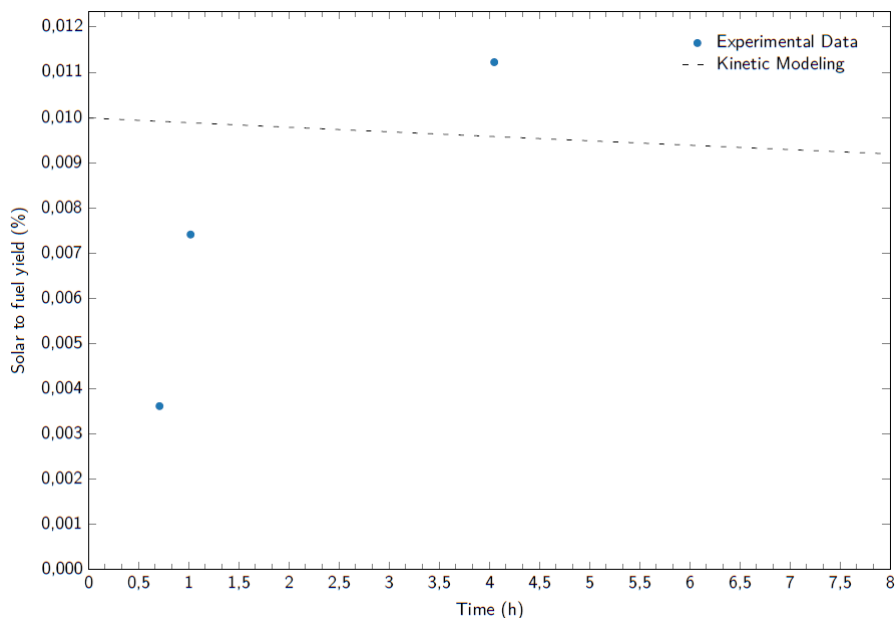
Figure G.74: Solar to fuel yield (%) of ITQ-75, obtained with Compound C as SDA and with a Fructose/SDA C molar ratio equal to 1, where the blue dots represent the experimental data and the black dashed line the kinetic modeling

Table G.24: ITQ-75, obtained with Compound C as SDA, with a Fructose/SDA C molar ratio equal to 1, main photocatalytic test results (n.a. - not available; [a] abitrary value for fit)

Initial simulated H$_2$ rate (μmol/h/g)	3,31
Initial simulated apparent quantum yield (%)	n.a.
Initial simulated solar-to-fuel yield (%)	0,010
Water splitting apparent kinetic constant k$_1$ (h^{-1})	7,20 · 10^{-4}
Back reaction apparent kinetic constant k$_{-1}$ (h^{-1})	1,00 · 10^{-10} [a]
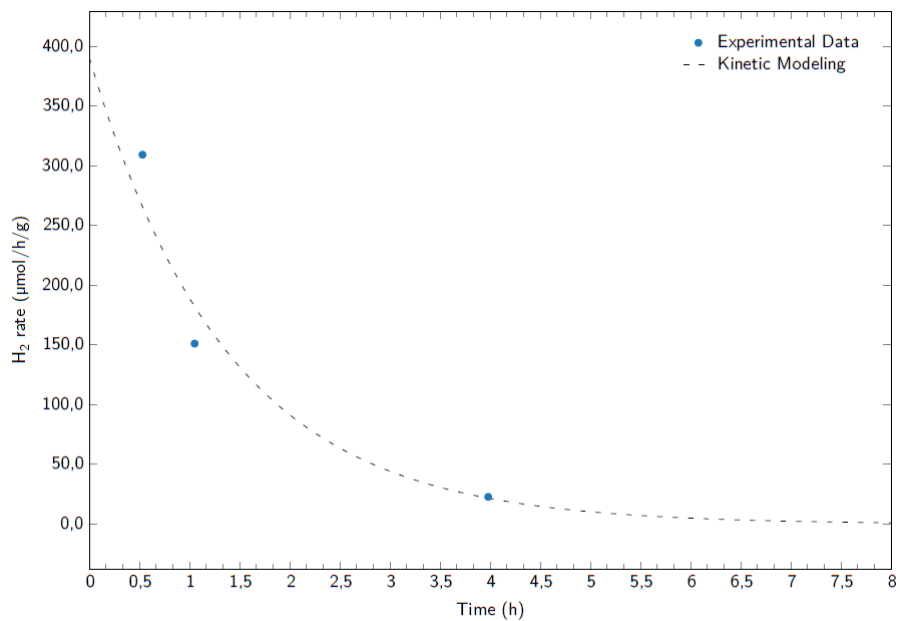
Figure G.75: H$_2$ rate (µmol/h/g) of ITQ-75, obtained with Compound C as SDA and with a Sucrose/SDA C molar ratio equal to 1, where the blue dots represent the experimental data and the black dashed line the kinetic modeling
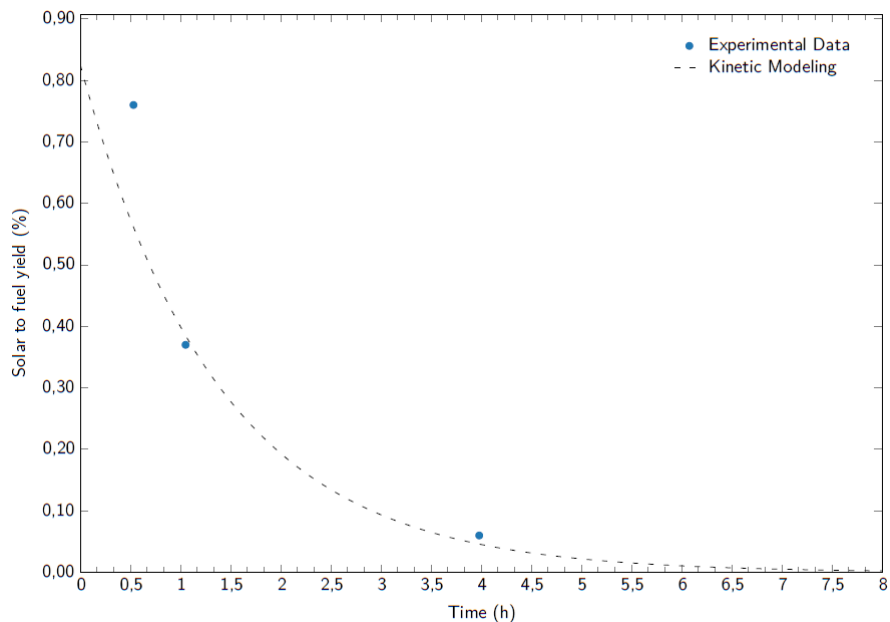
Figure G.76: Solar to fuel yield (%) of ITQ-75, obtained with Compound C as SDA and with a Sucrose/SDA C molar ratio equal to 1, where the blue dots represent the experimental data and the black dashed line the kinetic modeling

Table G.25: ITQ-75, obtained with Compound C as SDA, with a Sucrose/SDA C molar ratio equal to 1, main photocatalytic test results (n.a. - not available)

Initial simulated H_2 rate (µmol/h/g)	390,54
Initial simulated apparent quantum yield (%)	n.a.
Initial simulated solar-to-fuel yield (%)	0,83
Water splitting apparent kinetic constant k_1 (h^{-1})	$5,94 \cdot 10^{-2}$
Back reaction apparent kinetic constant k_{-1} (h^{-1})	$6,96 \cdot 10^{-1}$
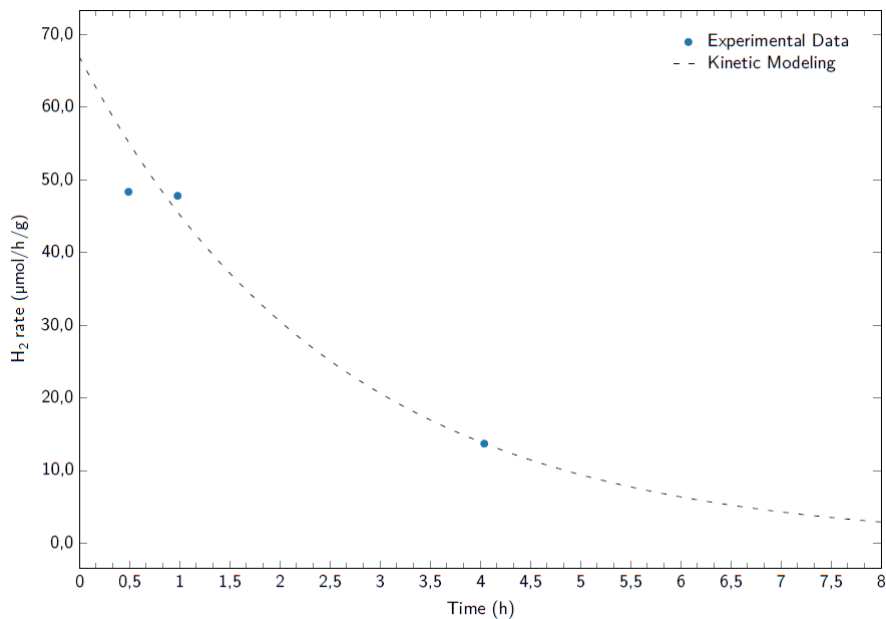
Figure G.77: H_2 rate (μmol/h/g) of ITQ-75, obtained with Compound C as SDA and after the Ball Mill treatment, where the blue dots represent the experimental data and the black dashed line the kinetic modeling
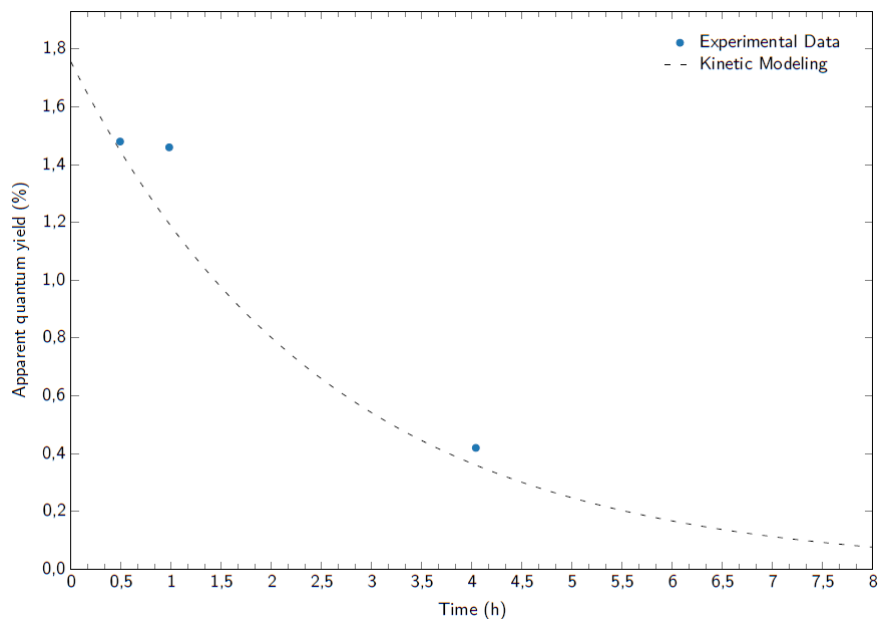
Figure G.78: Apparent quantum yield (%) of ITQ-75, obtained with Compound C as SDA and after the Ball Mill treatment, where the blue dots represent the experimental data and the black dashed line the kinetic modeling
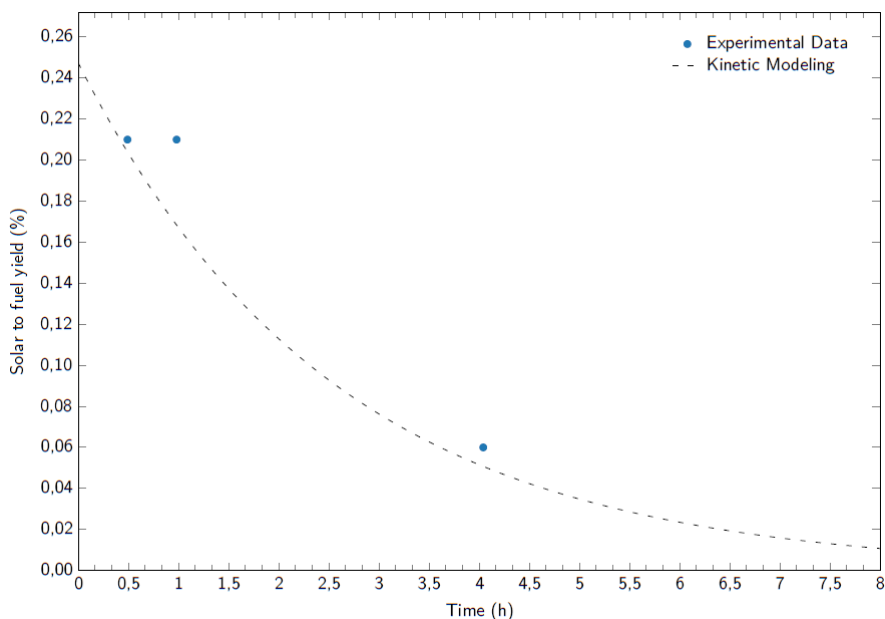
Figure G.79: Solar to fuel yield (%) of ITQ-75, obtained with Compound C as SDA and after the Ball Mill treatment, where the blue dots represent the experimental data and the black dashed line the kinetic modeling

Table G.26: ITQ-75, obtained with Compound C as SDA and after Ball Mill treatment, main photocatalytic test results

Initial simulated H_2 rate (µmol/h/g)	66,92
Initial simulated apparent quantum yield (%)	1,76
Initial simulated solar-to-fuel yield (%)	0,25
Water splitting apparent kinetic constant k_1 (h^{-1})	$1,78 \cdot 10^{-2}$
Back reaction apparent kinetic constant k_{-1} (h^{-1})	$3,83 \cdot 10^{-1}$
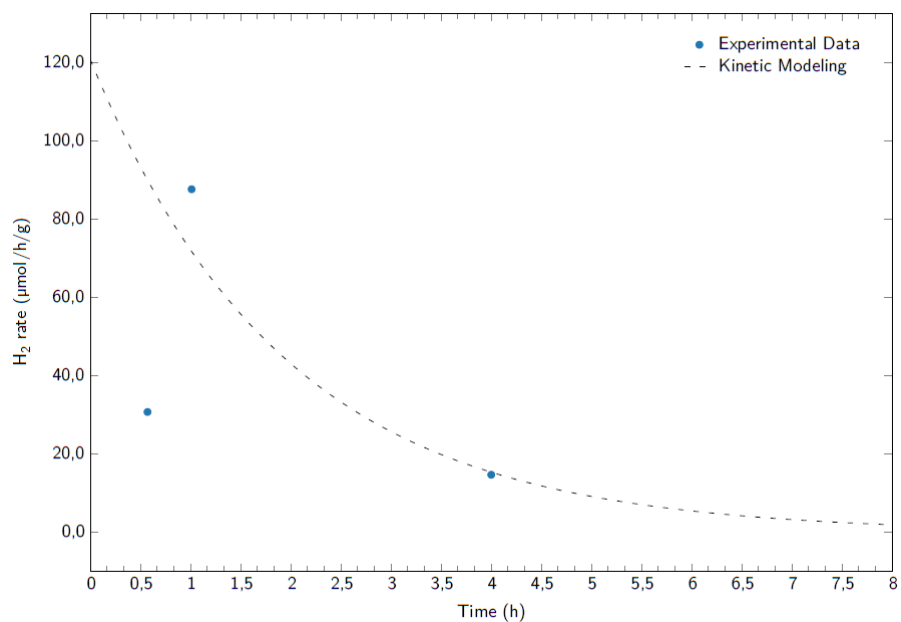
Figure G.80: H_2 rate (µmol/h/g) of ITQ-75, obtained with Compound C as SDA and after the BuLi treatment (recovered pellet), where the blue dots represent the experimental data and the black dashed line the kinetic modeling
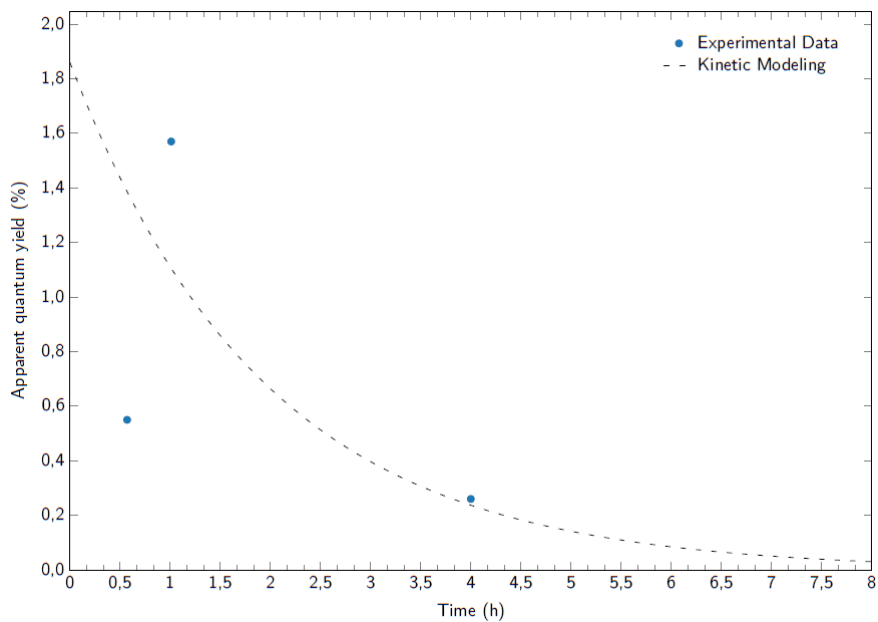
Figure G.81: Apparent quantum yield (%) of ITQ-75, obtained with Compound C as SDA and after the BuLi treatment (recovered pellet), where the blue dots represent the experimental data and the black dashed line the kinetic modeling
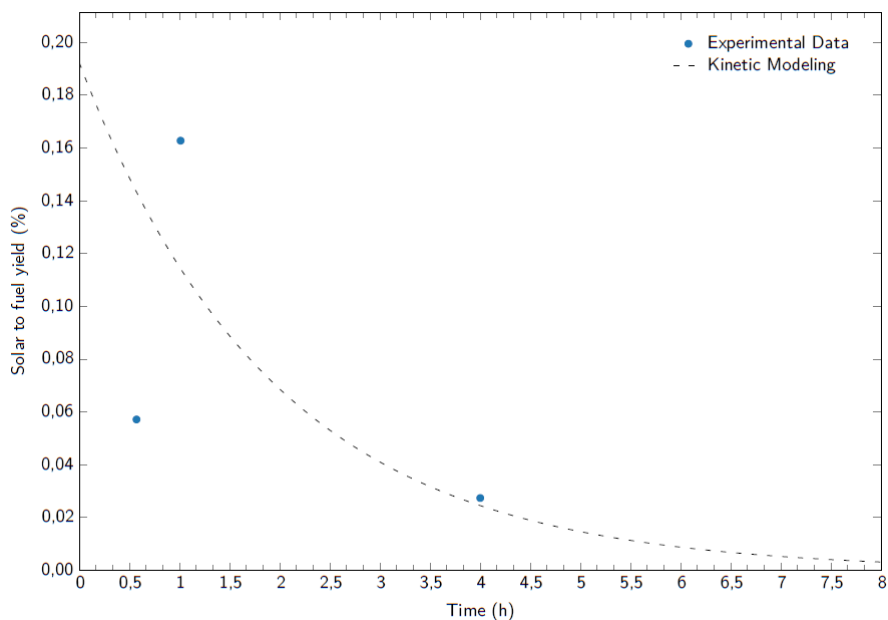
Figure G.82: Solar to fuel yield (%) of ITQ-75, obtained with Compound C as SDA and after the BuLi treatment (recovered pellet), where the blue dots represent the experimental data and the black dashed line the kinetic modeling

Table G.27: ITQ-75, obtained with Compound C as SDA and after the BuLi treatment (recovered pellet), main photocatalytic test results

Initial simulated H_2 rate (µmol/h/g)	120,75
Initial simulated apparent quantum yield (%)	1,86
Initial simulated solar-to-fuel yield (%)	0,19
Water splitting apparent kinetic constant k_1 (h^{-1})	$1,38 \cdot 10^{-2}$
Back reaction apparent kinetic constant k_{-1} (h^{-1})	$5,08 \cdot 10^{-1}$

G.4.4   Accessibility and doped modified samples
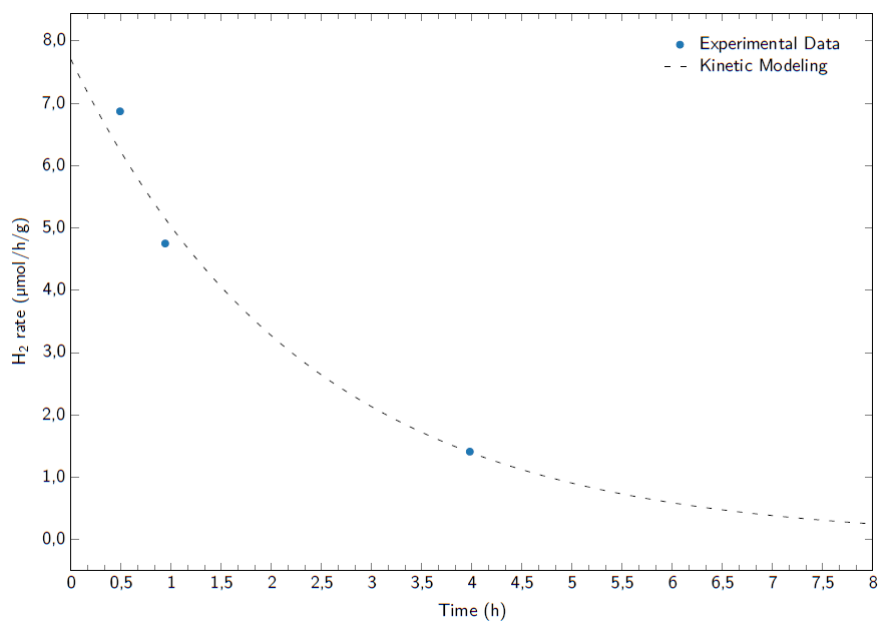
Figure G.83: H_2 rate (µmol/h/g) of ITQ-75, obtained with Compound B as SDA, with a Fructose/SDA B molar ratio equal to 1 and 0,1wt.% Cu, where the blue dots represent the experimental data and the black dashed line the kinetic modeling
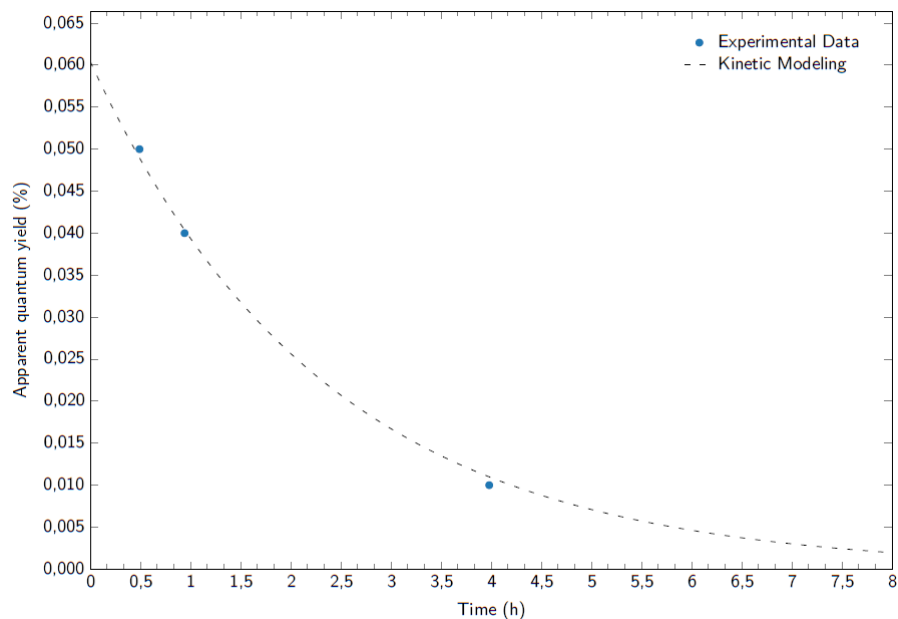
Figure G.84: Apparent quantum yield (&) of ITQ-75, obtained with Compound B as SDA, with a Fructose/SDA B molar ratio equal to 1 and 0,1wt.% Cu, where the blue dots represent the experimental data and the black dashed line the kinetic modeling
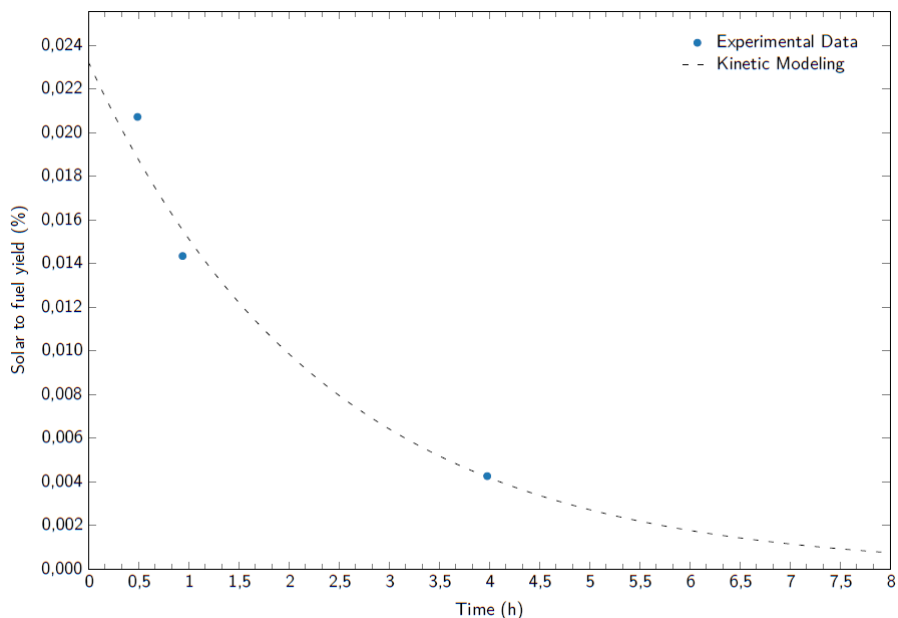
Figure G.85: Solar to fuel yield (&) of ITQ-75, obtained with Compound B as SDA, with a Fructose/SDA B molar ratio equal to 1 and 0,1wt.% Cu, where the blue dots represent the experimental data and the black dashed line the kinetic modeling

Table G.28: ITQ-75, obtained with Compound B as SDA, with a Fructose/SDA B molar ratio equal to 1 and 0,1wt.% Cu, main photocatalytic test results

Initial simulated H$_2$ rate (μmol/h/g)	7,70
Initial simulated apparent quantum yield (%)	0,06
Initial simulated solar-to-fuel yield (%)	0,023
Water splitting apparent kinetic constant k$_1$ (h^{-1})	$1,67 \cdot 10^{-3}$
Back reaction apparent kinetic constant k$_{-1}$ (h^{-1})	$4,27 \cdot 10^{-1}$
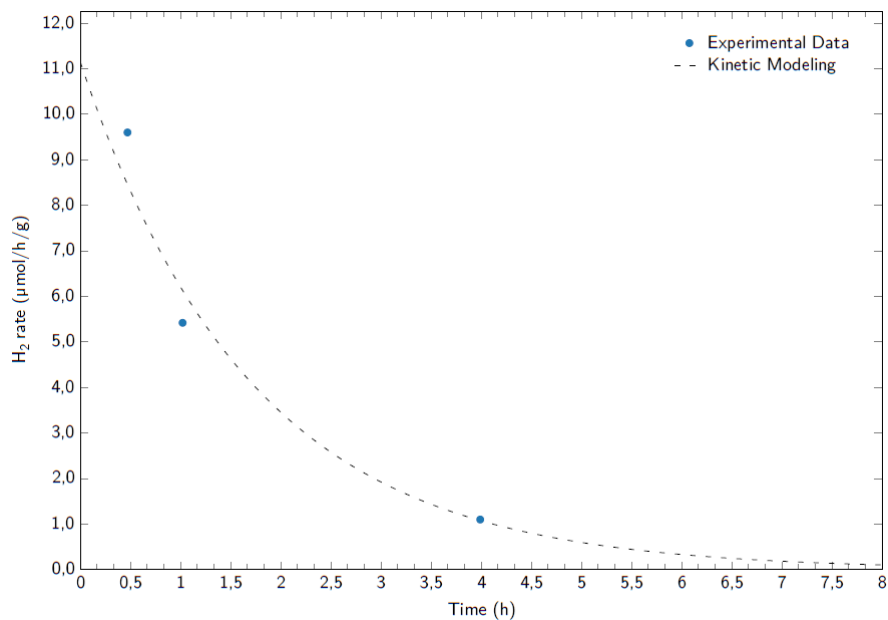
Figure G.86: H_2 rate (µmol/h/g) of ITQ-75, obtained with Compound B as SDA, with a Fructose/SDA B molar ratio equal to 1 and 0,1wt.% Co, where the blue dots represent the experimental data and the black dashed line the kinetic modeling
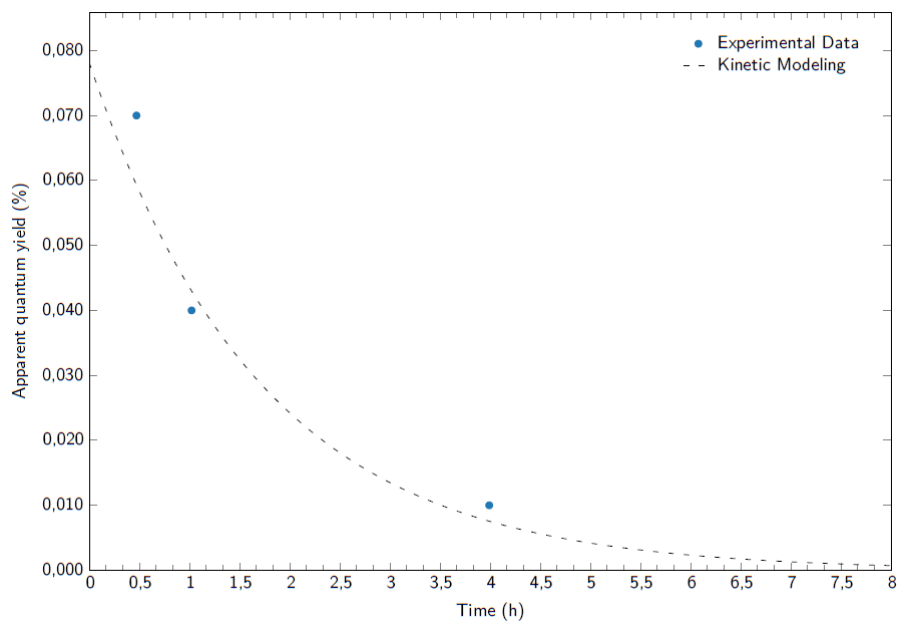
Figure G.87: Apparent quantum yield (&) of ITQ-75, obtained with Compound B as SDA, with a Fructose/SDA B molar ratio equal to 1 and 0,1wt.% Co, where the blue dots represent the experimental data and the black dashed line the kinetic modeling
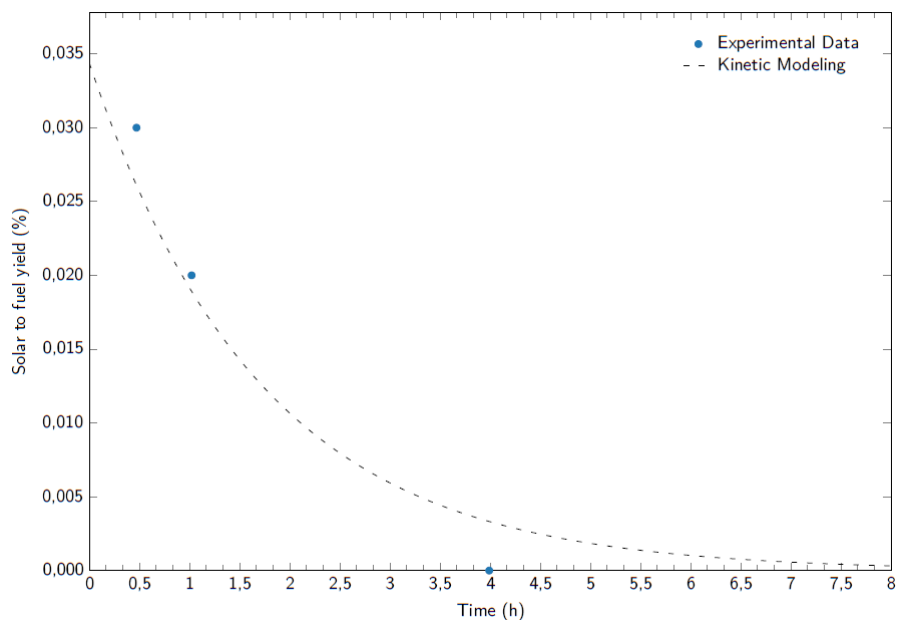
Figure G.88: Solar to fuel yield (&) of ITQ-75, obtained with Compound B as SDA, with a Fructose/SDA B molar ratio equal to 1 and 0,1wt.% Co, where the blue dots represent the experimental data and the black dashed line the kinetic modeling

Table G.29: ITQ-75, obtained with Compound B as SDA, with a Fructose/SDA B molar ratio equal to 1 and 0,1wt.% Co, main photocatalytic test results

Initial simulated H$_2$ rate (μmol/h/g)	11,14
Initial simulated apparent quantum yield (%)	0,08
Initial simulated solar-to-fuel yield (%)	0,034
Water splitting apparent kinetic constant k$_1$ (h^{-1})	2,48 · 10^{-3}
Back reaction apparent kinetic constant k$_{-1}$ (h^{-1})	5,84 · 10^{-1}

Appendix H

List of Figures and Tables

List of Figures

List of Tables